



01 Apr 1991

1991 OURE report, including the 1st Annual UMR Undergraduate Research Symposium – Entire Proceedings

University of Missouri--Rolla

Follow this and additional works at: <https://scholarsmine.mst.edu/oure>

Recommended Citation

University of Missouri--Rolla, "1991 OURE report, including the 1st Annual UMR Undergraduate Research Symposium – Entire Proceedings" (1991). *Opportunities for Undergraduate Research Experience Program (OURE)*. 111.

<https://scholarsmine.mst.edu/oure/111>

This Conference proceedings is brought to you for free and open access by Scholars' Mine. It has been accepted for inclusion in Opportunities for Undergraduate Research Experience Program (OURE) by an authorized administrator of Scholars' Mine. This work is protected by U. S. Copyright Law. Unauthorized use including reproduction for redistribution requires the permission of the copyright holder. For more information, please contact scholarsmine@mst.edu.

OPPORTUNITIES
FOR
UNDERGRADUATE
RESEARCH EXPERIENCE

University of Missouri-Rolla
1991

ACKNOWLEDGMENT

The Opportunities for Undergraduate Research Experiences program began in 1990. The aims were to enrich the learning process and make it more active, encourage interaction between students and faculty members, raise the level of research on the campus, help recruit superior students to the graduate program, and support the notion that teaching and research are compatible and mutually reinforcing. Chancellor Jischke made available an annual budget of \$50,000 to support the program.

As the papers herein attest, the OURE program is achieving its goals – UMR graduates have performed research on an enormous variety of topics, have worked closely with faculty members, and have experienced deeply both the pleasures and frustrations of research. Several of the undergraduates whose papers are included are now graduate students at UMR or elsewhere. Others, who have not yet graduated, are eager to submit proposals to the next OURE round.

I am sure all involved join me in expressing gratitude to Chancellor Jischke for inaugurating the program.

The first section of this volume is made up of papers presented at the first annual UMR Undergraduate Research Symposium, held in April 1991. Joining the UMR undergraduates in the Symposium were students from other colleges and universities who had participated in an NSF-sponsored summer program of research on parallel processing conducted by the UMR Computer Science Department.

We thank all who contributed.

H. J. Sauer, Jr.
Dean of Graduate Studies

CONTENTS

	Page
<i>Papers Presented at UMR Undergraduate Research Symposium</i>	
Session I: Improving Structures	
Measurement of Voltage and Current in Electric Power Systems, Michael L. Davis	3
Study of Joint Flexibility in Steel Frame Structures, Randy R. Frank (<i>Third Place</i>)	11
Modeling for Supersonic Missile Wing-Body Interference Lift, Howard S. H. Ho (<i>First Place</i>)	21
Vertical and Angular Motion of a Wing Model in Steady Flow: A Physical and Numerical Experimental Study, Andrew P. Johnston (<i>Second Place</i>)	47
The Edge Strength of Annealed and Heat-Strengthened Glass, Gregory P. Sallee	55
Session II: Improving Technology Through Computer Modeling	
Parallel Simulated Annealing Algorithm for the Composite Graph Coloring Problem, Kevin D. Alons	63
Parallel Implementation of the Sweep Algorithm for Vehicle Routing, Jana Beattie and Carol Spelman (<i>Third Place</i>)	67
Computer Visualization of Irrotational Flow Over Bluff and Streamlined Bodies, Nora Okong'o (<i>Second Place</i>)	75
Parallel Algorithms for the Traveling Salesman Problem, Tracy Orton and Lan Tran (<i>First Place</i>)	85
Session III: Improving the Interface Between People and Technology	
Identity Authentication Based on Keystroke Latencies Using Neural Networks, Angela G. Lammers and Sharon R. Langenfeld (<i>Second Place</i>)	95
Model Computational Approach to the Conformation of Adsorbed Polypeptide Fragments, Timothy J. McKeon	99
Development of a Learjet Model 24D for the UMR Flight Simulator, Richard Stigall (<i>Third Place</i>)	109
Development of a Large Commercial Transport Model for a Real-Time Digital Flight Simulator, John Francis Winkler (<i>First Place</i>)	119

UMR Opportunities for Undergraduate Research Papers

Synthesis and Characterization of an 18-Membered Macrocyclic Ligand Containing 2,2-Biimidazole for Selective Binding of Transition Metal, Mark Barnett	127
Influence of the McDowell Sanitary Landfill on Groundwater Quality, Phelps County, Missouri, Christine E. Bough	133
Analysis of Two Circuits for Detecting Superconducting Transition Temperatures, Terry Bowness	145
Stimulation of Amorphous Layers in the Co-Si System by Third Element Additions, Denise Brandt	149
Two-Phase Flow Measurement, Glenn Brenneke	155
Establishment of a Phase/Doppler Particle Analyzer for Two-Phase Flow Experiments, J. L. Burget	165
History and Development of Graduate Study at UMR, David G. Burwell (<i>Student failed to turn in Final Report</i>)	
Separation of Chemical Compounds via Thin Layer Chromatography, Lawrence K. Coffin (<i>Student failed to turn in Final Report</i>)	
Extrapolation of the Experimental Data of Electron Scattering, Hansen Chen	173
Investigation of the Products of Combustion of Patterns Material, David L. Cottrell (<i>Student failed to turn in Final Report</i>)	
Measurement of Voltage and Current in Electric Power Systems, Michael L. Davis (<i>Symposium Paper, See Page 3</i>)	
Study of Joint Flexibility in Steel Frame Structures, Randy R. Frank (<i>Symposium Paper, See Page 11</i>)	
Computer Modeling of a Liquid Fuel Spray, Clement R. Goodin, Jr.	181
Using Software to Demonstrate Kinematics of Gear Sets, John F. Hall	189
Modeling for Supersonic Missile Wing-Body Interference Lift, Howard S. H. Ho (<i>Symposium Paper, See Page 21</i>)	
Combustion Aerosol Morphology, Ronald P. Holland	195
Simulation Modeling in Manufacturing Cell Design, Debra A. Hunke	209
Aerosol Particle Bounding in Cascade Impactors, Bisma Husen	221
Attitudes Toward Animal Research Among Contemporary Psychologists, Carla A. Huskey	233

Fourier Transform Infrared (FTIR) Spectroscopy Analysis of Combustion Aerosol, Gary Jacquin	241
Vertical and Angular Motion of a Wing Model in Steady Flow: A Physical and Numerical Experimental Study, Andrew P. Johnston (<i>Symposium Paper, See Page 47</i>)	
Development of Thin Gold Targets for Precision Electron Polarimetry, Scott C. Johnston (<i>Student failed to turn in Final Report</i>)	
<i>Mathematica</i> Demonstrations for Calculus, Bryan Krueger	251
Implementation of the Articulated Total Body (ATB) Model on an Apollo Workstation, M. F. Laudon	255
Nonlinear Dynamics and the Lorenz Water Wheel, Rich Margis	271
Model Calculational Approach to the Conformation of Adsorbed Polypeptide Fragments, Timothy J. McKeon (<i>Symposium Paper, See Page 99</i>)	
Control and Data Reduction Software for UMR Neutron Spectrometer, Matthew K. McLaughlin	281
Students as Parents, A'sia M. McNeal	291
The Detection and Quantification of Atrophic Rhinitis Using Digital Image Processing Techniques, Timothy Mussman	297
Process for Scanning Photographic Slides of Laser Light Scattering with a Transmission Densitometer, Don Newburry	305
Measuring Hydrogen in Galvanized Steels, Timothy O'Hearn	311
Computer Visualization of Irrotational Flow Over Bluff and Streamlined Bodies, Nora Okong'o (<i>Symposium Paper, See Page 75</i>)	
Bonding Mechanism and Microstructure Development for Investment Casing, Joel Philliber (<i>Student failed to turn in Final Report</i>)	
The Synthesis and Characterization of Metal Binding Polymers Containing 2,2'-Biimidazole, Renee Proctor	319
The Electrochemical Characterization of Ferrocene as a Guest Molecule in the Presence of β -Cyclodextrin, Anne T. Roberson	327
The Edge Strength of Annealed and Heat-Strengthened Glass, Gregory P. Sallee (<i>Symposium Paper, See Page 55</i>)	
Enantiomeric Separation by Cloud Point Precipitation of Cyclodextrins, Deanna L. Schmid	333
A Measurement of the Relative Efficiency of a Channeltron, Steve Scott	337
Evaluation of Film Coated Window Glass Subjected to the Effects of Windstorms, Ronald B. Shankland, Jr.	343

Certain Mental Predicates and the Mind-Machine Controversy, Raymond A. Shelton (<i>Student failed to turn in Final Report</i>)	
An Overview and Evaluation: Computer Software to Aid Students in Prewriting, Writing, and Revision, Mary Lou Shomaker	353
Hybrid Ceramic Matrix Composites for Hypersonic Structures, Brian S. Snow (<i>Student failed to turn in Final Report</i>)	
<i>Mathematica</i> Calculus Illustrations, Jeremy Squires	367
Development of a Learjet Model 24D for the UMR Flight Simulator, Richard Stigall (<i>Symposium Paper, See Page 109</i>)	
A Computer Graphics Program for Displaying Water Molecules on a DN3500 Apollo Workstation, Michael A. Stuller	389
Border Detection of Skin Tumor Images, Mike Tiehes	393
Some Stability and Control Aspects of a Variable Pivot Wing Configuration, Paul Vitt	397
Bundled Cable Parameters and Their Impact on EMI Measurement Repeatability, Deanna L. Weil	407
A Computer Simulation of the UMR Reactor, H. Allen Wilkins	417
Development of a Large Commercial Transport Model for a Real-Time Digital Flight Simulator, John Francis Winkler (<i>Symposium Paper, See Page 119</i>)	
Suggestions for Improvements in Current Computer Image Processing Methods in Detection and Quantification of the Severity of Atrophic Rhinitis in Pigs, Jimmy Yu	421

Session I:
Improving Structures

MEASUREMENT OF VOLTAGE AND CURRENT IN ELECTRIC POWER SYSTEMS

Michael Davis

INTRODUCTION

A. B. Chance Company of Centralia, Missouri requested a study of the latest state-of-the-art technology to measure voltage and current on a normal distribution power line. (4kV - 35kV)

The particular device that A. B. Chance needs must be relatively inexpensive, \$200.00 per measurement, reliable, and capable of being manufactured by them.

Four types of power line measurement techniques were investigated; electrooptics/magnetooptics, present day measurement devices, the Raychem Line Monitor, and remote voltage and current sensing (RVCS).

The remote voltage and current sensing idea is the basis of the following report.

THEORY

One common type of voltage and current measurement technique used in power systems is voltage and current transformers. This type of measurement, while still effective, has just about reached its developmental maturity. Also, the devices have some draw backs. For instance: they are quite large and heavy, have the potential for catastrophic failure, and have low dynamic range.

Another possible way to perform power line measurements is with the use of optical sensors, meaning electrooptics and magnetooptics. The theory behind optical sensors is beyond my knowledge. However, the literature mentions that this technology needs much more research and development. Also, projected costs for the device are very high and the major application for these devices appears to be limited to the transmission level where voltages exceed 100kV.

Third, there is a device called the Raychem Line Monitor developed by the Raychem Corporation. The basic design is a coaxial capacitor that has a high voltage tap to measure the line voltage and a low voltage current transformer for measuring the line current. Even though the device has already been developed and does work, some development work would still be necessary to perform voltage and current measurement. Also, the projected cost of this device is about \$400.00 for both measurements.

Finally, an idea was proposed by Dr. Todd Hubing to use remote sensing to measure the

voltage and current of a power line. The basic theory behind this device is that if field sensors are placed near power lines the electric and magnetic fields could be measured. With this information, using electronics and an inexpensive digital signal processor the voltage and current on each line of a three phase distribution power line could be calculated. Also, the cost of such a device would be about \$200.00 per measurement, which is within the limits set earlier, and is capable of being produced by A. B. Chance.

REMOTE VOLTAGE AND CURRENT SENSING

Dr. Hubing's proposal is to place field sensors near the three phase distribution power line to detect the respective electric and magnetic fields produced. Figure 1 shows a possible arrangement of the field sensors around the power lines. Depending on how the sensors are arranged, a constant and unique 3×3 matrix of coefficients for each configuration can be developed. Calculation of the matrix coefficients will be explained later.

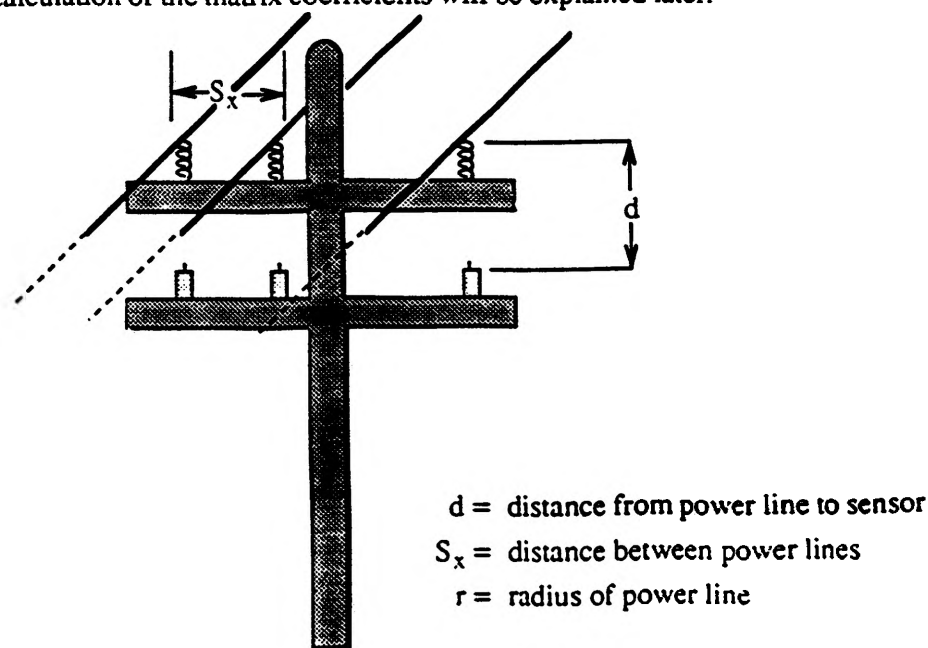


Figure 1:
Remote Voltage and Current Sensing

Assuming the matrix coefficients are known, Equation 1 shows the relationship between the electric field, line voltages, and the matrix coefficients. It should be noted that the same equations

can be related to magnetic field and line current. The only changes are to substitute magnetic field for electric field and line current for line voltage.

$$\begin{bmatrix} E_1 \\ E_2 \\ E_3 \end{bmatrix} = \begin{bmatrix} a_{11} & a_{12} & a_{13} \\ a_{21} & a_{22} & a_{23} \\ a_{31} & a_{32} & a_{33} \end{bmatrix} \times \begin{bmatrix} V_1 \\ V_2 \\ V_3 \end{bmatrix} \quad (1a)$$

$$\begin{bmatrix} V_1 \\ V_2 \\ V_3 \end{bmatrix} = \begin{bmatrix} a_{11} & a_{12} & a_{13} \\ a_{21} & a_{22} & a_{23} \\ a_{31} & a_{32} & a_{33} \end{bmatrix}^{-1} \times \begin{bmatrix} E_1 \\ E_2 \\ E_3 \end{bmatrix} \quad (1b)$$

Electromagnetic theory was employed to determine the matrix coefficients. Appendix A contains two lists of matrix coefficient equations. The first list of equations are valid for sensor configurations similar to Figure 1. The second list of equations is an approximated version of the first that assumes an infinite ground plane and considers the effect produced by the image. For this approximation to be valid there must be strong electric fields present and the distance between the power lines should be small compared to the distance of the sensor from the line. The approximated version will not be considered further. Dr. Hubing developed the matrix coefficient equations which are explained as follows:

Figure 2 shows a two dimensional view of a possible sensor configuration with electric field lines.

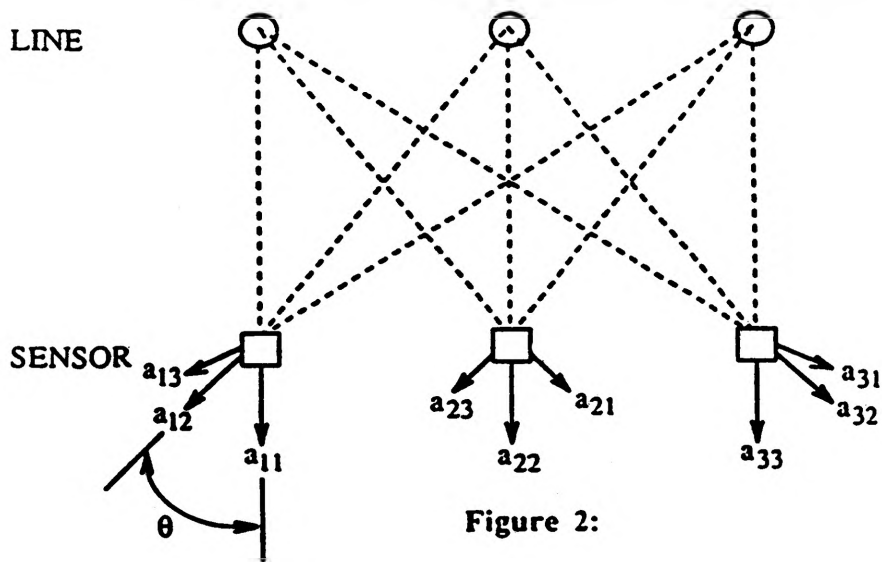


Figure 2:
Electrical Field Lines for Sensor Configuration

$$a_{xy} = \frac{\cos\theta}{z \times \ln(\sqrt{z}/r)} \quad (2a)$$

$$a_{xy} = \frac{2 \times \cos\theta}{z \times \ln(d/r)} \quad (2b)$$

Equation 2a & 2b show the basic form of the equations for the first and second list in Appendix A, respectively. The 2 in the numerator of Eq. 2b came from assuming an infinite ground plane and θ in Figure 2, is the angle that a_{12} , a_{13} , a_{21} , etc. makes with the vertical.

The theory behind the techniques is that each probe would be a single mono-pole that can detect the vertical component of the total electric field from each power line. However, a fault of some sort on one of the lines would cause a change in the voltage level and the resultant electric field. Since this would be detected by the field sensors, the calculated line voltages would reveal the fault.

With this in mind, initial development of the electronics to perform the matrix calculations for the device began under the guidance of Professor Herrick. The electronics development began on the TMS32010 Digital Signal Processing Development System. However, initial progress was slow, partly because of the need to learn Assembly Language programming and also due to limitations in the commands on the chip. Because of this, development was moved to the Computer Research Lab CRL25 Development System for the TMS320C25 DSP chip in the UMR computer lab. This system used the Fourth programming language. Converting a program from Fourth to Assembly language is relatively quick with only a few differences in the list of commands. Since the TMS320C25 is a higher member of the DSP family, the assembly language program can be performed by the TMS32010 chip with the only difference being that some commands on the TMS320C25 have to be two separate commands on the TMS32010.

The program was developed on the basis that there was a 60 Hz signal that could be sampled 32 times per period. This sample rate is high enough to catch most fault conditions; however, definitely not quick enough to detect faults from a lightning strike. A listing of the program is provided in Appendix B and deserves further explanation.

The program was written on fifteen screens of Fourth starting with screen #33 (SCR #33), screen #34 (SCR #34), etc. SCR #33 and #34 each contain a look up table for a 1.25 period sinusoid. The true values in the table are scaled for peak values of 1 and -1; however, the numbers listed in the table are between 32767 and - 32767 to make entering hexadecimal constants easier. SCR #34 differs from SCR #33 by a 5.625 degree phase shift. This was done to determine the error caused by not being able to represent +1 on SCR #33. SCR #34 eliminates this error. Further calculation for this program have been done with SCR #33. SCR #35 is a program that involves the electric field signal with the sinusoid look up table to produce the real and imaginary components of the measured signal along with their relative phase, for each A/D channel. An interesting feature of this is the fact that it extractes the 60 Hz component of the signal by taking the Fourier Transform, thereby eliminating the second and third harmonics. SCR #37 is used to plot sample waveforms to a printer. SCR #36 and #38 are used to derive three sample signals given the first three values of each waveform. Again, the amplitude of the waveforms are scaled to ± 1 . The formulas used to calculate the first three values of the waveform are shown in Equation 3.

$$u_K = 2 \times 2^{15} \times \cos[(2 \times 3.14) / 32] \quad (3a)$$

$$n_{Y2} = 2^{15} \times \sin[(2 \times 3.14) / 32 + \phi]; \quad \phi := \text{phase shift} \quad (3b)$$

$$n_{Y1} = 2^{15} \times \sin(\phi) \quad (3c)$$

$$n_{AMP} = \text{magnitude of electric field} \quad (3d)$$

SCR #39 is used to display the waveform on the monitor. SCR #40 was used to determine the worst case conditions. These calculations provided the overflow limitations on the output.

SCR #41 solves the three simultaneous equations shown in Eq. 1b. SCR #42 outputs the result on the monitor. The output includes scaling factors for the matrix coefficients and the line voltages.

SCR #43 is the main program and it links all the necessary programs together. Screen #44 thru #48 provide a list for matrix coefficients of different configurations and test cases to go along with them. The first matrix configuration is for a symmetrical situation where the sensors are about three meters away, called MATRIX1. A second matrix configuration is for the unsymmetrical case

about three meters away also. This one is called MATRIX2. Finally, the third matrix configuration is for the sensors close to the lines, only about .3 meters away, called MATRIX3. For the matrix coefficients, MATRIX1, the test cases that go along with it are; TEST1 - TEST4. For MATRIX2, the test cases are; TEST5 - TEST8. For MATRIX3, the test cases are: TEST9 - TEST12.

The type of tests they perform is, assuming there is a three phase, 30kV distribution line, Eq. 1a was used to calculate the electric fields generated. If phase A, B, or C were down, then this would result in different electric field calculations. After the electric fields are calculated, Eq. 3a - 3d are used to determine the first three points and the magnitude of each waveform. From these points, SCR #38 of the program generates the hypothetical electric field waveforms. The process just mentioned determines the theoretical signals detected by the field sensors for each A/D channel. Since the matrix coefficients are known, SCR #41 performs the calculation of Eq. 1b resulting in a scaled version of the voltage on each phase.

CONCLUSION

After it was determined that the line voltages could be calculated, a discussion with Dr. Stanton of UMR about the possible applications of such a device took place. Several comments from him were quite interesting and some appear below.

Such a device could be implemented in three ways. One way would be for it to simply detect if each individual line is energized or not. Even though this method is possible, it is quite primitive and will not be considered further.

Another possible application would be for it to actually reveal the calculated line voltage. If the actual line voltages were known, along with some detailed information about the line, it would be possible to determine the exact location of the fault, either direction from the measurement site. While this method might be used in the future, further developments of such an application are too sophisticated to be considered now.

The third way to implement the device would be to place the sensors at various locations

along the distribution line and have the device compare measured conditions to normal conditions. From this it would determine if each phase had normal voltage, no voltage, or some useful intermediate voltage range. For instance, if a fault occurred on phase C, then normal voltage would be detected on phase A & B, but the voltage detected on phase C would vary according to the impedance of the line. The same approach can be made for current measurement using a coil sensor. If voltage and current measurements were available, fault currents on each phase could be detected and combined with line voltages to provide even more information.

The results of this project showed that a Digital Signal Processing chip can easily perform the computational aspects of this technique. Also, using the TMS32010 DSP, which is about \$6.00 per chip, along with additional digital logic and circuitry make the projected cost for such a device to be about \$200.00 per measurement.

Finally, the next step would be to build a prototype and make tests and design changes as necessary.

ACKNOWLEDGEMENT

I would like to thank the 1990 Opportunities for the Undergraduate Research Experience (OURE) Program and the A. B. Chance Company for their financial support of the project.

Also, I extend a sincere thank you to my advisors on the project; Professor Thomas Herrick and Dr. Todd Hubing, for their excellent guidance.

Final thanks go to Dr. Dawson for inviting me to participate in the OURE Program, Kurt Hambacker for his programming assistance, and Dr. Stanton for his technical support.

STUDY OF JOINT FLEXIBILITY IN STEEL FRAME STRUCTURES

Randy R. Frank

I. ABSTRACT

Joint flexibility plays an important role in the distribution of strains and displacements in the frame structures of buildings, towers, automobiles, etc.. The objective of this project is to study the effect of flexibility (or rigidity) of two simple mechanical joints in frame structures on the stress and displacement distributions, using both experimental and analytical methods. Three welded and three bolted samples were fabricated using A-36 low carbon steel in a two column and horizontal cross-member (table) arrangement. This arrangement allows for both shear forces and axial forces in the joint. From a three element rectangular rosette strain gage attached to the bottom of the cross-member, strain readings were collected by a computer based data acquisition and processing system, during point and line loading (elastic range) of the specimens by a load frame. These results were compared to each other and to values found by analytical methods for the same arrangement with theoretically rigid and theoretically completely flexible joints.

The data for the line loading of the samples were plotted and compared with the analytical results. Also a quantitative flexibility index was developed and used to compare the bolted and welded joints. The flexibility index is defined as the ratio of the difference between the actual and theoretical rigid joint flexibility to the difference between the theoretical flexible joint and the theoretical rigid joint flexibility in percentage. These comparisons were made for each sample at load increments over 50 lbs and within the elastic limit of the specimen. This was chosen because of the linear relation of the data received in this range and the slight error of the experimental apparatus at low loads. The test was conducted for each of the six specimens of the bolted and welded joints (3 specimens per joint type) and then repeated. This allowed for error in the measurement and in the manufacture of the specimens. The average flexibility index for the bolted joint samples (line loading) were 52.23%, 50.46%, and 46.6% resulting in a total average flexibility index of 49.73% with standard deviation of 3.21. The average flexibility index for the welded joint samples (line loading) were 46.38%, 42.95%, and 42.27% resulting in a total average flexibility index of 43.87% with standard deviation of 2.78. The data from the point loading runs were used to see if anything unusual happened in this case. Because of averaging by the strain gage of the values of the strain at the center due to the stress concentration of a point loading the values were not used to compute a flexibility index. There were no unusual findings from the point loading data.

The results show that the bolted joints used in this experiment were more flexible than the welded joints for both line and point load. Furthermore, both joints did not act as completely flexible or completely rigid joints. This fact confirms the importance of the joint flexibility consideration in the design of steel frame structures.

II. INTRODUCTION

Steel frame structures are commonly used in the construction of buildings, bridges, towers and automobiles. An important aspect to the effective and efficient design of a frame structure is the flexibility in the joints. Most design theory does not account for the flexibility in joints. Thus, once an engineer has designed a frame structure, extensive testing would need to be performed to verify his design. This often results in redesign of the joints to reduce or increase the flexibility followed by further testing. This iterative process increases the development time and cost of the frames.

The objective of this project is to study the effect of flexibility (or rigidity) of two simple mechanical joints in frame structures on the strains and displacement distributions, using both experimental and analytical methods.

Figure 1 shows the design and dimensions of a bolted and welded steel frame structures subjected to flexure, which will be investigated in this research. From the literature survey conducted, no published literature was found on joint flexibility on frame structures which have elements subjected to flexure. Most of the published work found were limited to single plate framing shear connections, which consists of a plate welded to a support at one edge and bolted to a beam web [1,2].

Joint flexibility of frame structures subjected to flexure must be known to make efficient and effective design. Testing would be too time consuming and expensive in today's competitive markets. Standard sized bolted, welded, riveted and glued joints should be tested to evaluate the flexibility. Their flexibility should be indexed to allow comparisons between different joint types. The flexibility index information could be compiled and used as a reference for engineers when they design frames. Some indexing has been developed by some finite element software manufactures. They have setup an index called the Degree of Fixity, which is an index from 0-1 of how rigid a joint acts [3]. A rigid joint is given a value of 1. This index would be used in the finite element program to help model the actual stresses and displacements. The index was only done for four general categories of joints. In this research, an index will be developed to aid in comparison of the joints to different joints and to theoretical values of the joint flexibility Bolted and welded joints in a steel frame structures will be investigated.

III. SPECIMEN DESIGN AND ANALYSIS

General specimen: Three welded and three bolted samples were fabricated using A-36 low carbon steel in a two column and horizontal cross-member (table) arrangement. The specifications of the designs are shown in figure 1a and figure 1b for the bolted and welded joint respectively. This arrangement allows for both shear forces and axial forces in the joint. The legs of the table arrangement were designed to be rigid and the top plate to be flexible. Thus the thickness of the legs were chosen to be much greater than the thickness of the top plate. The top plate thickness and the distance between the legs were chosen by the relationship shown in equation (1) [4].

$$\frac{\text{Span between the legs } (l)}{\text{Top plate thickness } (t)} \geq 100 \quad (1)$$

The total length of the specimen was constrained by the size of the test equipment, corresponding to the leg span (l) being chosen as 12.5 inches. The thickness of the top plate (t) was then found by using equation 1 to be 0.125 inches. The requirement of equation (1) is then satisfied by $l/t = 12.5/0.125 = 100$. Standard sizes of material could now be used to fabricate the specimens.

Material: The material used was low carbon ASTM A-36 plate steel with properties shown in table 1 [5]. This material is widely used in frame structures and in general applications [1,2]. Therefore, it was readily available at a local welding shop for very low cost. Other types of materials proved to be too expensive be considered in this project.

FIGURE 1A: BOLTED SPECIMEN

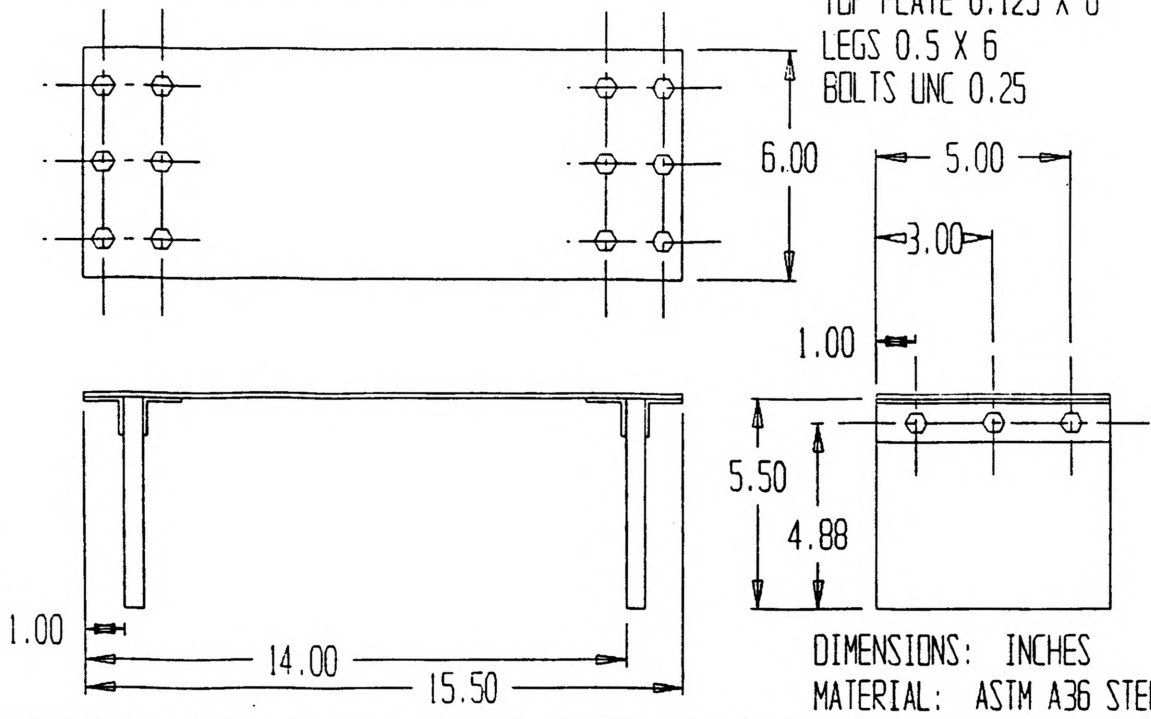


FIGURE 1B: WELDED SPECIMEN

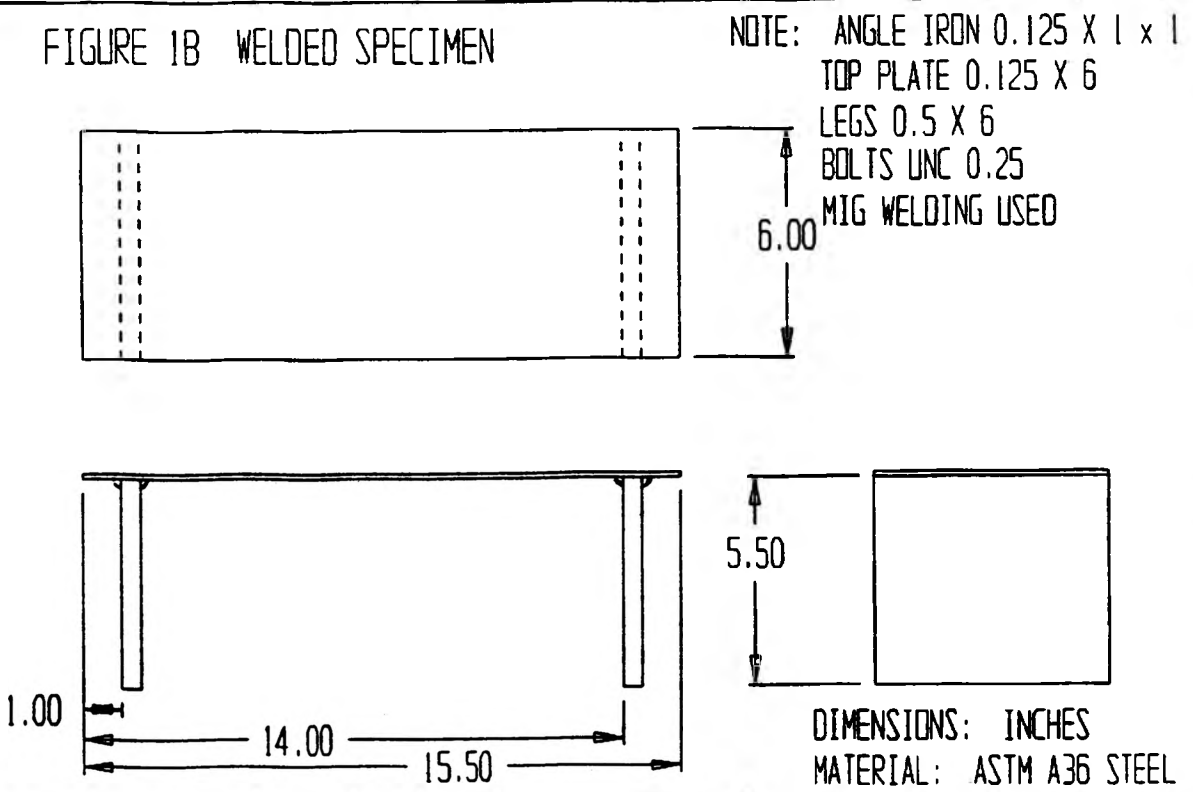


Table 1 PROPERTIES of TEST SPECIMENS: ASTM A-36 ASME SA36 LOW CARBON STEEL	
Tensile Strength (S_u)	65 KSI minimum
Yield Strength (S_y)	50 KSI minimum
Inertia of top plate (I)	0.0009765 in ⁴
Top plate thickness (t)	0.125 inches

Loading: Typically in frame design plastic deformation is undesirable. Therefore it is necessary to find the loading limits for the design. A safety factor of 2 for the specimen was chosen for maximum loading. This will guard against any accidental permanent deformation of the sample specimens.

The top plate, being the weakest pint in the specimen, will dictate the maximum load that can be applied to the specimen. Figure 2a shows a line force at the center of the top plate of the specimen acting downward parallel to the legs. The shear force and bending moment were found as a function of the applied line force (F) to the specimen as shown in figures 2b and 2c respectively. The maximum force (F_{max}) to be applied to the specimen was obtained from the maximum bending stress [2,8] given in equation (2).

$$S_{max} = \frac{S_y}{2} = \frac{M_{max}c}{I} \quad (2)$$

where (S_y) is the yield strength of the material and 2 is the factor of safety, (M_{max}) is the maximum bending moment, (c) is half of the top plate thickness (t/2) and I is the moment of inertia. The maximum bending moment (M_{max}) is obtained from figure 2c and is expressed as:

$$M_{max} = (F/2) \times 6.25 \quad (3)$$

The maximum force (F_{max}) that could be applied to the specimen was then obtained by substituting equation (3) into equation (2):

$$F_{max} = \frac{S_y I}{6.25c} \quad (4)$$

Substituting the values for yield strength (S_y), the inertia (I) and half of the top plate thickness (c), from table 1, the maximum loading force obtained was $F_{max} = 125$ lbs.

The force that could be applied for the point load was obtained in a similar fashion by replacing the line load with the point load in figure 3. The force obtained was the same as for the line load case.

Bolted Specimen Design: The main consideration in the bolted specimen was joint separation. It was assumed that the bolts should be strong enough to keep the joint from separating when loaded to the maximum force. This was done by making a few simple conservative assumption to find the deflection angle of the top plate (Theta) under maximum loading conditions with no bolts present

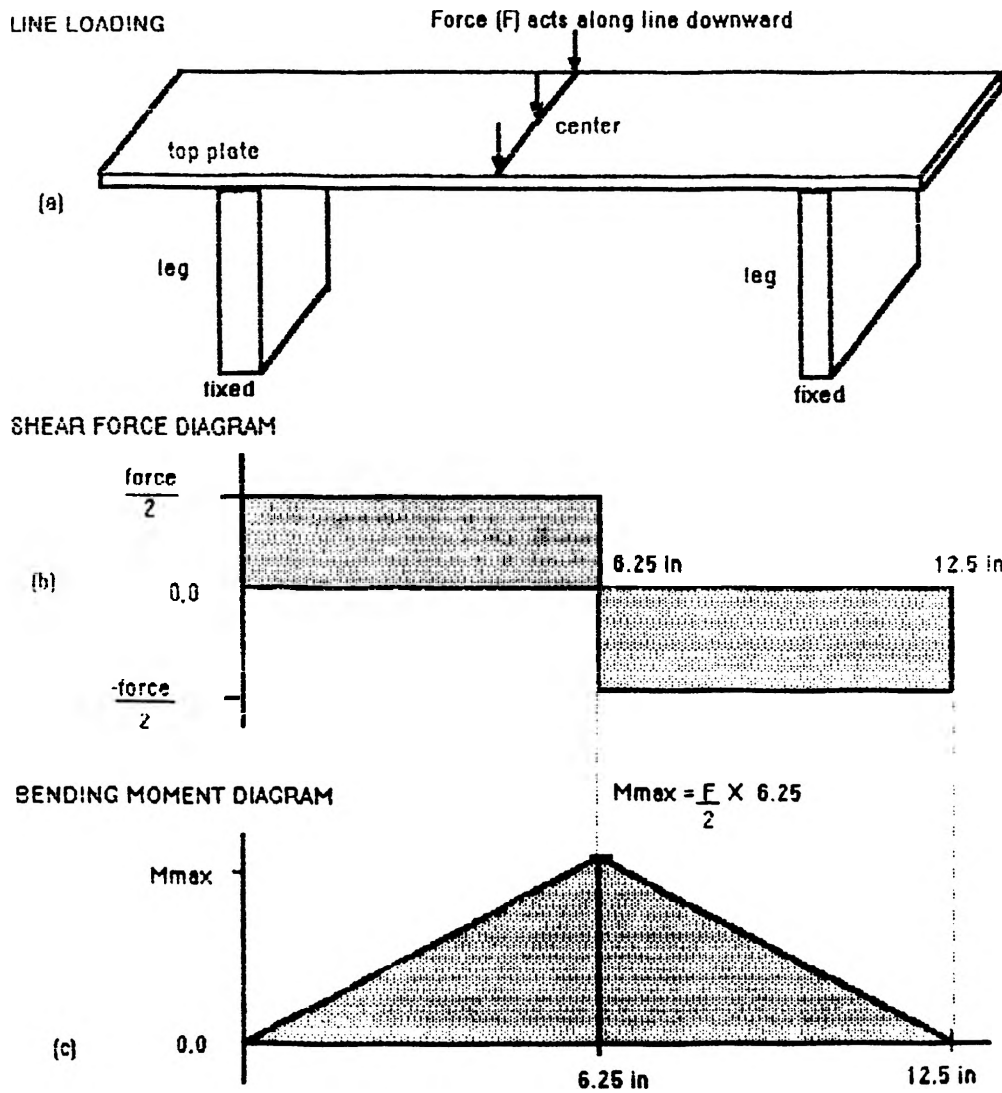


FIGURE 2 LINE FORCE LOADING, SHEAR FORCE and BENDING MOMENT DIAGRAMS.

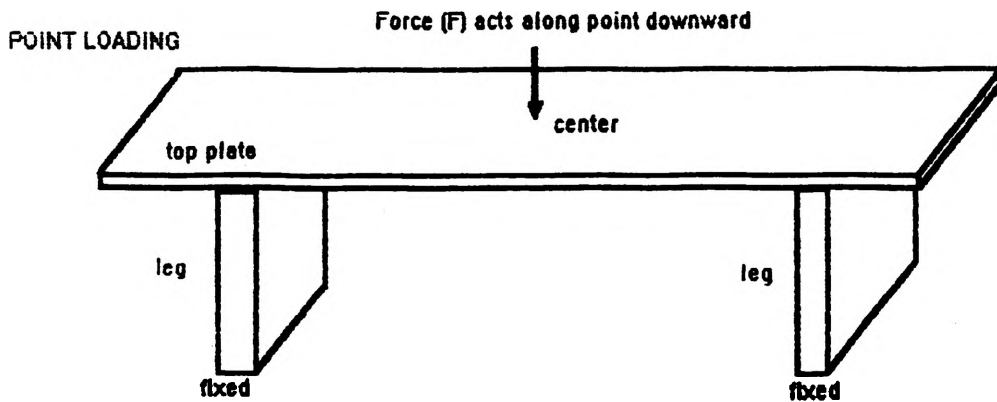


FIGURE 3 POINT LOADING OF SPECIMEN.

and the corresponding bolt force necessary to keep the joint from separating. This calculation was done using equation (5) [8] by substituting values of 125 lbs for the maximum force applied (F), 12.5 inches for the span length (L), 30,000 KSI for Young's Modulus (E) and 0.0009765 for the inertia (I). Therefore, Theta was found to be $\theta = 125 \times (12.5)^2 / (16 \times 30E6 \times 0.0009765) = 0.04167$ radians.

$$\theta = \frac{FL^2}{16EI} \quad (5)$$

The force necessary to bring the plate back to a horizontal position or no joint separation was calculated to estimate the force necessary for the bolts to withstand under maximum loading conditions. Using trigonometry and the computed θ value of 0.04167 radians and distance to the bolts the distance needed to return the plate to a horizontal position (Y) was found to be 0.04165 inches. Thus, the force necessary for the bolts to withstand (P) was found using equation (6) [8]. Values for Young's Modulus (E) and inertia (I) were taken from above to give $P = (3 \times 30E6 \times 0.0009765 \times 0.04165) / (12.5)^3 = 1.87$ lbs.

$$Y = \frac{PL^3}{3EI} \quad (6)$$

Stresses calculated using three 1/4 inch bolts on each side of the joint were found to be much less than the yield strength of the bolts. The shear stresses in the bolts through the legs were calculated and also found to be much less than the yield strength of the bolts. To confirm proper design of the bolted joint, it was checked using a procedure from a article Machine Design by Edmund J. Gohmann, Jr. of Purdue University [6]. Using Gohmann's procedure it was confirmed that joint separation (failure), under the maximum loads, would not occur. The drawing of the final bolted joint design used in this project is shown in figure 1a.

Welded Design: The welded joint was done using Metal Inert Gas Welding (MIG) to weld the joint on both sides of the legs to the top plate. This allowed for a smooth continuous weld to the thin top plate. The final drawing of the welded design used in this project is shown in figure 1b. Note that the overall dimensions are the same as the bolted design shown in figure 1a.

Strain Gage Selection: A strain gage was needed in order to record the strain at the center of the top plate of each specimen at different load levels. A six step procedure was used in the selection of an appropriate gage for this application. The procedure was taken from Measurements Group, Inc. Bulletin 309B [7,10]. This procedure resulted in picking a 3 element rectangular rosette strain gage (specification: CEA-06-250UR-120) from Micro-Measurements Division of Measurements Group, Inc..

Theoretical Analysis: Values for strain of the specimen under theoretically rigid and completely flexible joints were used for an analytically analysis of the data. Values for the strain at the bottom center of the top plate were found using equation (2), for a theoretically completely flexible joint. These values were compiled by a software program written in basic. Strain values for a theoretically rigid joint were found using the deflection at the center of a beam rigidly held (at the end of the span between the legs) and a trigonometric relationship. The deflection at the center of a

theoretically rigid joint specimen was found using equation (7) [9].

$$Y = \frac{FL^3}{192EI} \quad (7)$$

Where (Y) is the deflection at the center, (F) is the force applied, (L) is the span between the legs, (E) is Young's Modulus and (I) is the inertia. The strain was found using the relationship between right triangles to find the change in length of the top plate divided by the original length of the top plate. These values were compiled by a software program written in basic.

Flexibility Index: To compare the experimental results with the analytical results, a flexibility index was developed. The flexibility index (FI) is defined as the ratio of the difference between the actual and theoretical rigid joint flexibility to the difference between the theoretical flexible joint and the theoretical rigid joint flexibility in percentage. The flexibility index is expressed as:

$$FI = \frac{((\text{Actual flexibility}) - (\text{Rigid flexibility}))}{((\text{Flexible flexibility}) - (\text{Rigid flexibility}))} \quad (8)$$

The FI were computed for each sample at load increments over 50 lbs and within the elastic limit of the specimen. This was chosen because of the linear relation of the data received in the range and the slight error of the experimental apparatus at low loads. An average value of the FI was calculated for each test run. The data collected in this experiment was confirmed by multiple repetitions of each sample and by multiple samples. This allowed for correction of error in manufacture and measurement.

IV. EQUIPMENT AND EXPERIMENTAL PROCEDURE

Equipment: A computer based data acquisition and processing system was used to collect the data when the specimen was continuously loaded in a load frame. The computer read data from four channels. One channel was used for recording the load applied to the specimen. The other three channels were connected to strain indicators that were attached to each of the three elements of the rosette gage. This information was stored on disk for later evaluation. The software used in the data acquisition system was developed by Dr. Hornsey for the Basic Engineering Laboratory.

Procedure: The specimen was placed in the holding fixture and put in the load frame. The strain gage was connected to the strain indicator using a quarter bridge arrangement. Using two leads from one tab of the stain gage it was possible to connect the gage so that it was not sensitive to the lead wires. The gages were set to the proper gage factor of 2.06 and zeroed. The longitude gage was hooked to data channel 1 of the data acquisition system. The load applied, 45 degree gage and the transverse gage were hooked to data channels 0,2,3 respectively. The data collection program (Univrsl.tst) was executed. The load range setting was set for the 0-600 lb range. Strain ranges were set to 0-600 microstrain. A calibration was done for the collection equipment. This allows the software to set conversions for each channel so that the readings match the load readout and strain readouts on the equipment. The loading was done using a round bar placed horizontally on top of the plate under the load cell to apply a line load. A point load was achieved by using a ball

bearing in a similar fashion. Data collection was done at equal increments of load under a continuous loading of the specimen. Loading started at 5 lbs and continued to 125 lbs. After finishing a test the data was loaded into a file on disk. This data file was converted to a more usable format and loaded into a graphing program for graphical results. The file was also used by a program in basic which converted the values to FI for each increment. An overall average value of the FI for each test was also calculated. This procedure was repeated for all test of the specimens.

V. EXPERIMENTAL RESULTS

Line Loading: The line loading was run twice for each of the three specimens. The resulting data was then plotted using strain versus load for each run. A qualitative analysis of the plotted data was done to compare the flexibility of the bolted and welded joints. It was found that the bolted joint exhibited higher values of strain for equal loads. In general the bolted joint was more flexible than the welded joint. The flexibility index, developed in Specimen Design and Analysis, was used to quantitatively analyze the data. The average flexibility index for the bolted joint samples were 52.23%, 50.46% and 46.6% resulting in a total average flexibility index of 49.73% with standard deviation of 3.21. The average flexibility index for the welded joint samples were 46.38%, 42.95% and 42.27% resulting in a total average flexibility index of 43.87% with a standard deviation of 2.78. The individual average flexibility indexes for each sample were plotted versus load for the bolted and welded joint specimens in figure 4 and figure 5 respectively.

Point Loading: The point loading was run twice for each of the three specimens. The resulting data was plotted using strain versus load for each run. Like in the line loading case a qualitative analysis was done using these plots. The bolted joint was again more 'flexible' than the welded joint. A quantitative analysis was not done on this data because values for the theoretical cases were derived using a line loading of the sample. The purpose of the point loading was to qualitatively confirm the line loading data.

VI. CONCLUSIONS

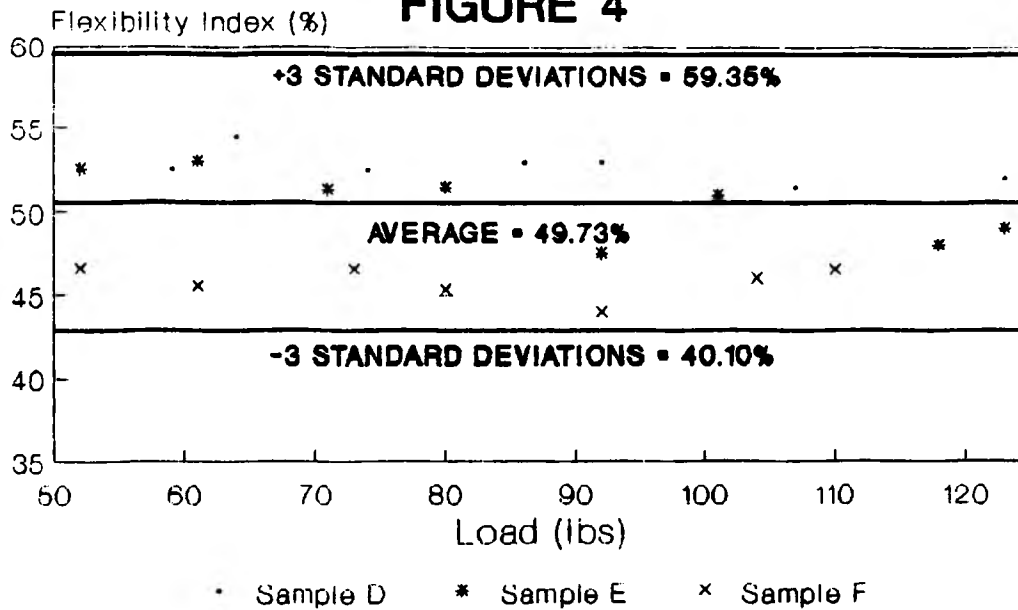
Based on the studies report here, the following conclusions were reached:

1. The bolted joints used in this experiment were more flexible than the welded joints for both line and point loading. Both joints did not act as a completely flexible or completely rigid joints. This fact confirms the importance of the joint flexibility consideration in the design of steel frame structures.
2. The flexibility indexes were converted to the degree of fixity and were found to meet the specifications given for the welded and bolted categories by the software manufacturer.
3. It is recommended that standards should be setup for joint flexibility. This could be done using the flexibility index developed in this experiment or by using the degree of fixity used by some finite element software manufactures.
4. The average flexibility index for the bolted joint samples were 52.23%, 50.46% and 46.6% resulting in a total average flexibility index of 49.73% with standard deviation of

Flexibility Index vs. Load

Bolted Specimens

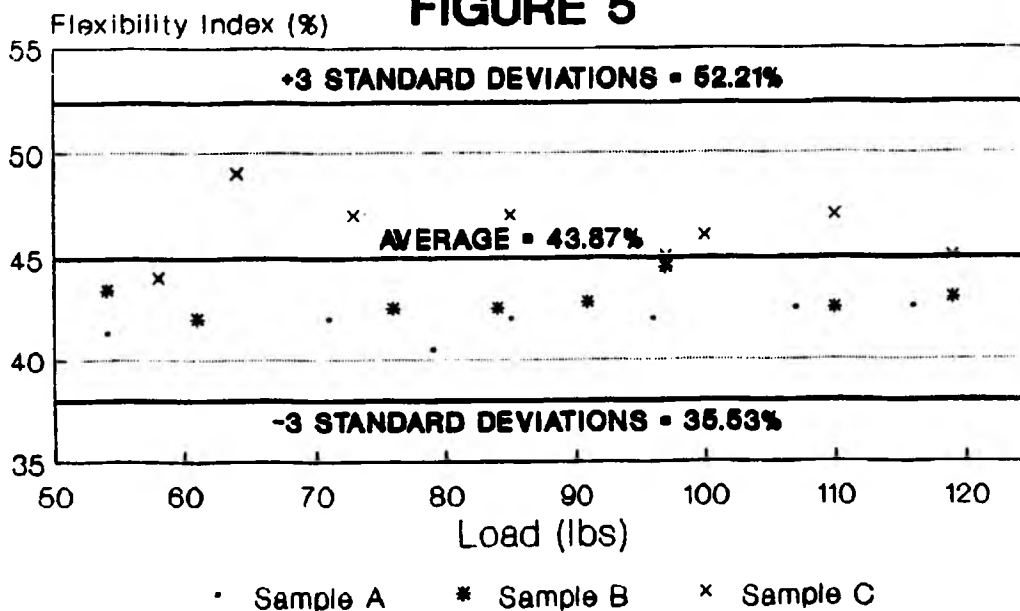
FIGURE 4



Flexibility Index vs. Load

Welded Specimens

FIGURE 5



3.21. The average flexibility index for the welded joint samples were 46.38%, 42.95% and 42.27% resulting in a total average flexibility index of 43.87% with a standard deviation of 2.78.

5. Further work is proposed to evaluate the effect of different plate thickness, beam thickness, span to thickness ratio, number of bolts and type of weld.

VII. ACKNOWLEDGEMENTS

The project was performed using the equipment in the Basic Engineering laboratory. The availability of the data acquisition system in the laboratory enable more accurate results to be obtained. The use of the laboratory equipment and support in execution of the experiment provided by Dr. Edward E. Hornsey was sincerely appreciated. Special thanks also go to Bob Hribar and Ken Schmid both of mechanical engineering department who helped in fabricating the test specimens and mounting the strain gages respectively.

VIII. REFERENCES

1. A. Astanch, S.M. Call and K. M. McMullin, "Design of Single Plate Shear Connections", Engineering Journal, American Institute of Steel Construction, First Quarter 1989. pp 21-32.
2. R. M. Richard, P.E. Gillett, D. Kreigh and B. A. Lewis, "The Analysis and Design of Single Plate Framing Connections", Engineering Journal, American Institute of Steel Construction, 2nd Quarter 1990, pp 38-52.
3. International Business Machine, Computer-Aided Engineering Design System Analysis, (CAEDS), Users Manual, 1984.
4. Young W. Kwon, Assistant Professor, Naval Post-Graduate School, Monterey, California.
5. Joseph T. Ryerson & Sons Inc., Ryerson Stock List & Data Book, 1987-88 Edition, pp 386.
6. E. J. Gohmann, Jr., "Evaluating Loads in Bolted Joints", Machine Design, January 22, 1987, pp 103.
7. Measurement Group Inc., "Student Manual for Strain Gage Technology, Bulletin 309B, 1983.
8. Higdon, A., E.H. Ohlsen, W.B. Stiles, J.A. Weese, W.F. Riley, Mechanics of Materials, Fourth Edition, 1985, pp 65-124, 708.
9. J.E. Shigley, C.R. Mischke, Mechanical Engineering Design, Fifth Edition, McGraw - Hill, 1989, pp 325-405, 741.
10. J.W. Dally, W.F. Riley, Experimental Stress Analysis, Second Edition, McGraw - Hill, 1978, pp 153-163, 318-329.

MODELING FOR SUPERSONIC MISSILE WING-BODY INTERFERENCE LIFT

Howard S. H. Ho

ABSTRACT

During the initial phase of a missile design, a quick and simple way of estimating wing-body interference is essential. A simple panel model based on the cross flow over a cylinder is developed to estimate the effect of the body on the wing lift. This model produces quick and reasonably accurate results, while little user expertise is needed. This model determines K_{WB} (upwash interference factor) and K_{ϕ} (sideslip interference factor), and is applicable to infinitely thin delta and clipped delta fins on missiles in supersonic flight. The effects of the fin semivertex angle, span, taper ratio, free stream Mach number, angle of attack, and roll angle are investigated. The free stream Mach number ranges from 2 to 5. The angle of attack varies from 5 to 15 degrees. The rolling angle varies from 0 to 6 degrees. Fin semivertex angles of 30, 45, and 60 degrees are tested. The fin span varies from 1 to 6 body radii. The model predicts acceptable results for conceptual and preliminary design.

NOMENCLATURE

- A_F = Area of fin
 A_i = Area of individual panel
 AR = Aspect Ratio of the wing
 b = Wing span
 C_L = Lift force coefficient
 $C_{L(w)}$ = Lift force coefficient of the fin
 $C_{L(wB)}$ = Lift force coefficient of the fin in the presence of the body
 $C_{L\alpha}$ = Lift curve slope
 $C_{L\alpha_w}$ = Lift curve slope of the wing alone

C_r	= Fin root chord
C_t	= Tip chord for a clipped-delta fin
K_{WB}	= Fin-body upwash interference factor
K_ϕ	= Fin-body sideslip interference factor
L_w	= Lift on the fin alone
L_{WB}	= Lift on the fin in the presence of a body
LPT	= Linearized Potential Theory
M	= Mach number
R	= Radius of the missile body
r	= Distance from body centerline to the point of interest
S	= Fin span measured from the centerline of the body
SBT	= Slender Body Theory
S/R	= Ratio of fin span to body radius
V_C	= Circumferential velocity component of flow over a cylinder
V_H	= Velocity component in the horizontal direction
V_N	= Velocity component normal to the fin
V_V	= Velocity component in the vertical direction
V_∞	= Free stream velocity
x,y	= Coordinate axes based at the center of the missile body
α	= Angle of attack of the missile
α_{eq}	= Missile equivalent angle of attack
α_o	= Angle of attack for wing alone
$\Delta\alpha$	= Change in angle of attack due to interference
$\Delta\alpha_{eq}$	= Vortex interaction interference factor
β	= Missile sideslip angle
ϵ	= Fin leading edge semivertex angle

- μ = Mach angle
- ϕ = Missile sideslip angle

INTRODUCTION

The complex flow field around a finned missile in supersonic flight is governed by nonlinear partial differential equations¹⁻³; however, the knowledge about aerodynamic interaction between the fins is vital for proper missile design. The effect of the aerodynamic interaction is especially important for missile design due to their small span and multi-numbers of fins. Numerical schemes for solving the flow field are available⁴⁻⁵, but they require high computing power, lengthy computing time and a great deal of user expertise. During the preliminary phase of a missile design, changes in configuration are frequently encountered. Therefore, a quick and simple way of predicting the aerodynamic interaction accurately and economically is essential.

For preliminary design purpose, the component buildup method is often used because it is capable of calculating the force and moment coefficients rapidly and accurately. The component buildup method⁶⁻⁸ is based on the assumption that one can obtain the forces and moments on a missile by summing the individual values on the isolated missile parts (ie, fuselage, fins, tails). These individual values are added to calculate the overall loading by incorporating interference factors to account for mutual interference effects. An important component buildup method is based on the concept of the equivalent angle of attack⁹, which relates the normal force coefficient of a fin-body combination to a fin-alone wing lift curve slope. The overall lift coefficient of the missile is related to wing lift curve slope as:

$$C_{Lmissile} = \alpha_{eq} * C_{L\alpha}(W)$$

The equivalent angle of attack is defined as:⁹

$$\alpha_{eq} = K_{WB} \alpha + (4/AR) K_{\phi} \alpha \beta + (\Delta\alpha_{eq})_v \tag{1}$$

where the terms on the right hand side represent the effect of body upwash, fin sideslip and vortex interaction, respectively. The body upwash interference factor K_{WB} , is defined as^(10,11):

$$K_{WB} = V_C/V_V = C_{L(WB)} / C_{L(W)} \quad (2)$$

where $C_{L(WB)}$, is the lift coefficient of the fin in the presence of the body and $C_{L(W)}$ denotes the lift coefficient of the wing alone. The sideslip interference factor K_ϕ is defined as^(9,10) :

$$K_\phi = (\Delta C_L / C_{L(W)}) \cdot (AR / 4 \sin\beta) \quad (3a)$$

$$\Delta C_L = C_{L(\alpha, \beta)} - C_{L(\alpha, \beta=0)} \quad (3b)$$

where ΔC_L is the change in lift coefficient on a fin due to sideslip while $C_{L(W)}$ is the lift coefficient for the wing alone.

The analytical solution for K_{WB} and K_ϕ can be found in Ref 11; in which Nielson derives K_{WB} and K_ϕ as a function of S/R and the number of fins using Linearized Potential Theory (LPT). The K_ϕ and K_{WB} values calculated by LPT are independent of flight conditions such as angle of attack, Mach number, sideslip angle and fin configuration; they are functions of the ratio of the fin span to the body radius (S/R) only . The purpose of this project is to develop a simple, accurate and quick model to calculate K_{WB} and K_ϕ , and investigate the effect of various flight conditions and fin configurations on K_{WB} and K_ϕ . Special interest is focused on the influence of roll angle on K_ϕ since¹²

$$\sin\beta = \sin\alpha \sin\phi \quad (4)$$

where β is the sideslip angle, α is the angle of attack and ϕ is the roll angle. From the dynamics of flight, rolling is always accompanied by simultaneous sideslipping, although the vice versa does not hold true. In other words, when the missile rolls, the fins experience a sideslip velocity component as well as the circumferential velocity component simultaneously. Based on this roll–sideslip relationship and with the effort to keep this model simple, it is desirable to evaluate the K_ϕ –sideslip relationship in terms of roll angle ϕ instead of sideslip angle β . Nonetheless, one should keep in mind that effects of rolling and sideslipping are physically identical for K_ϕ calculation.

Two different fin configurations are used in this model: delta and clipped delta. Much work has been done on delta fin interference factors, which provides a proper base for evaluating the vali–

ality of the model developed here.^(9,10,11) Clipped delta fins have become a popular choice for many supersonic missile designs. Therefore, the aerodynamic interference characteristics of clipped delta fins are part of the interest for this research. The results for these two configurations will be discussed and compared. The modeling is kept as simple as possible. Therefore, shockwaves are not included, though the flight Mach number is supersonic. All fins are assumed to be infinitely thin, and located along the centerline of the body. All angles of perturbation are small and follow the right-hand rule. Figure 1 shows the schematic of the missile configuration and helps to define the nomenclature.

ANALYTICAL METHODOLOGY

Equation Formulation

The modeling of K_ϕ is based on Slender Body Theory (SBT), which is a simplified version of Linearized Potential Theory. SBT assumes that axial flow could be neglected compared to cross-flow over the body when calculating the forces and moments. The cross flow is equivalent to the basic flow over the cylinder expressed in terms of flight parameters. Given a cylindrical cross section, the circumferential flow (Fig. 2) perpendicular to the fin is written as:

$$V_C = V_V \left(1 + \frac{R^2}{r^2} \right), \quad (5a)$$

where $V_V = V_\infty \sin\alpha \cos\beta$ (5b)

But once the missile body rolls, V_C is no longer perpendicular to the fin. To calculate the the velocity component normal to the fin, one more remote velocity component is used. From Fig. 3, V_H can be expressed as:

$$V_H = V_\infty \sin\beta \left(1 - \frac{R^2}{r^2} \right) \quad (5c)$$

V_N , the velocity component normal to the fin, can be expressed as:

$$V_N = V_\infty \sin\alpha \cos\beta \cdot \cos\phi \left(1 + \frac{R^2}{r^2}\right) + V_\infty \sin\beta \sin\phi \left(1 - \frac{R^2}{r^2}\right) \quad (6)$$

at a finite r . V_N is a function of r and f . As r goes to infinity, V_N becomes

$$V_N = V_V \cos\phi + V_H \sin\phi \quad (7)$$

The angle of attack (α) can be broken into two parts

$$\alpha = \alpha_0 + \Delta\alpha \quad (8)$$

where α_0 is the angle of attack of the missile when $\phi = \beta = 0$ and $\Delta\alpha$ is the perturbation in α due to roll (sideslip). Recall that $\sin\beta = \sin\alpha \sin\phi$, which describes the direct relationship between roll and sideslip. Define angle of attack as:

$$\alpha = V_N/V_\infty$$

$$\text{so that } \alpha = \sin\alpha \cos\beta \left(1 + \frac{R^2}{r^2}\right) \cos\phi + \sin\beta \sin\phi \left(1 - \frac{R^2}{r^2}\right) \quad (9a)$$

Note that α is a function of of position (r) along the fin span, the sideslip angle β and the roll angle ϕ . Since α_0 is the angle of attack at $\phi = \beta = 0$, it can be written as

$$\alpha_0 = \sin\alpha \left(1 + \frac{R^2}{r^2}\right) \quad (9b)$$

and the angle of attack of the wing (two fins joined at the root) becomes $\alpha_{ow} = \sin\alpha$ because the body radius R is zero in this case.

Recall the definition of K_ϕ

$$K_\phi = \frac{AR}{4\beta} \left(\frac{C_{L_{\alpha\beta}} - C_{L_{\alpha\beta 0}}}{C_{L_\alpha}} \right) = \frac{AR}{4\beta} \left(\frac{\alpha_{\alpha\beta} - \alpha_{\alpha\beta 0}}{\alpha_{\alpha_w}} \right) \quad (10)$$

thus

$$K_\phi = \frac{AR}{4\beta} \left(\frac{\alpha_0 + \Delta\alpha}{\alpha_{\alpha_w}} - \frac{\alpha_0}{\alpha_{\alpha_w}} \right) = \frac{AR \Delta\alpha}{4\beta \alpha_{\alpha_w}} \quad (11)$$

Apply Eqs. (9a) and (9b), and express $\Delta\alpha/\alpha_{ow}$ (Eq. 12a) as:

$$\frac{\Delta\alpha}{\alpha_{\alpha_w}} = \left\{ \left\{ \sin\alpha \cos\beta \left(1 + \frac{R^2}{r^2}\right) \cos\phi + \sin\beta \sin\phi \left(1 - \frac{R^2}{r^2}\right) \right\} - \sin\alpha \left(1 + \frac{R^2}{r^2}\right) \right\} / \sin\alpha$$

which can be simplified to

$$\frac{\alpha}{\alpha_{o_w}} = \left(1 + \frac{R^2}{r^2}\right) (\cos\beta \cos\phi - 1) + \left(1 - \frac{R^2}{r^2}\right) \sin\beta \sin\phi / \sin\alpha \quad (12b)$$

when β and ϕ are small, Eq. (12b) can be expressed as:

$$\frac{\alpha}{\alpha_{o_w}} = \left(1 - \frac{R^2}{r^2}\right) \sin\beta \sin\phi / \sin\alpha \quad (12c)$$

This yields the final expression for K_ϕ

$$K_\phi = \frac{AR}{4 \sin\beta} \left(1 - \frac{R^2}{r^2}\right) \frac{\sin\beta \sin\phi}{\sin\alpha} \quad (13)$$

with the restriction of small α and ϕ .

From Ref. 9, the aspect ratio for a delta fin is written as

$$AR = 4 \tan\epsilon \quad (14a)$$

For a clipped delta fin, its aspect ratio is defined as

$$AR = 4(S/R - 1) / \{(1+\lambda) C_t/R\} \quad (14b)$$

where λ is the taper ratio of the clipped delta fin, $\lambda = C_t / C_r$

The formulation of K_{WB} starts from the definition, as given by Eq. (2), where

$K_{WB} = V_C/V_V$ and from Eq. (5a) where $V_C/V_V = (1 + R^2/r^2)$. As a result of combining Eq. (2) and Eq. (5a), one can express K_{WB} in terms of r and missile body radius R only

$$K_{WB} = \left(1 + \frac{R^2}{r^2}\right) \quad (15)$$

Panel Analysis

The K_ϕ and K_{WB} formula given by Eq. (13) and (15) represent the local value of the interference factor at a given distance, r , from the centerline. In order to calculate the interference factors of the fin, a panel analysis is used. In the panel analysis, the fin is divided into an arbitrarily selected number of panels. Panels are bounded by Mach lines as shown in Fig. 4. The panel size and shape

are thus dependent of Mach number and fin aspect ratio. As the Mach number increases, the Mach angle (μ) approaches zero, which implies the panel boundary becomes parallel to the root chord. The Mach line boundaries limit the effect of disturbances at the fin leading edge to the regions interior to the Mach line as occurs in supersonic flight. The results of panel analysis yield the overall expressions for K_ϕ and K_{WB} for a given S/R as:

$$K_\phi = \frac{AR}{4 \sin \beta} \sum_{i=1}^I \frac{\sin \beta \sin \phi}{\sin \alpha} \left(1 - \frac{R^2}{r_i^2} \right) \frac{A_i}{A_F} \quad (16)$$

$$K_{WB} = \sum_{i=1}^I \left(1 + \frac{R^2}{r_i^2} \right) \frac{A_i}{A_F} \quad (17)$$

where A_i is the area of i th panel and A_F is the area of the fin.

The number of panels (I) is chosen arbitrarily. A total of 20 panels per fin is used throughout the analysis. The calculations of K_ϕ and K_{WB} are based on the cross flow velocity along the fin leading edge; therefore, the r_i value represents the distance between the midpoint of the i th panel and the centerline of the missile body.

The analysis is done on one fin only since the cross flow is symmetrical for K_{WB} . Although this assumption does not apply to rolling, the K_ϕ calculation is focused on one fin only.

RESULTS AND DISCUSSION

A FORTRAN code was developed to calculate for K_ϕ and K_{WB} at various flight conditions and fin configurations. The calculations consist of the following parameter ranges: 4 Mach numbers (2, 3, 4, and 5), 3 angles of attack (5° , 10° , 15°), 3 semivertex angles (30° , 45° , 60°), and 3 roll angles (0° , 3° , 6°). Two fin configurations are considered: delta and clipped delta. A taper ratio of 0.6 is selected arbitrarily for clipped delta wings. A nominal case based on $\alpha = 10^\circ$, $\epsilon = 45^\circ$, $\phi = 6^\circ$, and $M = 3$ is chosen for reference. The range of S/R varies from 1.0 to 6.0. Typical S/R values for missiles range from 2.5 to 4.0 (Table 1). All results are presented by changing one parameter at a time from the nominal case.

According to SBT, the values of K_ϕ are functions of S/R and the number of fins only. The model presented here, suggests that K_ϕ is also influenced by M , α , ϵ , and ϕ . Special attention is focused on the effect of roll angle on K_ϕ . Though K_ϕ is defined as sideslip interference factor, dynamics of flight always couple sideslip with roll as indicated by Eq. (13). The K_{WB} values, on the other hand, are expected to be primarily a function of S/R . Results of K_ϕ and K_{WB} are plotted against S/R . Every graph contains several curves displaying the effect of one particular variable. The results between the delta fins and clipped delta fins are discussed. An sample application of the results is also presented.

Delta Fins

Effects of angle of attack (α). Figs. 5 & 6

Figure 5 shows that K_{WB} is unaffected by the changes in angle of attack, which is predicted by LPT. Figure 6 shows the relationship between α and K_ϕ . As α increases from 5° to 15° , K_ϕ curves shift downward and thus, K_ϕ decreases as α increases.

Effects of Semivertex angles (ϵ). Figs. 7 & 8

Changes in semivertex angles alter the fin shapes, aspect ratios and areas. Figure 7 shows the relationship between K_{WB} and ϵ at $M=3$, $\alpha = 10^\circ$, and $\phi = 6^\circ$. K_{WB} is insensitive to changes in semivertex angles. As ϵ increases, K_{WB} increases slightly because the fin area decreases. As a result, Fig. 7 suggests that increasing aspect ratio increases K_{WB} slightly for a delta fin at a given S/R value. Figure 8 shows that K_ϕ is strongly influenced by changing ϵ . For a delta fin, $AR = 4\tan\epsilon$, a higher semivertex angle means greater AR . Since K_ϕ is an explicit function of AR , higher ϵ results in higher K_ϕ .

Effects of Mach number (M). Figs. 9 & 10

From Figs. 9 & 10, it is observed that both K_ϕ and K_{WB} are relatively insensitive to Mach number. Figure 9 shows slight increases in K_{WB} as Mach number moves from 2.0 to 5.0, which suggests more lift is generated by the body at high Mach number. On the other hand, K_ϕ degenerates slightly

as a result of increasing Mach number, which suggests that lower lift is contributed from sideslip at higher Mach number.

Effects of roll angles (ϕ). Figs. 11 & 12

Figure 11 shows that K_{WB} is completely independent of roll angles. Since sideslip is always coupled with rolling, results from Fig.11 suggest that K_{WB} is also independent of sideslip angle β . When $\phi = 0^\circ$, K_ϕ is simply zero since no sideslipping occurs at 0° roll. K_ϕ is proportional to ϕ , hence higher ϕ values yield higher K_ϕ values as shown in Fig. 12.

Clipped Delta Fins

Upon inspecting Figs. 13 to 20, one sees that different fin configurations do not change the relationship between interference factors with the flight condition and fin semivertex angles. Despite the fact that both configurations follow the same trends when responding to changes, differences in curve curvature and magnitudes are apparent. For the same flight condition, clipped delta fin yields consistently lower K_ϕ and K_{WB} values, and steeper curves than delta fins. The differences are due to greater individual panel areas of clipped delta fins. Though interference factors are proportional to panel areas, the effect is decreased by smaller local velocities and larger overall wing area. The clipped delta fins also have lower aspect ratios than delta fins at a given S/R and ϵ value.

Comparisons

Numerical solutions for K_ϕ are available from the work of Jenn and Nelson⁹, which are used here for comparison. Jenn and Nelson used a finite-difference Euler code (SWINT) to solve the nonlinear flow field, and the results obtained from SWINT are well established and proven accurate for K_ϕ calculations. A special flight condition of $M = 3$, $\alpha = 10^\circ$, $\epsilon = 38.7^\circ$, and $\beta = 3^\circ$ is evaluated to provide a comparison of this model. The results and comparison of these two models are plotted in Fig. 21. The K_ϕ values from this model is very sensitive to roll angles as indicated by the graph. Small roll angles yield low K_ϕ values which are below SBT and SWINT value. For a roll angle of 10° , this model underestimates K_ϕ up to the $S/R = 5.0$. For $\phi = 15^\circ$, the K_ϕ value agrees with to both SWINT and SBT well up to $S/R = 1.75$.

Sample Application

A sample application is performed to show the practical use of K_ϕ and K_{WB} . The sample application is done at the flight condition of Mach number = 3, $\alpha = 10^\circ$, $\epsilon = 45^\circ$, and $\phi = 6^\circ$. The span(S/R) value is chosen to be 3.5 arbitrarily. Base on these specified parameter, K_ϕ and K_{WB} values are found to be 0.7 and 1.3, respectively, for a delta fin. Recall the

$$\alpha_{eq} = K_{WB} \alpha + (4/AR) K_\phi \alpha \beta + (\Delta\alpha_{eq})_v, \text{ where } \Delta\alpha_{eq} = 0 \text{ for fixed fins.}$$

$$\begin{aligned}\alpha_{eq} &= (10.0 \cdot \pi/180) \cdot \{1.3 + (4/(4 \tan \epsilon)) \cdot 0.70 \cdot \sin^{-1}(\sin \alpha \sin \phi)\} \\ &= (10.0 \cdot \pi/180) \cdot \{1.3 + (1/\tan 45^\circ) \cdot 0.70 \cdot \sin^{-1}(\sin 10^\circ \sin 6^\circ)\} \\ &= 0.2455 \text{ rad} \\ &= 14.07^\circ\end{aligned}$$

$$\text{Recall } C_{L_{missile}} = \alpha_{eq} \cdot C_{L_{\alpha v}}$$

$$\begin{aligned}\text{where } C_{L_{\alpha v}} &= \frac{4}{\sqrt{M^2 - 1}} \\ &= \frac{4}{\sqrt{3^2 - 1}} \\ &= 1.414\end{aligned}$$

Therefore,

$$\begin{aligned}C_{L_{missile}} &= 0.2455 \cdot 1.414 \\ &= 0.3471\end{aligned}$$

Similarly, for a Clipped-delta fin with the same parameters and $K_\phi = 0.18$, $K_{WB} = 1.18$, $AR = 1$.

$$\begin{aligned}\alpha_{eq} &= 0.2251 \text{ rad} = 12.90^\circ \\ C_{L_{missile}} &= 0.2251 \cdot 1.414 \\ &= 0.3183\end{aligned}$$

From this sample application, one can conclude that delta fins will generate more lift forces

than clipped delta fins at a given flight condition and a specified span.

CONCLUSIONS

A quick, simple and reasonably accurate model using SBT panel analysis is developed herein to calculate aerodynamic interference factors K_{WB} and K_ϕ for supersonic missiles. This model determines the effect of angle of attack, Mach number, fin semivertex angle, and roll angle on K_{WB} and K_ϕ . The results indicate that K_{WB} is virtually unaffected by all changing these parameters, while K_ϕ is sensitive to most of these variables. The variation of K_ϕ and K_{WB} along the span agree with published work. K_{WB} has the highest value of 2 for a very narrow fin span and then gradually decrease as the fin span grows wider. K_ϕ is the lowest for missiles with vanishingly small fins, but K_ϕ then gradually increases as the fin span increases. The results obtained from this model compare favorably with theoretical values and SWINT output for its simplicity. This model is over sensitive to roll angle; however, the sensitivity of this model can provide more insight into the effects of various parameters on K_ϕ . This model's ability to offer reasonable accuracy and user friendliness makes it suitable for preliminary design use. However, the users should be fully aware of the model's limitation. This model is limited in the range of roll and sideslip angles and is prone to errors at higher angles. This SBT panel-method does not take into account of shockwaves therefore the effect of pressure jump behind the shockwave is not included.

This model offers great potential for further development. Inclusion of shockwaves should greatly enhance the realism of this model. Users are encouraged to expand the program capability to handle trailing edge sweep to cover a wider variety of fin configurations. The effect of negative roll angles should be evaluated and compared to the positive values. The application is not limited to missile use only, greater S/R values could be used to simulate aircraft wings.

ACKNOWLEDGEMENT

This research is sponsored by UMR Opportunity for Undergraduate Research Experience (OURE) program. Research topic is formulated by Dr. H.F. Nelson of Aerospace Engineering Department here at University of Missouri–Rolla. Assistance and direction provided by Dr. Nelson is greatly appreciated.

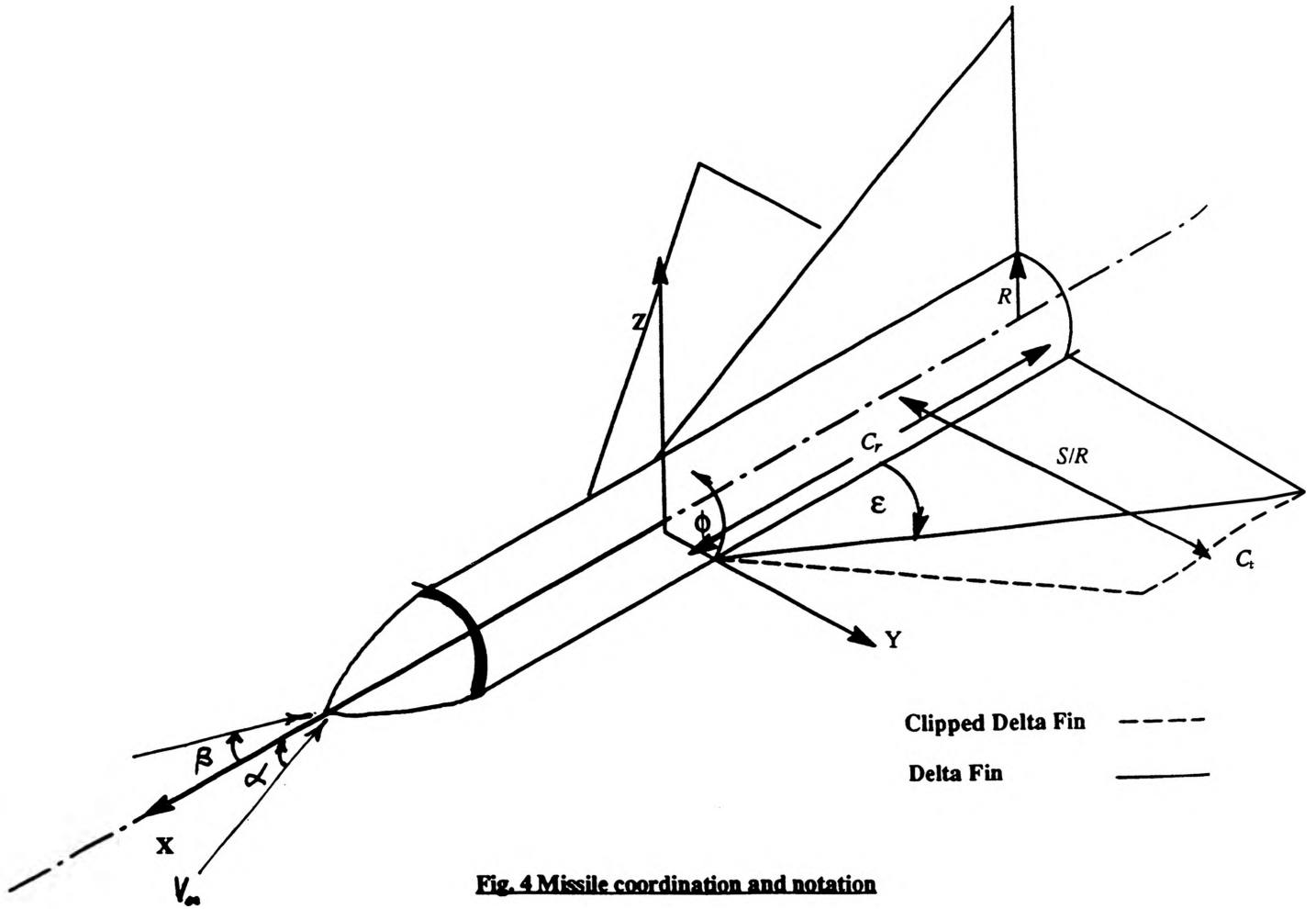


Fig. 4 Missile coordination and notation

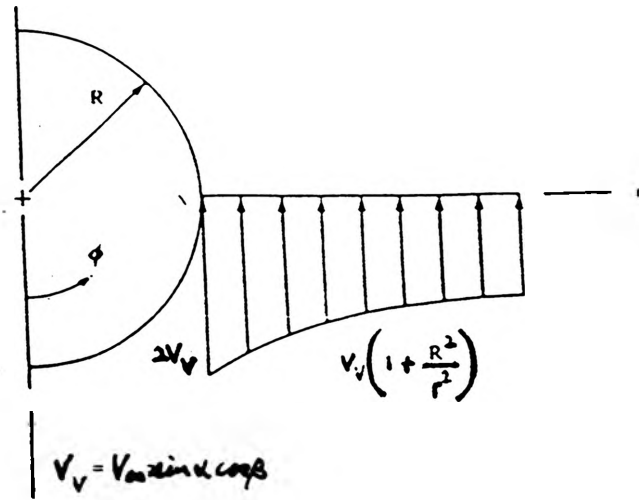


Fig.2 Circumferential flow distribution for flow over the cylinder

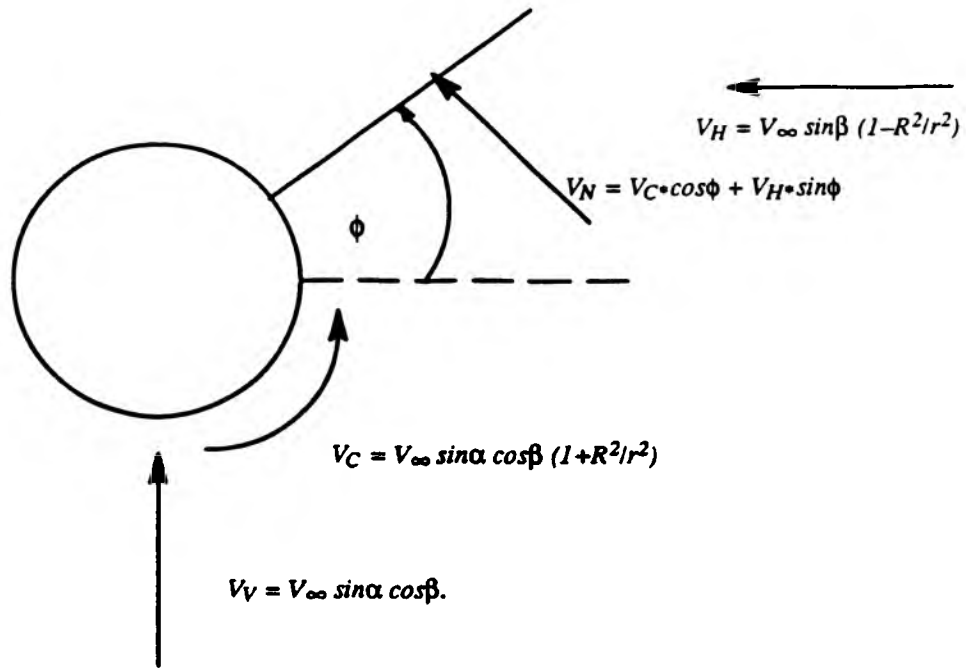


Fig. 3 Flow pattern and velocity nomenclature under rolling

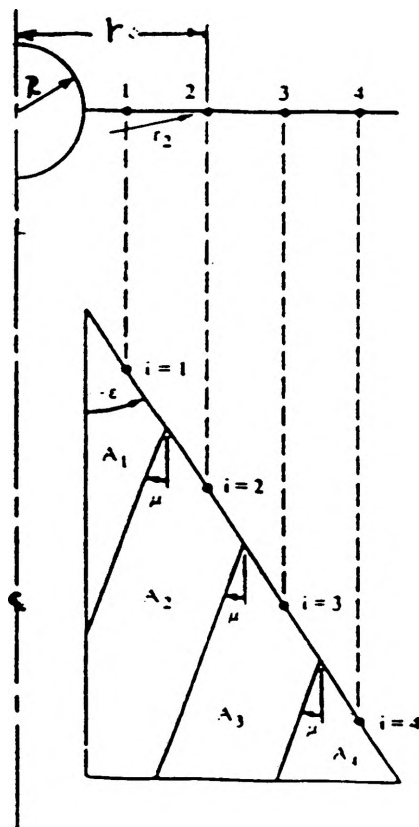


Fig. 4 Illustration for panel layout and nomenclature

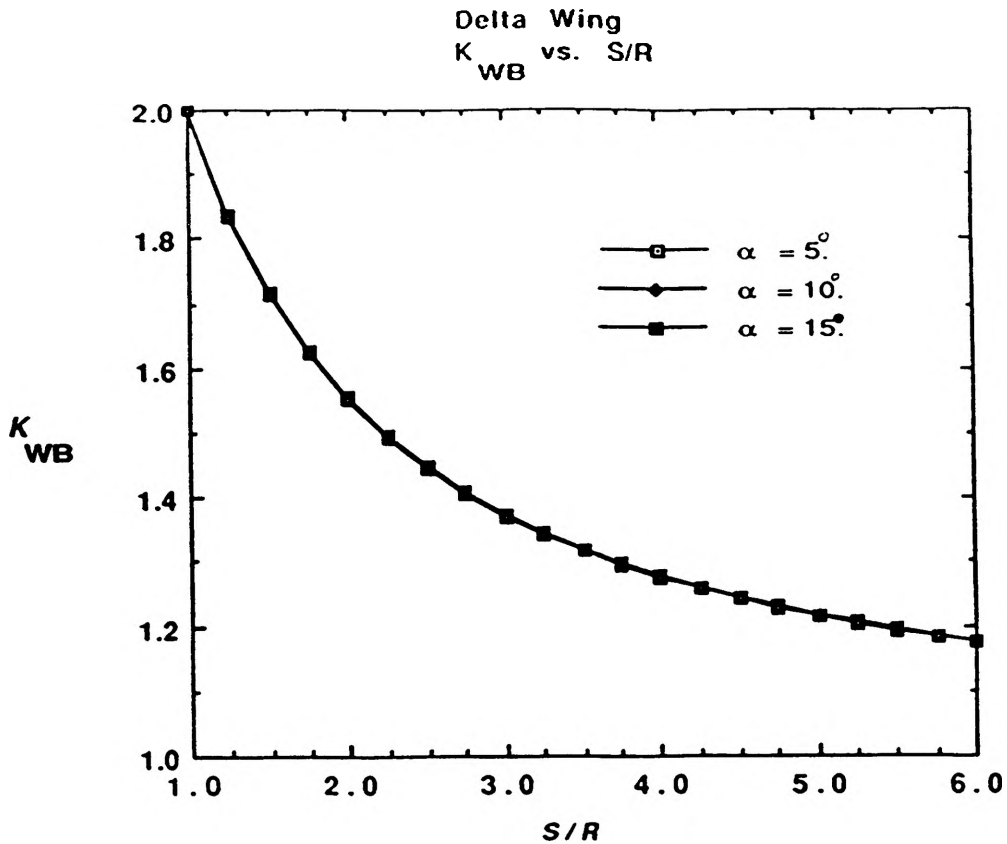


Fig. 5 The effect of angles of attack on K_{WB} vs. S/R , $\epsilon = 60^\circ$, $\phi = 6^\circ$, $M = 3$

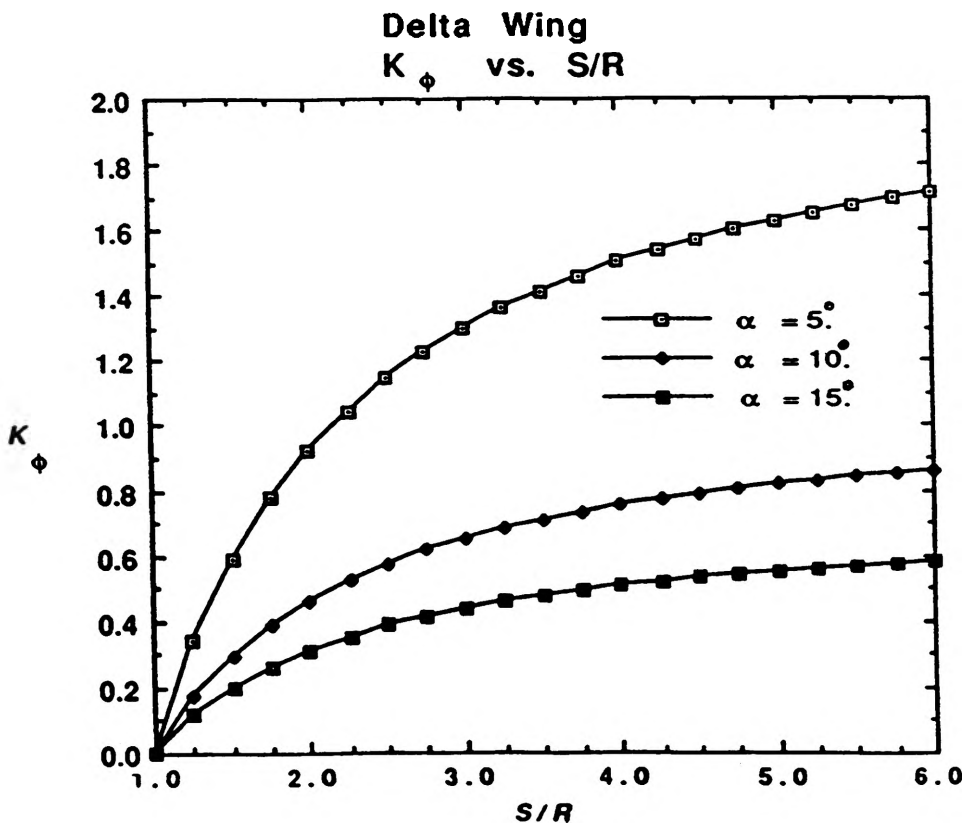


Fig. 6 The effect of angles of attack on K_ϕ vs. S/R , $\epsilon = 60^\circ$, $\phi = 6^\circ$, $M = 3$

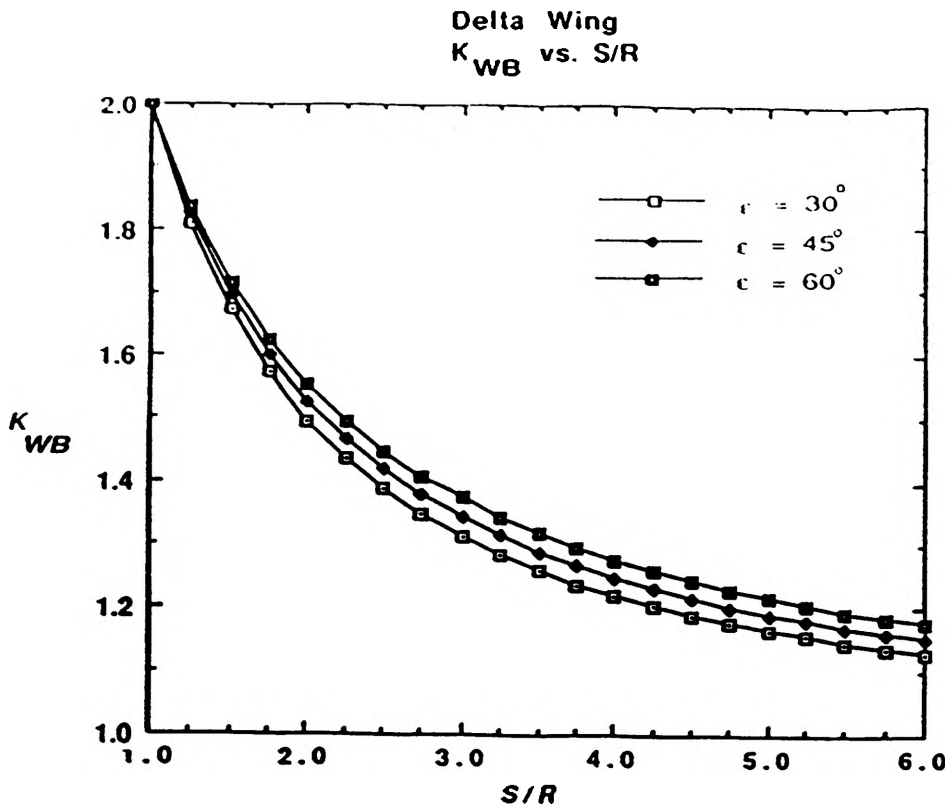


Fig. 7 The effect of semivertex angles on K_{WB} vs. S/R , $\alpha = 10^\circ$, $\phi = 6^\circ$, $M = 3$

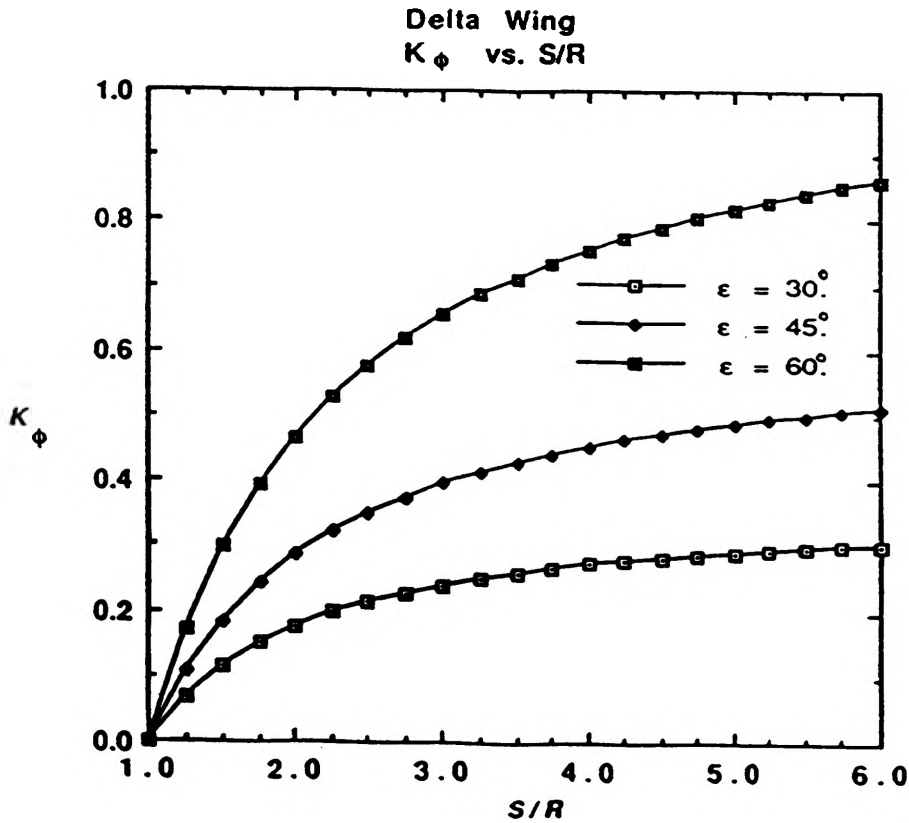


Fig. 8 The effect of semivertex angles on K_ϕ vs. S/R , $\alpha = 10^\circ$, $\phi = 6^\circ$, $M = 3$

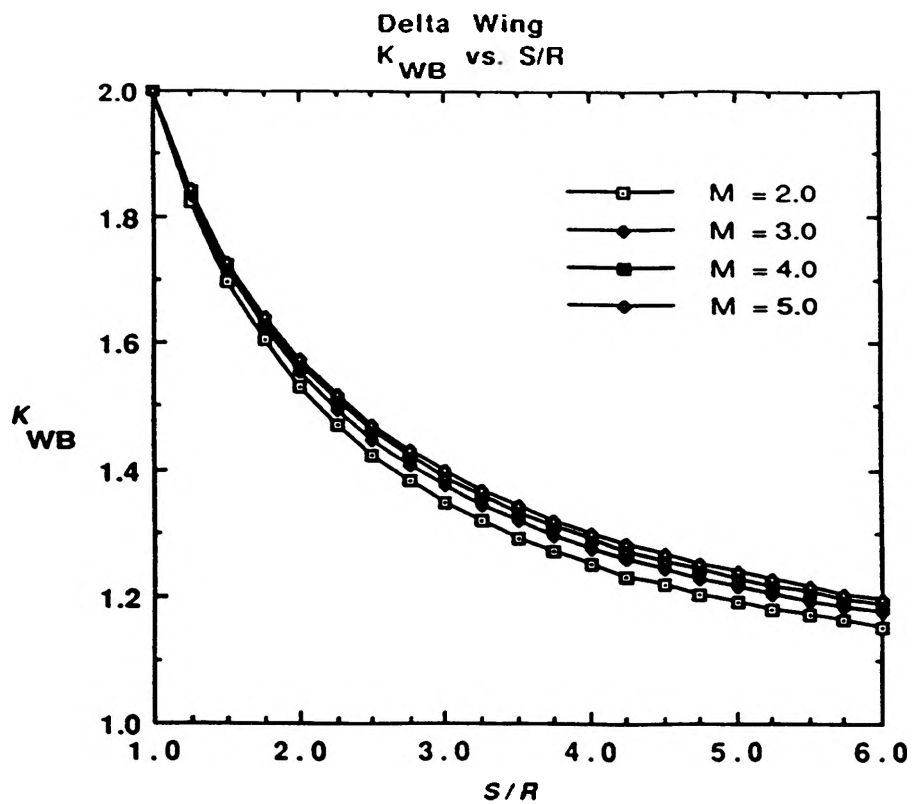


Fig. 9 The effect of free stream Mach number on K_{WB} vs. S/R , $\alpha = 10^\circ$, $\epsilon = 60^\circ$, $\phi = 6^\circ$

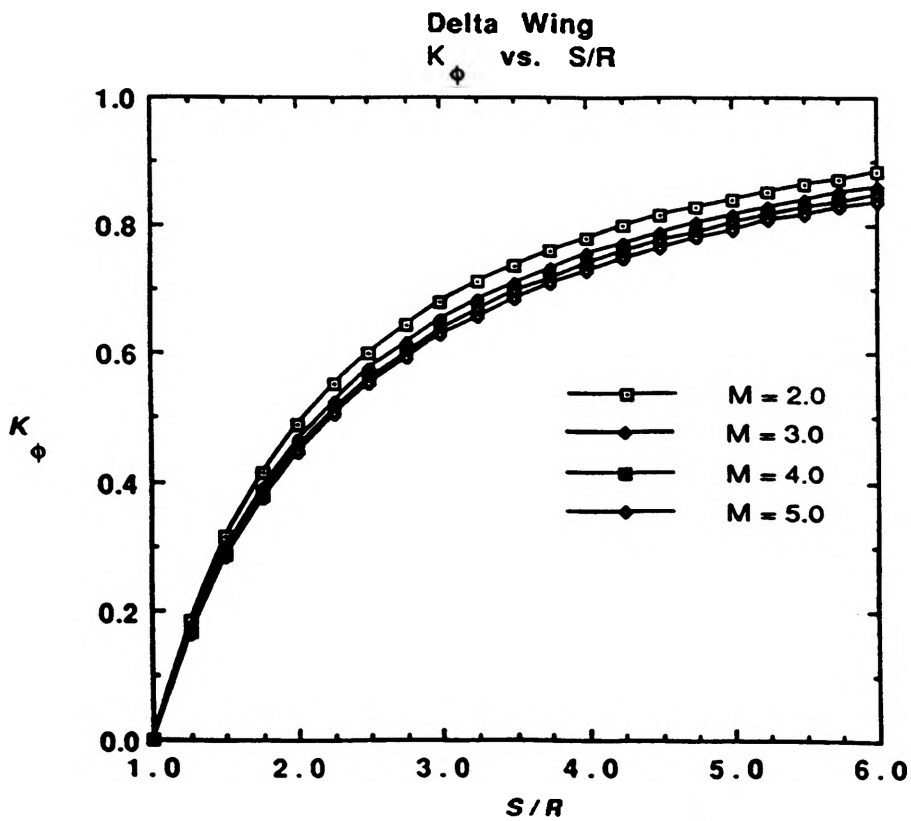


Fig. 10 The effect of free stream Mach number on K_ϕ vs. S/R , $\alpha = 10^\circ$, $\epsilon = 60^\circ$, $\phi = 6^\circ$

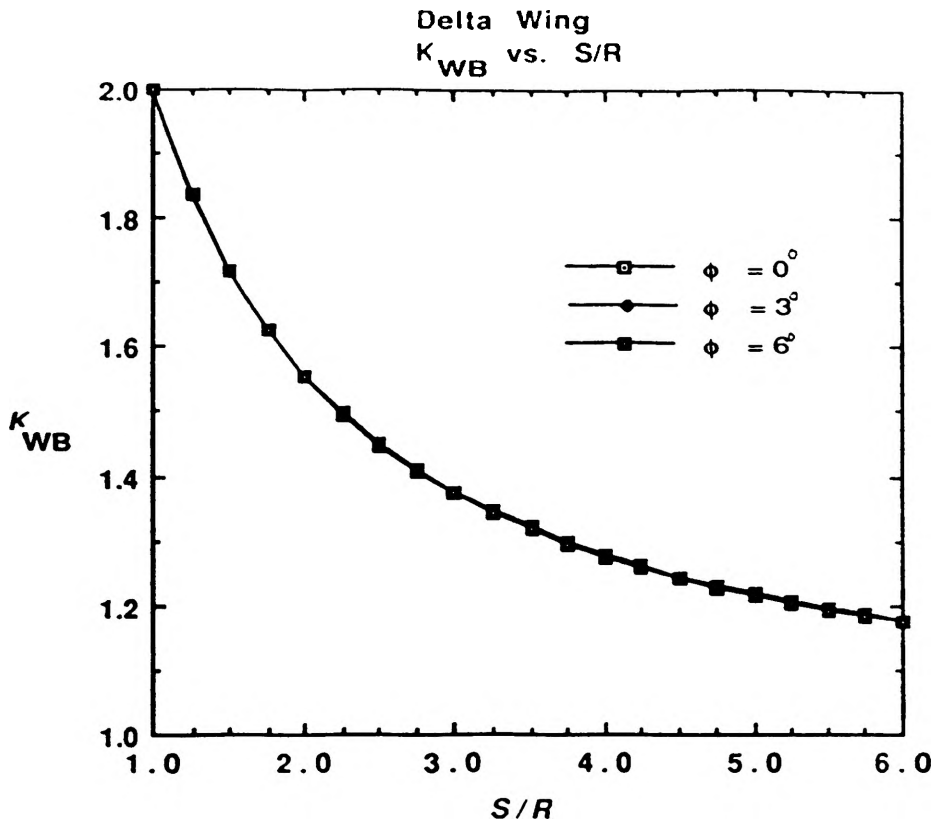


Fig. 11 The effect of roll angles on K_{WB} vs. S/R , $\alpha = 10^\circ$, $\epsilon = 60^\circ$, $M = 3$

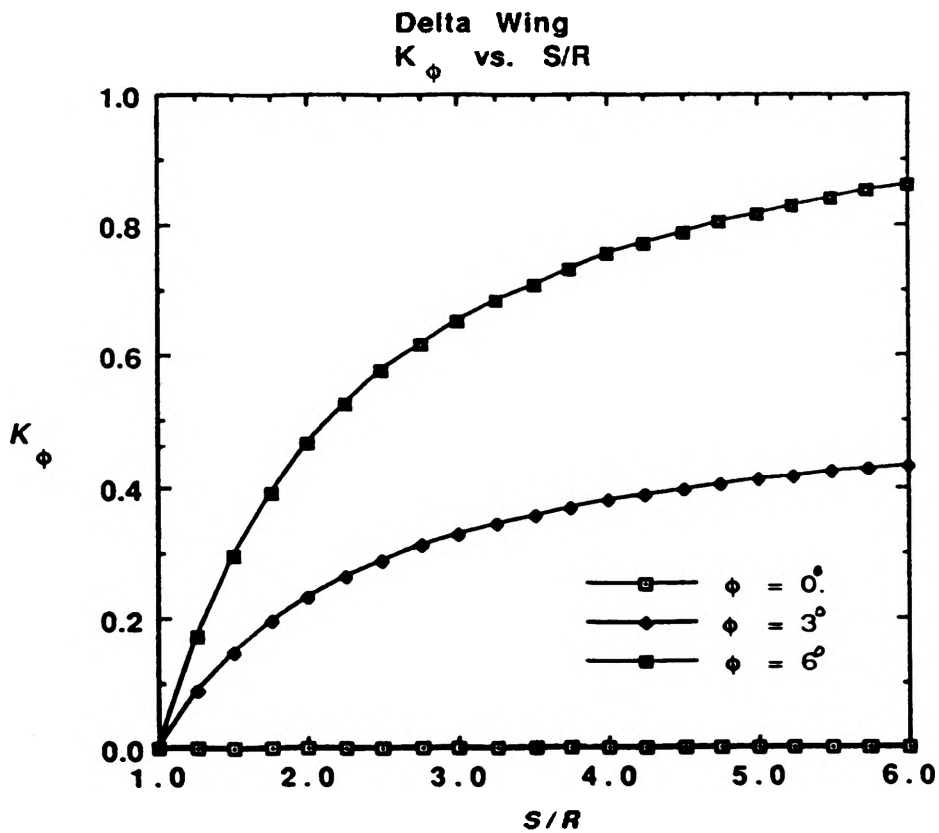


Fig. 12 The effect of roll angles on K_ϕ vs. S/R , $\alpha = 10^\circ$, $\epsilon = 60^\circ$, $M = 3$

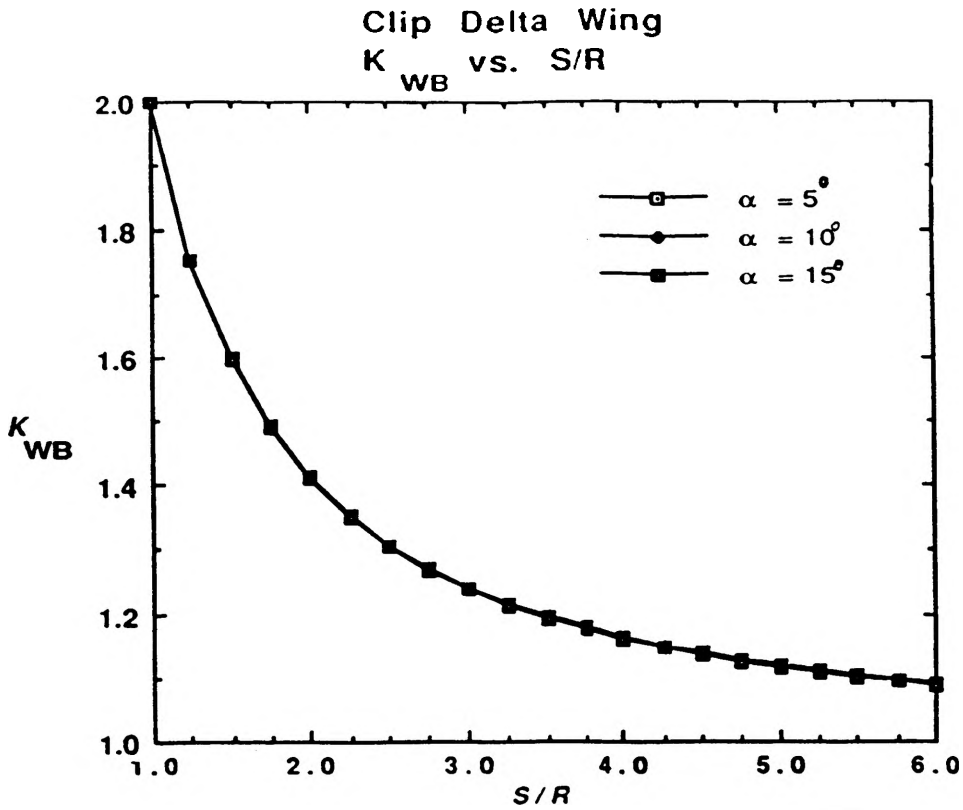


Fig. 13 The effect of angles of attack on K_{WB} vs. S/R , $\epsilon = 60^\circ$, $\phi = 6^\circ$, $M = 3$

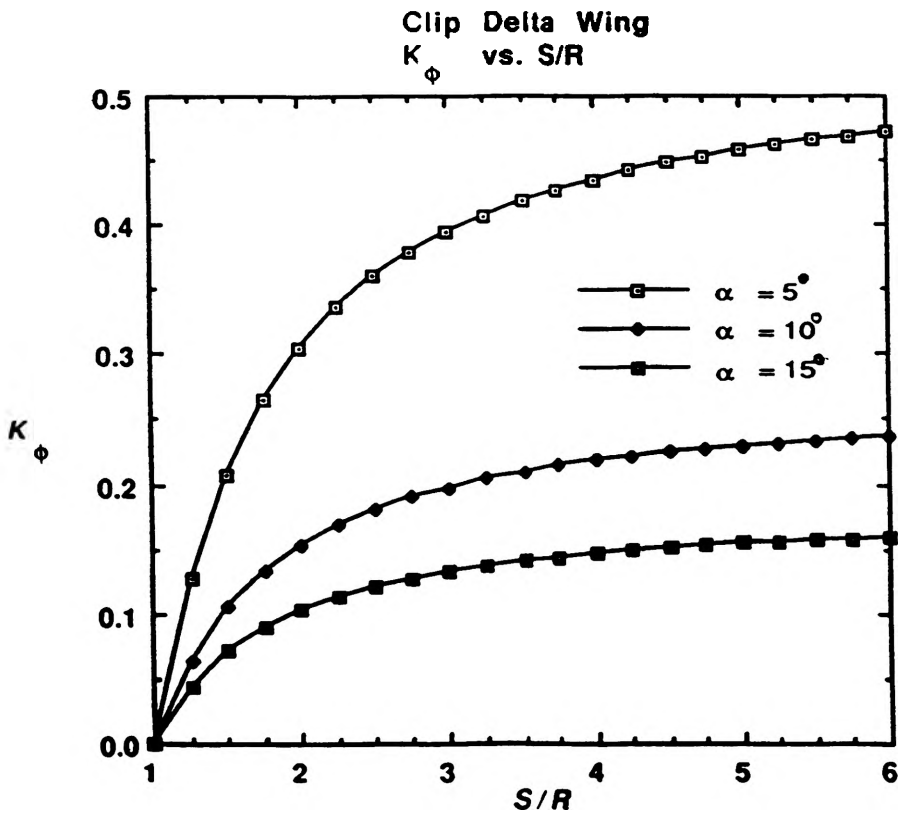


Fig. 14 The effect of angles of attack on K_ϕ vs. S/R , $\epsilon = 60^\circ$, $\phi = 6^\circ$, $M = 3$

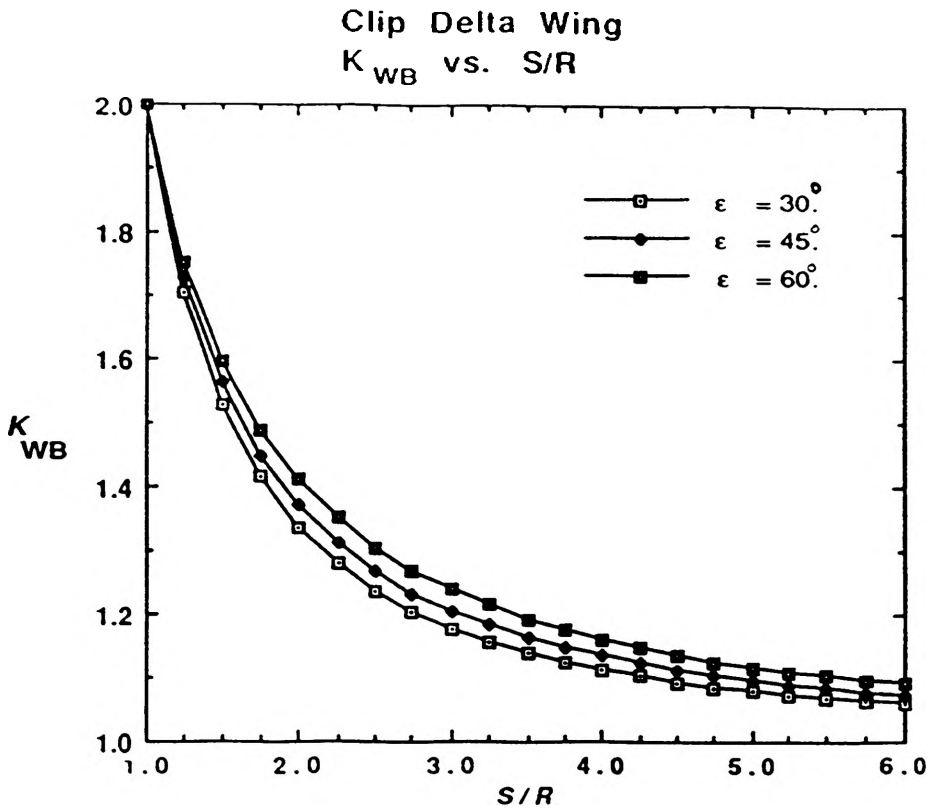


Fig. 15 The effect of semivertex angles on K_{WB} vs. S/R , $\alpha = 10^\circ$, $\phi = 6^\circ$, $M = 3$

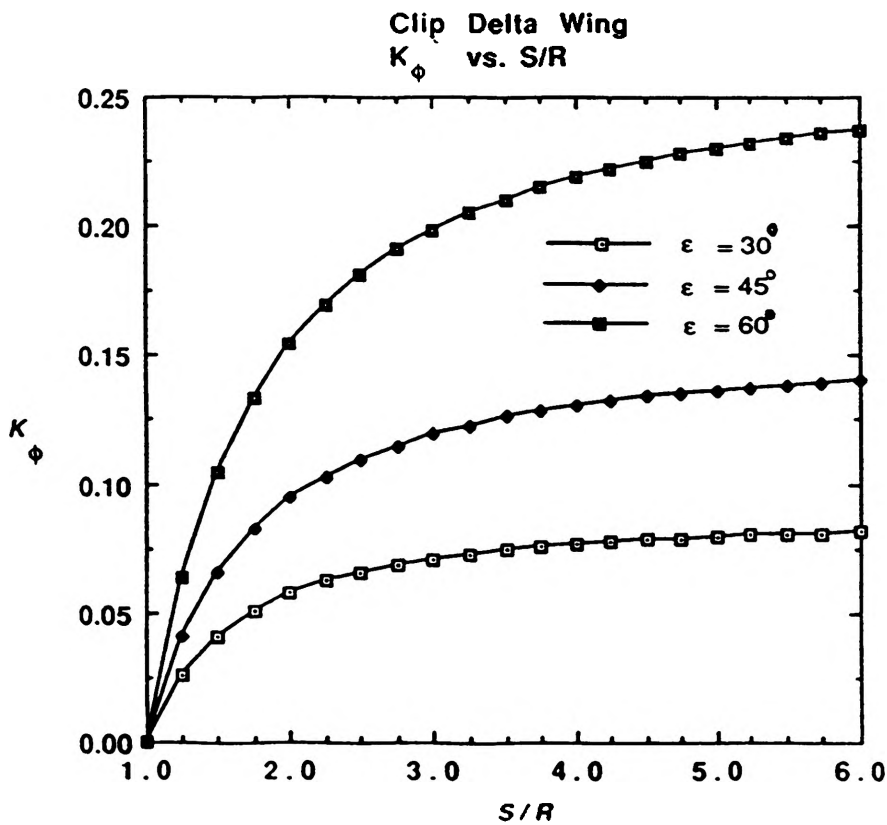


Fig. 16 The effect of semivertex angles on K_ϕ vs. S/R , $\alpha = 10^\circ$, $\phi = 6^\circ$, $M = 3$

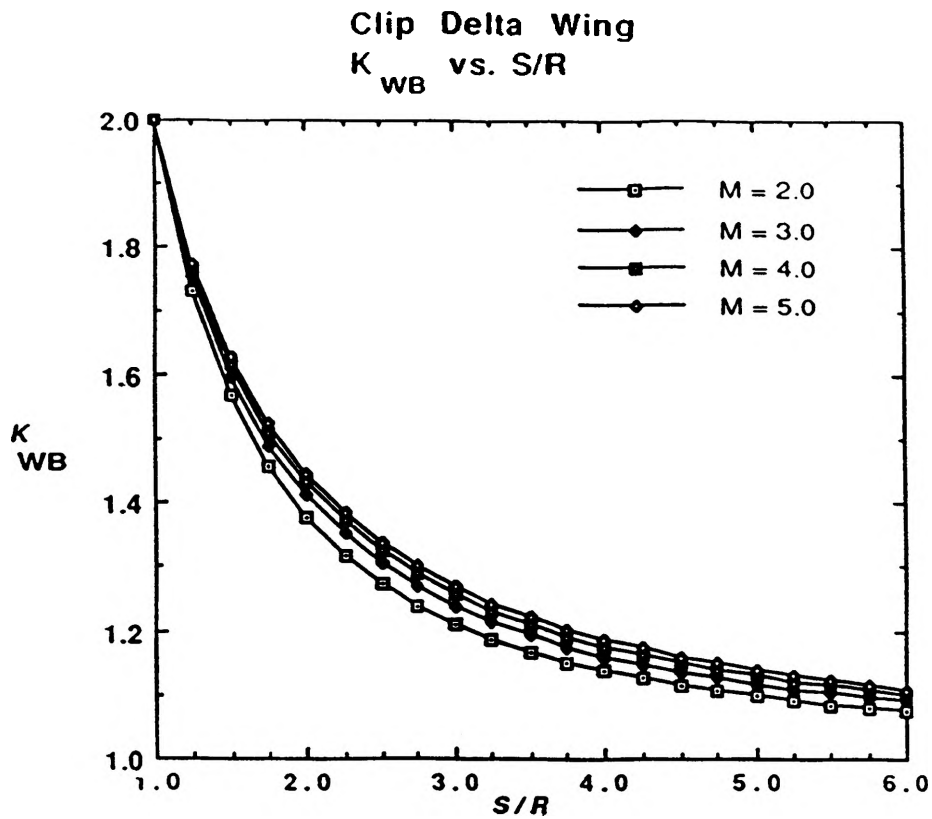


Fig. 17 The effect of free stream Mach number on K_{WB} vs. S/R , $\alpha = 10^\circ$, $\epsilon = 60^\circ$, $\phi = 6^\circ$

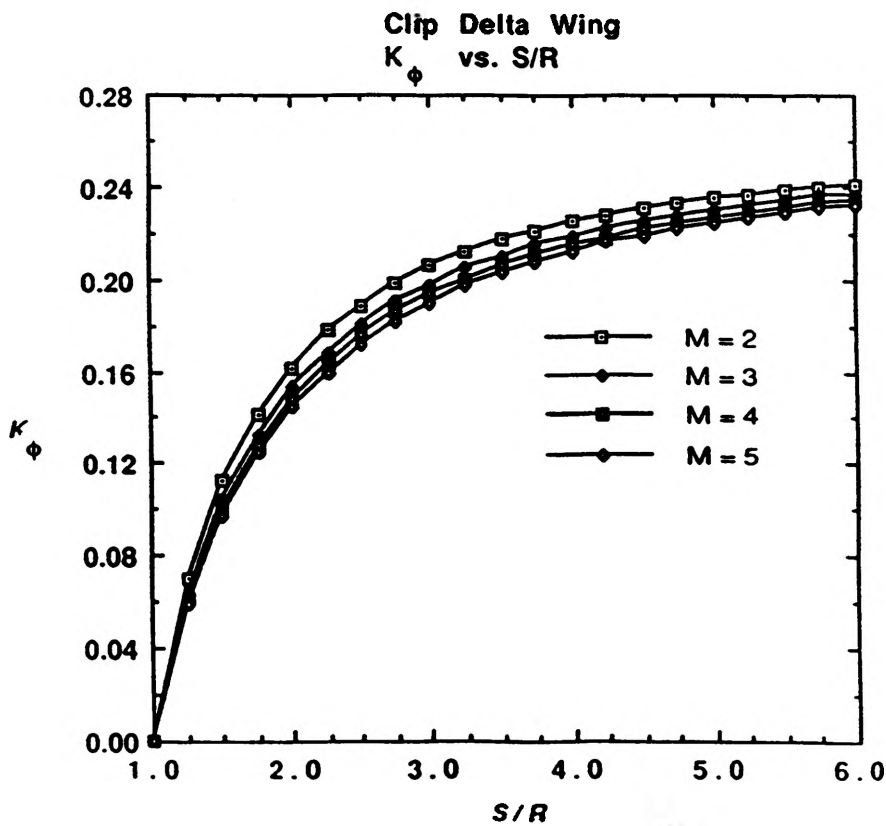


Fig. 18 The effect of free stream Mach number on K_ϕ vs. S/R , $\alpha = 10^\circ$, $\epsilon = 60^\circ$, $\phi = 6^\circ$

Clip Delta Wing
 K_{WB} vs. S/R

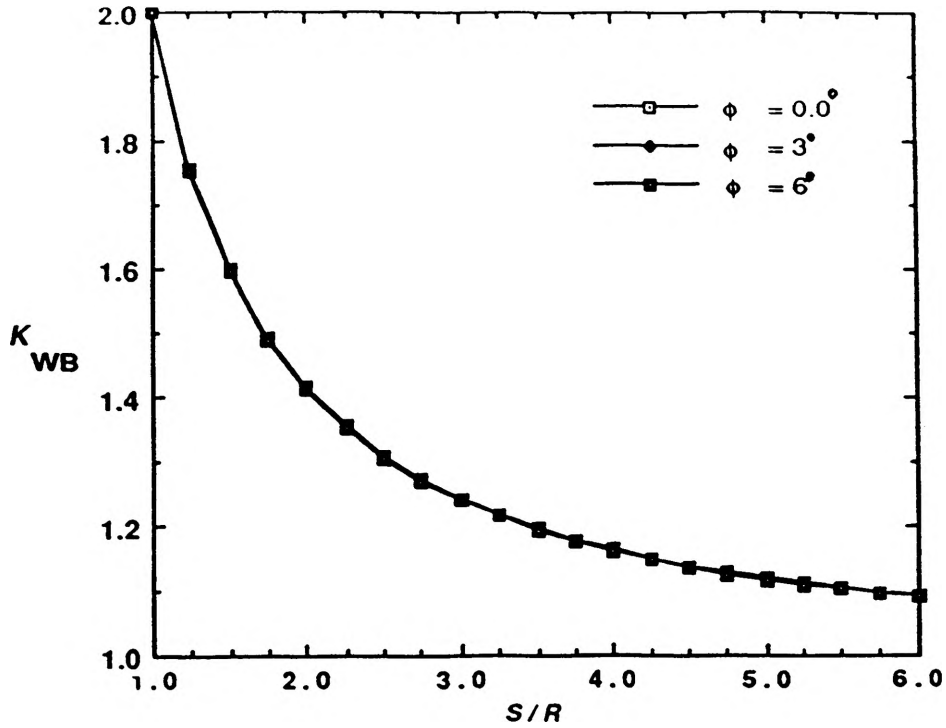


Fig. 19 The effect of roll angles on K_{WB} vs. S/R , $\alpha = 10^\circ$, $\epsilon = 60^\circ$, $M = 3$

Clip Delta Fin
 K_ϕ vs. S/R

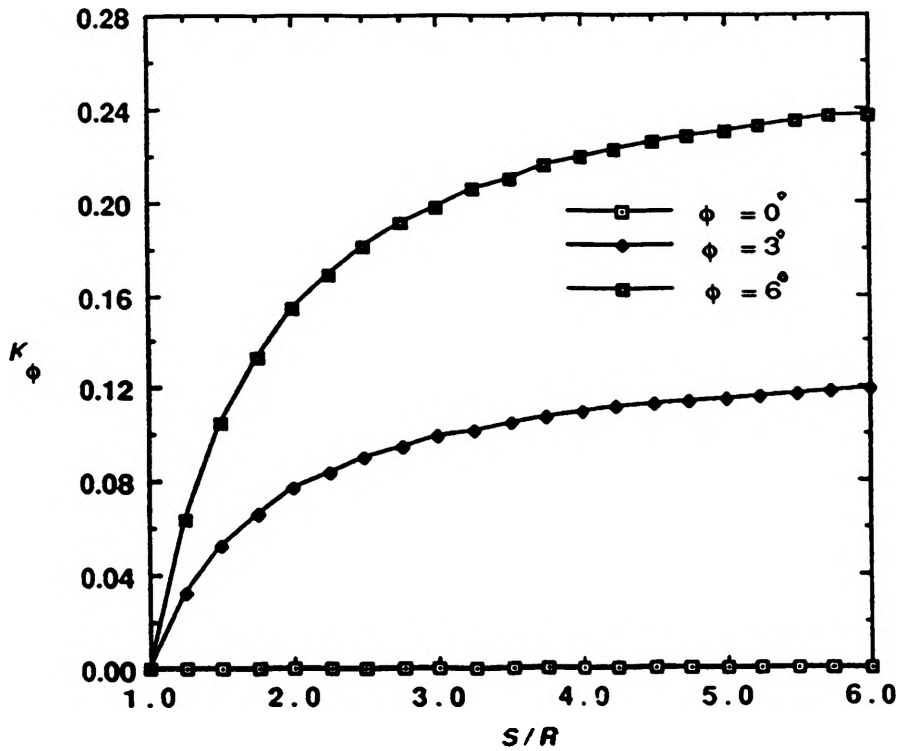


Fig. 20 The effect of roll angles on K_ϕ vs. S/R , $\alpha = 10^\circ$, $\epsilon = 60^\circ$, $M = 3$

Comparison between SWINT, SBT and result from this model (at 3 different roll angle) for a delta fin

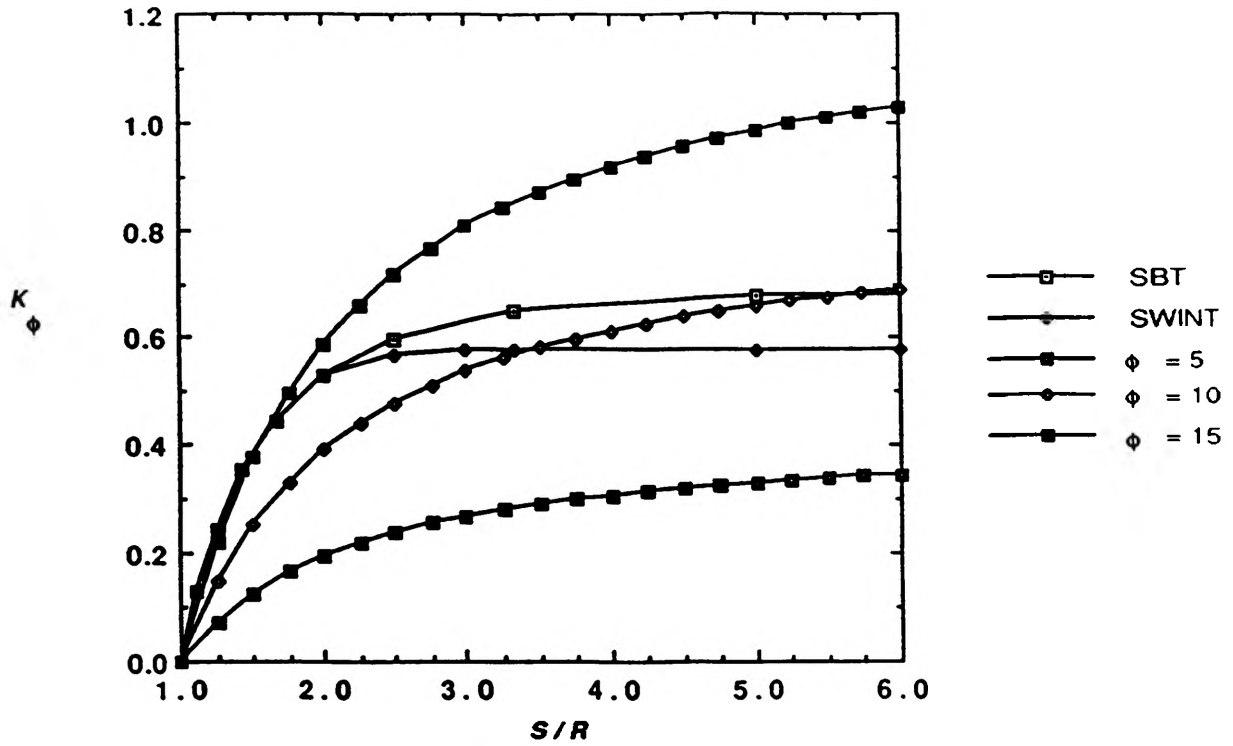


Fig. 21 The comparison of K_ϕ values between SWINT, SBT and the model

Table 1

Table 1 Missile S/R values	
Type of Missile	S/R
Air to Air Missile	3.0-5.0
Sparrow	5.00
Sidewinder	4.88
Air to Surface Missile	2.4-4.9
Shrike	2.40
Harpoon	2.68
Surface to Air Missile	2.8-4.8
Hawk	3.30
Chapparel	4.80
Surface to Surface Missile	2.2-4.8
Vigilant	2.55
Dragon	2.54
Surface to Surface/Air Missile (Ship-borne)	2.5-5.0
Albatros	4.00
Sea Chapparel	4.92

REFERENCE

1. Agnone, A.M., "Supersonic Flow Over a Cruciform Configuration at Angle of Attack," *Journal of Spacecraft and Rockets*, Vol. 23, Sept–Oct. 1986, pp. 451–452.
2. Larson, E.S., "Normal Force Characteristics at Supersonic Speeds of Sharp Edged Delta Wings," AIAA Paper 87–0214, 1987.
3. Spreiter, J. R. and Sacks, A.H., "A Theoretical Study of the Aerodynamics of Slender Cruciform–Wing Arrangements and Their Wakes," NACA Rept. 1296, 1957.
4. Shang, J.S. and Scherr, S.J., "Navier–Stokes Solution of the Flow Field Around a Complete Aircraft," AIAA Paper 85–1509, 1985.
5. Wardlaw, A.B., Baltakis, F.P., Martin, F.M., Priolo, F.J., and Jettmar, R.U., "A Godunov Method for Supersonic Tactical Missiles," *Journal of Spacecraft and Rockets*, Vol. 24, Jan.–Feb. 1987, pp. 40–47.
6. Vukelich, S.R. and Jenkins, J.E., "Missile DATCOM: Aerodynamic Prediction of Conventional Missiles Using Component Build–Up Techniques," AIAA Paper 84–0388, 1985.
7. Vukelich, S.R. and Jenkins, J.E., "Evaluation of Component Build–up Methods for Missile Aerodynamic Predictions," *Journal of Spacecraft and Rockets*, Vol. 19, Nov.–Dec. 1982, pp. 481–488.
8. Stoy, S.L. and Vukelich, S.R., "Prediction of Aerodynamic Characteristics of Unconventional Missile Configurations Using Component Build–Up Methods," AIAA Paper 86–0489, 1986.
9. Jenn, A.A. and Nelson, H. F., "Sideslip Effects on Fin–Fin Interference in Supersonic Missile Aerodynamics," *Journal of Spacecraft and Rockets*, Vol. 25, No. 6, Nov.–Dec. 1988, pp. 385–392.
10. Talpallikar, M. and Nelson, H.F., "Potential Flow Approach for Wing–Body Interference for Missiles in Supersonic Flow," AIAA Paper 90–0277, 1990.
11. Nielson, J.N. *Missile Aerodynamics*, McGraw–Hill Book Company, 1960, pp.119–165.
12. Rozkan, J, *Aircraft Flight Dynamics and Automatic Flight Controls*, 1971, pp. 105–150.
13. Jenn, A.A. and Nelson, H.F., "Wing Vertical Position Effects on Lift for Supersonic Delta Wing Missiles," *Journal of Spacecraft and Rockets*, Vol. 26, No.4, July–Aug. 1989, pp. 210–216.

VERTICAL AND ANGULAR MOTION OF A WING MODEL IN STEADY FLOW: A PHYSICAL AND NUMERICAL EXPERIMENTAL STUDY

Andrew P. Johnston

Abstract

The dynamic response of a rigid wing in steady flow mounted on translational and rotational elastic supports is investigated. This study presents both a numerical and a physical experimental arrangement that can be employed to investigate the effect of a wide range of parameters on the response of the wing subjected to steady flow. An interactive computer program, which utilizes the fourth order Runge-Kutta integration scheme to solve the governing differential equations, is discussed. The program output allows for quick visualization of the change in response due to parameter changes. An experimental arrangement that utilizes the new 18" x 18" subsonic wind tunnel is also developed. The experimental setup allows for quick parameter changes as well as being adaptable to other one or two degree of freedom systems. Low frequency oscillation at low speeds for flow visualization is obtainable along with chaotic responses at higher flow speeds. Periodic, quasi-periodic, and chaotic responses are observed in both experiments. A qualitative comparison of the results from the two experimental setups is given.

Nomenclature:

A	=	Dimensionless aerodynamic parameter = $\rho L_c S / 2m$
a	=	Distance from aerodynamic reference to axis of rotation
C_z	=	Dimensionless translational damping constant = $c_z / (m/t_c)$
C_α	=	Dimensionless rotational damping constant = $c_\alpha / (I/t_c)$
c_l	=	Wing lift coefficient
c_z	=	Translational damping coefficient
c_α	=	Rotational damping coefficient
g	=	Acceleration due to gravity
I	=	Wing mass moment of inertia
K_z	=	Dimensionless translational stiffness = $k_z / (m/t_c^2)$
k_z	=	Translational spring stiffness
K_α	=	Dimensionless rotational stiffness = $k_\alpha / (m L_c^2 / t_c^2)$
k_α	=	Rotational spring stiffness
L	=	Wing lift
L_c	=	Characteristic length
M	=	Dimensionless inertia parameter = $m L_c / I$
m	=	Wing mass
S	=	Wing area
t	=	Time
t_c	=	Characteristic time
T	=	Dimensionless time = t/t_c
U_∞	=	Free stream velocity
U	=	Dimensionless velocity in x-direction = U_∞ / w_c
v	=	Vertical flow (wing) velocity, $v = dz/dt$
V	=	Dimensionless velocity in z-direction = v / w_c
w_c	=	Characteristic velocity
z	=	Vertical amplitude
Z	=	Dimensionless wing vertical displacement = z/L_c

- α = True angle of attack
- α_o = Static angle of attack
- δ_α = Induced angle of attack
- ω = Angular wing velocity, $\omega = d\alpha/dt$
- Ω = Dimensionless wing angular velocity = $\omega / (1/t_c)$
- ρ = Air density
- d/dt = First derivative with respect to time
- d^2/dt^2 = Second derivative with respect to time
- D/DT = Dimensionless first derivative with respect to time

Introduction

The response of dynamic systems is an important topic in the education of future engineers and is included in several college courses. However, a majority of the systems studied is not fully investigated by the students. The experimental arrangements presented will enable the user to investigate the response of a wing with two degrees of freedom through the use of parametric studies. The opportunity to perform parametric studies becomes valuable when there is a large parameter space involved and the response is no longer intuitive. The dynamic system investigated is that of a rigid wing in steady flow mounted on translational and rotational elastic supports. The objective of this paper is to present a guide on the design and construction of numerical and physical experimental arrangements that allow for exploring the dependence of the translational and rotational wing motions on the parameter space. The governing equations, the numerical experiment, the physical experiment, and the results are discussed in subsequent sections.

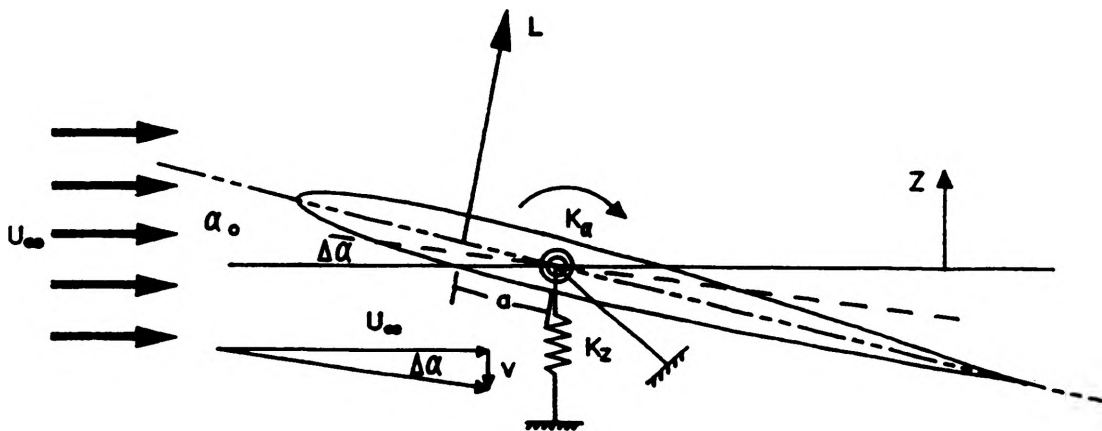


Figure 1. A wing model mounted on translational and rotational elastic supports.

Governing Equations

A schematic of the dynamic system investigated in this study is presented in Figure 1. The rigid wing is supported by translational and rotational springs with spring constants k_z and k_α respectively. It is assumed that the wing can only rotate and move vertically, and hence it is a two-degree of freedom system. Damping in the vertical and angular directions is represented by the damping coefficients c_z and c_α respectively. The length a represents the distance from the axis of rotation to the quarter chord. In the absence of flow, the wing makes

and angle α_0 with the horizontal, and its axis of rotation sets at a height $z = 0$. When the model is subjected to flow velocity U_∞ , the wing angle of attack can be written as

$$\alpha = \alpha_0 - \delta_\alpha = \alpha_0 - \tan^{-1} [v/U_\infty] \quad (1)$$

where v is the vertical flow velocity due to vertical wing motion. The wing lift normal to the flow direction is given by

$$L = 1/2 \rho (U_\infty^2 + v^2) S c_\ell \quad (2)$$

where ρ is the air density, S is the wing planform area, and c_ℓ is the airfoil lift coefficient. The lift coefficient can be approximated as²

$$c = 2\pi\alpha \quad (3)$$

The assumption here is that the airfoil is thin and symmetric with a large aspect ratio and the wing angle of attack is below the static stall angle of attack. Also for this type to wing, the lift acts along the quarter-chord line, and the airfoil moment coefficient is zero. In the numerical experiment, the wing is considered to be stalled, $c_\ell = 0$, for angles of attack whose magnitudes are greater than 12 degrees. With these assumptions the equations for vertical and angular motions can be written as

$$m d^2 z/dt^2 = -c_z dz/dt - k_z z + L \cos(\delta_\alpha) \quad (4)$$

$$I d^2 \alpha/dt^2 = -c_\alpha d\alpha/dt - k_\alpha (\alpha - \alpha_0) + a L \cos(\delta_\alpha) \quad (5)$$

Using equations (2) and $\cos(\delta_\alpha) = U_\infty / \sqrt{U_\infty^2 + v^2}$ one can write

$$m d^2 z/dt^2 = -c_z dz/dt - k_z z + 1/2 \rho c_\ell S U_\infty \sqrt{U_\infty^2 + (dz/dt)^2} \quad (6)$$

$$I d^2 \alpha/dt^2 = -c_\alpha d\alpha/dt - k_\alpha (\alpha - \alpha_0) + 1/2 a \rho c_\ell S U_\infty \sqrt{U_\infty^2 + (dz/dt)^2} \quad (7)$$

Characteristic quantities for length, time, and velocity are chosen in order to write the governing equations in a dimensionless form. The period of free oscillation of the system is taken as a reference time t_c and the deformation of the spring due to the wing weight is taken as the reference length ℓ_c . The ratio of ℓ_c/t_c is chosen as a characteristic velocity w_c . Based on these quantities, the characteristic quantity for time, length, and velocity can be written as follows:

$$t_c = 2\pi \sqrt{m/k_z} \quad (8)$$

$$\ell_c = mg/k_z \quad (9)$$

$$w_c = g/(2\pi \sqrt{m/k_z}) \quad (10)$$

The second order governing Equations (6) and (7) can be rewritten as four first order ordinary differential equations. Substituting Equations (8), (9), and (10) into Equations (6) and (7), will lead to the following dimensionless equations:

$$DZ/DT = V \quad (11)$$

$$DV/DT = -(2\pi)^2 Z - C_z V + A c_{\ell} U \sqrt{u^2 + V^2} \quad (12)$$

$$D\alpha/DT = \Omega \quad (13)$$

$$D\Omega/DT = -(2\pi)^2 K_{\alpha}(\alpha - \alpha_0) - C_{\alpha}\Omega + A M c_{\ell} U \sqrt{U^2 + V^2} \quad (14)$$

where A and M are the dimensionless aerodynamics and inertia parameters, C_z and C_{α} are the translational and rotational damping parameters and K_{α} is the rotational stiffness parameter. These dimensionless parameters are given as follows:

$$A = \rho g S / 2k_z \quad (15)$$

$$M = a g m^2 / I k_z \quad (16)$$

$$C_z = 2\pi c_z / \sqrt{m k_z} \quad (17)$$

$$C_{\alpha} = 2\pi c_{\alpha} \sqrt{(m k_z)} / I \quad (18)$$

$$K_{\alpha} = m k_{\alpha} / I k_z \quad (19)$$

As can be seen, the number of parameters is reduced to five dimensionless constants. Each set of values of these constants represents a large number of combinations of the dimensional parameters.

Computational Approach and Program Structure

The objective of the computer program is to integrate the governing equations in order to enable the user to perform parametric studies to investigate the dynamic response of a rigid wing with two degrees of freedom. To integrate the governing differential equations, the fourth order Runge-Kutta integration scheme is employed. This method requires the evaluation of the right hand side of Equations (12) and (14) at each time step. These functions represent the force and the moment acting on the wing respectively. The integration scheme and the results thereof are sensitive to the choice of the time step, and the program enables the user to investigate this sensitivity.

[AIRFOIL]	Input >
COMPUTE	Vrt & Ang Motion of an Aircraft Wing in Steady Flow
GRAPH	
FILE	Flow Speed, (m/s) 6.
HELP	Wing Angle of Attack, (deg) 5.
EXIT	Maximum Time, (sec) 10.
	Translational Stiffness, (N/m) 500.
	Translational Damping, (N/m/s) 50.
	Rotational Stiffness, (N m/rad) 3.5
	Rotational Damping, (N m/rad/s) 0.1
	Elastic Axis Location, (m) 0.05
	Time Increment, (sec) 0.02

Figure 2. User interaction environment. The main menu is on the left and the AIRFOIL submenu is on the right.

All computer routines are written in C, employing the Microsoft Quick C compiler. The language was selected because it provides direct access to most capabilities of a machine-language instruction set. It has a large variety of data types and concise syntax for effective conversions and indirections. Also, it has a very high degree of portability from one machine to

another. These capabilities make C powerful, efficient, and well suited to PC applications that involve user interfaces.³ An IBM PC/2 model 30-286 running at 10 MHz with a math co-processor was used to integrate the system of equations.

The program consists of several functions that perform different tasks when called by the main driver. The program interacts with the user with the use of a main menu, shown in Figure 2 on the left side of the screen, which allows for changing the parameter values, running the program, visualizing the results in a graphical presentation, storing the results, obtaining help, and exiting the program.

Once the input parameters are set and the option to perform the calculations is entered, the program computes the required size of arrays based on the time interval requested by the user and allocates memory for these arrays. This step is followed by functions that assign the initial conditions and integrate the governing equations. Once the integration is complete, the main menu is used to enable the user to visualize and/or store the results. Parametric investigations can continue until the program is exited. As can be seen in the AIRFOIL submenu, Figure 2 on the right side of the screen, nine parameters are involved in the parametric study. Fixed variables are the wing mass, moment of inertia, and surface area. The graphical presentation of the results is in the form of four graphs: Amplitude *vs.* Time, Angle of Attack *vs.* Time, Velocity *vs.* Amplitude (phase plot), and Angular Velocity *vs.* Angle of Attack (phase plot). The results may be stored on disk as an ASCII file for future plotting by selecting the FILE option. The user interaction environment of this program allows for efficient parametric investigations.

Physical Experiment

The objective of this portion of the paper is to present an approach to the design and construction of a physical experiment used to observe the dynamic response of a wing model with two degrees of freedom and subjected to steady flow. The design goal is to create a simple experimental setup which enables the user to observe a pure two degree of freedom system and perform parameter changes easily. The parameters that may be changed are the flow velocity, static angle of attack, spring constants k_z and k_ω , and the location of the axis of rotation, a . The new 18"x18" subsonic wind tunnel is used in conjunction with a removable test section with a length of 54 inches. The tunnel is driven by a 20 hp DC motor that provides feedback control for a tubular acustafan. Test section flow velocities can be controlled in a range between 0 and 120 ft/sec.

As shown in Figures 3a and 3b, the majority of the wing support structure is located outside of the wind tunnel to provide for clean flow and quick changing of the parameters. A "flexible fork" was developed to transmit the lift of the wing to the translational springs located underneath the wind tunnel. A flexible tube is used to connect the support uprights and provide a self-aligning fork. This eliminated the necessity of having to construct a perfectly square fork and having to align the linear bearings exactly. A set of five linear bearings and two rotational bearings confine the system to 2 degrees of freedom. The wing itself is a semi-symmetrical airfoil constructed of a polystyrene core coated with clear epoxy. The wing is mounted by the use of a connecting rod which passes through the rotational bearings and a tube running spanwise in the wing. One rotational bearing is mounted on top of each of the uprights. There are currently two tubes placed spanwise in the wing, one at the quarter-chord and one 4.5 cm. aft of the quarter chord, which allow for the location of the rotational axis to be changed. On one side of the fork a spring holder/angle of attack adjuster is mounted to the connecting rod, and the angle of attack is adjusted by loosening the setscrews and repositioning the wing. The rotational spring is a flat spring with one end cantilevered and the other end simply supported. The spring constant is varied by repositioning the rotational spring rate adjuster, which slides along the upright. The translational spring constant is adjusted by using different sets of

compression springs. The height of the translational spring housing is adjustable to accommodate a wide variety of spring sizes. The translational spring housing is mounted on a separate platform which is not connected to any portion of the tunnel in order to help eliminate any vibration caused by the running of the wind tunnel.

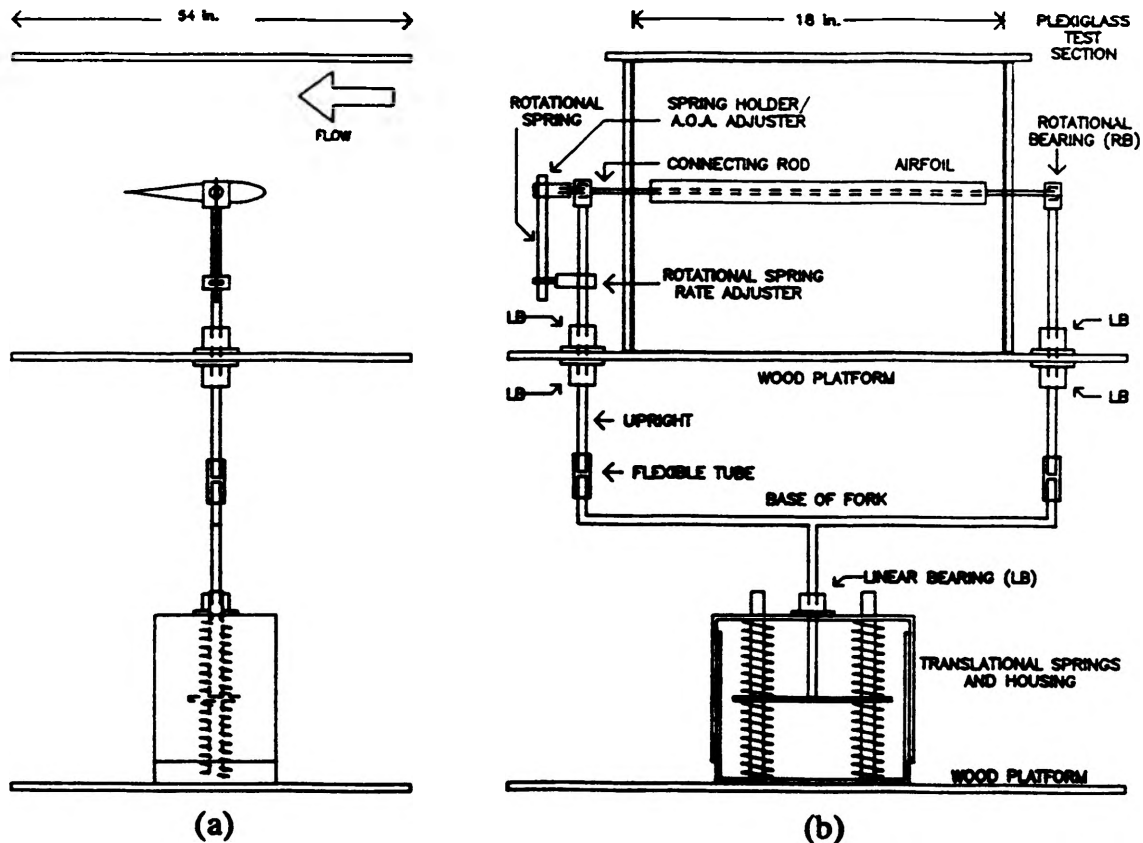


Figure 3. a) Side view of the experimental arrangement; b) Front view.

The experimental setup meets the design goals of being simple and adaptable. The entire test section is removable, and the experimental setup can be assembled or disassembled in a half hour. All of the parameters, except the location of the elastic axis, can be changed while the wind tunnel is running. Data gathering devices include an angle of attack indicator, a vertical displacement indicator, and a Pitot-static tube used to measure the flow velocity.

Results and Discussion

Computational Experiment

The program proves to be a success in the ability to observe a wide range of dynamic responses such as periodic, quasi-periodic, and chaotic oscillation. An example of the graphical presentation of the results is provided in Figures 4a through 4d. A wing reference area of 0.2 m^2 is selected. The wing mass and inertia are 2.0 kg and 0.2 kg m^2 respectively. The results show that initially the aerodynamic lift raises the wing upward from its static equilibrium position and exhibits underdamped behavior as the wing moves to a steady state height. The system is obviously stable. With a case such as this, the user can proceed to investigate the effect of different parameters on amplitude, frequency, and stability.

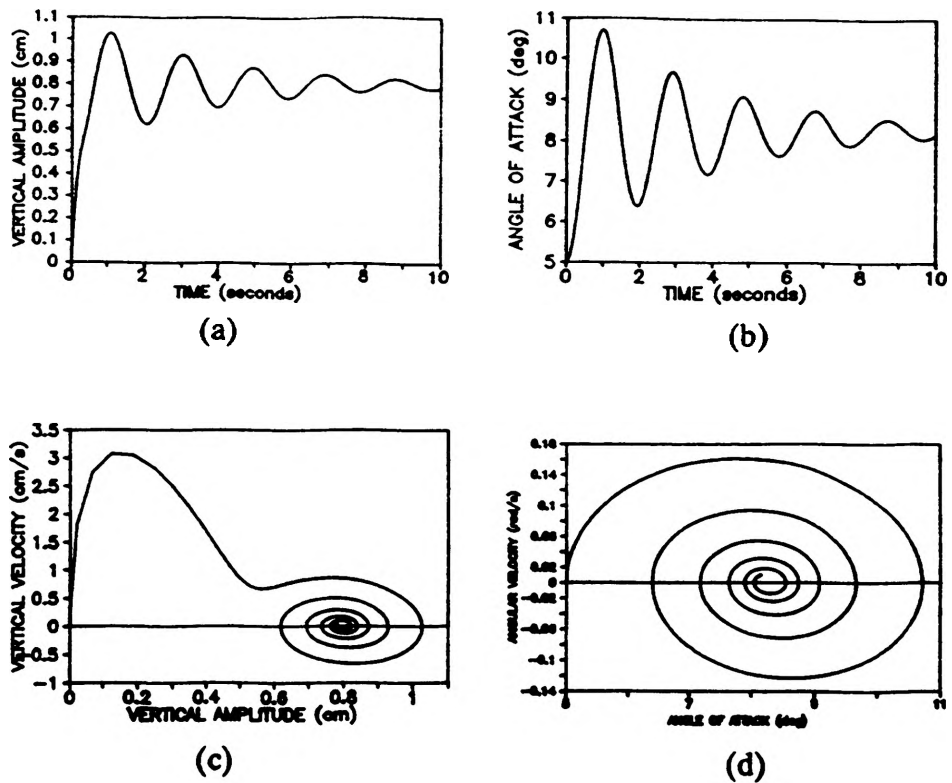


Figure 4. Results for an underdamped case (see Figure 2 for values). 4a) Amplitude vs. Time. 4b) Angle of Attack vs. Time. 4c) Vertical Velocity vs. Amplitude. 4d) Angular Velocity vs. Angle of Attack.

This dynamic system may be used to simulate the stiffness of an airplane wing in order to investigate wing flutter. Figures 5a and 5b present results for a divergent response which would be characteristic of a wing in flutter. The transition speed between stable and unstable behavior is found by a simple parametric study. The program also demonstrates that modes of flutter occur at different flow speeds.

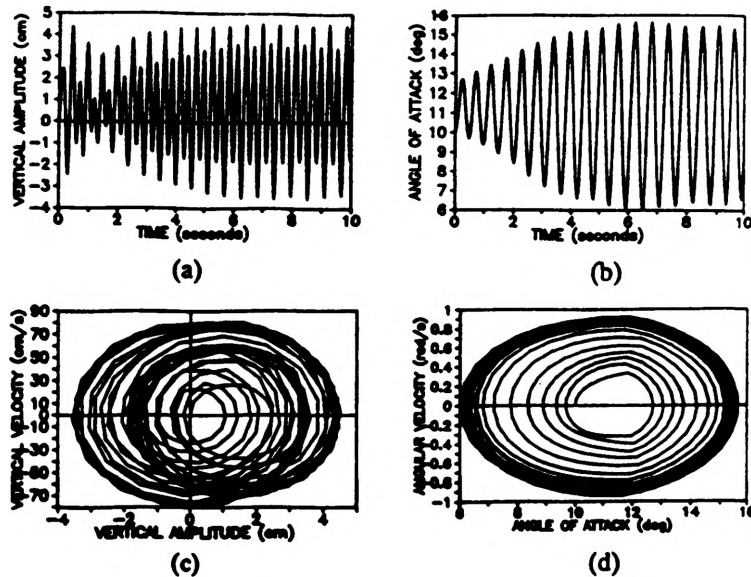


Figure 5. Results for a flutter case. 5a) Amplitude vs. Time. 5b) Angle of Attack vs. Time. 5c) Vertical Velocity vs. Amplitude. 5d) Angular Velocity vs. Angle of Attack.

Physical Experiment

The physical experimental setup meets the design goals and provides an interesting yet effective opportunity to enable the user to see the true dynamic behavior of the system. The wing used in this study has a surface area of 0.07 m^2 and a mass moment of inertia of 0.00015 kg m^2 . The mass of the structure that is free to oscillate in the vertical direction is 1.0 kg . Steady oscillations begin to appear at speeds of 5 m/s using the rotational spring with the lowest rate, approximately 0.2 N m/rad . The system is usually self excited, however manual excitation is easily performed due to the experimental arrangement. The entire range of responses has been observed, including modes of flutter at different speeds. The typical ranges for the amplitudes of the vertical and rotational oscillations are 0.1 to 3.0 cm and 5° to 30° respectively. The frequency of oscillation varies from 100 cycles per minute to upwards of 500 cycles per minute. The setup can also be used to observe destructive flutter at high speeds if caution is used.

Direct quantitative comparison of the results from the two experimental setups is not easily obtained due to the current inability to measure the damping coefficients. One case has been investigated and the results of the program appear to correspond to the behavior observed by the model. The case involved low frequency oscillation (flutter) at a speed of 5.5 m/s . With the mass, surface area, spring constants and inertia known, reasonable damping coefficients were found using parametric iteration to find the calculated response that matched the behavior observed in the tunnel. Qualitative comparison is easily achieved by a general observance of the effect of the individual parameters. Both experiments are extremely sensitive to the location of the elastic axis and the rotational spring constant.

Concluding Remarks

A physical and a numerical experimental arrangement used to investigate the translational and rotational dynamic response of a rigid wing model mounted on elastic supports and subjected to steady flow is presented. Both experimental arrangements allow the user to perform parametric studies to investigate the response of the system and the effects of the parameters. These investigations enable the user to study a wide range of responses which are generally not intuitive. The two arrangements can be qualitatively compared. These experiments have been recently introduced into the aerospace laboratory course curriculum with success.

Acknowledgement

This study was supported by the Opportunities for Undergraduate Research Experience program of the University of Missouri-Rolla. The guidance and support of Dr. F. Finaish throughout the project is greatly appreciated. My gratitude also goes to Robert Hribar for his help in machining necessary parts for the physical experiment.

References

1. Finaish, F. and Johnston, A., "Dynamic Response of an Elastically-Supported Wing Model in Steady Flow: Numerical Experiment for Undergraduates", submitted to the Intl. J. Mech. Eng. Educ.
2. Kuethe, A. M. and Chow, C. Y., 1986, "Foundation of Aerodynamics", John Wiley and Sons, New York.
3. The Waite Group, 1988, "Microsoft Quick C Programming", Microsoft Press, Redmond, Wash.
4. Mathews, E.H., 1987, "A Windtunnel Model to Demonstrate the Principles of Flutter", Intl. J. Mech. Eng. Educ., Vol.15, No.2.

THE EDGE STRENGTH OF ANNEALED AND HEAT-STRENGTHENED GLASS

Gregory P. Sallee

Pre-Testing Setup and Research

It was once stated that "a chain is only as strong as its weakest link." In the specific discipline of large commercial building design, this axiom takes no exception. Indeed, the required strength and stability of a structure can be obtained only if its individual components are sound.

It is for this reason, therefore, that engineers devote a great deal of their attention to the design of structural elements and to the strict control and inspection of plan interpretation and subsequent construction. Consider, for example, the analogous comparison of a modern skyscraper building to the human body. Undoubtedly, the framework is of primary importance, as it will determine how the structure will withstand physical loading. This framework takes the form of steel and concrete beams and columns in the skyscraper, and bones, tendons, ligaments and muscles in the human body. Also, the plumbing, electrical, and communication network systems are very instrumental in an operational building, just as circulatory and nervous systems are vital to the body's proper functioning. Yet, perhaps the most important element from a standpoint of serviceability and aesthetics is the protective barrier which lies between the structure's in-service functions and the harsh external environment. In the case of the human body, the skin serves this purpose well. Similarly, the "skin" of a skyscraper takes the form of glass windows.

Inarguably, the beauty of a building is a function of the condition of its glass covering. Furthermore, cracked or broken windows are not only distracting in appearance, but also fail to serve their primary purpose of weatherproofing and more importantly, thermal energy conservation. Moreover, in today's world of engineering economy and accompanying monetary significance, the need for properly designed glass units is of great importance and therefore, deserves much attention.

Sadly, up until now, very little research has been conducted in the field of glass window strength. The purpose of this research, therefore, is to explore the topic of glass window strength such that we might offer some conclusive evidence as to the probable in-situ performance of structural windows. Our intention is to examine the specific phenomenon of thermally-induced stress and its effect on glass strength. J. G. Croll explains the existence of this well-documented problem. "Whenever a structure is subjected to a varying temperature distribution, or where it is prevented from free expansion, stresses will be induced that are generally proportional to the difference in temperature from the unstressed state" (Croll, pp.181-182).

The importance of this research is clear in the case of the glass failure of the Merchants National Bank and Trust Company Building in Fargo, North Dakota. In the fall of 1964, the building began losing tinted, heat-absorbing panes due to thermally-induced stresses. Specifically, the glass in the sunlight was heated while portions of the panes in the shadow, or near the building's cool walls along the pane's edges, stayed relatively cold. The resulting uneven thermal expansion caused cracks. These cracks were significant enough to require replacement of the individual 10x14 feet panes which cost \$1200 apiece (Ross, p. 274). Before the problem was diagnosed, hundreds of windows had to be removed, costing tens of thousands of dollars. Clearly, a better working knowledge of this problem could have saved the headaches resulting from this particular incident. Our experimentation should be of great help in an effort to obtain this working knowledge.

The initial steps in this research involved theorizing and some guesswork, just as in any new process. We began by narrowing the scope of our problem to avoid too many experimental variables. Since field observations have shown that the window failures are governed by an initial cracking originating at the pane edges (i.e. a corner in the glass window cross section), we decided to focus our testing on this "weakest link". Hence, if we could experimentally analyze the average edge strength of a window, we could then determine the probable governing strength of the entire glass window.

Development of Testing Procedure

The primary difficulty we faced lay in the development of an accurate testing procedure that would lead us to good results. Although the ideal modeling and testing procedure would involve some type of thermal-loading, this could not guarantee us accurate information that would lead us to our specific goal of obtaining the edge strength; therefore, another alternative was developed. The design which we used involved a mechanical loading procedure that would maximize stresses at the targeted edge of the glass. The testing equipment consisted of glass samples, a hydraulic manually-operated load bar, an adjustable aluminum block, and load measuring devices.

First, the most important consideration in our experimental design lay in the development of a good loading procedure. From a practical standpoint, the procedure needed to be simple to limit possibilities of experimental error. This simplicity was found to be optimum in a third point bi-axial beam loading scheme. This type of loading would maximize a pure bending stress at the edge of a glass beam, and consequently, would allow us to determine the strength of the edge through simple mechanics of materials calculations.

The next step in building our testing procedure was to develop the size and dimensions of our glass samples. The sample thickness of 2.5 mm was an already present property of the large glass panes from which our beams were cut. This dimension controlled the depth of the beam since a critical angle of loading, which is created by a depth/width ratio of 10:1, is necessary in order to develop the maximum loading stress at the edge. This is a result of the bi-axial bending theory found in advanced mechanics of materials. Also, we chose the length of our samples to be 150mm (approximately 6 in.) along with the depth of 25mm. The reason for these numbers lies in the fact that a ratio of length to width larger than this would result in warping problems whereas a smaller ratio would have accompanying shear difficulties in the loading.

After determining an appropriate sample size, we began considering exactly how we would categorize our tests. We opted to test both annealed glass and heat-strengthened glass in their respective subgroups of scored (cut) edge/ other (uncut) edge and air side edge/tin side edge so that we could create a comparative edge strength study.

Samples from the annealed glass sheets were easy to obtain through a simple steel roller scoring and manual breaking process. The heat-strengthened samples, however, could not be obtained in this manner. Instead, they were manufactured by utilizing the state-of-the-art water jet technology available in the Mining Engineering department at the University of Missouri-Rolla. The water jet was altered experimentally until it could successfully cut the glass to the size we had specified. At this point, the samples were polished at a local glass shop so that their testing quality rivaled that of in-situ glass windows. Enough samples of both annealed and heat-strengthened glass were cut so that we could obtain enough successful tests to satisfy our quest for the glass edge strength.

The next most important experimental consideration concerned the loading apparatus itself. We designed and fabricated a manually-operated hydraulic loading bar which could be lowered onto two small points on the adjacent edge of the edge to be tested. This would model the third-point, pure bending load scheme which we desired. Also, an adjustable aluminum support block was machined so that the glass beams could be rigidly placed under the loading bar with the intention of loading to edge failure. Finally, the magnitude and rate of the bar loading was monitored via stress/strain gages and experimental graphing of bar load versus time. Importantly, these monitoring procedures were used to determine the failure stress in the samples.

In short, our preparations were carefully researched and planned so that our experimentation would yield satisfactory results. From these results, we could determine if there are appreciable differences between the average edge strengths of annealed and heat-strengthened glass.

Testing

The majority of the glass testing took place during the summer months of 1990. The samples were all cut and effectively marked so that they could be re-examined for future analysis. Also, the testing apparatus was manufactured and calibrated to avoid unnecessary errors. But, as is the case with any experimental process, some unanticipated difficulties and required changes were encountered during the testing.

One particular problem which needed to be addressed concerned the rate at which the samples should be loaded. This could only be examined through actual testing. Accordingly, many "test" samples were loaded at various rates so that we could determine the rate which would give us the most consistent and reasonable results. Rates of 50 lbs./min, 100 lbs./min, 200 lbs./min, and 250 lbs./min, and 300 lbs./min were all examined. After graphing and interpreting the data from each of these rates, it was determined that the loading rate of 100 lbs./min yielded the most consistent results for both annealed and heat-strengthened glass. Thus, this was the rate chosen for the sample testing.

The next problem we encountered was how to actually model the third point loading on the inclined beam. Our solution was to transfer the bar load directly to two very small square steel "shoes" which would be glued on the compression edge of the glass beam. These shoes were carefully machined to sit on the inclined sample so that their tops would be in contact with the horizontal load bar without creating an eccentricity in the beam. As a result, the distributed bar load could be transferred directly to the two points on the beam.

Other additions were also employed during the course of the testing. For example, plastic cushions were installed to prevent stress concentrations and resulting undesirable failures at the beam supports. Also, thin strips of tin and copper were inserted in the contact regions of the beam ends and the aluminum block support so that the uneven torsion and beam slippage could be avoided.

Notwithstanding the pre-planning and changes, some problems were encountered. This fact is clear when the low percentage of successful tests in the annealed samples is examined: only 26.2% of the tests were satisfactory for experimental consideration. These problems were seen as failures at points other than the theoretical location of maximum stress. Specifically, uneven loading due to machine misalignment, torsional stress, and shear stress concentrations caused failures to occur in undesirable places in the beam. However, all of these problems were diagnosed and successfully corrected so that we could obtain enough data to satisfy our requirements. In fact, we were able to achieve an 88.2% success rate in the second series of heat-strengthened glass tests once we corrected our experimental sources of error.

Furthermore, we were able to successfully test enough samples to be assured of a 95% confidence level in our our final edge strength statistical calculations.

Results and Analysis

The primary objective of this research was to determine the relationship among the six series of tests in regard to edge strength. We accomplished this goal by examining the samples through the application of the basics of statics and mechanics of materials.

First, the failure loads were recorded for 20 samples in each of the following test situations: annealed air side, annealed tin side, annealed scored edge, annealed other side edge, heat-strengthened air side, and heat-strengthened tin side. It should be noted that the air side is the side of the glass plate which is facing up during the manufacturing process. Conversely, the tin side faces downward during the manufacture process. The scored edge is the side which is cut with a steel wheel before breaking. The other edge is the side which is not cut before before breaking.

Next, the bending stresses about both the x and y axes were calculated using a modeling scheme developed from statics and mechanics of materials. The beam was analyzed as a simply supported beam in bending about its short axis, and a double-fixed end beam in bending about its long axis. The corresponding stresses were thus calculated and added linearly to give a maximum theoretical total stress at the edge.

In comparing the heat-strengthened tin side to the air side, there was only a 0.13% difference in failure stress. However, in the annealed glass air side/tin side, a difference of 8.6% was found. A comparison of annealed scored edge to other edge yielded a difference in failure stresses of 17%. The greatest percent difference, 34% was found to exist between the annealed and heat strengthened glass specimens. Therefore, we concluded that the heat strengthened samples would be more resistant than the annealed samples to thermally-stressed failures occurring at their edges. Also, the other edge would resist stress better than the scored edge on annealed glass.

Theoretically, these hypotheses seemed accurate. The only problem we faced after this statistical analysis was to account for failures occurring at places other than at the point of maximum theoretical stress. In fact, we observed many failure indications beginning at points along the long side of the sample cross section. This lead us to focus our attention to determining the cause of these unforeseen failures.

We examined the possibility of changes in the loading angle as the cause for stresses exceeding the desired maximum at the edge. However, calculations proved this effect was minimal and therefore was of no consequence in our experimental analysis.

Our second hypothesis was formed using the possibility of shear and torsion developing in the critical failure section of theoretical pure bending. A load differential at the two loading points could have caused both shear and torsion to devleop in the failure section. After extensive research and theoretical calculations, we found that only a 3% or less differential in loading between the two points could cause a maximum stress to occur at a point other than at the edge due to the combined loading of bending, shear, and torsional stresses. Our theory was proven correct after we attached strain gages to the two loading points of the beam and observed a difference that proved the 3% stress difference theory was correct.

One final portion of the experimentation process which has not yet been completed involves the correlation of our results with previous work. There has been a proposed theory which gives a direct relationship between failure stresses and glass fracture mirror radii. We

are in the process of measuring, via microscope and micrometer, the radii of our sample fracture mirrors. If the stresses we calculate from the theory correspond with our experimental stresses, we can be much more confident that our results are good enough to give us the ability to suggest how to best utilize glass from the standpoint of edge strength in thermally adverse conditions. Moreover, our results thus far have certainly lead us very close to the completion of this goal.

Session II:

Improving Technology Through Computer Modeling

Simulated Annealing on the Composite Graph Coloring Problem

*Kevin Alons
Northwestern College
Orange City, Iowa 51041*

The composite graph is a finite undirected graph G with no loops and no multiple edges and with positive integers associated with each vertex of G . The number of integers associated with each vertex is the chromaticity of the vertex. The chromatic degree of a vertex v is the sum of the chromaticity of v and the chromaticities of all vertices adjacent to v . The graph G is a v -composite graph if the chromaticities are not equal.

The v -composite graph coloring problem (CGCP) is the problem of assigning consecutive integers to each vertex of a graph in such a way that each vertex is assigned a number of integers equal to its chromaticity, no adjacent vertices have an integer in common and the number of integers used is a minimum. The minimum number of integers required to color a graph is referred to as the chromatic number of the graph.

The composite graph coloring problem is closely related to the non-composite graph coloring problem (GCP) and both are NP-complete. Exact algorithms for either of these problems exist only for very small graphs, so heuristic algorithms must be applied to solve practical problems.

For NP-complete problems, there is no known algorithm whose worst-case complexity is bounded by a polynomial in the size of the input. Local optimizing heuristic algorithms are often used to solve NP-complete problems approximately, i.e. to find "reasonable" solutions that are somewhat close to optimum. These algorithms explore a discrete space of reachable configurations, S , in a deterministic fashion. The set of solutions that can be reached in one change from a given configuration A is called the neighborhood of A . This is a generic description of local optimization:

1. Get an initial configuration S .
2. While there is an untested neighbor of S do the following:
 - 2.1 Let S' be an untested neighbor of S .
 - 2.2 If $cost(S') < cost(S)$, set $S = S'$.
3. Return S .

Starting from an initial configuration, a sequence of configurations is selected until a locally optimal solution is found. Typically, this local optimum is far from the globally best solution. Nonetheless, a better configuration cannot be reached from this local optimum as to escape this local region, an initial "bad" move must be accepted.

Simulated annealing (SA) is a randomizing heuristic algorithm recently applied to many NP-complete problems. While similar in many ways to its local optimization brethren, it differs in one important aspect. SA algorithms avoid local optimum through probabilistically accepting "uphill" or bad moves, in order to escape local optimum regions. This acceptance of uphill moves is controlled by a monotonically decreasing "temperature". As the temperature decreases, less uphill changes are allowed. This guides the algorithm to the global optimum region where it finds the best configuration. The following is the basic structure of simulated annealing in general:

1. Get an initial solution S .
2. Get an initial temperature $T > 0$.
3. While not yet "frozen" do the following:
 - 3.1 Perform the following loop L times:
 - 3.1.1 Pick a random neighbor S' of S .
 - 3.1.2 Let $\Delta = Cost(S') - S$.
 - 3.1.3 If $\Delta \leq 0$ (downhill move),
Set $S = S'$.
 - 3.1.4 If $\Delta > 0$ (uphill move),
Set $S = S'$ with probability $e^{-\Delta/T}$.
 - 3.2 Set $T = rT$ (reduce temperature).
4. Return S .

SA algorithms share four basic functions: accept, generate, update, and cost. The accept function decides whether to accept the proposed configuration, S' . The generate function generates this adjacent configuration, S' . The update function decreases the temperature by multiplying it by a cooling ratio r , $0 < r < 1$. The cost function generates the relative cost of a configuration, which is used in comparing different configurations.

Simulated annealing has been applied to the non-composite graph coloring problem. The results of these experiments prove that simulated annealing can perform as well as, if not better than most existing algorithms for the CGP. Since the two types of graph coloring are closely related, a method developed for the CGP was used for the CGCP.

Of the CGP simulated annealing methods developed, the penalty function method, was the most suitable for conversion to the CGCP. An initial solution using this algorithm is a partitioning of the vertices into color classes. This coloring (solution) is not required to be feasible. An adjacent solution is generated by randomly choosing a non-empty color class and a vertex within this color class. This vertex is then moved to a different randomly chosen color class which may be empty. This allows the number of color classes to increase, reducing the number of "bad edges" (adjacent vertices sharing colors).

The cost function used for penalty function annealing has two components, the first of which favors large color classes, the second which favors independent sets. It is:

$$cost(\Pi) = -\sum_{i=1}^k |C_i|^2 + \sum_{i=1}^k 2|C_i| \cdot |E_i|$$

This cost function does not explicitly count the number k classes in Π ; it minimizes this number as a side-effect of minimizing the cost of the configurations.

To convert this algorithm for use on the CGCP, modifications are needed. In generating a random neighboring configuration, the complexity in finding a valid vertex is increased. Instead of moving any random vertex, a vertex either starting or ending with the chosen color class must be found. This is due to the fact that vertices must have consecutive colors (integers). If a valid vertex in this color class does not exist, a new color class must be chosen. The constant in the second part of the equation used to penalize bad edges was increased to place more emphasis on independent sets. To ensure consistent convergence to feasible solutions, this additional penalizing of bad edges with composite graph coloring is required.

A functioning sequential algorithm was developed, which did converge to feasible, while not optimal, solutions. Developing the data structures to effectively implement simulated annealing required considerable time and effort. While improvements could be made to the

actual C program, it did incorporate dynamic lists and other techniques to reduce execution time and conserve memory. Run times of this algorithm on substantial graphs are quite large, which limited actual testing and timing of the algorithm. Instead, a parallel version of this algorithm was developed for a distributed memory parallel processing computer.

The parallel version was designed for and executed on a 16-node IPSC/2 hypercube. This application required the development of three separate programs: a host, a controller, and the node program. The host program acquires the requested number of nodes, and initializes and loads the cube. One node gets the controller program, the remaining nodes receive the worker program. This parallel application can be massively parallelized -- it can utilize any number of processors.

The controller program is essentially a copy of the sequential version with the inclusion of message passing within the outer loop. The worker programs contain only the inner loop of the sequential version and are coordinated by the controller. This coordination is not achieved through explicitly synchronized message passing, but is instead an inherent part of the algorithm design. Each node traces a different path through the solution space S by executing its inner loop a pre-specified number of times, then returning its best-solution-to-date to the controller. The controller takes the best *feasible* solution received and returns this solution and the decremented temperature to all nodes. This continues until the controller terminates the entire algorithm in the same manner as the sequential version.

This application appears to offer increased consistency in convergence to optimal feasible solutions with reduced running times. Since more paths from each common origin in the solution space are investigated, it stands to reason (and limited observance) that an optimal path will be located more efficiently in parallel. These predictions have yet to be proven, as conclusive data was not obtained.

A major goal of this program was to learn about and design a reliable, efficient parallel algorithm. While the sequential version took considerable work, the parallel version was the end result. Once the sequential algorithm was reliable, conversion to parallel required only an efficient system of message passing. This was especially critical as distributed memory parallel machines have high communication overhead. The goal was met as the program was reliable and promised increased efficiency.

Both the sequential and parallel versions of this algorithm prove that simulated annealing are applicable to the CGCP. Since the research done was primarily a study on parallelization and parallel algorithm design, little time was allocated for confirming the actual results of simulated annealing. More work is needed optimizing the many different parameters used (required by any simulated annealing application) before any realistic comparison can be done to existing CGCP algorithms.

Works Cited

Johnson, D. S., C. R. Aragon, L. A. McGeoch, and C. Schevon. 1990a. Optimization by Simulated Annealing: An Experimental Evaluation, Part II (Graph Coloring and Number Partitioning).

VEHICLE ROUTING USING THE SWEEP ALGORITHM IN PARALLEL

Jana G. Beattie (Hendrix College)
and
Carol L. Spelman (Principia College)

ABSTRACT

This paper presents a parallel version of the Sweep Algorithm, a heuristic solution to the single-terminal vehicle routing problem. The Sweep Algorithm uses a cluster-first, route-second approach in finding a near-optimal set of routes. The clusters of delivery points are formed by using the terminal as the center and moving around it in a sweeping fashion. After a cluster is defined, the route is found with a traveling salesperson algorithm.

The parallel version begins the sweep at different angles and performs both forward and backward sweeps. Each node handles a sweep and returns information concerning total distance traveled to the host. The host then decides which node has the best routes and requests the specific information.

The traveling salesperson algorithm is the nearest neighbor method. This starts the route at the point in the cluster nearest the terminal and proceeds by visiting the nearest unvisited point. Since this procedure is called many times in the course of finding all the routes, the quick but good results that this method yields were attractive.

Also discussed are other parallel implementations of this problem and ideas for further research.

Vehicle Routing Using the Sweep Algorithm in Parallel

Vehicle routing is a generalization of the infamous Traveling Salesman Problem. The main difference between the two is that the vehicle routing problem can have more than one "salesman." Also of concern in the vehicle routing problem is truck capacity, maximum traveling distance for the driver, simultaneous pickup and delivery, and seasonal demand. Bott and Ballou point out several reasons for research in the area in their article "Research Perspectives in Vehicle Routing and Scheduling." The most telling of the reasons cited is that the "typical firm spends 10% of its sales dollar, and from one third to two thirds of its logistics budget on transportation."¹ Parallel processing provides a new arena to search for better and more efficient results.

Many algorithms exist for solving vehicle routing problems. These can be broken into three basic groups, including exact, interactive, and heuristic approaches. [1] The exact methods use mathematical programming which consumes computation time and storage space.² The interactive approaches require a person to formulate the routes and acts more as a "cost calculator." There are various ideas in the heuristics approaches.

First, in the heuristic category, are the insertion procedures which begin with one stop per route and combine routes until no gain is made by further recombination. Next are improvement procedures which work with routes to reduce costs while maintaining feasibility. Third is the route first, cluster second approach where a large, infeasible route of all the delivery sites is broken into clusters. Finally is the cluster first, route second approach in which the delivery sites are first clustered and then routed. [1] This is where the Sweep Algorithm falls.

The Sweep Algorithm

The Sweep Algorithm is an approach designed by Dr. Bill Gillett (University of Missouri-Rolla) and Dr. Leland Miller (Bowling Green State University) in 1970. Using the coordinates of the delivery sites and the depot, the demand at each site, the maximum distance for any one route, and the maximum capacity for a truck, the sites are broken into clusters and then routed. This is a generalized version that can be altered to meet the specific demands of a given situation. This might involve assigning distances rather than using the coordinate distances or making some other modifications to fit the situation. The algorithm generally lends itself to alterations for many variations. [1]

With the information above given, the first step is to order the sites by polar coordinates with the depot being the origin. With this ordering the sweep begins. Sites are added to a cluster in this order until the next one cannot be added without exceeding the maximum capacity of the truck. The cluster is then sent to a TSP procedure for distance evaluation. If the distance returned from this procedure is greater than the maximum distance for a route, then sites are subtracted from the cluster until the distance constraint is satisfied. This cluster, now ordered by the TSP procedure, is considered a route.

¹ Bott, K. and Ballou, R. H., "Research Perspectives in Vehicle Routing and Scheduling," Transportation Research, May 1986: 239.

² Bott and Ballou actually cite an interesting example of a branch and bound exact method, which could provide an interesting parallel implementation. (Christofides, Mingozzi, and Toth, 1981)

Next begins an evaluation of the route. The points closest (C) and next closest (NC) to the route are defined, as well as the point in the route which is both closest to the depot and the next cluster (called KII). KII is chosen as such because it will be the easiest point to add to the next route. If the points C and NC are not in the first five sites after the current cluster, then the evaluation is complete and the route is saved as is. This is because adding either of these points to the route would only cause too much disturbance in the sweep. If the sites are within the five site limit, the route is re-evaluated including each of C and NC and excluding KII . If this re-evaluation provides a better route, then the better route is saved, and the sweep for the next cluster is begun. The sweep continues until all points have been routed.

Implementation

First, the algorithm was implemented sequentially in "C", as it was originally implemented in FORTRAN. To store the delivery site information, a doubly-linked list of structures was used. Each structure holds the x and y coordinates, the polar coordinates, the demand, and the list position, route and route order number for a delivery site. A doubly-linked list was implemented because of the ease of ordered insertion and dynamic storage.

Once the list is created and the elements of the structure assigned, the "sweep" is performed by proceeding down the list using the information stored in the structures. The TSP applied is a nearest neighbor algorithm. The algorithm requires starting at the site in the cluster nearest the depot and successively visiting the nearest unvisited site until all sites have been visited. This algorithm was chosen because of its ease of coding and good, fast results, as compared to several other simple TSP heuristics. [2] The latter is of the utmost importance, since the procedure is called many times in the course of the sweep. The results of the completed sweep are recorded into a file for the user.

The original version of the Sweep Algorithm was modified by Gillett and Miller to ask the user if another sweep was desired. By starting in a different position or sweeping a different direction, different routes are achieved and perhaps a better set found. This modification was implemented in the "C" version as well.

The parallel implementation involved many options. This program is in data parallel, meaning that the same program is run on each of the nodes with different data input. The algorithm had a natural inclination to this type of parallelization, because a different sweep could be done at each node. The host program creates the list from a file created by the user, and sends this list to the nodes. The host also tells each node where to begin its sweep and in which direction to proceed. The values of the starting angles and the directions are dependent on the number of nodes used. This is to say that if there are four nodes used there will be two forward sweeps from 0 and π and two backwards sweeps from π and 2π , etc. This is the obvious advantage to the parallel version, because in the time it took to run one sweep in serial many (dependant upon the number of nodes) sweeps could be performed by the parallel version.

Although the time sending messages is cause for concern, the serial program required user interaction and interpretation of the output. The parallel program makes its own decisions on the best set of routes according to specified criteria. In its current implementation the host program chooses the best set by the number of trucks used and the minimum total distance. Other criteria could be implemented as well by adding weights to

the structures. The final action of the host is to create a file for the user that contains the necessary output

Conclusions

As previously mentioned, the parallel version has the obvious advantage of completing several sweeps in the time the serial version completes one sweep. One extension to the program which would provide even more benefit would be to have the nodes sweep from each site within their angle range. A node would keep track of the best set of routes internally then return that to the host. This would mean that a sweep, both forward and backward, would be done from each delivery site.

Although complete testing with the nearest neighbor TSP procedure has not been done, the results should prove to be favorable. The idea behind the TSP in this program is for it to be "quick and dirty." This means that the focus is not on optimization, but speed, because of the numerous times the procedure is called. A comparison between the program with this TSP procedure and another (perhaps the spacefilling curves heuristic discussed in [2]) would be interesting. A parallel TSP algorithm was considered, but the results were not quick or optimal. Simplicity is a key here.

Parallel implementation seems to be a good option for vehicle routing problems. The previously mentioned exact algorithm (see footnote 2) implemented in parallel would provide an interesting comparison to this algorithm. As well, a route first, cluster second approach could be organized in a parallel manner similar to the Sweep Algorithm. After each of these are implemented and tested, a recent article in the ORSA Journal on Computing gives an idea for using neural networks for choosing between different vehicle routing heuristics. [3] The article claims that vehicle routing problems with different characteristics are better solved by different heuristics. This is as well a further idea for research in parallel processing in the arena of vehicle routing.

Results

The following results were obtained using a consecutive point TSP procedure, which does not provide even close to optimal solutions. This TSP was used as a substitute due to the time constraints of the summer NSF program. Results with the nearest neighbor procedure have not been produced. The main objective of the Sweep Algorithm is the clustering and this output shows the different clusterings.

Problem

Number of Locations is 22.

Depot Coordinates are (145 , 215).

Maximum Load Capacity is 6000.

Maximum Distance is 200.

Position	X	Y	Demand
7	151	264	1100
5	159	261	700
10	130	254	800
11	128	252	1400
4	163	247	2100
8	146	246	400
3	161	242	800
9	142	239	100
2	163	236	500
6	148	232	600
12	128	231	1200
1	156	217	1300
13	129	214	1300
18	146	208	300
21	164	208	900
17	141	206	2100
15	147	193	1000
20	164	193	900
14	129	189	2500
19	155	185	1800
16	139	182	700

The clusters formed with one node are

Route 1

21 20 19 18 15 16

Route 2

17 14 13

```

Route 3
  12 11 10 9 8 7 6
Route 4
  5 4 3 2 1

```

Notice that the sweep was a backwards one and the switching of positions 15 and 17, which would have been accomplished in the KII re-evaluation.

The clusters formed with 4 nodes are

```

Route 1
  1 2 3 4 5 6
Route 2
  7 8 9 10 11 12 13
Route 3
  14 15 16
Route 4
  17 18 19 20 21

```

Note that the above clusters are the same ones that are formed with 16 nodes. Thus in this case the forward sweep from 0 provides the best results.

Looking at the best ratio of trucks/distance with 18 nodes gives the following clusters.

```

Route 1
  16 15 14
Route 2
  13 12 11 10 9 8 7 6
Route 3
  5 4 3 2 1
Route 4
  21 20 19 18 17

```

In this case the sweep that gave the best results was a backwards sweep starting at $3\pi/2$.

The above results show several of the scenarios that are possible from different sweeps.

References

1. Bott, K. and Ballou, R. H. "Research Perspectives in Vehicle Routing and Scheduling" Transportation Research May 1986: 239 - 243.
2. Platzman, L. K. and Bartholdi, J. J. "Spacefilling Curves and the Planar Travelling Salesman Problem," Journal of the Association for Computing Machinery 4 October 1989: 719 - 737,
3. Nygard, K. E., Juell, P., and Kadaba, N. "Neural Networks for Selecting Vehicle Routing Heuristics," ORSA Journal on Computing Fall 1990: 353 - 364.

COMPUTER VISUALIZATION OF IRROTATIONAL FLOW OVER BLUFF AND STREAMLINED BODIES

Nora Okong'o

ABSTRACT

Computer programs were developed to visualize irrotational flow over bluff bodies (circular cylinders and half-bodies) and streamlined bodies (elliptical cylinders and airfoils). The method of superposition of flows was used, with stream functions or complex velocity potentials for fundamental flows being added to obtain the flows over the bodies. For the flow over the circular cylinders, half-bodies and elliptical cylinders, the stream function was calculated directly. The flow over the airfoil was obtained by Joukowski mapping of the imaginary part of the complex velocity potential for flow over a circular cylinder.

The programs developed will be valuable learning tools for undergraduate aerospace engineering students. The students will be helped to understand the equations used to describe the flows by studying the effects of varying various parameters. Future work on these programs may include modifying them to calculate and plot the velocity and pressure distributions, and to calculate the aerodynamic forces on the bodies.

NOMENCLATURE

a	Radius of circular cylinder
c	Joukowski mapping constant
d	Source-sink separation in flow over elliptical cylinder or complex doublet flow
h	Asymptotic height of half-body
l	Length of elliptical cylinder
q	Source, sink or doublet strength in complex flow
r	Distance from origin in cylindrical coordinates
u	x-component of velocity
v	y-component of velocity
V_∞	Magnitude of freestream velocity
x	Cartesian coordinate abscissa
x_0	Source, sink, doublet or vortex x-location
x_p	Joukowski mapping parameter
xx	x-coordinate of point on streamline
y	Cartesian coordinate ordinate
y_0	Source, sink, doublet or vortex y-location
y_p	Joukowski mapping parameter
yy	y-coordinate of point on streamline
z	Complex coordinates, $x + iy$
z_0	Source, sink, doublet or vortex location in complex coordinates
z_p	$x_p + iy_p$
α	Uniform flow angle of attack
Γ	Vortex strength
Δ	Increment in quantity

θ	Angle from x-axis in cylindrical coordinates
K	Doublet strength
Λ	Source or sink strength
ϕ	Velocity potential
ψ	Stream function
Ω	Complex velocity potential

INTRODUCTION

The purpose of the project described in this report was to develop computer programs to visualize two-dimensional, irrotational (potential) flow over bluff and streamlined bodies. The bluff bodies were half-bodies and circular cylinders, the streamlined bodies were elliptical cylinders and airfoils. The stream function was used to describe the flow over the various bodies. The computer programs are designed as learning tools to introduce undergraduate aerospace engineering students to the principles involved in visualizing irrotational flows. The computer programs calculate and plot the streamlines for the various types of flows.

The programs are written in the C programming language. (Refs. 1-3). C was used since it has several advantages over FORTRAN for programs of this type. The main advantages are: powerful and built-in graphics routines, ease of interaction with the user, a high degree of modularity, and ease of implementation on personal computers. When the program is compiled and linked, a DOS-based executable file is produced.

GENERAL METHODS

The general method for visualizing the flows over the various bodies consists of two main steps: finding the points on the streamlines, and plotting the streamlines. The points on the streamlines are found by: generating a grid, calculating the stream function values at points on the grid, finding the points with the same stream function values, calculating the body profile, and eliminating the points inside the body. A grid is defined by x- and y-coordinates ranging from -1 to 1. Grid divisions of 0.1 are used.

The stream function is found by the method of superposition of flows--stream functions for fundamental flows are added to obtain the stream functions for flows over various bodies. The method used to find the points with the same given stream function value is based on that described by Chow. (4) The method used is similar to subroutine SEARCH in program 2.2. The essence of the method is to approximate the location of a point (xx_k, yy_k) that has a given stream function value, ψ_a . (See figure 1 for terminology.) Its location is approximated by:

$$xx_k = x_i$$

$$yy_k = y_j - \frac{|\psi_a - \psi_{ij}| \Delta y}{|\psi_a - \psi_{ij}| + |\psi_a - \psi_{ij-1}|} \quad (1)$$

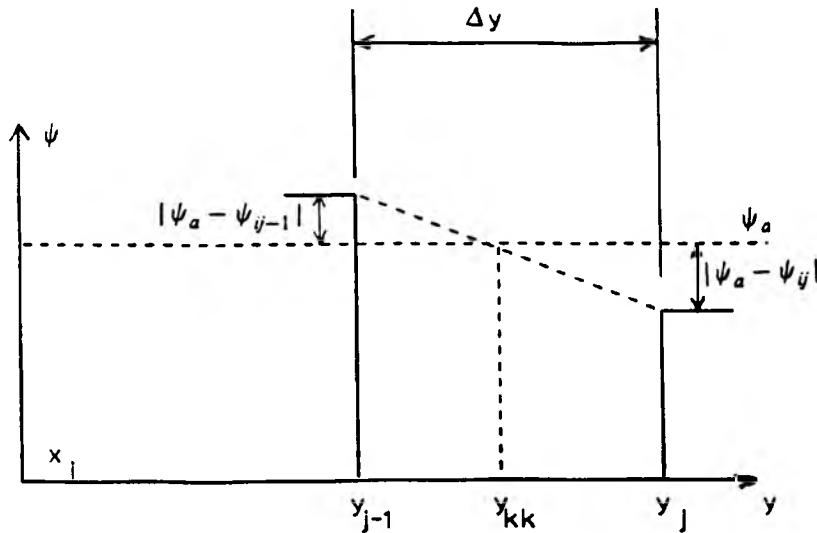


Figure 1. Approximating location of point with stream function value ψ_a

The equation for the body profile is obtained by setting the stream function equal to zero. The equation may be solved analytically or numerically to find the coordinates of the points on the body profile. Since the equations used to describe the flow are only valid for irrotational two-dimensional flow, they are not valid for points inside the body shape. Using the equation of the body profile, it is possible to determine if a point calculated as being on a streamline is inside the body shape. If it is, it is eliminated. For this project, a maximum of forty points can be plotted per streamline, and, at most, fifteen lines, including the body shape, are plotted.

FLOW OVER CIRCULAR CYLINDERS

The flow over the circular cylinder is obtained by adding uniform, doublet and vortex flows. For the vortex and the doublet located at the origin, the stream function is given by (5):

$$\psi = V_{\infty} y \left(\cos \alpha - \frac{a^2}{r^2} \right) - V_{\infty} x \sin \alpha + \frac{\Gamma}{2\pi} \ln \left(\frac{r}{a} \right) \quad (2)$$

where $r = \sqrt{x^2 + y^2}$ and $a = \sqrt{\frac{K}{2\pi V_{\infty}}}$

The body shape is a circle of radius a . To obtain the body shape, 2π radians are swept out in increments of $\Delta\theta$ radians, and the coordinates of the points on the body shape are calculated for each θ . The increment $\Delta\theta$ is :

$$\Delta\theta = \frac{2\pi}{\text{number of points to be plotted} - 1} \quad (3)$$

The x- and y-coordinates for the points on the circle are given by:

$$x = a \cos \theta, \quad y = a \sin \theta \quad (4)$$

Points are eliminated if $(x^2 + y^2) < a^2$.

FLOW OVER HALF-BODIES

The flow over a half-body is obtained by adding uniform and source flows. For the uniform flow at zero angle of attack and the source on the x-axis, the stream function is given by (5):

$$\psi = V_{\infty}y + \frac{\Lambda}{2\pi} \tan^{-1}\left(\frac{y}{x-x_0}\right) \quad (5)$$

or

$$\psi = V_{\infty}\left(h \frac{\theta}{\pi} + y\right) \quad (6)$$

where $h = \frac{\Lambda}{2V_{\infty}}$ is the asymptotic height of the half-body.

The body shape, obtained by setting $\psi = 0$, is given by:

$$y = -\frac{\Lambda}{2\pi V_{\infty}} \tan^{-1}\left(\frac{y}{x-x_0}\right) \quad (7)$$

To calculate the x- and y-coordinates of the points on the body, equation (7) is solved numerically; $(2\pi - 2\beta)$ radians are swept out, where

$$\beta = \tan^{-1}\left(\frac{h}{x_{\max} - x_0}\right) + \frac{\pi}{2 \times \text{number of points to be plotted}} \quad (8)$$

A point is eliminated if $y \leq \frac{-\Lambda}{2\pi V_{\infty}} \tan^{-1}\left(\frac{y}{x-x_0}\right)$

FLOW OVER ELLIPTICAL CYLINDERS

The flow over an elliptical cylinder is obtained by adding uniform flow along the x-axis to a source and a sink. If the source and sink have the same strength and are at the same distance from the origin, the stream function for the flow is (6):

$$\psi = V_{\infty}y + \frac{\Lambda}{2\pi} \left[\tan^{-1}\left(\frac{y}{x-d}\right) + \tan^{-1}\left(\frac{y}{x+d}\right) \right] \quad (9)$$

The body shape is obtained by setting $\psi = 0$. The length of the body is given by:

$$l = \sqrt{\frac{\Lambda}{\pi V_{\infty} d} + 1} \quad d \quad (10)$$

Also, from equation (9)

$$y = \frac{\Lambda}{2\pi V_{\infty}} \tan^{-1}\left(\frac{2dr \sin \theta}{r^2 - d^2}\right) \quad (11)$$

Equation (11) has to be solved iteratively for x and y. To do this, 2π radians are swept out in $\Delta\theta$ increments and l length units are swept out in Δr units where

$$\Delta\theta = \frac{2\pi}{2 \times \text{int}\left(\frac{\text{number of points to be plotted} - 1}{2}\right)} \quad (12)$$

$$\Delta r = \frac{l}{\text{number of points to be plotted}} \quad (13)$$

Points are eliminated, if

$$y < \frac{\Lambda}{2\pi V_\infty} \left| \tan^{-1}\left(\frac{y}{x-d}\right) - \tan^{-1}\left(\frac{y}{x+d}\right) \right| \quad (14)$$

FLOW OVER AIRFOILS

To visualize the flow over the airfoil, the Joukowski transformation is used. Both the body shape and the streamlines of the flow over the cylinder are mapped to the flow over an airfoil.(7) The transformation parameters are shown in figure 2: the circular cylinder is in the $x''-y''$ plane, and the airfoil is in the $x-y$ plane.

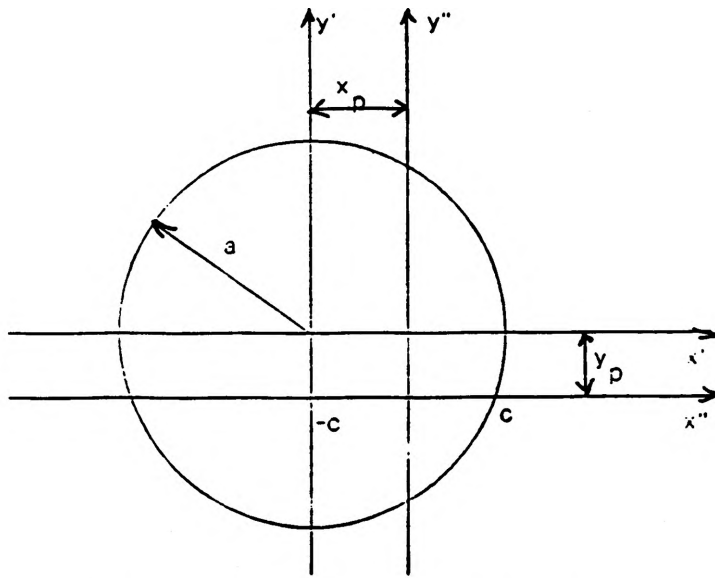


Figure 2. Mapping parameters for Joukowski transformation

The circular cylinder is first shifted to the $x'-y'$ plane, with its center at (x_p, y_p) , with x_p always less than zero. The system of equations for the coordinate transformation from $x''-y''$ to $x-y$ is:

$$z_p = x_p + iy_p \quad (15)$$

$$z' = z'' + z_p \quad (16)$$

$$z = z' + \frac{c^2}{z'} \quad (17)$$

where c is a constant. y_p determines the camber of the airfoil, and is zero for a symmetrical airfoil. A negative value of y_p will give an airfoil that is curved downward.

Since the transformation uses complex coordinates, the complex potential for flow over a circular cylinder is used (6):

$$\Omega = V_{\infty}z + V_{\infty}\frac{b^2}{z} + \frac{i\Gamma}{2\pi}\ln z \quad (18)$$

where $b^2 = \frac{qd}{\pi V_{\infty}}$

The stream function is obtained as the imaginary part of the complex velocity potential. Once the stream function for the flow over the cylinder is found, streamlines and body profile are found as for the flow over the circular cylinder, and are then mapped using the Joukowski transformation.

SPECIAL CONSIDERATIONS

Since the programs developed to visualize the flow are intended as learning tools, it is important to obtain results quickly but with reasonable accuracy. The numerical schemes used in visualizing the flow are intended to give the user a general idea of what the streamlines and body shape look like.

The method for finding the points on the streamlines works best for flows approximately parallel to the x -axis. So, there are problems in finding points on a streamline that has orientations parallel to the other coordinate axis. Because the numerical calculations for the body shape would take too long, the program cannot visualize flow over very thin elliptical cylinders.

RESULTS AND DISCUSSION

Sample results of the programs developed are shown in figures 3 through 6. Figure 3 shows the results for flow over a circular cylinder. The circulation (or vortex) in figure 3 removes the symmetry of the streamlines about the x -axis. The streamlines are closer together on top of the cylinder for clockwise circulation. Figure 4 shows the results for flow over a half-body. A larger source strength increases the height of the half-body. Figure 5 shows the results for flow over an elliptical cylinder. Decreasing the distance between the source and the sink results in a smaller, rounder body. Figure 6 shows the results for flow over an airfoil. Decreasing c increases the thickness of the body, and a non-zero value of y_p gives a cambered airfoil.

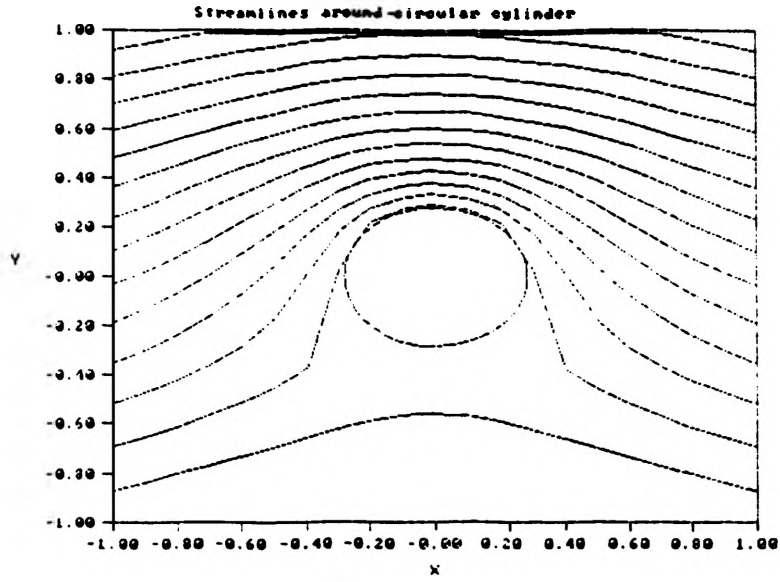


Figure 3. Flow over circular cylinder; $V_\infty = 1$, $\alpha = 0$, $K = 0.5$, $\Gamma = 3$

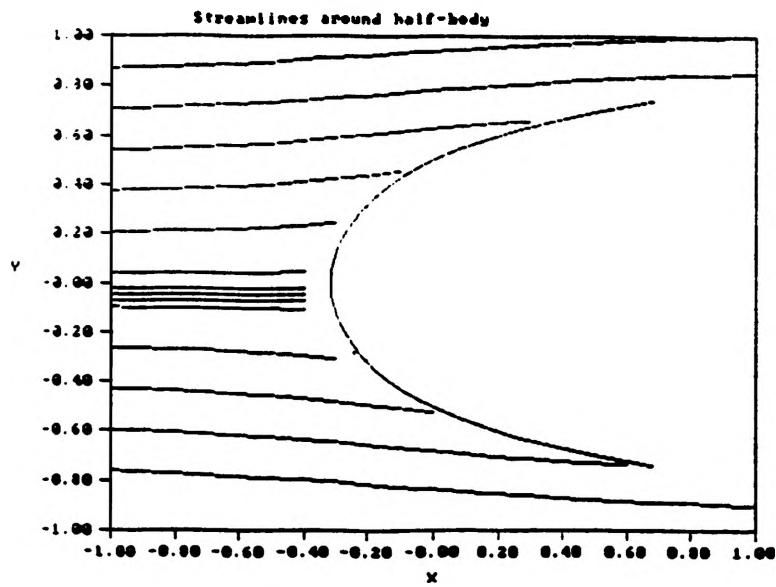


Figure 4. Flow over half-body; $V_\infty = 2$, $\Lambda = 4.0$, $x_0 = 0$

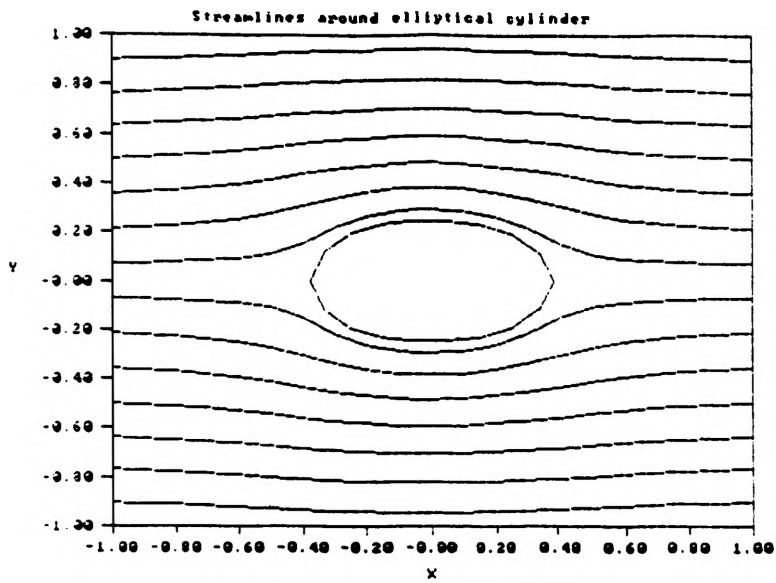


Figure 5. Flow over elliptical cylinder; $V_\infty = 1$, $\Lambda = 1$, $d = 0.25$

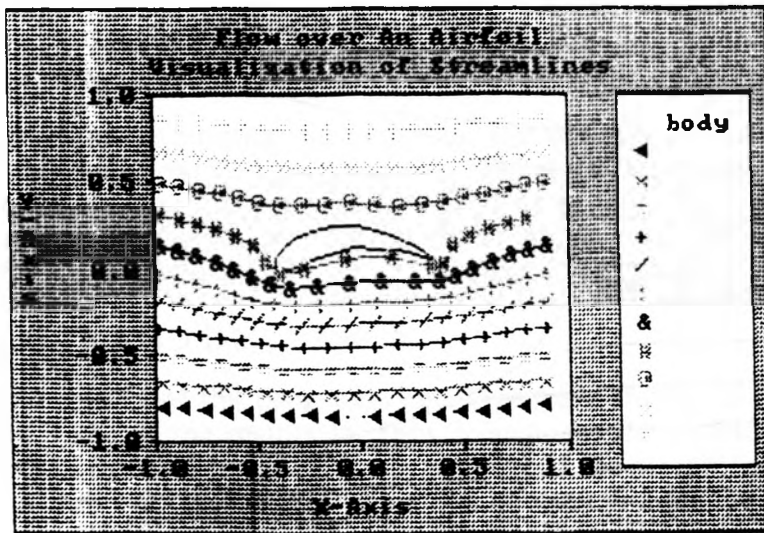


Figure 6. Flow over airfoil; $V_\infty = 1$, $q = 1$, $d = 0.2$, $\Gamma = 1$, $y_p = -0.1$, $c = 0.2$

CONCLUSIONS AND RECOMMENDATIONS

The program developed in this project should prove to be valuable learning tools for undergraduate aerospace engineering students. The visualization programs may be used to explore the effect of varying various parameters on the flow pattern and body shape obtained, and to give the users an idea of how the equations used to describe the flow translate into a physical flow pattern.

The programs have a few limitations, some of which may be removed by incorporating different numerical methods or optimization techniques. The effects of decreasing the grid divisions or of increasing the number of points and/or streamlines that are plotted might be investigated to optimize computational time and accuracy. Future work on the visualization software may include comparison of the computer-generated results with experimental results, and visualization of flow over additional bodies, and incorporation of routines to calculate and plot the pressure and velocity distribution, as well as to calculate the aerodynamic forces on the bodies.

ACKNOWLEDGEMENTS

I would like to thank the OURE program for its support and funding, and Dr. Fathi Finaish for his encouragement and direction.

REFERENCES

1. Microsoft QuickC Compiler: Tool Kit. Version 2.5. Microsoft Corporation; 1990
2. Microsoft QuickC Compiler: C for Yourself. Version 2.5. Microsoft Corporation; 1990
3. Barkakati, N. The Waite Group's QuickC Bible. Indianapolis, IN: Howard W. Sams & Company; 1989
4. Chow, C.-Y. An Introduction to Computational Fluid Mechanics. Boulder, CO: Seminole Publishing Company; 1983
5. Kuethe, A. M. and Chow, C.-Y. Foundations of Aerodynamics: Bases of Aerodynamic Design. 4th ed. New York, NY: John Wiley & Sons; 1986
6. Granger, R. A. Fluid Mechanics. New York, NY: CBS Collge Publishing; 1985
7. Currie, I. G. Fundamental Mechanics of Fluids. New York, NY: McGraw-Hill Publishing Company; 1974

**THE TRAVELING SALESMAN PROBLEM
A PARALLEL BRANCH AND BOUND SOLUTION**

Tracy Orton (Mid-America Nazarene College)

and

Lan Tran (Rockhurst College)

ABSTRACT

A book published in Germany in 1852 said of the successful traveling salesman: "The most important aspect is to cover as many locations as possible without visiting the same location twice." This quote is the earliest mention of the "Traveling Salesman Problem" (TSP). There are many algorithms to solve the TSP, the one we implemented was the Branch and Bound algorithm. The TSP graph G is completely connected by a set of edges E , with a non-negative cost C_{ij} associated with each edge. A tour of the graph is a cycle containing all vertices once and only once, starting and ending at the same vertex. A graph with N vertices has $(N-1)!$ possible tours through the graph. A 50 city graph would require 10^{17} years to solve on a computer running at 10^7 additions per second.

The Branch and Bound algorithm consists of starting at a given vertex and calculating the cost of the edge from V to all of the other vertices in the graph. There are three main heuristics that describe how to choose the next vertex in the cycle, they are breadth-first, depth-first, and best-first; we implemented the best-first algorithm.

To implement the B&B algorithm in parallel, we used a distributed list, with and without load balancing. In the distributed list algorithm, the supervisor creates N initial nodes and sends them to the N workers, where N is the number of processors. Each worker has its own separate list. A worker expands the nodes from its list. It also puts the children back on the same list. When a worker finds a new best cost, it updates its best cost and broadcasts the new best to others. Each worker will stop when its list is empty. The algorithm terminates when all the workers have finished.

In the load balancing algorithm, we used the nearest neighbor method. The worker asks its nearest neighbors for work when it is finished. The neighbors then share their loads with the requester.

Our results were not quite what we had expected. The best speed up that we accomplished was 1.56 times when we increase the number of processors from 2 to 4. This is less than the ideal 2.0. In other cases, we did not achieve much speed up. When increasing the number of processors from 2 to 16, we only achieve 2.6 times speed up, which is much less than the expected 8.0.

THE TRAVELING SALESMAN PROBLEM
A PARALLEL BRANCH AND BOUND SOLUTION

Our project was to solve the Traveling Salesman Problem (TSP) using the Branch and Bound heuristic. We implemented this heuristic on a iPSC/2 Hypercube using a distributed list, and distributed list with load balancing.

The term "Traveling Salesman Problem" arose in mathematical circles in the early 1930's. The TSP is the problem of a salesman visiting all the cities in his route once and only once while minimizing the cost by taking the shortest route possible.

In 1954, the paper "Solution of a Large-Scale Traveling Salesman Problem" in the *Journal of the Operational Research of America* by Dantzig, Fulkerson, and Johnson was a major event in the study of combinatorial optimization. The authors proposed an algorithm to solve a large TSP (42 cities), but they refused to claim the credit it.

Mathematically speaking, the TSP graph G is completely connected by a set of edges E with every vertex V is connected to every other. There is a non-negative cost C_{ij} to connect each pair of vertices with $C_{ij} = \infty$. A tour of G is a cycle that includes each vertex once and only once and ends up where it started. The cost of a tour is the sum of the edges in the tour. To find the optimal tour one must minimize the cost while still maintaining a complete tour. The mathematical expressions for the TSP are as follow:

$$\sum_{i \in V} \sum_{j \in V} C_{ij} X_{ij}$$

Subject to the constraints of no subtours and only visiting each city only once.

$$\sum_{j \in V} X_{ij} = 1 \text{ for every } i \in V \text{ and } \sum_{i \in V} X_{ij} = 1 \text{ for every } j \in V$$

$$\sum_{i \in S} \sum_{j \in V-S} X_{ij} \geq 1 \text{ for all } S \in V, S \neq \emptyset$$

$$X_{ij} = 0 \text{ or } 1 \text{ for every } i, j \in V$$

Where $X_{ij} = 1$ if the path from vertex i to vertex j is included in the solution and $X_{ij} = 0$ if not.

The TSP is part of the NP-hard class of problems for which for all known algorithms require exponential time as the problem grows. There are $(N-1)!$ possible solution to a N city TSP. The time to find all possible solutions to a 50 city problem and add up all the costs of all the tours, would require 10^{67} years to solve on a computer running at 10^9 additions per second [3]. This is, however, only the worst case, which is extremely rare.

THE BRANCH AND BOUND HEURISTIC

Since it is impractical to solve the TSP by examining every possible solution, heuristics have been developed. The TSP has been solved using Neural Networks and Simulated Annealing, but the most popular approach is Branch and Bound (B&B).

The origins of B&B go back to Dantzig, Fulkerson, and Johnson when they attempted to solve the 42-city TSP. The basic concept in B&B is to breakup (branch) the feasible-solution-set into successively smaller subsets, then calculate the bounds (lowest cost) for those subsets. Using the newly found lowest cost we can discard all the subsets that have greater cost. This branching and bounding process forms a "Branch and Bound" tree. This tree has the original set as its root. When the root is branched, it produces subsets or children. As the process continues, the tree is further expanded.

Generally speaking, the Branch and Bound heuristic consists of 3 main parts: selecting, branching, and bounding. When branching, the B&B tree produces many children (or nodes). We need a method to select which node is to be expanded. The popular methods are best-first, depth-first, and breadth-first. Best-first selects the node that has the lowest cost. Depth-first selects the node that is at the highest level of the B&B tree. Breadth-first selects the node that is at the lowest level of the tree. In this project, we used the best-first method.

Once a node is selected, it is branched into many children. Branching is accomplished by incrementing the number of cities in a given path. For example, in a 50 city problem, the path of the root has only 1 city: city number 1. Since it is possible to travel from city 1 to 49 other cities, we can branch the root by creating 49 other nodes going from city 1 to city 2, 1 to 3, 1 to 4 and so on.... When we finish branching the root, we should have 49 children.

After branching a node, we have to find its bound. This bounding process consists of 2 parts: solve the relaxation problem and prune the B&B tree. In the beginning of B&B, we set the best cost (the bound) to infinity. We then "relax" the TSP by allowing subtours in a path (a path that has a subtour contains a city more than once). Fortunately, the relaxation problem of the TSP is the Assignment Problem, which is easy to solve and requires less time than the TSP. The solution for the Assignment Problem is the lowest cost path for a given node. If the returned path is NOT a tour (i.e., it has sub-tour) and its cost is less than the current best cost, we store it in a list for later expansion. If the path IS a tour and its cost is less than the cost of the current best cost, we have found a new best cost. If neither of the above conditions is met, we discard the node. Once we obtain a new best cost, we go back to the list and remove the nodes that have greater cost. This is called pruning the tree.

IMPLEMENTATION OF B&B ON THE iPSC/2 HYPERCUBE

There are two popular ways to implement B&B on the hypercube: the centralized list and the distributed list. The centralized list has a controller and $(N-1)$ workers, where N is the number of processors on the hypercube. The controller keeps the list of the nodes to be expanded. It sends each worker a node to expand. The worker expands the node and returns the children to the controller. If a worker finds a new best cost, it broadcasts this cost to all processors. When all the nodes are expanded, the current best cost is the solution.

Since the centralized list has already been done by others, we will only use the distributed list. Unlike the centralized list, the supervisor of the distributed list (not the controller) creates N initial nodes and sends them to the N workers. Each worker has its own separate list. A worker expands the nodes from its list and puts the children back on the same list. When a worker finds a new best cost, it updates its best cost and broadcasts the new best cost to others. Each worker will stop when its list is empty. The algorithm terminates when all workers have finished.

The distributed list is quite easy to implement, however, it has a problem: A worker may finish expanding its list after a few expansions, while others may have to work much longer. Since the speed of the algorithm is measured by the speed of the slowest worker, this can be disastrous. The way to eliminate this problem is to use load balancing: Share the load among the workers until all are finished. In this project, we used the load balancing algorithm suggested by Ma, et al, [2]. When a worker is finished, it sends requesting messages to all processors. If others have work to share, they will share their works with the requester. Each processor keeps track of its neighbors' condition. If the request message is denied (no work to share), the processor will mark the denying process as finished. When all processors are marked as finished, the final processor will terminate itself. We made a minor change in Ma's algorithm. Instead of sending requesting messages to all of its neighbors, a processor only sends request messages to its nearest neighbors according to the hypercube architecture. For example, if the dimension of the hypercube is 2, which means the 4 processors are arranged in a rectangular configuration with the vertices in the order of 0, 1, 3, 2. Processor 0's neighbors are 1 and 2. The threshold index, the minimum length of the list when a processor ignoring its neighbors' request, is set a 4. When a processor receives a work request from its neighbor, if it has more than 4 nodes, it send $(\text{length}/(\text{dim}+1))$ nodes to the requester, where length is the length of the list and dim is the dimension of the iPSC/2. By changing Ma's technique, we reduce the number of requesting messages and allow a processor more working time.

RESULTS

The results are not what we had expected. Ideally speaking, when we increase the number of processors, the run time should decrease linearly. In other words, we should achieve linear speed up. The best speed up that we obtained from the distributed list, when we increase the number of processors from 2 to 4, is 1.58. This is less than the 2.0 expected, but it is acceptable. However, when we increase the number of the processor from 2 to 16, the best speed up we obtained was 2.6, which was much less than the linear speed up of 8.0. In some cases, the run time increases as the number of processors increases! The results from the distributed list and the distributed list with load balancing are essentially the same (see table 1 and table 2). Theoretically, they should be different. We suspect that this problem is the result of the matrices that were used. For each problem we used 10 matrices. These matrices were generated randomly (using the random function provided by the C math library). We take the average the run times at the end. Observing the run times of a problem, we discover that some matrice has very long run time while others have relatively short run time. In taking the average run times, one long run time can distort the entire set of data. We believe that we need better random matrices to achieve better results.

Table 1

DISTRIBUTED LIST WITHOUT LOAD BALANCING

Number of Cities	Dim	Run_time (sec)	Worker Efficiency	Nodes Expanded
10 cities	1	1.176	0.6758	89
	2	0.652	0.5169	77
	3	0.503	0.4678	81
	4	0.451	0.6651	94
20 cities	1	34.060	0.8345	305
	2	17.886	0.7106	299
	3	17.890	0.5249	371
	4	19.920	0.5010	599
30 cities	1	64.810	0.8421	140
	2	52.030	0.7277	179
	3	135.780	0.5724	980
	4	141.960	0.4460	1692
40 cities	1	59.040	0.8444	117
	2	47.770	0.7153	149
	3	41.370	0.5473	228
	4	63.554	0.6024	322
50 cities	1	146.050	0.8700	279
	2	85.070	0.7185	365
	3	87.000	0.3475	317
	4	78.240	0.4308	323

Table 2

DISTRIBUTED LIST WITH LOAD BALANCING

Number of cities	Dim	Run_Time (in sec)	Worker Efficiency	Nodes expanded
20 cities	1	43.2490	0.7664	414
	2	34.3096	0.7200	514
	3	25.5300	0.5318	509
	4	20.9656	0.5626	550
30 cities	1	288.3795	0.8547	480
	2	224.9050	0.6927	876
	3	230.2425	0.4897	1638
	4	130.7876	0.5503	2722
40 cities	1	119.1140	0.8117	242
	2	84.5110	0.5232	241
	3	94.9791	0.3856	298
	4	75.7183	0.3789	345
50 cities	1	168.9500	0.7905	379
	2	206.4330	0.5737	695
	3	210.5000	0.4245	835
	4	150.2670	0.2553	837

REFERENCES

- [1] Lawler, et al, editor. The Traveling Salesman Problem.
John Wiley & Sons, New York, 1985.
- [2] Ma, et al. "A dynamic Load Balancer for a Parallel Branch
and Bound." Third Conference on Hypercube Concurrent
Computers and Applications, the Association for
Computing Machinery, 1988, pp 1505-1513.
- [3] Rottman, Mike. A Parallel Implementation of the Traveling
Salesman Problem. Air Force Institute of Technology,
- Wright-Patterson AFB, Ohio, 1989.

Session III:

Improving the Interface Between People and Technology

Identity Authentication Based on Keystroke Latencies Using Neural Networks

*Angela Lammers, Rockhurst College
and
Sharon Langenfeld, Briar Cliff*

Most computer security systems verify the identity of a user through objects in the user's possession such as keys or magnetic cards, or through knowledge the user has, such as a password or PIN number. There are, however, two other methods of user verification, which have as yet received little or no attention. There has been some work done on the third method, recognition of physiological patterns (such as finger prints, retinal patterns, or voice patterns), but this work has been limited and requires expensive hardware to implement. The final method of user verification is through actions such as signature or behavior patterns.

Because each person's signature is unique, it has been used for verification and authentication since man learned to write. This uniqueness is due to the complex physiology of the human hand. The factors that make the human signature characteristic of a single person, also produce a unique pattern of latency times (or time lapsed between keystrokes). It has been shown that this pattern remains fairly constant, especially within words often entered [Joyce & Gupta].

Some work has been done on the use of keystroke latency patterns for user identification and verification. The majority of the systems involve the entry of a particular string several times initially in order to form a mean reference signature of latency times. The standard deviation of this reference signature was used as a measure of tolerance for each login attempt. When a person wants access to the system, he identifies himself by typing his password. The latency vector this produces is compared to the reference signature entered previously, and access is granted if the two are statistically similar [Joyce & Gupta].

Our system makes use of neural networks rather than statistical references in order to classify login attempts as acceptable or non-acceptable. Rather than performing a sequential set of instructions, neural networks are capable of exploring many competing hypotheses in parallel. Because of this quality, neural networks are considered to have the greatest potential in the area of pattern recognition [Lippmann]. The neural network we have developed is trained to recognize a person's unique keystroke latency pattern and will accept or reject subsequent login attempts based on the attempt's approximation of the previously learned pattern.

Inherent in the system is the desire to maximize the number of times the correct user is accepted (called a user success) and the number of times an intruder is rejected (called an intruder failure). At the same time it is desirable to minimize the number of times the correct user is rejected (a false alarm) and the number of times an intruder is allowed access to the system (a break-in).

To make the system more robust, multiple neural networks are trained and tested. One

neural network is located at each processor, thus parallelizing the learning and testing. Each processor or neural network receives its own unique initial weight vector which is produced by a random number generator. The neural networks are trained on the inputs and each ends up with its own unique learned weight vector depicting the user's signature.

The first step involves educating the neural networks by entering a password string many times and teaching each neural network to recognize the string. As the string is typed in repeatedly, the system records the time between keystrokes. These times are used to train the neural networks, one located at each processor of the system, to recognize the latency pattern.

Neural networks learn the electronic signature of the user by adapting the set of weights associated with the input until the result is within a desired range [fig. 1]. The initial weights are obtained through a random number generator. After the learning has taken place, these weights represent the digital signature of the user.

Each neural network learns by taking the inputs (the array of latency times) and multiplying each of the elements of the time vector by its associated weight vector and summing:

$$R = \sum X_i W_i$$

where R is the result, X the input vector, and W is the weight associated with the input [fig. 2].

If the result of the summation converges to 1 (the desired output), then the neural network is said to have learned the inputs. The network converges due to adjusting the weights of the neural net and sending the inputs back through the network again.

The weights are adjusted accordingly: The error ϵ is calculated by subtracting the result obtained (R) from 1 (the desired result):

$$\epsilon_i = 1 - R$$

The change in weight W is then found using the equation:

$$\Delta W_i = a\epsilon(X_i - \epsilon W_i)$$

This function is a variation of the Hebbian rule:

Our function has some interesting properties including:

1. It looks like a Hebbian algorithm with error instead of output.

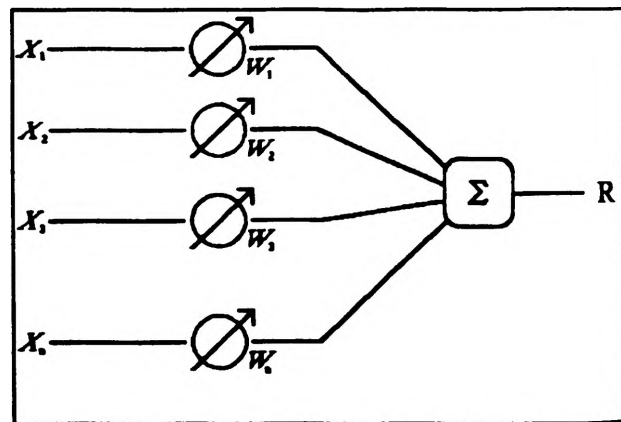


Figure 1

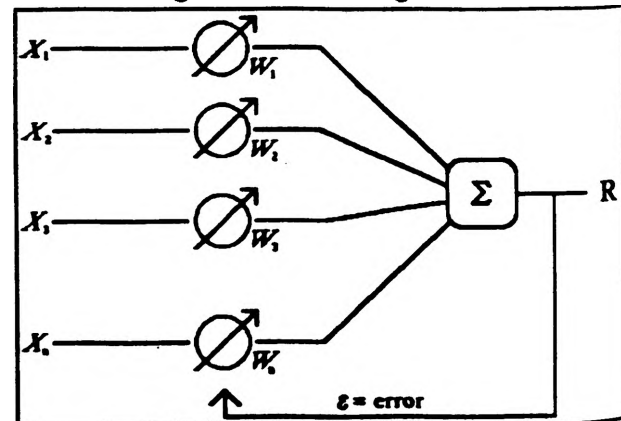


Figure 2

$$\Delta W_i = a \epsilon X_i$$

2. It reduces weights and keeps them from growing too large.
3. It controls excessive jumps in response to the error.

We found our function caused the output to converge to the desired output (1) rather quickly.

Once the networks have learned the user's signature, the program requests attempts for access to the system. Each attempt is taken as input to each of the trained neural networks. The inputs are multiplied by the learned weights and summed to produce a result. If the result of an individual network falls within the allowed acceptance range, the processor sends a message of acceptance back to the controller. If the majority of the processors accept the signature, the user is granted access to the system and the attempt is integrated into all the networks. If there is not a majority acceptance, the user is denied access and the attempt is discarded.

In the experimentation with the program, many parameters were varied. First, the size of the acceptance range and the size of the password were tested. Not surprisingly, using small passwords (3 characters in length) and a small acceptance range (.90 to 1.10) rendered the most break-ins and the most false alarms. Meanwhile, using medium sized passwords (7 characters in length) and a bigger acceptance range (.85 to 1.15) yielded the same number of break-ins, but fewer false alarms. Using big passwords (9 characters in length) and a small acceptance range (.90 to 1.10) produced no break-ins, but incurred the greatest number of false alarms. The best alternative was a medium sized password (7 characters in length) and a small acceptance range (.90 to 1.10) This combination provided few break-ins and even fewer false alarms.

Next, the use of input to the system was altered. Originally, the neural networks were trained on five separate inputs from the user -- one after the other. This, however, invoked the problem of an inaccurate digital signature if the last password entered was not indicative of the user because of a pause or slip during entry. Because the last entry was learned most recently, the neural network looked for the inaccurate pattern during the attempt stage. Therefore, the average of the inputs was used as a basis for training the neural networks. Not surprisingly, the average of the inputs produced more user successes than did the sequential learning of the individual passwords, while maintaining the same number of break-ins.

Finally, the function in the learning algorithm was altered. Using a linear function:

$$R = \sum X_i W_i$$

where R is the result, X is the input vector, and W is the weight vector, provided 10% more user successes than did the nonlinear function:

$$R = \sum X_i^2 W_i$$

where the input vector was squared before being normalized. Altering the function type had no effect upon the number of break-ins incurred: as user successes increased, false alarms decreased.

Therefore, the best combination of the parameters tested are: taking the average of the inputs of medium sized passwords trained on neural networks containing a linear function and

tested in a small acceptance range. Figure 3 shows the number of user successes, intruder failures, false alarms, and break-ins for each of the four program types we tested (sequential inputs with a linear function, sequential inputs with a nonlinear function, averaged inputs with a linear function, and averaged inputs with a nonlinear function). Tests shown were conducted with mid-sized password and small acceptance range. Our tests overall produced a 75% success rate (user successes and intruder failures). Of the 25% failure rate, only 3% were due to break-ins. (22% were due to false alarms.)

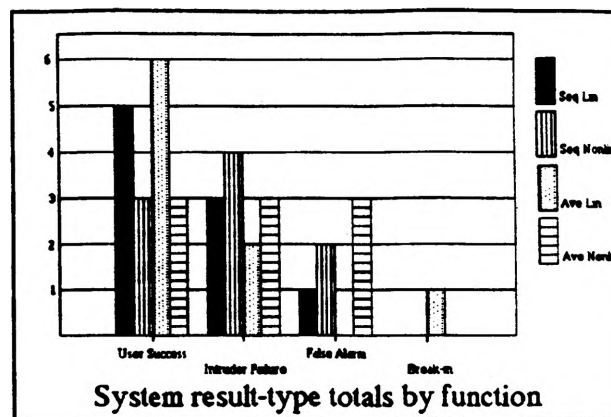


Figure 3

From our results we are able to conclude that keystroke latency is a valid measure of security when implemented with password checking and other common security measures. Neural networks not only make the implementation of the keystroke latency security system easier, but also grow and adapt with each user--thus making them superior to statistical keystroke security systems by increasing the flexibility of the system. Parallelizing the system makes it more robust than when implemented on a single processor since more than one neural net is trained and tested on each input.

REFERENCES

- Joyce, Rick and Gopal Gupta, "Identity Authentication Based on Keystroke Latencies", *Communications of the ACM* 33 (2) (Feb '90) 168-176.
- Lippmann, Richard P., "An Introduction to Computing with Neural Nets", *IEEE ASSP Magazine* (Apr '87) 4-22.

MODEL CALCULATIONAL APPROACH TO THE CONFORMATION OF ADSORBED POLYPEPTIDE FRAGMENTS

Timothy J. McKeon

Introduction

The focus of the paper is to examine possible conformational changes of peptides when placed in the presence of a poly-synthetic material. A major concern in the pharmaceutical industry is the loss of potency of polypeptide drug products during processing, packaging and storage. An example of this is polymer syringes being used in place of glass ones. The effect is that some protein-derived products experience structural changes due to contact with the polymer. This is otherwise known as surface denaturation. In order to understand the energetics of interfacial polypeptide systems, a calculational approach was used via the program Alchemy. The organization of this paper is as follows: first, is the manner in which the peptide bonds are arranged and the ways in which they were synthesized on the computer screen and shown in three dimensional space. Ideas incorporated into the "experiments" will follow. In conclusion, a comparison of the stable structures to those in the model interfacial systems will be given. If these experiments can be shown to give reasonable results this setup could potentially save time and money, and further be used in the development and understanding of potential laboratory experiments.

Background

In discussing this project and its concepts it is necessary to have a basic working knowledge of the peptide nomenclature. Polypeptide structures generally have four types of structures, primary, secondary, tertiary and quaternary. In this paper, the secondary structure is the most significant. The secondary structure or conformation has three specific subgroups within it, alpha-helical, beta-sheet and random coil structures. These structures become stable due to the internal hydrogen bonding. In setting up the model molecules bond angle information was needed. More specifically what was discovered is that the two main structures of interest alpha-helix and beta-sheet were described in terms of torsion angles. The peptide bond is often considered to be planar which infers that the HNCO atoms all lie within the same plain. Then, came the more difficult task of defining phi and psi, the torsion angles on either side of the peptide bond. These can be more fully explained by referring to Figures 1 and 2, in which phi is described as the rotation of the the HN bond about the NC bond with respect to CC' bond. Psi however resides on the other side of the peptide bond, and is rotation of the NC bond about the CC' bond with respect to the OC' bond. Where C refers to the alpha-carbon with the R group attached to it, and C' is the carbon double bond oxygen. These angles are said to be zero when the molecule was flat and the bonds on each end of the torsion angle are in a cis configuration.¹ In other papers x-ray data had been used to determine regions of stability and the phi and psi angles that corresponded to these low energy states. These stable regions can be seen in Figure 3.²

The modeling package being used to complete the calculations and minimum energy state determinations is Alchemy. Alchemy contains programs for some good "hands on structure building" and the minimizer program which were the two main features which brought it to be the package of choice. Alchemy takes into account all the energies in the molecules from bond energies to van der Waal effects. The equation used by Alchemy for the total energy is $E = E_{str} + E_{eng} + E_{str} + E_{vdw} + E_{cop}$ where the subscripts describe the energies considered as follows:

str - bond stretching
 ang - angle bending
 tor - torsion deformation
 vdw - van der Waal's interactions
 oop - out-of-plane bending

The bond stretching and angle bending are self-explanatory. The torsion deformation is the moving of a torsion angle away from the zero torsion angle. The van der Waal's interactions are the attractions and repulsions between two atoms in a molecule as determined by their atomic radius, the distance between them and any charge they might contain. This includes bonded and nonbonded atoms within the molecule. Out-of-plane bending is the term that takes into account the interactions of perimeter atoms attached to a central atom, this includes sp^2 and aromatic atoms in which a modification to the equation is used. In the case of sp^3 atoms, the plane refers to the trigonal base opposite the atom in question. For the latter cases the out-of-plane distance refers to the distance from the base line between the two adjacent atoms.³

Experimental Design

In experimental design the idea was to choose appropriate molecules such that the experiments could be easily visualized and manipulated, since some of the concepts were very complicated. Also, there was some need to attempt to keep the experiment relevant to a process environment. With this in mind, the two polymers chosen for study were polyethylene and polyvinylalcohol. Since, many of today's storage media are polymeric materials rather than glass these seemed to be good choices. They were simple structures and both hydrophilic and nonhydrophilic interactions could be studied. The peptide chosen was glycine, since it had the simplest R group side chain. At times the pictures become confusing and difficult to understand, so it was necessary to use one that was simple in the beginning.

The alpha-helix that was used is a right hand structure and if it had chiral centers would be an L-amino acid, as these are more common. From figure as described above stable angles of phi and psi equal to 120 degrees. This structure was built as well as the structures for the polymers and each was minimized individually. Then, each of the polymers was placed in the presence of the alpha-helix and these were each minimized.

Results

	E(kcal/mol)	E_{str}	E_{ang}	E_{tor}	$E_{oop}E_{vdw}$
alpha-helix alone	23.48	3.09	9.40	48.11	.3287-37.45
ethylene	12.44	4.05	9.97	48.46	.4135-50.46
alcohol	26.83	7.03	20.0	56.17	.2544-56.61

The overall energy of the alpha-helix and polyvinylalcohol system is slightly higher than the alpha-helix alone, and the alpha-helix and polyethylene system is by far the lowest. The alpha-helix and polyvinylalcohol system has the largest potential for intermolecular interactions as reflected by the large E_{ang} of 20 kcal/mol as opposed to 9-10 kcal/mol for the other 2 systems.

Conclusions and Future Work

From the data obtained it can be seen that there is a significant difference in the overall energy of the molecules in the different systems. It can be seen also from Figures 3, 4, and 5 that there is a difference in the structure from the initial alpha-helix consisting of bond angles of 120 degrees for phi and psi. The angles varied in some instances by as much as 20 degrees. The low value for E in the polyethylene system shows that adsorption would be probable. Since the

major influencing factor is the large value with respect to E_{vdw} , while the other values are essentially the same as those in the single molecule system. The slight difference in overall energies of polyvinylalcohol/alpha-helix systems shows that there would be none, or maybe slight adsorption.

In the future these ideas will hopefully be carried on and the systems under consideration will become more realistic. There is another system to be considered called Sybil which is more accurate and could possibly handle larger systems. Another consideration is certainly the dynamics of such a system, how long does it take for this change to occur. In the future this could hopefully provide insight without the loss of costly chemicals and/or time.

References

1. "A Proposal of Standard Conventions and Nomenclature for the Description of Polypeptide Conformations"; *Biopolymers*; Vol. 4, 1966; pp. 121-130
2. Walton, A. G. and Blackwell, J.; *Biopolymers*; Academic Press, 1973; New York; pp. 34-37
3. *Alchemy Handbook*

TOP OF PAGE
LETTER RIGHT
 ϕ , phi
3/2/11
L configuration

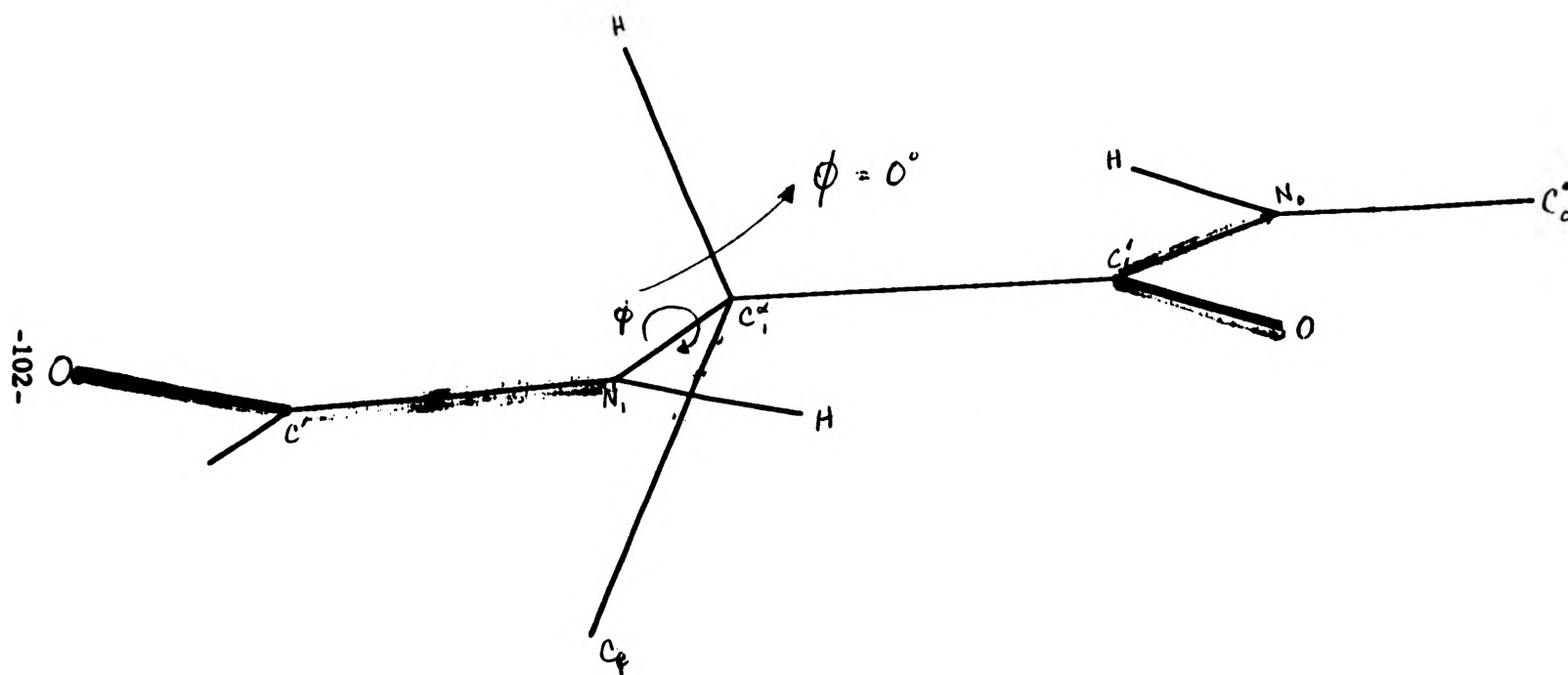


Figure 1: Torsion Angle, ϕ , when equal to zero degrees

TOP OF PAGE
UPPER RIGHT

ψ , psi

2/26/91

L configuration.

-103-

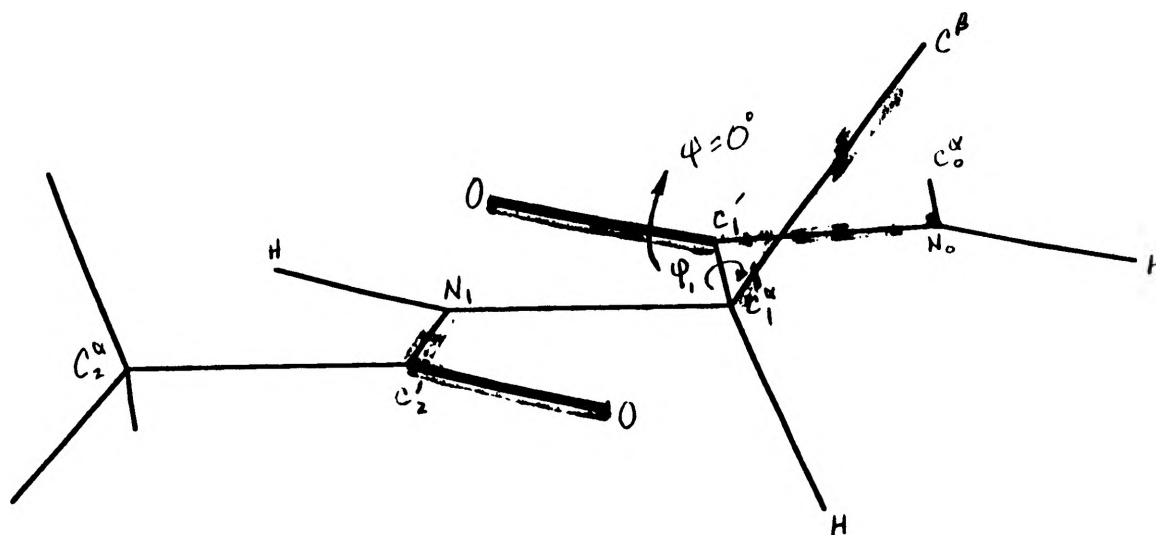


Figure 2: Torsion Angle, ψ , when equal to zero degrees

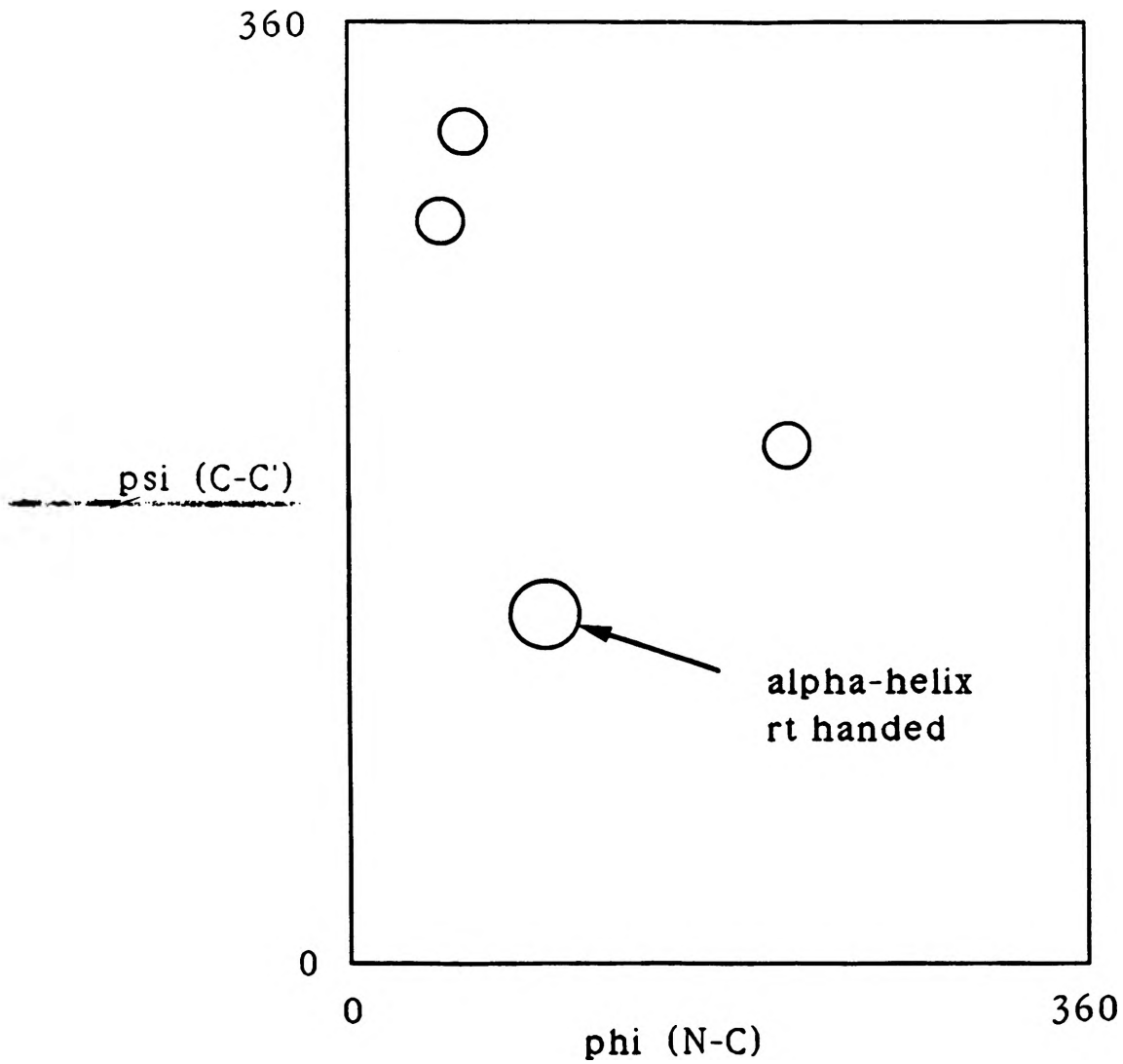


Figure 3: Stable regions for phi and psi angles

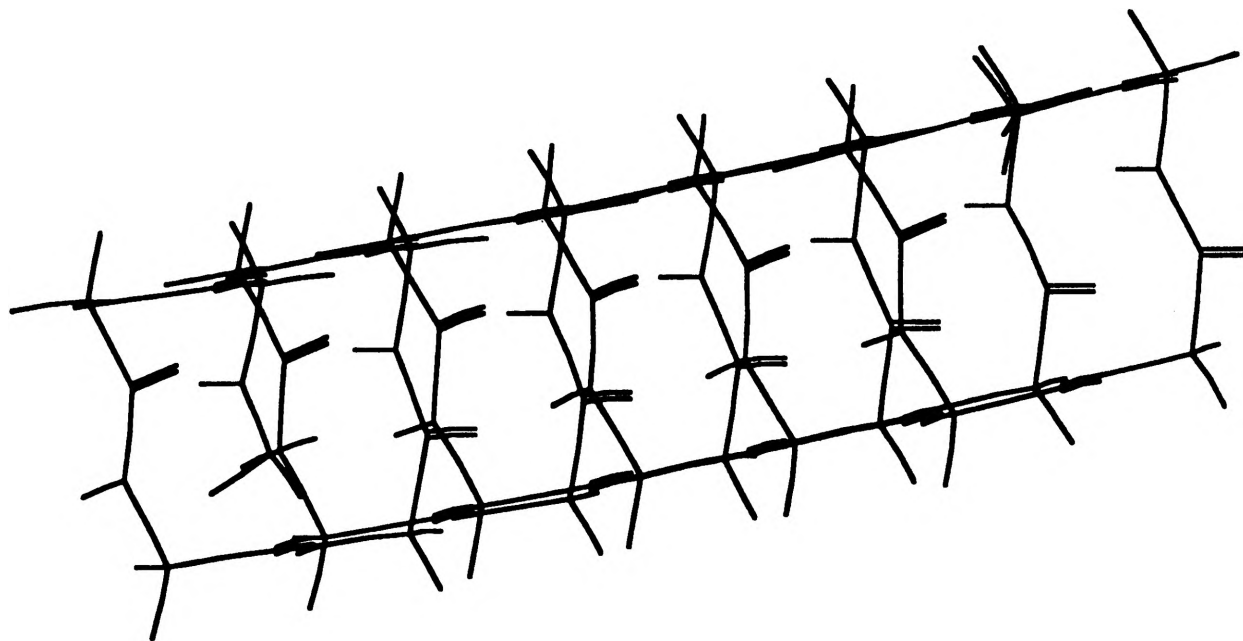


Figure 4: α -helix molecule, right handed $\phi = \psi = 120^\circ$

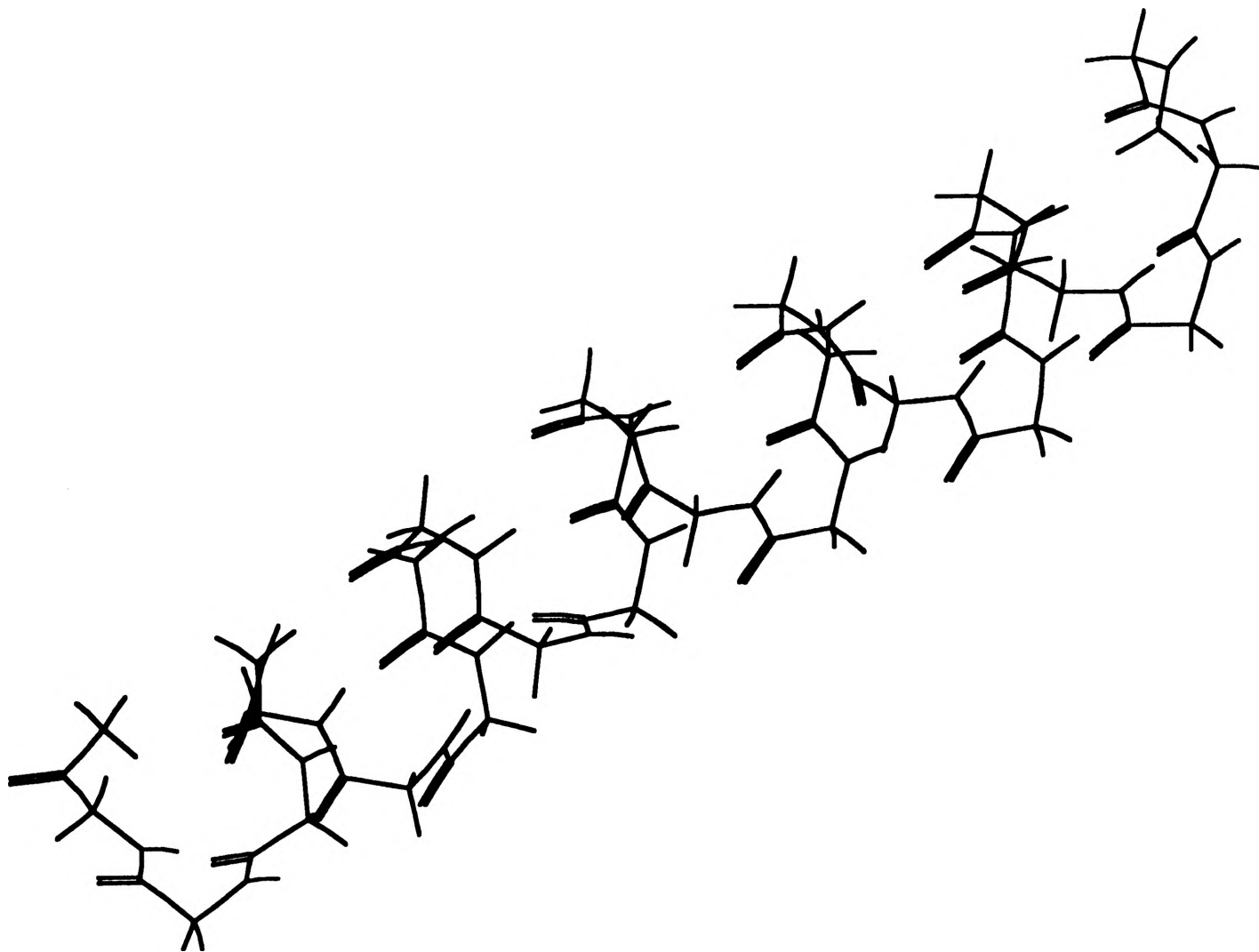


Figure 5: α -helix, right handed, after minimization in presence of polyvinyl alcohol.

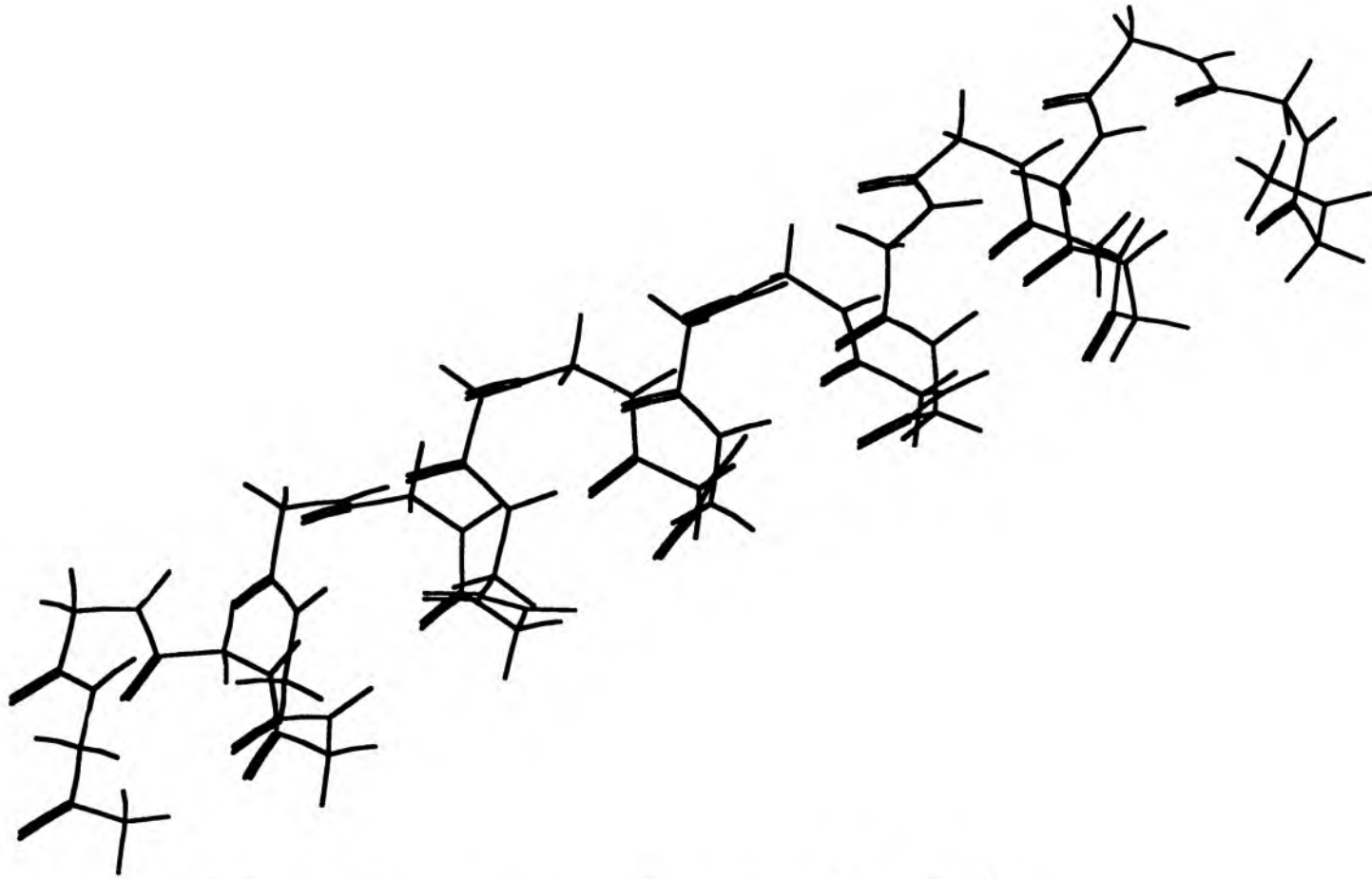


Figure 6 : α - helix, right handed , after
minimization in presence of polyethylene

Development of a Learjet Model 24D for the UMR Flight Simulator

Richard Stigall

**Department of Mechanical and Aerospace Engineering
and Engineering Mechanics**

ABSTRACT

A flight simulator was recently developed at the University of Missouri-Rolla for a single engine aircraft. The need soon arose for a higher performance aircraft. After exploring several possibilities, a Learjet Model 24D was chosen to include the high performance aircraft.

The purpose of this project was to develop a model for the Learjet 24D. This was accomplished by examining the computer code previously written and determining the changes needed. The code for the simulation is located in various subroutines. Each subroutine was analyzed to determine if changes needed to be made. When a modification was needed, appropriate methods were used to determine the parameter. When this process was complete, the aircraft was flown on the simulator. Each flight was used to analyze the performance of the aircraft and then compared to the Operating Manual for the Learjet. After evaluating the performance of the flights, changes were again made to meet the performance of the Learjet. Several assumptions were made in this process with the end justification being the performance of the simulation. The completed Learjet model has produced a simulation which flies much like the actual aircraft.

This report will outline the steps employed to develop the Learjet model, the assumptions made, and the results of evaluating the model performance.

1. Introduction

Flight Simulation is becoming an increasing alternative to the high cost of aircraft operational costs, and is being used by industry to train new pilots, refresh veteran pilots, and train emergency techniques that are too dangerous to perform in actual operations. For university students, the flight simulator can be used as an inexpensive and safe way to teach the basic principles of piloting an aircraft, as well as to reinforce principles of performance and stability & control learned in the classroom. Based on these motivations a set of computer programs, written in Fortran and run on an Apollo DN10000VS computer were developed. The Apollo computer is capable of operating at speeds which allow the simulation to occur in real time. The simulator setup is designed to receive input from the pilot through a keyboard, mouse, and joystick and display graphics output to the user via a 10 foot projection screen and a computer terminal. The computer terminal is used to display a basic instrument cluster consisting of five instruments and sixteen text outputs. The instruments include an airspeed indicator, an artificial horizon, a clock, a

vertical compass, and a vertical speed indicator. The text instruments are capable of being changed to read practically anything the pilot desires to see.

The flight simulator was originally developed modeling a single engine propeller driven Cessna 210. The need for a high performance aircraft was considered and found to be an appropriate addition to the simulator. Work began in January 1990 on the modeling of a small business jet. After looking at several aircraft, a Learjet Model 24D was chosen to fulfill the role.

2. Simulation Process

As shown in the block diagram of Figure 1, the simulation begins by accessing shared memory. Shared memory access prepares the shared memory between the aircraft and graphics programs for parallel processing. The next step in the simulation is initializing the timing mechanism, which defines the rate at which the simulation is ran. Aero_Load and Atmos_Load subroutines initialize variables needed in the simulation. Aero_Load loads the lift, drag, and moment data tables, and Atmos_Load loads the standard atmosphere tables. Table_prep prepares these tables for the simulator to use.

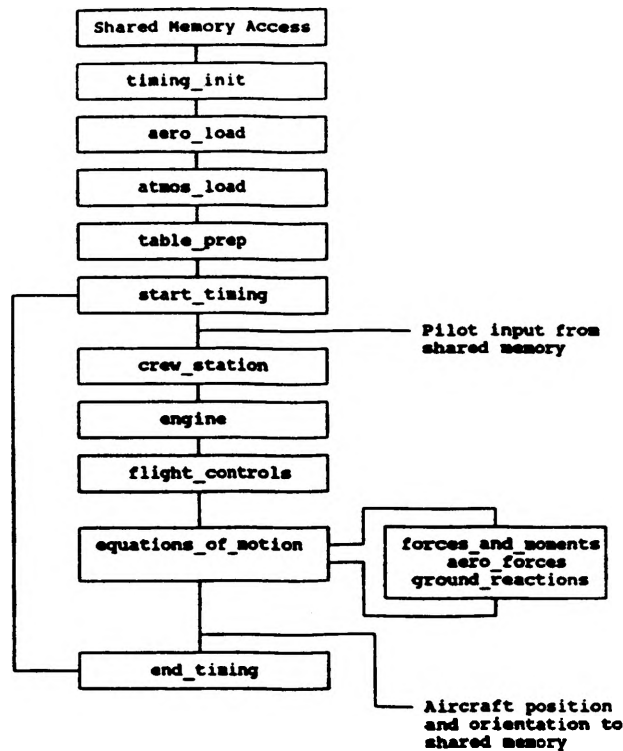


Figure 1. Simulation Process Flowchart

The real-time portion of the simulation is begun with the `start_timing` block. A real-time process is one in which the execution time of the computer is synchronized with the actual time of the system being modeled. If the computer calculates all the information needed it must wait until the next pass is required. This process is accomplished in the timing mechanism of the program.

The pilot inputs generated by the stick, mouse, and keyboard are supplied to the shared memory. According to this pilot input data, the subroutine `Crew_station` then calculates stick, throttle, rudder pedal, and flap switch position. The engine subroutine is then called to calculate the engine thrust based on throttle position and altitude. The flight controls subroutine then calculates the aileron, rudder, elevator, and flap positions. The next subroutine called is equations of motion, which then calls `Ac_forces_and_moments` to determine the total forces and moments acting on the aircraft. This subroutine then calls the `aero` subroutine to calculate the aerodynamic forces and moments. `Ac_forces_and_moments` also calls the ground reactions subroutine which calculates the forces due to inertia, friction, braking, and nose wheel steering while the aircraft is on the ground. Once these subroutines have been called, the equations of motion subroutine integrates the angular and linear acceleration equations once to yield linear and angular velocities and again to yield positions and orientations. The velocities and orientations are then sent to shared memory for use by the graphics to update the visual displays. End timing determines whether it is time to begin a new pass through the simulation. This process is then repeated until the pilot elects to stop the simulation.

This brief review of the flight simulation should be enough to give a basic understanding of how the simulator operates. It is not the purpose of this report to outline the entire operation of the flight simulator. For additional details, the reader may refer to [1].

3. The Learjet Model 24D

The Learjet is designed to carry 8-10 people, cruise at Mach numbers around 0.8, Velocities around 470 knots, and at altitudes up to 45,000 feet. There is a single low wing which is swept back to allow operation at high speeds. The aircraft is equipped with two engines mounted on the aft fuselage, each capable of producing 2,950 pounds of thrust at sea level. The total amount of fuel carried is approximately 5,590 pounds. With full fuel the aircraft has a maximum takeoff weight of 13,000 pounds. The jet incorporates conventional control surfaces: ailerons, elevator, and a rudder. Flaps can be used to aid in takeoff and landing.

4. Modifications

4.1 Stability and Control Derivatives

Stability derivatives are changes in aerodynamic forces or moments due to motion about one of the aircraft axes. Several of the derivatives for this simulation were obtained from

[2], many of these are located in a namelist called `s_and_c.nml` in the `Learjet_data` directory. For this simulation many of the stability derivatives were assumed to be constant over the range of speeds and weights the aircraft will operate. This assumption is justified in part by the fact that many of the derivatives change very little throughout the flight envelope. The derivatives, which do change, were taken as the values at the high speed end of the flight envelope. This was done in part because this is where the majority of the simulation time will be spent. Normally the aircraft will takeoff then cruise at speeds where the derivatives are correct. Another reason for choosing the high speed derivatives was the handling qualities of the aircraft. At high speeds the plane became hard to control if the low speed values were used.

Some of the derivatives are located in the `aero` subroutine. These derivatives are changed through each pass of the simulation. One major difference in the Learjet model and the Cessna model is the coefficient of lift. The Cessna model uses table lookups to determine this value, but the Learjet model calculates the value. All equations for modifications came from either [3] or [4].

Another difference between the two models is the moment curve slope. The slope for this simulation is allowed to change with a change in the center of gravity location. At stall, a decrease in lift should cause a pitching down of the nose. Since the lift and moments are calculated separately, the decrease in lift near stall did not directly cause a nose down pitching moment. To overcome this problem a new variable, `cm_stall` was selected. Below stall, `cm_stall` equals zero, but at stall and above, `cm_stall` takes on a value to cause the needed moment to pitch the nose down.

4.2 Control Surfaces

The Learjet has a movable horizontal stabilizer which is used to trim the plane. The input for this horizontal stabilizer deflection is located in the `Cst.sub` subroutine. The movable horizontal stabilizer allows the pilot to fly the simulator without constantly holding the stick forward, which is what would have to be done when flying at high speed. The trim tab was developed for the Learjet, but was also installed on the Cessna model. The keys to activate the trim tab are: 'u' for nose down, 'j' to zero the tab, and 'm' for nose up. The variable introduced to accomplish this task was called `delta_tab`. The deflection of `delta_tab` is limited to five degrees up and down.

The actual control surface deflections are calculated in the flight controls subroutine, `Fc.sub`. The Learjet has different ranges of control surface deflections than the Cessna so all these had to be changed. The deflections are: aileron 18 degrees, elevator 15 degrees, and rudder 30 degrees, these deflections were obtained from [6]. The flap operating speeds are also located in this subroutine. The flaps are extended by two settings. The maximum speed to extend the flaps to eight degrees is 190 knots, the maximum speed to extend the flaps to 40 degrees is 153 knots.

To ease the pilot in controlling the aircraft with the small joystick at high speeds, the elevator and aileron deflections are scaled above 200 knots by the ratio of the aircraft

velocity to 200 knots. A similar equation is used for `delta_a`, the aileron deflection.

4.3 Forces and Moments

Forces and moments are dealt with in `f_m.sub` and `ground.sub`. `F_m.sub` contains the equations that compute the forces and moments while the aircraft is in the air. Two values that had to be changed in this subroutine were the maximum structural g's the aircraft could withstand. The values from [5] are +4.5 to -1.5 g's. These values were not used in the simulation due to the joystick. The joystick is so sensitive that at high speeds with the low values of g limitation the wings were to easily torn off. For this reason slightly higher values of +5 to -2 were chosen.

Several other values that had to be changed in this subroutine dealt with geometric distances involving the landing gear. A drawing of the meaning of the geometric data can be found in [1]. The geometric distances for the Learjet were obtained from [6]. Some of these distances include the x, y, and z positions of the gear fully retracted and fully extended. These distances are needed to perform the simulation of the gear being raised and lowered. The gear in the Cessna move in two motions, first moving in, then back to stow in the fuselage. The gear on the Learjet only move up into the wings so this process had to be changed.

The ground subroutine contains the forces acting on the aircraft when the aircraft is on the ground. Several variables in this subroutine had to be modified. There are some geometric distances in this subroutine as well as `f_m.sub`, which had to be changed. The damping coefficients and the spring constants of the landing gear had to be modified. Two values of each constant were used, one for small displacements of the struts and one for larger displacements. These values were determined by trial and error. The values had to be larger for this aircraft, but care had to be taken in raising them.

4.4 Additional Modifications

The weight and balance subroutine contains information about the loading of the aircraft and the moments of inertia. The aircraft for this simulation is loaded with 4 people, 414 gallons of fuel, and 50 pounds of baggage. This brings the takeoff weight to 11000 pounds, which would be a typical configuration for this aircraft. Provisions have been made to easily modify the weight by simply choosing a different passenger loading. The center of gravity is also calculated in this subroutine. The `ac_moment` needed for the center of gravity calculation is acquired by adding the weights of different components multiplied by there moment arm. The weights of the components as well as the moment arms are listed in [5]. The moments of inertia were obtained from [2].

The engine subroutine contains the equation for thrust. The method used for determining thrust assumes that the thrust of the engines varies directly with air density. This subroutine was changed to reflect the Learjets more powerful engines.

The instrument panel for a Learjet is much different than a Cessna's, so two instruments

were changed. The airspeed indicator for the Cessna went to 200 knots, the maximum speed of the Learjet is much faster, so the airspeed was increased to 600 knots. The code for the airspeed indicator is located in the instruments directory in the file airspeed.ftn. Similar adjustments for the vertical speed indicator were also performed. The Cessna vertical speed indicator range was between -2000 feet per minute and 2000 feet per minute, this was changed to ± 6000 feet per minute. All the other instruments were compatible with the Learjet.

Another modification made to the simulator was not specific to the Learjet model. A new scene was created. For details on how to create a new scene, see [7]. The scene created was a night scene, which included a lighted runway and lighted cities.

5. Results

The purpose of this project was to create a model of the Learjet for the existing simulator at UMR. The justification for all the changes made, rested in the final performance of the simulation. The main analysis for the results came from flying the aircraft and checking the performance against the Operating Handbook, [5]. Several phases of flight were evaluated in great detail. These were takeoff, cruise, landing, and flight at slow speeds, including the stall. Final flight tests indicated the simulation performs very close to the actual aircraft. A table of comparisons between actual and simulation performance numbers appears below.

Table I
Results

Performance Parameters	Flight Manual	Simulation Results
takeoff speed (knots)	115	118
takeoff ground roll (feet)	2250	2050
maximum Mach number	0.82	0.82
landing ground roll (feet)	1500	1450
stall speed, flaps at 0° (knots)	107.0	110.0
stall speed, flaps at 8° (knots)	95.0	93.0
stall speed, flaps at 40° (knots)	86.0	83.0
climb gradient at 10000 feet (%)	3.2	3.3
climb gradient at 20000 feet (%)	0.5	0.55

6. Conclusions and Recommendations

The purpose of this project was to modify existing code to perform similar to a high performance aircraft, the aircraft chosen was the Learjet Model 24D. Steps were taken to

analyze and determine the changes needed in the original code, then obtain new information for the simulator by various methods. The performance of the aircraft was then compared with the Operating Manual. Once the performance tests were completed, changes were made to correct the simulation to more closely match the performance numbers in the Manual. Final flight tests indicate a very good simulation of a high performance aircraft has been developed. In the future, this simulation will be used with the other models currently in the simulator to benefit all Aerospace Engineering students at the University of Missouri-Rolla.

The simulation could be greatly improved with the addition of a cockpit and real controls. The joystick does not provide the feel of an actual control stick. The rudder controls are currently on the keyboard, which does not allow the pilot of feeling the position of the rudder. With the addition of a cockpit, a q-feel system could be incorporated into the model. Q-feel is a system by which the velocity of the aircraft is felt in the controls. As it is now, the pilot can move the stick as easily at 500 knots as can be done at 100 knots, which is not the case in an aircraft. The cockpit would also give more of an impression of flying, than is currently felt with the simulation.

One of the most important uses for the simulator could be the simulation of aircraft being designed in the senior design class. With the aid of this paper and reference [8] it should be a fairly simple task to modify the code to fit a generic model. This would benefit the design students, and offer something that very few, if any other university could offer a senior design student.

Acknowledgements

I would like to thank Mike Sinnett and Randy Johnson for providing help in the beginning of the project, Marcus Adkins also helped in programming and final evaluation. The support by the OURE program is also greatly acknowledged.

References

- [1] M. K. Sinnett. "The Development of a Real-Time Digital Flight Simulator on the Apollo DN10000VS." M. S. Thesis: Department of Mechanical and Aerospace Engineering and Engineering Mechanics. Univ. of Missouri-Rolla, 1990.
- [2] J. Roskam. "Airplane Flight Dynamics and Automatic Flight Controls." Roskam Aviation and Engineering Corporation, Ottawa, Kansas, 1982.
- [3] B. Etkin. "Dynamics of Flight—Stability and Control." New York: John Wiley & Sons, Inc., 1982.
- [4] McDonnell Douglas Corporation, Douglas Aircraft Division. "United States Air Force Stability and Control DATCOM." Long Beach, California: Douglas Aircraft Division, 1978.

- [5] **Gates Learjet Corporation. "Gates Learjet 24D Flight Manual." Wichita, Kansas: Gates Learjet Corporation, 1983.**
- [6] **Gates Learjet Corporation. "Gates Learjet General Information." Wichita, Kansas: Gates Learjet Corporation, 1983.**
- [7] **M. S. Adkins. "Scene Creation Manual for the UMR Flight Simulator." Internal Report, Department of Mechanical and Aerospace Engineering and Engineering Mechanics. Univ. of Missouri-Rolla, 1991.**
- [8] **R. A. Stigall. "Development of a Learjet Model 24D for the UMR Flight Simulator." Honors Paper: Department of Mechanical and Aerospace Engineering and Engineering Mechanics. University of Missouri-Rolla, 1991.**

DEVELOPMENT OF A LARGE COMMERCIAL TRANSPORT MODEL FOR A REAL-TIME DIGITAL FLIGHT SIMULATOR

John Francis Winkler

Abstract

In order to test the adaptability of the University of Missouri-Rolla's flight simulator to different types of aircraft, a basic mathematical model of a large commercial transport aircraft is developed. The original aircraft model is based on the Cessna 210, and in order to accommodate the drastic differences between the Cessna 210 and the Boeing 747, many changes are made to the simulation code. The aircraft geometric data, stability and control derivatives, and weights data are altered to match those of the 747. Changes are made within the various subroutines to include thrust reversal, spoilers, and a variable incidence horizontal stabilizer. In order to simplify the model, various modifications to the 747's lift, moment, and drag data are made based on an order of magnitude analysis.

This paper gives an overview of the procedure used in creating the new mathematical model and the various problems encountered during the model's implementation. The various assumptions that are made to simplify the modeling of the transport aircraft and the reasoning behind each assumption are discussed in detail. Finally, the flight characteristics of the developed model are compared with those of a real-world aircraft to determine the validity of the model.

It appears from flight testing that the final model does indeed offer the flight characteristics of a large transport aircraft.

Introduction

Recent rises in fuel costs make the need for practical and realistic flight simulation extremely important. With a well-designed flight simulator, industry can train pilots on the ground, thereby saving flight time and fuel. An engineer can model a slight configuration change on an aircraft and immediately see its effects on the flight characteristics. Moreover, by changing the magnitude of the stability and control derivatives, one may be able to see the difference in the handling of the aircraft. Large aerospace companies are currently using advanced flight simulators to optimize the flight characteristics of an aircraft in the initial design stage. In this sense, they may eliminate a large number of problems before the aircraft is ever built. Test pilots are now finding that the test aircraft are flying very close to the simulator model on which they were trained.

The University of Missouri-Rolla flight simulator project was started in 1987 by graduate student Michael Sinnett, and a mathematical model of a Cessna 210 general aviation type aircraft was completed in 1989. The computer code for the simulator is written in FORTRAN and runs on an Apollo 10000vs workstation. The program itself is divided into two major routines: the math model and the graphics model. Each model runs on a different central processing unit, and they communicate with one another through a shared memory location. An instruments program runs interactively with the math model and graphics model on an Apollo 4500 workstation. The graphics are displayed on a 10' diagonal glass screen with an overhead rear projector. At this time the pilot input is read in through the use of a joystick, mouse, and keyboard.

Since the completion of the Cessna model in 1989, new graphic scenes have been added and a weather model containing wind, turbulence, and microbursts was developed to enhance

the realism of the simulation.⁶ Furthermore, an interest has come about in being able to develop mathematical models for different types of aircraft.

The purpose of this project was to develop a mathematical model of a large commercial transport type aircraft for the digital flight simulator at the University of Missouri-Rolla. The large transport aircraft model is based on the Boeing 747, and it is clearly apparent that this aircraft is much different and much more complex than the Cessna 210. Many changes had to be made to the Cessna model to accommodate the drastic differences between the two aircraft.

This report discusses the differences between the Cessna 210 and the Boeing 747 and the changes that have to be made to model the 747 properly, and it gives a very basic overview of the various problems encountered during the model's implementation. The various assumptions that are made to simplify the modeling of the transport aircraft and the reasoning behind each assumption are discussed in detail. Finally, the flight characteristics of the developed model are compared with those of a real-world aircraft to determine the validity of the model.

Problem Formulation

As it was previously mentioned, UMR's flight simulator was originally designed to model a Cessna 210 general aviation aircraft. The Cessna is a fairly simple plane driven by a single Propeller engine, and it contains only the basic required control surfaces (Figure 1). Ailerons are used for roll control; simple flaps are used to augment the lift, and a basic elevator and rudder are used for pitch and yaw control, respectively. Moreover, this aircraft flies in the low subsonic flight regime where lift, drag, and moment calculations are relatively simple to perform.

The Boeing 747, however, is a very large and complicated jet aircraft (See Figure 2). It is Propelled by 4 turbofan engines, and it contains numerous control surfaces. Outboard ailerons are used for low-speed roll control while inboard ailerons are used for high-speed roll control. The flap system on the 747 is very complicated, containing a combination of leading edge Krueger flaps and triple-slotted trailing edge flaps which can be used together to augment the lift. This larger aircraft also possesses inboard and outboard elevators for pitch control along with a split rudder for yaw control at different speeds. The flight envelope of the 747 is much greater, as it may fly at altitudes up to 45000 feet above sea level and at speeds around 800 nautical miles per hour. Its maximum cruise speed lies within the transonic regime, and therefore supersonic pockets may form on the wings, complicating lift, drag, and moment calculations.

Although the simulator was originally written in a fairly general format, it is easy to see that several changes and additions will have to be made to model the more complex Boeing 747 aircraft. It should be noted here that the original intent of this project was to model a large commercial transport based on the 747, and hence the final developed model was not intended to behave exactly like the Boeing aircraft. Nevertheless, many changes still had to be made in order to develop a simplified generic commercial aircraft.

Modeling Data and Table Lookups

The original Cessna model only has a few different table lookups due to the lack of a large amount of information, as it is very difficult to get companies to release detailed and accurate information pertaining to the lift, drag, and moments acting on their aircraft. Therefore the Cessna model has only four one-dimensional lookups to determine the atmospheric temperature based on altitude, the atmospheric density based on altitude, the change in the zero-lift pitching moment due to flap deflection, and the ground effect on drag based on

the height above the ground. It also has two three-dimensional lookups to determine the lift coefficient and drag coefficient based on angle of attack, flap deflection, and Mach number.

Lack of data was not a problem for the commercial transport model, as Boeing¹ provided the same data that its engineers initially used to model the 747 in a NASA simulator. Lift, drag, moment, and ground effect data are all given in graphical form. This graphical data was employed to generate tables that can be utilized by the computer code. The procedure for creating tables of data from graphical data was used to create tables for the lift, drag, and moment coefficients as functions of angle of attack and Mach number and as functions of angle of attack and flap deflection.

All in all, the commercial transport model contains the original one dimensional lookups to determine the atmospheric temperature and pressure based on altitude, and 10 two-dimensional lookups to determine the values of the above variables. This extra data involved setting up new variable arrays and adding them to the common blocks in the subroutines. The data tables and new variable arrays can be seen in the Subroutine Aero-load. found in Winkler.¹¹

Aircraft Geometry Changes

The areas and dimensions of the aircraft were taken from Boeing,² stored in a data file, and read into a menu structure. These values may be changed within the menu substructure to see the effect on the flight characteristics of the aircraft, but the default values may always be restored from the data file.

Weight Properties

Aircraft Weight and Balance

The maximum takeoff weight for a Boeing 747 aircraft varies anywhere from 620000 lb to 820000 lb depending on the model and configuration (See Janes⁹). A value of 660000 lb was chosen for simulation use. In reality, this weight would depend on the number of passengers, the amount of payload, and the amount of fuel. Moreover, over a long range flight, the weight of the aircraft would vary as fuel is used up.

For simulator purposes, however, the weight is assumed to remain constant throughout the flight time. One will normally not be flying the simulator for a long period of time that will cause the weight to change substantially. For short flight times on the order of an hour or so, this kind of assumption appears to be relatively valid.

According to Boeing,¹ the center of gravity (cg) may vary anywhere from about 14% of the mean aerodynamic chord to about 33% of the mean aerodynamic chord. The center of gravity will depend on the number and positioning of passengers, the amount and location of payload, and the amount and location of fuel.

The simulation of the commercial aircraft assumes the cg to remain constant at 25% of the mean aerodynamic chord, which is 1250 inches from the nose of the aircraft (See Boeing²). Again, one will probably not be flying the simulator for a long period of time, and hence the weight and location of the fuel will not change drastically enough to warrant changing the aircraft cg. Moreover, it can be assumed with reasonable accuracy that the majority of the passengers will remain in their seats during the flight and hence the cg will remain relatively constant.

Aircraft Moments of Inertia

The aircraft moments of inertia are required by the simulation to integrate the equations of motion. The values of I_{xx} , I_{yy} , I_{zz} , and I_{xz} will change with the weight distribution of the aircraft. For the Cessna model, it was a valid assumption to make $I_{xz} = 0$, but because of size of the 747 and the nonsymmetrical weight distribution in its xz plane, this is not true for the 747. Values of the moments of inertia for landing gear up and landing gear down were obtained from Roskam.⁷

Stability and Control Derivatives

The original Cessna model assumes that the stability and control derivatives remain constant throughout the flight envelope. For the low altitude and low speed envelope of the Cessna 210, this is a reasonable assumption. The 747, however, has a much larger flight envelope; it can cruise at altitudes up to 45000 feet and Mach numbers up to 0.92. Because many of the basic stability and control derivatives are functions of both Mach number and altitude, some way had to be devised to take the compressibility effects into account.

The Cessna 210 is equipped with one set of ailerons, one elevator, and one rudder. Hence, the Cessna model is only set up to model this simple case. The 747, however, is equipped with inboard and outboard ailerons, inboard and outboard elevators, and a split rudder. This is to insure that the aircraft will have good control characteristics over its entire flight regime. At lower speeds, the outboard ailerons are used to roll the aircraft, and at high speeds, the inboard ailerons are used for roll control. The elevators and split rudder are used likewise.

These multiple control surfaces cause their respective control derivatives to vary substantially with velocity. The values of the important stability and control derivatives were obtained from Roskam⁷ for three different flight conditions and can be found in Winkler.¹¹ Each flight condition pertains to a specific velocity. In order to include the effect of these multiple control surfaces, an expression is set up to vary the magnitude of the aileron, elevator, and rudder control derivatives with velocity as per each flight condition. Because the control derivative for the aileron, elevator, and rudder varies automatically with velocity, it is in effect modeling both the inboard and outboard control surfaces. Hence, the single control derivative for the ailerons can be thought of as an average of the control derivatives of the inboard and outboard ailerons, and this removes the requirement of having two separate derivatives – one for the inboard ailerons and one for the outboard ailerons. The same analysis applies to the split rudder and the inboard and outboard elevators.

Aerodynamic Forces and Moments

The original equations for the total lift, drag, and pitching moment coefficients in the Cessna model had to be altered for the commercial transport model because of the different type of data that was obtained from Boeing.¹ The Boeing data was very detailed, and in order to simplify the model, the higher order terms for each force and moment coefficient were thrown out. Because the purpose of this project was to develop a basic model of a commercial transport, neglecting the higher order terms seems to be reasonable. A detailed analysis of the changes made in the calculation of each coefficient is given in Winkler.¹¹

Landing Gear

The original Cessna model uses a simple landing gear setup with one nose gear and two main gear. When retracted, the main gear rotates inward and then backward, and the nose gear rotates forward.

Only the nose gear and the inside back main gear were modeled for the commercial transport aircraft. This simplification was made in order to keep from having to rewrite the entire Ground Subroutine. The aircraft model will still take off and land without problems, and such a simplification does not affect the flight characteristics.

The simulation code was altered slightly to change the rotation of the gear. The nose gear on the 747 rotates backward during retraction while the inside main gear rotate forward. The spring constants and damping coefficients for each set of gear were increased until the gear provided a reasonable response during landing and takeoff (See Winkler¹¹).

VISUAL OUTPUT

The cockpit of the original Cessna model is set about 3 feet above the ground; the Boeing 747 cockpit, however, is about 27 feet above the ground, and therefore the visual output had to be modified. This was accomplished by adding an increment of height to the altitude which is sent to the Graphics Model.

The instruments on the original Cessna model have maximum values that apply to that particular aircraft. The airspeed indicator has a maximum value of 200 knots, while the rate of climb indicator has a maximum value of 200 feet per minute. Since the Boeing 747 can fly at speeds over 500 knots (See Janes⁹) and climb at a maximum rate of 16000 feet per minute (See Boeing¹), the maximum value on the airspeed indicator was therefore changed to 600 knots, and the maximum/minimum values on the rate of climb indicator were changed to 16000 feet per minute.

The original simulation world has several small aviation airports with 2000 foot runways. These runways can easily handle the small Cessna for takeoff and landings, but they realistically cannot handle an aircraft the size of the 747. According to Janes,⁹ a fully loaded 747 may take just over 10000 feet to take off and clear a 36 foot obstacle. In order to compensate for this takeoff distance, a 10000 foot runway was created and placed in a large commercial airport.

Flight Controls

It was desired to employ spoilers, thrust reversal, and a variable incidence stabilizer on the commercial transport model to simulate the 747 more accurately. Changes are therefore made in the Crew Station Subroutine so that a stabilizer switch can be set, thrust reversal can be turned on or off, and spoilers can be deflected or retracted.

Additional code was added to the flight Controls Subroutine so that it can calculate the stabilizer position based on the information calculated in the modified Crew Station Subroutine.

The subroutine checks to see if the flaps are deflected past their maximum value for a given airspeed, and if they are, it automatically retracts them to the next lower setting. The maximum speed for any flap deflection can be found in TWA.³ The Flight Controls Subroutine also keeps the control surfaces from deflecting past their maximum deflections. The maximum values of deflection for the rudder, aileron, and elevator for the 747 were obtained from Boeing¹ and can be found in Winkler,¹¹ along with the previously mentioned subroutines.

Engine Routine

The original engine model is a very simple subroutine which calculates thrust based on throttle position and density. At full throttle setting and sea level, the thrust calculated will

basically be equal to the static sea level thrust of the engine. As altitude increases, the thrust of the engine is decreased by the density ratio factor. For the commercial transport model, a check was added to see if reverse thrust is being employed to slow the aircraft during landing. If so, the sign of the thrust is made negative.

The engine options for the Boeing 747 are numerous, and Janes⁹ lists several different types along with their maximum static sea level thrust. The Rolls-Royce RB211-524D4 engine with a static sea level thrust of 53110 pounds was chosen for the simulation. Hence, with four of these engines, the simulation model is able to develop 212440 pounds of thrust at sea level.

Performance Evaluation

There is really no exact method for evaluating the performance of the commercial transport model on the simulator. It was easy to get a pilot's opinion on the simulator's realism for the Cessna model, as general aviation pilots are numerous and easy to find. Boeing 747 pilots, on the other hand, are too few and extremely hard to find, and there were none available to test the flight characteristics of the simulator model. The model does seem to behave like a large aircraft would, as it appears to react slower than the corresponding Cessna model. The following performance of characteristics of the commercial transport were evaluated and compared with the corresponding characteristics of the Boeing 747.

- **Takeoff Distance** - The takeoff distance obviously varies between the different models of the 747, and it depends immensely on the takeoff weight. According to Janes,⁹ the 747-100B takes 10000 feet to take off and clear a 35 ft high obstacle, while the 747-200 will take as much as 10,800 ft to take off and clear a 35 ft high obstacle, depending on the version. The commercial transport model, with the horizontal stabilizer deflected downward, will lift off before the end of the 10,000 ft runway. The exact ground roll distance depends on the deflection of the stabilizer. The aircraft climbs rather quickly after takeoff, and it therefore will clear a 35 ft high obstacle right around 10000 ft.
- **Maximum level speed** - The maximum level speed for the Boeing 747-100B at an altitude of 80,000 ft above sea level is given by Janes⁹ as 525 knots, and the maximum level speed for the 747-200 ranges from 623 knots to 630 knots, depending on the version. The commercial transport model has shown its capability of reaching a level speed of right around 520 knots at a 30,000 ft altitude.

Concluding Remarks

A simplified model based on Boeing 747 that will give the flight characteristics of a large commercial transport aircraft was developed for the University of Missouri-Rolla flight simulator. This model met the performance characteristics of the 747 with reasonable accuracy.

With this new model, students in aerospace engineering should be able to get a better feeling of how a large commercial transport actually flies through "hands on experience." By using the menu structure, they can change various stability and control derivatives and see what happens to the flight characteristics of the aircraft. Through altering the flight conditions, the students ought to be able to see how varying the altitude, velocity, and weather conditions affect the aircraft's performance. Moreover, with this new model, students could learn more about how and why wind shear has caused various airliner accidents during takeoff and landing.

In the future, if one wanted to change the model from a generic transport model to a more exact representation of the 747, several things could be done. The engine subroutine could be rewritten to calculate thrust as a function of throttle position, Mach number, and altitude. A new subroutine could be written that would calculate the stability derivatives as a function of Mach number and altitude to take compressibility into account, thus bypassing the menu structure. Lastly, one could include the higher order terms that were neglected in the various coefficient calculations. The task of obtaining an exact model of the 747 would take a long time and a lot of hard work, but it may be well worth attempting.

Flight simulation is becoming more and more important as the rising fuel and maintenance costs make actual flight testing of aircraft extremely expensive. The more work that can be accomplished through simulation, the larger the savings will be to industry. The development of flight simulation on the university level is therefore extremely important, as new research may bring forth many advances in the modeling of various aircraft. The advancement and continuation of flight simulation research will clearly benefit not only industry and education, but the entire scientific community.

Acknowledgments

The author would like to thank Doctors Kamran Rohkaz and Fathi Finaish, and graduate student Marcus Adkins for their continued support throughout the project. The grant from OURE is greatly appreciated.

References

1. Boeing. The Simulation of Jumbo Jet Transport Aircraft. Volume 2: Modeling Data. Boeing Company. Wichita. Kansas. Sep 70.
2. Boeing. General Arrangement Model 747P Passenger. Boeing Drawing J5B00090. Revision C. Boeing Company, Renton, Washington, Oct. 67.
3. TWA 747 FLIGHT HANDBOOK. TRANS WORLD AIRLINES. Kansas City. Missouri.
4. Sinnett, M. "The Development of a Real-Time Digital Flight Simulator on the Apollo DN10000VS". M.S. Thesis, University of Missouri-Rolla, 1990.
5. Adkins, M. "Development of a Turbulent Atmospheric Model For An Experimental Flight Simulator." M.S. Thesis. University of Missouri-Rolla, 1990.
6. Sinnett, M. "Notes on UMR's Flight Simulation Facility." Unpublished notes, University of Missouri-Rolla, 1990.
7. Roskam, J. Airplane Flight Dynamics and Automatic Flight Controls. Roskam Aviation and Engineering Corporation. Ottawa. Kansas.
8. Etkin, B. Dynamics of Flight - Stability and Control. New York: John Wiley and Sons, Inc., 1982.
9. Janes. Jane's All The World's Aircraft. Jane's Information Group Limited. Sentinel House, United Kingdom. 1990.
10. Anderson, J. Introduction To Flight. New York: McGraw-Hill Book Company, 1989.
11. Winkler, J. "Development of a Flight Simulation Model for a Large Commercial Transport Aircraft." Department of Mechanical and Aerospace Engineering and Engineering Mechanics, University of Missouri-Rolla, 1991.

UMR
Opportunities for Undergraduate
Research

Papers

SYNTHESIS AND CHARACTERIZATION OF AN 18 MEMBERED MACROCYCLIC LIGAND CONTAINING 2,2'-BIIMIDAZOLE FOR SELECTIVE BINDING OF TRANSITION METAL IONS

Mark Barnett

Abstract

A description of the synthetic approach to the preparation of an 18 membered macrocyclic ligand containing 2,2'-biimidazole is presented. A diol derivative of 2,2'-biimidazole is tosylated with p-toluene sulfonyl chloride making it susceptible to bimolecular substitution with a disodium salt of tetratosylated triethylenetetraamine. The final desired product is an 18N6 macrocycle, 4,7-(1,1'-(2,2'-biimidazolo))-1,4,7,10,13,16-hexaazacyclooctadecane, potentially capable of binding transition metal ions in various combinations with three chelating sites. Initial characterization includes NMR and IR spectroscopic analysis.

Introduction

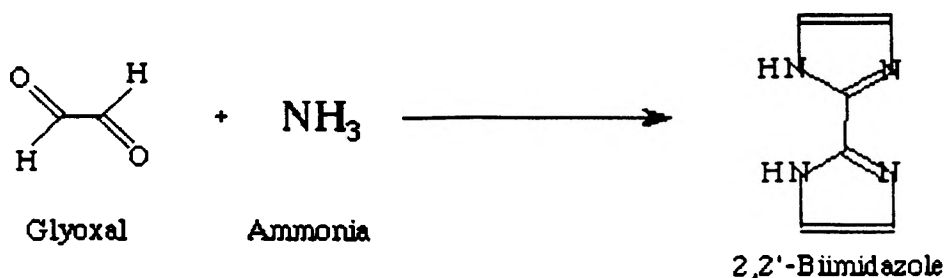
Natural biological chemical systems that contain macrocyclic chemical units can be extremely complicated molecules and characterization to discern their structure and function is very difficult. Thus, whenever possible, it is desirable to chemically prepare and characterize very basic macrocycles as models that may allow understanding the more complex nature of such entities found in naturally occurring species. These models may typically imitate behaviors related to structure, molecular interaction, or chemical reactivity found in natural systems. Studies that are of interest today include reversible reactions with small molecules, such as that demonstrated with reversible dioxygen binding by the heme macrocycle of hemoglobin; roles as active sites in catalytic processes (30% of enzymes contain transition metal complexes of macrocyclic ligands that provide catalytic activity); and selective metal ion binding that is useful in studying chelation processes. The characteristic properties of macrocyclic complexes, i.e., after metal complexation, include marked kinetic inertness, stabilization of high oxidation states of bound metal ions, and high thermodynamic stability.

The goal of this project is to investigate the synthesis of a unique 18-membered macrocyclic ring system containing 2,2'-biimidazole and characterize it via the application of electronic spectral analysis before and after metal ion complexation. The use of electrochemical, elemental, and magnetic characterization methods will ultimately be used to provide a more thorough investigation of this ligand.

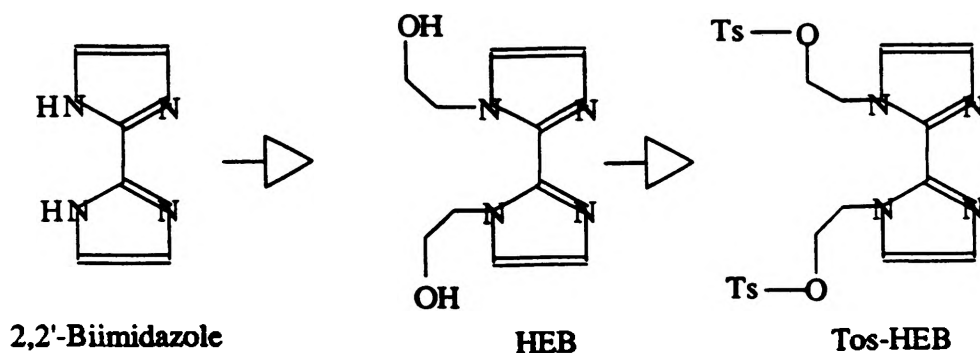
Experimental

Preparation of 1,1'-Dihydroxyethyl-2,2'-biimidazole Ditosylate

The preparation of the macrocycle which this paper describes begins with the synthesis of 2,2'-biimidazole, first reported in 1856 by Debus. The formation of 2,2'-biimidazole is achieved via the exothermic and spontaneous reaction of glyoxal and ammonia. Glyoxal, usually obtained as a 40% solution in water, is added to an equal volume of concentrated aqueous ammonia with constant stirring. The reaction results in a mixture of dark brown liquid and a brown biimidazole precipitate. The solid biimidazole is collected by filtration and recrystallized several times from boiling water producing an off-white or light tan crystalline solid. Typical yields ranged from 10 to 20%.



The biimidazole is then transformed into 1,1'-dihydroxyethyl-2,2'-biimidazole (HEB) by replacing the protons on the nitrogen atoms with hydroxyethyl groups. For this preparation, a 5.0 gram quantity (0.0373 mol) of biimidazole is placed in a three-necked, 500 mL round-bottom flask. A 200 mL portion of ethanol and 50 mL portion of water are added to the flask and slowly heated to 50 degrees C. Then a solution of 5.96 grams of NaOH in 25 mL of water is added to the mixture and stirred for four hours. An additional 2.25 grams (0.017 mol) of biimidazole is added during the first hour. After four hours, 7.34 mL (d-1.201 g/mL, 0.108 mol) of 1-chloro-2-ethanol is carefully added over a one-hour period. The mixture is then neutralized with dilute HCl, roto-evaporated to one-third the initial volume and then filtered. To the collected yellow-orange solution is added successive amounts of acetone followed by azeotropic roto-evaporation of the solvents and filtration to remove precipitated salts. The sample is then dried and redissolved in boiling acetone and filtered again. The acetone solution contained both HEB and mono-HEB (a side product in which only one of the biimidazole protons is substituted with an hydroxyethyl group). This solution is roto-evaporated to approximately one-third its initial volume and allowed to stand at room temperature for several days to permit crystallization of the mono-HEB derivatives. The HEB enriched solution is decanted, leaving the red-orange crystals of mono-HEB behind. Thin layer silica-gel chromatography analysis was used to confirm the purity of the soluble portion obtained. The enriched soluble component can be further purified by a redissolved dried sample in methanol and treating the mixture on a flash chromatographic column. The mono-HEB followed by HEB (distinct yellow band) are eluted using a 3:8:1 solvent mixture of propanol:hexane:ethanol to give a 20-25% yield of the pure HEB derivative.



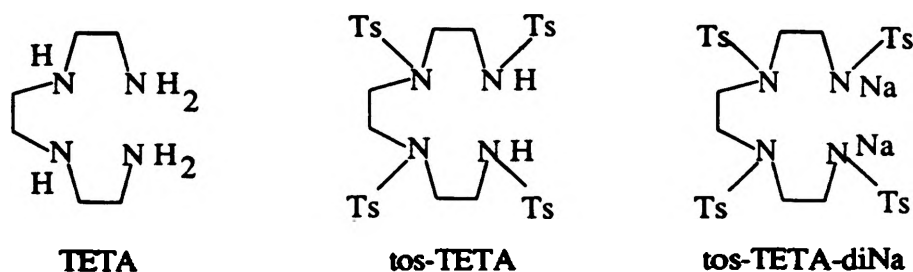
In order to make the diol reactive, it is tosylated with p-toluene sulfonyl chloride. To a chilled solution of 0.2 g HEB (8.8×10^{-4} mol) dissolved in approximately 10 mL pyridine, 0.34 g TsCl (1.76×10^{-3} mol) was added in small portions; the solution was maintained around 20 degrees C, as the reaction is extremely exothermic, giving off HCl which is adsorbed by the pyridine. The resultant solution was stirred for an additional three hours and after unsuccessful attempts to remove the pyridinium hydrochloride, the mixture was allowed to set several days while the solvent evaporated. The reaction went mostly to completion. In this form, the

tosylated HEB is susceptible to bimolecular substitution by strong base, the preparation of which is described next.

Preparation of DiSodium Salt of TetraTosTETA

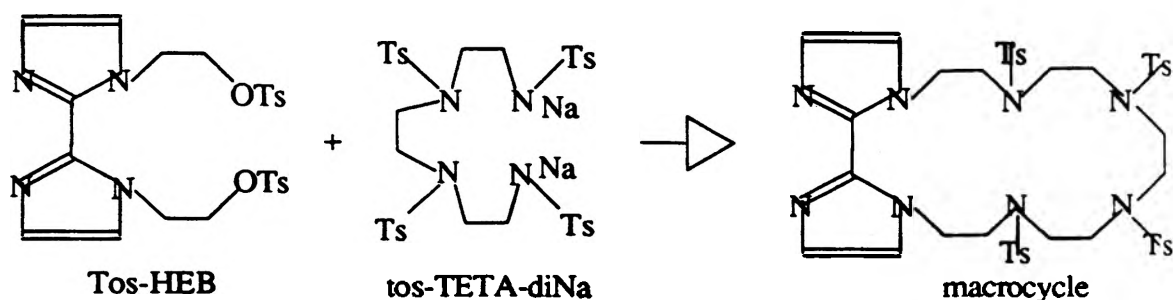
4.4 Grams of triethylenetetraamine (0.03 mol TETA) was dissolved in a solution of 7.2 grams of NaOH in 25 mL water. While this was vigorously stirred, a solution of 22.9 g p-toluene sulfonyl chloride (0.12 mol) dissolved in 60 mL diethyl ether was added dropwise resulting in the white precipitate tetratosylated triethylenetetraamine, tos-TETA, and stirred for one hour. This tosylation was to deter undesired attack on the non-terminating nitrogen atoms. The tos-TETA was washed with ethanol/water, filtered, and dried. The yield was approximately 40%.

86.7 Grams of tos-TETA was refluxed in ethanol for two hours. To this was added dropwise an ethanol solution of sodium (0.63 g Na in 18.25 mL ethanol). The solution was refluxed for an additional two hours, filtered, and the filtrate was rotoevaporated to about half its initial volume. Upon standing a day or two, a white crystalline precipitate formed. The salt was filtered and washed with an ethanol, giving a typical yield of 40%.



Preparation of Macrocycle

The macrocycle is formed by the reaction of the tosylated diol, tos-HEB, and tosylated disodium salt of TETA, tos-TETA-diNa. Each of these materials was dissolved in N,N-dimethylformamide (DMF) to form very dilute solution; 0.62 g tos-HEB (0.0012 mol) in 20 mL DMF was added dropwise over a period of four hours at 110 degrees C to 0.946 g tos-TETA-diNa (0.0012 mol) in 50 mL DMF and stirred for an additional hour. However, it was discovered that this dibase reacted mostly with the troublesome pyridinium hydrochloride to form tos-TETA and NaCl. So, another stoichiometric equivalent of dibase was added under the same conditions to form the macrocycle. The macrocycle is believed to form via a bimolecular nucleophilic substitution, where one end of the base displaces the tosylate, which is an excellent leaving group. The solutions are dilute so as to minimize the possibility of another base molecule substituting the remaining tosylate of the tos-HEB. The other end of the base then displaces the other tosylate leaving group, forming the macrocycle. Most of the DMF was removed by azeotropic distillation with water under reduced pressure using rotoevaporator. In aqueous solution, the unreacted amine becomes insoluble tos-TETA, leaving the macrocycle in solution. Yields are around 20%.



Discussion and Conclusions

Nomenclature

In general, macrocycles are classified according to the size of the ring and number of nitrogen atoms contained in the ring structure. The macrocycle discussed in this paper is an 18N6; the first number represents the number of atoms composing the ring structure, N for nitrogen, and the last number represents the number of nitrogen atoms in the ring. Specifically, the completed macrocycle has the following formal name, in accordance with the nomenclature rules of the Union of International Pure and Applied Chemistry (UIPAC):

4-7-(1,1'-(2,2'-biimidazolo))-1,4,7,10,13,16-hexaazacyclooctadecane

Initial Characterization by NMR and IR

Initial spectroanalysis by proton NMR supports the formation of the tosylated macrocycle; for peak assignments refer to *Table of NMR Assignments* at the end of this paper. Without detosylation, the final macrocycle was complexed with copper (II) chloride resulting in a maize colored material. It was found that the IR peaks of the complexed macrocycle were shifted towards higher energies when compared to the non-complexed material. This evidence indeed, supports the formation of the macrocycle, see *Table of IR Assignments* at the end of this paper.

Future Investigation

Initial evidence supports the formation of the tosylated macrocyclic ligand. The next step is to detosylate and characterize the macrocycle. After this, the ligand will be exposed to a variety of metal cationic salts for binding studies. There are potentially three binding sites in this macrocycle. It is desirable to gain insight as to which chelating cavity is preferred by the metal cation or whether the cavities have priorities for the binding of various metals simultaneously. Ultimately, characterization of this specific macrocycle will not only help us gain insight into more complex naturally occurring macrocycles, but may lead to exciting new applications in microelectronics as a molecular semiconducting material.

Result

<u>Material</u>	<u>Mol. Wt (g/mol)</u>	<u>Exp. Yield</u>	<u>Description</u>
Biimidazole	134.0	20%	Lt tan-off white, crys.
HEB	226.3	20%	Yellow solid (pure)
Tos-HEB	530.5	99%	Yel-brown cryst.
tos-TETA	763.1	38%	White solid
tos-TETA-diNa	807.0	40%	White crys. solid
tos-Macrocyclic	949.1	20%	Pumkin orange residue

Table of IR Assignments

NMR Characterization of 18-Membered Macrocyclic Ligand

<u>Group Assignment</u>	<u>Tos-Mac (ppm)</u>
C-H (Biimidazole)	7.8 - 8.8
Ar-H (Tosyl)	7.2 - 7.7
D2O (solvent)	4.7
C-H (Triene)	3.7 - 4.5
CH3 (Tosyl)	2.3
TMP (zero std)	0.0

IR Characterization of 18-Membered Macrocyclic Ligand and Complexed Ligand

<u>Group Assignment</u>	<u>Frequencies, cm⁻¹</u>	
	<u>Tos-Mac</u>	<u>Complex</u>
S-N (tosyl)	1399	1399
Ar-C-H (tosyl)	3038	3038
para subst Ar (tosyl)	814	814
C=N (biimidazole)	1599 m	1599 vw
C-N (aliph)	1638	1638
C-N (biim)	1668	-
C-H (asym/sym str, triene)	2921	2921
In-plane C-H bend (biim)	1044	1049
Out-of-plane C-H bend (biim)	955	-
Ring Torsional vibr (biim)	683	696

REFERENCES

- Sugimoto, M.; Nonoyama, M.; Ito, T.; Fujita, J. *Inorg. Chem.* **22**, 950 (1983).
- Melloni, P.; Metelli, R.; Bassini, D.; Confalonieri, C.; Logemann, W.; de Carneri, I. *Arzneim-Forsch (Drug Res.)* **25**, Nr.1, 9 (1975).
- Melloni, P.; Bassini, D.; Dradi, E.; Confalonieri, C. *J. of Heter. Cyl. Chem.* **11**, 731 (1974).
- Debus, H. *Ann. Chem.* **607**, 199 (1856).

INFLUENCE OF THE McDOWELL SANITARY LANDFILL ON GROUNDWATER QUALITY, PHELPS COUNTY, MISSOURI

Christine E. Bough

Abstract

This is a case study of the groundwater quality near the McDowell Sanitary Landfill in Phelps County, Missouri. The landfill is located in section 21 of T37N R8W off of Missouri State Highway CC. This landfill is a near surface solid waste disposal facility above the groundwater table located in an abandoned area of a rock quarry. The thickness, lithology, and structure of the material beneath the landfill, and the design of the landfill itself, will influence the time of contaminant transport and degree of modification in the event that leachate escapes the landfill. Among the more important topographic features in Phelps County, Missouri, is the widespread occurrence of karst features, which results from solution and erosion of limestone and dolomite bedrock. Karst features in Phelps County pose a threat to groundwater contamination because of the potential large capacity for open channel flow. There are two major aquifers in Phelps County that could be contaminated by a leaking landfill. These are the Roubidoux Sandstone and the Gunter Member of the Gasconade Dolomite. The Roubidoux Sandstone is the shallowest aquifer and thus is the one that has the highest probability of being contaminated. Based on our Atomic Absorption analysis for calcium, magnesium, sodium, potassium, total iron, and chloride, it was found that the groundwater is not contaminated in Phelps County near the McDowell Sanitary Landfill. These results show that if landfills are properly designed for each hydrogeologic setting, groundwater contamination can be avoided.

Introduction

This report describes the investigation of groundwater quality near the McDowell Sanitary Landfill. The landfill is owned and operated by the Phelps County Landfill Board, which was organized in August 1973 and is comprised of the chief elected official of each city in Phelps County, in addition to the presiding Judge of the Phelps County Court.

Landfills are surface or near surface solid waste disposal facilities above the groundwater table. Soluble substances in the waste material may be gradually removed by solution in percolating waters that originate from precipitation, surface runoff, or addition of fluids to the landfill. These soluble substances, known as leachate, often form a liquid sometimes containing heavy metals and organics. The thickness and character of the unconsolidated deposits beneath a landfill, and the design of the landfill itself, influence the time of waste transport and degree of modification before leachate reaches the water table. Both bedrock lithology and structure may also influence the travel time and chemistry of the leachate.

Leachate reaching the water table tends to maintain its chemical integrity with dilution occurring mainly where it contacts the groundwater. If the leachate escapes the landfill it will move in the direction of groundwater flow as a plume whose shape is determined by the flow characteristics of the aquifer, a geologic unit that supplies water for wells and springs.

This report discusses the general characteristics of the physiography, geology, and groundwater near the landfill site. It also discusses specific details on the groundwater quality of the study area.

Site Description

Location

The landfill is located in Phelps County off of Missouri State Highway CC approximately 2 miles west of U.S. Highway 63 in section 21 T37N R8W. The site is in an abandoned area of a rock quarry on the William McDowell property. The site location is shown in figure 1 below.

McDowell Sanitary

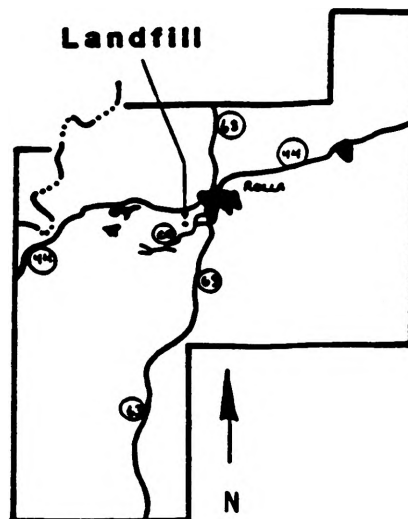


Figure 1. Map of Phelps County Showing Location of Landfill

Physiography

Phelps County lies in the northeastern part of the Salem Plateau section of the Ozark Plateau physiographic province just west of the divide between the Gasconade and Meramec River Basins. The Salem Plateau is underlain by essentially flat Cambrian and Ordovician sandstones, limestones, and dolomites; therefore, the topography of the area is controlled by the stratigraphy.

Topography and Drainage

Among the more important topographic features in the Ozark Region of Missouri is the widespread occurrence of karst features, which result from solution and erosion of limestone and dolomite bedrock. The term karst designates areas characterized by thin clayey soils and bedrock, sinkholes connecting surface and groundwater, caverns and small openings serving as underground conduits, springs bringing groundwater to the land surface, and losing streams transporting water underground. These features form a unique topography with very irregular surface and subsurface drainage patterns. There are no significant springs, caves, or sinkholes in the area that would effect the landfill.

The entire eastern part of Phelps County is deeply dissected by short, abrupt, deeply cut stream channels separated by narrow ridges. The ridge tops are nearly level, continuous, and remarkably uniform in shape. They are covered by residual materials to depths of 30 feet or more. The lowest point in the area, 640 feet above sea level, is at Boulware Ford in the northwest corner of the County, and the highest point, 1244 feet, is Pilot Knob in the southeast quarter. Therefore, the maximum relief of the area is 596 feet. The elevation at the landfill is approximately 980 feet with a slightly rolling topography.

The surface drainage of the area empties into the Gasconade and the Meramec River Basins. The Little Piney Creek, gathering the largest percentage of the Phelps County drainage, flows from the southeastern corner north to the center of Phelps County and then turning west to join the Gasconade River. Several smaller creeks collect the drainage of the southern and eastern parts of the area and flow into the Little Piney Creek. The basin of the Little Piney creek is limited on the north by Pea Ridge which crosses the Phelps County from Rolla to the Gasconade River. The surface drainage from nearby points that are higher than the rim of the landfill was routed around the landfill by diversion ditches to the natural drainageway lying to southwest of the landfill to prevent ponding in the pit. There are no significant creeks or lakes in the area that would have an affect on the landfill.

Climate

Phelps County has a humid climate with relatively mild winters and warm summers. The annual average temperature is 56.2 degrees Fahrenheit. The average temperature for July is 77.8 degrees Fahrenheit and for January is 32.9 degrees Fahrenheit. The average annual precipitation is 39.7 inches per year. See figure 2, a graph of average monthly precipitation values.

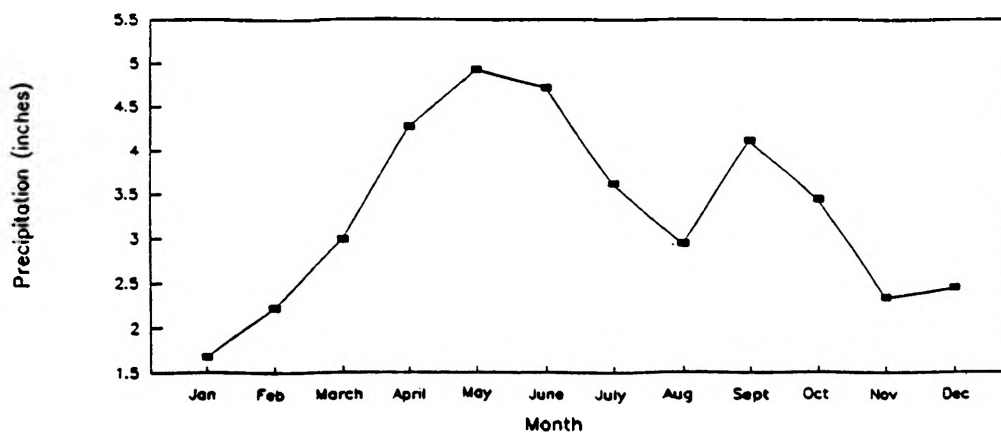


Figure 2. Average Monthly Precipitation (National Weather Service)

Geology

Stratigraphy

All of the stratigraphic units that outcrop in Phelps County are part of the Canadian Series of the Ordovician System. The strata of the Canadian Series in Central Missouri are composed predominantly of arenaceous and cherty dolomite and sandstone. The stratigraphic units will be discussed from youngest (the Jefferson City Formation) to oldest (the Gasconade Formation). See figure 3 for the stratigraphic column, which is a graphical representation of the geologic units discussed here.

The Jefferson City Formation is composed of crystalline dolomite with chert as nodules and lenses. Green shale partings and sand are present along bedding planes but are not subordinate. The dolomite beds are thin except for one, the "Quarry Ledge", which is about 20 feet thick. Much of the dolomite is earthy and weathers to a buff stone locally called, "cotton rock". The Jefferson City forms the tops of the uplands in the Rolla area. It has a thickness ranging from 125 feet to 350 feet. The landfill is located in the Jefferson City Formation.

The Roubidoux Formation consists of three well developed sandstone beds with inter-bedded chert and dolomite. The sandstones tend to form red-stained outcrops and the dolomite dissolves away when weathered. The Roubidoux forms a pronounced upland surface. The thickness of the Roubidoux ranges from 100 to 250 feet.

The Gasconade formation consists of three units: an upper unit of coarsely crystalline dolomite with very small amounts of chert, a middle unit characterized by a cherty horizon, and the lower unit consisting of a basal sandstone, the Gunter Member. The upper unit tends to be cavernous and is readily leached by groundwater. The steep walled valleys of the Gasconade and the Little Piney rivers are developed in this upper portion of the formation. The Gunter Member varies from a sandy dolomite to a true sandstone. The average thickness of the Gasconade formation is 300 feet.

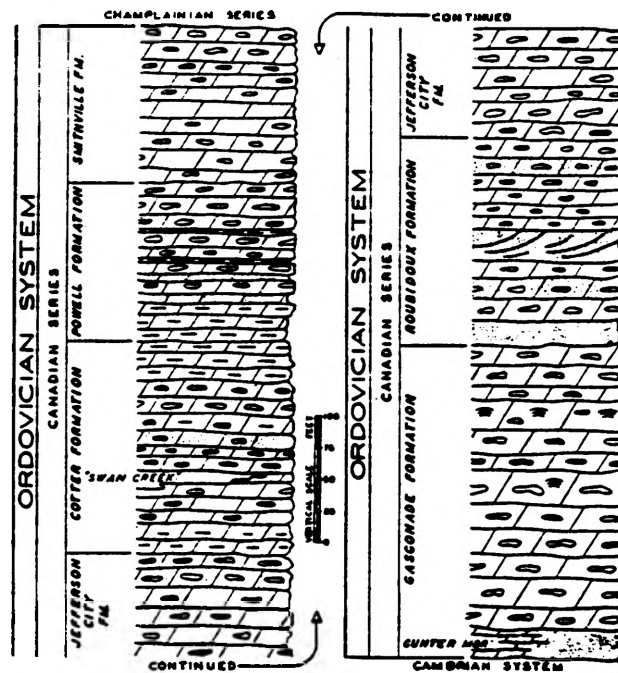


Figure 3. Geologic Units in Phelps County (Howe, 1961).

Structure

Phelps County lies within the stable Mid-Continent area. The dominant structural feature is the Ozark Uplift that is responsible for the uplift of the St. Francois Mountains in southeastern Missouri. There have been at least six mild uplifts since the time of the St. Francois Mountains which are shown by unconformities in the stratigraphic record. The uplift is asymmetrical and dips steeply on the southeast and east into the Illinois Basin.

There has been a considerable amount of faulting and folding associated with the Ozark uplift. However, the strata in Phelps County is relatively flat with only minor faulting occurring. The largest area of faulting occurs in a belt about two miles south of Newburg, Missouri. These faults trend in a northwest - southeast direction. These faults do not appear to affect the hydrology of Phelps County.

A test hole drilled in April 1980 revealed a 17 foot layer of dense dolomite below the floor of the proposed landfill. This thick layer of rock suggests that the landfill should not cause any harmful fracturing to occur that would result in the escape of leachate into the groundwater.

Investigation of Groundwater Quality

Groundwater

Aquifer Characteristics

There are two principle fresh-water aquifers that yield a dependable supply of water in Phelps County. They are the Roubidoux Formation and the Gasconade Formation. See figure 4 for the relationship of the aquifers. The groundwater reservoir in this area consists of a section of more than 2000 feet of Cambrian and OrdoVICIAN dolomite and sandstone. The aquifers will be discussed from youngest to oldest.

System	Series	Formation	Thickness	Lithology	Hydrogeology
Ordovician	Canadian	Cotter Dolomite	55-355	Cherty dolomite	This unit acts as a major aquifer in this area.
		Jefferson City	125-350	Dolomite with chert lenses	
		Roubidoux	100-250	Sandstone and cherty dolomite	Water from this aquifer is a calcium-magnesium bicarbonate type
		Upper Gasconade	40-100	Crystalline dolomite and chert	
		Lower Gasconade Gunter Member	235-320 25-50	Quartzose Sandstone	

Figure 4. Relationship of Aquifers

The Roubidoux formation consists of sandstone, dolomitic sandstone, and cherty dolomite. In central Missouri, the formation consists of sandstone horizons between bedded dolomite and chert. The sandstone is composed of fine to medium grained quartz sand which is characteristically sub-rounded and frosted. The sandstone is, in many places, characterized by well preserved ripple marks, mud-cracks, and cross bedding. The thickness of the Roubidoux ranges from 100 to 250 feet. The Roubidoux produces approximately 20 gallons per minute (gpm), which is enough for ordinary household and small farm use.

The Gasconade dolomite is a light brown to gray, cherty dolomite that averages 300 feet in thickness. The upper 50 to 75 feet is dense crystalline dolomite with very little chert. This dense rock forms a good aquitard. The next 100 to 150 feet consists of fractured chert and dolomite. This zone produces 25 gpm and is an adequate aquifer for small farms and industries when large yields are not required. The City of Rolla utilizes the Gasconade dolomite for part of its municipal water supply.

The Gunter Member, which is the 25 foot thick basal member of the Gasconade Dolomite, is composed of sandstone and sandy dolomite. It is the lower most Ordovician unit in Missouri. The depth to the Gunter Member is about 575 feet in depth at Rolla. This unit produces between 50 and 100 gpm throughout the area.

The Roubidoux formation is the closest aquifer to the Jefferson City Formation in which the landfill is located. The water producing zone lies approximately 165 feet below the bottom of the landfill. Because the Roubidoux Formation is the closest aquifer to the landfill, it has the highest potential for groundwater contamination.

Groundwater Flow

Groundwater, like surface water, flows in a down gradient direction. This down gradient direction of groundwater flow was determined from Water Well Records obtained from the Missouri Geological Survey. This was done to determine the area in which to look for possible groundwater contamination. In general, groundwater flows from wells with a higher static water level than those with a lower static water level.

As one can see from figure 5 the groundwater in Phelps County flows in a southwest direction. This map was created by using static water levels taken from Water Well Records at the Missouri Geological Survey. Once the static water level was obtained each point was given a unique x-y coordinate, with the landfill located at point (12,12), in order to create the 3-D surface map. It is

not only important to know which direction the groundwater is flowing, but also to know at what rate it is flowing. The exact rate at which the groundwater flows in this area was not determined but because of the well developed karst topography it can be assumed to have a high rate of infiltration and flow.

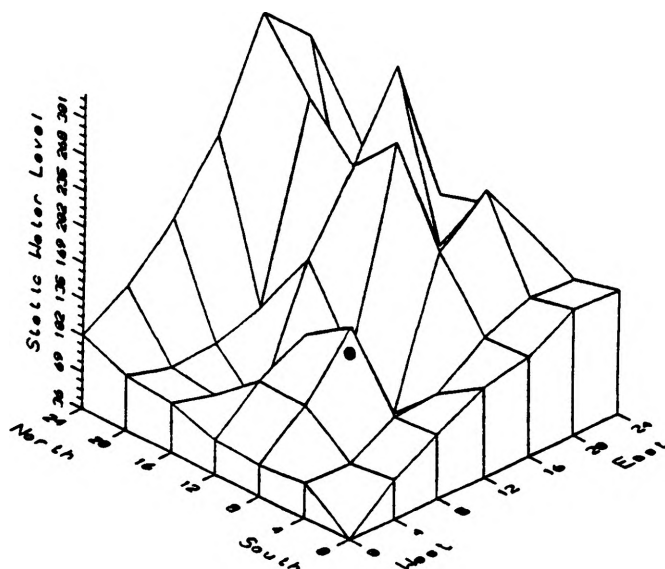


Figure 5. Southwest Direction of Groundwater Flow in Phelps County

Sample Collection and Treatment

Water samples were collected from residential housing and springs within the study area. They will be referred to by either the section number or by the distance and direction from the landfill.

At each site a 1 liter sample was collected directly from an indoor tap in a new sample bottle that had been rinsed in the lab with nitric acid and distilled water. Before a sample was taken the water was run for a period of 5 to 10 minutes and the sample bottle was washed 3 to 5 times. This was done so that the system could be purged of any solid materials that may have precipitated out of solution and settled in the pipes and to avoid metals, for example copper, which might have gone into solution during prolonged contact time with the pipe system.

Each sample was then tested for pH in the field immediately after collection and in the laboratory at the end of the day. After the pH had been tested in the laboratory, the samples were acidified with concentrated nitric acid (10 ml / L) to preserve the sample for storage.

Chemical Analysis of the Samples

The samples were analyzed in the Geochemistry Laboratory at the University of Missouri-Rolla. The equipment used for the analysis is a specific ion electrode for the pH and chloride concentration and a Perkin Elmer (Model 2100) Atomic Absorption Spectrophotometer for calcium, magnesium, sodium, potassium, and iron. See figure 6 for tabulated chemical analysis data.

Section	pH	Calcium	Magnesium	Sodium	Potassium	Total Iron	Chloride
1		70.00	41.00	3.45	1.65	0.01	4.50
3	8.05	64.00	48.50	4.95	2.00	0.10	8.00
4	7.90	71.00	50.00	3.60	2.40	0.64	5.50
5	8.00	50.00	31.00	4.30	0.82	0.01	12.50
7	7.70	55.00	37.00	4.50	1.20	0.06	18.00
10	7.85	51.75	33.95	3.40	1.25	0.65	5.75
14	7.15	85.50	49.50	11.38	1.86	0.71	15.00
15	7.80	45.00	39.50	2.85	1.81	3.10	5.50
16	7.80	54.00	31.00	11.30	1.39	0.08	16.00
21	7.40	63.00	49.50	12.65	0.98	0.45	16.50
22		59.00	36.00	4.55	1.48	0.03	5.00
23	7.65	73.00	50.40	6.30	2.05	2.31	9.20
24	7.27	137.67	89.00	7.83	3.00	3.22	9.67
29		47.00	27.00	2.57	1.03	0.03	4.50
31	8.20	40.00	25.00	2.00	0.85	0.90	3.00
36	7.70	72.50	44.00	7.78	2.00	1.05	11.25
Average	7.68	63.52	41.74	5.41	1.54	0.75	8.55
Standard Deviation	0.33	21.32	13.97	3.33	0.59	1.02	5.07

Figure 6. Tabulated Chemical Analysis of Groundwater Samples.

Specific ion electrodes are used to measure the concentration of a selected ion in solution. The concentration is measured by inserting an indicator electrode and a reference electrode into a test solution, creating a galvanic cell. The voltage of the cell, which varies with the concentration of the ions to which the indicator electrode is sensitive, is measured and compared to a calibration plot in which the measured potential is plotted as a function of the concentration in known standards of the specific ion.

Atomic Absorption (usually referred to as AA) is an analytical method based on the absorption of ultraviolet or visible light by gaseous atoms. The sample is converted into atomic vapor by spraying the solution into a flame. A hollow-cathode lamp containing the element to be determined is used as the light source. The atoms of this element in the flame absorb at precisely the wavelength emitted by the light source. The wavelength spread is extremely narrow, both for the emission line of the light source and the absorption line of the same element in the flame. For this reason, interference from the spectral lines of other elements is almost zero.

Results and Discussion

The data from the collected samples were statistically analyzed and compared to water quality data obtained from the Missouri Geological Survey. The sample sets were compared and tested for homogeneity by a simple f-test. The results of the f-test indicate that there is no significant differences in water quality since 1985.

In order to have the most information available to study the trends in ionic concentration near the landfill the two data sets were combined and the average concentration for each ion was determined for each section. Cross-sectional graphs were created using the average concentration for each section as described. A diagram of T37N R8W sections used to create the graphs can be seen in figure 7 below.

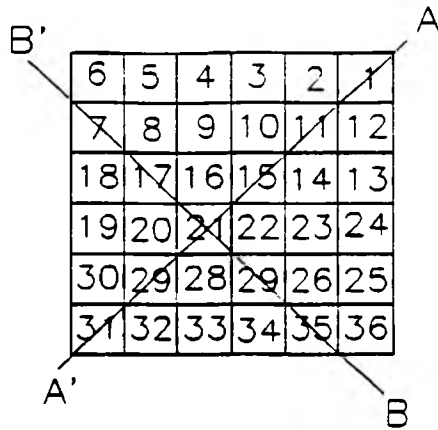


Figure 7. Diagram of T37N R8W sections used to create graphs.

The landfill is located in section 21 and is point 0 on the graph. For the graph in the northeast-southwest direction data was taken along the line from A to A'. For the graph in the northwest-southeast direction data was taken along the line from B to B'. The negative and positive ends were chosen such that the negative end is the area behind the landfill and the positive end is the area in front of the landfill in terms of the flow direction. The graphs of ionic concentration vs. distance can be seen in figure 8.

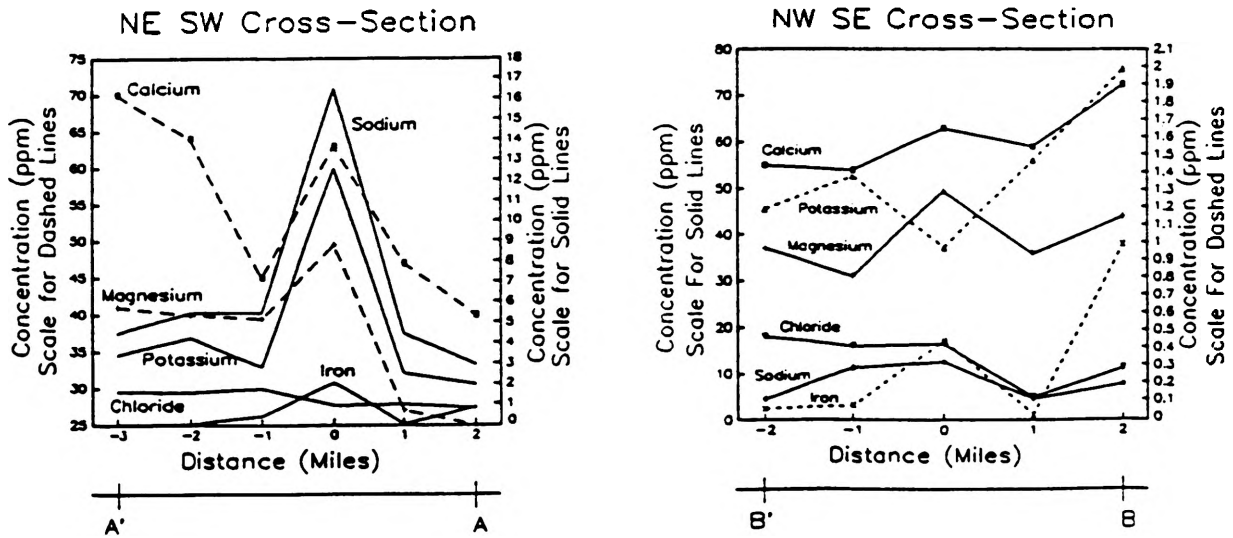


Figure 8. Graphs of Concentration vs. Distance.

As you can see in the graphs of concentration vs. distance the concentration of all the ions, except chloride, show a high concentration over the landfill in the northeast southwest direction. In the northwest southwest direction sodium and magnesium show a peak concentration; calcium, potassium, and iron show an intermediate and increasing concentration; and chloride shows an intermediate and decreasing concentration. It is interesting to see the concentration peak in the northeast southwest direction, however the ionic concentrations are well within recommended concentration limits set by the U.S. Environmental Protection Agency.

Summary and Conclusions

The McDowell Sanitary Landfill is located in Phelps County, Missouri off of Missouri State Highway CC. The topography in the area is controlled by the stratigraphy and is composed of very irregular surface and subsurface drainage patterns that are caused by extensive karst development.

Landfills are surface or near surface solid waste disposal facilities above the groundwater table. The buried refuse in sanitary landfills is subject to leaching by percolating water derived from precipitation and surface runoff. The thickness, lithology, and structure of the material beneath a landfill, and the design of the landfill itself, influence the time of waste transport and degree of modification before leachate reaches the water table.

There are two major aquifers in Phelps County that could be contaminated by a leaking landfill. These are the Roubidoux Sandstone and the Gunter Member of the Gasconade Dolomite. The Roubidoux Sandstone is the shallowest aquifer and thus is the one that has the highest probability of being contaminated.

If landfills are situated in appropriate hydrogeologic settings groundwater contamination can be avoided. This study has concluded that the shallow groundwater, within a 4 mile radius of the McDowell Landfill, is not contaminated. This investigation could be expanded by analyzing for certain trace elements (e.g. heavy metals and mercury), other anions (e.g. nitrate, phosphate, and ammonium), and dissolved organic compounds.

Acknowledgments

I wish to thank the University of Missouri-Rolla for the award of an Undergraduate Research Fellowship. I am also grateful for the help and encouragement which I received from my advisor, Dr. Ernst Bolter and the staff of the Missouri Department of Natural Resources Division of Geology and Land Survey, especially Mr. Don Miller.

References

1. Gann, E.E. 1976. Water Resources of South-Central Missouri. U.S Geological Survey. HA-550.
2. Howe, W.B. 1961. The Stratigraphic Succession in Missouri. Missouri Department of Natural Resources, Division of Geology and Land Survey. Vol XL, Second Series. pp. 13-21.
3. Lee, W. 1912. The Geology of the Rolla Quadrangle. Missouri Department of Natural Resources, Division of Geology and Land Survey. Vol. XII, Second Series. 111 pp.
4. Missouri Department of Natural Resources, Division of Geology and Land Survey. 1967. Mineral and Water Resources of Missouri. Vol. XLIII, Second Series. pp. 253-322.
5. White, W.B. 1988. Geomorphology and Hydrology of Karst Terrains. Oxford University Press, Inc. 450 pp.

ANALYSIS OF TWO CIRCUITS FOR DETECTING SUPERCONDUCTING TRANSITION TEMPERATURES

Terry Bowness

Introduction

When measuring the transition temperature of large numbers of high T_c superconducting samples it is desirable to have available equipment that is both easy to operate and reliable. In addition, should anything malfunction, the device should be relatively simple to repair. One method of measurement involves placing a sample in the magnetic field of an inductor, the inductor being an active member of some type of oscillating circuit. There are many standard oscillator designs which can be used for this type of application. In this report two such circuits, the tunnel diode and Hartley oscillators, will be examined and evaluated on their potential as measurement devices for superconductor transition temperatures.

Experiment and Observations

Indirect measurement of transition temperatures is possible via direct measurement of the resonant frequency of some oscillator circuit. Placing any conductor in the time-varying magnetic field of an inductor will create eddy currents in that conductor, thereby decreasing the inductance, L , of the inductor. Consider for example a parallel LC circuit whose resonant frequency is simply

$$\omega = (L \cdot C)^{-0.5}.$$

Clearly, a change from $L = L_0$ to $L = .25L_0$ would double the frequency. A superconducting sample occupying space in the magnetic field of an inductor would have little effect on L until the transition temperature is reached, at which point the sample's eddy currents would cause significant change in L and, as a result, ω .

The shape of the inductor is important here. A previous experiment utilized a cylindrical coil wound around an insulating tube of 1/8" inner diameter and 1/4" outer diameter. Inside the tube was placed some amount of superconducting powder. Samples generally come as solid discs, so rather than grinding each one up as was done before we opted to wind a flat coil 5/8" in diameter, one layer thick from 28 gauge copper wire.

The Tunnel Diode Oscillator

The first to be examined is the tunnel diode oscillator (TDO). Illustrated in Figure 1, this circuit's resonant frequency is expressed as¹

$$f = \frac{1}{2\pi (L C)^{0.5}} \left[1 - \frac{C}{G^2 L} \right]^{0.5}$$

After turning up several diodes it was determined that only about 120 mV_{dc} across the diode was needed to produce oscillation. The resulting sinusoidal output ranged from 400 to 500 mV_{pp}. With no sample attached to the coil the circuit specified in Figure 1 resonated at 7.85 MHz.

The TDO falls short in several areas. For one, the diode itself is relatively expensive, several dollars. Given the ease with which one can be inadvertently fried, the TDO is

FIGURE 1--TUNNEL DIODE OSCILLATOR

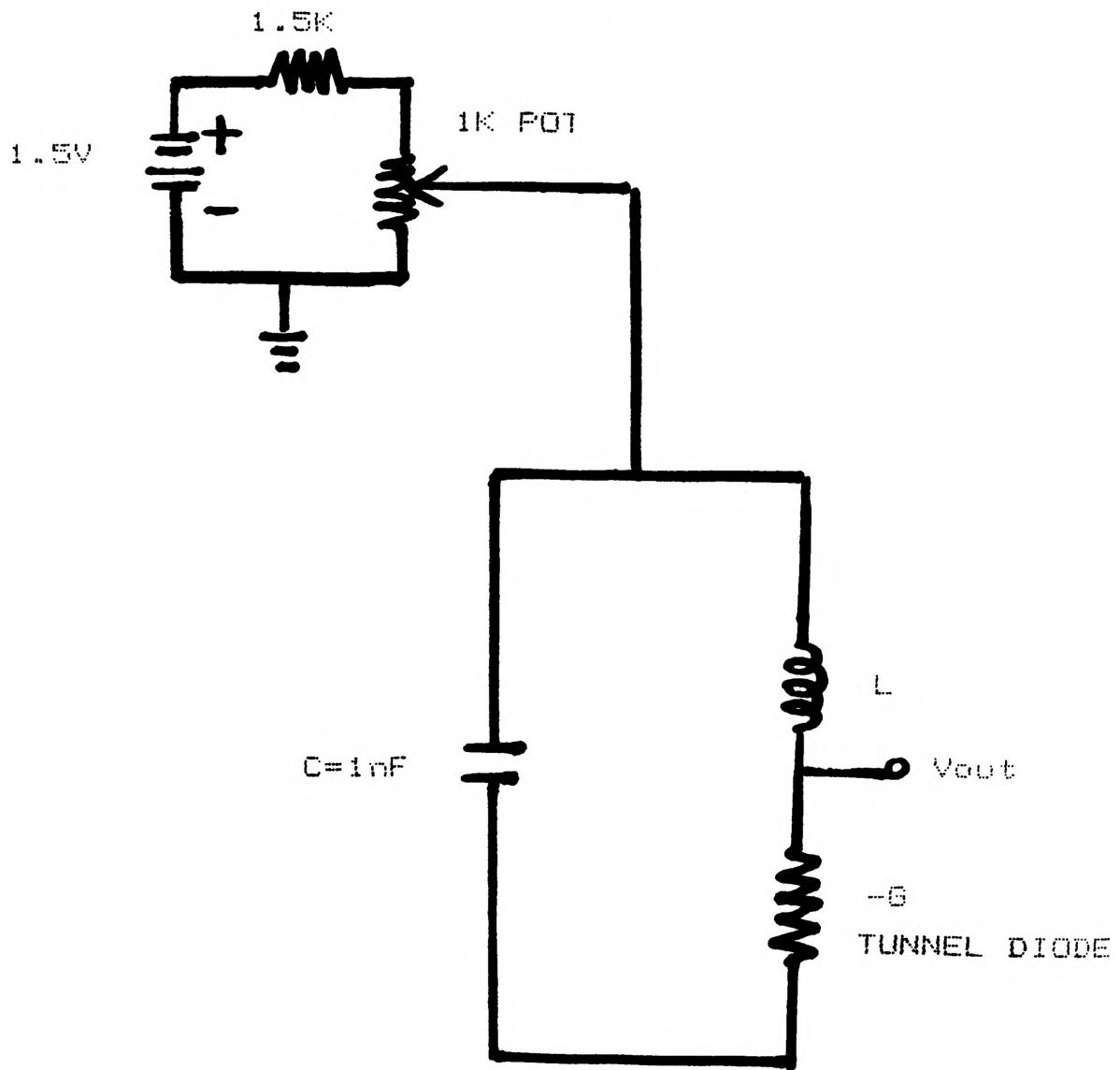
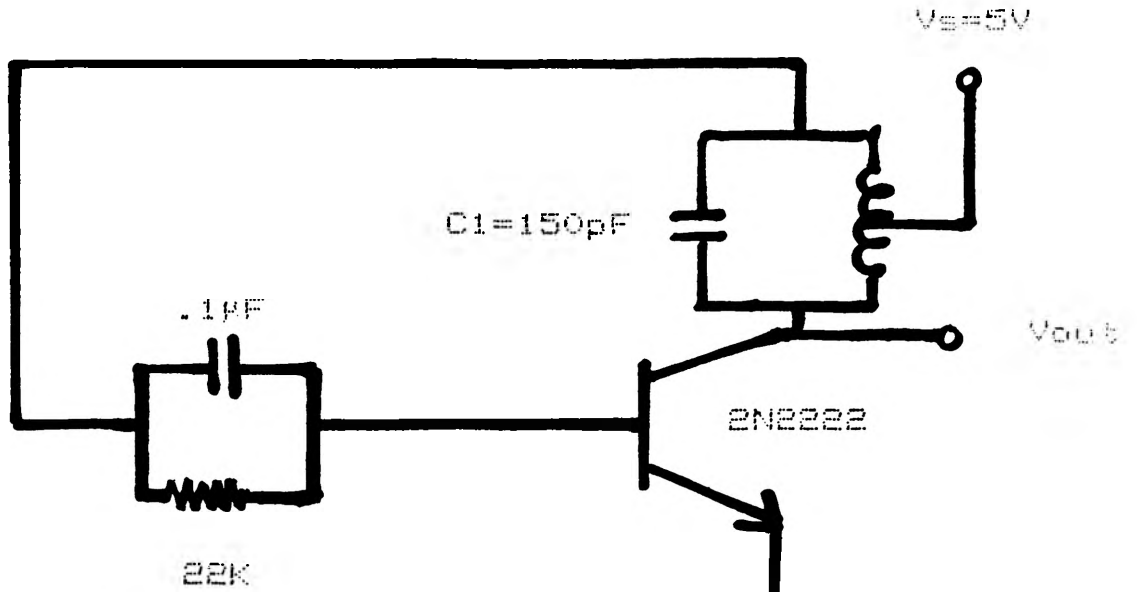
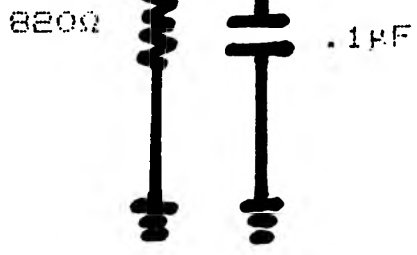
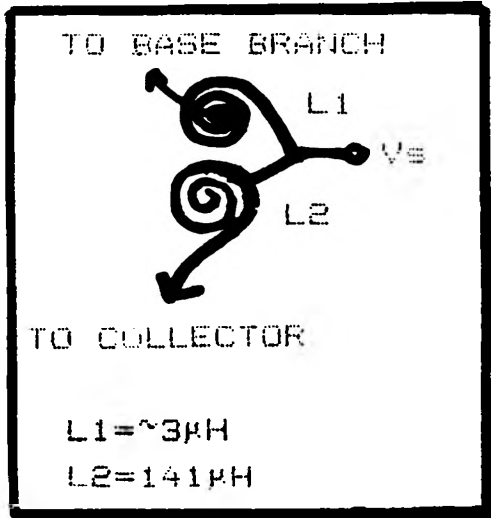


FIGURE 2--HARTLEY OSCILLATOR



INDUCTOR COIL CONFIGURATION



unreliable and could quickly become unnecessarily expensive. Furthermore, this circuit was seen to be extremely sensitive to environmental conditions. A region exists from about one to five feet away in which the presence of a human being causes all oscillation to cease. Finally, the output voltage is too small; a voltage follower would be needed to send the signal to a scope or meter with a relatively low input impedance.

The Hartley Oscillator

We turn now to the Hartley oscillator shown in Figure 2. This design is of interest particularly because of its simplicity. One problem present in actually building this circuit arose from the supply voltage being connected to a center-tapped coil. Again, it was important that a flat inductor be used. The arrangement worked by having two of them face-to-face as shown in the Figure 2 insert. Through trial and error it was found that the relative size, position, and winding direction of one to the other is very crucial.

With the component values listed in Figure 2 the output was a healthy 6 V_{pp}. No need for a voltage follower here! Below is a sketch of v_o.



The Hartley oscillator fails in one crucial way: at superconducting temperature the transistor does not operate. For it to work, the transistor must be separated from the rest of the circuit or isolated from the cold in some other way. Despite this obstacle, the Hartley oscillator is extremely reliable; it is composed of no special components, and is, unlike the TDO, not extremely susceptible to outside interference.

One noteworthy observation was made as the circuit (sans transistor) was dunked into a cup of liquid nitrogen. The frequency dropped initially but then increased to level off above the original, room-temperature frequency, f_0 . Sample data from one particular dunk shows

$$\begin{aligned} f_0 &= 904.5 \text{ kHz} \\ \text{liquid nitrogen } f_{\min} &= 886 \text{ kHz} \\ \text{liquid nitrogen } f_{\max} &= 967 \text{ kHz} \end{aligned}$$

This sort of behavior was also observed when a cylindrical coil was substituted for the flat ones.

Conclusions

To build a device for simultaneously measuring the transition temperature(s) of several superconducting samples it would be beneficial to explore the possibilities of oscillators other than the two described in this report. The TDO is easily damaged yet very simple. The Hartley oscillator is quite simple and dependable but hindered by the necessity of having to isolate the transistor. It would be wise to examine designs not employing transistors or special parts such as tunnel diodes.

References

1. "Contactless Transition Temperature Measurements in High T_c Superconductors", Matt Commens.

Much of the information throughout this paper was provided by Dr. D. M. Sparlin.

STIMULATION OF AMORPHOUS LAYERS IN THE CO-SI SYSTEM BY THIRD ELEMENT ADDITIONS

Denise Brandt

Introduction

Multilayer thin films play an important role in our technology today. They can be found in many devices such as magnetic hard disks, microelectronic circuits, and x-ray optical elements. In many of these metal-metal and metal-metalloid multilayers, amorphous layers have been discovered using various techniques such as extended x-ray absorption fine structure (EXAFS) and high resolution transmission electron microscopy (HTEM). These amorphous layers enhance the magnetic and electrical properties of the alloy. They also affect the mechanical and structural properties of the system.

The solid state amorphous reactions (SSAR) occur whether the layers are formed by epitaxy or by sputtering. The amorphous phase occurs if there is a large negative heat of mixing between the initial components.¹ This indicates that it requires less energy for the amorphous phase to form than for the crystalline phases to form. The reaction is also limited by diffusion rates. In order for the amorphous phase to form, one of the components must have a much larger diffusion rate in the intermixed layer between the components.^{1,2}

Although SSAR is a very active research subject, no studies have explored the possibility that the formation of amorphous layers might be promoted by adding a third element to the layers. To be effective, the third element should lower the free energy of the system and promote faster diffusion of the mobile component in the system. Research is currently being done on this idea. In this paper, the first stages of this research will be discussed. The research is being conducted on the Co-Si system. The Co-Si system is similar to the Ni-Si system but while the Ni-Si system forms amorphous layers the Co-Si system does not. Ti and Rh are to be used as the third elements in the system. The samples are made by two different sputtering techniques. This will show the effect of the quality of vacuum on the amorphous reaction.

The Co-Si System

Nickel and cobalt have lattice parameters that are within 2% of each other, their atomic sizes are within 1%, their melting points are within 50 C, they are both the mobile element during silicide formation, and they form similar phases with Si. Therefore, one may expect the systems to react similarly under the same conditions. However, this is not the case when thin films of the two systems are formed. The Ni-Si system forms amorphous layers that grow during the annealing process.

In the Co-Si system interlayers of 4.5 nm thickness are formed. The interlayers are mostly amorphous with a small amount of compound crystallites, which are unaffected by annealing at 250 C. Annealing at 300 C produces a mostly crystalline microstructure.² From previous experiments it has been determined that nickel-silicon reactions occur approximately 10^5 times more rapidly than cobalt-silicon reactions. This implies that by increasing the reaction rate of Co-Si reactions, amorphous layers might be produced. The reaction time can be increased by reducing the heat of mixing or by increasing the diffusion rate. The addition of a third element may increase the reaction rate.

Third Element

By examining free energies of mixing and relative sizes of atoms in comparison with Co and Si, educated guesses were made of third element additions that might alter the diffusion factor or the thermodynamic factor independently. Ti and Rh respectively, were selected for the Co-Si system based on the above criteria and experimental convenience.

The diffusion factor was estimated using an empirical equation developed by Bernardini³ that predicts the diffusion behavior of impurity elements in the grain boundaries of binary alloys. The equation was developed from an equation of grain boundary energy and theories on adsorption. The addition of solute B to A affects the grain boundary self-diffusion of A according to the formula:

$$D_b^{AB/A} = D_b^{A/A}(1 + (b_v^{AB/A} - 2 s^B)c^B).$$

Where $D_b^{AB/A}$ is the boundary diffusion coefficient of A in AB, $D_b^{A/A}$ is the self diffusion coefficient of A along the grain boundaries, $b_v^{AB/A}$ is the temperature dependent coefficient for the effect of solute B on the lattice self-diffusion of A, s^B is the ratio of solute concentrations in the boundary and in the lattice, and c^B is the bulk concentration of B. This equation suggests that solutes having small s^B values and large b_v values have been established for few combinations of elements, so they must be estimated more indirectly from heats of solution⁴ and other empirical correlations.⁵

These estimates led to the choices of Ti and Rh. For Ti, b_v is large, which indicates that it will speed up the diffusion of the Co, which is the rate controlling step in the Co-Si system. Its s^B value is also large, but not large enough to overcome the effect of b_v . Thermodynamically, Ti behaves similarly to Si, so Ti should exert its effect mainly on the diffusion factor. On the other hand, for Rh, b_v is unknown and s^B is small, which indicates that it will not segregate appreciably. Accordingly, rh would be a suit third element to examine the effect of the thermodynamic factor in the Co-Si system.

Sample Preparation

Co-Si layers were formed by sputtering instead of epitaxy because sputtering requires less of a vacuum, it produces larger grains which should minimize the effects of grain boundary diffusion within the layers, and it is faster and cheaper than epitaxy. The sputtering was performed on two different types of sputtering machines. 100 nm and 50 nm layers were made on a (100) Si wafer about 1 in square on a high vacuum sputtering machine at the National Nanofabrication Facility at Cornell University. Similar samples are to be made on a table top sputtering machine that is normally used to sputter gold and palladium on SEM specimens.

The samples from the table top sputterer will consist of one layer of sputtered Co on a silicon wafer and a second silicon wafer similarly coated and inverted on top of the cobalt layer. These layers are not bonded very well to the Si and therefore will be annealed under pressure in hydrogen at 300 C for a short time to improve the bonding. The samples will then be cut to approximate TEM specimen size before the anneal so that they will later fit in the specimen holder. Once the layers are bonded the specimens are ready for the addition of the third element.

The third element will be deposited from an aqueous solution on to the faces perpendicular to the layers before being annealed. After the anneal, TEM specimens will be prepared for inspection of the extent of penetration of third element along the layers and changes in the extent of intermixing.

Holding Device

The holding device required for the first anneal of the samples made from the tabletop sputtering machine had to be designed. To promote the bonding of the layers in these samples, the first anneal must occur under pressure. The final design is shown in Figure 1.

The pressure was accomplished by using two different alloys with two entirely different coefficients of linear expansion. From the expansion coefficient and the annealing temperature, the strain in the materials can be determined using

$$e = a\Delta T$$

and the effective strain determined from:

$$e_{\text{effective}} = e_{\text{screw}} - e_{\text{tube}}$$

Then the stress in the screw can be determined by

$$\sigma = eE.$$

Using Invar for the tube and 316 stainless steel for the screw, a pressure of approximately 135 ksi would be reached in the screw at 300 C and thus in the sample. The actual pressure should be smaller because the coefficient of expansion reduces at higher temperatures for the stainless steel while the coefficient for invar remains constant for this temperature range. Using

$$\sigma = F/A$$

the stress in the tube can be determined. For the dimensions shown in Figure 1, the pressure in the tube is only 2.9 ksi.

The tensile and compressive strengths of these materials must also be taken into consideration. The Invar has a strength of approximately 72 ksi which is well above the pressures applied and is not of concern. However, the screw must withstand much higher pressures. The 316 stainless steel when cold rolled achieves tensile strengths of 100 to 150 ksi and yield strengths up to 135 ksi. These high strengths should support the pressure produced by the temperature with little plastic deformation occurring. Many alloys would lose their increased strength from cold work at 300 C but for steels the recrystallization temperatures are much higher and they can maintain high strength at this temperature.

Precautions must be taken to ensure that the threaded portions of the device do not strip under pressure. The minimum length of thread contact can be determined by the following equation:⁶

$$L_e = 2A_t / [3.1416K_n \max [1/2 + .57735n(E_s \min - K_n \max)]]).$$

The above equation is valid for threads of the same material. The values needed for calculations can be found on the attached table.⁶ If the threads are of two different materials, the following calculation must be done:

$$J = \frac{A_s \times \text{tensile strength of external thread material}}{A_n \times \text{tensile strength of internal thread material}}$$

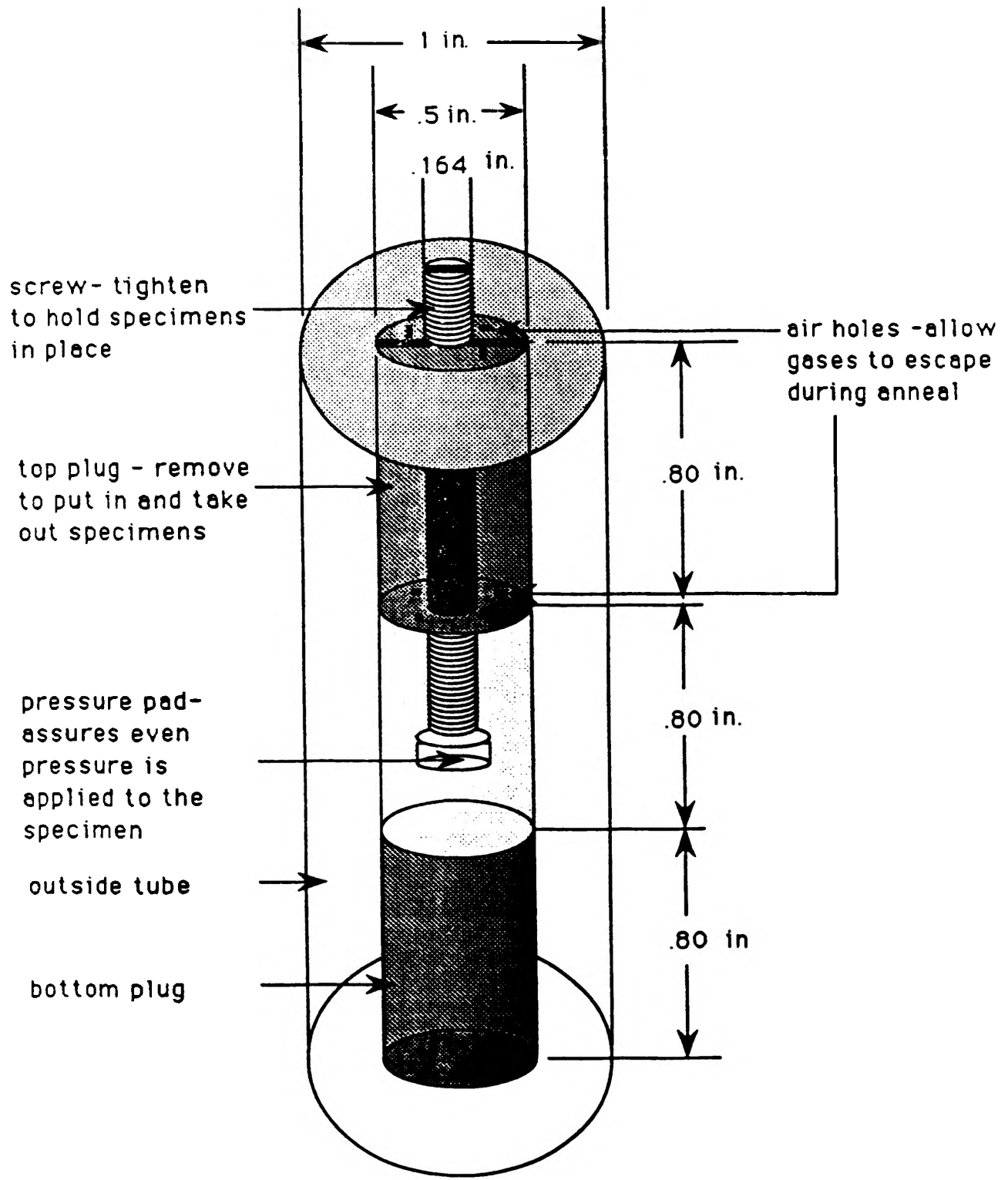


Figure 1. holding device

Table 3b. Fine-Thread Series, UNF and UNRF — Basic Dimensions

Sizes No. or Inches	Basic Major Diam., D	Thds per Inch. n	Basic Pitch Diam., ^a E	Minor Diameter		Lead Angle A at Basic P.D.	Area of Minor Diam. at D-2n ^b	Tensile Stress Area ^c	
				Ext. Thds., ^d A ₁ (Ref.)	Int. Thds., ^e A ₂				
				Inches	Inches				Deg.
0 (.060)	0.0600	80	0.0519	0.0451	0.0465	4	23	0.00151	0.00136
1 (.0731) [*]	0.0730	72	0.0640	0.0565	0.0580	3	57	0.00237	0.00228
2 (.086)	0.0860	64	0.0759	0.0674	0.0691	3	45	0.00339	0.00324
3 (.100) [*]	0.0990	56	0.0874	0.0778	0.0797	3	43	0.00451	0.00427
4 (.112)	0.1120	48	0.0985	0.0871	0.0894	3	51	0.00576	0.00541
5 (.125)	0.1250	44	0.1102	0.0979	0.1004	3	45	0.00716	0.00670
6 (.138)	0.1380	40	0.1218	0.1082	0.1109	3	44	0.00874	0.00818
8 (.164)	0.1640	36	0.1460	0.1309	0.1339	3	28	0.01285	0.01224
10 (.190)	0.1900	32	0.1697	0.1528	0.1562	3	21	0.0176	0.0169
12 (.216) [*]	0.2160	28	0.1928	0.1734	0.1773	3	22	0.0226	0.0218
1/4	0.2500	28	0.2268	0.2074	0.2113	2	52	0.0326	0.0312
3/16	0.3125	24	0.2854	0.2629	0.2674	2	40	0.0524	0.0503
1/2	0.3750	24	0.3479	0.3254	0.3299	2	11	0.0809	0.0788
7/16	0.4375	20	0.4050	0.3780	0.3834	2	15	0.1091	0.1067
1 1/2	0.5000	20	0.4675	0.4305	0.4359	1	57	0.1470	0.1439
9/16	0.5625	18	0.5264	0.4864	0.5024	1	55	0.189	0.185
5/8	0.6250	18	0.5889	0.5489	0.5649	1	43	0.241	0.236
3/4	0.7500	16	0.7094	0.6703	0.6823	1	30	0.351	0.343
7/8	0.8750	14	0.8286	0.7900	0.7977	1	24	0.470	0.460
1	1.0000	12	0.9459	0.9001	0.9098	1	36	0.625	0.603
1 1/8	1.1250	12	1.0709	1.0258	1.0348	1	28	0.812	0.788
1 1/2	1.2500	12	1.1959	1.1508	1.1598	1	16	1.024	1.003
1 3/8	1.3750	12	1.3209	1.2758	1.2848	1	9	1.260	1.238
1 1/2	1.5000	12	1.4459	1.4008	1.4098	1	3	1.521	1.481

^a Secondary sizes.
^b British Effective Diameter.
^c See formula, page 1279.
^d Design form for UNF threads. (See figure on page 1281.)
^e Basic minor diameter.

where

$$A_s = 3.1416nL_e K_{n \max} [1/(2n) + .57735(E_{s \min} - K_{n \max})] \text{ and}$$

$$A_n = 3.1416nL_e D_{s \min} [1/(2n) + .57735(D_{s \min} - E_{n \max})].$$

If J is greater than 1, then

$$Q = JL_e$$

where Q is the length of thread engagement required to prevent stripping. For the holding device the length of the thread contact was calculated to be .758 in for a size 8 screw with a thin thread series. To have a small safety factor we made a contact length of .800 in.

At the annealing temperature under pressure the threads will have a tendency to weld together. A boron nitride spray is sprayed on to the threads before the anneal to prevent this problem. The boron nitride contains additives that will allow it to stick to the metal and form a protective coating that remains at high temperatures.

One end of the screw is rounded to about a 3/8 in radius. A metal pad is placed on the rounded end. The pad can then move to assure even distribution of pressure on the specimens. The screw is tightened just enough to hold the specimens in place. The actual pressure is applied gradually with the temperature change before the anneal.

Continuing Research

This project is being carried on by another student next semester. This student will make the samples in the tabletop sputter, anneal them, anneal all of the samples with third elements, prepare TEM specimens from these samples, view them with the TEM, and determine the results.

References

1. B. M. Clements and R. Sinclair, "Metastable Phase Formation in Thin Films and Multilayers", MRS Bulletin, Feb. 1990, pp. 19-28.
2. K. Holloway, R. Sinclair, and M. Nathan, "Amorphous Silicide Formation by Thermal Reaction: A Comparison of Several Metals-Silicon Systems", J. Vacuum Sci. Tech, A 7(3), May/June 1989, pp. 1479-1483.
3. I. Kaur and W. Gust, "Fundamentals of Grain and Interface Boundary Diffusion", Stuttgart, 1989, pp. 305-309.
4. F. R. DeBoer, R. Boom, W. C. M. Mattens, A. R. Miedema, and A. K. Niessen, Cohesion in Metals Transition Metal Alloys, 1989.
5. H. Bakker, Diffusion in Crystalline Solids, 1984, pp. 189-258.
6. Machinery's Handbook, 23rd Ed., H. H. Ryffel, ed., pp. 1278-79.

TWO-PHASE FLOW MEASUREMENT

Glenn Brenneke

INTRODUCTION:

Liquid fuel engines have many applications in today's world. Diesel, spark-ignition, and gas turbine engines, and furnaces are just a few of the many applications of liquid fuel sprays. With the rising cost of fuel and need for energy conservation it is imperative that more efficient engines be developed. Analyzing liquid fuel spray characteristics non-intrusively could unlock the door to powerful highly efficient engines in the future.

The vaporization of fuel is mandatory in liquid fuel combustion. Vaporization and the fuel to air ratio are important characteristics of the spark-ignition engine. Compression ignition is controlled by the parameters of the injected fuel spray. By developing an accurate non-intrusive method of measuring the fuel spray parameters, data collected could be used to develop fuel injection methods that increase the power output, and raise the fuel efficiency of an engine.

The infrared absorption method of determining fuel spray characteristics provides a non-intrusive method to measure vapor concentration, but little is known of its accuracy. The goal of this project, which is being sponsored by the National Science Foundation, is to develop an accurate method of measuring evaporating sprays and their spray distribution. The non-intrusive laser method uses the known absorption of hydro-carbon fuels at a wavelength of 3.39 microns to measure spray characteristics namely accurate quantitative measurements of the vapor phase.

GOALS OF THE PROJECT:

The goal of the project is to develop a method to test the accuracy and limitations of the infrared absorption method. To do this the infrared method will be used in an environment with a known flow rate in order to test the accuracy of the hardware as well as the method itself. To simulate the two-phase spray, polystyrene seed will be injected into a methane gas spray. This "two-phase flow" gives more flexibility in two-phase measurement because of the range of vapor-solid ratios that can be varied. Since the vapor-solid ratio is known, the accuracy of the infrared technique can be easily tested. In order to develop an environment with a known flow rate and an adjustable vapor-solid ratio input, a two-phase flow test section was developed.

The focus of the summer project was to develop a two-phase flow test section to meet the criteria of the project as suggested in the NSF proposal. This test section injected a methane spray with polystyrene seed into a moving air flow. A window in the test section would allow the laser based diagnostic

equipment to measure the characteristics of the two-phase spray including particle size, and fuel vapor concentration. A schematic of the test section is attached. A design for the air moving system and preliminary sizing of the test section had to be completed. In addition, a translating fuel nozzle system, and an air filtration system, which provided clean air, had to be developed for the test section. Supply companies needed to be contacted for materials, and organization of the building of the section needed to be completed.

PROJECT OVERVIEW:

To begin the project a review of the project proposal was necessary. Jumping into the design cold could be time consuming as well as lead to a faulty design. The design criteria, which were outlined in the proposal, would be met more completely when a solid feel for the project was gained. Although the design criteria did not specifically outline the size and shape of the test section, certain characteristics needed to be met. First, a two meter per second flow speed in the section was needed. This speed provided ample exhaust for the combustible gases, but maintained uniform flow in the test section. Secondly, the test section must be wide enough to accommodate the spray patterns to be tested. It was decided that the test section needed to sustain a 30 degree cone 15 inches from the injector. To maintain this spray pattern the section needed to be 10 inches wide. Finally, the section must be long enough to provide a relatively smooth uniform flow in the section. A flow straightener, which is nothing more than an aluminum sheet with a honeycomb pattern, helped develop the uniform flow. The added length of the test section above the view window helped maintain uniform flow as well. By skimming other similar project proposals, ideas were developed on how to overcome these obstacles and develop the best test section design possible.

DESIGN:

Section Size and Shape:

Preliminary sizing of the section was needed next. The test section shell shape, which would be either square, round or hexagonal, needed to be determined. After discussion with Professor Drallmeier, a ten inch square design was decided upon. This would allow for the nozzle movement necessary for testing. This size would also provide the needed fuel nozzle spray area. A square design would allow for easy placement of fused quartz windows in each side providing the viewing area for the laser based infrared extinction equipment. In the round or hexagonal shape the window placement would be more difficult. The square design also provided an easy method of attachment to the support stand, and could be easily fabricated out of the materials purchased. (Diagrams of the test section are attached following the report.)

Air Moving System:

Next the design consisted of developing an air moving system for the test section. The air moving system had to develop two meter per second flow in the section but also have a high enough exhaust flow rate so that back pressure would not develop in the section. Two meter per second flow in a 10 inch square section, requires a flow rate of about 300 cfm. A flow rate greater than 300 cfm was needed from the lab hood exhaust. Checking the specifications of two blowers owned by the University indicated that at the proper speed one of the blowers would provide the air flow needed for the experiment. After finding the proper blower, aluminum ducting to run from the blower to the section entrance and from the section exit to the exhaust hood was ordered. With the proper blower found, sufficient exhaust provided, and the adequate duct work ordered the air moving system was complete.

Acquiring Materials:

In order to build the section and get the project off the ground supply companies needed to be contacted. One task was to determine materials that were needed for the test section and then order those from various companies. Names and telephone numbers of various supply companies were found in the Thomas Register. By consulting the Thomas Register an idea of the materials that were available for the design of the test section was obtained. After studying the register it was decided that many of the designs had to be adjusted to fit the materials that could be acquired for the test section, with material availability being a limiting factor. Minimum orders hampered the material acquisition process. The first design for the test section was a ten inch square tube. This tube could not be purchased without a sizeable order, therefore the design needed to be changed. The square test section needed to be formed out of four aluminum sheets. Problems such as this one slowed the project and forced many design changes.

Leveling Mechanism and Test Section Shell:

After gaining an understanding of the materials available, plans for the design were put down on paper. The plans were to be developed using the MacIntosh Draw II software available for project use, after gaining a working knowledge of the software.

A leveling stand for the structure was needed to insure accurate experimental results. This leveling stand provided a means not only to level the two-phase flow test section but also to transverse the section in the horizontal direction. Movement of the section was important to provide enough measurement positions for the laser based flow measuring device. Drawings of the leveling stand are attached. Plans were also drawn for the test section shell itself. It was to be constructed of one-fourth inch aluminum plate on the viewing sides and one-eighth inch aluminum sheet on the non-viewing sides. The one-eighth inch sides would then be screwed to the one-fourth inch viewing

side plate. This method provided a sturdy section which resists buckling and also provided a thick side to attach the fused quartz window. The drawings of all designs were reviewed, approved by Professor Drallmeier and then turned into the machine shop for construction. The test section shell drawings are attached.

Window:

The window design was a baffling problem, but with a few ideas from Professor Drallmeier the problem was soon conquered. The window was to be rigidly supported but also maintain a smooth inside surface so as not to disrupt air flow inside the test section. A four and one-half inch window was agreed upon to give the needed size for the spray measurements to be taken by the laser. To support the window to the front plate of the test section the plate was machined to a depth of three-sixteenth of an inch to fit the window dimensions. The one-sixteenth of an inch of aluminum supported the quartz on the inside, and a small aluminum plate was added over the outside edge to fasten the fused quartz firmly to the test section shell. This design provided the needed support of the window, and the small inside section variation would not disrupt the air flow inside the test section. (Figure attached)

Injector Movement:

Now that the support stand and test section shell had been completed it was time to concentrate on the fuel injector movement. The injector needed to be capable of horizontal movement and vertical movement. As mentioned before, the support stand provided horizontal movement in one direction. A mechanism for vertical and perpendicular horizontal movement needed to be designed. This movement problem was overcome by using threaded rod movement of a small support inside the section itself. By turning the threaded rod outside the section the injector inside is moved horizontally to the correct position. A simple set screw in the block is loosened to allow the fuel injector vertical movement to any position needed in the desired test zone. The traversing method provided the means to measure the fuel spray in any position deemed necessary.

Intake and Exhaust Convertors:

Intake and exhaust from the ten inch square section was also a design problem that developed during the summer project. The unusually large size of the test section shell raised problems in finding the necessary duct work fittings. From the blower a six inch round aluminum duct was used in order to provide enough air flow and because of the ease with which the flexible aluminum duct could be positioned. But a round six inch to square ten inch convertor was needed to complete the blower connection. After consulting the Thomas Register again it was decided that this fitting could not be purchased and would have to be

designed. A local sheet metal shop fabricated a convertor for both the top and bottom of the section. The bottom convertor section consisted of a sheet metal box with a six inch exhaust outlet, enough room at the bottom for any liquid that might collect there if a liquid spray were used, and a small drain to allow for the removal of this liquid. The much simpler top convertor section again consisted of a sheet metal box, but the six inch air inlet was at the top instead of the side as in the bottom section. The top convertor was long enough so that the entering air would become relatively uniform over the test section cross-section before being probed with the laser. These convertors completed all but one major part of the air flow network.

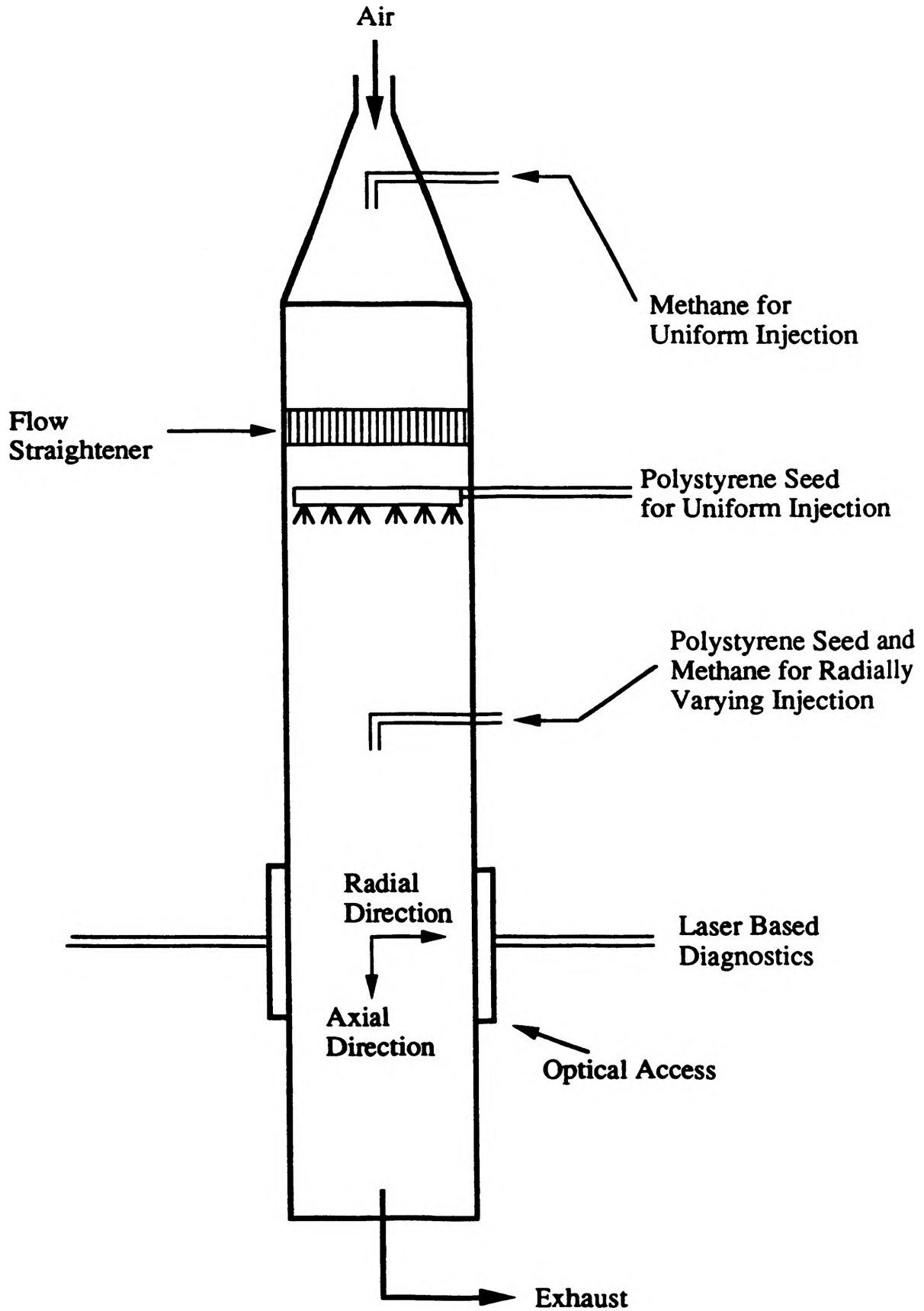
Filters:

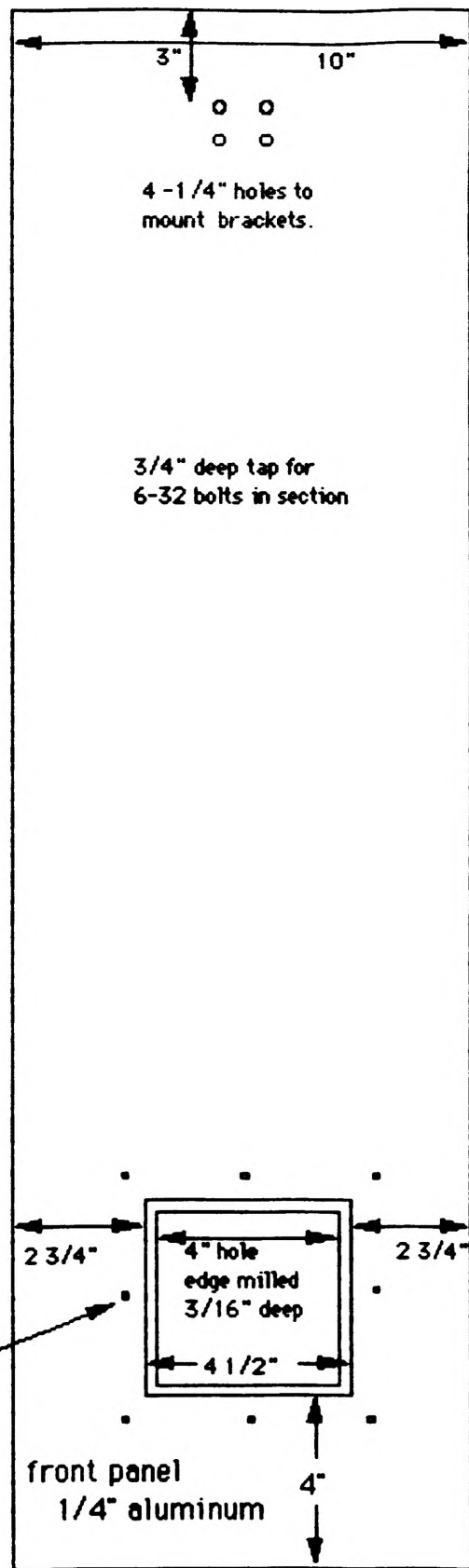
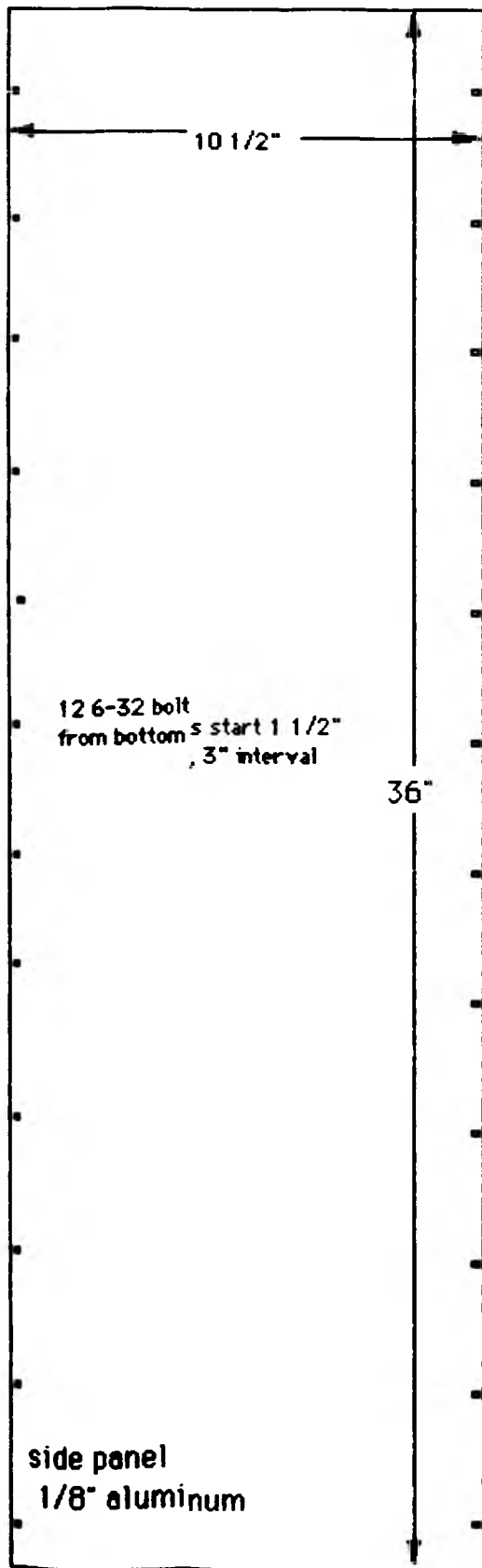
Filters are used to clean the entering air, and collect seed from the exiting air. Both the entrance and exit filters needed a small pressure drop with a flow rate of nearly three hundred cubic feet per minute, and also required a high efficiency at the one to three micron range. Filtering particles of this size would eliminate some measurement errors caused by particle interference. Also, due to the expense of the polystyrene seed a method of recovering the seed was necessary to keep experimental cost as low as possible. An exit filter would be needed to carry out this task. After discussing the project and filter parameters with several companies it was found that the necessary filters could be acquired, and the design of the test section as a whole was then complete.

Conclusion:

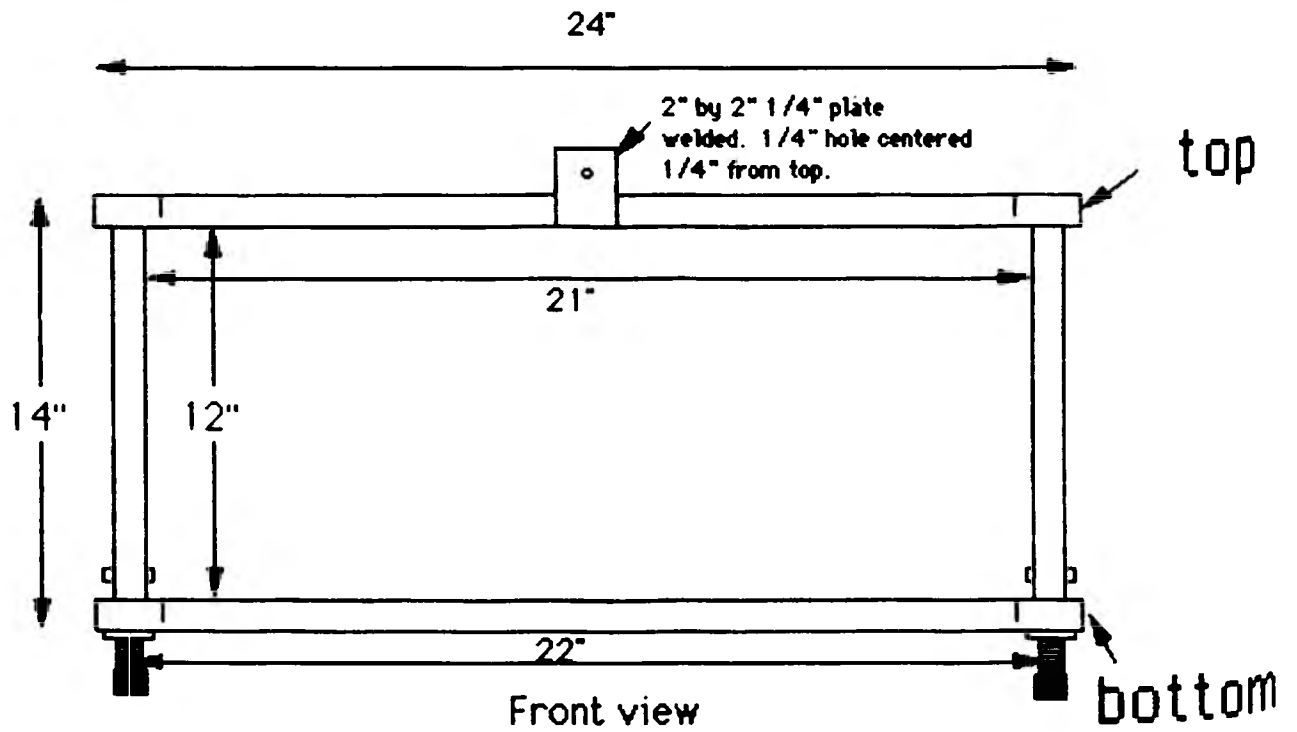
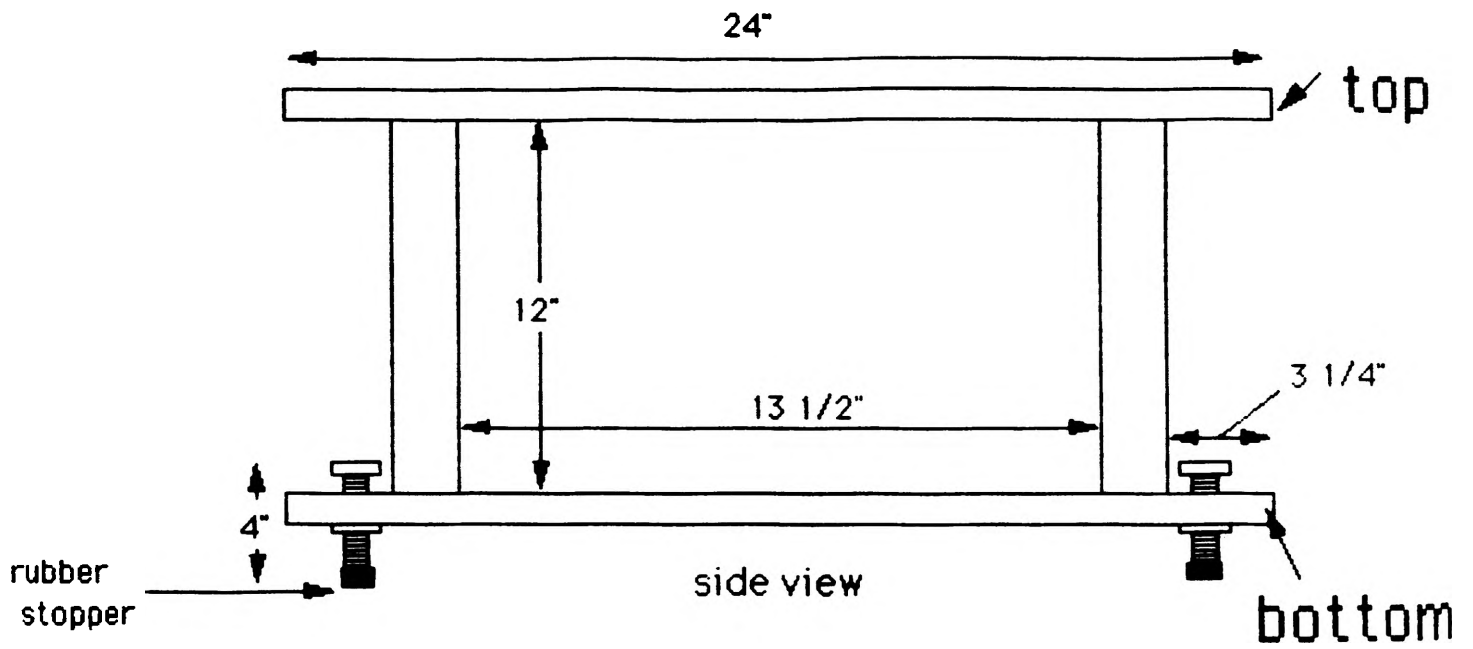
The design of the test section components was not an easy task and many difficulties arose. Many first designs were changed because better ideas were suggested, or because of the lack of the necessary materials needed to build the design. A minimum order, which was required by many companies, also hampered plans for the project. But despite the problems encountered along the way I enjoyed working on the project tremendously and I believe I learned a great deal from working one on one with Professor Drallmeier.

The summer research program is not only an excellent method to attract students to graduate school, but it is also a good learning experience for undergraduate students. By working with the professors in a one on one environment much can be learned about project design, research, and personal relation with outside companies. The research program gives the student an opportunity to get a taste of graduate studies and also gain knowledge that will help in the outside world. Professor Drallmeier used the test section project to give me first hand knowledge of research work but also showed me design techniques, company research, and methods to communicate project needs with outside companies. When a professor works closely with a student the many problems encountered in a project can be overcome.



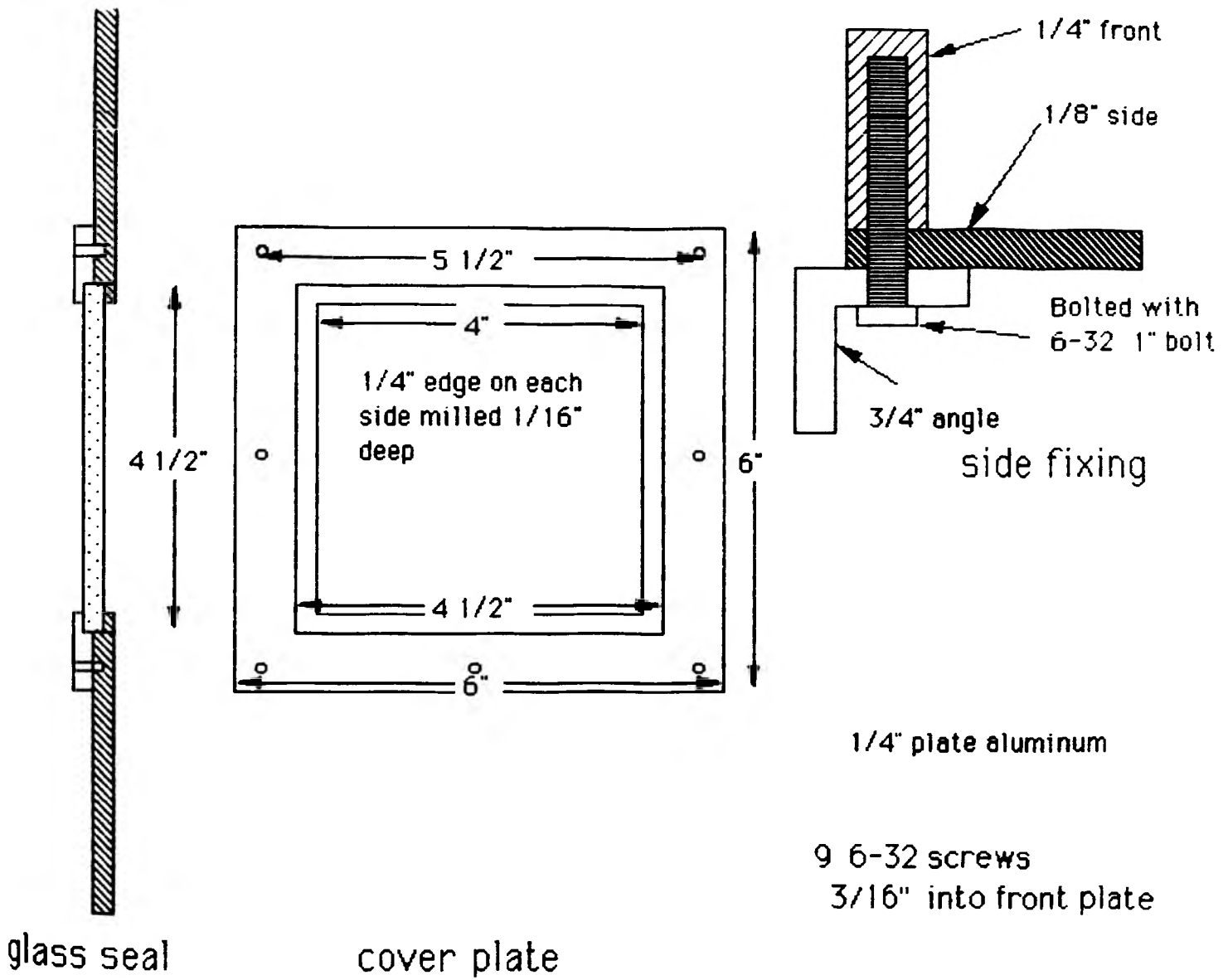


section size

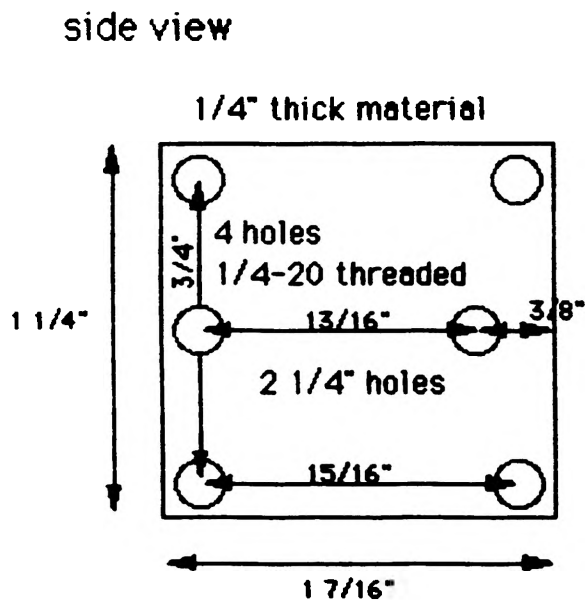
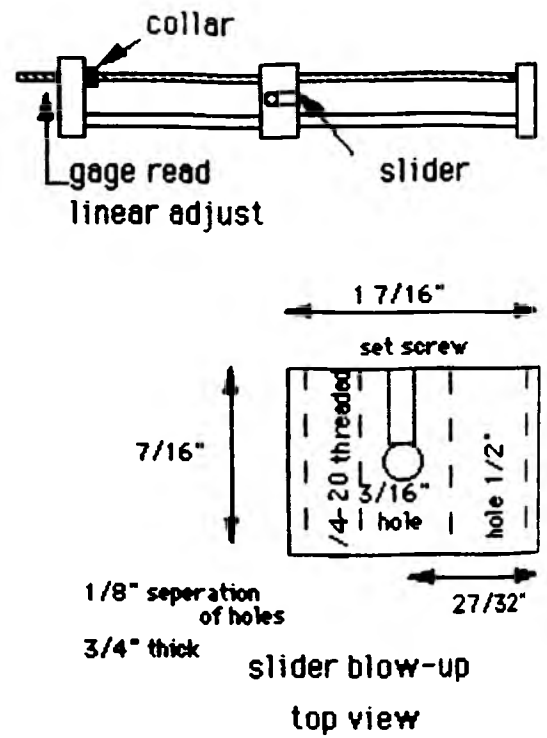
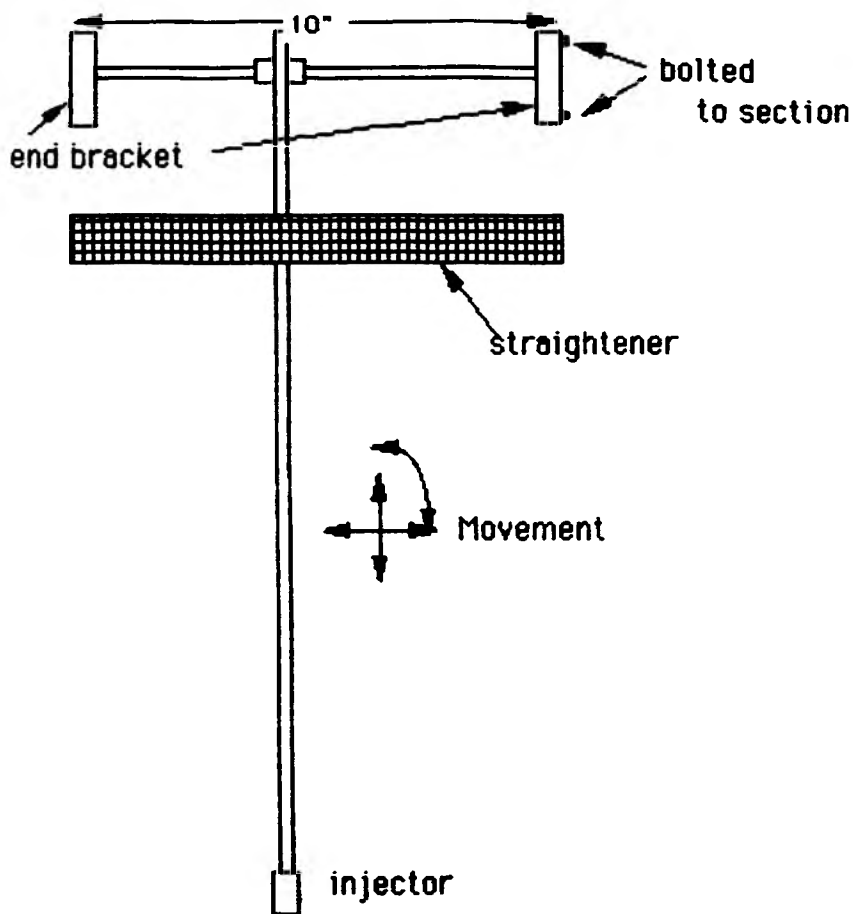


Leveling Stand

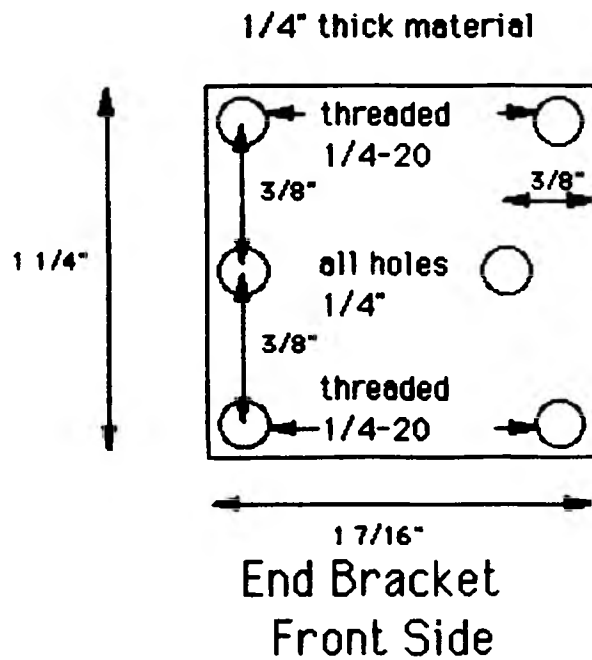
All structural material 1 by 2" tubing.



Window Mount



End Bracket Back Side



Injector Movement

ESTABLISHMENT OF A PHASE/DOPPLER PARTICLE ANALYZER FOR TWO PHASE FLOW EXPERIMENTS

J. L. Burget

Introduction

The accurate measurement of liquid spray drop size and velocity is important in a variety of applications. These applications include agricultural sprays, furnaces, spark ignition and compression ignition engines, gas turbines, and a variety of industrial processes. Because of the need to improve combustion efficiency and minimize soot and other harmful emissions, one of the most active areas of research is fuel spray combustion. Quantitative measurements of the vapor phase in fuel sprays is vital to the understanding of spray dynamics and the operation of combustion devices.

There are various measurement techniques available to measure vapor phase characteristics in a fuel spray including schlieren photography, vapor fluorescence using exiplex emission, and mechanical isokinetic probes. Schlieren photography and vapor flux fluorescence using exiplex emission are nonintrusive techniques which provide only a qualitative picture of the vapor phase. Mechanical isokinetic probes have provided a quantitative picture of the vapor phase, but have the disadvantage of disrupting the flow field.

The Aerometrics Phase Doppler Particle Analyzer (P/DPA) is a laser based instrument that provides a quantitative, nonintrusive method to obtain simultaneous size and velocity measurements. This instrument incorporates the Laser Doppler Velocimeter for flow measurements with particle sizing methods.

My role in this project consists of setup and validation of the P/DPA. This includes developing an appropriate spray set up and making measurements in a variety of spray environments for the validation of drop size, velocity, and liquid volume flux measurements. The instrument will ultimately be used in the investigation of two phase flows, including the measurement of particle size and velocity distributions in fuel sprays.

Experimental Setup

Spray Setup For validation of the P/DPA a spray apparatus using water was constructed. This apparatus provides the ability to deliver water at a constant pressure to the nozzle. The basic spray apparatus is shown in Figure 1. The spray apparatus functions in the following manner. With the air line valve off, water is introduced into the tank by the T-valve located at the bottom of the tank. When the tank is filled to an appropriate level, the T-valve is shut off and the tank is pressurized by turning on the air line valve and adjusting the pressure regulator. A readout of the pressure in the tank is provided by a pressure gage. To produce spray, the T-valve is opened in the direction of the line flowing to the nozzle. The spray collection bucket functions to collect the spray through the aid of gravity and a vacuum port, which draws the spray into the bucket. The manually operated pump functions to expel the water from the bucket into a laboratory drain. The pressurized water tank was attached to the side of a moveable cart, and the cart was modified with an additional set of wheels and frame structure to hold the collection bucket. This was done to provide mobility of the spray apparatus.

P/DPA Background Theory

The optical diagram for the P/DPA is shown in Figure 2. A drop passing through the intersection of the two beams produces a scattered light interference fringe pattern similar to the one shown in Figure 3. The spacing between these projected fringes is proportional to the drop diameter, light wavelength, beam intersection angle, drop refractive index, and the location of the receiver. These fringes move past the detectors at the Doppler difference frequency and produce a Doppler burst signal at each detector which is similar to the one shown in Figure 4. The Doppler burst produced at each detector is shifted in phase from one another. Figure 5 shows the Doppler burst produced at each detector after high pass filtering to remove the low frequency component. The phase shift between detector 1 and 2 is determined by measuring the time difference between zero crossings of each signal and dividing by the measured Doppler frequency.

$$\Phi_{12} = \frac{\Delta L}{\Gamma D} \times 360^\circ \quad (1)$$

These measurements are averaged over all cycles occurring in the burst signal. This phase shift is related to the drop size by the linear relationship shown in Figure 6. This relationship was computed from a mathematical representation of the scattered light fringe pattern. In this figure, the drop size is made non dimensional by a parameter (DELTA) which is an assumed fringe spacing formed at the intersection of the beams, and which is a function of light wavelength and laser beam intersection angle. Three detectors are used to eliminate the uncertainty in measurement and to provide two sensitivity ranges shown as curves ϕ_{1-2} and ϕ_{1-3} in Figure 6.

Assuming the drops remain spherical, the method described above provides the ability to measure drop sizes in the range of 0.5 to 3,000 micrometers. Because the drop size and velocity are measured simultaneously, the P/DPA is capable of providing a complete description of the drop distribution within the spray.

P/DPA System Description

The P/DPA consists of five major components. These components are a transmitter, receiver, signal processor, motor controller, and computer. A very general description of each component follows.

The Aerometrics, model XMT-1100-4S transmitter shown in Figure 7 generates two equal intensity laser beams and focuses them at an intersection point which serves as the measurement region. The transmitter contains a Spectrum-Physics model SP-106, 10 milliwatt, polarized helium-neon laser and optical components which serve to focus, partition, and collimate the laser beam.

The Aerometrics model RCV-2100 receiver shown in Figure 8 collects scattered light and provides the signal phase shift required for determination of drop size. The package consists of a highly efficient lens system for light collection, a spatial filter for exact probe volume definition, a light partitioning prism assembly, and multiple detectors complete with preamplifiers.

The Aerometrics DSA 3000 signal processor, not shown, is a state-of-the-art frequency domain signal processor which analyzes and processes the Doppler burst signals. The proper selection of instrument parameters is necessary in order to obtain reliable data. The selection of instrument parameters is accomplished through software that provides complete control of the processor in all stages of data acquisition, analysis, and presentation. Some of the instrument

parameters selected through the software includes various filtering networks, mixer frequency, frequency shifting, sampling frequency, number of samples, signal threshold, and velocity range.

The Aerometrics model MCB-71001-1 motor controller, not shown, monitors both the frequency shift and track select motors located in the transmitter. In addition, the motor controller serves as a multiplexor for other accessories connected to the system.

The data management system consists of a Kapro personal computer, Amdek color monitor, and a Fujitsu DL3300 Printer. The personal computer is enhanced with expanded memory, an 80287 math coprocessor, and an EGA card. The computer contains the system software which allows control of the signal processor, and is used for data handling and reduction. The system produces histograms of the droplet size and velocity on the monitor as the data is accumulated. Sample time and the number of samples recorded is also displayed. When a preset number of samples have been measured, the tabulated results can be printed or stored on disk.

Results

The original goal of this project was to use operate the Phase Doppler Particle Analyzer to make measurements in a variety of spray environments under controlled conditions for the validation of drop size, velocity and liquid volume flux measurements. This was a new piece of equipment being purchased by the university and was scheduled to be delivered prior to the beginning of the project. Due to a series of delays on the part of the manufacturer, the equipment did not arrive until the middle of the fall semester and validation of the system became unrealistic given the time constraints. Therefore, the sensitivity of the system to variation in a few setup parameters was investigated using the spray apparatus discussed previously.

The setup parameters investigated were the photomultiplier tube (PMT) voltage and the high pass filter settings. The effect of these setting on Sauter mean diameter (SMD) and mean velocity can be seen in Figures 9 through 12. The PMT voltage basically provides a gain to the Doppler burst signal and therefore determines the size of particle data that will be processed. Figures 10 and 12 show a decrease in SMD and mean velocity as the PMT voltage is increased from 300 to 350 Volts and then an increase in both quantities as the voltage is increased to 400 Volts. The low pass filter helps to improve the signal to noise ratio before the signal is sampled. Figures 9 shows a decrease in SMD as the filter setting in increased past 10 MHz, and Figure 11 shows a decrease in mean velocity as the setting is increased from 5 MHz to 20 MHz and then an increase in mean velocity at the 40 MHz setting.

Conclusions

Due to a series of delays by the manufacturer of the equipment that the major part of this project was dependant upon, the objective of validating the system was not accomplished. Even though this major objective was not accomplished, a spray apparatus was constructed and a small amount of time was spent operating the system and investigating its sensitivity to variations in system parameters. The system was found to be sensitive to variations in both of the parameters investigated. A more complete picture of the variation of the system could be obtained if a larger number of data points are obtained with a spray setup that produces a known, constant size particle. Even though the major objectives of the project were not accomplished, this project provided experience in the area of experimental research, and an introduction to fuel spray characterization and basic laser diagnostic principles.

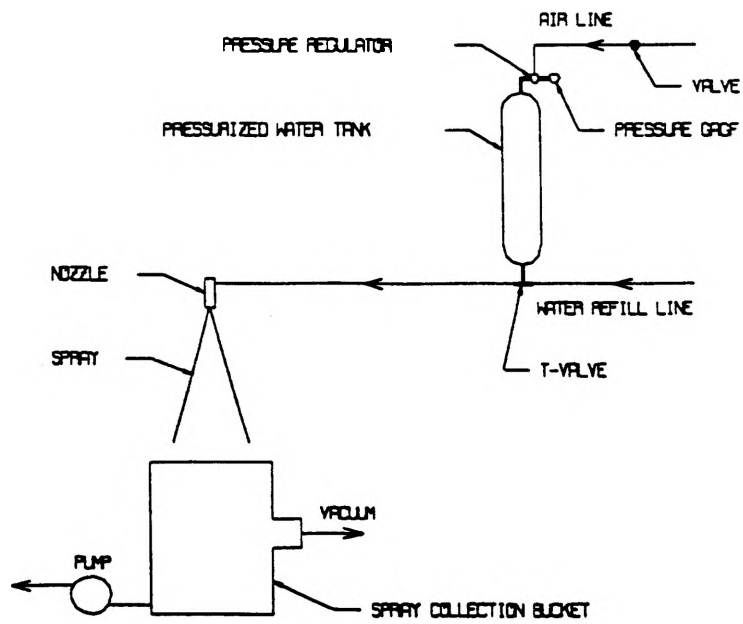


Figure 1 Spray Setup

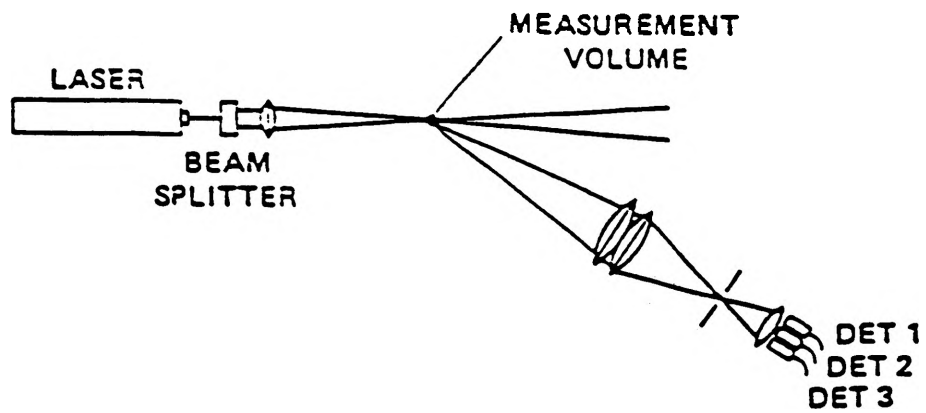


Figure 2 P/DPA Optical Diagram

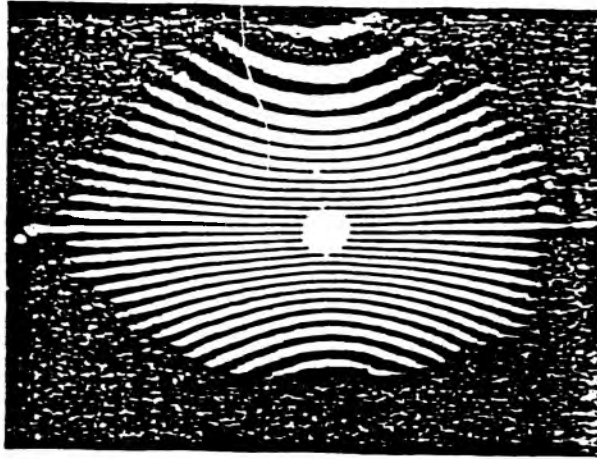


Figure 3 Scattered Light Interference Fringe Pattern

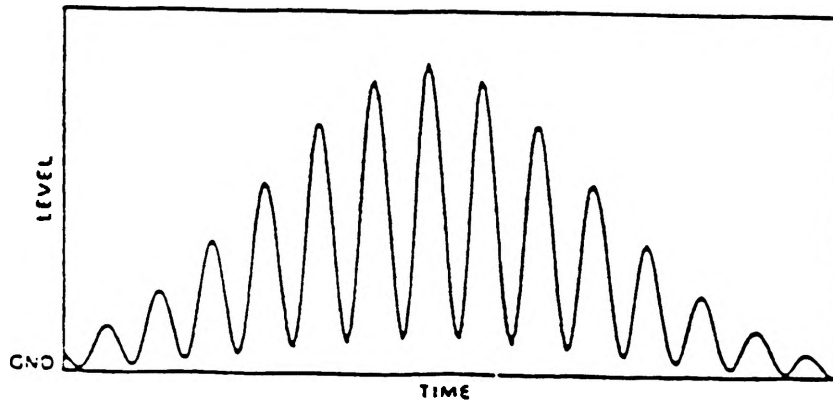


Figure 4 Doppler Burst Signal

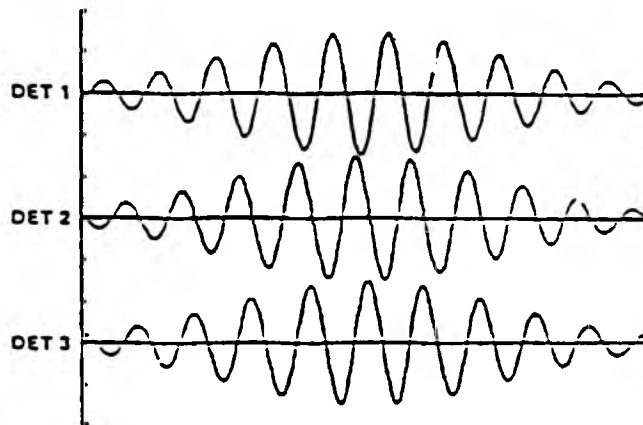


Figure 5 Filtered Signal Produced at each Detector

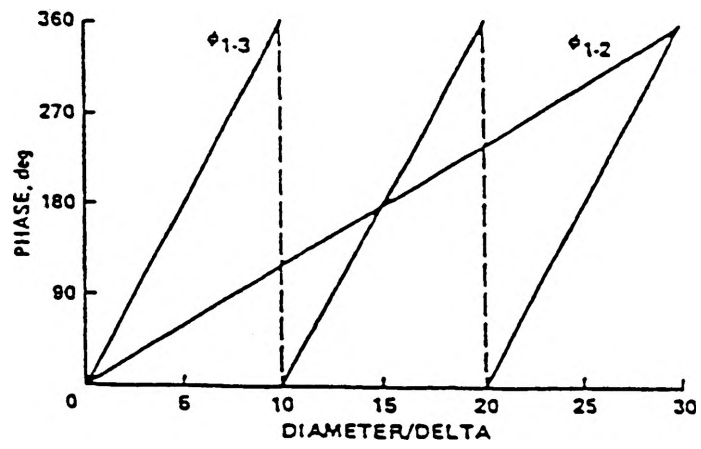


Figure 6 Linear Phase Shift Variation with Drop Size

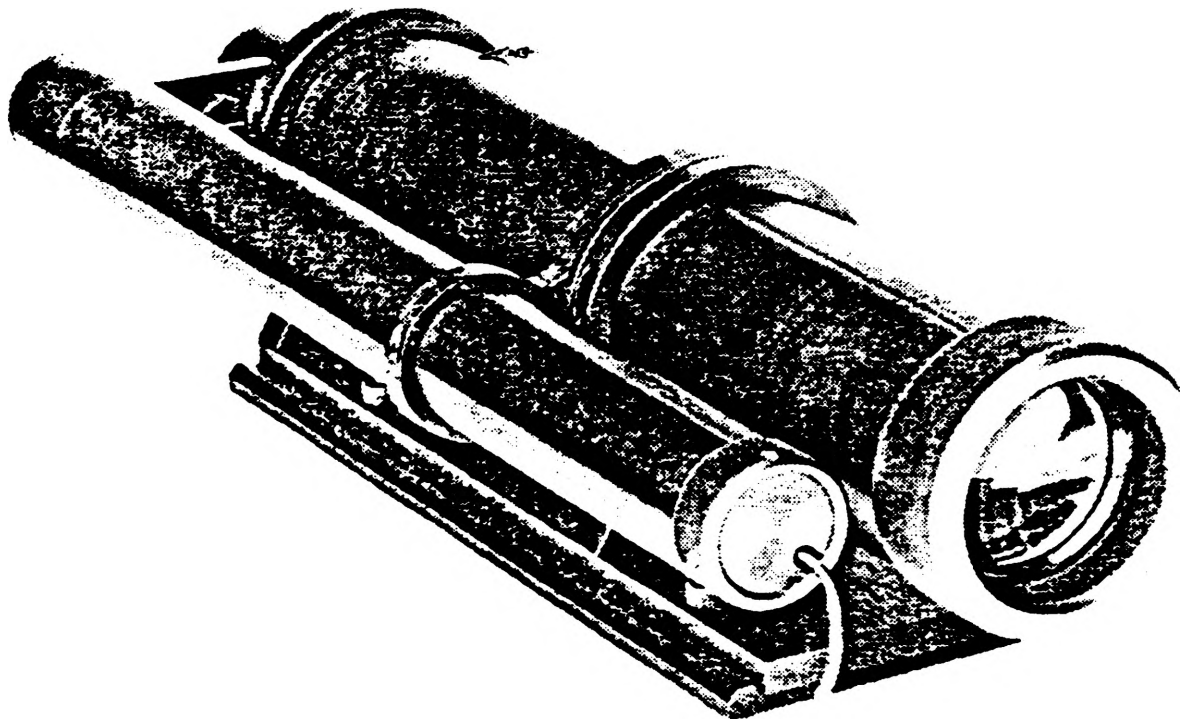


Figure 7 Transmitter Model XMT-1100-4S

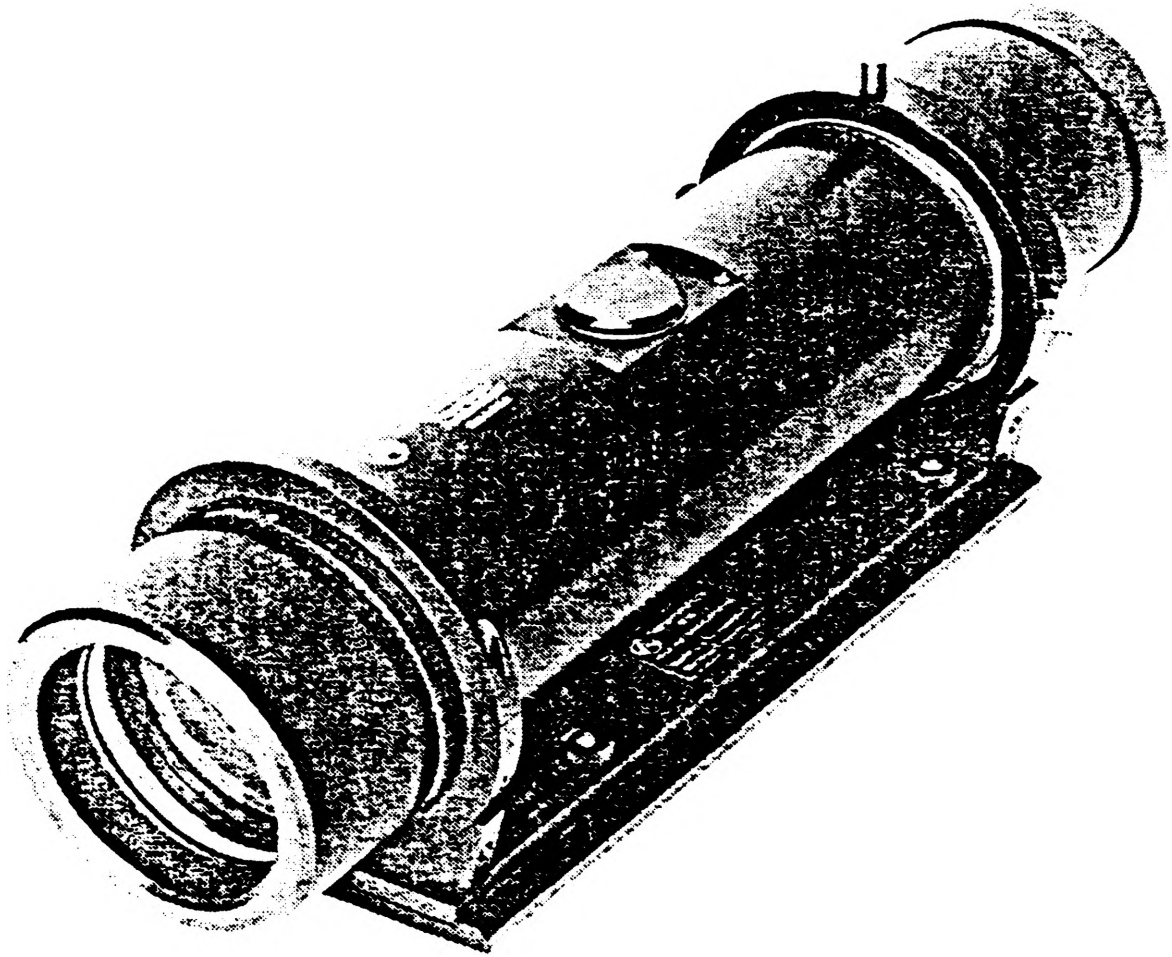


Figure 8 Receiver Model RCV-2100

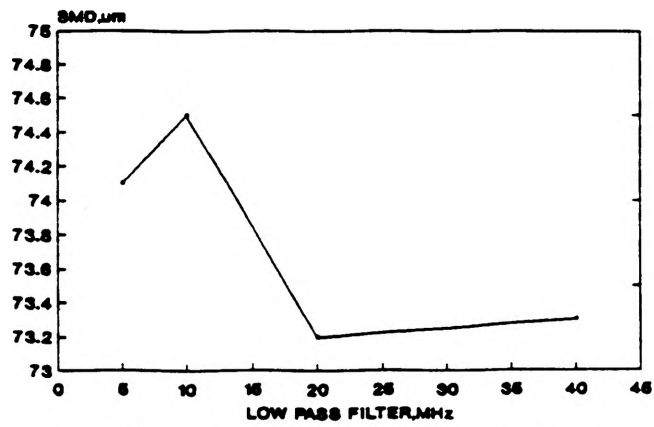


Figure 9 Plot of SMD vs. Low Pass Filter Setting

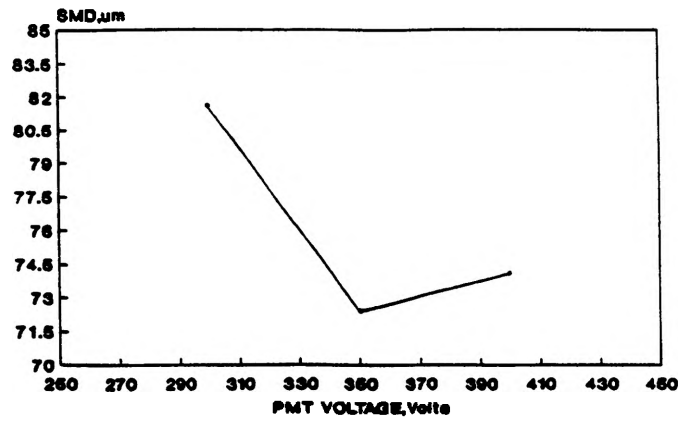


Figure 10 Plot of SMD Vs. PMT Voltage

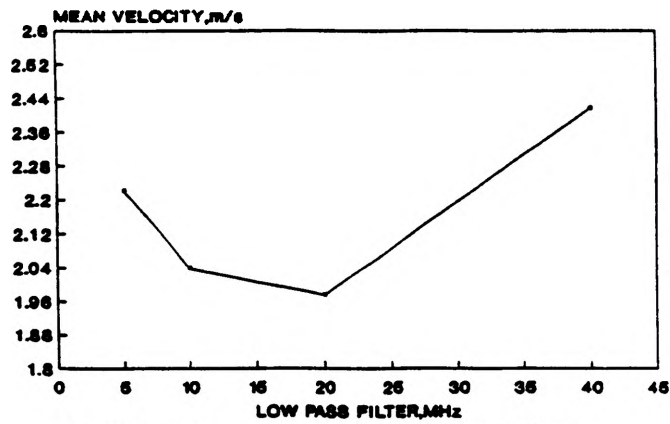


Figure 11 Plot of Mean Velocity Vs. Low Pass Filter Setting

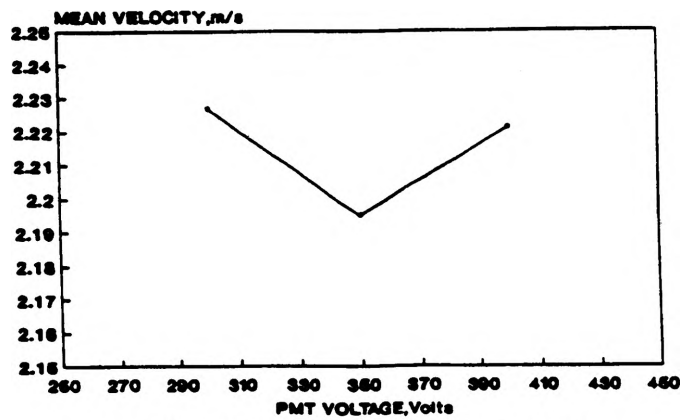


Figure 12 Plot of Mean Velocity Vs. PMT Voltage

EXTRAPOLATION OF THE EXPERIMENTAL DATA OF ELECTRON SCATTERING

Hansen Chen

Physics Department, University of Missouri-Rolla

I Introduction

Our problem of interest is electron-atom scattering. One type of experiment is to measure the number of electrons exciting an atom from a initial s-state to a final p-state. These measurements are proportional to the differential cross section (DCS). Theoretically the DCS is given by

$$DCS = \partial\sigma/\partial\Omega = \sum_m |T^{(m)}|^2 \quad (1)$$

where $T^{(m)}$ is an complex amplitude for exciting a particular magnetic sublevel with magnetic quantum number m , and $T^{(-1)} = -T^{(1)}$.

Experimentally it is very difficult to measure absolute scattering cross sections. There is a quantity called the generalized oscillator strength (GOS) which is proportional to the DCS

$$GOS = f = \Delta E/4 k_i/k_f q^2 \sum_m |T^{(m)}|^2 \quad (2)$$

where

$$q^2 = k_i^2 + k_f^2 - 2k_i k_f \cos\theta \quad (3)$$

Here θ is the scattering angle for the electron, and ΔE is the energy change of the atomic electron. Since $k_i \neq k_f$, it is experimentally impossible for q to be 0. However, experimentalists conjectured that for a final p- state, the GOS will extrapolate to the OOS for $q=0$, where OOS stands for the optical oscillator strength. One of the reasons this method is so attractive is that OOS is independent of the initial electron energy, and only depends on ΔE .

The purpose of this project was to investigate validity of the extrapolation procedure. We used the following mathematical basis for our extrapolation procedure. We consider f , the generalized oscillator strength, as an restriction of an analytic function on an appropriate domain, containing a closed interval with left end point 0, and right end point the physically obtainable

maximum of q^2 , the square of the magnitude of the change in momentum of the outgoing and incoming electron. A well known theorem in complex analysis states that, if two analytic functions in a common domain coincide on an infinite point set with one of its cluster points inside the domain, they will be constantly equal to each other everywhere in the domain. As a result, if we could find an analytic extension function of f , it would be the only one we are after. Consequently we searched for a method to extend the function from the physically allowed interval on the q^2 -axis to that appropriate domain to determine if the values of f at $q^2=0$ were the same independent of initial energy.

The simplest theoretical treatment of this problem is called the plane wave Born approximation. In this approximation, f is a fractional function with only a simple pole off the positive real line of the q^2 -axis. It has the optical oscillator strength as its value at the origin.

The plane wave Born approximation is known not to be accurate enough. However Lassetre¹ claims that even if PWBA (plane wave Born approximation) is not reliable, a more accurate theory should still extrapolate to the optical oscillator strength.

The theory we are using is significantly better than the PWBA. According to Lassetre's theorem, our theory should extrapolate to the optical oscillator strength. The objective of this research project was to check this theory.

II Methodology

In our theory,

$$T^{(m)} = \sum_{l,m} a_l C(l,m) P_l^m(z) \quad (m=-1, 0, 1) \quad (4)$$

$$z \in f$$

and

$$z = \cos\theta \quad \text{while } z \in [-1, 1] \quad (5)$$

where a_l , $C(l,m)$ are coefficients of the expansion generated by the theory, and θ stands for the scattering angle.

¹ Lassetre, Edwin N., J. Chem. Phys. 43, p.4479-4486 (1965)

We proved² that if any function is analytic inside and on an ellipse with foci $-l$ and l , its Legendre polynomial expansion uniformly converges on that compact ellipse. $T^{(m)}$ must approach infinity at $q=0$ so that f will be finite at the origin. Since $q=0$ corresponds to a pole, there is a potential problem for large numerical errors as we approach the pole. We hoped that we could get a good result by the following method. Set up a smaller major axis such that the ellipse excludes $z_c > l$, which is such that $q(z=z_c)=0$, and keep on approaching the major axis to z_c . If the numerical result is accurate enough, we should be able to see the trend. Since this is a singularity, however, a small shift of the zero point of q and the pole of $T^{(m)}$ in the numerical calculation will possibly result in serious deviations, which is what we unfortunately found.

We generated a Fortran code to evaluate the Legendre Polynomials with recurrence functions. The coefficients we calculated for the physical region should remain valid for that enclosed by the ellipse. Consequently it is only necessary to calculate the value of f at $z = \text{major axis}$ using equation (1) and (2).

Appendix I and Appendix II show the comparisons between the analytical PWBA result and the corresponding results obtained from our numerical method. The columns labeled "Analytical" denote the result of the analytical calculation; those labeled "numerical" are of numerical calculation. We can see that the analytic results deviate from the numerical calculation significantly as z approaches closer to the critical point z_c , which is equal to 1.005219 when the initial energy $E_i = 54.4$. In fact the numerical results do not ever have the proper behavior near z_c , which indicates that there is a serious problem in the numerical method for calculating $T^{(m)}(z)$ and $f(z)$, when $|z| > l$.

We first suspected that there may be a problem with the accuracy of our evaluation of the Legendre polynomial $P_{lm}(z)$. We tested the subroutine used to calculate them and compared the generated value for both $|z| \leq l$ and $|z| \geq l$ with those on a handbook. They agreed with each other.

Finally, we checked the accuracy of the coefficients of the Legendre expansion calculated by the numerical method. We recalculated these Legendre coefficients using the conventional inversion:

$$a_{lm} = (l-m)!/(l+m)! \int_{-l}^l T^{(m)}(x) P_{lm}(x) dx \quad (6)$$

where a_{lm} is the coefficient of

$$T^{(m)} = \sum_l a_{lm} P_{lm}(z) \quad (7)$$

² The proof is too long to be typed and presented here.

However, from Appendix III, we can see that the cross sections for $m=0$ obtained by using eq(6) and (7) are even worse than the those generated numerically, even in the normal region $[-1, 1]$.

III Conclusion

We were not able to obtain an extrapolation procedure which was numerically stable. Evidently the Legendre series expansion is unable to produce values for the pole of $T^{(m)}$ which are sufficiently accurate numerically. As a result, we have not been able to determine whether or not the experimental extrapolation are valid.

Appendix I

The following is a comparison of the cross sections obtained from the numerical solutions and the analytical solutions for initial energy 54.4eV. Z_c is the critical point of z .

CROSS SECTIONS FOR M = 0

z	CROSS SECTION		z	CROSS SECTION	
	Numerical	Analytic		Numerical	Analytic
0.99640	1.658E+01	1.665E+01	1.00240	1.745E+02	1.505E+02
0.99680	1.817E+01	1.824E+01	1.00280	2.408E+02	2.004E+02
0.99720	2.001E+01	2.007E+01	1.00320	3.465E+02	2.800E+02
0.99760	2.215E+01	2.219E+01	1.00360	5.213E+02	4.184E+02
0.99800	2.465E+01	2.466E+01	1.00400	8.207E+02	6.918E+02
0.99840	2.761E+01	2.757E+01	1.00440	1.351E+03	1.357E+03
0.99880	3.116E+01	3.103E+01	1.00480	2.316E+03	3.773E+03
0.99920	3.546E+01	3.517E+01	$Z_c=1.00520$	4.118E+03	3.413E+04
0.99960	4.075E+01	4.020E+01	1.00560	7.548E+03	3.360E+04
1.00000	4.736E+01	4.639E+01	1.00600	1.418E+04	3.753E+03
1.00040	5.580E+01	5.412E+01	1.00640	2.712E+04	1.353E+03
1.00080	6.684E+01	6.396E+01	1.00680	5.258E+04	6.903E+02
1.00120	8.164E+01	7.674E+01	1.00720	1.028E+05	4.176E+02
1.00160	1.021E+02	9.377E+01	1.00760	2.020E+05	2.796E+02
1.00200	1.313E+02	1.172E+02	1.00800	3.977E+05	2.002E+02

CROSS SECTIONS FOR M = 1

z	CROSS SECTION		z	CROSS SECTION	
	Numerical	Analytic		Numerical	Analytic
0.99640	4.612E+00	4.681E+00	1.00240	3.544E+01	3.156E+01
0.99680	4.518E+00	4.592E+00	1.00280	5.717E+01	4.940E+01
0.99720	4.376E+00	4.454E+00	1.00320	9.380E+01	7.949E+01
0.99760	4.174E+00	4.252E+00	1.00360	1.575E+02	1.347E+02
0.99800	3.892E+00	3.967E+00	1.00400	2.718E+02	2.493E+02
0.99840	3.507E+00	3.574E+00	1.00440	4.821E+02	5.420E+02
0.99880	2.985E+00	3.039E+00	1.00480	8.779E+02	1.657E+03
0.99920	2.277E+00	2.314E+00	$Z_c=1.00520$	1.637E+03	1.637E+04
0.99960	1.316E+00	1.332E+00	1.00560	3.114E+03	1.749E+04
1.00000	0.000E+00	0.000E+00	1.00600	6.019E+03	2.110E+03
1.00040	1.827E+00	1.821E+00	1.00640	1.177E+04	8.177E+02
1.00080	4.408E+00	4.336E+00	1.00680	2.320E+04	4.469E+02
1.00120	8.136E+00	7.863E+00	1.00720	4.596E+04	2.886E+02
1.00160	1.367E+01	1.291E+01	1.00760	9.121E+04	2.056E+02
1.00200	2.211E+01	2.031E+01	1.00800	1.810E+05	1.562E+02

Appendix II

The following is a comparison of the generalized oscillator strength obtained from the numerical and analytic solution for 54.4 eV. Z_c is the critical point of z .

Generalized Oscillator Strength FOR AN ENERGY OF 54.40 EV

z	CROSS SECTION		z	CROSS SECTION	
	Numerical	Analytic		Numerical	Analytic
0.99640	3.482E-01	3.509E-01	1.00240	4.660E-01	3.930E-01
0.99680	3.508E-01	3.536E-01	1.00280	4.930E-01	3.960E-01
0.99720	3.536E-01	3.562E-01	1.00320	5.240E-01	3.990E-01
0.99760	3.566E-01	3.589E-01	1.00360	5.562E-01	4.021E-01
0.99800	3.598E-01	3.616E-01	1.00400	5.812E-01	4.052E-01
0.99840	3.634E-01	3.644E-01	1.00440	5.789E-01	4.083E-01
0.99880	3.674E-01	3.671E-01	1.00480	5.031E-01	4.114E-01
0.99920	3.719E-01	3.699E-01	$Z_c=1.00520$	2.519E-01	4.146E-01
0.99960	3.772E-01	3.727E-01	1.00560	-3.972E-01	4.178E-01
1.00000	3.834E-01	3.755E-01	1.00600	-1.927E+00	4.210E-01
1.00040	3.909E-01	3.784E-01	1.00640	-5.376E+00	4.243E-01
1.00080	4.001E-01	3.812E-01	1.00680	-1.297E+01	4.276E-01
1.00120	4.115E-01	3.841E-01	1.00720	-2.943E+01	4.309E-01
1.00160	4.259E-01	3.871E-01	1.00760	-6.470E+01	4.342E-01
1.00200	4.438E-01	3.900E-01	1.00800	-1.396E+02	4.376E-01

Appendix III

The following is the comparison of the cross sections for $m=0$ calculated using the coefficients from eq(6) (by numerical calculation), the numerical and analytic solutions. Z_c is the critical point of z .

z	CROSS SECTION		
	eq(6)	numerical	analytic
0.9964000	17.59354	1.658E+01	1.665E+01
0.9968000	19.30448	1.817E+01	1.824E+01
0.9972000	21.27625	2.001E+01	2.007E+01
0.9976000	23.56468	2.215E+01	2.219E+01
0.9980000	26.24119	2.465E+01	2.466E+01
0.9984000	29.39923	2.761E+01	2.757E+01
0.9988000	33.16152	3.116E+01	3.103E+01
0.9992000	37.69249	3.546E+01	3.517E+01
0.9996001	43.21677	4.075E+01	4.020E+01
1.000000	50.04342	4.736E+01	4.639E+01
1.000400	58.61216	5.580E+01	5.412E+01
1.000800	69.55167	6.684E+01	6.396E+01
1.001200	83.78282	8.164E+01	7.674E+01
1.001600	102.6775	1.021E+02	9.377E+01
1.002000	128.3184	1.313E+02	1.172E+02
1.002400	163.9262	1.745E+02	1.505E+02
1.002800	214.5656	2.408E+02	2.004E+02
1.003200	288.3530	3.465E+02	2.800E+02
1.003600	398.4980	5.213E+02	4.184E+02
1.003999	566.8372	8.207E+02	6.918E+02
1.004399	829.9591	1.351E+03	1.357E+03
1.004799	1249.917	2.316E+03	3.773E+03
Z_c=1.005199	1932.939	4.118E+03	3.413E+04
1.005599	3062.533	7.548E+03	3.360E+04
1.005999	4957.213	1.418E+04	3.753E+03
1.006399	8172.682	2.712E+04	1.353E+03
1.006799	13680.27	5.258E+04	6.903E+02
1.007199	23179.92	1.028E+05	4.176E+02
1.007599	39644.59	2.020E+05	2.796E+02
1.007999	68271.29	3.977E+05	2.002E+02

COMPUTER MODELING OF A LIQUID FUEL SPRAY

Clement R. Goodin, Jr.

The initial phase of this project involved manipulation of a lengthy FORTRAN computer code named "Kirwan." The code originated from England many years ago and was transferred to UMR by Dr. Drallmeier. Dr. Drallmeier had the code on a series of 5.25 inch floppy diskettes and the objective of the project was to load the code on to the Apollo computer system and be able to use it. Basically, the code was designed to accept several parameters concerning the liquid fuel type and the injector type and predict what the fuel droplet size and distribution was after a finite period of time and flow distance. The code had previously ran successfully on the University of Illinois Urbana-Champaign campus. It was realized from the onset of the project that once the code was loaded, the FORTRAN compiler used here could possibly be incompatible with the code and compilation would be impossible. The first few weeks of the project involved becoming familiar with the Apollo system. Once this was achieved, the assistance of Michael Johnston was employed in operating the "PC emulator" of the Apollo system. The PC emulator is an integral program of the Apollo system which allows the shell/batch system to be transformed into a personal computer environment. This area allows for transference of code, which is how the Kirwan code was transported. Once the code was contained in account, attempts were made to compile. A lengthy list of errors were reported with compilation attempts. Upon reviewing the code, it was found that these errors stemmed from the numerous data statements throughout the code. The worst case was realized. Obviously, the U of I

compiler had allowed data statements to go unchecked, whereas the Apollo compiler did not. Solving this problem would have involved deleting and adding data, which would be a very tedious project manageable only by a participant who had intricate knowledge of the program's internal workings. Dr. Drallmeier deemed this incompatible with my involvement in the program and this phase was halted.

The second phase of the project was begun in early November 1990 and is currently ongoing. The objective of this project is to predict "Rosin-Rammler" (RR) distribution equations for a fuel spray, given scattered intensity data. The RR distribution is given as:

$$V(D) = \frac{\delta D^{\delta-1}}{D\delta} \text{Exp} \left\{ - (D/\bar{D})^\delta \right\}$$

where \bar{D} , the mean droplet diameter, and δ , the distribution width parameter, are constants for a particular fuel spray and are the points of interest here.

The project centers around the experimental setup of Figure 1. In this experiment, a laser beam is directed through a projected fuel spray flow, scattering light. This scattered light is detected by a flat, concentric ring detector (Figure 2) which detects the light as an energy, given by:

$$\text{Energy} = L_{ik} = C \int_0^\infty \left\{ \left[J_0^2 + J_1^2 \right]_{\alpha\theta_i} - \left[J_0^2 + J_1^2 \right]_{\alpha\theta_k} \right\} \frac{1}{D} V(D) dD$$

This gives the energy incident upon one ring.

The energy given by Equation 2 is measurable and is recorded data. Note, however, the containment of $V(D)$, the size distribution, in the integral of Equation 2. The distribution is unknown and, to be solved for, must be assumed. Several distributions have been suggested by various researchers. As noted, this project assumed the function to be a Rosin-Rammler distribution, given by Equation 1. This is a widely accepted assumption.

Note also in Equation 2 the α term. α is given by:

$$\alpha = \frac{\pi D}{\lambda}$$

The dependence of α upon drop diameter, D , makes Equation 2 all the more complicated (λ is wavelength of the laser light, a known constant). In addition, α is an argument of the Bessel functions, complicating matters further still. Also, note the θ term in Equation 2. $(\theta_i - \theta_k)$ is the angle from the bottom of the ring to the top of the ring.

An iterative procedure has been chosen to solve Equation 2 for $V(D)$, or more specifically, \bar{D} and δ . To do this, a curve-fit method is to be employed.

Educated guesses will be made for \bar{D} and δ and energies calculated from Equation 2. This will then be compared to energy data from experiment and adjustments made in \bar{D} and δ with repetition until the calculated energies equal the experimental energies. Once the energies are equal, the correct \bar{D} and δ values are known. Although this appears as a cookbook operation, Equation 2 is not a simple equation to solve. The first step in this project has been to write computer code to evaluate this integral equation. To do so, data from a calibration reticle was employed. A calibration

reticle is a thin gold foil slide which has been precisely etched. The gold is etched away to leave a known number of known diameter particles, simulating fuel drops on a slide. With all numbers of particles and particle diameters known, the \bar{D} and δ parameters of the Rosin-Rammler distribution equation are also known. This data can then be inserted into Equation 2. The second step in creating the simulation code was actually writing the code. The first hurdle overcome was writing from scratch a Bessel function subroutine. This was completed by using polynomial expressions for Bessel functions as displayed in a math CRC handbook. Once the Bessel function subroutines were operable and checked with CRC table values, the integral equation had to be encoded. This was done by using a Simpson Rule approximation from calculus. The function is integrated from a minimum diameter to a maximum diameter in incremental steps of discrete diameter sizes (all of this information for diameter sizes came from the calibration reticle data). Note that Equation 2 computes energy for a finite angle range. To decide upon this range, a radius for the rings must be decided upon. Initial calculations were run using a logarithmic radius for each ring. The calculations were then run again using inner and outer radii of each ring. The inner and outer radii calculations were used since this was the basis for the calibration reticle calculations.

Figure 3 is a plot of calibration reticle energy values and the energy calculations made by the Simpson code discussed here. The trends match very well with the exception of one data point which is suspected to be a data entry error. Once it has been established that this code makes an accurate prediction of ring energies (which

it appears that a little polishing of the code will bring about), it will then be used for the iterative procedure discussed above. It is conceivable that the present code will be integrated into a much larger code which will accept Rosin-Rammler parameters and produce the calculated energies. An extension of this plan is for the code to automatically run through a group of RR parameters and match up the best calculated energy with the inputted experimental energy. This would resemble a linear best fit routine, but would instead be non-linear.

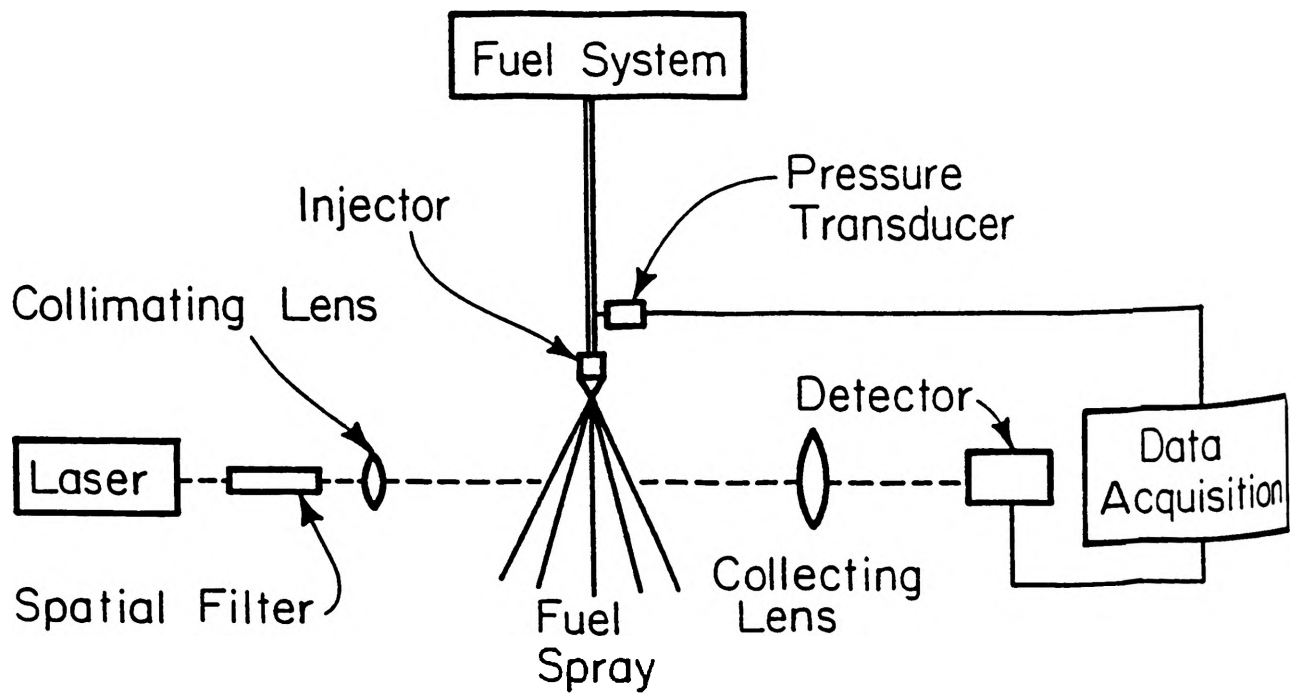


Figure 1) Experiment Setup

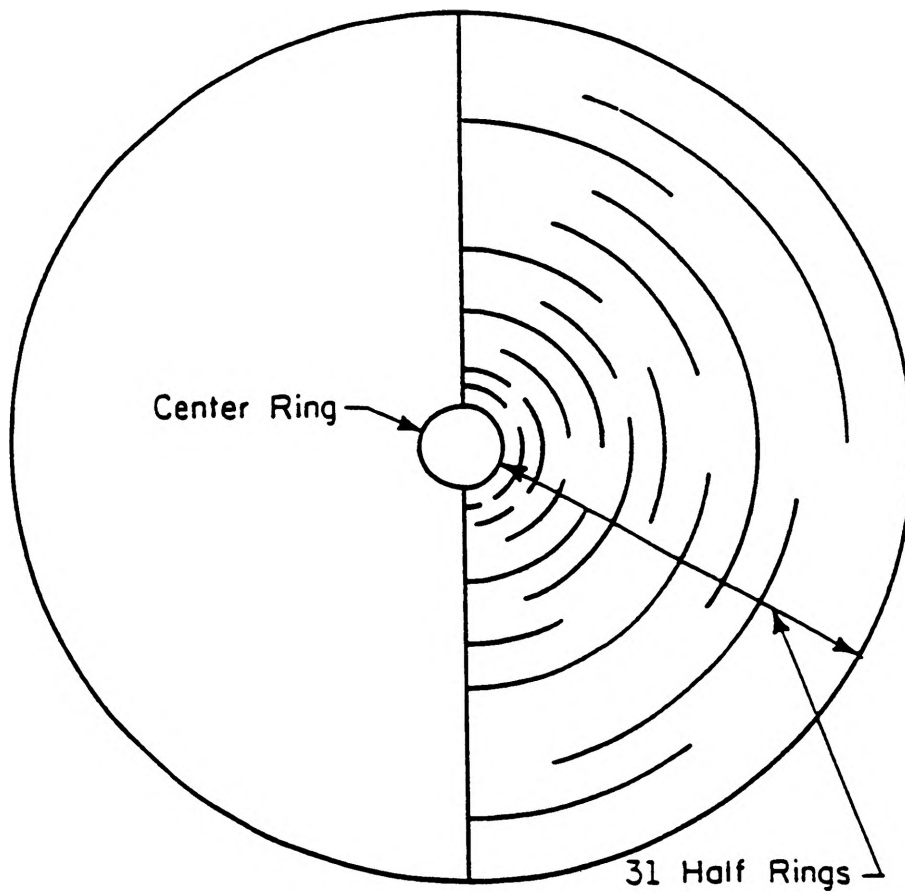
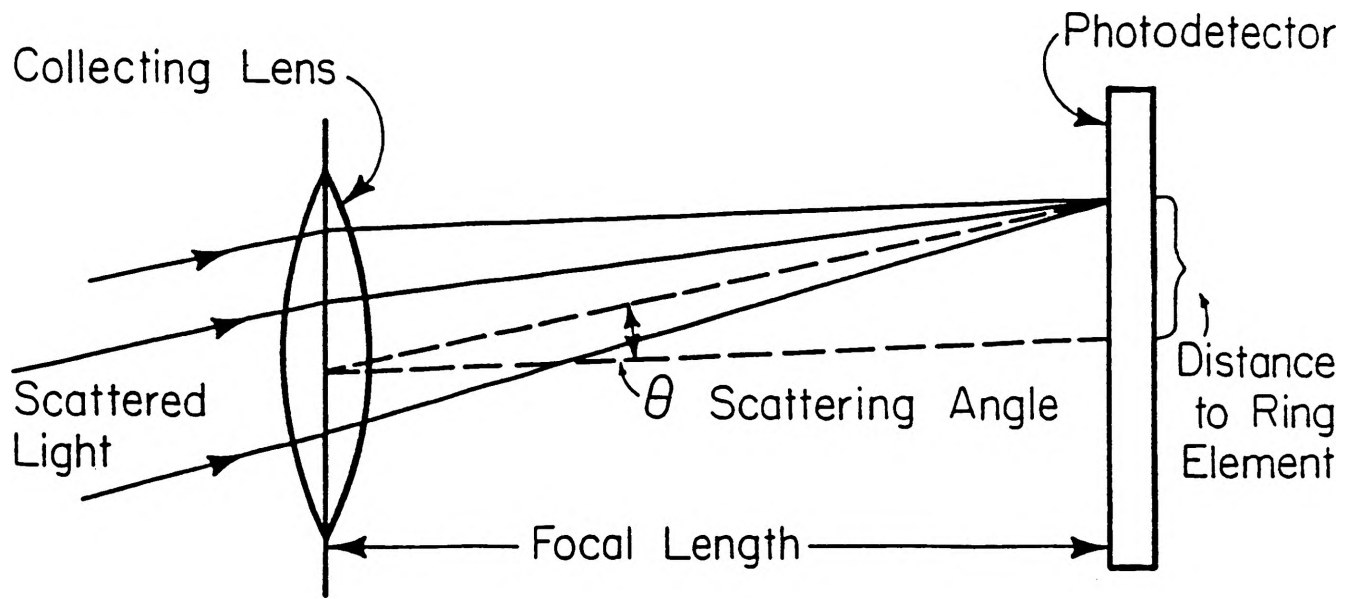


Figure 2) Ring Detector

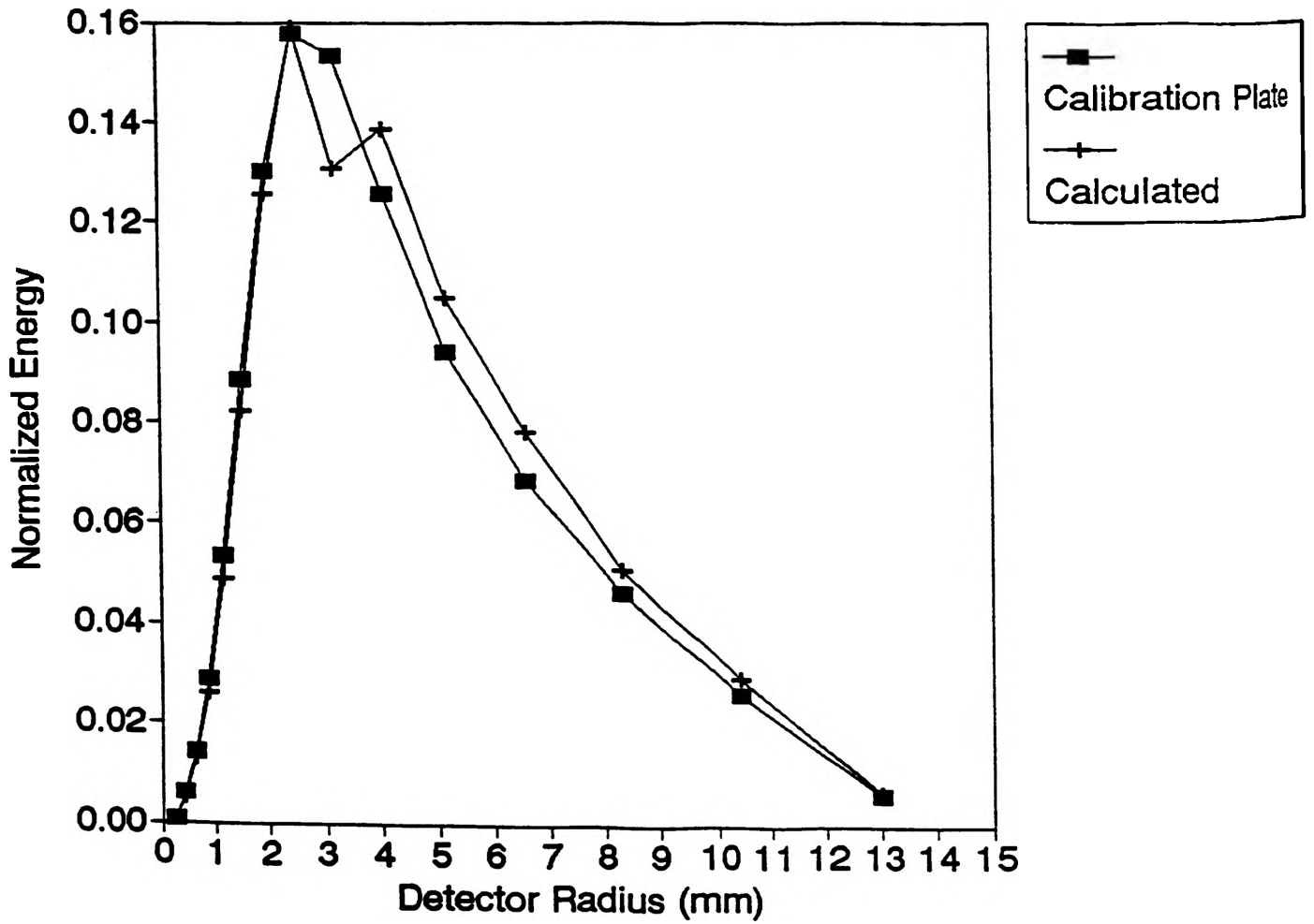


Figure 3) Plot of Results

USING SOFTWARE TO DEMONSTRATE KINEMATICS OF GEAR SETS

John F. Hall

Abstract

The research was done in the area of developing software which could be used to demonstrate the motion of gears. To demonstrate this motion involved learning about programming using graphics. Engineering skills were used in the programming in various ways. One way was in developing and implementing the equations and theory. The more critical engineering aspect of this project is in determining what is effective in demonstrating the kinematic principles associated with gear sets.

The programs will be a helpful aid in showing students what is happening with the motion of gear sets. Not only will instructors be allowed to display drawings of gears quickly, but the important data will be displayed also. The instructor will be able to demonstrate how a slight change in a gear size will change the output in an instant. Overall this program will allow students to cover much more material pertaining to gear sets in much less time.

Introduction

The design and analysis of gear trains involves geometrical restraints, angular velocity ratios, and iteration. As a consequence of these factors visualization of the motion of gear sets is not always intuitive. This is particularly true for planetary gear sets in which some of the gear axes are not stationary.

The basic equation which governs gear ratios is:

$$e = \frac{\text{Product of teeth which are driving}}{\text{Product of teeth which are being driven}}$$

where 'e' is the train value for a set of gears which are in mesh with each other. This equation will allow the output speeds to be found since 'e' is proportional to gear speeds.

The first program, Gear Train Design, makes computations for a gear train and will also create a scaled display of a model designed by the user. There is no actual movement in Gear Train Design, however, the program is able to demonstrate the direction of motion from the computations made.

The second program, Planetary Gear Design, will make computations for a planetary gear set. This program involved displaying the rotation of gears. The program is still in the developing stage. However, the subroutines which animate the motion of the gears have been written as well as a subroutine which verifies data.

In the following text, the ways that these programs will be helpful to students of engineering will be shown by discussing the usage. The design of the program will also be discussed to give a better feel for the program.

Gear Train Design

Program Usage

Gear Train Design was written as a means to analyze and design a five-gear gear train. The user is asked to enter certain characteristics of the gears, such as size and input speed, and in doing so a system is generated. The program itself is user-friendly and self explained.

There are five gears available to the user to construct the gear train. There are four available gear axles which means that two gears must be placed on a single axle when using all five gears. The components can be seen on the following page. Gear 2 serves as the driver gear, while gears 3 and 4 share a common axis to control the speeds of the following gears, gear 5 can be used to give the desired direction for the output, and gear 6 is the output gear. The user has the option to use only the driver and output gears, but he/she may incorporate the other two axles which gears 3 and 4, and 5 rotate about. The user must use either both or neither of gears 3 and 4 since 3 is only in contact with gear 2 and gear 4 is only in contact with gear 5 or 6 (depending on whether or not gear 5 is used as an idler). The program is very descriptive in explaining use of the program functions. There are axis examples of gear trains, along with a description, which can be designed with Gear Train Design.

Not only could students use Gear Train Design to visualize the working part of a gear train and to make basic computations, but design is also possible. For example, say that one wanted to design a gear train with a certain train value; The user would start off by entering what is thought to give the desired output value. Once the output is obtained it can be checked to see if the value was correct. If the output is incorrect, say the train value was too low, the user could press the 'R' key to redesign the train. Once we have the desired values, we may want to reduce the size gear 5 for space purposes. However we also should consider wear on the axle bearings.

The user has the opportunity to interact with the program. To start with, the user will have the opportunity to enter gear sizes based on radius, diameter, or number of gear teeth. The next screen will give the user an organized table where values can be entered. Once the user has entered the values, the program makes some computations and then graphically displays the designed gear train with direction arrows and output table which contains calculated gear speeds. At this time the design part of the program becomes possible. At the output screen the user may enter 'R' to Redesign the gear train. For example, the user may leave out gear 5 to change the direction of the output, decrease the output speed by making gear 3 larger or gear 4 smaller, or completely take out gears 3 and 4. Minor to major modifications can be made an unlimited number of times. While in the design mode, the user may enter a piece of data which the program finds to be unsuitable (i.e. a negative gear value). However, the program will catch the error and alert the user with an explanation.

After the user has decided to exit the design mode (by pressing a key other than 'R' after new gear screen), there will be an opportunity to exit the program or to design another gear train. The program is capable of doing this by recording the last data input by the user and then allowing the user the option to reuse this data.

The help screens at the start of the program have made it possible for a student, even with little understanding of gear ratios, to use the program. Once the student has begun to use Gear Train Design, the student will be made aware of any mistakes he/she has made in entering data and why. Students can find this program to be a great time saver. Computations can be made in an instant as well as scaled diagrams. A copy of the screen can be made by pressing 'PrtSc' on the keyboard while the system is in the GRAPHICS mode.

Program Design

Gear Train Design was written using Borland Turbo Basic Software. The program has a main body, which consists mainly of gear train computations, and a series of subroutines at the end. Subroutines are used to generate the graphical displays. A brief description of each part of the program will help an observer to understand the logic behind the program. Some of the general parts of the program which pertain mostly to this project will be discussed.

At the beginning of the program we can observe help screens to explain the program. As we go down the page, we see a label entitled 'GEARTRAIN', this is the heart of the program. 'GEARTRAIN' consists of a structured IF-THEN statement which is about 75 lines long. In 'GEARTRAIN' I have actually made the computer determine if the user is entering useful data while at the same time having the capacity to make computations for the gear speeds. Towards the top of the 'GEARTRAIN' block we can see the calculations being made for a gear train which consists of all five gears. As we move even lower, the input error messages can be seen.

Some other features that I would like to point out is that one part of the program actually centers the gear train in the upper part of the screen, while another part of the program looks at the horizontal and vertical distances to allow the largest gear train possible without going off the screen.

Planetary Design

Program Usage

Planetary gear design is a program which will delve into the motion and computations associated with a planetary gear set. The gear sets will be based on the twelve types gear sets according to Levi.¹

This program will be useful to the student as it will be very user friendly. The data entry subroutine will make sure that no 'bad' data is entered. In a planetary gear set, such as one where we have some gears in between a center gear and an outer gear with inside teeth, we must make sure that the number of teeth will mesh. For example, suppose that we have a sun gear of diameter 12 inches in the center of the gear train and on the outside we have a ring gear with a diameter of 24 inches. This means that the planet gear must be at a diameter of:

$$d = (24 - 12)/2 = 6 \text{ inches}$$

If the diameter is any bigger the gear will not fit into the mesh. On the other hand, if the planet gear is too small, and it is the only one in between, it will not work either. For this reason, the computer will only allow the user to enter the sizes of a certain amount of gears since the computer will be able to compute the sizes needed for the remaining. This also goes for the input of gear speeds. The program will only allow the user to enter a certain amount so that the remaining can be computed. I should mention that the program does let the user decide what gears are going to be assigned which values pertaining to size and speed.

Once the program is operational, the student will be able to see the motion of the gear set by both a front and side view. I felt as if both were needed due to the complex configuration of some planetary gear sets. When looking at the front view, one can only see the gears which are in front. However, in some cases, where we have many gears composing the planetary gear set, we may not be able to see the background work. By the side view, we can completely understand what is going on with the program. Although I have not yet experimented with showing a back view of the gear set, this is one of my future plans and it will be even better in helping one

grasp an understanding of planetary gear sets. The program is useful for students to visualize what happens with the motion of a planetary gear set since the planet gears have rotation about their own axis, which is itself being carried by the arm in a circular path. This has been found to be a particularly difficult concept to visualize.

Program Design

To understand the usage of the program utilizing motion we will begin by analyzing what happens with the motion of a single gear. The gear looks like four arcs of 75° each. The arcs are separated by 15°. With these four arcs in a circular formation, we can change the orientation of the arcs to animate rotation. There is a part of the program which determines how much rotation is needed for each arc. I used about 0.1 radians for rotation since this proved to give a smooth rotating effect. Each time the program runs through the subroutine for the arcs, the value which represents the start of an arc is decreased by 0.1 while the value which represents the end of the arc is increased by 0.1 for counter-clockwise motion. Since counter-clockwise motion is positive for programming, motion in the clockwise direction requires another subroutine. The program will go through this loop of rotating the arcs for a number of times which corresponds to the speed at which the gear is turning. I should also note that the program could be changed to make the gear rotation increment correspond to the gear speed instead of using 0.1 radians. In doing this we would only need to send the program through the rotation procedure one time per gear. However, our rotation may not appear to be as smooth for incrementation which is large.

The next item which should be incorporated with gear rotation is actual movement of a gear from one location to another. This will need to take into consideration the speed at which the arm of the planetary gear set is moving. By considering the amount of rotation of the arm we can determine how far a gear has moved around the center of the planetary gear set. We must now move the gears which are attached to the arm in a circular path and rotate it at the same time. What I have done is made the program look at each gear to determine if its location has changed since the last time it went through the rotation loop. If the gear has changed, the program completely erases the old and re-draws the new gear with the appropriate rotation.

I have established the screen format for the program and error traps for the data which is entered. The screen is laid out so that the data is entered in the left side of the screen while the gear is drawn in the right side of the screen. Two views of the planetary gear set will be seen, a front view and a side view.

Conclusions

Writing this program not only made use of technical skills that I have learned through my studies in mechanical engineering, but it also required intuitive skills. I had to decide which functions should be created to best aid the engineer who uses the program.

Whenever I wrote this program, I thought of a similar project I once had during a co-op term with General Motors. It pertained to having a certain amount of gears which could be used in a transfer cased to cause certain motion of the output gear. With a program like this I now see how much time one can save.

Future plans include animation of the motion of the gears. The capacity for this can be seen in the planetary gear program. Other future plans include allowing the user unlimited number of axles and gears to design a gear train.

Reference

Shigley J. E. and Uicker, J. J., Theory of Machines and Mechanisms, McGraw Hill Book Company, New York, New York, 1980.

COMBUSTION AEROSOL MORPHOLOGY

Ronald P. Holland

Introduction

The following report entitled **Carbon Aerosol Morphology** is the result of research done through the University of Missouri - Rolla Graduate School program entitled Opportunities for Undergraduate Research Experience (OURE). My appointment was for the Summer - 1990 with the Cloud and Aerosol Sciences Laboratory, Department of Physics, located in Norwood Hall. The goal of this appointment was to study the size and morphology of combustion aerosols whose characteristics are dependent on the history of the particle, e.g. exposure to chemicals, scavenging effects, and other time dependent factors. Computer image processing software is available in the department for this purpose.

This research experience included several facets with the main portion of time spent on the development and perfection of a combustion chamber, specifically the burner assembly itself. This combustion chamber is used in the Cloud Physics laboratory to supply combustion aerosols of liquid fuels, primarily aviation fuel JP-4 supplied by McDonnell Douglas Corporation. These aerosols are used in the study of the effects of jet engine emissions in the atmosphere and thus upon global environment.

The appointment began with exposure to the operation of the equipment and instruments used within the Cloud Physics laboratory. This equipment being used to isolate and characterize aerosols by size, mobility, and critical supersaturation (SSc), the latter being a measurement of the amount of water vapor present in air to cause the particle to grow by the accumulation of water vapor. The understanding of these methods is important as they are used routinely to classify and characterize aerosols produced by nebulizers and by combustion processes.

As my project goal was to study aerosols produced by combustion processes, it was first necessary to perfect the operation of the combustion equipment which operated inadequately for the collection of these aerosols. The torch assembly used for combustion produced a flame which was unsteady in nature and not easily controlled. This problem had to be eliminated as the oscillations of the flame produced particles of inconsistent nature as seen by production of varying amounts of soot. The torch was analyzed and its problems were found. Based on a great deal of research time, the burner assembly was modified to produce a flame which was very stable and easily controlled. This required at least a month of the summer to accomplish.

Upon the perfection of the torch, it was then possible to produce a consistent flame pattern from which carbon aerosols were collected and analyzed by scanning electron microscopy. Due to the amount of time required to perfect the torch assembly it was not possible during the summer to complete the goal of the project. As such, time was taken during the Spring 1991 semester to continue to collect and analyze particles. It is from this work that significant data and conclusions have been possible. This information is in the following report.

In addition to the improvements of the combustion process, time was used to improve the operation of a wire-egression droplet generator which is currently being used by another department for the production of single droplets. Also, a computer software system (JAVA) for image processing was studied for its application to the characterization of the carbon aerosols collected.

Additional plans related to this research appointment include two presentations at regional science meetings. The first of these is the Missouri Academy of Sciences Meeting (MAS) on April 19, 1991 in Fulton, Missouri for a presentation entitled **Combustion Aerosol Morphology**. The second is at the Midwest Association for Cloud and Aerosol Physics (MACAP) at the University of Wisconsin, Madison, on May 17, 1991 for a presentation entitled **A laboratory liquid fuel burner and the properties of the associated combustion aerosols**.

Pollution

One of the greatest concerns facing the world today is the need to regulate and reduce environmental pollutants. Of particular interest are anthropogenic, that is man-made, air pollutants which arise from combustion processes as in power plants and factories. These atmospheric pollutants subsequently affect global surface conditions as they are removed from the atmosphere by natural precipitation processes like rainfall. Air pollutants pose immediate health hazards to man such as lung disease due to particulate matter. These pollutants also cause long-term global effects associated with chemical reactions and the Greenhouse Effect. As these effects are critical to the environment and its stability the need for pollution control becomes increasingly important.

Pollutants fall into five major categories which are particulate matter, nitrogen oxides, sulfur oxides, hydrocarbons and carbon monoxide. Each of these categories is associated with a damaging process to the environment such as acid rain production. This research is associated with the production and effects of particulate matter to the atmosphere, particularly that which is produced by organic fuel combustion.

Airborne particulate matter can arise from different sources. These sources can be of mineral origin such as milling and demolition operations or as organic origin such as forest fires and fossil fuel combustion. Organic particulate matter includes soot and flyash which may be as large as 100 microns or larger in diameter and combustion nuclei which may be as small as 0.01 micron in diameter. Figure 1 provides information relating particle sizes with associated features for reference.

Aerosols

An aerosol is a suspension of solid or liquid particles dispersed in a gas medium which is air in this case. The

combustion of fossil fuels produces carbon aerosols whose sizes range from those of nuclei to those of soot. This study is concerned with the particles produced by aviation fuels which have a size range from 0.01 micron to 0.10 micron in diameter. This aerosol size range is important to study as they act as initiation sites for the phase change of water vapor within the atmosphere. Particles which act as sites for the accumulation of liquid water are known as cloud condensation nuclei (CCN). If the particles acts as sites for ice crystal deposition they are called ice nuclei (IN). Scavenging theory, that is the rate at which particles are removed from the atmosphere, was first studied by Greenfield (1957) who studied scavenging processes by Brownian diffusion, turbulent shear diffusion and inertial capture. He found that small particles (less than 0.1 micron radius) and larger particles (greater than 1.0 micron radius) are affected by Brownian diffusion and inertial capture resulting in greater scavenging rates for those particles. This produces a minimum scavenging rate for particles between those minimum and maximum radii which is referred to as the Greenfield Gap. This relationship between scavenging rate and particle size was also demonstrated by Slinn and Hales (1971) with a minimum scavenging rate of particles with a radius of 0.01-0.15 micron (0.02-0.30 micron diameter). This is pertinent to the particles which we are studying whose sizes fall within this minimum scavenging range suggesting that these particles will be long-lived in the atmosphere.

Cloud condensation nuclei occur by natural phenomenon such as salt particles generated by bursting bubbles over oceans. Other sources for such nuclei occur by man-influenced chemical reactions within the atmosphere such as ammonium sulfate formation or particles produced by combustion processes. As already mentioned these nuclei act as sites where water vapor can change phase to a liquid or solid depending on temperature. As such, their presence reduces the amount of supersaturation, that is the amount of water vapor present, required for a phase change to occur. Much higher supersaturation levels are necessary in the absence of nuclei to initiate the phase change which will occur at lower supersaturation levels in the presence of nuclei. Once the phase change is initiated, the water droplet continues to grow by vapor deposition until its size and interaction with other particles plays a greater role in its growth than does vapor deposition. The particle as a droplet may begin to fall and impact with other droplets at that point. Thus, the presence of carbon aerosols results in their action as condensation nuclei which influence the behavior of water vapor within clouds. The combustion aerosols produced by jet engines are studied for their actions and influences as condensation nuclei.

Production of Aerosols

To study the size and morphology of the carbon aerosols produced from jet fuel, a laboratory combustion and aerosol collection

system is used. This system consists of a combustion chamber in which liquid fuel and air are mixed for rapid combustion and a commercial instrument which removes the aerosols produced. Other Cloud and Aerosol Laboratory equipment is available for further characterization of the aerosol produced. Description of these systems follow and are represented visually by the attached Figure 2.

In an effort to study the production of combustion particles by a jet engine a chamber, made of a cylindrical stainless steel bell jar (44 cm diameter x 61 cm height) equipped with sealed viewing ports is used to house a torch-like liquid fuel burner. Within this sealed chamber is fixed a burner assembly in which pressurized liquid fuel and filtered air enter, preheat and premix before combustion occurs. This burner allows the control of temperature, fuel flow and air flow to any desired parameter. It is entirely accessible from outside the chamber to ensure a controlled combustion environment within the chamber. The burner head itself is constructed of stainless steel with interchangeable cores by which the flame diameter may be altered. The head also uses an internal jet passage which ensures the atomization and mixing of the fuel and air. Combustion occurs with a flame stabilized at the head by a fine stainless steel mesh. Figure 3 illustrates a lean-burn flame produced by the combustion of JP-4 aviation fuel in the combustion chamber.

The ability to control the flame parameters is critical to this study as it predicts the type of particle produced. Flame stability is necessary for the stability of the resulting combustion aerosol. Aerosol stability, in turn, is needed to accommodate the various aerosol characterization facilities available in the Cloud Physics aerosol laboratory. The actual combustion process is very complex in which the chemical reactions take place. This process amounts to reaction zones in which the fuel and oxidizer are heated to reaction temperatures. Reaction zones occur in which rapid oxidation of the jet fuel produces heat, flame, water vapor, carbon dioxide, aerosols, and other by-products. Control and stability of the flame is essential to study a particular flame type without which combustion aerosols ranging from nuclei to soot are produced. This combustion system is perfected to allow continuous laminar flow flame conditions ranging from a high temperature, high velocity, blue flame to a much lower temperature, low velocity, yellow flame. These differences are due to the amounts of fuel and oxygen present during the combustion process. These different flame conditions are found to produce measurably different combustion aerosols.

Another parameter of this system is that it can be used to produce the major flame types, either premixed or diffusion type. The premixed flame is the one usually employed in which the reactants are homogeneous before the point of combustion. With modification of the burner head a diffusion type flame can be obtained in which the fuel and oxidizer meet and react within a reaction zone limited by the diffusion of fuel on one side to the oxidizer on the other. Flame types of mixed nature between

premixed and diffusion can also be obtained if necessary. The versatility of the combustion chamber also extends to the ability to burn different liquid fuels for the study of other combustion products as well.

Collection of Aerosols

The flow of combustion products exits the top of the combustion chamber and enters an ice-cooled condensation container. This container serves to cool the gases present and to remove water vapor which is generated by the combustion process. The "dried" products are then prepared for entry into a commercial electrostatic aerosol sampler. This preparation is done by passing the combustion products through a commercially available bipolar charger. This unit uses a radioactive source to produce a known charge distribution on the particles as they exit the unit. This is needed as many combustion products carry large electrostatic charges due to the combustion process. This unit equalizes and quantifies the particle charge distribution. From the bipolar charger, the combustion products enter the electrostatic aerosol sampler which ionizes the aerosol present and intermittently precipitates the aerosol onto treated slides by use of an electric field force. Upon completion of a suitable number of cycles the treated slides are submitted for scanning electron microscopy (SEM).

The slides used for electrostatic precipitation of the particles are glass cover slips which are cleaned and coated with approximately 300 Angstroms of gold-palladium (Au-Pd) alloy. This Au-Pd serves as a viewing substrate for the SEM analysis. After collection of the aerosol, the slide is again coated with Au-Pd, about 200 Angstroms thick, which stabilizes the aerosol and increases the contrast for SEM analysis.

Analyzing Aerosols

SEM analysis is done by the University of Missouri - Rolla electron microscope laboratory located in McNutt Hall. The slides are examined and pictures of the slides are taken at magnifications ranging from 3500X to 75000X. Pictures are taken at locations chosen so that there is no bias towards the particles/area selected for analysis. Series of photographs are taken for particle analysis at higher magnifications. Figures 4-7 are examples of the electron micrographs analyzed.

In addition to analyzing areas in which particles are deposited, areas on the slides are covered as control regions. These areas are photographed in a duplicate manner as the actual test regions for analysis. A system control is performed as well in which the collection process is performed in its entirety except that combustion is not performed. This allows for a check of the entire system and the particles which may arise inherent to the system and not due to combustion. These control slides

are analyzed by the same procedure as the actual test slides with masked control areas and Au-Pd coatings.

A particle size distribution is desired from the electron micrographs to see the correlation between SEM analysis and size distributions readily obtainable from other aerosol characterizing methods already used and accepted. This correlation will provide information on the ability to use SEM analysis for the further characterization of carbon aerosols and their study. The method of determining this size distribution is to measure and record the diameters of the particles present on slides photographed by SEM and prepared using a lean burning laminar flow premixed combustion flame from JP-4 aviation fuel. This data follows; however it is important to note the criteria used for determining and measuring the particles.

A characteristic of the photographs is that an irregular background appearance occurs on almost all of the electron micrographs including those which are controls. See Figure 7. After consideration of what this could be - whether an actual particle collected or an anomaly associated with the Au-Pd substrate - it was decided to consider it something besides a particle layer. This decision arises from the fact that it occurs on control slides and the size distribution and appearance is not like that of a particle deposited to the surface. This will be discussed later with the following criteria used for determining which features constitute a particle as seen on Figures 5,6:

- (1) the image appears distinct and defined at its edges,
- (2) the image does not appear to be the size and shape of the background associated with the control pictures,
- (3) the diameter of the particle is taken as the outermost defined border of the particle,
- (4) particles found on the edge of the micrograph are included provided the diameter can be determined.

The consideration and measuring of the particles is somewhat subjective to the person performing the task, however with these criteria it is believed that suitable guidelines are set for determining an accurate size distribution.

Data

The following data is taken from a single collection date in which carbon aerosols are collected from JP-4 aviation fuel. The fuel was burned with a lean (excess oxidizer), laminar flow premixed flame. Two slides were analyzed and the particles were counted from the micrographs obtained by SEM. This amounted to a total of 24 pictures for a total of 327 particles. The data is recorded as follows. Note all dimensions are in microns.

Photo Number	No. Part. Counted	Mean Diameter	Standard Deviation	Minimum Diameter	Maximum Diameter
SLIDE 1					
030904	10	0.072	0.014	0.056	0.094
030906	09	0.074	0.021	0.056	0.12
030908	19	0.065	0.019	0.036	0.11
030909	19	0.064	0.014	0.039	0.086
030910	16	0.070	0.021	0.042	0.12
030911	15	0.068	0.013	0.053	0.10
030912	10	0.068	0.023	0.044	0.12
030913	15	0.076	0.023	0.047	0.13
030915	12	0.064	0.014	0.044	0.094
030917	07	0.067	0.008	0.058	0.081
030918	18	0.065	0.012	0.047	0.099
030919	11	0.073	0.014	0.056	0.10
SLIDE 2					
030924	14	0.074	0.011	0.053	0.089
030926	12	0.080	0.018	0.050	0.11
030928	15	0.071	0.009	0.056	0.089
030929	20	0.075	0.016	0.056	0.11
030930	17	0.065	0.014	0.044	0.094
030931	10	0.068	0.021	0.036	0.10
030932	14	0.068	0.010	0.047	0.086
030933	10	0.068	0.021	0.042	0.12
030935	10	0.078	0.017	0.047	0.10
030937	09	0.093	0.012	0.072	0.11
030938	25	0.073	0.021	0.039	0.12
030939	10	0.075	0.013	0.047	0.089

The following is a summary of the particles counted from each slide and an overall summary for all particles counted. Again, all dimensional values are given as microns.

Summary of:	Number of Particles	Mean Diameter	Standard Deviation	Minimum Diameter	Maximum Diameter
Slide 1	161	0.068	0.017	0.036	0.13
Slide 2	166	0.073	0.017	0.036	0.12
Combined	327	0.071	0.017	0.036	0.13

Discussion

The summary of results gives an overall mean particle diameter of 0.071 microns with a standard deviation of 0.017 microns. This provides a particle range of 0.054-0.088 microns. This distribution is compared with the size distribution as measured by an alternate technique used in the Cloud Physics laboratory. This technique is based on particle electric mobility and uses the electric aerosol classifier (EAC) for sizing and the alternating gradient cloud nucleus counter (ALGR) for particle detection and counting. Data from the EAC/ALGR was computer processed to yield a size distribution with a mean particle diameter of 0.054 microns and standard deviation of 0.029 microns. This indicates a particle range from 0.025-0.083 microns. Good agreement is achieved between the size distributions determined by the two different methods.

Particle morphology (shape) is studied in addition to particle size. This is important as morphology affects particle hydration properties, mobility and scavenging rates which will affect the evolution of the particle in the atmosphere. Electron micrographs indicate that flame type is critical to particle morphology as shown on the attached figures. A yellow flame produces soot, hence large particle agglomerates, and a blue flame produces small spherical particles with little agglomeration. This production and analysis of small spherical particles validates the EAC/ALGR classification techniques which work well for spherical particles and not-so-well for large chain aggregates. It is seen from the data and the results of SEM that carbon aerosols can be produced and classified by several methods. These methods being SEM analysis and standard lab methods currently used such as EAC/ALGR counting of nuclei. The SEM method being studied is found to produce results which fall within the range of the currently accepted means of nuclei measurement. The studied method by SEM analysis not only produces a size distribution close to accepted methods but it provides additional information dealing with the morphology of carbon aerosols. This ability to characterize morphology opens many opportunities to explore particle characteristics based on the history of a particle. That is, the effects of an aerosol's exposure to moisture, chemicals, and storage conditions as functions of time. This information can then be used to determine the effects of carbon aerosols upon the environment.

Several areas of investigation remain with this study to improve and enhance the ability to characterize carbon aerosols by SEM analysis. These include (1) the collection process which may enhance particle collection efficiency, (2) improvement of SEM analysis by use of different substrates, (3) chemical analysis which can precisely describe the content of particles collected and (4) improvement of the quality of the micrographs, computer analysis equipment is available which can be used to collect data for size as well as area distributions.

This work will benefit future university aerosol research, e.g. environmental effects associated with jet engine exhaust by future high speed high altitude commercial aircraft as in NASA's high speed civil transport (HSCT) program.

Acknowledgements

I would like to thank all those who made my OURE appointment such an enjoyable research experience. These include M. B. Trueblood and Dr. D. E. Hagen of the Cloud and Aerosol Sciences Laboratory, Scott Miller of the McNutt Hall Electron Microscopy Laboratory, and the University of Missouri - Rolla Graduate School for providing the opportunity to do this research.

Bibliography

Hagen, D.E., Trueblood, M.B., White, D.R., (1989). Aerosol Science and Technology, 10:63-69.

Hidy, G.M. (1987) "Aerosols," Encyclopedia of Physical Science and Technology, Volume 1, Academic Press, Inc., New York.

Monastersky, R., (1991) "Time for Action," Science News. Volume 139, No. 13, pp. 200-203, Science Service Publication, Washington, D.C.

Williams, F.A., (1987) "Combustion," Encyclopedia of Physical Science and Technology, Volume 3, Academic Press, Inc., New York.

General Reference

McGraw Hill Encyclopedia of Science and Technology, (1987), 6th Edition, McGraw Hill Book Company, New York.

The New Encyclopedia Britannica, (1987), 15th Edition, Chicago.

Scientific Encyclopedia, (1989), 7th Edition, VanNostrand Reinhold, New York.

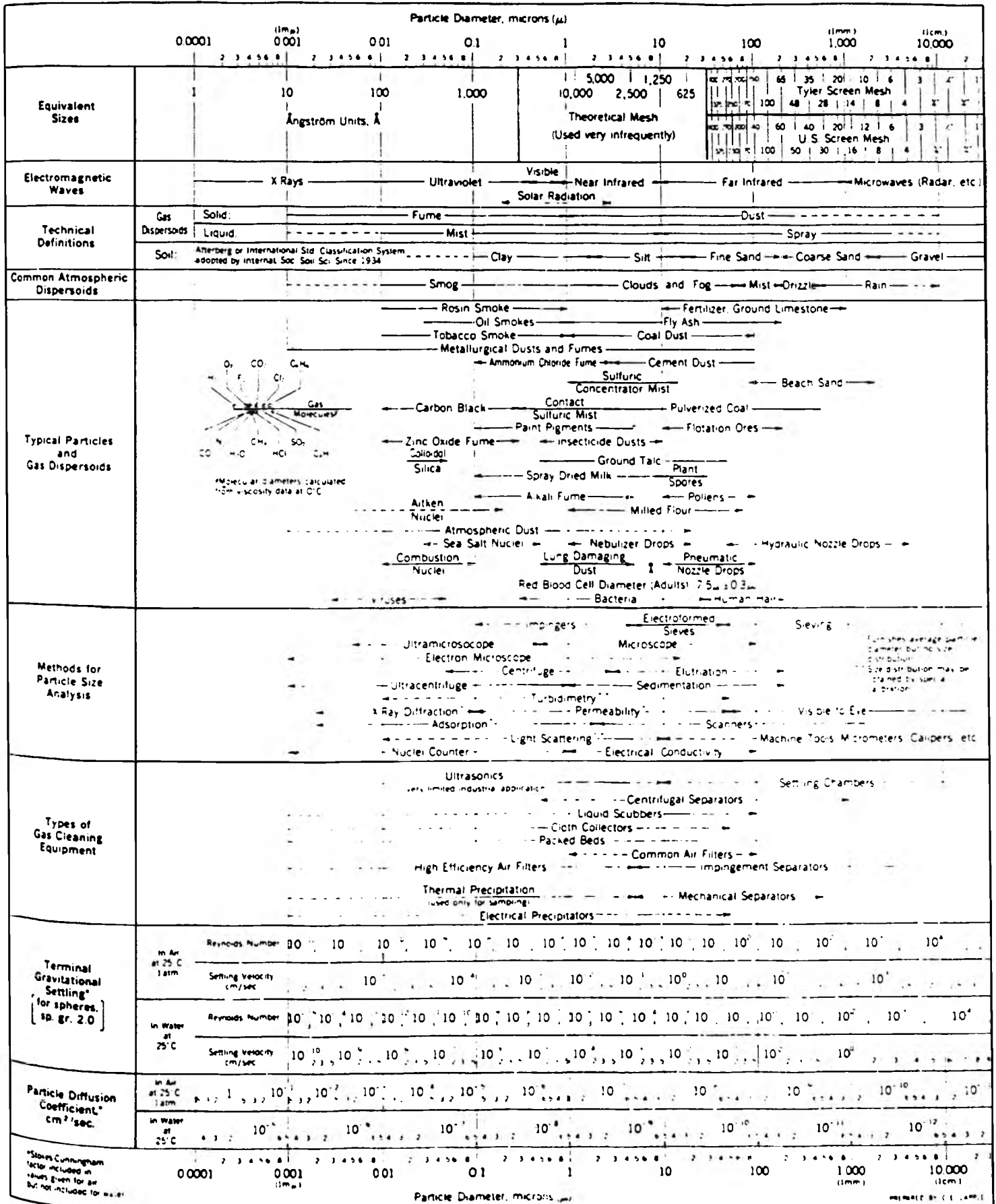


FIG. 1. Summary diagram of particle properties as a function of size, including measurements and gas-cleaning technology. (Courtesy of Stanford Research Institute.)

Combustion Aerosol Generation/Collection Diagram

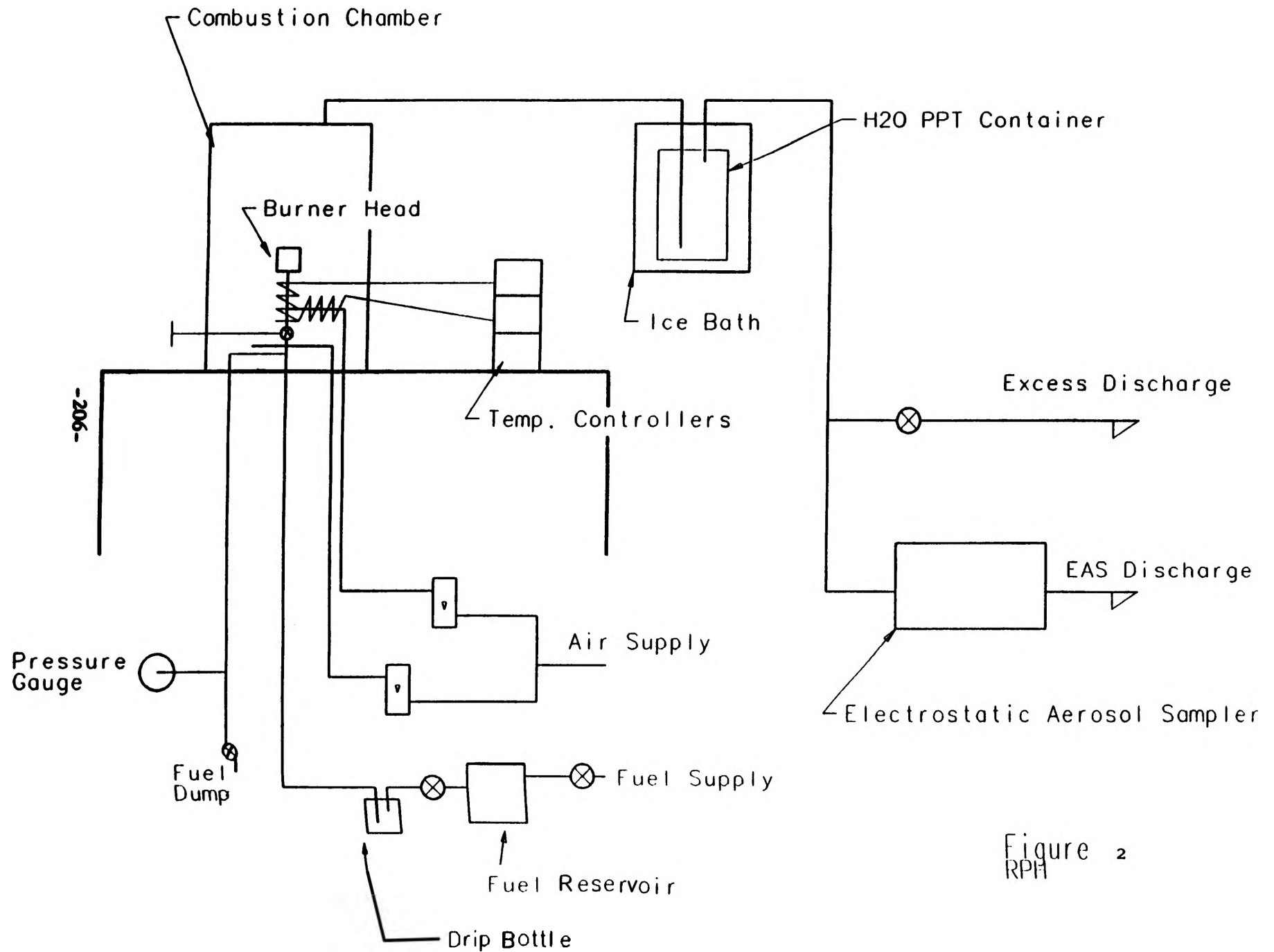


Figure 2
RPH

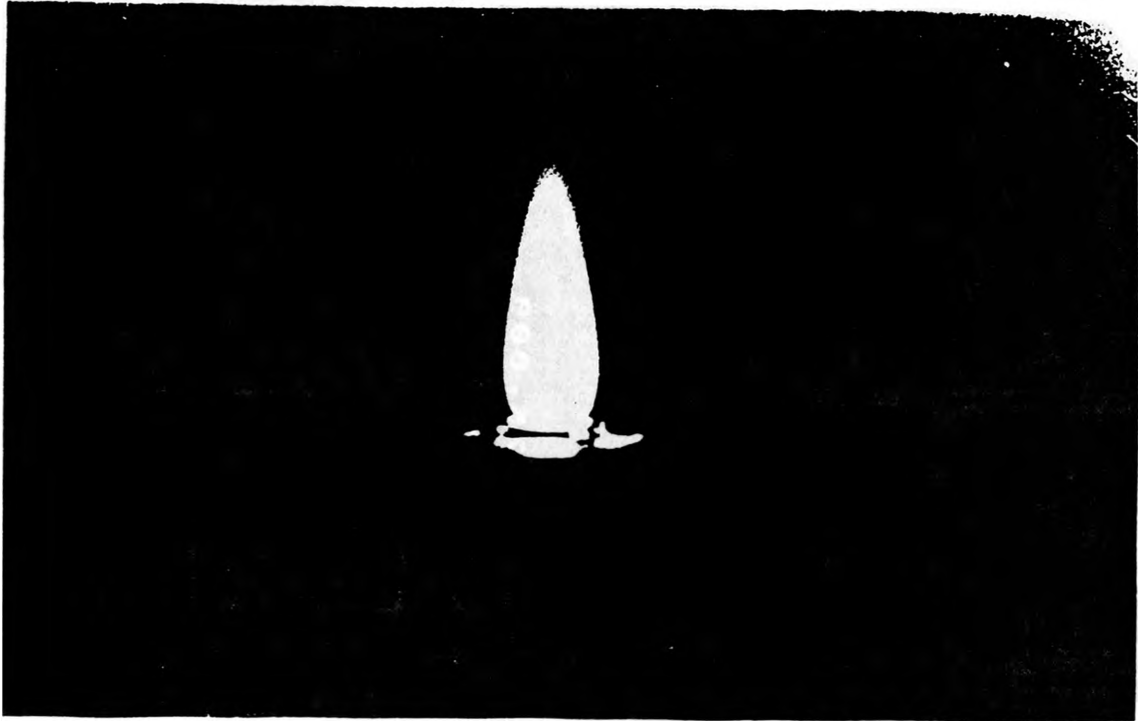


Fig. 3

Flame produced by improved torch

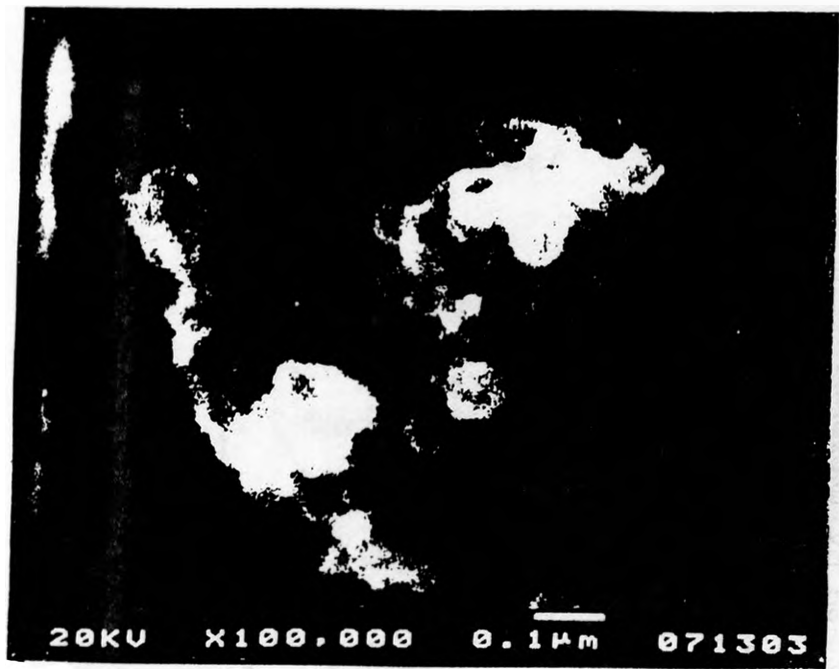


Fig. 4 - Large soot agglomerate (SEM)

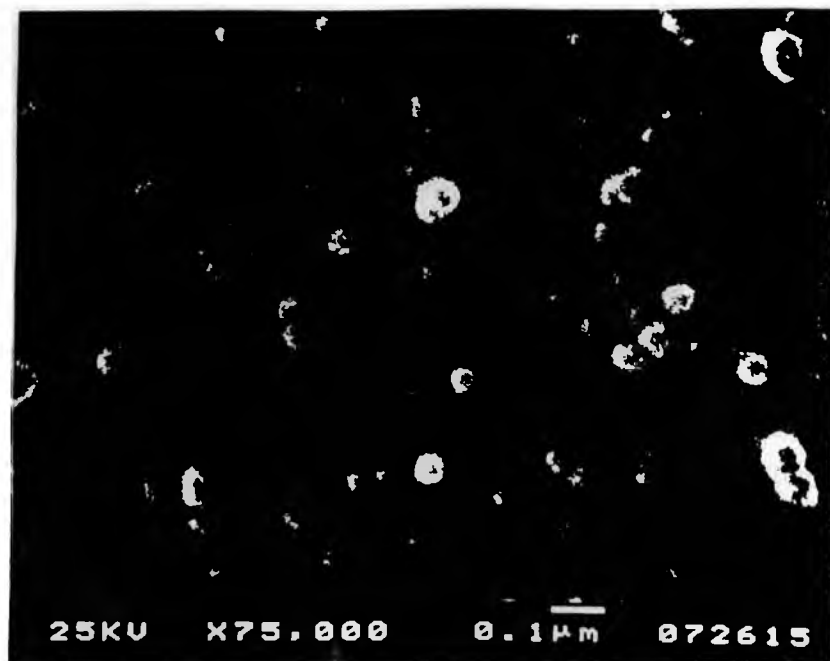
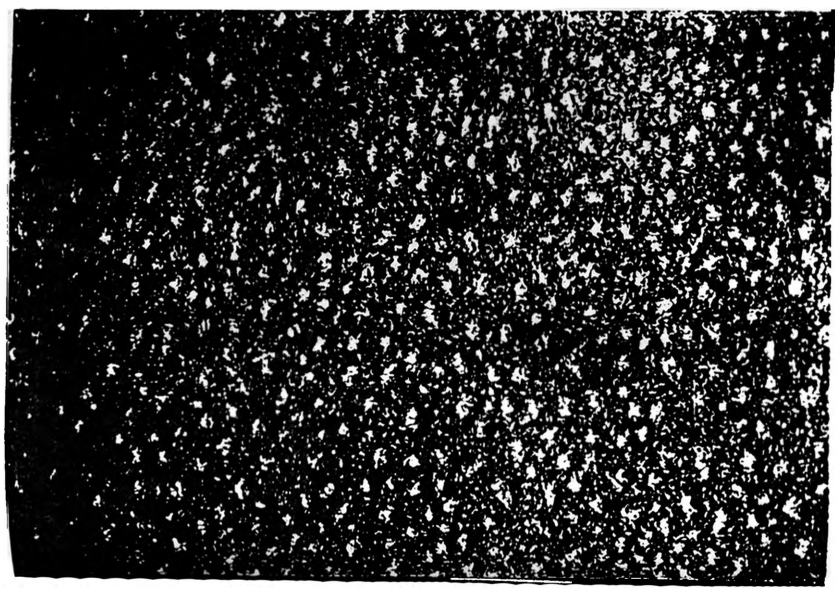
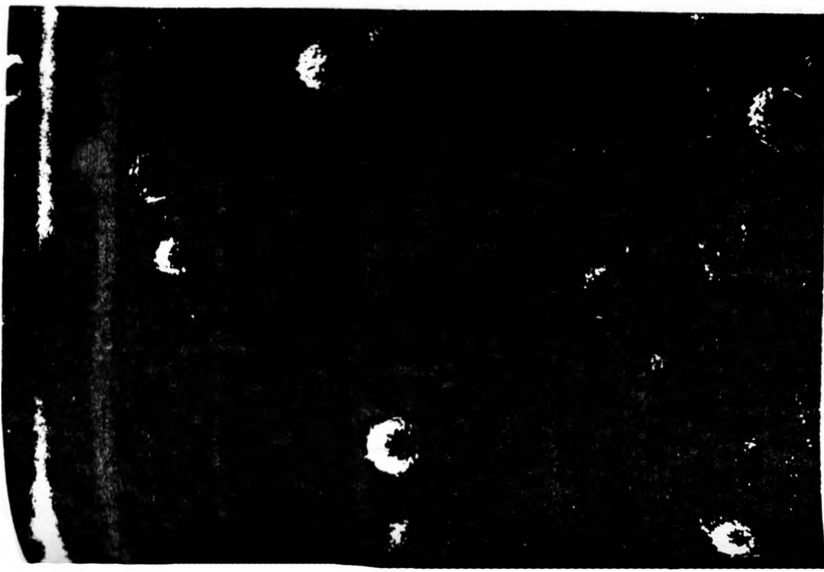


Fig. 5 - Single aerosol particles (SEM)



Simulation Modeling in Manufacturing Cell Design

Debra A. Hunke

ABSTRACT

The interwoven phases of the manufacturing process in Computer Integrated Manufacturing (CIM) require a carefully designed facility. Simulation modeling can be combined with other techniques to provide a rigorous methodology for CIM system design. This paper describes CIM, simulation and their relationship. A case study demonstrates the described methodology in the design of a flexible manufacturing cell.

Introduction

Computer Integrated Manufacturing (CIM) combines all phases of the manufacturing process - design, manufacturing planning, manufacturing control, and business functions. The technology applied in CIM makes extensive use of computer networks and data processing techniques to control and integrate automation at all levels of the manufacturing process.

Simulation modeling is a technique used to evaluate a manufacturing system's design before implementation. Simulation can uncover problems in the layout and material handling system as well as provide a means to perform sensitivity analysis on the components of the system.

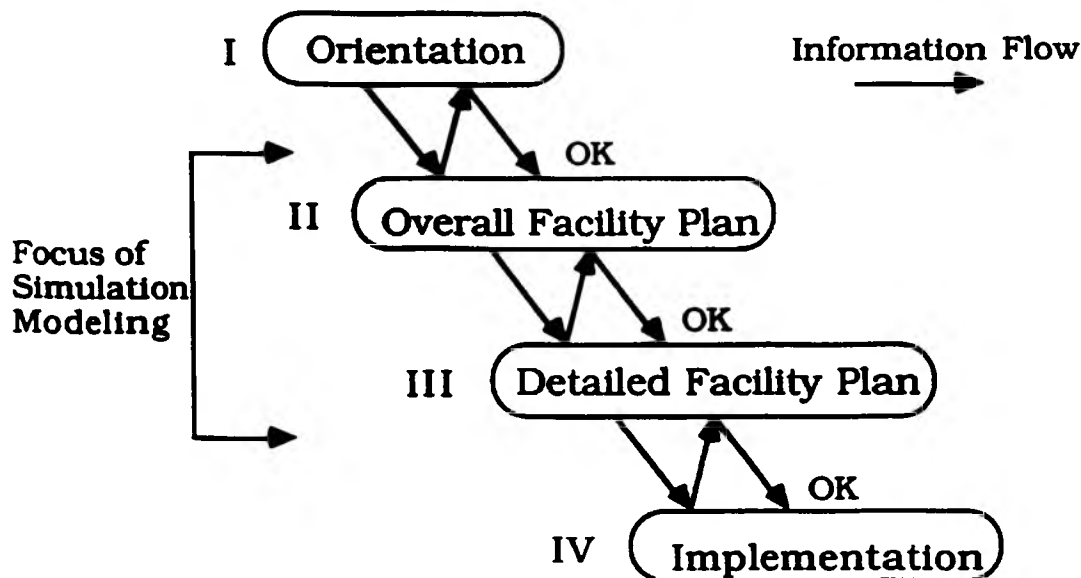
Simulation modeling can be successfully integrated into CIM system design. This paper describes simulation modeling and its application in CIM system design. These techniques are then demonstrated in a case study involving the design of a flexible manufacturing cell.

Computer Integrated Manufacturing

Computer integrated manufacturing (CIM) denotes the use of computers to design the products, plan the production, control the operations, and perform the various business related functions needed in a manufacturing firm. CIM brings all of these processes in an automated factory together by performing the information-processing functions necessary to support the production operations (1).

The process of planning and implementing a CIM facility can be divided into four phases as shown in Figure 1.

Figure 1 Phases of Integrated Facilities Planning



The orientation phase, Phase I, begins with the definition of the project and its objectives. It involves an evaluation of all constraints and influencing factors, such as: machinery to be used, projected capacity, and costs. A preliminary economic analysis should be done in this phase also.

Phase II, the overall facility plan, involves the development of an initial plant layout. This layout may be revised upon evaluation.

Phase III, the detailed facility plan, includes a second, more detailed economic analysis and the development of detailed layouts. This phase also includes development of the computer software for integrating and controlling the system elements.

Implementation is Phase IV. In this phase, the plant is built, debugged and put into operation.

An effective methodology for designing a CIM system layout is Systematic Layout Planning (SLP) developed by Richard Muther (2). The steps involved in this manual method are shown in Figure 2.

Simulation Modeling

Simulation modeling is one of several modeling techniques available to Facilities Planners and Designers. These techniques range in decreasing level of abstraction from mathematical models through computer simulation to pilot plants (3).

The results of a 1980 survey by Shannon et al (4) indicated that Operations Research practitioners in U.S. industry felt that simulation modeling was the second most widely used OR technique and the one most respondents were eager to learn more about. This is supported by the recent study conducted for the Society of Manufacturing Engineers (SME) (5).

Simulation modeling utilizes a computer to emulate the manufacturing system. After the important components have been modeled, the system can be analyzed. Simulation can be used to perform sensitivity analysis to optimize goals such as production volumes as well as to pinpoint problems in the layout or materials handling system.

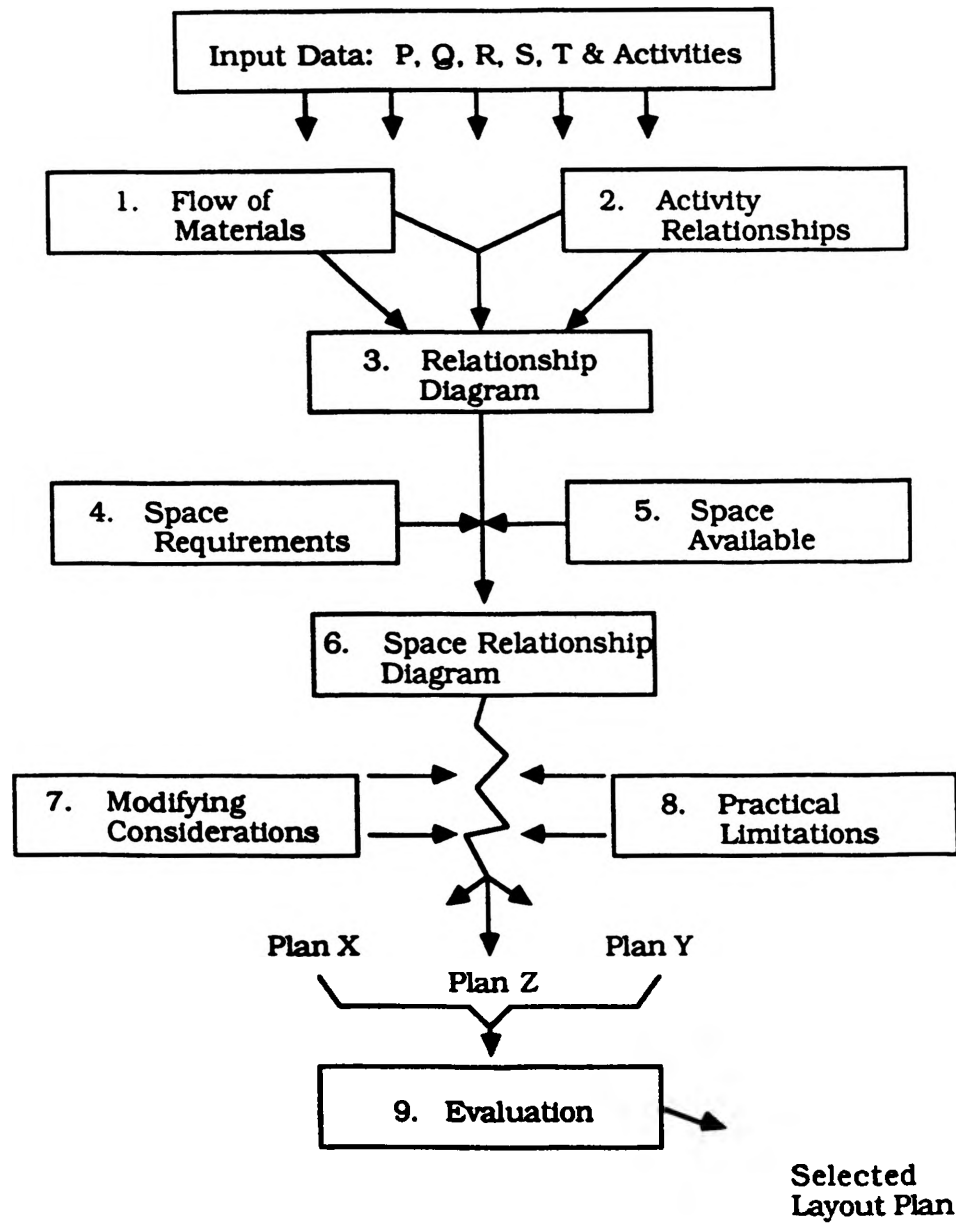
Simulation is also useful in generating funds for the project as it increases the confidence of planners and investors. Animation is a very useful enhancement in this situation. Animation makes it easier for the observer to understand the process being modeled.

There are a few limitations with simulation. First, any simulation requires a lot of programming time. This problem is currently being addressed with programs which allow the user to develop a model without actually programming. Secondly, simulation cannot optimize the system. It can only describe the results of a "what-if" question. Finally, the simulation model is only as accurate as the input data and it can only describe system characteristics that have been explicitly modeled.

A simulation study should follow the same four phase process discussed earlier.

Phase I, orientation, begins with the formulation of the problem. The external considerations should be examined and the study planned.

Figure 2 SLP Pattern of Procedures



Phase II is system modeling. In this phase, data is collected and the model is defined. Then the model is validated. This phase includes the construction and verification of a computer-based version of the model. Pilot runs of the model are made and the validity is again checked.

System analysis, Phase III, includes designing simulation experiments and making production runs. The output data is analyzed, results interpreted, and decisions made.

The final phase, Phase IV, is implementation. Here the model and work are documented. Funding for the project is acquired now and the results are applied.

There are several software packages available for developing a simulation model. These packages range in price from \$500 to \$100,000 and must be evaluated on several factors: animation features, underlying simulation language, brand and type of required hardware, and the special class of problems which can be modeled (6), (7).

Applying Simulation in CIM System Design

Simulation modeling is most effective in Phases II and III of facilities planning. During Phase II, simulation modeling can be used to evaluate different layout alternatives. A simple model will provide a quantitative measure to the evaluation procedure.

In Phase III simulation modeling can be used to further evaluate the system. Here a more detailed model is appropriate. The model can be used to fine-tune the layout and to evaluate the material handling system. The simulation can also lay the foundation for the controlling computer software.

Simulation can also be used after the plant has begun operations. In an operating plant, simulation assists management in scheduling and staffing. It can also determine equipment availability and estimate production capacity.

The Flexible Manufacturing Cell - A Case Study

The Flexible Manufacturing Cell (FMC) is a 900 square feet educational facility equipped with industry grade equipment. This includes a CNC mill and CNC lathe, a loop conveyor, a GE robot, an IBM robot, a Mercury robot, a bagging machine, three controllers and one CAD/CAM workstation.

The FMC is capable of producing six small toys and souvenir items: a key chain, a 3-D maze, the Tower of Hanoi, the Cam Critter, a single-hole pencil holder, and a multi-hole pencil holder.

The key chain displays the company's logo as well as other alpha-numeric characters. The maze is a tri-level plexiglass maze. The Tower of Hanoi consists of a horizontal base with three vertical pegs. On the middle peg are seven disks arranged largest to smallest. The Cam Critter is a pull-toy that has a cam attached to the front axle to cause the critter to bob up and down. The pencil holders consist of a dumbbell shaped body with holes in the top surface to accommodate pencils.

Since the FMC is to be used for educational purposes, it must be designed with several factors in mind. It must demonstrate the principles involved in CIM. It must be safe and easily accessible for demonstrations. Richard Muther's SLP methodology was used in designing the layout for the FMC.

Following the design of the layouts, the alternatives must be evaluated. The alternatives were evaluated on the following factors: ease of servicing, ease of expanding, safety, ease of material flow, ease of machine control and supervision, and accessibility for demonstrations. A simulation model was attempted at this point to help in the evaluation process. However, due to the restricting relationships between the machines, the layouts did not differ enough to affect a model. For layout alternatives which vary a great deal, simulation modeling can help in determining the most effective layout.

For each of the factors, Alternative 3 rated as well as or better than Alternatives 1 and 2. Therefore, Alternative 3 is the "best" layout. The dimensioned "best" layout for the Flexible Manufacturing Cell is shown in Figure 3. Having chosen the "best" layout, simulation modeling can be used for further evaluation.

The educational version of XCell + was used first to model the FMC. XCell + is a computer program which allows the user to build a simulation model without actually programming. It is an interactive program with animation which also utilizes graphics during the construction phase (8).

The educational version of XCell + was not capable of handling all of the processes in the FMC. Since the production version was not available, two simplified models were designed. The two models, designated Group 1 and Group 2, differed only in the mix of products. Group 1 modeled the production of the Tower of Hanoi, the single-hole pencil holder, the 3-D maze, and the Cam Critter. Group 2 consisted of the key chain, the multi-hole pencil holder, and the 3-D maze.

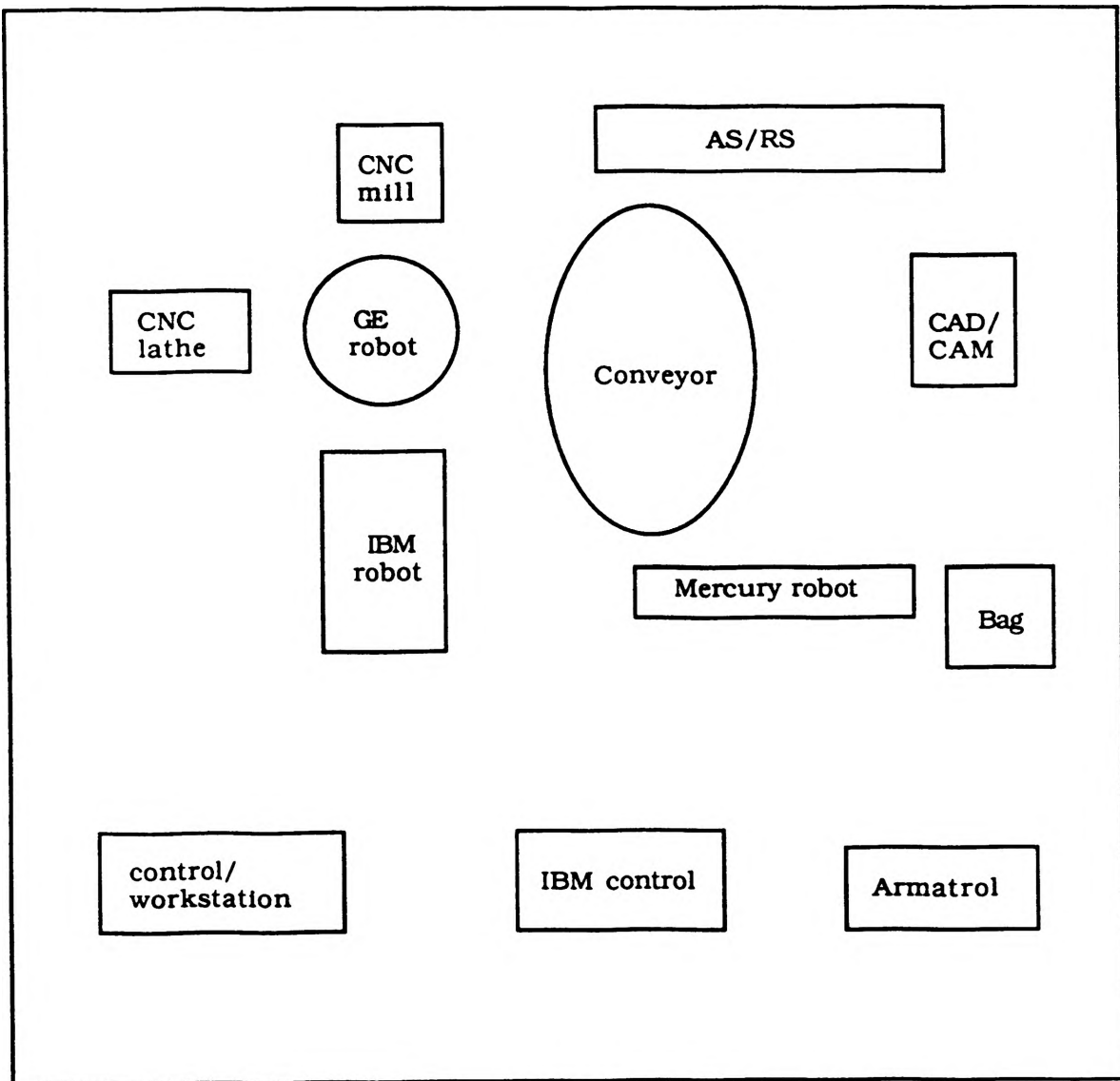
Because of the required processes, the GE robot was modeled with three and four workstations. Thus, when analyzing the data, these workstations must be combined. Although this is not a perfect model of the FMC, it is a good approximation.

The models were each run for a period of 740 minutes. The factory throughput of Group 1 was 264 units while Group 2's throughput was 241 units. An analysis of Group 1's workcenter utilization indicates that the GE robot (W1 + W2 + W3) was busy 20.15% of the time, the CNC lathe (W4) was used 31.28% of the time, and the assembly cell (W5) was used 27.29% of the time. This model indicates that although the machines aren't utilized to their fullest potential, the FMC is fairly well balanced.

A similar analysis of Group 2 reveals that the GE robot (W1 + W2 + W3 + W8) was used 39.12% of the time, the CNC lathe was busy 38.52% of the time, the assembly cell was used 20.10% of the time, and the CNC mill was busy 55.03% of the time. Again there is low machine utilization, but this time the FMC is not balanced. The mill is in use more than the rest of the cell and it will be the limiting factor in cell throughput. A second mill might be needed.

Since the FMC was simulated with two separate models, a more detailed simulation incorporating everything into one model was done. A knowledge-based program called EXSEMA was used to select the appropriate simulation software (9). EXSEMA is an expert system using the Level Five knowledge engineering shell. A typical consultation

Figure 3 FMC "Best" Layout



session prompts the user for information describing the proposed application and existing constraints. EXSEMA then identifies the simulation system which provides the best fit with the user's needs. The system is based on the 1989 survey by Law and Haider (6). The following guidelines were used in selecting the software for this model:

- ◆ time is restricted
- ◆ programming expertise is not available
- ◆ application orientation is manufacturing
- ◆ input modes are interactive
- ◆ cost range is medium
- ◆ available computer class is pc
- ◆ animation is necessary
- ◆ animation development concurrent with model construction is required

SimFactory, a menu-driven program written in the SimScript II.5 simulation language, met all of these criteria (10).

SimFactory was capable of handling all of the required processes, so one model was designed to simulate the system. Each machine was represented by one station, thus providing a more accurate model.

This model was also run for a period of 740 minutes with a warm-up period of 30 minutes. The total throughput of the cell was 348 units. An analysis of the output indicates that the GE robot is in use 79.45% of the time, the lathe 37.12% of the time, the assembly cell 29.05% of the time, and the mill 44.57% of the time. This again suggests that the FMC is not balanced. However, in this model the GE robot is used the most. The mill is still utilized more than the lathe and assembly cell, but the GE robot is the limiting factor.

The utilization of the GE robot was not accurately represented in the XCell + models since three and four workstations were used to emulate it. The workstations could operate at the same time, essentially performing two or three jobs at once. The SimFactory model used one transporter to emulate the GE robot, thus successfully representing its utilization.

"What-if" analysis can now be done on the SimFactory model. Areas of investigation should include the GE robot and the mill. "Could a faster robot be helpful?" "Should a larger, faster mill be acquired?" "Could another robot be added to the system to transfer material?" All of these are questions which should be addressed in further study.

Finally, the SimFactory model can be used to optimize the throughput and minimize the raw material queue by adjusting the raw material arrival times and quantities.

Conclusion

Simulation modeling is an effective OR technique to use during the design of a CIM system. It enables the planner to evaluate and improve the system without costly physical models or pilot plants. Used with animation, simulation becomes an effective communication tool, allowing the observer to easily understand the process being modeled. Simulation also is a powerful evaluation tool during the manufacturing cell design process.

These benefits show that simulation modeling can indeed serve the manufacturing company and is a worthwhile investment.

REFERENCES

1. Mikell P. Groover, Automation, Production Systems, and Computer Integrated Manufacturing, Prentice-Hall, Englewood Cliffs, NJ, pp. 4, 1987.
2. Richard Muther, Systematic Layout Planning, Missouri: Management & Industrial Research Publications, 1973.
3. R. Borchelt and S. Alptekin, "Physical Modeling - A Tool for CIM Educators", International Journal of Applied Engineering Education, January, 1990.
4. R.E. Shannon, S.S. Long, and B.P. Buckles, "Operations Research Methodologies in Industrial Engineering: A Survey", AIIE Transactions, Vol. 12, No. 4, pp. 364-367, 1980.
5. D.F. Koska and J.D. Romano, Countdown to the Future: The Manufacturing Engineer in the 21st Century, A.T. Kearney Research Study, Profile 21, Executive Summary, SME, Fall 1988.
6. A.M. Law and S.W. Haider, "Selecting Simulation Software for Manufacturing Applications: Practical Guidelines and Software Survey", Industrial Engineering, May 1989.
7. J.W. Grant and S.A. Weiner, "Factors to Consider In Choosing A Graphically Animated Simulation System", Industrial Engineering, August 1986.
8. R. Conway, W.L. Maxwell, J.O. McClain, and S.L. Worona, User's Guide to XCELL + Factory Modeling System, 2nd Edition, The Scientific Press, Redwood City, CA, 1987.
9. C.O. Benjamin and O. Hosny, "EXSEMA - An EXpert System for sElecting simulation software for Manufacturing Applications", Department of Engineering Management Working Paper No. 90-12-37, University of Missouri -Rolla, Rolla, Missouri, May 1990.
10. SIMFACTORY with Animation. Version 1.6. User's and Reference Manual, CACI Products Company, La Jolla, CA, 1988.

BIBLIOGRAPHY

- Bachers, R., Augustin, M., and Dangelmaier, W. "Using simulation in the planning of final assembly: a case study from a German car manufacturer", Simulation in Manufacturing, Proceedings of the 2nd International Conference, June 24-26, 1986, Chicago, Illinois, U.S.A.
- Ben-Arieh, D. "A Knowledge based system for simulation and control of a CIM", Simulation in Manufacturing, Proceedings of the 2nd International Conference, June 24-26, 1986, Chicago, Illinois, U.S.A.
- Branstrator, J. and McCormick, M. "Computer Simulation Justifies Construction of CIBA-GEIGY Dyestuff Production Facility", Industrial Engineering, May 1989, pp. 22-26.
- Benjamin, C.O. and Smith, M.L. "Simulation Modeling in Cim System Design", Department of Engineering Management Working Paper No. 90-13-38, University of Missouri-Rolla, Rolla, Missouri, May 1990.
- Benjamin, C.O. and Smith, M.L. "The CIM Laboratory Facility", Case Study, Case Clearing House of Great Britain and Ireland, Cranfield Institute of Technology, England, May 1990.
- Carlier, J., "Simulation as a planning tool for an FMS", Simulation in Manufacturing, Proceedings of the 2nd International Conference, June 24-26, 1986, Chicago, Illinois, U.S.A.
- Chaharbaghi, K., Davies, B.L., and Rahnejat, H. "Application of simulation in planning the design of flexible assembly systems", UK Research In Advanced Manufacture, Proceedings of the Institution of Mechanical Engineers, 1986.
- Godziela, R. "Simulation of a Flexible Manufacturing Cell", 1986 Winter Simulation Conference, December 8-10, 1986, Washington, D.C.
- IIE, Simulation: Modeling Manufacturing and Service Systems, Industrial Engineering and Management Press, Norcross, Georgia, 1987.
- Law, A.M. and McComas, M.G. "Pitfalls in the Simulation of Manufacturing Systems", 1986 Winter Simulation Conference, December 8-10, 1986, Washington, D.C.
- Makin, A.J. "The use of simulation-from specification of an FMS through to its operation-a case study", Simulation in Manufacturing, Proceedings of the 2nd International Conference, June 24-26, 1986, Chicago, Illinois, U.S.A.
- Martin, D. "Simulation Analysis of an FMS during Implementation", 1986 Winter Simulation Conference, December 8-10, 1986, Washington, D.C.
- Mishra, P.K., Pandey, P.C., and Singh, C.K. "Simulation studies of flexible manufacturing systems", Simulation in Manufacturing, Proceedings of the 2nd International Conference, June 24-26, 1986, Chicago, Illinois, U.S.A.

- Roy, R. and Grinsted, S.E. "The role of simulation in manufacturing and how to use it effectively", Simulation in Manufacturing, Proceedings of the 2nd International Conference, June 24-26, 1986, Chicago, Illinois, U.S.A.
- Smith, Charles A. "The Role of Simulation Analysis in Improving the Manageability of Integrated Systems", Autofact '85. Conference Proceedings, November 4-7, 1985, Detroit, Michigan.
- Warnecke, H.-J., Steinhilper, R., and Zeh, K.-P. "Simulation as an integral part of an effective planning of flexible manufacturing systems (FMS)", Simulation in Manufacturing, Proceedings of the 2nd International Conference, June 24-26, 1986, Chicago, Illinois, U.S.A.
- Wortmen, David and Miner, Robin "The Role of Simulation in Designing Manufacturing Systems", Autofact '85. Conference Proceedings, November 4-7, 1985, Detroit, Michigan.

AEROSOL PARTICLE BOUNCING IN CASCADE IMPACTORS

Bisma Husen

ABSTRACT

Particle deposition characteristics were observed from the aerosol sampling results of a UNICO cascade impactor. A simple model of particle motion combined with Hiemenz flow of stagnation flow on a flat plate were developed and discussed.

Both results and analysis were compared to recent models on particle bouncing errors or secondary deposition which included vortices formation around the edge of the slot, back spin (Magnus effect), and hydrodynamic conditions of the particles. The analysis was limited to a laminar inviscid and incompressible case. The main obstacle in the observation was the fact that impactor nozzles were unsymmetrical to a considerable degree, thereby deviating particle trajectory significantly from the predicted situation.

NOMENCLATURE

c_s	Slip correction factor
c_i	Particle concentration far away from deposition plane
d_p	Particle diameter
g	Vector gravitational acceleration
m_p	Particle mass
t	Time
u_∞	Fluid velocity far away from deposition plane
v	Particle velocity vector
u_{x0}, v_{y0}	Components of initial particle velocity
v_{x1}, v_{y1}	Components of particle velocity at edge of boundary layer
$x_1, d_p/2$	Final particle position after deposition
α	Constant descriptive of flow field, $ u_\infty /H$, x-axis
α'	Constant for y-axis
β	Friction coefficient, $3\pi\mu d_p/c_s m_p$
δ	Boundary Layer's thickness
ω	Particle's angular velocity
η	Kinematic viscosity
μ	Dynamic viscosity
ϕ	Function defining velocity profile inside boundary layer

INTRODUCTION

Aerosol is defined as any relatively stable suspension of particles in a gas, especially in air, including both the continuous (gaseous) and discontinuous (particulate) phases. During the last decade, great advances have been made in our knowledge of the behavior of aerosols and in the techniques available for studying them. Perhaps the greatest incentive for the present research has been the growing concern about the impact of man on his environment, particularly the extent to which he is polluting the atmosphere -locally, regionally, and worldwide. Another incentive is the need in many modern devices for closer tolerances that can be achieved only by manufacturing them in relatively dust-free rooms, the so-called clean rooms. Study of airborne particles are the main aspect of industrial hygiene, weather modification, and studies of the natural atmosphere. Investigation of the production, characterization and behavior of aerosols has therefore become a scholarly discipline.

The most important thing of aerosol investigation is the measurement of the suspended particles. Measurement refers to the

determination of size distributions, concentration and shapes. Many methods have proposed to such measurement. Impaction method of measuring microstructural characteristics of a coarsely dispersed aerosol are one of those methods that are widely used. Impaction method means the settling of aerosol particles from the stream on obstacles due to their inertia.

Cascade impactor is one of many types of impactors that are being used. First introduced by May (1945) it has been gaining popularity due to its simple operation. A cascade impactor is a multistage impaction device used to separate airborne particles into aerodynamic size classes. In use, an aerosol is drawn through a series of progressively narrower jets, each followed by an impaction surface, usually placed at right angles to the axis of the jet and coated with certain substances such as gelatin or other chemicals. The jet may be a circular or rectangular slit. Each jet and its associated impaction surface is a "stage". Particle with the largest inertial mass are impacted, and deposited, onto the first stage substrate, and smaller particles are deposited successively on the following stages.

Many theoretical studies of the mechanism of particle deposition under a jet or rectangularly shaped nozzle illuminated well the main parameters affecting the motion of the solid particles or droplets under the nozzle and along the substrate sideward (May 1975, Ramarao and Tien 1989, Fuchs 1964). The results of these studies are briefly reviewed and several most salient and still unanswered questions are formulated. Among these is the particle bouncing at the substrate and its dependence on the flow pattern, state of the particle, and of the substrate at different environment conditions represents still one of the most attractive subjects of the particle separation and two-phase flow research (Dzubay 1976, Fuchs 1973, Berner 1988, Markowski 1987).

Most of the particle bouncing investigations in cascade impactors dealt with the jet flow pattern which might seemingly be simpler for mathematical modeling of particle deposition and comparison of the theoretical results with the experimental work. In this research, we used a simple two-dimensional Hiemenz flow model of boundary layer over a flat plate (Currie 1974) superimposed to the hyperbolic potential flow describing the particle deposition under a rectangularly shaped long nozzle, as noted by Ramarao and Tien (1989), which can be compared with the particle deposition in a four-stage UNICO impactor frequently used in our laboratory (figure 1). The main goal was to discuss the main question raised by several authors whether the particle bounce errors in impactor are caused by the flow pattern and vorticity formation around the nozzle's edge (Berner 1976) or by the back spin caused by some kind of Magnus effect (May 1975) acting on spherical particles in a shear flow close to the impactor's wall.

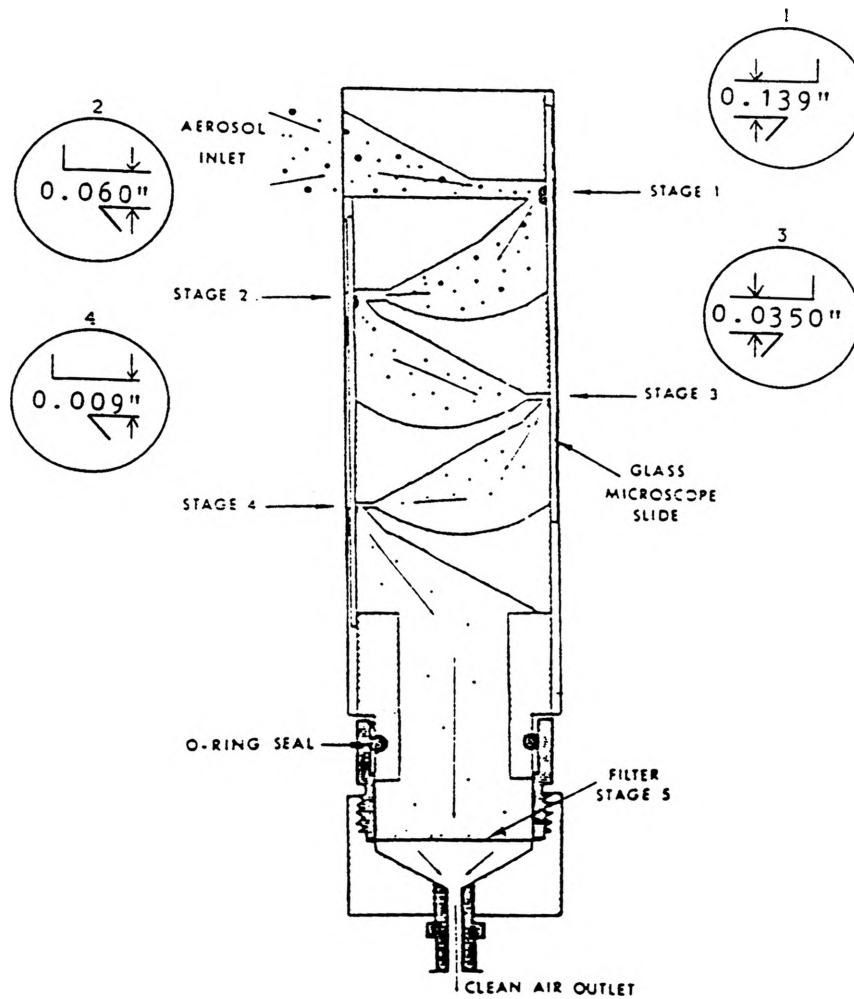


Figure 1

TWO-DIMENSIONAL STAGNATION FIELD

Classical stagnation flow is shown in figure two. The deposition plane is situated at $y = 0$, and the flow is directly towards the plane. Except for a region immediately adjacent to the deposition plane, $y \leq \delta$ (δ is boundary layer's thickness), flow is considered to be ideal, i.e.

$$u_y = -\alpha' y \quad (1)$$

$$u_y = -\alpha' y \quad (2)$$

assuming symmetrical slot, we can assume that $\alpha' = \alpha$.

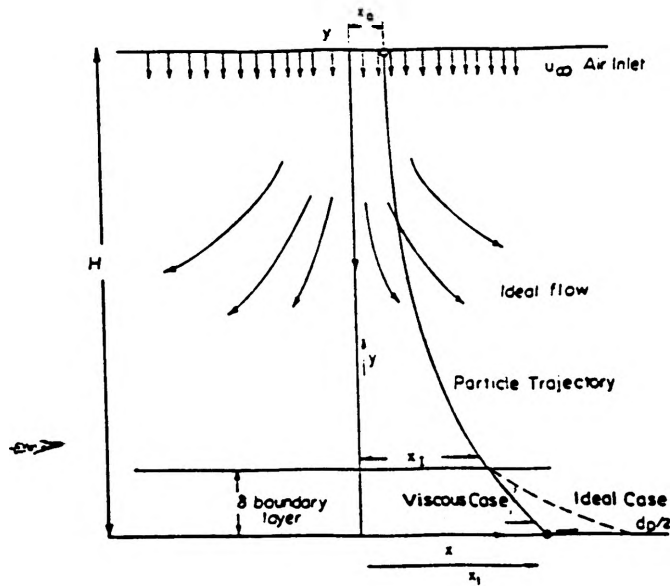


Figure 2

Within the boundary layer, according to Schlichting (1968)

$$u_x = x f'(y) \quad (3)$$

$$u_y = -f(y) \quad (4)$$

Hiemenz suggested $f(y)$ as :

$$f(y) = \sqrt{\alpha v} \phi(\eta) \quad (5)$$

where v is the kinematic viscosity of the gas and η is the

$$\eta = \sqrt{\alpha/\nu} y \quad (6)$$

similarity variable for boundary layer flow. Then $\phi(\eta)$ is the solution of the following non-linear differential equation :

$$\phi'''' + \phi'' - \phi^2 + 1 = 0 \quad (7)$$

boundary conditions for this equation :

$$\phi(0) = \phi'(0) = 0, \phi'(\infty) = 1 \quad (8)$$

Equation 8 was expanded using Taylor's series. Let $\phi' = u/U_\infty = R$, we get

$$-\left(1 + \frac{\Delta\eta}{2} \phi_i^n\right) R_{i+1}^{n+1} + 2R_i^{n+1} - \left(1 - \frac{\Delta\eta}{2} \phi_i^n\right) R_{i-1}^{n+1} = \Delta\eta^2 [1 - (R_i^n)^2] \quad (9)$$

Using Tridiagonal Matrix Algorithm, we have the equation in the form of

$$-AR_{i+1}^{n+1} + BR_i^{n+1} - CR_{i-1}^{n+1} = D_i^n \quad (10)$$

We postulate the solution in the form of

$$R_i = E_i R_{i+1} + F_i \quad (11)$$

then substitute back to equation 10 we get

$$E_i = \frac{A}{B - CE_{i-1}} \quad (12)$$

The solution, according to Schlichting (figure 3), shows

$$F_i = \frac{D + CF_{i-1}}{B - CF_{i-1}} \quad (13)$$

that δ may be taken to be $2.4 (\eta/\alpha)^{0.5}$ for u_x to reach 99% of the value given in equation 1. Ramarao and Tien (1989) suggested taking $\delta = 20 (\alpha/\eta)^{0.5}$ to match within 2 % of the value given in equation 1. This last equation will be used for the equation of particle motion in the boundary layer.

Hiemenz Flow

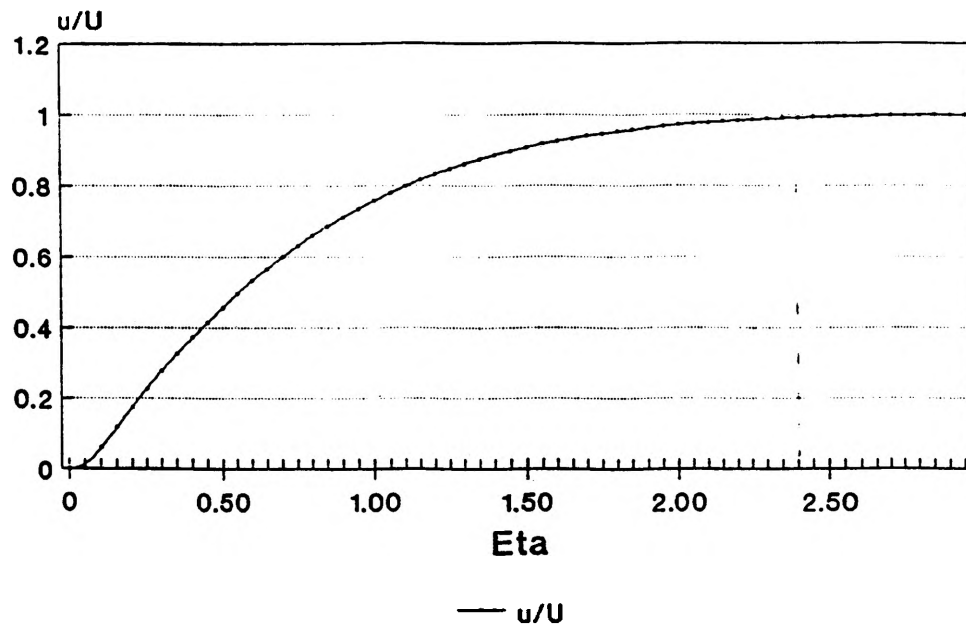


Figure 3

PARTICLE MOTION IN IDEAL FLOW

The equations that describe this situation :

$$\frac{d^2x}{dt^2} + \beta \frac{dx}{dt} - \beta \alpha x = 0 \quad (14)$$

$$\frac{d^2y}{dt^2} + \beta \frac{dy}{dt} + \beta \alpha y = -g \quad (15)$$

x, y are coordinates of the center of the particle and β is the slip factor expressed as :

$$\beta = \frac{3\pi\mu d_p}{c_s m_p} \quad (16)$$

where μ and d_p are the dynamic viscosity and diameter of the particle, and c_s is the Cunningham's correction factor mentioned in Marple and Willeke (1979).

Solutions to these equations subject to initial conditions $x = x_0, v_x = v_{x0}$ at $t = 0$

$$x = A_x e^{m_{1x}t} + B_x e^{m_{2x}t} \quad (17)$$

$$v_x = m_{1x} A_x e^{m_{1x}t} + m_{2x} B_x e^{m_{2x}t} \quad (18)$$

$$A_x = \left[v_{x0} + \left(\frac{\beta_{1x} + \beta}{2} \right) x_0 \right] / \beta_{1x} \quad (19)$$

$$B_x = \left[-v_{x0} + \left(\frac{\beta_{1x} - \beta}{2} \right) x_0 \right] / \beta_{1x} \quad (20)$$

$$m_{1x} = \frac{\beta_{1x} - \beta}{2} \quad (21)$$

$$m_{2x} = -\frac{(\beta_{1x} + \beta)}{2} \quad (22)$$

Similarly, the solutions of equation 15 subject to the initial conditions, $y = y_0 = H$, $v_y = v_{y0}$ at $t = 0$, given as :

$$y = A_y y_{c1} + B_y y_{c2} + Y_p \quad (23)$$

$$y_p = -g/\beta\alpha \quad (24)$$

The discriminant is $\Delta = \beta^2 - 4\alpha\beta$. For clean room application it is likely to be positive. The trajectory solutions are given by :

$$y = \left[v_{y0} + H \frac{\beta_{1y} + \beta}{2} - \frac{2g}{\beta_{1y} - \beta} \right] \frac{e^{(\beta_{1y} - \beta)t/2}}{\beta_{1y}} - \left[v_{y0} - H \frac{\beta_{1y} - \beta}{2} + \frac{2g}{\beta_{1y} + \beta} \right] \frac{e^{-(\beta_{1y} + \beta)t/2}}{\beta_{1y}} - \frac{4g}{\beta^2 - \beta_{1y}^2} \quad (25)$$

$$v_y = \left[v_{y0} + H \frac{\beta_{1y} + \beta}{2} - \frac{2g}{\beta_{1y} - \beta} \right] \frac{(\beta_{1y} - \beta)}{2\beta_{1y}} e^{(\beta_{1y} - \beta)t/2} + \left[v_{y0} - H \frac{\beta_{1y} - \beta}{2} + \frac{2g}{\beta_{1y} + \beta} \right] \frac{(\beta_{1y} + \beta)}{2\beta_{1y}} e^{-(\beta_{1y} + \beta)t/2} \quad (26)$$

where

$$\beta_{1y} = (\beta^2 - 4\alpha\beta)^{1/2} \quad (27)$$

If the boundary layer effect is considered, the equation of particle motion become :

$$\frac{d^2x}{dt^2} + \beta \frac{dx}{dt} - \alpha \beta x \phi' \left(\frac{y}{\sqrt{\alpha/v}} \right) = 0 \quad (28)$$

$$\frac{d^2y}{dt^2} + \beta \frac{dy}{dt} + \beta \sqrt{\alpha v} \phi \left(\frac{y}{\sqrt{\alpha/v}} \right) = 0 \quad (29)$$

Since ϕ is a complicated function of η , the solution of these equations must be made numerically and beyond the discussion of this paper. Equations 17, 18, 25, and 26 are sufficient to determine the trajectory path of the particle at the impaction plate.

The boundary layer effect in this problem will cause an aerosol particle to spin. Particles which escape the initial impaction will be skimming outward exceedingly close to the impaction plate, as implied by the ideal gravitational effects discussed above. It can be seen that the particles will initially experience a velocity gradient, their upper edge being urged forward by the outflowing air and their lower edge being retarded by the stationary boundary layer, causing them to spin. As the outflowing air rapidly slows, the particles by their inertia overshoot the air stream and dip into the plate by the so-called Magnus effect (May 1975), creating a secondary deposition on the same stage. Hapel and Brenner (1965) formulated the hydrodynamic frictional force and torque on a spinning rigid spherical particle using Faxen's laws. According to this, if a sphere to which fluid adheres is immersed in an unbounded fluid in motion at infinity with velocity v_∞ and if the sphere center translates with velocity U while the sphere spins with angular velocity ω , then the force and torque on the sphere are

$$F = 6\pi\mu r_p ([v_\infty]_o - U) + \mu\pi r_p^3 (\nabla^2 v_\infty)_o \quad (30)$$

$$T_o = 8\pi\mu r_p^3 \left(\frac{1}{2} [\nabla \times v_\infty]_o - \omega \right) \quad (31)$$

where r_p is the sphere radius, and subscript o implies evaluation at the location of the sphere center.

EXPERIMENTAL RESULTS

The schematic of the experiment is shown in figure 4. The aerosol was generated using a nebulizer. Three samples were taken, i.e. water, salt (NaCl), and Titanium Oxide. Within the

confines of the wind-tunnel the aerosol can be set to produce initial evaporated drops in the range of 0.2 to 30 μm by control of the air pressure to the spray. The main sample was the dry salt particles which was collected using a glass slide covered with a very thin gelatine layer. The Liesegang circle (spot test) technique was used for detecting the deposited salt particles (containing chlorides) if they impacted a gelatine layer sensitized by a weak solution of silver nitrate (to 8% gelatine solution 10% of AgNO_3 was added in the ration of 20:1).

The results are shown in figure 5 which corresponds to particle deposition in stage I, II, III, and IV of the impactor. Similar pattern of deposited salt particles shown reveals that the wave length of the deposited particles is comparable and does

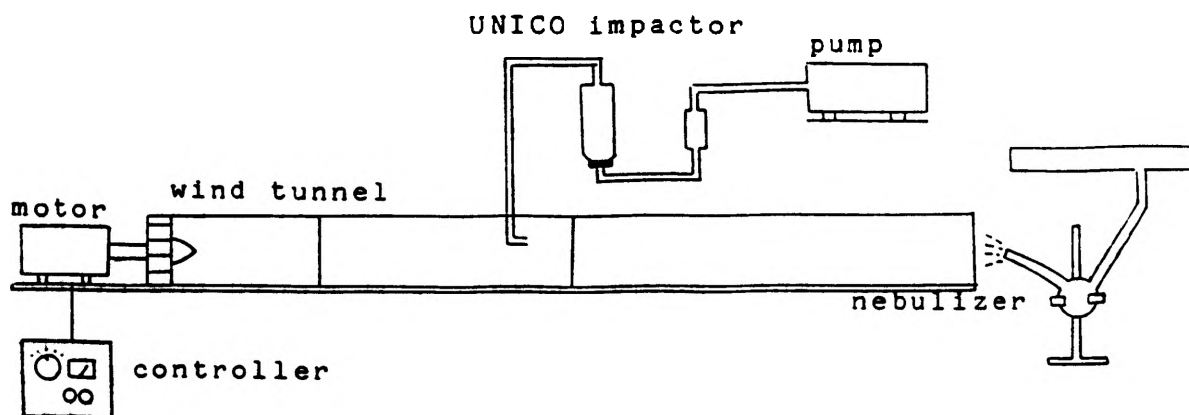
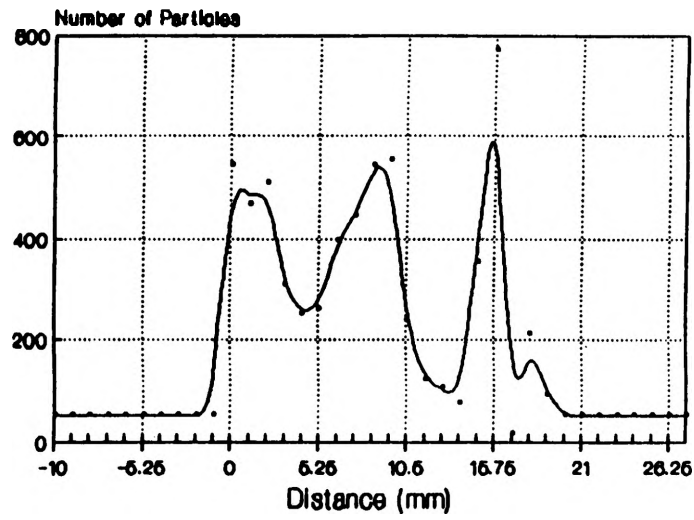


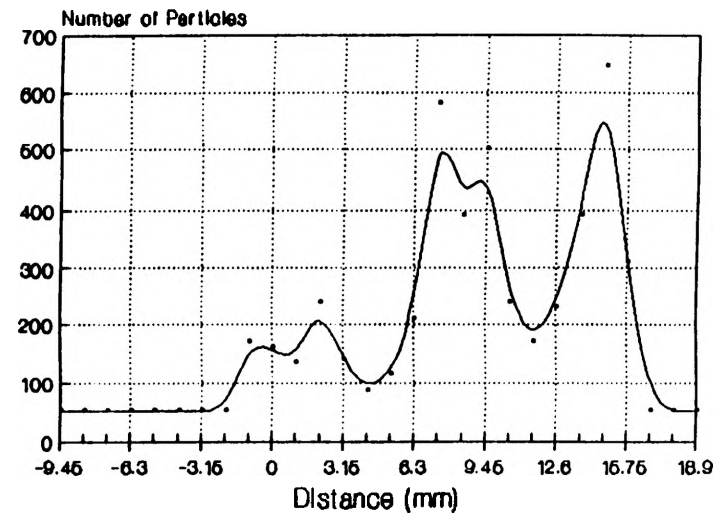
Figure 4

not depend very much on the different geometry and different air speed in the individual nozzles of the impactor. For comparison, a similar investigation has been done with insoluble titanium oxide particles impacting a dry glass slide. The difference in deposited particle pattern is explained by the different state of the sampling substrate, by different environmental conditions, and, possibly, by the different properties of the deposited particles (mainly their aerodynamic diameters). The main effect seems to have, however, the space behind the slightly unsymmetrical nozzle which affects the formation and possibly the releasing of vortices at the sharp edge due to the increasing pressure and bouncing of particles at the subsequent stage. The formulas suggested by several authors for determining the location of a stable vortex at the nozzle's edge from its dimension

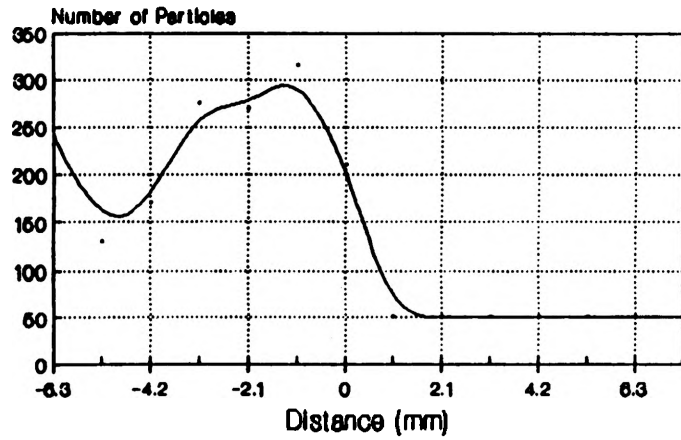
**UNICO Impactor
Stage I**



**UNICO Impactor
Stage II**



**UNICO Impactor
Stage III**



**UNICO Impactor
Stage IV**

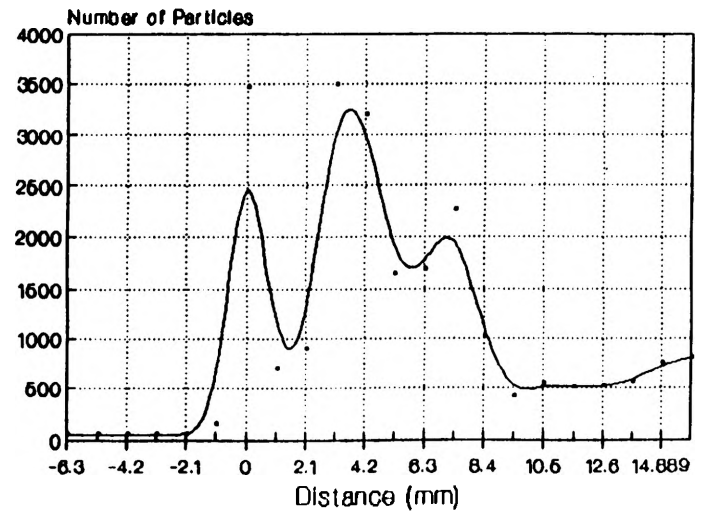


Figure 5

distance from the sampling substrate and air flow parameters of a jet-impactor is not applicable for UNICO instruments. As can be noticed, α and α' in equations 1 and 2 will have different values, and will complicate the particle trajectory solution. Different approach on an unsymmetrical flow field or a more general derivation of Hiemenz stagnation flow is therefore needed for this kind of conditions.

CONCLUSION

In conclusion, we suggest the air flow conditions in and around the nozzle affect most the particle deposition in UNICO impactor. The particle back spin near a shear flow, state of the particle and of the substrate might explain well the bouncing of the large particles and their deposition on the subsequent (smaller particle) stages. This research itself had therefore provided basic introduction to a more in depth study on aerosol reentrainment characteristics.

REFERENCES

- Berner, A.W. (1988); "The Collection of Fog Droplets by A Jet Impaction Stage"; The Sci of The Total Environ vol.73, pp 217-228
- Cadle, R.D. (1948); "The Measurement of Airborne Particles"; Environmental Science and Technology; 1948
- Currie, I.G. (1974); "Fundamental Mechanics of Fluids"; McGraw-Hill Publishing Co.; 1974
- Dzubay, T.G. (1976); "Particle Bounce Errors in Cascade Impactors"; Atm. Environ. vol 10 pp 229-234
- Fuchs (1964); "The Mechanics of Aerosols"; Pergamon Press; 1964
- Fuchs (1973); "Preliminary Report on The Efficiency of Collisions between Dust Particles and Water Droplets"; Staub vol 33 no 4, 1973
- Happel & Brenner (1965); "Low Reynolds Number Hydrodynamics with Special Applications to Particulate Media"; Prentice-Hall Inc., 1965
- Lodge, Chan; "Cascade Impactor Sampling and Data Analysis"; Ame. Indust. Hygiene. Assc. 1986
- Markowski, G.R. (1987); "On Identifying and Correcting for Reentrainment in Cascade Impactor Measurements"; Ae.Sci. & Tech. 7:143-159, 1987
- Marple & Rubow (1986); "Theory and Design Guidelines"; from "Cascade Impactor Sampling and Data Analysis"; Lodge & Chan; Am. Ind. Hyg. Assc, 1986
- Marple & Willeke (1979); "Inertial Impactors"; from "Aerosol Measurement"; editor Lundgren et.al.; Univ. Presses of Florida, 1979
- May (1975); "Aerosol Impaction Jet"; J.Ae.Sci. 16:403-411; 1975
- Ramarao & Tien (1989); "Aerosol Deposition in Two Dimensional Laminar Stagnation Flow"; J.Ae.Sci. vol 20 no 7 pp 775-785
- Ranade, M.B. (1987); "Adhesion and Removal of Fine Particles on Surfaces"; Ae.Sci.&Tech 7:161-176(1987)
- Schlichting (1955); "The Boundary Layer Theory"; McGraw-Hill Book Co., 1955
- Tillery, M.I. (1979); "Aerosol Centrifuges"; from "Aerosol Measurement"; editor Lundgren et.al.; Univ. Presses of Florida, 1979
- Vanderpool & Lundgren, Marple & Rubow (1987); "Cocalibration of Four Large-Particle Impactors"; Ae.Sci. & Tech 7:pp177-185, 1987

ATTITUDES TOWARD ANIMAL RESEARCH AMONG CONTEMPORARY PSYCHOLOGISTS

Carla A. Huskey

Ethical considerations in the use of animals in biomedical and psychological research has become an increasingly controversial topic of debate. The recent broad media coverage over animal use in experimentation is unmatched and has brought the controversy to the attention of a greater number of people (Dewsbury, 1990). On June 10, 1990 nearly 50,000 people from across the United States participated in a rally in Washington, D.C. to promote the humane treatment of animals, including research animals (Gainesville Sun). Critics of animal research have charged that much research is unnecessary and viable alternatives do exist. They have asserted that research inflicts needless pain and suffering and that scientists involved are concerned more with monetary and professional advantages at the expense of the animals involved (Dewsbury, 1990).

Graham Mitchell, in *Current Contents* (1990), has divided arguments concerning animal research into two clearcut views. Holders of the first view believe in most cases, that animal lives have no moral significance. Once minimal standards have been met such as the avoidance of willful cruelty, or legal requirements to perform experiments have been met, then no further issues are relevant. Basically, proponents of this view hold that humans are unique and have a "moral authority" to use animals as equipment in research. The second view Mitchell presents is that of the "informed antagonist". This view questions the ethics of using animals in experiments and knowingly subjecting them to pain, distress and suffering, in the pursuit of knowledge. Some advocates of this view hold to the Kantian idea that using animals as objects results in a hardness and insensitivity to suffering which could ultimately lead to a cheapening of life and abuse of people: Mitchell also noted that there is a major communications deficit between the research community and the animal-rights community, and a "middle ground" must be reached so that both humans and animals are protected.

Harold Herzog (1990) identified two philosophical positions held by those who question the ethics of using animals in research. The first position was presented by Peter Singer in his publication *Animal Liberation* (1975). Singer argued for the "principle of equality" or "equal consideration of interests". This principle professes that all sentient creatures have equal stakes in their own existence. Further, there is no reason to promote the interests of one species over another, a phenomena he terms "speciesism". Singer asserted that differences such as intelligence, race and gender are not valid reasons for exploiting humans, and thus differences in species is an equally irrelevant reason for exploiting animals. He further argued that the only relevant criterion for discriminating between species is the capacity to suffer. Singer indicated research with animals is permissible only if it was so important that human subjects would also be used.

The second philosophical position identified by Herzog (1990) is the principle of equal rights. The rights position has been argued most notably by Regan (1983, 1985). Typically, this position holds that some creatures have certain fundamental rights such as the right to moral consideration and the right not to be harmed. Animal rights theorists include animals as rights holders. Regan argues that the fundamental criterion for having rights is "inherent value". He claims that sentient creatures, including humans, all have equal inherent value and so are entitled to fundamental rights such as respect and the right not to be harmed. Regan believes there is no justification for animal research even if it would benefit a majority of humans. His foremost reason for abolishing animal research is that scientists treat animals as "renewable resources", not as creatures with "inherent value", so thus are violating the "respect principle".

Herzog (1990) claimed that few psychologists are informed about the intellectual foundations of the animal rights movement. He noted the scientific community often dismisses animal rights activists as "intellectual lightweights". However, Dewsbury (1990) noted that the controversy over animal rights is nearly as old as the field of psychology as a whole, and both sides of the issue have been responsibly debated by psychologists throughout its history. For example, prototypical psychologist William James was very concerned about questions of ethics and openly condemned some reported animal uses as "revolting excesses" (p. 318). T. Wesley Mills, founder of the first Association for the Study of Comparative Psychology, is an example at the opposite end of the debate. In an address to the American Humane Association in 1892, Mills proposed that "it will be wise for all societies with a humane object to think well before interfering with scientific investigation of any kind" (p. 319).

Little research has addressed the attitudes of contemporary psychologists on issues related to the animal rights controversy. Gallup and Beckstead (1988) surveyed undergraduates' attitudes about animal rights. They concluded their results indicated that opposition to animal research had not yet reached substantial proportions among most college students at the State University of New York at Albany. However, a majority of their subjects were concerned about pain and suffering in research animals (76%), and most believed that more regulations were needed governing the use of animals in research (57%).

The present research examined the attitudes of a national sample of contemporary professional psychologists concerning the use of animals in research. A survey was developed similar to that used by Gallup and Beckstead (1988). Additionally, psychologists were asked about their agreement with the two fundamental philosophical positions outlined by Herzog (1990): the principle of equality and the principle of specific rights.

Method

Subjects

Psychologists holding non-student, full-membership status in the American Psychological Association (APA) and the American Psychological Society (APS) were surveyed by mail. Because of the probability that the APA would have a larger percentage of its members in the human service fields, psychologists from both the APA and APS were surveyed. The initial sample consisted of 800 members of APA and 100 members of APS randomly selected from the most current membership directories for each organization, the Directory of the American Psychological Association (1989) and the Membership Directory of the American Psychological Society (1990). Sixty-four surveys were returned from APA members due to incorrect addresses and two from APS members. It was possible to remail eleven surveys with corrected addresses to APA members. The final sample consisted of 354 returned APA surveys and 55 APS surveys.

Materials and Procedure

An anonymous questionnaire was used to maximize the return rate and the chances that subjects would be comfortable expressing their true opinions. Thus, specific information regarding geographic area, sex of subject, education, etc., was not available. However, subjects were asked to voluntarily indicate their area of specialization.

A questionnaire modeled after Gallup and Beckstead's (1988) questionnaire was developed (see Appendix A). Subjects indicated their extent of agreement, using a 1 to 5 rating scale, with questions asking about issues related to the use of animals in research. On this scale, a rating of 1 indicated "strongly agree," 2 indicated "agree," 3 reflected "neither agree nor disagree," 4 indicated "disagree," and 5 reflected "strongly disagree." Since Gallup and Beckstead made no distinction between attitudes toward use of animals in biomedical and

psychological research, the present questionnaire was divided into three sections: general issues, issues related to biomedical, and issues related to psychological research. A section was also added asking about the extent to which subjects agreed with two fundamental philosophical positions: the principle of equality, defined as "From an ethical point of view, all species should be treated equally;" and the principle of specific rights, defined as "All species have the right to be treated with respect and the right not to be harmed."

Numerous other modifications were made in Gallup and Beckstead's questionnaire to make the items either more objective and/or more clearly referring to either psychological or biomedical research. An item asking about the extent of agreement with the statement "I would rather see humans die or suffer from disease than to see animals used in research" was restated in more positive terms and included as a separate item under both the biomedical and the psychological research sections (i.e., "I think biomedical research with animals is justified if it reduces human death and suffering from accidents and/or diseases;" "I think psychological research with animals is justified if it reduces human suffering from accidents and/or diseases"). The statement "Animal research cannot be justified and should be stopped" was restated as "some...is unjustified and should be curtailed" and was also included under both the biomedical and psychological research sections. Similarly, the statement "There are plenty of viable alternatives to the use of animals in biomedical and behavioral research" was changed into two items, one asking about psychological and one asking about biomedical research, and restated as "There are viable alternatives..." Two questions were dropped. One asked whether the subject had seriously considered becoming a vegetarian to save animal lives and the other asked about the extent of agreement with the statement that most laboratory animals were treated better than many humans. Also, the word "very" was deleted from an item asking about concern "about pain and suffering in animals." Moreover, the item indicating "animals should be granted the same rights as humans" was dropped since it was felt that the two philosophical questions included in the present study more adequately assessed this issue. Finally, a question asking about the "need for more regulations governing the use of animals in research" was left unchanged, but an additional item was added asking about the need for "more effective enforcement" of these regulations.

Results and Discussion

Nature of Samples

The return rate for both professional organizations was noteworthy. Forty-eight percent of APA members and 55 percent of APS members returned questionnaires within two months.

Although the total number of returned questionnaires was 409, 20 of the subjects did not indicate a specialty area. Subjects indicating an area of specialization were classified into one of four categories: basic experimental, which included the areas of sensation and perception, animal learning, comparative, physiological, and experimental psychology, and behavioral pharmacology; human services, which included the areas of clinical, counseling and school psychology; other research, which included personality, developmental, cognitive and social psychology; and other applied, which included industrial, organizational, consumer and environmental psychologists. The percentages of professionals representing these different areas in the two professional organizations are presented in Table 1. It is apparent that the APA sample was dominated by human service psychologists (69%) and that the APS sample had larger percentages of both basic experimental (19% vs. 7%) and other research psychologists (44% vs. 13%). In general, it was hypothesized that since basic experimental psychologists were the most likely to have actually used, or worked with colleagues who have used animals in research, they will have the most positive attitudes about animal research.

Questionnaire Results

All 19 items on the questionnaire were analyzed with 2 x 4 analyses of variance (APA vs. APS x Area of Specialization). There were no significant interactions, but significant main effects were found for both APA versus APS and area of specialization.

Table 1. Specialty Areas in APA and APS.

	APA (n=337)	APS (n=52)
Basic Experimental	25/7%	10/19%
Human Services	234/69%	13/25%
Other Research	43/13%	23/44%
Other Applied	35/10%	6/12%

Table 2 shows the average ratings for all items given by members of APA versus APS. Overall, there were more instances of agreement than disagreement between the two groups of professional psychologists (i.e., similar ratings on 13 of the 19 items). However, as expected the APS, with its larger percentage of basic experimental and smaller percentage of human service psychologists, showed the most pro-animal research attitudes. For example, APA members were neutral with regard to the need for more regulations and agreed that more enforcement of regulations governing the use of animals in research was needed, while APS members disagreed that more regulations are needed and were neutral with regard to the need for more enforcement of regulations. Additionally, APA members were neutral on the existence of viable alternatives to biomedical animal research, while APS members disagreed that there are viable alternatives to biomedical animal research. It is also noteworthy that APA members agreed with the principle of specific rights while APS members were neutral. APA members also agreed that some biomedical animal research is unjustified and should be curtailed while APS members gave this item a more neutral rating.

Significant main effects for area of specialization occurred on 10 of the 19 items. Table 3 shows the average ratings by these different groups of psychologists on all items. As expected, in every instance, the basic experimental psychologists had the most positive attitudes toward animal research. Also, in general, the human service psychologists appeared to have the most questions concerning the use of animals in research. For example, basic experimental psychologists agreed most strongly with the value of basic animal research and with the possibility that many important questions cannot be answered by doing experiments on people. They also disagreed with the need for more regulations while the other areas were more neutral regarding this issue. However, the human service psychologists agreed that more enforcement of the regulations was needed. Additionally, basic experimental psychologists disagreed that viable alternatives exist to using animals in biomedical research, while the other areas were essentially neutral about this issue. The experimental research psychologists were also neutral regarding the possibility that some biomedical animal research may be unjustified while the psychologists in the other areas agreed with this statement. Similarly, the basic experimental psychologists disagreed that viable alternatives exist with regard to the use of animals in psychological research while all other areas gave essentially neutral ratings to this item. However, it is noteworthy that none of the psychologists disagreed with the statement that some psychological research is unjustified and should be curtailed. In fact, the basic experimentalists were neutral on this issue and the other three areas actually agreed with it.

Table 2. Average Ratings APA Versus APS Members.

<u>Items</u>	<u>APA</u>	<u>APS</u>	<u>F Value</u>	<u>P Level</u>
<u>General</u>				
1. Animal research has no bearing on peoples' problems.	4.39	4.64	2.27	.08
2. Intrinsic interest is sufficient justification.	2.54	2.04	3.36	.07
3. Concern about pain and suffering in animals.	1.67	1.64	.25	.62
4. More regulations needed.	2.85	3.58	9.62	.002**
5. More enforcement needed.	2.40	3.00	7.55	.006**
<u>Biomedical Research</u>				
1. Animal research justified in reduced suffering.	1.60	1.39	.00	.99
2. New surgical procedures and drugs first tested on animals.	1.77	1.60	.00	.96
3. Important breakthroughs are from animal research.	1.64	1.42	.03	.87
4. Viable alternatives exist.	3.14	3.68	9.45	.002**
5. Most biomedical research is necessary and valid.	2.45	2.27	.05	.83
6. Some biomedical animal research is unjustified and should be curtailed.	2.23	2.51	4.20	.04*
<u>Psychological Research</u>				
1. Animal research justified if reduces suffering.	1.78	1.52	.03	.86
2. No alternative to animal research since many questions not answerable with research of people.	2.34	2.10	.08	.78
3. Important breakthroughs are from animal research.	2.13	1.87	.52	.47
4. Viable alternatives exist.	2.88	3.35	8.65	.004**
5. Most psychological research is necessary and valid.	2.67	2.65	.06	.81
6. Some psychological animal research is unjustified and should be curtailed.	2.27	2.39	.85	.36
<u>Philosophical Positions</u>				
1. All species should be treated equally.	3.38	4.02	3.11	.08
2. Rights to respecty and not be harmed.	2.44	3.30	11.32	.0008***

Note: All ratings made using a 1 (strongly agree) to 5 (strongly disagree) rating scale.

Lastly, the ratings with regard to the philosophical issues showed similar patterns. All areas disagreed with the principle of equality except for the human service psychologists who gave this item a neutral rating. Not surprisingly, the basic experimental psychologists most strongly disagreed with this position. On the other hand, with regard to the principle of specific rights, the human service psychologists agreed with it while the other three groups gave it a more neutral rating.

Although there were more areas of disagreement than agreement among the psychologists in different specialties, there were also numerous instances of clear agreement: all disagreed that research on animals has no bearing on problems confronting people, all were concerned about pain and suffering in animals, and all agreed that both biomedical and psychological research with animals is justified if it reduces human suffering. Both groups also agreed that important biomedical and psychological breakthroughs have occurred as a consequence of animal research. Additionally, all clearly agreed that new surgical procedures and drugs should be tested on animals before they are used with people.

Table 3. Average Ratings by Psychologists with Different Areas of Specialization.

<u>Items</u>	<u>Basic Exp.</u>	<u>Human Serv.</u>	<u>Other Res.</u>	<u>Other Appl.</u>	<u>F Value</u>	<u>P Value</u>
<u>General</u>						
1. Animal research has no bearing on people's problems.	4.80	4.40	4.30	4.41	1.75	.19
2. Intrinsic interest is sufficient justification.	1.80	2.58	2.44	2.49	3.32	.02*
3. Concern about pain and suffering in animals.	1.63	1.63	1.53	2.07	.63	.60
4. More regulations needed.	3.74	2.76	3.12	3.13	3.22	.02*
5. More enforcement needed.	3.14	2.35	2.52	2.64	2.63	.04*
<u>Biomedical Research</u>						
1. Animal research justified if reduces suffering.	1.20	1.66	1.46	1.56	1.70	.17
2. New surgical procedures and drugs first tested on animals.	1.29	1.85	1.70	1.66	1.58	.19
3. Important breakthroughs are from animal research.	1.26	1.66	1.55	1.70	1.62	.18
4. Viable alternatives exist.	3.74	3.13	3.19	3.30	3.08	.03*
5. Most biomedical research is necessary and valid.	2.12	2.48	2.39	2.40	.78	.50
6. Some biomedical animal research is unjustified and should be curtailed.	2.67	2.24	2.14	2.39	3.20	.02*
<u>Psychological Research</u>						
1. Animal research justified if reduces suffering.	1.31	1.87	1.55	1.71	1.55	.20
2. No alternative to animal research since many questions not answerable with research on people.	1.46	2.43	2.20	2.48	5.21	.001***
3. Important breakthroughs are from animal research.	1.54	2.16	2.15	2.12	2.42	.07
4. Viable alternatives exist.	3.60	2.85	2.88	3.03	4.92	.002***
5. Most psychological research is necessary and valid.	2.17	2.70	2.77	2.70	2.42	.07
6. Some psychological animal research is unjustified and should be curtailed.	2.69	2.25	2.17	2.34	3.33	.02*
<u>Philosophical Positions</u>						
1. All species should be treated equally.	4.30	3.25	3.72	3.65	3.30	.02*
2. Rights to respect and not be harmed.	3.47	2.36	2.63	2.87	5.24	.001***

Note: All ratings made using a 1 (strongly agree) to 5 (strongly disagree) rating scale; * $p < .05$, ** $p < .01$, *** $p < .001$.

Comparison with Gallup and Beckstead's Results

A comparison of ratings of psychologists with Gallup and Beckstead's (1988) undergraduate students on the six overlapping items is presented in Table 4. Not surprisingly, it appeared the psychologists disagreed more than the students with the statement that animal research has no bearing on problems confronting people, and agreed more strongly with the statement on the value of basic animal research. It is noteworthy that all psychologists seemed to be as concerned as students about pain and suffering in animals. On the other hand, students appeared to support more regulations governing the use of animals in research, while members of APA were neutral and APS members disagreed with this statement. Psychologists also agreed more strongly with the value of trying out surgical procedures and drugs on animals than did the students. All students and psychologists, however, agreed with the statement that some animal research is necessary since many important questions cannot be answered by doing experiments on people.

Table 4. Comparison of Average Ratings of Present Results With Gallup and Beckstead's (1988) Results.

	<u>Gallup and Beckstead</u>	<u>APA</u>	<u>APS</u>
Research on animals has little to no bearing on problems confronting people.*	3.81	4.39	4.64
An intrinsic interest in the animal for its own sake is ample justification for doing animal research.*	2.99	2.54	2.04
+I am concerned about pain and suffering in animals.	1.98	1.67	1.64
We need more regulations governing the use of animals in research.*	2.30	2.85	3.58
New surgical procedures and experimental drugs should be tested on animals before they are used on people.	2.22	1.77	1.60
Since many important questions cannot be answered by doing experiments on people, we are left with no alternative but to do animal research.	2.43	2.34	2.10

*Significant differences APA versus APS
+word "very" deleted in present survey

Subjective Comments

A wide range of comments were made on the questionnaires (total = 52). They ran the gamut from clearly supporting animal research (23%), to supporting animal research within ethical limits (56%), to neutral opinions (6%), to being clearly against animal research (15%). The majority of psychologists making a comment supported animal research, but with ethical limits. Many of these psychologists emphasized the necessity and appropriateness of animal research, but stressed the importance of weighing the costs in terms of animal pain and suffering. Some noted that in many cases, research is trivial and is cruel and destructive. Those clearly in support of animal research noted the superiority of the human race and several commented on the "fanaticism" and misguided ways of the animal rights groups. Psychologists clearly against animal research expressed the importance of all species in the preservation of our natural world and emphasized that human beings do not have any ethical right to harm non-human animals to benefit the human species.

Conclusions

The results of this survey demonstrated that most psychologists do not see the issues related to the use of animals in biomedical or psychological research as representing a simple, "all animal research is good" or "all animal research is bad" issue. All psychologists across all areas agreed that there are justifiable uses of animals in biomedical and psychological research. However, all were also concerned about pain and suffering in research animals and the vast majority of psychologists agreed that some biomedical and psychological animal research is unjustified and should be curtailed. Moreover, there was a large number of psychologists, especially in the human service fields, who were also concerned about animals' right not to be harmed and agreed that more effective enforcement of regulations governing the use of animals in research is needed. Thus, it appears that many psychologists, in the tradition of William James, continue to remain concerned about the use of animals in research and to raise ethical questions. Moreover, for a small sub-group of psychologists to dismiss everyone who raises questions about the use of animals in research as misguided extremists is for them to

dismiss the views of a majority of their colleagues in psychology and to perhaps also show the very irrationality that they accuse their opponents of displaying.

References

- American Psychological Association. (1989). Directory of the American Psychological Association (1989 ed.). Washington, D.C.: Author.
- American Psychological Society. (1990). Membership Directory of the American Psychological Society (1990 ed.). Washington, D.C.: Author.
- Dewsbury, D. A. (1990). Early interactions between animal psychologists and animal activists and the founding of the APA committee on precautions in animal experimentation. American Psychologist, 45, 315-327.
- Gainesville Sun. (1990, June 11). 24,000 march for animals.
- Gallup, G. G. and Beckstead, J. W. (1988). Attitudes toward animal research. Animal Psychologist, 43, 474-476.
- Herzog, H. A. (1990). Discussing animal rights and animal research in the classroom. Teaching of Psychology, 17, 90-94.
- Mitchell, G. (1990). Guarding the middle ground: the ethics of experiments with animals. Current Contents, April 9, 7-13.
- Regan, T. (1983). The case for animal rights. Berkeley: University of California.
- Regan, T. (1985). The case for animal rights. In P. Singer (Ed.), defense of animals (pp. 13-26). Oxford, England: Basil Blackwell.
- Singer, P. (1975). Animal liberation: A new ethics for our treatment of animals. New York: Avon.

FOURIER TRANSFORM INFRARED (FTIR) SPECTROSCOPY ANALYSIS OF COMBUSTION AEROSOL

Gary Jacquin

Introduction

In conjunction with my co-op program at McDonnell-Douglas, my current OURE project is the analysis of combustion aerosols using Fourier Transform Infrared (FTIR) Spectroscopy. Aerosol science is a very important field as it is concerned with atmospheric chemistry, atmospheric physics, climate, public health, and environmental issues.

In the Cloud and Aerosol Sciences Laboratory (CASL) at UMR, combustion aerosols are generated by an in-house designed torch or burner. The fuels, JP4 and JP5, are provided by McDonnell-Douglas. Some other commercial fuels are also used.

The primary objective of my OURE project was to generate and collect combustion aerosols for chemical analysis. I was also involved in the construction of an automated cloud condensation nucleus (CCN) counter. A more thorough description of these efforts is now offered.

Redesigning the Liquid-Fuel Burner

Background

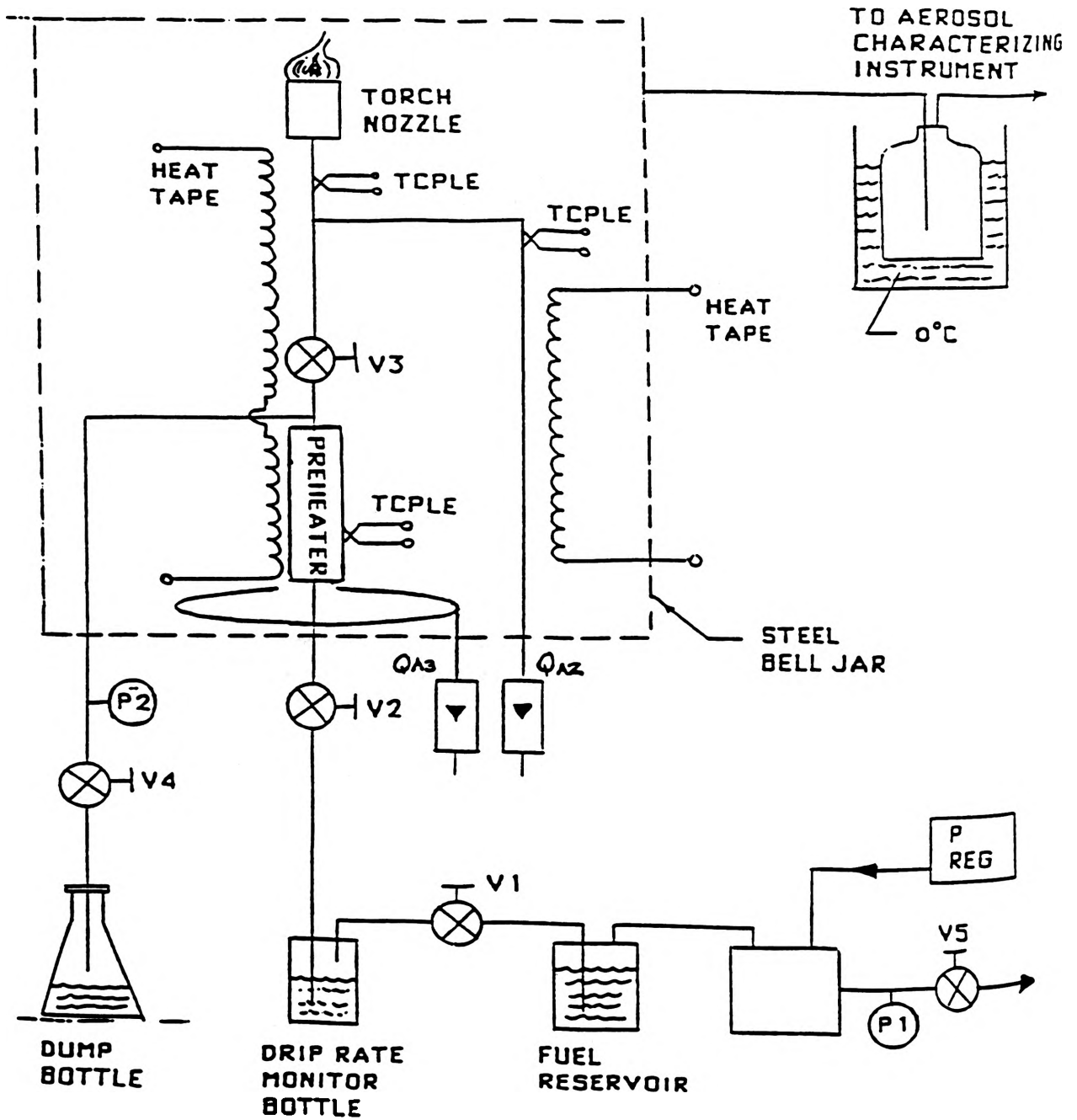
One question that arose early on was whether or not the carbon aerosol from the UMR burner truly simulates the emissions from a jet aircraft. The size distributions found in earlier works (Refs. 1-3), dealing with jet engine exhaust, indicated that the mean carbon particle diameter D_p was approximately 0.04 microns. Figure 1 shows the basic set-up of the UMR burner. Before the improvements were made to the burner, carbon produced by the burner was deposited onto slides coated with Au-Pd and examined by scanning electron microscopy. The carbon was found to be huge strands (about 1 microns in diameter) of interconnecting carbon conglomerates. This was believed to be a characteristic of the flame, which frequently turned yellow. Clearly the UMR torch needed to be improved before it would simulate a jet engine.

Actual Work

Many internal improvements were made to the torch or burner head to obtain a highly-controllable flame. There were also improvements made to the external mechanism. These include:

- 1) A port used as a pressure tap and fuel dump was added to the fuel injection system. This greatly decreases start-up and shut-down times, and allows the monitoring of fuel pressure, thus enhancing day to day reproducibility.
- 2) A shaft with several universal joints was installed to allow external control of the final fuel valve, and an externally operated ignition system was designed and implemented. These modifications allow the torch to be operated without raising and lowering the bell jar.
- 3) A photoresistance circuit was designed and partially installed to monitor the flame and sound an alarm should the flame go out. This is a big safety improvement.

FIGURE 1



- 4) The most significant improvement, however, was the design of a new burner tip. Previously the burner used to use a porous ceramic tip which produced a ball-shaped flame consisting of many individual flames that flickered out of each pore. This was unsuitable for the McDonnell-Douglas experiment which required a single large stable flame with all distinct areas of the flame accessible for probing. A new burner tip and inserts were then constructed of aluminum. This new design offers the following features:
- a) It accepts "inserts" of differing diameters to allow for variation of burn surface areas.
 - b) It holds the inserts in place by pulling a fine stainless steel wire screen down over it. The screen causes the base of the flame to sit slightly above the burner head giving access to all parts of the flame.
 - c) It has a threaded hole in the bottom for easy installation of fuel jets of various orifice size. The orifice forces the fuel-air mixture to become turbulent, thus ensuring a thorough mixing. Having different diameter orifices provides the ability to use different fuels having different vapor pressures for a given torch temperature.

There was some concern that the high temperature of the flame might cause some of the aluminum in the tip to sublime away contaminating the aerosol. Thus the final version was machined from stainless steel. As a result of the improvements, the burner is now able to produce a wide variety of very stable flames, from a pure blue flame with an inner bright blue cone and an outer dark blue cone (premixed flame) to a sooty, yellow flame. This is desirable because we can now simulate the jet engine (premixed flame) for McDonnell-Douglas. It is also able to simulate other combustion aerosol sources such as an uncontrolled oil refinery fire (sooty, yellow flame). Such a flame is at the center of the nuclear winter controversy.

After the improvements to the burner, a sample was again taken and there were no longer any strands of carbon conglomerates, and the vast majority of the particles were single spheres with diameter in the .02 to .1 microns range. Thus the UMR liquid fuel burner produces carbon aerosol with size distribution simulating the carbon from jet aircraft. This is clearly a direct effect of the burner modifications.

Aerosol Samples From the Torch

Once the torch was finished, samples of the combustion aerosol were sent to McDonnell-Douglas for Fourier Transform Infrared (FTIR) analysis. This was accomplished with an Electrostatic Aerosol Sampler (EAS). The EAS charges the aerosol, then electrically deposits the particles onto slides. The aerosol was sampled directly from the burner and after passing it through an Electric Aerosol Classifier (EAC), which discards from the aerosol stream all particles except those within a very narrow range of diameters. Such an aerosol is termed monodisperse. The slides were then sent to McDonnell-Douglas to undergo FTIR analysis to determine the aerosol's chemical nature. The main focus of the chemical analysis was on the aerosol's hydration properties. This is part of an ongoing effort to determine the effect of jet exhaust on the atmosphere.

The origin of hydration properties of combustion aerosols is a heated topic. One school of thought believes it is based on the amount of soluble material in the aerosol particles, while others argue that it is mainly due to morphological effects. This was the main topic of discussion at the Third International Conference on Carbonaceous Particles in the Atmosphere held at Lawrence Berkeley Laboratory in October, 1987 and at the conference titled Lab Studies of Smoke/Cloud Microphysical Processes Workshop held in Los Angeles, Calif. in December

1987. The present research at UMR is helping to uncover the answer by investigating whether certain soluble materials do actually exist on combustion aerosols. Initial results of the FTIR analysis do show the presence of soluble sulfates in the combustion aerosols. This is a positive and exciting result (I plan to monitor further developments in the future).

Infrared spectroscopy was chosen to analyze the aerosol because it is a powerful tool for chemical characterization, since it is capable of detecting picogram quantities of material for both organic and inorganic functional groups. This makes it possible to collect enough aerosol to perform a chemical analysis in a day.

Figure 2 shows the size distribution of carbon from JP4 aviation fuel that is available downstream of the EAC. The octagons denote the size distribution of the aerosol with the combustion air flow rate (QA2) of 5.5 liter per minute. The mean particle diameter (D_p) is about 0.045 microns. The crosses denote the size distribution for QA2 equal to 2.1 liter per minute. The mean particle diameter (D_p) is about 0.06 microns. Thus at higher combustion air flow rate, the mean carbon particle diameter is slightly smaller. Although not shown here, similar characteristics are also found for JP5. This seems to indicate a more thorough combustion of the fuel as expected. For the sake of comparison, the size distribution of the aerosol produced by the combustion of ethanol is also shown. Note that both its mean size D_p and the concentration of particles are smaller than those of JP4. One might very well expect oily fuels such as JP4 and JP5 with long chain-like molecules and many carbon atoms/molecules to provide more unburned carbon than a fuel such as ethanol.

Figure 3 shows the size distribution of carbon from JP4 that is available just after the burner. Although the mean particle diameter D_p is approximately the same for the octagons and crosses here, the crosses (lower QA2) still have a higher concentration of large particles. Again ethanol is shown for comparison.

The data for Figure 3 is obtained from the data in Figure 2 through a somewhat sophisticated computer inversion. The basic premise of this inversion is that what exits the EAC at a particular diameter D_p is only a fraction f of what enters the EAC at that D_p . Boltzmann's distribution correctly describes the charge distribution on aerosol particles. At a given D_p only the fraction f of those particles carry a charge and can thus be extracted from the rest of the aerosol.

Note that the D_p in Figure 3 (at exit from torch) is approximately 0.03 microns, which is smaller than that in Figure 2 (exit of EAC). This is because the value of f is smaller for the smaller particles, and the EAC is less efficient, therefore, in extracting them.

While collecting the samples, a part of the aerosol was extracted by the EAC (i.e., a particular D_p) and put through a Continuous Flow Diffusion Chamber (CFD). This instrument introduces the particles to a precisely controlled supersaturation. An optical particle counter counts drops that are grown from the aerosol. This allows the calculation of the critical supersaturation (SSc) for the particle of a certain diameter and chemical species. This is necessary to correlate the results of the chemical analysis with the results predicted by theory. Figure 4 shows the critical supersaturation (SSc) vs. carbon particle diameter (D_p) produced by burning ethanol, JP4, and JP5. For reference, the behavior of NaCl is also shown. First note that for a given D_p , NaCl has lowest SSc. The carbon from ethanol has the highest SSc. This is entirely to be expected since the pertinent theory states that the more soluble material there is in the particle, the lower the SSc. All of the material in an NaCl particle is soluble and one would expect very little, if any, soluble material in a carbon particle from burning reagent grade ethanol. The carbon from JP4 and JP5 is another matter though. Such fuels contain small amounts (about 0.1%) of sulfur. When burned, these fuels give rise to sulfur oxide which combine with the water of combustion forming sulfuric acid. The sulfuric acid is, of course,

FIGURE 2

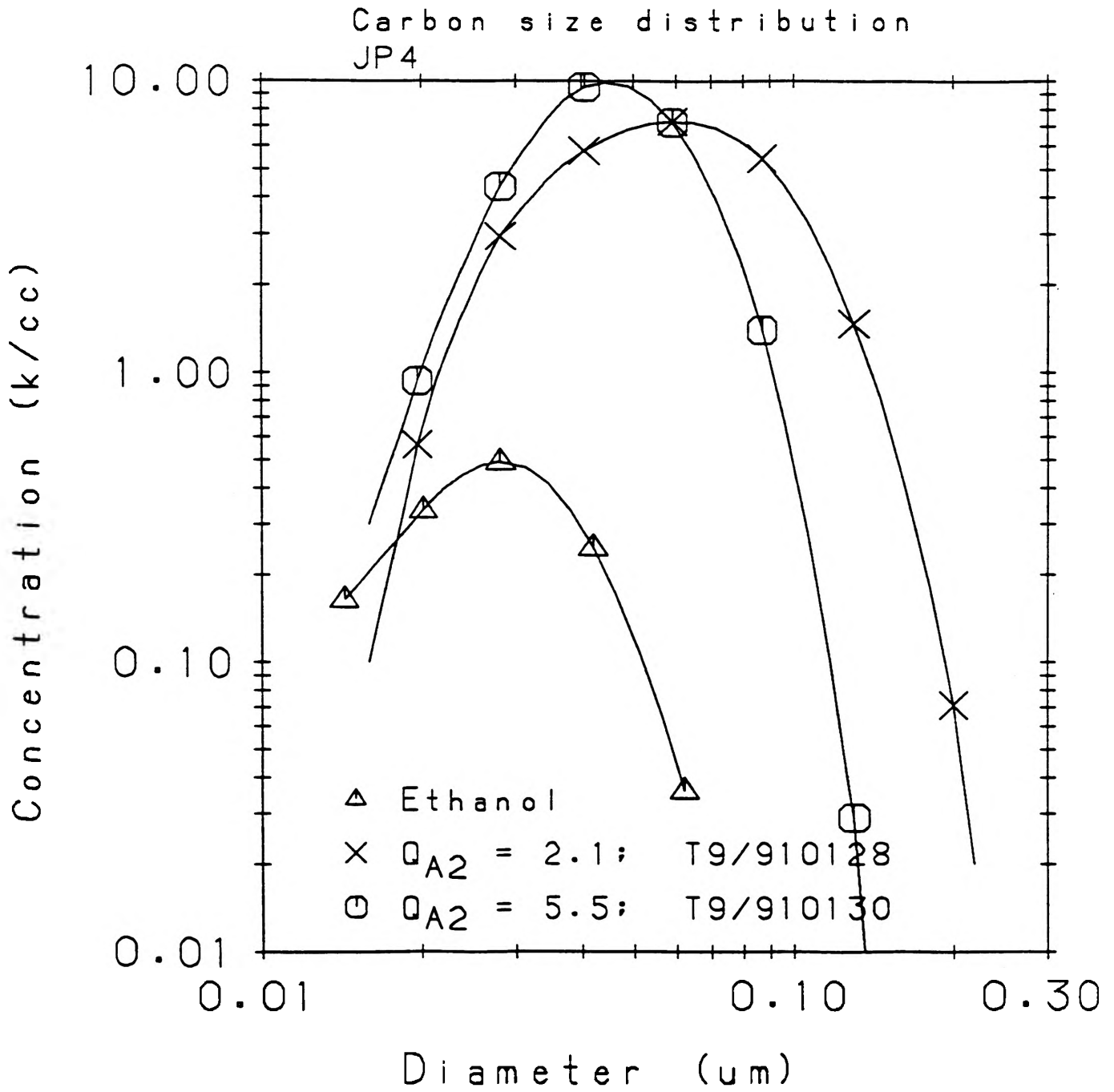


FIGURE 3

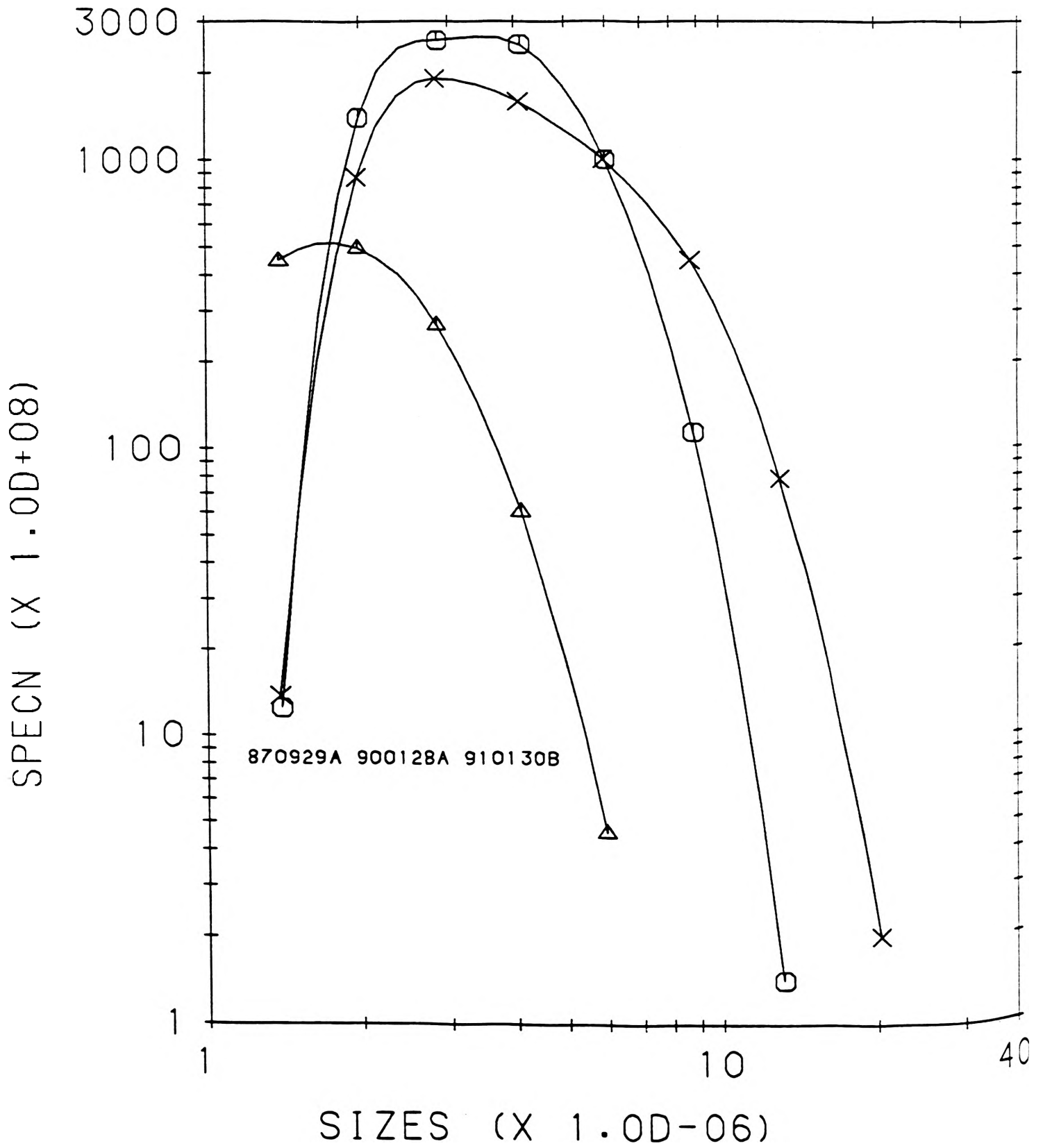
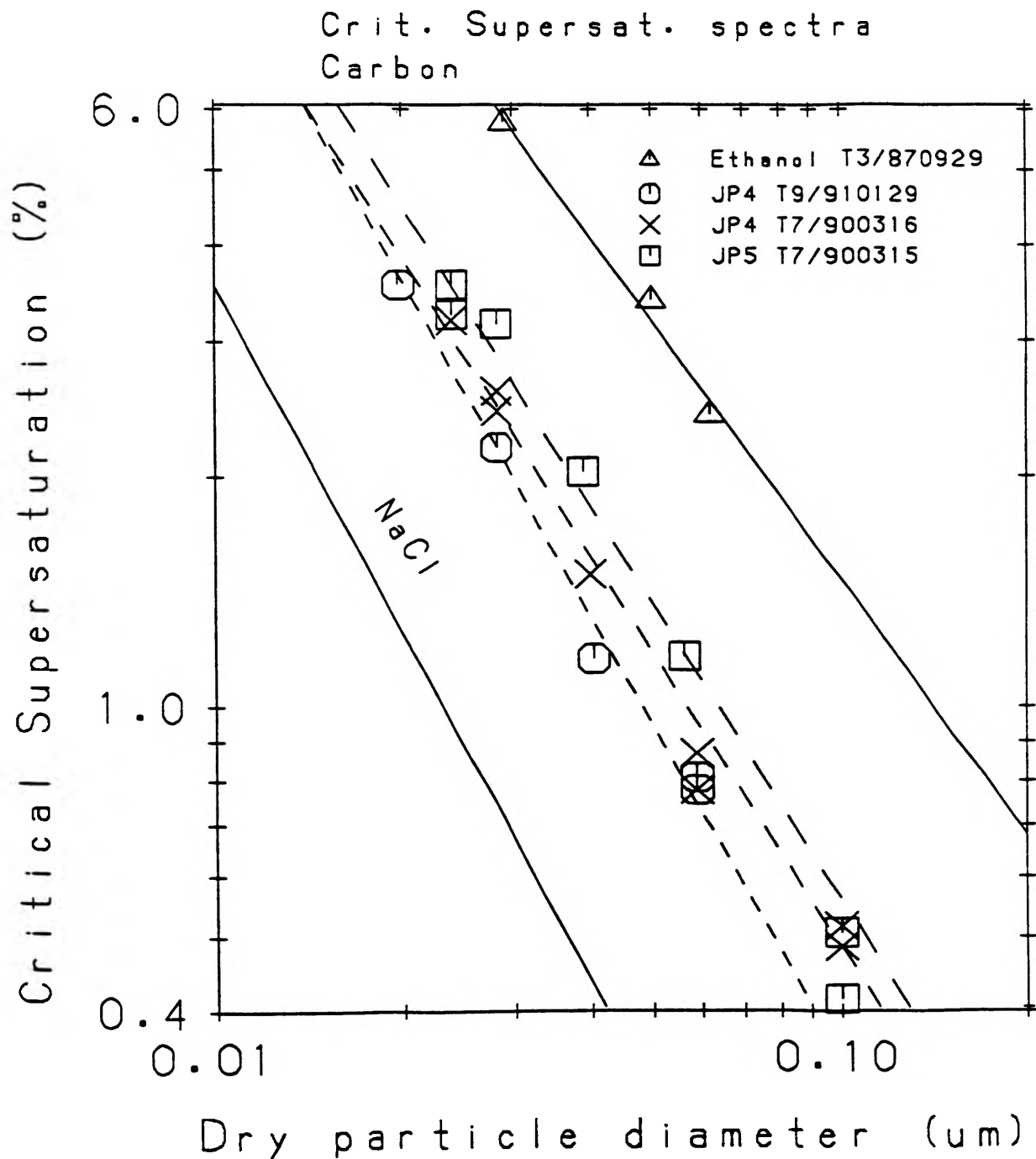


FIGURE 4



soluble. If it finds its way to a carbon particle, as some of it surely must, it would then cause the carbon particle to have a lower SSc than that from ethanol.

Note that the highest SSc value (the squares) are for JP5. The two batches of JP4 provide particles with lower SSc values. This also is to be expected since the analyses of sulfur content of JP4 and JP5 revealed that the JP4 had more sulfur than the JP5.

Other Experimental Work

There was considerable turn around time between supplying McDonnell-Douglas with samples and getting instructions from them on what type of samples to take next. Therefore, I also worked on a project designed to determine the chemical composition of cloud condensation nuclei (CCN). CCN make up only about 1% of the atmospheric particulate matter, yet are responsible for cloud condensation, fog, etc. Thus, these are very important particles. The problem is that they are at the extreme small end of the aerosol size spectrum. This makes it difficult to collect the mass required to do a chemical analysis. Recent advances in chemical analysis now make it possible to perform quantitative analysis on the amount of material that can be obtained by collecting these CCN over a reasonable of time (about 24 hours).

This project requires the design and construction of a much larger and improved version of the fore mentioned CFD. I was involved in the construction and initial testing of a smaller prototype of the new instrument. Figure 5 shows a diagram of the prototype. We are having good initial success with the still uncompleted prototype.

In addition to the FTIR McDonnell Douglas experiment and the CCN chemical composition experiment, I was involved on a smaller scale in many other experiments. One such experiment was the study of scavenging rate. Scavenging is a process whereby one aerosol particle captures another particle of smaller diameter. This process creates a third particle with D_p and SSc different from either of the original two. As stated earlier, this is of considerable importance in environmental issues. This experiment again made use of both the EAC and CFD. The burner produced carbon particles which were then sent to the EAC and a monodisperse slice of diameter D_{p1} extracted. Meanwhile the nebulizer atomized a solution of polystyrene latex (PSL) particles and this aerosol was sent to a second EAC where a monodisperse slice of diameter D_{p2} was extracted. These two aerosols were put in a 200 liter plastic bag for a few hours. Then the resulting aerosol was extracted from the bag, and its SSc measured using the CFD. Repeating this procedure many times using different diameter particles and varying scavenging times allowed the scavenging rate and resulting SSc to be measured as a function of D_{p1} and D_{p2} and scavenging time.

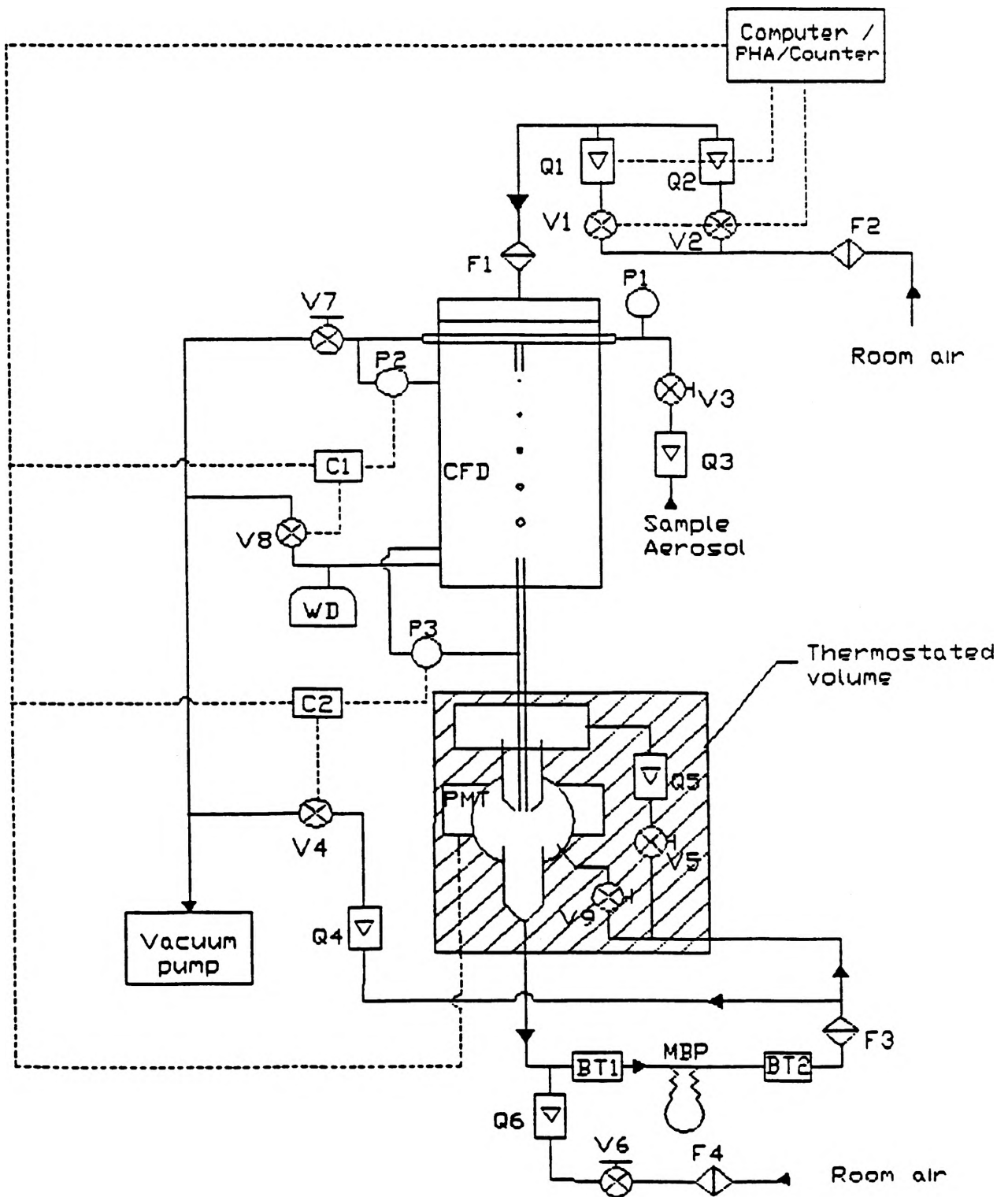
I also spent some time developing a drop generator to be used in ice nucleating experiments. A drop generator is an instrument that can create drops of liquid of various diameter at various rates. The drop generator I worked on used a ball-tipped wire connected to a motor driven cam to pull a drop away from a meniscus of liquid.

In addition, Ron Holland, another OURE student with whom I worked closely over last summer, and I spent a week learning to use an image processor called JAVA. Ron Holland plans to use the processor to analyze Scanning Electron Microscope results of his morphology experiments.

Conference Presentations

With the support of Dr. Donald Hagen and Max Trueblood, I have entered a paper in the Missouri Academy of Sciences (MAS) meeting to be held April 19. Ron Holland is also presenting a paper at the meeting. I have included a copy of my abstract in this report. I feel

FIGURE 5



this will be a very valuable experience for me and I look forward to participating in the meeting. This work will also be reported at the 9th Midwest Association for Cloud and Aerosol Physics Meeting, May 1991, at the University of Wisconsin-Madison, in a paper entitled "A laboratory liquid fuel burner and the properties of the associated combustion aerosols".

With the MAS meeting being April 19, I will not be able to participate in the UMR Undergraduate Research Symposium being planned for the same date. I regret not being able to present a talk at both events.

Postscript

I have restrained from introducing the theoretical and mathematical aspect of the experiments in favor of simple, direct explanation of the subject in the belief that this approach would better serve prospective future OURE students who may read this report in trying to decide where they may want to work. Along these same lines I would like to conclude by saying I had a very enjoyable and beneficial OURE experience. Everyone I worked with on a daily basis was extremely helpful and supportive. I have gained immeasurable knowledge from the project, not only in cloud physics, but also in research methods and the many difficulties involved in research. Therefore, I strongly recommend future OURE involvement in the Cloud and Aerosol Science Laboratory.

References

- 1) "Particle Size Measurement Program From the Exhaust of the J79-GE-80 Engine", test cell 20, Naval Air Rework Facility, North Island Naval Air Station, San Diego, Calif. Taken from the Aircraft Environmental Support Office (AESO) Report No. 110-01-84, January 1985.
- 2) "Physical Characterization of Particulate Material From a Turbine Engine." Taken from Proc. Gas Turbine Conf., San Diego, Calif. 1979, ASME Publication 79-GT-179.
- 3) "Electrical Aerosol Analyzer: Operation, Maintenance, and Application." Taken from Aerosol Measurement, D. A. Lundren ed., University Press of Florida, Gainesville 1979.

MATHEMATICA DEMONSTRATIONS FOR CALCULUS

Bryan Krueger

Introduction

The objective of this research was to generate useful classroom demonstrations of fundamental Calculus concepts. Herein are the code listings of two *Mathematica* "programs." The first displays individual plots of two dimensional Taylor Series approximations. The second set of code creates a TNB frame on a three dimensional space curve. Following this introduction is a complete listing of each "program" along with an example of its function.

Each set of *Mathematica* commands follows a simple format. The special functions are loaded first, then an input routine, followed by the calculation/graphics output section. One thing to note about these demonstrations is the input section. Previously, new functions were put in a single block statement which utilized commands written in a format such that they could be loaded the same way as other special functions, i.e. the cross product (<<:LinearAlgebra:Cross.m). As the necessary input increases these block statements become lengthy and confusing. To avoid this, *Mathematica's* built in user active input is used. This allows for better control over output such as the number of plots generated and their size. It may even speed usage as memorization and constant reference are not required to place the needed values in their exact location and format. Hence, fewer errors and frustrations are created while interest is kept high.

Just these few examples are consistent with the great usefulness and versatility of *Mathematica*. The code lines can easily be taken apart, added to, and used in other student exercises. Each program generates a separate plot for every iteration. The plots can then be combined for colorful examples and high quality animations. *Mathematica* built-in organization and text functions are very useful in the production of reports such as this one and insure its capabilities will be used for other courses aside from mathematics.

Taylor Series

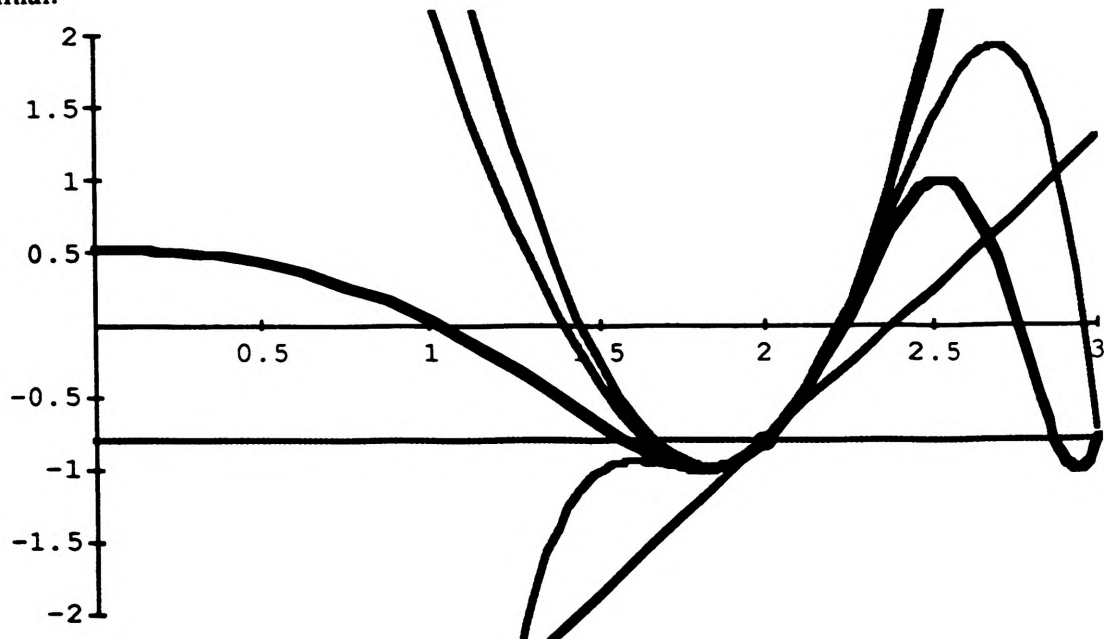
This code produces plots of a user-supplied function and a specified number of approximating Taylor polynomials about a user-given point.

(*Two-Dimensional Taylor Series Approximations*)

```
f[x_] = Input["Enter a function in terms of x:"];
p = Input["Enter the point about which to approximate:"];
x1 = Input["Enter the MINIMUM x value for viewing:"];
x2 = Input["Enter the MAXIMUM x value for viewing:"];
y1 = Input["Enter the MINIMUM y value for viewing:"];
y2 = Input["Enter the MAXIMUM y value for viewing:"];
t = Input["Enter the number of iterations to perform:"];
t = t - 1;
ts[x_,a_] = 0;
pt = Graphics[{RGBColor[0,0,1], PointSize[.02], Point[{p,f[p]}]}];
Do[ts[x_,a_] = ts[x,a] + (D[f[a],{a,n}]) (x - a)^n/n!;
```

```
Show[Plot[{f[x],ts[x,p]},{x,x1,x2},
  PlotStyle->{Thickness[.0075], RGBColor[1,0,0]},
  DisplayFunction->Identity],
pt, PlotRange->{{x1,x2},{y1,y2}},
AspectRatio->1/GoldenRatio,
Axes->{0,0}, DisplayFunction->{$DisplayFunction},
{n, 0, t}]
```

Here is $f[x] = \text{Cos}[\text{Cosh}[x]]$ and its first five Taylor polynomials expanded about $x = 2$. These have been merged into one plot - the command above gives a separate cell for each polynomial.



The TNB Frame

The following command creates frames for an animation showing the unit tangent, unit normal, and unit binormal vectors for a given space curve. On a color monitor these can be assigned different colors for easy identification. The output shows some frames when the space curve is

$$\{x[t], y[t], z[t]\} = \{\text{Cos}[t], \text{Sin}[t], \text{Sin}[2t]\}.$$

```
<<:Graphics:ParametricPlot3D.m
```

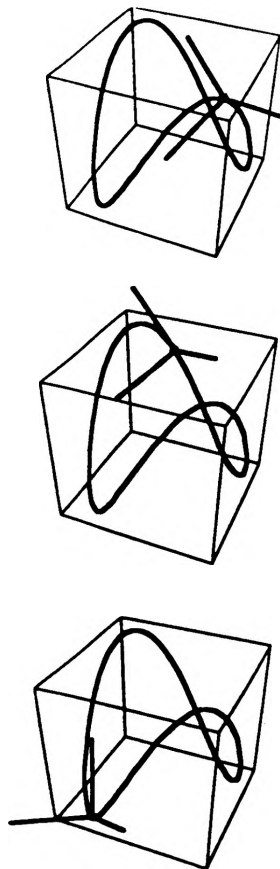
```
<<:LinearAlgebra:Cross.m
```

```
rvx[t_] = Input["Enter the x-component for a position vector:"];
rvy[t_] = Input["Enter the y-component for a position vector:"];
rvz[t_] = Input["Enter the z-component for a position vector:"];
t0      = Input["Enter the initial value of t:"];
t1      = Input["Enter the final value of t:"];
dt      = Input["Enter the stepsize for t (used when drawing the curve):"];
tvm     = Input["Enter the scalar multiplier for the tn timer:"];
min     = Input["Enter the largest NEGATIVE number any function achieves:"];
max     = Input["Enter the largest POSITIVE number any function achieves:"];
m       = Input["Enter the number of frames in the animation:"];
rv[t_] = {rvx[t], rvy[t], rvz[t]}
```

```

tv[t_]=D[rv[t],t]/Sqrt[D[rv[t],t].D[rv[t],t]]
nv[t_]=D[tv[t],t]/Sqrt[D[tv[t],t].D[tv[t],t]]
bv[t_]=Cross[tv[t], nv[t]];
tstep=(t1-t0)/nn;
sc=SpaceCurve[{rvx[t], rvy[t], rvz[t]}, {t, t0, t1, dt}, DisplayFunction->Identity];
Do[Show[Graphics3D[{PointSize[.03], RGBColor[.5,.5,.5], Point[rv[n]]},
Graphics3D[{Thickness[.01], RGBColor[1,0,0],
Line[{rv[n], rv[n]+tvm tv[n]}]},
Graphics3D[{Thickness[.01], RGBColor[0,1,0],
Line[{rv[n], rv[n]+tvm nv[n]}]},
Graphics3D[{Thickness[.01], RGBColor[0,0,1],
Line[{rv[n], rv[n]+tvm bv[n]}]},
Graphics3D[Thickness[.01], RGBColor[0,0,0]], sc,
BoxRatios->{1,1,1},
PlotRange->{{min, max}, {min, max},{min, max}},
DisplayFunction->$DisplayFunction],
{n, t0, t1, tstep}]

```



IMPLEMENTATION OF THE ARTICULATED TOTAL BODY (ATB) MODEL ON AN APOLLO WORKSTATION

M. F. Laudon

The Articulated Total Body Model (ATB) is used for predicting gross segmented body response in various dynamic environments. The ATB computer program, originally written by the Department of Transportation as a Crash Victim Simulation (CVS) program, was later modified by the Calspan Corporation and More recently by the Armstrong Aerospace Medical Research Laboratory (AAMRL) to allow for aerodynamic force applications, harness belt capabilities and hyper-ellipsoidal graphical display of the modeled segments. The ATB model has been successfully used to investigate gross human body responses to bodies placed in such complex dynamic environments as high-speed aircraft ejection. This ATB model is quite versatile due to the variety of inputs it can handle. Because of this versatility, a wide range of physical systems may be simulated.

In this work, the ATB computer program has been modified for use on the Apollo workstation and utilized to predict limb and joint limitations a modeled human arm for the purpose of creating more effective rehabilitation schedules. A patient's left shoulder, left-upper and left-lower arm have been modeled for a case study. The required information consists of segment physical dimensions, weight, center of gravity and maximum forces and torques obtainable from various body muscles. From this information, forces a graphical display of desired segment positions, and numerical approximations of forces, torques, positions, velocities, and accelerations of any desired point of the modeled segment. A comparison of this numerical output found from the ATB will be made with actual patient response, further input will be created tracking the patient's rehabilitation progress. A mathematical model of this will be incorporated into the ATB for the purpose of predicting future patient responses and a predicted schedule for disabled patient rehabilitation.

An accurate numerical and visual prediction of patient responses and limitations would be very beneficial in the creation of rehabilitation schedules. For such a service to be obtainable in a hospital environment, the ATB must be executable on a personal computing level. The Apollo workstation was selected for this project due to its relative mobility and availability. Many similar computing systems could be used where the criteria of mobility, large memory capabilities and superior graphics are obtainable. These criteria must be met so that the ATB could eventually be used by physicians in a clinic or office environment.

INTRODUCTION

The Articulated Total Body Model (ATB) is a computer model of the human body used for predicting gross segmented body response in various dynamic environments. The ATB program evolved from the Crash Victim Simulation (CVS) Program which was created by the Department of Transportation in 1973. Aerodynamic force applications and a harness belt capability were added to the CVS by Calspan Corporation in 1975 for the Armstrong Aerospace Medical Research Laboratory (AAMRL). The resulting program became known as the Articulated Total Body Model. In 1980, Calspan made a number of modifications to the ATB model, combining it with the then current 3-D Crash Victim Simulation program to form the ATB-II model. A new version, ATB-III, was generated which included improvements made by J&J Technologies, Inc. AND used to model the body response to wind blast for AAMRL. The ATB-III is the program version used for implementation on an Apollo workstation.

In this paper, first a general description of the human body model is treated. This description consists of the actual FORTRAN code within the ATB and its capabilities found from numerous executions (successful and unsuccessful) of the ATB program. This paper does not attempt to explain the actual computer coding of the ATB or any of the non-biodynamic options available to the ATB Model. Then a brief case study of a modeled human limb is presented to demonstrate successful implementation on the Apollo workstation for possible utilization of the model in a clinical environment. It should be emphasized that this model and the corresponding output obtained are simplified cases of a full body model. Although much more complex models could be presented, this simplicity has been emphasized so that the huge amounts of input and output data would not distract from the main point which is to demonstrate the utility of a computer model in a clinical setting. The unique aspect of this work is the use of the ATB model on a personal computing level with graphical display capabilities for determining the dynamic characteristics of various limbs and joints of the human body while carrying out prescribed motion. The Apollo workstation was selected for this project due to its relative mobility and availability. Many similar computing systems could be used where the criteria of mobility, large memory capabilities and superior graphics are obtainable. These are essential if the ATB were to eventually be used by physicians in a clinical environment. In that environment, an accurate numerical and visual prediction of patient responses and limitations would be very beneficial in the assessment of reach and flexion of the injured patient under a rehabilitation program, for example.

GENERAL FORMULATION OF THE ATB MODEL

"The Articulated Total Body (ATB) Model is primarily designed to evaluate the three-dimensional dynamic response of a system of rigid bodies when subjected to a dynamic environment consisting of applied forces and interactive contact forces." (Calspan Co 3). The structure of the ATB program input is quite versatile making the ATB a very general model. "The ATB Model has been used to model such widely diverse physical phenomena as human body dynamics, the motion of balls in a billiards game and transient response of an MX missile suspended from cables in a wind tunnel"(Calspan Co. 3).

To avoid confusion between the individual segments and the total body model, the term "segment" will be used to refer to the individual rigid bodies and the term "body" will refer to the overall modeled body. A model of a human body structure

showing the labeling of each segment and corresponding joints is shown in Figure 1. The ATB model divides the human body into individual rigid segments. These segments are linked together into a "tree" of coupled segments. Segments are assigned center of gravity, mass, moment of inertia, physical dimensions and are joined at positions representing human joint locations such as shoulders and elbows. Segments branch out from a central segment to form open chains analogous to limbs branching out from a tree trunk. A maximum of 30 segments can be modeled without program changes. The ATB input format is quite flexible and allows wide variation in the number and make-up of the segments.

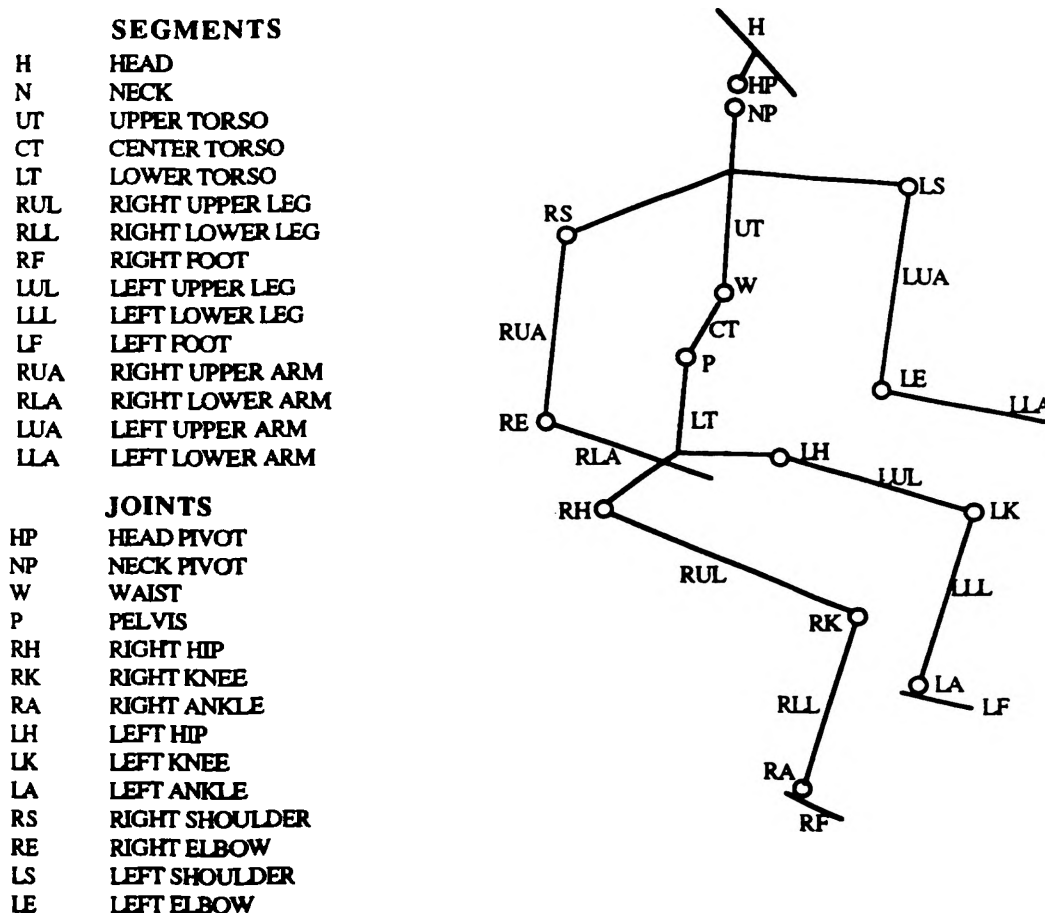


FIGURE 1- Body Dynamics Model

A chain structure is used to identify and relate the segments and their corresponding joints. The body models are composed of a Number of body SEGments, NSEG, and a Number of JoiNTs, NJNT. An example of a 15-segment, 14-joint human body model, and a 3-segment, 2-joint left arm model along with the methods of numbering these segments and joints are presented in Figures 2 and 3 respectively.

The ATB model utilizes many reference coordinate systems with respect to which position in space and segment orientations are calculated. The primary coordinate systems used in the model are the inertial, vehicle, local body segment, principal, joint and contact ellipsoid. The specification of each reference coordinate system requires an origin and a direction cosine matrix defined by three rotation angles yaw, pitch and roll- which relate one reference coordinate system to another. All the above mentioned coordinate systems are orthonormal. The inertial coordinate system represents the ground and can be positioned at the user's convenience. The inertial frame of reference is specified by defining a gravity vector as seen in Figure 2. Any values can be used for the vector components, however a convenient method is to assign the frame values of (zero, zero, g), defining the Z axis as pointing downward. In terms of a standing patient, the positive force of gravity would be pointing from head to foot. By assigning the positive X axis from the patients back to front, the right hand rule defines the positive Y axis as pointing in the lateral direction from the patients left to right side (see Figure 2). Segment coordinate systems are then defined with respect to the inertial system. These local segment coordinate systems are used to define the joint, force, vehicle, contact ellipsoid, and external planar coordinate systems.

FULL BODY MODEL					
I	SEGMENT	J	JOINT	JNT(J)	CONNECTS
1	LT	1	P	1	LT-CT
2	CT	2	W	2	CT-UT
3	UT	3	NP	3	UT-H
4	N	4	HP	4	NH
5	H	5	RH	1	LT-RUL
6	RUL	6	RK	6	RUL-RLL
7	RLL	7	RA	7	RLL-RF
8	RF	8	LH	1	LT-LUL
9	LUL	9	LK	9	LUL-LLL
10	LLL	10	LA	10	LLL-LF
11	LF	11	RS	3	UT-RUA
12	RUA	12	RE	12	RUA-RLA
13	RLA	13	LS	3	UT-LUA
14	LUA	14	LE	14	LUA-LLA
15	LLA				

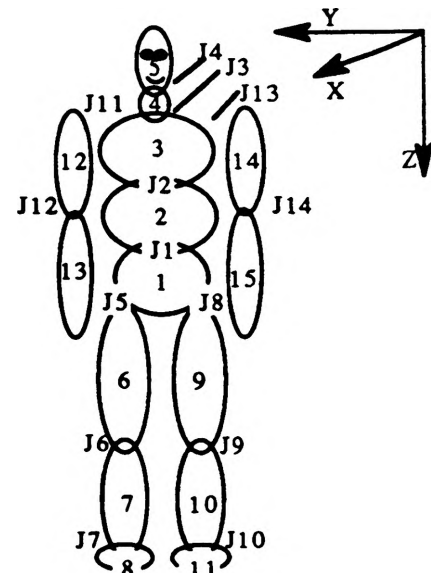


FIGURE 2- Example of segment, joint, and connectivity assignments (Full Body Model)

LEFT ARM MODEL					
I	SEGMENT	J	JOINT	JNT(J)	CONNECTS
1	B-Body	1	LS	1	B-LUA
2	LUA	2	LE	2	LUA-LLA
3	LLA				
4	*-Vehical				

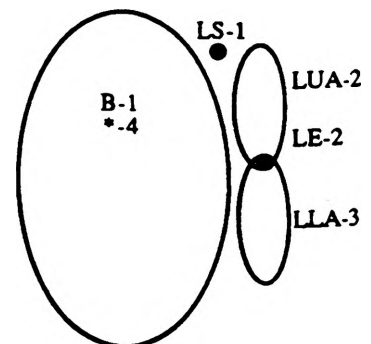


FIGURE 3- Example of segment, joint, and connectivity assignments (Left Arm Model)

LEFT ARM UNDER A CONSTANT ELEMENT TORQUE

To relate segments and joints to each other, the identification numbers $i=1$ to NSEG and $j=1$ to NJNT are used along with the array, JNT(j) which defines the connectivity of the segments. Referring to the left upper and lower arm model in Figure 3, the torso or body (BODY) is assigned the segment number, NSEG=1, defining the torso as the reference segment. Although any segment can be defined as the reference segment, a segment with maximum joint connections and minimal acceleration is desirable for the reference segment in order to avoid errors with the program integrator. After selection of the reference segment, the first joint j , must be defined. For the arm model, the left shoulder (LS) is defined as joint number 1. The requirement for sequential numbering of segments results in the upper arm (LUA) being designated as segment number 2, with the lower arm (LLA) being assigned segment number 3. The elbow (E) joint connects segment 2 and 3 and is assigned joint number 2.

To accurately model the human arm structure, the arm needed to be joined to a relatively stable structure via a joint. Originally an ellipsoid-planar contact was defined at the shoulder joint position. The planar surfaces are actually defined as finite rectangles which contact the segment ellipsoids at a finite number of points. For this type of contact, the contact force is determined by a force deflection routine which allows for energy losses (hysteresis), permanent offset, and impulsive forces. The force deflection is associated with each paired contact. Mutual force deflection characteristics which allow for the specific paired contacts must be accurately specified. For this particular ellipsoid-planar contact, unrealistic contact forces were continuously encountered.

Instead of the planar contact, the BODY segment was introduced along with a fourth segment defined as a vehicle segment. By defining the vehicle with respect to BODY and mounting BODY upon the vehicle, the numerical descriptions of both segments were used to create a stationary segment to which the shoulder joint could be connected. To obtain this stationary position, the BODY segment was defined to have extremely large x , y , and z components of moment of inertia: 5000 (lbs-sec²-in). The velocity and acceleration of the vehicle were then set to the constant value of zero.

As mentioned above, the BODY segment was created to act as an anchor for the modeling of the 2-segment left arm. The BODY segment was given a weight of 210 lbs and a contact ellipsoidal semi-axis of 6.0, 8.7, and 36.0 inches (x , y , z) which somewhat corresponds with the physical dimensions of the arm. The upper arm was given a weight of 5.542 lbs with a contact ellipsoidal semi-axis of 2.212, 2.212, and 7.497 inches (x , y , z) where the left lower arm weight was set at 5.901 lbs with ellipsoidal axes of 1.871, 1.871 and 10.269 inches (x , y , z respectively). These values were obtained from recorded human dimensions, with this example representing a 95th percentile male. Referring to Figure 4 and the corresponding table, both the linear positioning and the prescribed physical dimensions of each segment can be seen. The shoulder joint is located at (0.0, 9.0, 0.0) inches in the BODY coordinate system. The shoulder joint is located at (0.0, 0.0, -5.42) with in the upper arm coordinate system, which is located at the center of gravity of segment 2. The elbow and the shoulder joints are defined to be 8.2 and 19.04 inches respectively in the negative Z direction of the left lower arm coordinate system.

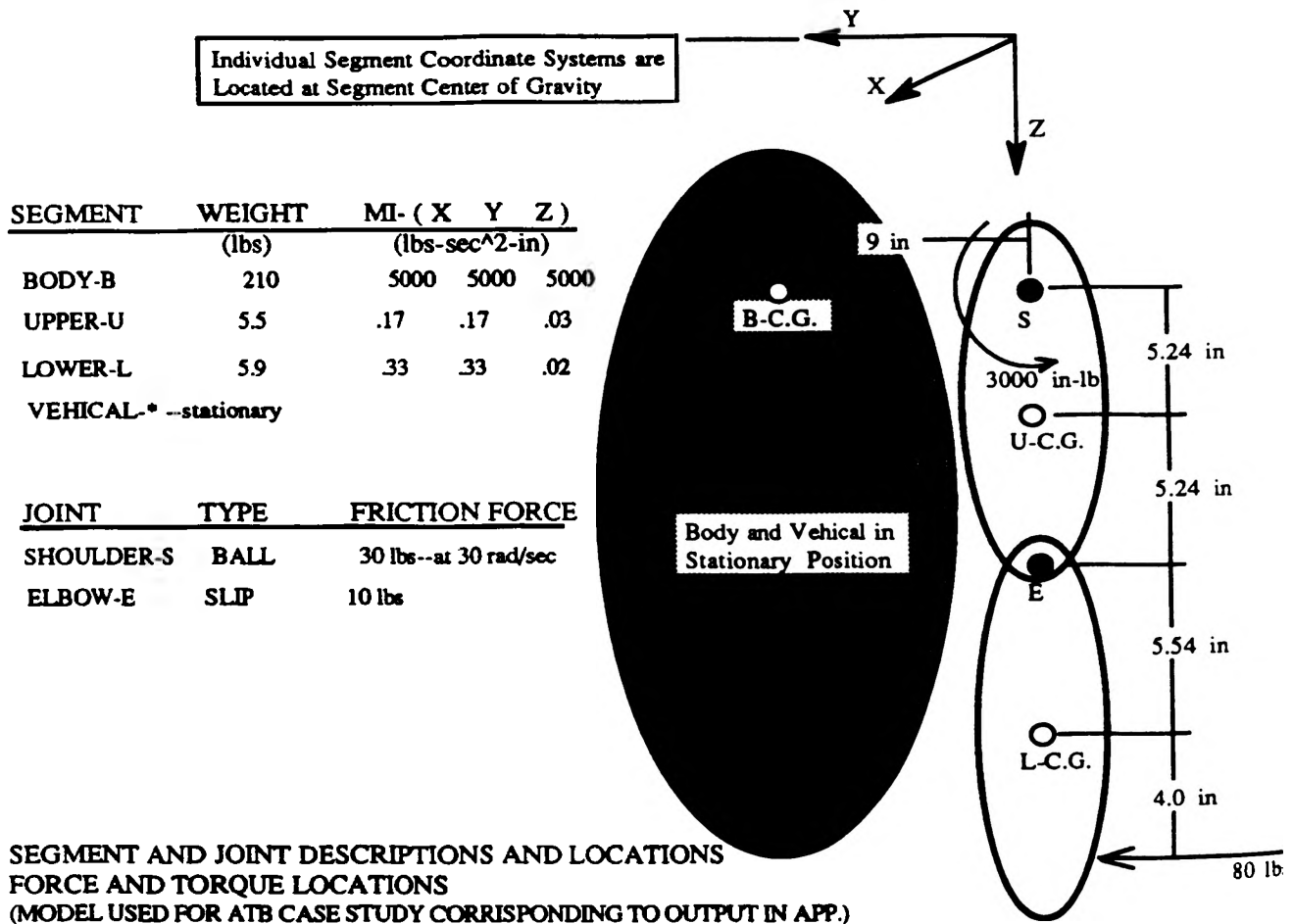


FIGURE 4- Left Arm Model Physical Description

The ATB has the ability to accurately model standard ball and pin, hinge, Euler, slip, and universal joints. These joints can be linear or angular locking joints with maximum and minimum locking and unlocking joint forces. For simplicity, a totally free ball joint was specified for the shoulder joint of the modeled arm. The elbow was specified as a slip joint with a coulomb frictional force applied when joint angular velocities exceed 30 rad/sec. This slip joint allows small linear motion between the joint's segment coordinate systems. Although this particular joint is unlocked, joints can easily be locked to limit rotation, and angular velocity. Joint torques can be both applied and calculated for each joint by relating joint parameters and yaw, pitch, and roll with all related local segments.

The ATB model has the capability to apply time-dependent forces and torques to body segments. A force or torque coordinate system is defined such that a positive force is applied in the positive X direction of the force or torque coordinate system and a positive torque is applied about the positive X axis of the coordinate system using the right hand rule. The origin and orientation (rotation) of the force or torque coordinate systems are specified with respect to the local reference coordinate system of the segment to which the force or torque is being applied. Each time dependent force can be subdivided over the time domain that it acts on. The force

over each of these smaller domains can be defined either as a constant force, a polynomial, or the force can be defined over an even smaller domain by using tabular data to describe the force. For the arm model, a constant torque was placed on the left upper arm at (0, 0, -4) with respect to the left upper arm center of gravity.

MODEL RESPONSE

The ATB outputs requested time histories of selected total and angular accelerations, velocities, displacements, joint parameters, joint forces and torques, and total body properties. For the 2-segment arm model, only relative positioning and joint parameters were requested. For this run, end point positioning of the upper and lower arm segments (segments 2 and 3) were calculated with respect to segment 1 (BODY). The positioning of segment 3 with respect to segment 2 was also calculated and this tabular output can be seen in Appendix B. The shoulder joint forces and torques on the upper arm were also tabulated and can be seen in Appendix C. These tables of displacements represent the displacements of each of the specified points over the specified time frame of 40 msec. This 40 msec is divided into specified one time units which for this case was 1 msec.

The tabulated position data is depicted as Y-Z, X-Z, and X-Y plane views of the body segments in Appendix D. These printer plots, also called "stickman plots" give the location in the primary vehicle reference coordinate system. This is an optional feature to the ATB, and any or all of the three plots can be suppressed. These printed output pages consist of 60 lines of 120 characters each. The top line represents the Z axis and the first column or left side edge, running top to bottom, represents the plot X or Y axis. Rotating the pages 90 degrees in a counter-clockwise direction, the printed page becomes more familiarly orientated. In this position the negative Z is up and the positive X or Y is to the right from lower left corner. The X-Y axis has tick marks located every one length unit from input data. Table 1 gives the joint or segment center of gravity identifying symbols used in this plotting option.

Table 1
Identifying Symbols for Printer Plots App. B1

<u>Segment C.G. or Joint</u>	<u>Number</u>	<u>Symbol</u>
Body	S-1.	B
Upper Arm	S-2.	U
Lower Arm	S-3.	L
Vehicle	S-4.	*
Shoulder	J-1.	S
Elbow	S-2.	E

From these plots, the motion of the modeled segments can clearly be seen. It should be noted that the shoulder and body segment have very little motion forcing the two arm segments to respond to the torque placed on the upper arm. The response to the specified torque is extremely similar to the actual motion of a human raising a upper arm through a contraction of a series of shoulder muscles.

CONCLUSION

The Articulated Total Body Model (ATB) is a computer model of the human body used for predicting gross segmented body responses in various dynamic environments. In this paper a general description of the human body model and a case study of the human limb behavior are given. A brief case study of a modeled human limb using the ATB was also given. The purpose of this case study was to show the possibilities of adapting the ATB model for clinical applications. It should be emphasized that this model and the output are simplified cases of a full body model.

The ATB model is a useful tool. Although the flexibility of the input does initially cause the program to seem highly complex, once the system is mastered, the ATB has numerous possibilities for modeling most any rigid bodied structure in a dynamic environment. The ATB uses both Newtonian and Lagrange methods to formulate the equations of motions for these rigid bodies. The boundary conditions of these bodies are extremely well defined and a finite element analysis routine for evaluation of these rigid body structures could be implemented.

Before the ATB could be used in a hospital or clinical environment to predict human dynamic responses, very specific input would have to be prescribed. A program used in such a situation could also access generalized input data with only a limited amount of required patient data to be entered for individual computer runs. Whichever the method used, the next step is to understand what output would be needed in a rehabilitation environment and to specify what patient data would be required to obtain the desired output. For example, a mathematical model of rehabilitation prograess could be incorporated into the model and a clinical evaluation could be made. The modeling of such systems does seem inevitable due to the success and accuracy obtainable from computerized models as simply demonstrated by the ATB's ability to raise its own hand.

WORKS CITED

Armstrong Aerospace Medical Research Laboratory Articulated Total Body Model Enhancements. Volume 2. No. AAMRL-TR-88-043. Wright-Patterson AFB, OH. : 1988

Calspan Corporation Advanced Technology Center. Validation of the Crash Victim Simulator. U.S. Department of Transportation Report No. ZS-5881-V-1. Washington, D.C. :1981

Calspan Corporation, J&J Technologies Inc. AAMRL Articulated Total Body (ATB) Model. FORTRAN Program ATB-III. : 1983

APPENDIX

INPUT DATA-LEFT ARM-SHOULDER TORQUE-----	A1
DEFINED POINT MOTION	
POINT TOTAL POSITION-----	B1
POINT TOTAL VELOCITY-----	B2
POINT TOTAL ACCELERATION-----	B3
SHOULDER JOINT FORCES-----	C1
GRAPHICAL POSITIONING OF ARM SEGMENTS-----	D1

APPENDIX A1

MMJ-23-91: LEFT ARM-DYNAMIC JNT TEST

SLIP JOINT / 3000 IN-LBS TENSION ELE TORQUE

IN. LB.SEC.	0.0	0.0	386.088								CARD A3	
4 20	0.002	0.0005	0.001	.0000625							CARD A4	
1 0 1 0 2 1 1 1	0 0 0 0 0 0 0 0	0 0 0 0 0 0 0 0	0 0 0 0 0 0 0 0	0 0 0 0 0 0 0 0	0 0 0 0 0 0 0 0	0 0 0 0 0 0 0 0	0 0 0 0 0 0 0 0	0 0 0 0 0 0 0 0	0 0 0 0 0 0 0 0	0 0 0 0 0 0 0 0	0 0 0 0 0 0 0 0	CARD A5
3 2	95TH PERCENTILE MALE										CARD B1	
BODY B	210.0	5000.	5000.	5000.	6.000	10.50	36.00	0.000	0.000	26.00		CARD B2a
DRM U	5.542	.1743	.1743	.0259	2.122	2.122	7.497	1.000	1.000	1.000		CARD B2b
LARM L	5.901	.3331	.3331	.0214	1.871	1.871	10.269	1.000	1.000	1.000		CARD B2c
SLDR S	1 0	0.00	9.00	0.00	0.00	0.00	-5.42	1	0.00	0.00		CARD B3a
		0.00	0.00	0.00	0.00	0.00	0.00					
ESW E	2 S	0.00	0.00	5.42	0.00	0.00	-8.20	1	0.00	0.00		CARD B3b
		0.00	0.00	0.00	0.00	-67.19	0.00					
.00	.00	.00	.00	.00	.00	.00	.00	.00	.00	.00	.00	CARD B4A
.00	.00	.00	.00	.00	.00	.00	.00	.00	.00	.00	.00	CARD B4B
0.0	0.0	10	0.0	0.0				0.0	0.0			CARD B5A
0.0	0.0	30.	0.0	0.0				0.0	0.0			CARD B5B
.00	.00	.00	.00	.00	.00	.01	.01	.001	.001	.001	.001	CARD B6A
.00	.00	.00	.00	.00	.00	.01	.01	.001	.00	.00	.00	CARD B6B
.00	.00	.00	.00	.00	.00	.01	.01	.001	.00	.00	.00	CARD B6C
EQUILIBRIUM-0 INFL MOTION-STATIONARY TORSO												
0.0	0.0	0.0	0.0	0.00	0.00	0.00	9.00	-3	0.0	2.30		CARD C2A
2	1	3										CARD C2B
0.000	0.000	0.000	0.000	0.000	0.000	0.000	0.000	0.000	0.000	0.000		CARD C5A
0.000	0.000	0.000	0.000	0.000	0.000	0.000	0.000	0.000	0.000	0.000		CARD C5B
2.300	0.000	0.000	0.000	0.000	0.000	0.000	0.000	0.000	0.000	0.000		CARD C5C
4.600	0.000	0.000	0.000	0.000	0.000	0.000	0.000	0.000	0.000	0.000		CARD C5D
0	0	0	0	0	0	0	0	0	0	2		CARD D1
0	0	0	0	0	0	0	0	0	0	0	0	CARD D7
-2	1	0.0	0.0	-4.0	0.0	0.0	0.0	0.0	0.0	0.0		CARD D9a
3	2	0.0	0.0	8.0	90.0	0.0	0.0	0.0	0.0	0.0		CARD D9b
1 SHOULDER TORQUE												
0.0	0.0	-3000.0	0.0	0.0	0.0	0.0	0.0	0.0	0.0	0.0		CARD E2
2 +X FORCE ON HAND												
0.0	0.0	-80.0	0.0	0.0	0.0	0.0	0.0	0.0	0.0	0.0		CARD E2
0	0											CARD F3A
0	0											CARD F4A
20.0	20.0	60.0	0	0	0	0	0	1				CARD G1A
0.00000	0.00000	0.00000	0.0	0.0	0.0	0.0	0.0	0.0	0.0	0.0		CARD G2A
0.00	-2.00	0.00	0.00	0.00	0.00	0.00	0.00	3	2	1		CARD G3A
0.00	-2.00	0.00	0.00	0.00	0.00	0.00	0.00	3	2	1		CARD G3B
0.00	-2.00	0.00	0.00	0.00	0.00	0.00	0.00	3	2	1		CARD G3B
3 2 3	0.0	0.0	21.82									CARD H1A
1 2	0.0	9.0	10.84									CARD H1B
1 3	0.0	9.0	27.24									CARD H1c
3 2 3	0.0	0.0	21.82									CARD H2A
1 2	0.0	9.0	10.84									CARD H2B
1 3	0.0	9.0	27.24									CARD H2c
3 2 3	0.0	0.0	21.82									CARD H3A
1 2	0.0	9.0	10.84									CARD H3C
1 3	0.0	9.0	27.24									CARD H3C
0												CARD H4
0												CARD H5
0												CARD H6
1 1												CARD H7
0												CARD H8
1 1 1												CARD H9
												CARD H10

APPENDIX B1

POINT REL. LINEAR DISPLACEMENT (IN.)

TIME (MSEC)	POINT (0.00, 0.00, 21.82) ON SEGMENT NO. 3 - LARM				POINT (0.00, 9.00, 10.84) ON SEGMENT NO. 2 - UARM				POINT (0.00, 9.00, 27.24) ON SEGMENT NO. 3 - LARM			
	IN UARM REFERENCE				IN BODY REFERENCE				IN BODY REFERENCE			
	X	Y	Z	RES	X	Y	Z	RES	X	Y	Z	RES
0.000	0.000	0.000	35.440	35.440	0.000	18.000	16.260	24.257	0.000	18.000	46.280	49.657
0.500	0.000	-0.029	35.440	35.440	0.000	18.007	16.256	24.259	0.000	17.986	46.285	49.656
1.000	0.000	-0.115	35.440	35.440	0.000	18.027	16.245	24.267	0.000	17.943	46.299	49.654
1.500	0.000	-0.258	35.439	35.440	0.000	18.062	16.226	24.280	0.000	17.871	46.323	49.651
2.000	0.000	-0.459	35.437	35.440	0.000	18.110	16.199	24.297	0.000	17.770	46.356	49.645
3.000	0.000	-1.034	35.425	35.440	0.000	18.246	16.121	24.348	0.000	17.482	46.448	49.629
4.000	0.000	-1.837	35.392	35.440	0.000	18.436	16.011	24.418	0.000	17.077	46.571	49.603
5.000	0.000	-2.867	35.323	35.439	0.000	18.679	15.865	24.507	0.000	16.554	46.720	49.566
6.000	0.000	-4.122	35.197	35.438	0.000	18.971	15.683	24.614	0.000	15.908	46.889	49.514
7.000	0.000	-5.596	34.991	35.436	0.000	19.310	15.462	24.738	0.000	15.139	47.068	49.443
8.000	0.000	-7.278	34.676	35.432	0.000	19.693	15.200	24.877	0.000	14.241	47.247	49.347
9.000	0.000	-9.156	34.222	35.425	0.000	20.115	14.894	25.029	0.000	13.210	47.415	49.220
10.000	0.000	-11.208	33.593	35.414	0.000	20.570	14.544	25.192	0.000	12.040	47.555	49.056
11.000	0.000	-13.405	32.757	35.394	0.000	21.049	14.149	25.363	0.000	10.724	47.652	48.844
12.000	0.000	-15.708	31.679	35.359	0.000	21.545	13.712	25.538	0.000	9.257	47.683	48.573
13.000	0.000	-18.065	30.331	35.303	0.000	22.046	13.236	25.714	0.000	7.633	47.622	48.230
14.000	0.000	-20.414	28.692	35.213	0.000	22.539	12.731	25.886	0.000	5.848	47.440	47.799
15.000	0.000	-22.677	26.756	35.073	0.000	23.012	12.209	26.050	0.000	3.905	47.098	47.260
16.000	0.000	-24.768	24.537	34.864	0.000	23.451	11.685	26.201	0.000	1.818	46.557	46.593
17.000	0.000	-26.596	22.071	34.561	0.000	23.844	11.182	26.336	0.000	-0.388	45.775	45.776
18.000	0.000	-28.081	19.420	34.142	0.000	24.181	10.721	26.451	0.000	-2.668	44.713	44.793
19.000	0.000	-29.162	16.663	33.587	0.000	24.456	10.320	26.544	0.000	-4.962	43.347	43.630
20.000	0.000	-29.808	13.883	32.883	0.000	24.669	9.994	26.616	0.000	-7.202	41.666	42.284
21.000	0.000	-30.020	11.156	32.026	0.000	24.823	9.749	26.668	0.000	-9.319	39.679	40.759
22.000	0.000	-29.822	8.539	31.020	0.000	24.923	9.584	26.702	0.000	-11.250	37.410	39.064
23.000	0.000	-29.253	6.070	29.876	0.000	24.977	9.494	26.720	0.000	-12.945	34.891	37.215
24.000	0.000	-28.359	3.771	28.609	0.000	24.991	9.469	26.725	0.000	-14.367	32.164	35.227
25.000	0.000	-27.185	1.651	27.235	0.000	24.972	9.501	26.719	0.000	-15.492	29.269	33.116
26.000	0.000	-25.770	-0.290	25.772	0.000	24.925	9.580	26.703	0.000	-16.304	26.249	30.900
27.000	0.000	-24.153	-2.054	24.240	0.000	24.855	9.696	26.679	0.000	-16.795	23.143	28.595
28.000	0.000	-22.364	-3.647	22.660	0.000	24.765	9.842	26.649	0.000	-16.965	19.990	26.218
29.000	0.000	-20.431	-5.077	21.053	0.000	24.658	10.010	26.613	0.000	-16.817	16.825	23.789
30.000	0.000	-18.379	-6.350	19.445	0.000	24.539	10.195	26.572	0.000	-16.358	13.683	21.327
31.000	0.000	-16.227	-7.472	17.864	0.000	24.408	10.392	26.528	0.000	-15.601	10.593	18.858
32.000	0.000	-13.994	-8.449	16.346	0.000	24.268	10.596	26.480	0.000	-14.559	7.584	16.416
33.000	0.000	-11.696	-9.286	14.934	0.000	24.122	10.803	26.431	0.000	-13.248	4.680	14.050
34.000	0.000	-9.347	-9.986	13.678	0.000	23.972	11.010	26.380	0.000	-11.684	1.905	11.839
35.000	0.000	-6.961	-10.554	12.643	0.000	23.819	11.215	26.327	0.000	-9.888	-0.723	9.914
36.000	0.000	-4.550	-10.991	11.895	0.000	23.666	11.414	26.275	0.000	-7.878	-3.187	8.498
37.000	0.000	-2.123	-11.298	11.496	0.000	23.515	11.606	26.223	0.000	-5.674	-5.471	7.882
38.000	0.000	0.308	-11.477	11.481	0.000	23.368	11.788	26.173	0.000	-3.298	-7.563	8.250
39.000	0.000	2.734	-11.527	11.847	0.000	23.226	11.959	26.124	0.000	-0.768	-9.453	9.484
40.000	0.000	5.147	-11.446	12.550	0.000	23.092	12.116	26.078	0.000	1.895	-11.133	11.293

APPENDIX B2

POINT REL. VELOCITY (IN./SEC.)

TIME (MSEC)	POINT (0.00, 0.00, 21.82) ON SEGMENT NO. 3 - LARM IN UARM REFERENCE				POINT (0.00, 9.00, 10.84) ON SEGMENT NO. 2 - UARM IN BODY REFERENCE				POINT (0.00, 9.00, 27.24) ON SEGMENT NO. 3 - LARM IN BODY REFERENCE			
	X	Y	Z	RES	X	Y	Z	RES	X	Y	Z	RES
0.000	0.000	0.000	0.000	0.000	0.000	0.000	0.000	0.000	0.000	0.000	0.000	0.000
0.500	0.000	-54.926	-0.045	54.926	0.000	27.492	-15.232	31.429	0.000	-57.342	19.183	60.466
1.000	0.000	-109.852	-0.362	109.853	0.000	54.944	-30.533	62.858	0.000	-114.746	38.174	120.929
1.500	0.000	-164.775	-1.221	164.780	0.000	82.318	-45.973	94.286	0.000	-172.274	56.780	181.390
2.000	0.000	-219.690	-2.895	219.709	0.000	109.570	-61.619	125.708	0.000	-229.988	74.810	241.849
3.000	0.000	-329.442	-9.770	329.587	0.000	163.518	-93.787	188.505	0.000	-346.238	108.377	362.804
4.000	0.000	-438.923	-23.165	439.534	0.000	216.354	-127.516	251.136	0.000	-464.040	137.347	483.939
5.000	0.000	-547.770	-45.265	549.637	0.000	267.531	-163.204	313.382	0.000	-583.988	160.184	605.558
6.000	0.000	-655.384	-78.282	660.043	0.000	316.362	-201.125	374.882	0.000	-706.747	175.312	728.166
7.000	0.000	-760.846	-124.472	770.961	0.000	361.995	-241.373	435.087	0.000	-833.063	181.063	852.512
8.000	0.000	-862.817	-186.155	882.670	0.000	403.398	-283.790	493.220	0.000	-963.760	175.583	979.624
9.000	0.000	-959.396	-265.733	995.517	0.000	439.356	-327.875	548.211	0.000	-1099.702	156.711	1110.811
10.000	0.000	-1047.924	-365.663	1109.889	0.000	468.477	-372.668	598.625	0.000	-1241.683	121.821	1247.644
11.000	0.000	-1124.714	-488.365	1226.165	0.000	489.226	-416.615	642.580	0.000	-1390.204	67.637	1391.849
12.000	0.000	-1184.713	-635.959	1344.615	0.000	499.984	-457.426	677.659	0.000	-1545.057	-9.926	1545.088
13.000	0.000	-1221.160	-809.732	1465.230	0.000	499.180	-491.971	708.868	0.000	-1704.628	-115.801	1708.557
14.000	0.000	-1225.418	-1009.176	1587.478	0.000	485.505	-516.299	708.717	0.000	-1864.894	-255.487	1882.313
15.000	0.000	-1187.345	-1230.577	1710.003	0.000	458.261	-525.940	697.579	0.000	-2018.211	-434.168	2064.383
16.000	0.000	-1096.772	-1465.437	1830.414	0.000	417.822	-516.691	664.488	0.000	-2152.452	-654.968	2249.896
17.000	0.000	-946.407	-1699.679	1945.403	0.000	366.078	-485.929	608.391	0.000	-2251.522	-916.512	2430.915
18.000	0.000	-735.544	-1915.021	2051.421	0.000	306.540	-434.046	531.379	0.000	-2298.265	-1210.871	2597.735
19.000	0.000	-472.453	-2093.114	2145.772	0.000	243.804	-365.120	439.036	0.000	-2279.367	-1523.614	2741.699
20.000	0.000	-173.197	-2220.713	2227.457	0.000	182.433	-286.006	339.236	0.000	-2189.689	-1836.783	2858.061
21.000	0.000	142.893	-2292.741	2297.190	0.000	125.859	-204.250	239.914	0.000	-2033.203	-2133.305	2947.016
22.000	0.000	458.258	-2311.684	2356.668	0.000	75.905	-126.085	147.170	0.000	-1820.344	-2400.257	3012.455
23.000	0.000	760.000	-2284.635	2407.729	0.000	32.998	-55.505	64.573	0.000	-1564.114	-2629.755	3059.749
24.000	0.000	1040.250	-2220.246	2451.859	0.000	-3.303	5.605	6.506	0.000	-1277.131	-2818.122	3094.006
25.000	0.000	1295.118	-2126.760	2490.068	0.000	-33.811	56.866	66.159	0.000	-970.251	-2964.515	3119.252
26.000	0.000	1523.335	-2011.181	2522.974	0.000	-59.398	98.769	115.254	0.000	-652.290	-3069.778	3138.315
27.000	0.000	1725.149	-1879.119	2550.926	0.000	-80.836	132.212	154.966	0.000	-330.264	-3135.677	3153.021
28.000	0.000	1901.592	-1734.959	2574.128	0.000	-98.752	158.215	186.505	0.000	-9.757	-3164.466	3164.480
29.000	0.000	2054.043	-1582.102	2592.709	0.000	-113.627	177.774	210.986	0.000	304.758	-3158.659	3173.327
30.000	0.000	2183.987	-1423.191	2606.774	0.000	-125.819	191.793	229.379	0.000	609.671	-3120.907	3179.899
31.000	0.000	2292.894	-1260.297	2616.431	0.000	-135.583	201.056	242.500	0.000	902.062	-3053.932	3184.371
32.000	0.000	2382.165	-1095.055	2621.803	0.000	-143.099	206.236	251.019	0.000	1179.586	-2960.482	3186.829
33.000	0.000	2453.104	-928.764	2623.036	0.000	-148.489	207.891	255.475	0.000	1440.389	-2843.296	3187.327
34.000	0.000	2506.916	-762.453	2620.298	0.000	-151.825	206.488	256.297	0.000	1683.052	-2705.073	3185.919
35.000	0.000	2544.707	-596.936	2613.784	0.000	-153.146	202.403	253.813	0.000	1906.544	-2548.438	3182.679
36.000	0.000	2567.479	-432.841	2603.709	0.000	-152.461	195.939	248.267	0.000	2110.184	-2375.916	3177.712
37.000	0.000	2576.139	-270.634	2590.315	0.000	-149.751	187.328	239.827	0.000	2293.605	-2189.898	3171.163
38.000	0.000	2571.484	-110.635	2573.863	0.000	-144.972	176.738	228.590	0.000	2456.722	-1992.614	3163.225
39.000	0.000	2554.205	46.969	2554.637	0.000	-138.856	164.274	214.582	0.000	2599.694	-1786.101	3154.135
40.000	0.000	2524.868	202.125	2532.945	0.000	-128.984	149.977	197.760	0.000	2722.895	-1572.181	3144.187

DATE: MAR 23, 1991

PAGE 18

RUN DESCRIPTION: RUN_3-23-91: LEFT ARM-DYNAMIC JMT TEST

SLIP JOINT / 3000 IN-LAS TENSION ELA TORQUE

PAGE: 23.01

VEHICLE DECELERATION: EQUILIBRIUM-0 INFL MOTION-STATIONARY TORQUE

APPENDIX B3

POINT TOTAL ACCELERATION (G'S)

TIME (MSEC)	POINT (0.00, 0.00, 21.82) ON SEGMENT NO. 3 - LARM IN UARM REFERENCE				POINT (0.00, 9.00, 10.84) ON SEGMENT NO. 2 - UARM IN BODY REFERENCE				POINT (0.00, 9.00, 27.24) ON SEGMENT NO. 3 - LARM IN BODY REFERENCE			
	X	Y	Z	RES	X	Y	Z	RES	X	Y	Z	RES
0.000	0.035	-238.710	0.999	238.712	0.035	140.781	-77.844	160.870	0.035	-298.653	100.536	315.120
0.500	0.035	-238.710	0.498	238.711	0.035	140.681	-78.023	160.868	0.035	-298.812	100.039	315.114
1.000	0.035	-238.709	-1.006	238.712	0.035	140.377	-78.558	160.863	0.035	-299.292	98.551	315.100
1.500	0.035	-238.704	-3.513	238.730	0.035	139.859	-79.442	160.847	0.035	-300.095	96.071	315.098
2.000	0.035	-238.686	-7.024	238.789	0.035	139.113	-80.668	160.809	0.035	-301.229	92.603	315.141
3.000	0.035	-238.570	-17.063	239.179	0.035	136.838	-84.084	160.607	0.035	-304.524	82.709	315.556
4.000	0.035	-238.244	-31.154	240.272	0.035	133.307	-88.639	160.086	0.035	-309.284	68.870	316.859
5.000	0.035	-237.531	-49.382	242.609	0.035	128.193	-94.070	159.005	0.035	-315.663	51.033	319.762
6.000	0.035	-236.172	-71.914	246.878	0.035	121.101	-99.992	157.047	0.035	-323.860	29.037	325.160
7.000	0.035	-233.778	-99.044	253.893	0.035	111.582	-105.856	153.805	0.035	-334.090	2.535	334.100
8.000	0.035	-229.738	-131.213	264.569	0.035	99.165	-110.902	148.772	0.035	-346.523	-29.094	347.742
9.000	0.035	-223.082	-169.009	279.874	0.035	83.379	-114.104	141.322	0.035	-361.154	-66.841	367.288
10.000	0.035	-212.267	-213.078	300.765	0.035	63.801	-114.112	130.737	0.035	-377.576	-112.153	393.881
11.000	0.035	-194.913	-263.889	328.068	0.035	40.123	-109.207	116.345	0.035	-394.585	-166.950	428.451
12.000	0.035	-167.515	-321.229	362.283	0.035	12.271	-97.330	98.101	0.035	-409.577	-233.471	471.447
13.000	0.035	-125.319	-383.301	403.267	0.035	-19.399	-76.256	78.685	0.035	-417.739	-313.754	522.444
14.000	0.035	-62.728	-445.411	449.806	0.035	-53.815	-44.100	69.576	0.035	-411.271	-408.468	579.647
15.000	0.035	25.159	-498.635	499.269	0.035	-88.835	-0.307	88.836	0.035	-379.353	-514.943	639.590
16.000	0.035	139.447	-529.715	547.763	0.035	-121.055	52.924	132.119	0.035	-310.186	-624.852	697.606
17.000	0.035	273.607	-524.091	591.212	0.035	-146.207	109.540	182.689	0.035	-196.134	-723.352	749.470
18.000	0.035	412.011	-472.558	626.948	0.035	-160.498	160.320	226.853	0.035	-40.354	-792.250	793.277
19.000	0.035	534.238	-377.783	654.316	0.035	-162.439	196.216	254.730	0.035	140.573	-817.372	829.372
20.000	0.035	623.776	-254.380	673.651	0.035	-153.721	212.493	262.266	0.035	322.429	-795.217	858.097
21.000	0.035	674.331	-121.637	685.214	0.035	-138.224	210.311	251.668	0.035	483.899	-733.248	878.528
22.000	0.035	689.319	4.726	689.336	0.035	-120.057	194.800	228.825	0.035	613.373	-644.381	889.637
23.000	0.035	677.041	116.030	686.912	0.035	-102.179	171.923	199.995	0.035	708.719	-541.072	891.651
24.000	0.035	646.222	209.576	679.356	0.035	-86.115	146.438	169.882	0.035	773.356	-432.467	886.063
25.000	0.035	603.856	286.089	668.198	0.035	-72.331	121.352	141.273	0.035	812.555	-324.267	874.868
26.000	0.035	554.849	347.646	654.763	0.035	-60.711	98.226	115.473	0.035	831.404	-219.689	859.939
27.000	0.035	502.412	396.547	640.052	0.035	-50.906	77.669	92.865	0.035	834.097	-120.454	842.750
28.000	0.035	448.587	434.853	624.762	0.035	-42.525	59.763	73.348	0.035	823.897	-27.468	824.355
29.000	0.035	394.672	464.265	609.350	0.035	-35.213	44.326	56.611	0.035	803.320	58.786	805.468
30.000	0.035	341.504	486.153	594.113	0.035	-28.681	31.075	42.288	0.035	774.351	138.054	786.561
31.000	0.035	289.637	501.623	579.237	0.035	-22.702	19.703	30.060	0.035	738.607	210.216	767.939
32.000	0.035	239.447	511.579	564.844	0.035	-17.103	9.914	19.769	0.035	697.456	275.254	749.806
33.000	0.035	191.194	516.782	551.016	0.035	-11.749	1.444	11.837	0.035	652.090	333.231	732.301
34.000	0.035	145.056	517.884	537.815	0.035	-6.537	-5.944	8.835	0.035	603.570	384.296	715.528
35.000	0.035	101.150	515.466	525.297	0.035	-1.382	-12.459	12.535	0.035	552.849	428.673	699.573
36.000	0.035	59.543	510.051	513.514	0.035	3.787	-18.287	18.675	0.035	500.785	466.670	684.519
37.000	0.035	20.254	502.122	502.531	0.035	9.036	-23.600	25.271	0.035	448.150	498.668	670.453
38.000	0.035	-16.740	492.135	492.420	0.035	14.429	-28.562	32.000	0.035	395.624	525.125	657.476
39.000	0.035	-51.507	480.522	483.274	0.035	20.036	-33.334	38.892	0.035	343.802	546.571	645.709
40.000	0.035	-84.165	467.698	475.210	0.035	25.934	-38.086	46.078	0.035	293.182	563.607	635.302

DATE: MAR 23, 1991

PAGE

RUN DESCRIPTION: RUN_3-23-91: LEFT ARM-DYNAMIC JMT TEST

SLIP JOINT / 3000 IN-LAB TENSION ELE TORQUE

PAGE: 22.01

VEHICLE DECELERATION: EQUILIBRIUM-0 INFL MOTION-STATIONARY TORQUE

CRASH VICTIM: 95TH PERCENTILE MALE

APPENDIX C1

SLDR JOINT FORCES & TORQUES ON UARM IN BODY REFERENCE

TIME (MSEC)	JOINT FORCE (LB. 10**2)			JOINT TORQUE (IN.- LB. 10**2)		
	X	Y	Z	X	Y	Z
0.000	0.000	3.493	0.000	0.000E+00	0.000E+00	0.000E+00
0.500	0.000	3.493	-0.004	0.000E+00	0.000E+00	0.000E+00
1.000	0.000	3.493	-0.015	0.000E+00	0.000E+00	0.000E+00
1.500	0.000	3.493	-0.033	0.000E+00	0.000E+00	0.000E+00
2.000	0.000	3.493	-0.058	0.000E+00	0.000E+00	0.000E+00
3.000	0.000	3.490	-0.131	0.000E+00	0.000E+00	0.000E+00
4.000	0.000	3.483	-0.233	0.000E+00	0.000E+00	0.000E+00
5.000	0.000	3.468	-0.362	0.000E+00	0.000E+00	0.000E+00
6.000	0.000	3.441	-0.518	0.000E+00	0.000E+00	0.000E+00
7.000	0.000	3.397	-0.698	0.000E+00	0.000E+00	0.000E+00
8.000	0.000	3.329	-0.896	0.000E+00	0.000E+00	0.000E+00
9.000	0.000	3.230	-1.106	0.000E+00	0.000E+00	0.000E+00
10.000	0.000	3.092	-1.317	0.000E+00	0.000E+00	0.000E+00
11.000	0.000	2.906	-1.513	0.000E+00	0.000E+00	0.000E+00
12.000	0.000	2.662	-1.675	0.000E+00	0.000E+00	0.000E+00
13.000	0.000	2.353	-1.777	0.000E+00	0.000E+00	0.000E+00
14.000	0.000	1.974	-1.791	0.000E+00	0.000E+00	0.000E+00
15.000	0.000	1.530	-1.692	0.000E+00	0.000E+00	0.000E+00
16.000	0.000	1.043	-1.468	0.000E+00	0.000E+00	0.000E+00
17.000	0.000	0.556	-1.137	0.000E+00	0.000E+00	0.000E+00
18.000	0.000	0.129	-0.750	0.000E+00	0.000E+00	0.000E+00
19.000	0.000	-0.181	-0.383	0.000E+00	0.000E+00	0.000E+00
20.000	0.000	-0.346	-0.100	0.000E+00	0.000E+00	0.000E+00
21.000	0.000	-0.378	0.068	0.000E+00	0.000E+00	0.000E+00
22.000	0.000	-0.313	0.126	0.000E+00	0.000E+00	0.000E+00
23.000	0.000	-0.192	0.102	0.000E+00	0.000E+00	0.000E+00
24.000	0.000	-0.048	0.028	0.000E+00	0.000E+00	0.000E+00
25.000	0.000	0.100	-0.069	0.000E+00	0.000E+00	0.000E+00
26.000	0.000	0.242	-0.173	0.000E+00	0.000E+00	0.000E+00
27.000	0.000	0.373	-0.273	0.000E+00	0.000E+00	0.000E+00
28.000	0.000	0.495	-0.362	0.000E+00	0.000E+00	0.000E+00
29.000	0.000	0.606	-0.440	0.000E+00	0.000E+00	0.000E+00
30.000	0.000	0.710	-0.504	0.000E+00	0.000E+00	0.000E+00
31.000	0.000	0.808	-0.557	0.000E+00	0.000E+00	0.000E+00
32.000	0.000	0.900	-0.599	0.000E+00	0.000E+00	0.000E+00
33.000	0.000	0.990	-0.630	0.000E+00	0.000E+00	0.000E+00
34.000	0.000	1.077	-0.654	0.000E+00	0.000E+00	0.000E+00
35.000	0.000	1.163	-0.670	0.000E+00	0.000E+00	0.000E+00
36.000	0.000	1.249	-0.681	0.000E+00	0.000E+00	0.000E+00
37.000	0.000	1.336	-0.687	0.000E+00	0.000E+00	0.000E+00
38.000	0.000	1.425	-0.689	0.000E+00	0.000E+00	0.000E+00
39.000	0.000	1.518	-0.690	0.000E+00	0.000E+00	0.000E+00
40.000	0.000	1.615	-0.690	0.000E+00	0.000E+00	0.000E+00

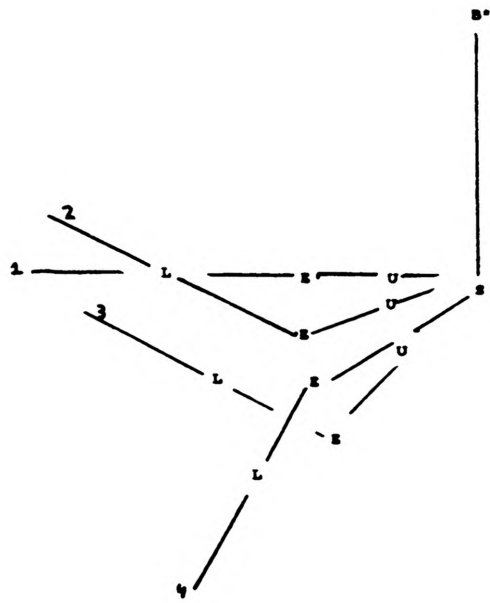
APPENDIX D1

//mem5/users/r094037/biotest_10.2/prhmb

page1

1 T= 0.000 Y0= 0.00000 Z0= 0.00000 Y-Z PLANE

03/28/91 12:06 W



NONLINEAR DYNAMICS AND THE LORENZ WATER WHEEL

Rich Margis

Undoubtedly one of the most exciting frontiers in physics today is the study of nonlinear systems, more popularly called chaos. Chaos is the key to many time-dependent processes in as varied fields as meteorology (such as weather modeling), mechanics (the three-body problem in gravitational fields), and economics (prediction of trends in the stock market).

An easy way to get a grip on the basic ideas of chaos is with the so-called Butterfly Effect. The Butterfly Effect is the idea that a disturbance in an air mass in Beijing created by the wings of a butterfly is enough to make the weather in New York City due to that air mass unforecastable. The basic idea here is nonlinearity. A linear function, for those who have not studied differential equations or linear algebra, is any function $y=f(x)$ such that $f(a+b)=f(a)+f(b)$ and $f(c*a)=c*f(a)$, where a and b are complex numbers or vectors. Simple linear functions include $y=x$ and $y=6$: simple nonlinear functions include $y=x^2$ and $y=\sin(x)$.

Nonlinearity is evident in the following sequence, investigated by the researcher early in the course of the experiment:

$$x_0 = x \quad x_{n+1} = q*x_n*(1-x_n) \quad \text{eqn. 1}$$

where x is the first term of the sequence, restricted to be between zero and one, and q is the driving coefficient, restricted to be between zero and four. Different values of the driving coefficient produce the following behaviors:

<u>value of q</u>	<u>behavior of sequence</u>
less than one	approaches zero as n goes to infinity
between one and three	approaches some constant as n goes to infinity
about 3 to 3.6	oscillates between increasingly many pairs as q increases
about 3.6 to 3.85	chaotic behavior
about 3.85 to 3.90	oscillates between increasingly many triples as q increases
above 3.90	chaotic behavior table 1

The sequence can be calculated easily with a hand calculator.

Naturally after investigating this intriguing sequence the researcher wanted to find out more about chaos. While reading the popular fiction book Chaos: Making a New Science by James Gleick the researcher discovered an interesting apparatus known as the Lorenz_ water wheel, which exhibits chaotic behavior. The apparatus is named for the meteorologist Edward Lorenz who invented it as a thought experiment in the early 1960's to explain the solution of a set of seven nonlinear heat convection differential equations derived by the physicist Barry Saltzman that reduce to three in certain ideal conditions. The form of these equations is:

$$dx/dt = -ax + ay \quad \text{eqn. 2}$$

$$dy/dt = -xz + bx - y \quad \text{eqn. 3}$$

$$dz/dt = xy - cz \quad \text{eqn. 4}$$

The traditionally chosen values for the constants, $a=10$, $b=28$, and $c=8/3$, give the famous strange attractor plot when the solution of the differential equations is graphed in phase space.

The Lorenz water wheel itself is an ordinary-looking apparatus that consists basically of a water source and drain and a wheel mounted on a base. Cups with small holes punched in their bottoms are

mounted to the outer radius of the wheel. This device works as follows. Water flows into the very top cup; the flow must be vertical such that it follows the diameter of the wheel down (unless the flow is intercepted by a cup) so that the flow itself exerts no torque on the wheel. Ideally, then, the wheel rotation will have to be started by hand unless the top cup is slightly off-center, but normally the flow exerts a small torque that overcomes the friction in the wheel and begins turning the wheel. Then the water in the cup slowly drains until the cup returns to the position at the top of the wheel. When the wheel is spinning slowly, the cups have a lot of time to fill at the top, as well as a lot of time to drain. This pulls the center of gravity of the wheel out close to the radius in the direction of the spin and puts a large torque on the wheel, increasing the angular acceleration. The wheel begins to spin faster and the cups get less and less time to fill and drain. Now the center of mass is pulled back toward center and over to the other side of the wheel, making the torque negative. The angular velocity begins to drop and the process repeats. After the initial awkwardness, the angular velocity seems to smooth out. But soon the fast-slow rhythm reappears, with barely noticeable but increasing amplitude. A little later the limps are highly pronounced, and the wheel almost stops once each rotation. Then it occurs that, on one rotation, the center of gravity of the wheel is far enough from the center that enough torque is exerted that the wheel stops and begins rotating backward! This is the beginning of the chaotic stage of the motion of the wheel and an example of the strange attractor in action. After this occurs, quantitatively predicting any long-term behavior of the wheel with any accuracy is

impossible, because, to do so, it is necessary to know the EXACT state of the system at some time. Even the tiniest errors grow into hundred-percent uncertainties within fifty or so iterations; this is an example of the butterfly effect in action.

With all of this in mind, the researcher and the researcher's supervisor, Dr. Ralph Alexander of the Physics Department, planned a set of goals for the experiment; which included the following. First, a Lorenz water wheel would be constructed according to the basic description above in order to collect qualitative data. Second, library research would be performed to check if any suggestions concerning the experiment had been published and if any crash courses on the solution of differential equations, particularly nonlinear ones, existed (although the researcher was familiar only with mathematics up to the second semester of calculus when the experiment was begun, this was not considered a serious difficulty at the time!). Third, computer work would be done in learning how to operate MathCAD, Quattro, and similar programs so that iterated solutions could be computed on them. Finally, measurement devices would be attached to the wheel so that quantitative data could be taken, and, at least for a few iterations, fit with a theoretical curve.

The experiment was begun in the spring of 1990 in Dr. Alexander's Physics 27 (First Semester Honors Laboratory) class with completion intended by the end of the semester; the wheel, constructed of tape cases and small medicine cups (the sort found with Nyquil medicine), was finished by the Physics Shop, Dr. Alexander, and the researcher by mid-semester. Immediately it was found that the wheel was unbalanced; holes half-drilled in one side of the wheel partially corrected the

problem. Then the job of playing with the wheel in order to find the parameters (number of cups, cup hole size, etc.) that make the wheel work correctly and easily was begun. In this task, there were no guides except somewhat vague ideas about the qualitative behavior of the wheel: it should rotate for awhile, uniformly after initial noise dies down and then with increasing limp, then the wheel should stop and begin rotating the opposite direction. To aid in further experimentation, more precise ideas of Lorenz water wheel behavior were needed.

To gain these ideas, the researcher proposed to try to model the water wheel's behavior by making successive ideal approximations of the wheel on the spreadsheet Lotus 1-2-3. The first step was to pick a set of variables that completely described the system. Variables to pick from included time, angle, angular velocity, angular acceleration, center of gravity, torque, flowrate of the water source, mass, and angular momentum. Angular momentum was immediately ruled out so that the problem would be defined in terms of easily visualized quantities, and time was ruled out soon after because it can be defined as the integral with respect to x of the reciprocal of the velocity and because time is implicit in many differential equations in mechanics and electrodynamics. Of the others, angle, angular velocity, and mass seemed the easiest to measure. Since center of gravity can be calculated from mass, position, and time, torque can be calculated from center of mass and mass, angular acceleration can be calculated from torque and mass, and mass can be calculated from flowrate, angle and time, all of the possible variables can be expressed in terms of the angle, the angular velocity, and the

flowrate of the water source. If the flowrate is kept constant, the problem has only two degrees of freedom.

The researcher proceeded to compute the iterated solution of the center of mass and torque due to the water on an ideal wheel spinning at a constant velocity. The graphs of the center of mass and the torque on such a wheel are included; see pp. 10-11.

To supplement this computer activity, researching was done in the Curtis Laws Wilson library. The article by Lorenz concerning convection, "Deterministic Nonperiodic Flow", that the researcher learned of in Gleick's Chaos, was found in the March 1963 issue of the Journal of Atmospheric Sciences there. The article contained a numerical solution of the system of three differential equations presented earlier, as well as a graph of one of the variables versus time. This graph gave the researcher a much better feel for the expected behavior of the water wheel and explained the nature of phase space as well.

A final addition to the researcher's chaos understanding came near the end of the semester in the form of Chaos Demonstrations, a IBM Physics Academic Software program by Julien C. Sprott and George Rowlands. This easy-to-use program contains eighteen demonstrations on chaos, including such examples as the three-body problem, the magnetic quadrupole, the driven pendulum, as well as the strange attractor.

With this done at the end of the 1990 spring semester, the researcher was ready to attack the problem of getting data and decided to continue the unfinished experiment as a summer project for the OURE program.

The summer portion of the experiment began optimistically with the nearly immediate confirmation that the behavior of the wheel is governed by a system of differential equations similar to equations 2, 3, and 4 above through the observation that a graph of the wheel's velocity over the fifteen or so minutes of each run would roughly agree with the graph mentioned above from Lorenz's article, as well as with the qualitative wheel predictions above.

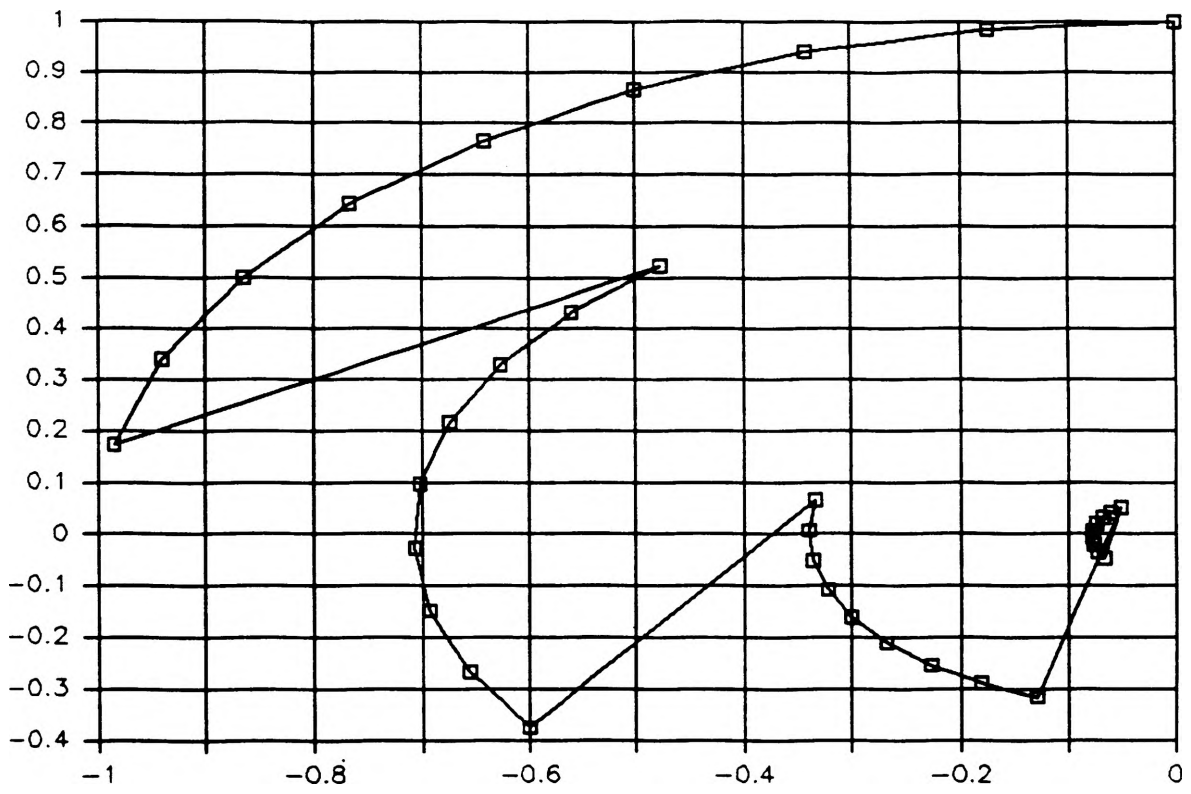
Next it was necessary to refine the apparatus in order to make sure that the form of the data, a strange attractor in phase space, would not be thrown off by the conditions (of course in any case there would be enough uncertainty to throw the data points off from any expected values). Noted among the problems with the apparatus were: the wheel was still unbalanced after the holes were drilled in it to balance it; during operation the wheel got wet enough to affect its center of gravity; during operation when no cup was at the top of its cycle on the wheel, water got into lower cups; water did not flow out of the cups at a uniform rate, but at a rate proportional to some function of the amount of water in the cup; when the flowrate was high, as much water splashed out of the cups as remained inside, while when the flowrate was low, friction between the wheel and the base as well as between the cups and their mounts on the wheel prevented and chaotic motion from occurring; and the flowrate of the water source was unknown, while the direction of the flow was not always strictly vertical. The fact that the wheel remained unbalanced threw any ideal calculations off considerably; from time to time the researcher added small weights to the wheel to temporarily balance it, but this never did much good. A more practical idea, however, was discovered to keep

the wheel from getting wet, namely, wax the wheel with car wax. Similar to the case of the unbalanced wheel, no good method to prevent water from falling in the lower cups on the wheel presented itself. The nonuniform flowrate out of the cups was more easily accounted for; one of the physicists Bernoulli investigated flow and his equation for flow can be found in the Physics 21 text by Pasachoff. The solution to the splash problem was to try to find an intermediate flowrate that avoided splashing as well as the nonchaotic behavior. Finally, the unknown flowrate could be held constant, ignored during datataking, and then solved for during analysis.

About midsummer came a period when Dr. Alexander was out of town and the researcher was occupied with other matters. When this ended, it was already quite late in the summer. The researcher began working on datataking apparatus, including some IBM data software, with the help of Dr. Alexander. Then, as the summer semester ended, it was decided that the project should not be prolonged into the succeeding semester for various reasons, so the project was terminated.

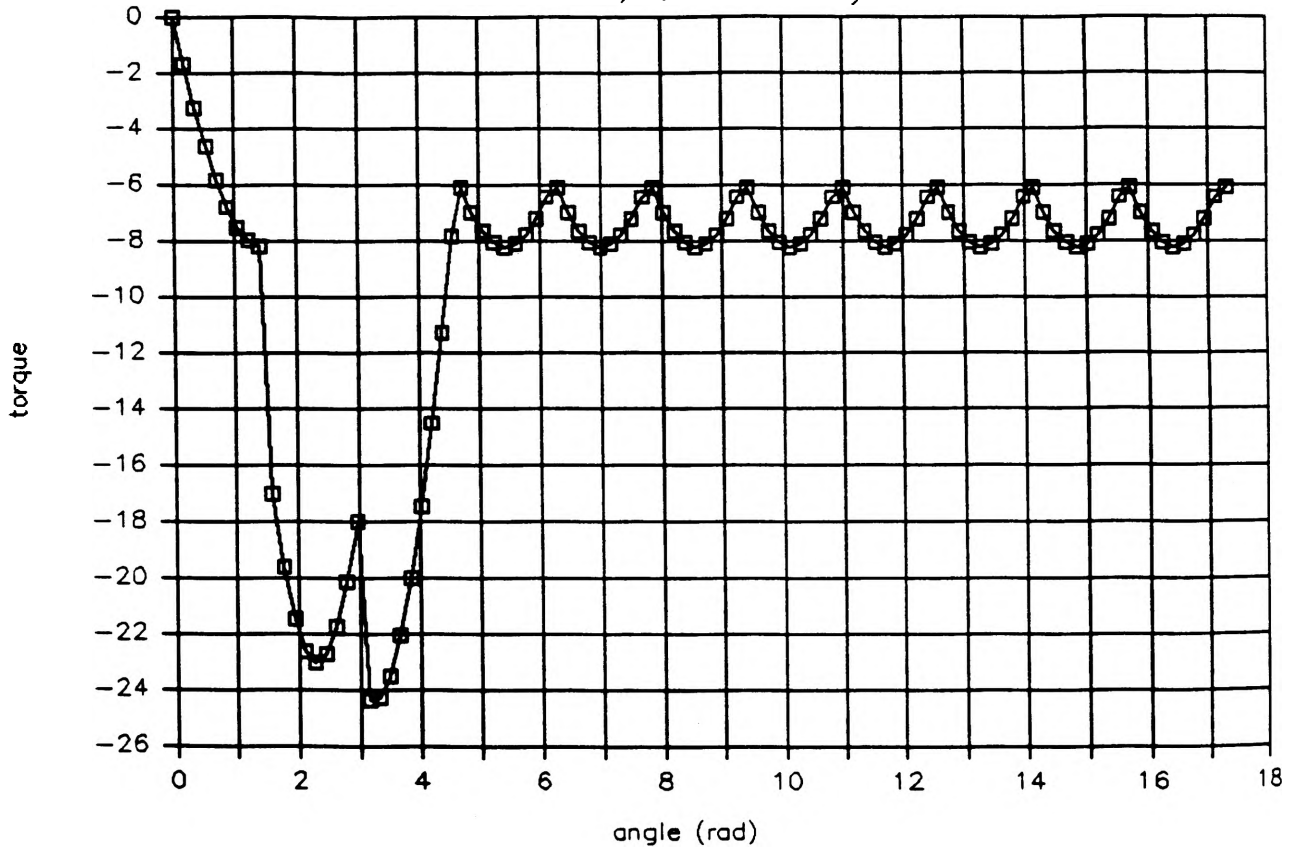
Although the project was never completed, the researcher still considers the experience a valuable one, for in doing the project the researcher gained experience in working with the nonidealities of the real world, as well as doing theory which tries to explain the phenomenon known as chaos. During the experiment, also, the researcher's appreciation of basic chaos ideas, such as the butterfly effect and nonlinearity, was enhanced. And finally, and perhaps most importantly, the researcher became aware of the beauty to be found in chaos.

Ideal Lorenz Wheel



Torque

4 buckets, constant velocity



CONTROL AND DATA REDUCTION SOFTWARE FOR UMR NEUTRON SPECTROMETER

Matthew K. McLaughlin

Introduction

A double-scatter time-of flight neutron spectrometer has been obtained by the Nuclear Engineering department of the University of Missouri-Rolla (UMR). As this device was an experimental prototype which was never brought to full operation, the chance to work with two of the original builders of the spectrometer at EG&G Idaho was an excellent opportunity. Part of the work being done with the detector is the development of a PC-based software package for machine control, data acquisition, and data reduction. It is this part of the project which has been supported by UMR's Opportunities for Undergraduate Research Experience (OURE) program.

History

The device originated at the research facility of Phillips Petroleum in Bartlesville Oklahoma. It was developed by A. M. Preszler, W. A. Millard, and S. E. Walker of Phillips working with T. J. Dolan of UMR, in 1984 and '85. The spectrometer was designed to provide information on the energy and angular characteristics of the neutron flux produced by an experimental fusion device. The project was abandoned when the company was forced to drop its fusion research program due to the combination of a loss of federal funding and the financial strain of hostile takeover attempts. In 1988, the spectrometer was donated to UMR by Phillips Petroleum. The next year Alan Preszler, now working at EG&G Idaho, and Dr. Dolan, on leave at the Idaho National Engineering Laboratory (INEL), proposed a joint project to develop the capabilities of the device. This project is currently underway at EG&G Idaho.

Spectrometer Description

The spectrometer is composed of a two-cell detector, a CAMAC crate containing the necessary electronics modules, and a microcomputer for control and data manipulation. The detector portion is made up of two scintillator cells separated by an adjustable distance. Each cell contains two sheets of NE102 plastic scintillator connected to photomultiplier tubes (PMT's) which collect the light impulses from the scintillators and convert them to electrical signals. These signals are collected, digitized, and processed through the CAMAC electronics for meaningful event data. Many of the CAMAC modules used were straight off the shelf, although some were modified and custom modules were developed for some purposes.¹ The resulting data is transmitted through a GPIB (IEEE 488) link to the microcomputer for evaluation.

The operation of the spectrometer is based on classic elastic scattering kinematics.² In an actual double scatter event, an incident neutron of energy E_0 collides with a proton (hydrogen nucleus) in the first cell, transferring a portion of its energy to the proton (E_{p1}). This energy is immediately deposited by the proton, and a light impulse proportional to E_{p1} is picked up by the PMT's. This also initiates a timing sequence. The neutron, with remaining energy E_{tof} , then travels to the second cell where it collides with another proton. The PMT pulse resulting from this reaction gives the time of flight from the first cell. Since the kinetic energy E_{tof} of the neutron is proportional to the square of the velocity, it is inversely proportional to the time of flight between the two cells:

$$E_{tof} = 0.5 * sep^2 / TOF^2, \quad (1)$$

where sep is the distance of separation between the two collisions. This gives us the energy of the incident neutron as the sum of the energy deposited in the first cell and the measured kinetic energy between the two cells:

$$E_0 = E_{p1} + E_{tof} \quad (2)$$

Since the fraction of energy deposited in the first cell is dependent on the incident angle of the neutron, the device can also be used to measure this angle. It is found by taking the arctangent of the square root of the ratio of the energy deposited in the first cell to the kinetic energy between the two cells:

$$\theta = \sqrt{E_{p1}/E_{tof}} \quad (3)$$

An illustration of the process is shown in Figure 1.

Certain tradeoffs are inherent in the design of the spectrometer. In order to maximize the efficiency of the detector, the first cell must occupy the largest possible solid angle with respect to the neutron source. Similarly, the second cell should occupy a large solid angle relative to the first cell. Therefore, efficiency demands that the cells be fairly large and relatively close together. Optimizing for efficiency, however, is detrimental to the resolution of the device for both angle and energy measurements. This is due to the larger possible deviation of the path of the scattered neutron from a line parallel to the axis of the detector. The design must balance these two considerations for the circumstances expected in use.

Since the spectrometer was originally developed for use with a fusion device, it was designed to cope with a very high event rate generated for a very short period of time. This required a relatively high efficiency, and the detector was built using one foot square sheets of scintillator in both the front and rear cells. The resulting resolutions for this configuration with a 100 cm separation were 34 keV and 10 degrees for 2.45 MeV neutrons at 45 degrees.²

Project Description

Equipment Configuration

The applications for which the Nuclear Engineering department is interested in using the spectrometer, as well as those in which EG&G is interested, are quite different from the original design purpose. Neutron energy spectra can be used in analysis of fission reactor behavior, determination of the content of nuclear materials, and experiments in radiation shielding and radiography. In each of these cases, the neutron source field is much more long term than in the case of a fusion device. Therefore, efficiency is not as limiting a factor and the configuration of the device can be changed to improve its resolution. This has allowed the design of a new detector with scintillator cells measuring about two inches on a side. While the reduction in efficiency is about 97%, there is about a thirty-fold decrease in the uncertainty of the path length. It is hoped that angular resolutions of one degree and energy resolutions of better than five keV will be obtained.

In addition to the change in the detector configuration, changes are being made in both the electronics packaging and the microcomputer control system. The CAMAC crate containing the instrument's electronics, which was originally mounted in the same structure as the detector, is being installed in a shock-resistant travel case. This affords advantages of portability and protection of the crate modules. The control and data handling of the system is being switched from the Hewlett-Packard Series 200 Model 9816 microcomputer to a Compaq Portable III, which is an IBM compatible 80286 based machine. The Compaq gives the

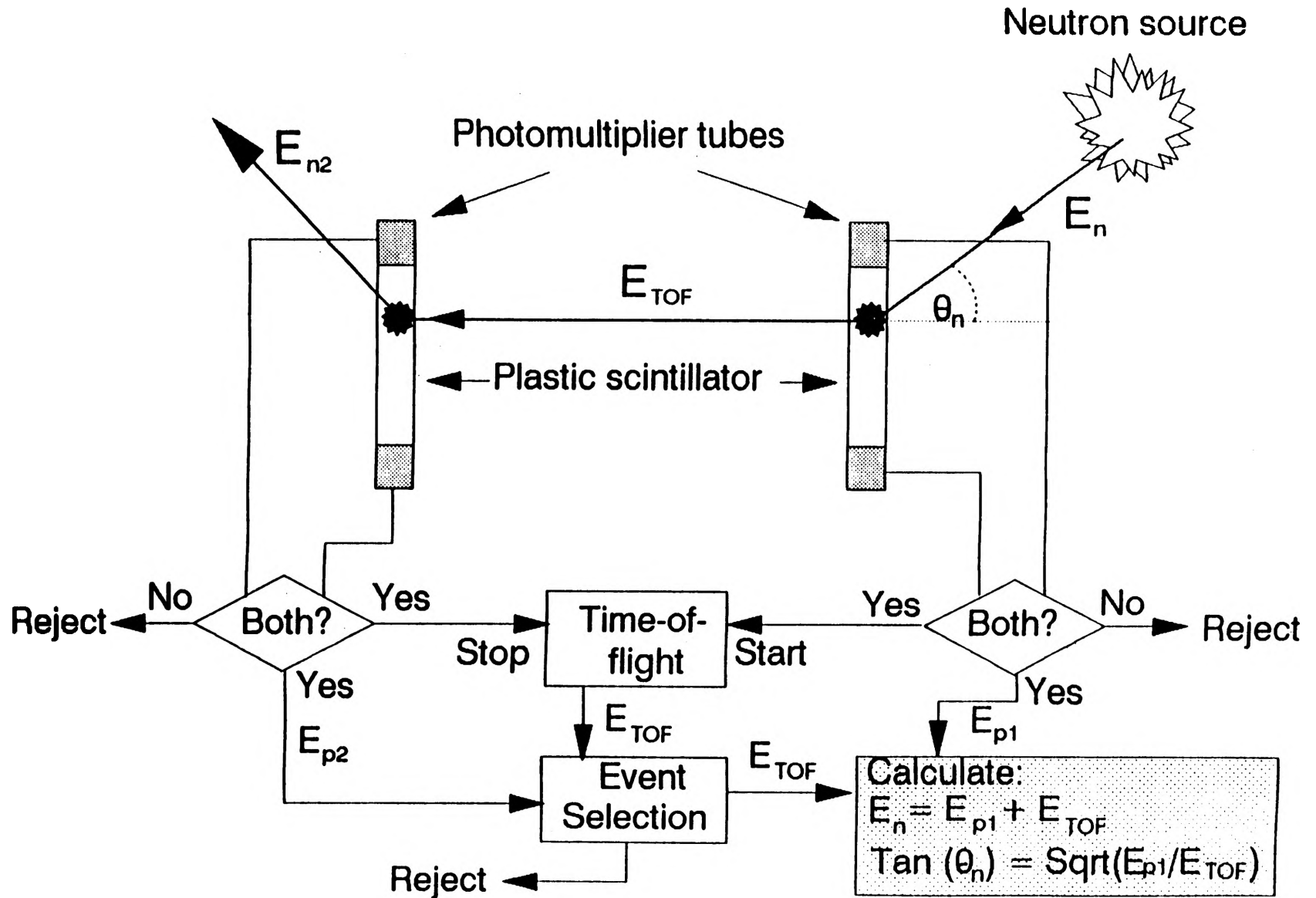


Figure 1: Spectrometer Operation

advantage of having the CPU, monitor, and hard disk all in a single easily portable unit, where the older HP machine consisted of four separate components which are not designed to be moved around.

The flexibility gained by the reconfiguration of the instrument will be substantial. In addition to the increased portability, the department will have available both the old and the new detector configurations, giving the option of using whichever is more suitable for a given project. Figures 2 and 3 illustrate the old and new configurations of the spectrometer.

Software Upgrade

In replacing the control computer, it has become necessary to rewrite the software which controls the instrument. This is being done in the C language, the old code having been written in BASIC. Writing the code in C will result in a faster and more efficient program. Additionally, it will make the program more easily portable to other machines. This is particularly important with the data reduction end of the program, where the need to run numerous variations on the analysis of the same data might make it worthwhile to work on a larger and faster machine. The version of C being used is Microsoft C 6.0. Care is being taken, however, to keep the program compatible with the ANSI C standard to ensure portability of the code.

Project Status

The building of the new detector is in progress at EG&G. It is expected to be completed in the summer of 1991. Work was started on the software in the summer of 1990 and the first version should be completed for the summer 1991 trial runs of the instrument.

Software

There are two major goals to meet in writing the software. The first is to improve on the efficiency of the code and reduce the time necessary for calculations and general operation. This includes changing the way in which the data is stored, changing the user interface, and including the ability to work with one set of data while monitoring the clock for collection of another data set. The second, and at least as important, is to write a program which can be readily maintained. Since this device is a prototype and of an experimental nature, it is very probable that the program will continue to evolve for some time. From working with the original program, it is very obvious how important this is. Additionally, the fact that the code is to be used in Idaho but written here in Missouri makes it imperative that it be as easy to use as possible.

There are effectively three main parts of the program. They are data handling, the user interface, and the CAMAC interface. Figure 4 is a basic flowchart of the program. The data which the program handles is actually rather straightforward. For each data point stored in memory records are kept for seven associated values. These are:

- the time of the event,
- the scintillator sheets involved,
- the energy deposited in the first cell,
- the time of flight between cells,
- the energy deposited in the second cell,
- the scaler rate of the first cell,
- and the scaler rate of the second cell.

Current Arrangement

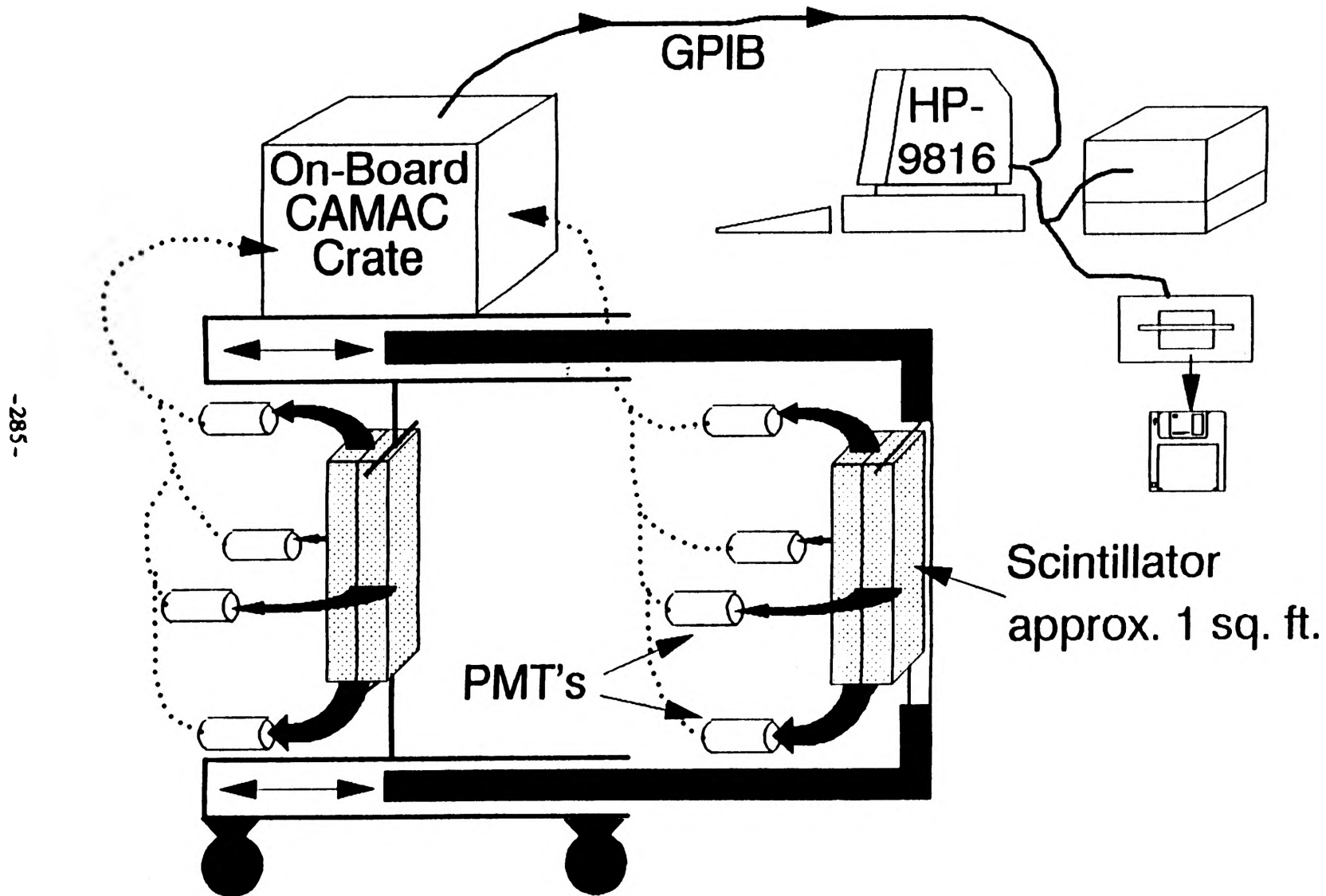
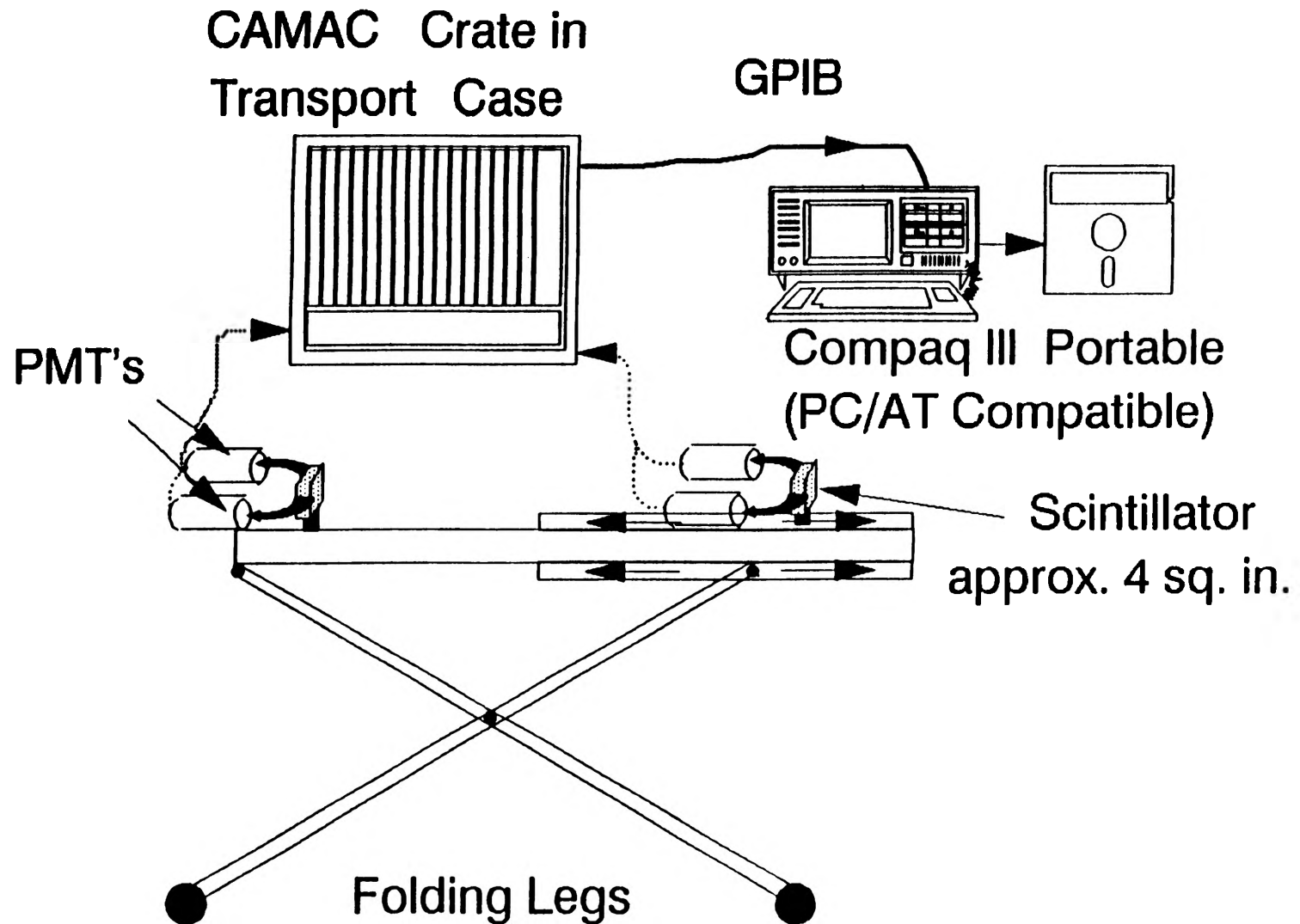


Figure 2: Original Configuration

Proposed Arrangement



-286-

Figure 3: Updated Configuration

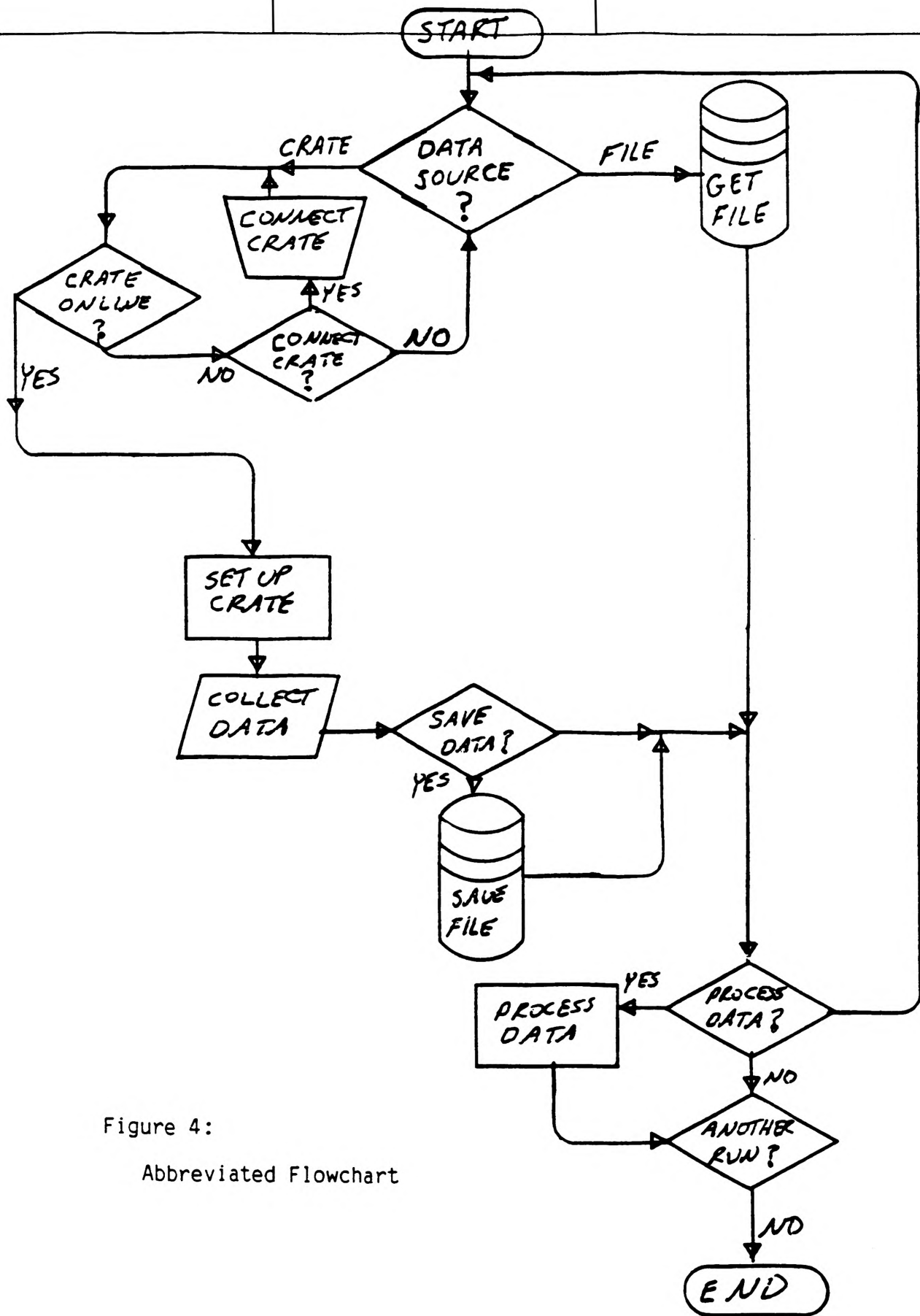


Figure 4:
Abbreviated Flowchart

These values are stored for each of up to 8184 events, and saved to a file if requested. Using this information, a wide variety of plots are produced, including polynomial fits and statistical distributions.

As it turned out, the data handling area showed the most room for improvement. In order to improve the efficiency, the most obvious areas to look for were those in which a time consuming operation was being performed repetitively. It became evident that one area in which time could be saved was the event selection routine. Since events are categorized by what sheets they deposit energy in, this information is recorded for each event. What the old program did was to determine which events were required, check each event (a maximum of 8184) against that requirement, and determine whether or not to include it in the data set to be worked with. If the requirements changed, even if just adding another set to the existing group, the entire process was repeated. This was necessary because the data points are kept in memory in the same order that they were read in from the digitizer.

To improve on the time spent sorting, the data is completely sorted when it is first read in and saved in that form. Since the sheet id's are simply yes or no for each of 4 sheets, there are sixteen possible permutations. This makes it possible to perform a simple sort on the entire set, leaving the events grouped according to which scintillator sheets fired. Coupled with this data array is a sixteen-element index array which tells how many events fall under each permutation. With all of the events in a contiguous array, these values can act as offsets which are added to the base address of the data array. This allows the use of pointer arithmetic to quickly access those events which are requested for a given plot. It also allows the use of a mask to identify qualifying events. For instance, if all events which deposited energy in the first sheet of the rear cell are wanted (sheet #3), only the third bit of the mask is set. A logical AND operator is then used to select the applicable elements of the index array.

Although the data reduction portion of the code is not complete, it does not appear that implementation of simultaneous control of a data run will be a large problem. The skeleton code which has been written for this portion includes all of the necessary function calls with time checks nested in between. Since the computer is not capable of multitasking, the strategy is to look at the time left on the data run, ensure that it is enough to complete the requested operation, and only then to execute the request. If the data run finishes in between two function call, the existing data will be written to a temporary file and the new data will be read from the crate and sorted. The new data will then be saved to disk, the old data recovered, and the operation completed. The problem with this part is estimating how long a given operation will take, which will not be possible until that part of the code is working.

The user interface is still primitive. Dr. Edwards has supplied a set of programs which allows the inclusion of windows and pull-down menus in a program. It is written for PC's, which limits its portability. The X-windows system, which is supposed to be a standard for graphics handling in C, is another possibility. This, in fact, would be preferable in order to make the graphics of the program available on other classes of computers. In the meantime, if the window and menu programs are used on the PC, the more primitive interfaces will be maintained for use with other machines. Since the program would have to be recompiled for use with another machines, this can be accomplished through standard structured programming practice, using different program modules for use with different machines. Of course, this will have to be well documented to prevent confusion.

The CAMAC interface portion of the code is essentially complete. A National Instruments GPIB-PCIII interface card is being used to interface the PC to the GPIB bus. A C language driver was included with the card. Although a header file for function prototypes was not included and there was a problem with the functions being listed in lower case and programmed in upper case, the driver worked fine after these problems were fixed. The most

difficult part was figuring out just what the problems were. Once the GPIB functions were prototyped and working, it was simply a matter of writing the CAMAC crate calls in terms of the GPIB functions. As soon as a simple framework is written around it for interface and data storage, it will be sent to Idaho for its first round of tests.

The documentation consideration largely becomes a discussion of lessons learned. Since this is the first time that the author has attempted a programming project of this magnitude, there have been many learning opportunities. One of the simplest to spot was the value of structured programming. The original code is all in one file, with innumerable calls to subroutines spread throughout. Care is being taken to write the code in a number of files. For instance, one file contains all CAMAC crate function calls and another the data manipulation routines. The code is also being heavily commented as to why things are done a given way. The old program is not very strong in this regard, and a lot of time has been spent chasing data trails to figure out what is going on.

Conclusion

Overall, this project has been a very rewarding experience. The experience working with research labs and writing programs that other people will be using will be invaluable in future work. Additionally, it has been an opportunity to make valuable contacts with professional researchers. Although still in progress, the program promises to be complete by the end of this summer, at which time a final report will be submitted.

References

1. W. A. Millard, A. M. Preszler, and S. E. Walker, "Electronics Implementation of a Double Scatter Neutron Time-Of-Flight Spectrometer for Fusion Plasma Measurements", Proc. 11th Symp. on Fusion Energy, Nov. 1985, 3C05.
2. A. M. Preszler, W. A. Millard, and S. E. Walker, "Double Scatter Neutron Time-of-Flight Spectrometer for Fusion Plasma Measurements", Proc. 11th Symp. on Fusion Energy, Nov. 1985, 3C04.
3. Ibid.

STUDENTS AS PARENTS

A'sia M. McNeal

Abstract

The effects extra responsibilities have on academic performance, attendance, and future career goals were investigated. These variables were especially of interest as they relate to the non-traditional student. College students (N=75) were asked to complete a questionnaire. All students were informed that factors concerning college attendance were being looked at and that all information would be confidential. There was a statistically significant difference between the overall GPAs of non-traditional students and traditional students. Despite the fact that non-traditional students have work more hours, they miss less classes per week than traditional students. Finally non-traditional student's primary reason for attending college was for self-improvement when compared to traditional students. This suggests that more difficult task make for a more highly motivated individual.

Each year, more and more parents enter the work force. In Keith Melville's book, "Marriage and Family", he acknowledges the difficulties of juggling work and parenting. In one recent study, cited in Melville's book, researchers interviewed 600 employees of a large corporation in Boston. They were seeking a better understanding of how family arrangements affected their work performance and vice versa. They found that one-third of the subjects both male and female felt guilty about leaving their children during the day. More than two in five said the strain for managing their family responsibilities was the main reason for their depression. Significantly, many of the participants felt frustrated about not having the time for household chores or events involving their children, or having time for themselves or their mates.

With these strains in mind, working parents are also entering undergraduate and graduate programs. In fact, the fastest growing segment of new entrants in colleges and universities are a group of individuals called non-traditional students. These students are older, and often have conflicting responsibilities as those described above. Currently, little is known about the effects additional responsibilities have on academic performance, attendance, or the career plans of non-traditional students. For the purpose of this research, non-traditional students are those individuals above the age of twenty-six. These students may be married or single, with or without children. Many studies have been done regarding the effects of task difficulty and effort on motivation. Rand (1967) treats task difficulty as interchangeable with goal difficulty. He describes a difficult task as hard to do, either because it is complex, that is it requires a high level of skill and knowledge, or because it requires a great deal of effort. Rand defines a goal as the object or aim of an action. An undergraduate program requires all of the above. For non-traditional college students, the extra responsibilities of economic support and family demands make their goal of receiving a degree become even more difficult. From these motivational studies of effort and task difficulty, there is evidence that more difficult challenges, as those facing the non-traditional student, can lead to enhanced performance.

Kaheneman (1973) argued that more effort is expended on hard tasks than on easy ones. Sales (1970) investigated and found that higher work loads produce higher levels of effort or drive. Higher goals produce higher performance than lower goals or no goals because individuals tend to work harder for the former. In research from a different perspective, that of cognitive expectancy theory, LaPorte and Nath (1976) allowed some subjects unlimited time to read a prose passage. Those asked to read the passage were also asked to get 90% of 20 post-reading questions correct. They spent more time on the passage than those subjects asked to

get 25% of the post-reading questions correct. Another study conducted by Rothkopf and Billington (1979) found that more time was spent on goal relevant than on incidental passages.

In totality, these studies suggest that non-traditional students may be more highly motivated due to all of their responsibilities than the more traditional students. Based on this information, it is hypothesized that regardless of all their other work and obligations, non-traditional students have better academic performance, and better attendance when compared to the more traditional students. Moreover, it is predicted that older students attend college more for self improvement than to fulfill future career goals.

Method

Materials

The self-report method was employed using a one-shot, questionnaire form. The form was prepared to evaluate six areas of a student's life. Of the thirty-six questions presented, thirty-three of them were fixed-response. These questions could be answered more easily and quickly with fewer scoring problems. In order to provide subjects with some flexibility, several questions required a one word response, and of the multiple choice responses, many included an other, please specify response. The remaining three questions were those of free-response. The goal of this survey was to ask a selected sample of traditional and non-traditional college students the same set of questions, so that their answers could be used as a basis for describing the characteristics of the population from which the sample was drawn.

A set of instructions summarized the purpose of the survey, explained the basis on which the subjects were selected, gave general directions on the method of response to the questions, and assured students that all information was confidential. The questions in this survey were developed to evaluate the subject's personal background, educational background, class attendance, their family situation, and their future career plans. As a precautionary measure, subjects were asked if they held any concerns that may be helpful in further evaluation of the questionnaire.

Procedure

Most students were obtained from the psychology pool at the University of Missouri-Rolla. There were specific times set for these subjects, and the survey was administered in a classroom setting. The accidental sample technique was employed to acquire the population of interest. This allowed every element to have an equal chance of being included in this sample. Each student was asked to read the directions and skim through the questionnaire form to see if there were any further questions. They were informed that the questionnaire took 5-10 minutes to complete, reconfirmed that their replies would be completely confidential and that they should answer each question as openly and honestly as possible.

Subjects

Seventy-five students from the University participated in the survey. These students were comprised of an accidental sample in nature. In order that non-traditional students were included, additional students were found on campus, and asked would they participate in the survey.

Results

The first hypothesis had to do with whether non-traditional students perform better in their coursework than did traditional students. To test this, the self-reported overall GPA and the GPA expected for the current semester were compared for the two groups. There was a statistically significant difference between the overall GPA, $F(1,57)=5.6$, $p<.02$, and the semester GPA, $F(1,65)=4.32$, $p<.04$. In line with predictions, non-traditional students reported higher overall GPAs ($M=3.19$) and GPAs for the current semester ($M=3.36$) than did traditional students ($M=2.75$ and 3.36 respectively).

The second hypothesis stated that, despite the likelihood of many conflicting demands, non-traditional students attend more classes. This hypothesis was confirmed, $F(1,65)=5.94$, $p<.02$. Non-traditional students reported having missed an average of 2.4 classes since the beginning of the fall semester whereas traditional students reported having missed an average of 3.4. This occurred despite the fact that non-traditional students were more likely to work, and to work slightly more hours ($M=20.18$) per week, than did traditional students ($M=13.00$, $F(1,32)=3.17$, $p<.08$).

The final hypothesis was that non-traditional students are more likely to be attending college for personal fulfillment than for specific career objectives. Table 1 summarizes the most important reason for why respondents were attending college. As predicted, more non-traditional students (43%) said the primary reason they were attending college was for self-improvement when compared to traditional students (7%). For traditional students, fulfilling career goals (54%) was more likely to be the primary reason for going to college than it was for non-traditional students (35%).

Discussion

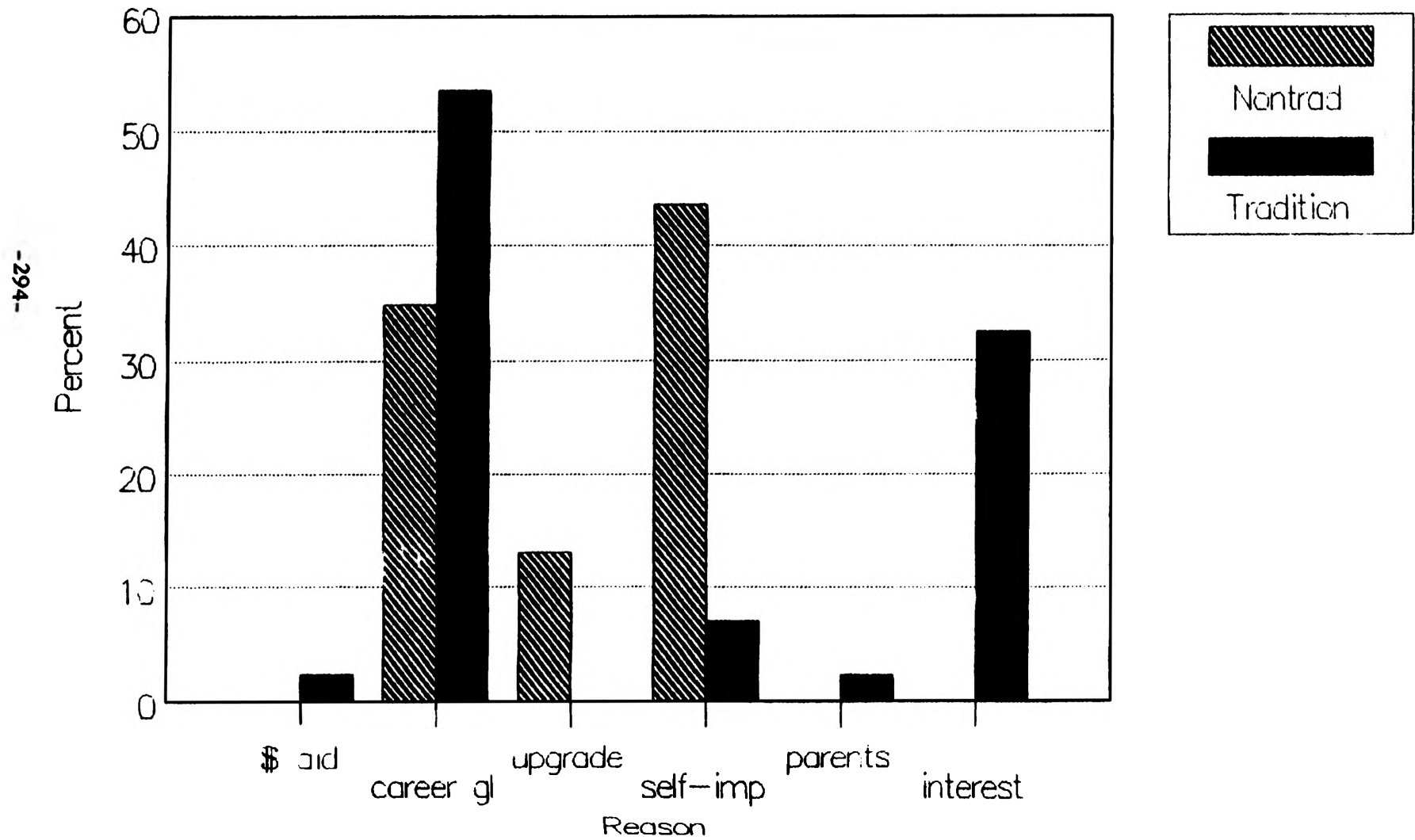
The present experiment investigated the effects that working, and family demands have on non-traditional students' academic performance, attendance, and future career goals. Despite what commonsense would seem to indicate—that the extra responsibilities of the non-traditional student would impair their performance in college—it was found that their performance is higher when compared to traditional students. Motivational studies such as that investigated by Sales (1970) allows us to understand this phenomenon. Higher work loads produce higher levels of effort or drive. Higher goals produce higher performance than lower goals. Rand (1967) describes a difficult task as hard to do, either because it is complex, that is, it requires a high level of skill and knowledge, or because it requires a great deal of effort. For non-traditional college students, the extra responsibilities of economic support and family demands make their goal of receiving a degree become even more difficult. From these motivational studies of effort and task difficulty, there is evidence that more difficult challenges, as those facing the non-traditional student, can lead to enhanced performance.

Task performance, attendance and future career plans were used in this study to test motivation. Though all necessary precautions were taken, the self-report method is not always valid. Assuming that the survey responses validly reflected students' true behaviors and feelings, the rate of attendance could account for the average difference in grade point averages. Non-traditional students reported missing 2.4 classes since the beginning of the fall semester; whereas, traditional students reported having missed an average of 3.4. Attendance is a very important factor in determining students' grades. This is especially true over time. In the case of this experiment, it would be necessary to look deeper into each individuals case to further analyze this possibility.

Intuitively, one might think that there is less time for a student to study if he or she works and tends to family demands. This brings up the issue of the way students study.

Figure #1

Decision to Attend School



Non-traditional students may study differently than traditional students. They may dedicate more of their time studying more general information, or they may study only to prepare for test and exams. In Melville's book, "Marriage and Family", he spoke of the guilt, despair and frustrations working parents felt about not having the time to spend with their families, nor having much time for themselves. Instead of attending many of the campus functions, or off campus parties, non-traditional students may use that time to study. The depression caused by all work and no play, may be rampant among these non-traditional students. Future research could address these concerns. Problem solving techniques would be valuable with regard to how working parents could effectively deal with the extra stress of attending college.

Non-traditional students chose self-fulfillment over and above other reasons for attending college. A student of this nature may take his/her education more seriously than other students. Age may also be a factor. Non-traditional students may have a much better idea of what they want, and therefore, choose fields of study that reflect the knowledge needed to participate in those specific career choices. This may also be relative to their age.

In summary, there are several questions left unanswered, and many avenues left untraveled. However, the present results confirm that non-traditional students do better academically, and they miss less classes when compared to traditional college students. They have chosen to attend college as a need to be self-improved. We are also more able to understand the effects extra responsibilities have on non-traditional students academic performance, class attendance and future career goals. The possibility of more research in this area is endless. As a future project, I would like to look at their schedules to analyze similarities that could be used in preventative measures and problem solving techniques for those seeking that extra challenge of a college education in their lives.

References

- Locke, A., Karyll, S., Saari, L., and Latham, G. (1986). Goal Setting and Task Performance: 1969-1980. In Frank J. Landy (Ed.), Readings in Industrial and Organizational Psychology. Chicago, Ill.: Dorsey Press, pp. 212-229.
- McClelland, D. C. (1985). How Motives Interact With Values and Skills to Determine What People Do. Human Motivation. Scott, Foresman, and Co., pp. 514-546.
- Melville, K. (1988). Marriage and Family. 4th ed. Random House, New York: Random House, pp. 235-238.
- Schwab, D., Olian-Gottlieb, J., and Heneman, H. III. (1983) Between-Subjects Expectancy Theory Research: A Statistical Review of Studies Predicting Effort and Performance. In Frank J. Landy (ed.), Readings in Industrial and Organizational Psychology. Chicago, Ill.: Dorsey Press, pp. 212-229.
- Shaughnessy, J. J. and Zechmeister, E. B. (1985). Research Methods in Psychology. New York: Alfred A. Knopf.

THE DETECTION AND QUANTIFICATION OF ATROPHIC RHINITIS USING DIGITAL IMAGE PROCESSING TECHNIQUES

Timothy Mussman

Abstract

This project focuses its attention on the detection and quantification of Atrophic Rhinitis (A.R.), a disease prevalent in pigs. A.R. causes some of the bony structure in a pig's snout to atrophy, which exposes the animal to other diseases that may effect its growth. It is studied by examining a cross section of the pig's snout. By comparing areas and perimeters of the nasal cavity to bony structures, or turbinates in the snout, one can determine the severity of the atrophy. Currently, the veterinarian's diagnosis is based on a subjective analysis of the snout. The problem with this method is that it varies among veterinarians. One would like to automate this procedure so that the system analyzes the same criteria (i.e. areas, perimeters) for all snouts. Semi-automated methods of manual planimetry are too slow and cumbersome to be of much use. The goal of this project is to develop a PC based system which could be installed in the slaughterhouse and could quickly determine the severity of Atrophic Rhinitis. This report describes the procedure and summarizes the results of software which has been developed to automate the task of determining the severity of A.R. Software has been developed to define the area of interest within the snout, create a histogram of the image, automatically threshold the gray level image, and compute areas and perimeters from the binary image.

Introduction

These automated methods will be used to compute known measurements for diagnosis of Atrophic Rhinitis. The measurements include the morphometric index (M.I.)[1], the turbinate area ratio (T.A.R.), and the turbinate perimeter ratio (T.P.R.)[2].

The core of this report is divided into four sections. The Materials section describes the systems and languages used to code the software. The Methods section discusses the various graphics and image processing techniques implemented. The Discussion section outlines the procedure taken to obtain measurements of atrophy. Lastly, the Results section tabulates the measurements taken and the correlation between the software and the subjective analysis.

I. Materials

This software was developed on an IBM XT model personal computer with 512kb of resident RAM. To display the snout images an image display board by HRH Electronics was used. This 8-bit, internally installed card, is capable of storing a 256 by 256 gray level image. Since each pixel is represented by an 8-bit number, each pixel value ranges from 0 (black) to 255 (white) and the total image occupies 65536 bytes of memory. These pixel values are set and modified by directly accessing memory which begins at a user set memory address. With the configuration used in this project, the 64kb block begins at \$E000. The output of the image board is then connected to a monochrome composite monitor for the display of the image. The software for the investigation of Atrophic Rhinitis was developed in Borland's TURBOPascal version 5.0.

II. Methods

In the process of writing this software, many interactive graphic and image processing techniques were obtained from various sources. The computer graphics methods provided the backbone of the software. Bresenham's line drawing algorithm and flood filling[3] were used to construct polygons to confine the area of interest and to mask unwanted regions of the image. For reasons outlined later, flood

filling was also used to count pixels in order to measure areas. Among the digital image processing methods used are automatic thresholding[4] to create a binary image and edge tracking[5] which was used to approximate perimeters.

III. Discussion

The following discussion describes the general procedure taken to obtain measurements of A.R. For a detailed outline of the software commands and source code listing, refer to (Mussman, 1990).

Upon displaying the snout image, it is obvious that there is much unwanted information. The snout should be located roughly in the center of the screen with the rest of the image being irrelevant. Thus it is necessary to remove this so as to focus all subsequent processing to the turbinates and nasal cavities, which are defined as the area of interest. This is accomplished by constructing a polygon around the area of interest and masking the outside region with a specific gray level, 255 in this case. This will serve as a mask, so the computer knows not to process this area. The masking is done by choosing a starting point in the region to be masked and then flood filling the region. When this is complete, the image should contain the snout in the center, surrounded by white pixels.

In order to compute areas or perimeters of any object, it is usually best to start with a binary image. The reason being that it is trivial to determine boundaries between the object and the background when one of two possible gray levels defines each region. Therefore, we must threshold this gray level image. To do this, a histogram of the image must first be created. The histogram contains the gray level intensity and number of pixels on the x and y axis respectively[6]. The histogram does not contain information on the location of the pixels but does contain information on the number of pixels in each gray level. Due to the nature of these images, the histogram has been normalized for ease of analysis.

In the case of pig snouts, the histogram has been assumed to be bimodal. Thus the histogram should contain a large number of pixels near or at gray level 0 and a large group near or at gray level 255. The threshold value is then chosen as the valley between the two peaks. Since the histogram is not very smooth in this case, it is divided up into sixteen bins of sixteen gray levels each. The peak and valley bins are then located by comparing each bin with the two bins next to it. Once the valley bin is located, the gray level with the fewest pixels is chosen as the threshold value. All pixels with a gray level at or below this threshold value are turned black and all pixels above are turned white. The snout is now a binary image with the darker nasal cavities black and the lighter turbinates white.

Due in part to the handling of the actual snouts and the noise in the system, all of the snouts had discontinuities in the nasal cavity regions. To measure the areas and perimeters efficiently, these areas must be connected. The software does allow for image editing. The user simply constructs a polygon to approximate the connection of the two separated regions and flood fills the polygon black. This same procedure is followed if part of the turbinate has been eroded due to a high threshold value. The only difference being that the user would fill the polygon white instead of black.

Once the binary image of the snout is editing, the perimeter and area of the nasal cavity can be found. The area is computed by simply counting pixels as the area is flood filled. The perimeter is found by using an edge tracking algorithm. This procedure also counts pixels, adding a correction factor for diagonals, as it tracks the boundary of the object.

To compute the areas of the turbinates, they need to be separated from the rest of the snout. The dorsal and ventral conchae, which are the upper and lower sections of the turbinate, are separated from the snout by drawing lines roughly tangent to the nasal cavities, which cut the conchae away from the bone. Area measurements

can now be taken on these enclosed regions by following the same procedure as above.

The last measurement needed is the perimeter of the entire snout, which includes the nasal cavities and the turbinates. This is found by filling all of the turbinates black, so that both halves of the snout are completely black, leaving a silhouette of the snout. Again, the perimeter of this shape can be found by using the edge tracker.

IV. Results

From the eight area and perimeter measurements, defined below, three ratios were calculated: M.I., T.A.R., and T.P.R.

Areas

CDR = right dorsal conchae
CVR = right ventral conchae
SR = right cavity space

CDL = left dorsal conchae
CVL = left ventral conchae
SL = left cavity space

Perimeters

C = perimeter of entire snout
D = perimeter of cavity space

Morphometric Index (M.I.)

$$M.I. = ((SL / (SL + CVL)) + (SR / (SR + CVR))) / 2$$

Turbinate Area Ratio (T.A.R.)

$$T.A.R. = (CDL + CVL + CDR + CVR) / (CDL + CVL + SL + CDR + CVR + SR)$$

Turbinate Perimeter Ratio (T.P.R.)

$$T.P.R. = (D - C) / C$$

The following four tables contain the data taken from the snouts. Table 1 and Table 2 contain the first and second area and perimeter measurements respectively, from the snout. However, when the data from Table 1 was recorded, the perimeter measurements had not yet been perfected, thus they are excluded. In both of these tables, samples M0-M5 are the plaster model snouts. They are labeled M#, where # is the A.R. score of the snout. In this project, the Weybridge system is used. Snouts are graded 0 (complete normality) to 5 (complete conchal atrophy)[1].

Table 3 provides a statistical analysis of the data in Tables 1 and 2 and of the subjective scores from the veterinarian (Vetscore) and pathologist (Pathscore). This data will be used to compute the correlation coefficients in Table 4, which contains the correlation coefficients between the pathologist and veterinarian as well as the individual ratios.

Some interesting results arise from Table 4. First of all, a correlation coefficient of 0.7543 between the pathologist and the veterinarian proves that subjective scoring is fairly consistent. On the other hand, coefficients below 0.5000 between the first and second M.I. and T.A.R.'s cause reason for alarm. In both cases,

these two measurements should be very close. One would expect a correlation coefficient of atleast 0.7500 for both of these. This extreme error is do to the editing procedure. Apparently the edited images of the first and second runs differed enough to produce a poor correlation coefficient. Since a single user produced these results, one can only assume that two different users would produce no better results.

Table 1: First run-Area data from snout samples

snout	left areas			right areas			M.I.1	T.A.R.1
	SL	CDL	CVL	SR	CDR	CVR		
1	did not record individual						0.5029	0.4970
2	measurements for						0.5291	0.4580
3	samples 1-3						0.5779	0.4220
4	1158	476	2697	1450	409	2497	0.3335	0.6990
5	2403	712	3106	2995	807	3764	0.4390	0.6090
6	3372	620	3003	3857	625	3216	0.5370	0.5080
7	3148	563	2470	3081	344	1984	0.5750	0.4630
8	3237	611	2515	3478	650	3080	0.5450	0.5050
9	2061	500	3209	1841	478	3198	0.3775	0.6540
10	2393	573	3217	2864	661	3199	0.4495	0.5930
11	1713	287	1594	1758	542	2286	0.4765	0.5760
12	2076	678	2865	2147	614	2985	0.4190	0.6280
13	2260	885	2442	2156	817	2615	0.4660	0.6050
14	1645	530	2281	1776	514	2291	0.4280	0.6210
15	2687	548	3412	2761	522	3201	0.4520	0.5850
16	3755	755	2896	2120	613	2481	0.5130	0.5340
17	2431	1228	3127	2506	801	3014	0.4460	0.6230
18	2194	700	2073	2508	769	1972	0.5370	0.5390
19	3162	828	3639	3505	552	2952	0.5040	0.5450
20-27	were not analyzed because of distortion present							
28	2337	661	3661	2245	361	3603	0.3870	0.6440
29	1925	388	2928	1279	345	3369	0.3360	0.6870
30	2157	512	3877	1951	299	4277	0.3350	0.6860
31	2453	287	3023	3530	654	3848	0.4630	0.5660
32	2303	655	3798	2231	683	4163	0.3630	0.6720
33	2392	278	2683	2418	341	2876	0.4635	0.5620
34	3278	505	4245	3327	423	4463	0.4315	0.5930
35	1714	521	3933	1332	457	3952	0.2780	0.7440
36	1361	921	4957	2079	632	4338	0.2695	0.7790
37	1885	521	3543	2207	731	3722	0.3595	0.6750
38	1125	278	3472	1308	421	3501	0.2585	0.7590
39	4166	446	1901	5203	800	1245	0.7470	0.3190
40	2880	618	3372	2799	555	3040	0.4700	0.5720
41	2792	846	3542	2943	482	3065	0.4655	0.5800
42	1513	382	3288	1573	482	2775	0.3385	0.6920
M0	4484	641	3796	5020	893	3888	0.5530	0.4920
M1	5719	601	3099	5289	934	3600	0.6220	0.4280
M2	4187	874	3225	4190	1050	3529	0.5540	0.5090
M3	5492	641	2792	8181	730	3532	0.6810	0.3600
M4	4394	331	1659	5243	693	2008	0.7245	0.3250
M5	6153	0	0	5418	0	0	1.0000	0.0000

Table 2: Second run-Area and perimeter data from snout samples

snout	left areas			right areas			perimeters		M.I.2	T.A.R.2	T.P.R.
	SL	CDL	CVL	SR	CDR	CVR	C	D			
1	2641	840	2921	2790	713	3715	1005	2781	0.4519	0.6012	1.767
2	2747	642	2885	2216	630	2820	889	2070	0.4652	0.5833	1.328
3	2413	585	1415	2520	676	2035	880	1572	0.5918	0.4885	0.7864
4	1448	615	2448	1448	590	2524	855	1885	0.3681	0.6808	1.205
5	2098	814	2838	2651	1018	3929	922	2632	0.4140	0.6442	1.855
6	2119	974	3600	3220	947	3928	1003	2474	0.4105	0.6390	1.467
7	3176	599	2468	2972	472	2053	932	1797	0.5771	0.4763	0.9281
8	3142	641	2669	3484	753	3194	993	2255	0.5312	0.5227	1.271
9	2565	631	3041	1989	699	3172	954	2331	0.4215	0.6235	1.443
10	2628	710	3147	2645	813	3453	921	2210	0.4444	0.6064	1.340
11	1642	441	1614	1699	754	2406	800	1793	0.4591	0.6100	1.241
12	2117	940	2875	2204	829	2869	937	2477	0.4292	0.6349	1.644
13	2208	942	2592	2239	931	2747	899	2074	0.4550	0.6186	1.307
14	1806	598	2216	2099	564	2191	858	2256	0.4692	0.5878	1.629
15	2913	678	3145	2687	609	3213	907	2626	0.4681	0.5772	1.895
16	4151	753	2770	2278	622	2357	974	2357	0.5456	0.5028	1.420
17	2507	1278	3037	2464	751	3067	959	2450	0.4488	0.6207	1.555
18	2379	645	2046	2608	740	2006	887	2148	0.5514	0.5216	1.422
19	2931	843	3848	3138	563	3219	991	2865	0.4630	0.5827	1.891
20-27	were not analyzed because of distortion present										
28	3022	553	3542	2712	443	3423	888	3026	0.4512	0.5813	2.408
29	2391	421	2831	2333	388	2733	838	2513	0.4592	0.5743	2.000
30	2961	325	3616	3982	345	3305	898	3067	0.4623	0.5609	2.413
31	2427	247	2970	3266	601	4046	948	3437	0.4482	0.5800	2.626
32	3130	488	3458	2612	620	3904	997	2940	0.4380	0.5960	1.949
33	2606	272	2662	2454	324	2892	800	2482	0.4769	0.5486	2.103
34	3980	399	4003	3822	676	4148	993	3494	0.4891	0.5418	2.519
35	3284	561	2915	2662	614	3099	923	2855	0.4960	0.5473	2.093
36	3113	898	3988	3124	663	3724	1016	3200	0.4473	0.5979	2.150
37	2824	459	3022	3343	483	2461	948	2712	0.5295	0.5102	1.861
38	2158	377	3080	2802	530	2790	878	2603	0.4565	0.5774	1.965
39	3275	434	2922	3653	554	2943	970	3046	0.5412	0.4973	2.140
40	3423	448	2595	3375	415	2600	943	2697	0.5506	0.4858	1.860
41	3485	906	3127	3314	504	2935	919	2641	0.5287	0.5236	1.874
42	2429	292	2536	2150	396	2537	790	2221	0.4740	0.5572	1.811
M0	4581	595	3738	5171	886	3949	1144	2972	0.5588	0.4846	1.598
M1	5728	626	3109	5327	983	3556	1137	2782	0.6240	0.4281	1.447
M2	4207	852	3193	4257	1028	3508	1076	2502	0.5584	0.5034	1.325
M3	5872	584	2734	8717	656	3202	1191	2997	0.7068	0.3297	1.516
M4	4395	357	1667	5268	688	1970	1016	2074	0.7264	0.3264	1.041
M5	6174	156	483	5442	159	390	958	1098	0.9303	0.0928	0.1461

Table 3: Statistical analysis of Tables 1 and 2

variable	N	mean	std. dev	median	minimum	maximum
Vetscore	42	0.7857	0.9509	0.5000	0.000	3.000
Pathscore	42	1.476	1.018	2.000	0.000	3.000
M.I.1	35	0.4420	0.1004	0.4500	0.2590	0.7470
T.A.R.1	35	0.5943	0.0968	0.5930	0.3190	0.7790
M.I.2	34	0.4769	0.0511	0.4626	0.3681	0.5918
T.A.R.2	34	0.5706	0.0509	0.5787	0.4763	0.6808
T.P.R.	34	1.742	0.4393	1.833	0.7864	2.626

Table 4: Correlation between the variables

Spearman correlation coefficient / prob > r under Ho:rho=0 / number of observations							
	Vetscore	Pathscore	M.I.1	T.A.R.1	M.I.2	T.A.R.2	T.P.R.
Vetscore	1.000	0.7543	0.6269	-0.6037	0.4390	-0.4117	-0.3856
	0.000	0.0001	0.0001	0.0001	0.0094	0.0155	0.0243
	42	42	35	35	34	34	34
Pathscore	0.7543	1.0000	0.3414	-0.2882	0.1559	-0.0969	-0.5944
	0.0001	0.0000	0.0447	0.0932	0.3787	0.5854	0.0002
	42	42	35	35	34	34	34
M.I.1	0.6269	0.3414	1.0000	-0.9746	0.4594	-0.3275	-0.4594
	0.0001	0.0447	0.0000	0.0001	0.0063	0.0587	0.0063
	35	35	35	35	34	34	34
T.A.R.1	-0.6037	-0.2882	-0.9746	1.0000	-0.4282	0.3204	0.3829
	0.0001	0.0932	0.0001	0.0000	0.0115	0.0647	0.0254
	35	35	35	35	34	34	34
M.I.2	0.4390	0.1159	0.4594	-0.4282	1.0000	-0.9343	-0.0738
	0.0094	0.3787	0.0063	0.0115	0.0000	0.0001	0.6783
	34	34	34	34	34	34	34
T.A.R.2	-0.4117	-0.0969	-0.3275	0.3204	-0.9343	1.0000	-0.1438
	0.0155	0.5854	0.0587	0.0647	0.0001	0.0000	0.4172
	34	34	34	34	34	34	34
T.P.R.	-0.3856	-0.5943	-0.4594	0.3829	-0.0738	-0.1438	1.0000
	0.0243	0.0002	0.0063	0.0254	0.6783	0.4172	0.0000
	34	34	34	34	34	34	34

Conclusions

This investigation of automated methods for the diagnosis of A.R. proved to be a limited success. The automatic thresholding procedure was successful for bimodal histograms, however, very few of the snout images produced a bimodal histogram. A solution to this problem would be to assume that the histogram is a combination of two gaussian distributions. One could then use statistical methods to separate the two distributions to find the threshold value.

Manual editing of the images proved to be inconsistent when the same images were processed more than once. A possible solution is to have the computer approximate the connection of the two separated regions, instead of the user. The software may produce a more predictable result.

Despite these shortcomings, the software did perform what it was designed for. This procedure for diagnosing A.R. is much more automated than before. However, there is still work to be done, especially in the area of pattern recognition, if this procedure is to be fully automated.

References

- [1] J.T. Done, "Atrophic rhinitis: Snout morphometry for quantitative assessment of conchal atrophy," The Veterinary Record, January 14, 1984.
- [2] M.T. Collins, "Turbinate perimeter ratio as an indicator of conchal atrophy for diagnosis of atrophic rhinitis in pigs," Am J Vet Res, Vol 50, No. 3, March 1989 -
- [3] J.D. Foley, Fundamentals of Interactive Computer Graphics, Addison-Wesley, 1984.
- [4] Timothy Mussman, EE300 VETPROJECT-Detection and quantification of Atrophic rhinitis, January 90-December 90.
- [5] Ballard and Brown, Computer Vision, Prentice Hall, Englewood Cliffs, New Jersey, 1982.
- [6] K. Castleman, Digital Image Processing, Englewood Cliffs, New Jersey, 1979.

PROCESS FOR SCANNING PHOTOGRAPHIC SLIDES OF LASER LIGHT SCATTERING WITH A TRANSMISSION DENSITOMETER

Don Newburry

Abstract

Non-symmetric variations in photographic slides of polarized laser light scattering experimental results are difficult to see. This paper explains a process developed for measuring the light density at points throughout the slide area using a transmission densitometer, so an accurate description of the laser light scattering may be obtained. A slide was tested using the described process and the results are presented. The results turned out well, but there were some errors introduced by the instability of the densitometer and by human error in reading the chart recorder output.

Introduction

Photographic slides of polarized laser light scattering experimental results are small in physical size and the nonsymmetric variations in light density are difficult to see. Therefore, an accurate method of scanning a slide, measuring the light density at points throughout the slide area, and digitizing the results was the goal of this project. Once obtained, the data can then be manipulated in any manner for study and presentation. For example, the constant intensity curves for any values of light intensity may be plotted on a percentage basis (i.e., 90% of max, 80% of max, and so on). These, in turn, give an accurate description of the laser light scattering as registered by the photographic film.

Thus, the purpose of this report is to describe just such a procedure. Throughout this project a Fisher Biotech 910 Transmission Densitometer (FB 910 - Fig. 1) was used along with a Kipp and Zowen Chart Recorder. The procedure for setting up the equipment and scanning a slide will be described along with the process for taking the data from the scan and converting it into distances for making plots.

Setup

The basic setup of this densitometer experiment was straight forward. Figure 1 also contains a photo of the setup. The recorder (reading 0 to 10 mV, max) was hooked up to the densitometer, and the SCAN/INTEGRATE switch was set to SCAN. At this point the equipment was ready to run with the exception of a warm-up period. In order to scan a slide, the lightest part of that slide was placed over the light source, and the ZERO knob was adjusted to a maximum value (100%). Then the slide was moved so the darkest portion of that slide was placed over the same light source, and the SPAN knob was adjusted to a minimum (0%). The carriage drive can then be turned to either low or high (the only choices), and the densitometer will scan down the object in a straight line.

The FB 910 operation had to be modified in order to scan the complete photographic slide. Two problems had to be overcome. First, due to the dark nature of photographic slides, the densitometer initially would not read in the dark regions of the slide. Two things were done in order to correct this problem. The first was to remove the narrow band optical filter that came with the densitometer and replace it with a broad band optical filter which could

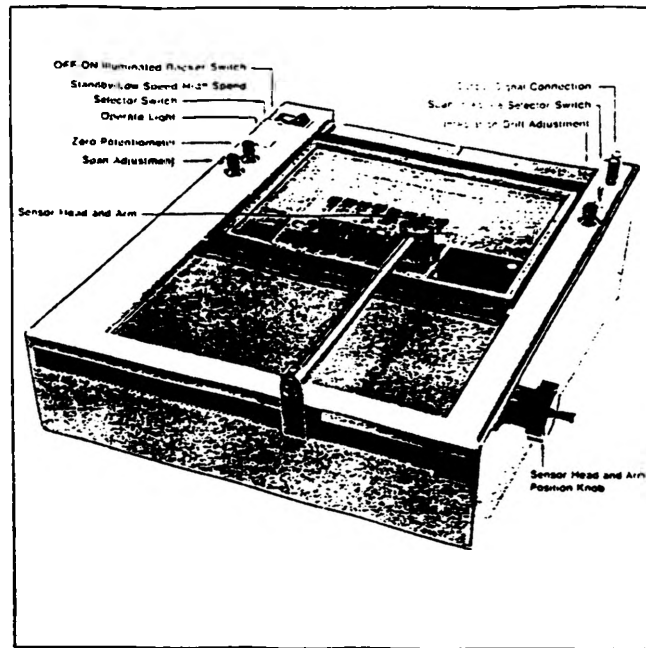


Figure 1a: FB 910 with labeled external controls.

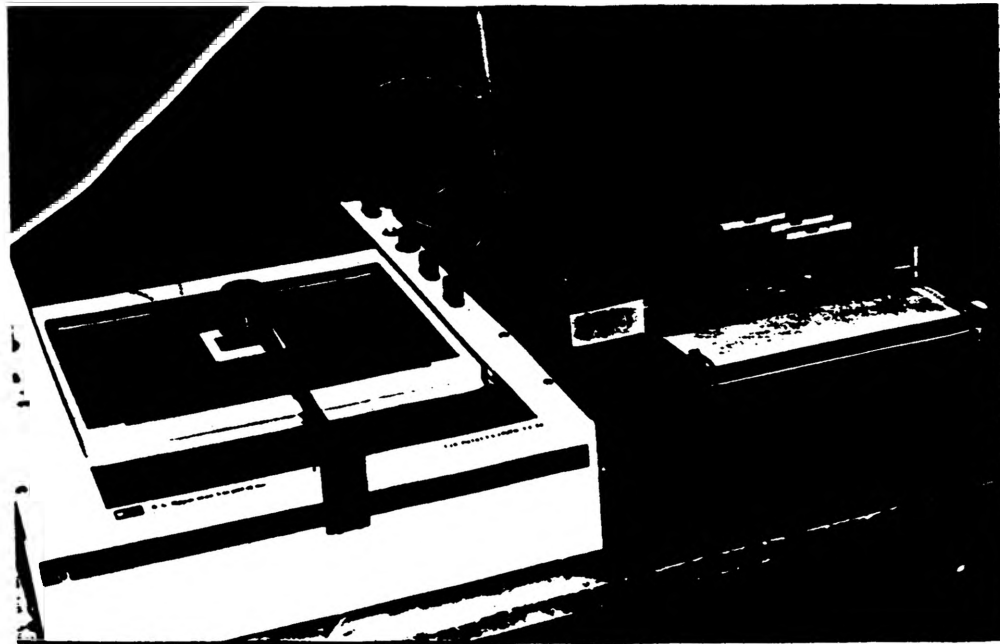


Figure 1b: Photograph of experimental set-up.

allow more red light to pass. The second action involved the light source of the densitometer; it is a tungsten filament light bulb which shines through an orifice. Initially, this orifice was a 0.05 mm in diameter circular hole and served as a point source. This orifice was the smallest obtainable from the manufacturer, so we assumed it would be the best size for very accurate results. However, the small source did not provide near enough light to penetrate the photographic slides. Therefore, larger and larger orifices were tried until the 0.4 mm point source produced the desired results (i.e., response to light variations throughout the slides).

Another problem with the FB 910 was the warm up time. When testing various slides, it was noticed that as time went on the magnitude of the output dropped, even if the same portion of the slide was being scanned repeatedly with all other settings fixed. Although the instruction manual for the densitometer stated it only needed 15 minutes to warm up, this was not found to be the case. A test was run over a 10 hour period of time with the densitometer simply scanning the same point. That is, the scanning mechanism was disconnected. During this test the densitometer was turned on (a cold start) and the chart recorder was set at the speed of 1 mm/minute. The results show that it took the densitometer at least 2.5 hours to reach a stable value. (See Figure 2.)

Another problem which was discovered was that the densitometer should be warmed up with nothing between the light source and the photodetector. An obstructed view keeps the photodetector from becoming fully warmed up. This causes error in the readings as of function of time as the photodetector does warm up during operation.

In order to test the long term stability of the scanner, while taking data, a slide was scanned vertically 20 times along the same line without changing any of the other settings. After the 20 scans, it could be seen on the chart recorder that the output magnitude of the last scan had dropped off approximately 5% from the output magnitude of the first scan. The cause of this error was still unknown. Further, after 20 scans the output continues to decrease. Therefore, this must be kept in mind when taking data of more than 20 scans and a data adjustment incorporated into the data to account for this drop.

Process

Since the scanner operates in only a straight line in the vertical direction, a method had to be developed in order to scan the entire slide. This was accomplished by starting at the left side of the slide, scanning down the slide, moving the light source and sensor head to the right (essentially the same as moving the slide to the left), and repeating the process across the whole slide. Depending upon how accurate the data needed to be and how much the slide varied in the horizontal direction, the distance between scans could be set as needed.

In order to determine the distances being scanned some operational procedures had to be developed. The motion in the horizontal direction was controlled by an unregistered knob on the machine. Therefore, a horizontal measurement standard had to be established. To accomplish this, the knob was marked at every 90 degrees. Then a Moire pattern (60 lines per inch) was scanned in the horizontal direction by turning the knob and keeping track of the number of revolutions. The peaks and valleys of the output were used to judge precisely where to start and stop counting the revolutions. Once this was finished the actual distance on the Moire pattern was measured and was divided by the number of revolutions. Thus the horizontal scale came out to be 2.5 mm/rev. of the knob.

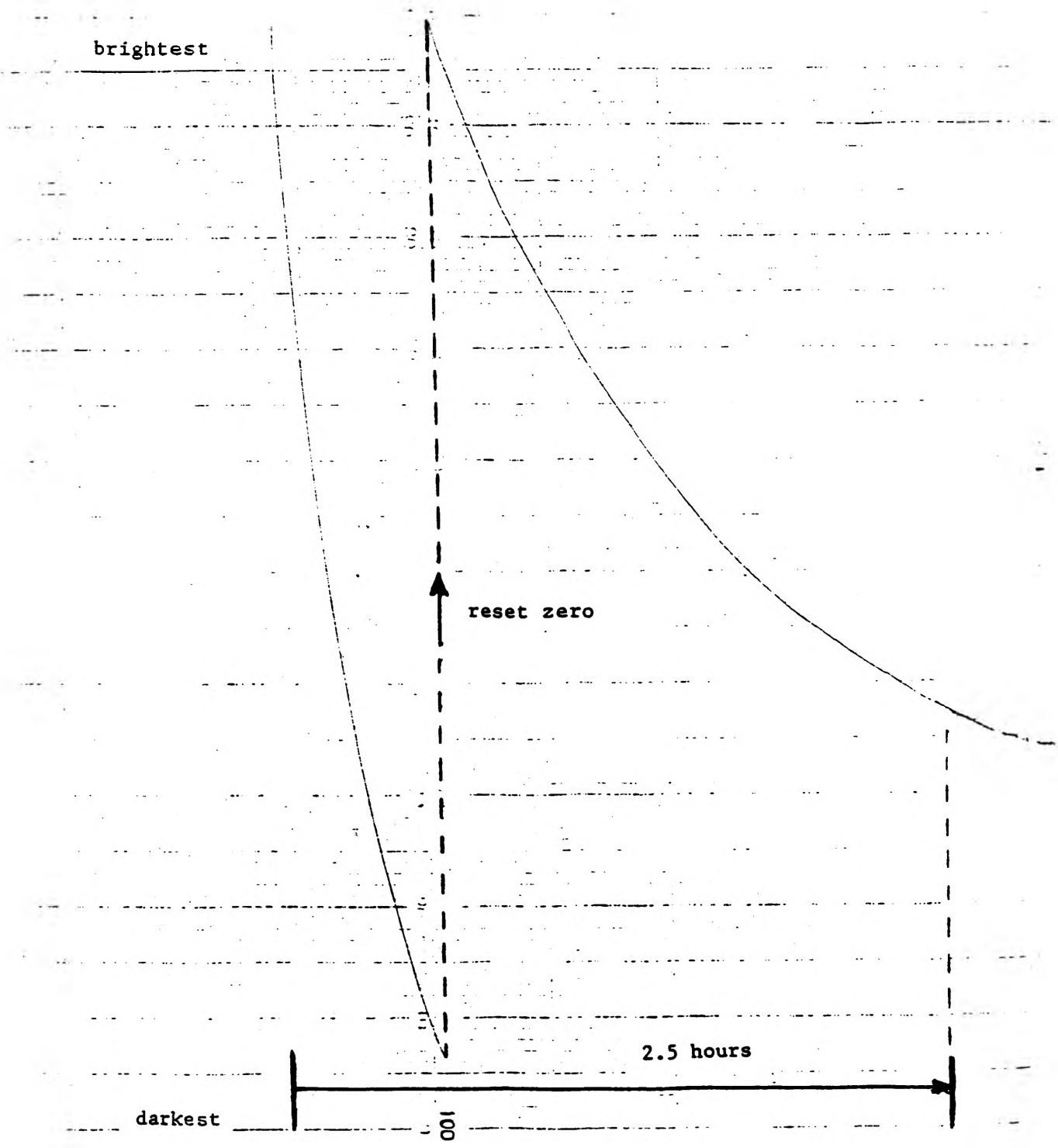


Figure 2: Chart recorder output of warm-up test.

In the vertical direction, the operational procedure was a bit more complicated. There were two motion aspects that needed to be considered: the recorder speed and the scanning speed. The scanning speed has two settings ("high - 2.2 in/min" or "low - 1.1 in/min"). These were verified by scanning a ruler of known length for a specified length of time. Since the recorder used metric distances, the scanning speeds were converted giving 0.932 mm/sec and 0.466 mm/sec, respectively. The scanning distance in the vertical direction was found by using the following definition:

R = the recorder speed in mm/sec

S = the scanning speed in mm/sec

f = R/S, which is the difference factor between the recorder and the scanner.

Therefore, the vertical distance on the slide is -y, (the scanner scans downward) and can be found from the distance travelled by the recorder along the time axis, d. Thus

$$-y = d/f$$

Using an easily recognizable position as a reference point, (the edge of the ruler for example), all the other vertical distances can be obtained with respect to it.

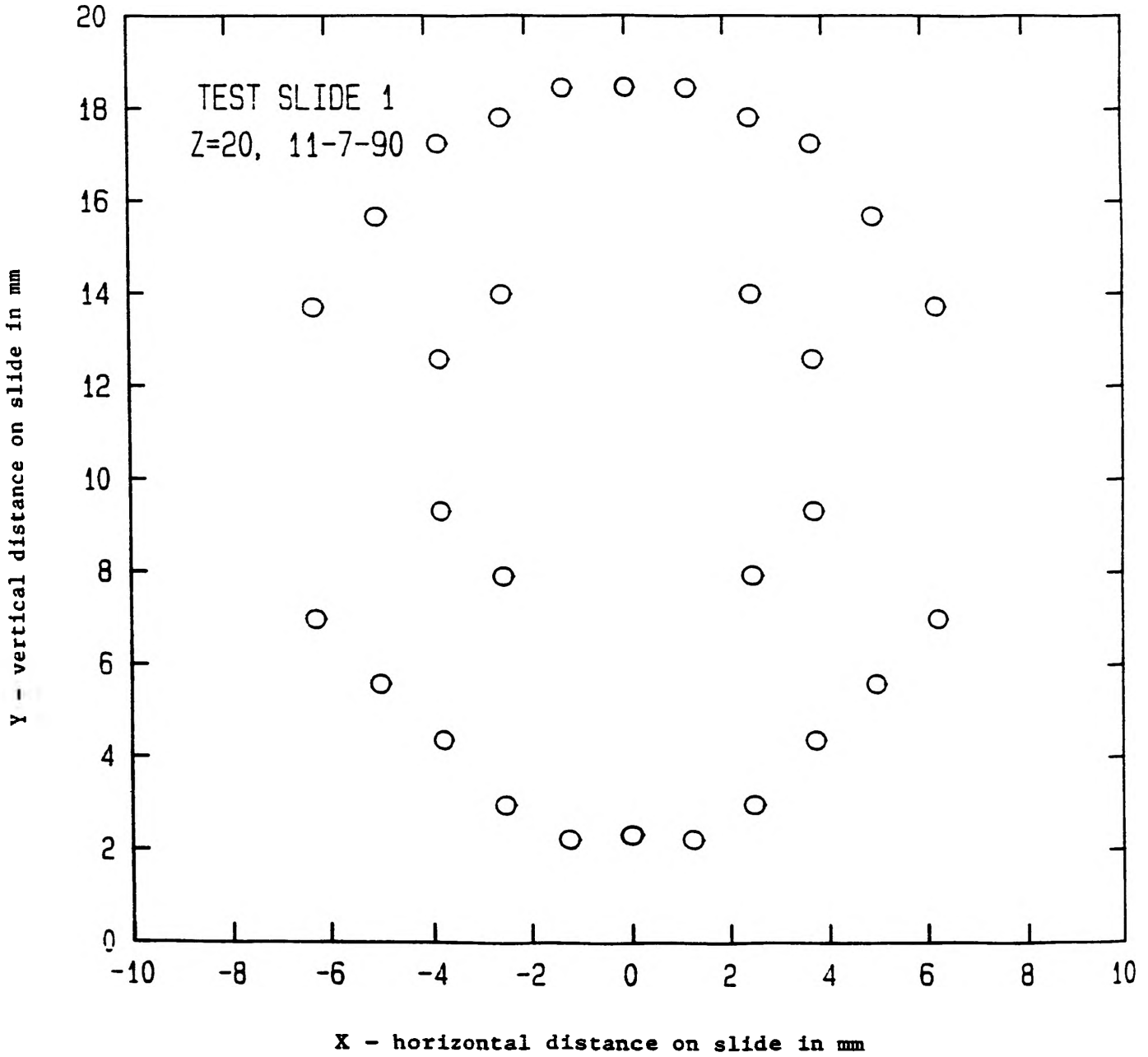
The brightness at each point could be measured directly off the slide at each point. By multiplying the maximum brightness by a percent, the value needed for that percent was given. Then everywhere that value occurred on the recorder charts could be found and used to plot a constant intensity curve.

Results and Conclusions

A slide was tested using the process described above, and the manipulated results are presented here. A plot was made for the relative brightness, z, equal to 20% of the maximum. (Fig. 3.)

Although the results turned out well for the test slide, there are some errors introduced by both the instability of the densitometer and by human error in taking the measurements. Also, the quality of the slide will effect the readings. Efforts are presently underway to pinpoint these errors and take corrective action. The results presented are encouraging. That is, the procedure presented outlines a reliable procedure of data acquisition from the slide. The results can, in fact, be presented as patterns which describe the scattering of laser light in a scattering medium.

Figure 3: Plot of relative brightness of 20% for the test slide



MEASURING HYDROGEN IN GALVANIZED STEELS

Timothy O'Hearn

Introduction

There has been much investigation in the past concerning ways to eliminate the embrittling effects of hydrogen in galvanized steel components.¹ Such galvanized parts are used extensively in the automotive industry. One solution that is commonly used is to anneal the galvanized parts at approximately 200 degrees Celsius for 4 to 24 hours. This annealing process does restore the ductility. However, very few if any experiments have been done to measure the amount of hydrogen released and the temperature dependence of the hydrogen release. This investigation is part of an on going effort to measure the hydrogen released from galvanized steels at various temperatures up to 800 degrees Celsius.

The Method of Modulated Beam Mass Spectrometry

To study the temperature dependence of the hydrogen release rate in galvanized steels a highly sophisticated technique known as modulated beam mass spectrometry was used. This technique was originally developed by Holister *et al.*² and applied to uranium dioxide studies by Srivastava (aka Kumar) and Olander³ and later used on copper and steels by Kumar.⁴ It has a highly superior sensitivity for measuring desorption rates.

Figure 1 shows how conventional mass spectrometry is used in conjunction with modulated beam technology to produce a highly sensitive instrument that can measure desorption rates as low as hundredths of a nanogram per second (0.01 ng/s). The apparatus is contained in a stainless steel ultrahigh-vacuum system. The sample is placed in a platinum crucible where it is heated by a furnace. The desorbed gases that travel up through an orifice are chopped by a rotating blade before passing into the mass spectrometer. A lock-in amplifier is used to read that part of the AC signal which has the same frequency as the chopper blade. Also connected to the apparatus is an ion pump which maintains the ultrahigh-vacuum.

Before an experiment can be performed the mass spectrometer must be calibrated. A gas of a known pressure and volume is bled into the system through a valve which has a known flow rate for the pressure of the gas. The mass spectrometer signal is measured to obtain a relationship between the mass spectrometer and the flow rate.

The Embrittling Mechanisms of Hydrogen in Steels

It has been generally agreed upon that there is a relationship between the hydrogen content in steels and their embrittlement. Many theories have been proposed to attempt to explain this phenomenon but so far none have proven to be totally satisfactory.

One theory that is presently considered is that hydrogen forms small gaseous voids which can lower the strain energy surrounding a stress concentrator when the specimen is under tension.⁵ The hydrogen lowers the stress energy by diffusing to the high energy region and forming a small void. The voids can act as microvoids in the void sheet mechanism of ductile failure.⁶ This type of mechanism would require slow strain rates to allow the hydrogen to diffuse to the high energy regions of the material. This is consistent with the findings of past strain rate experiments of hydrogen charged specimens.⁷ Slow strain rates were found to enhance the effects of hydrogen embrittlement, which is opposite the effects of most other types of embrittlement.

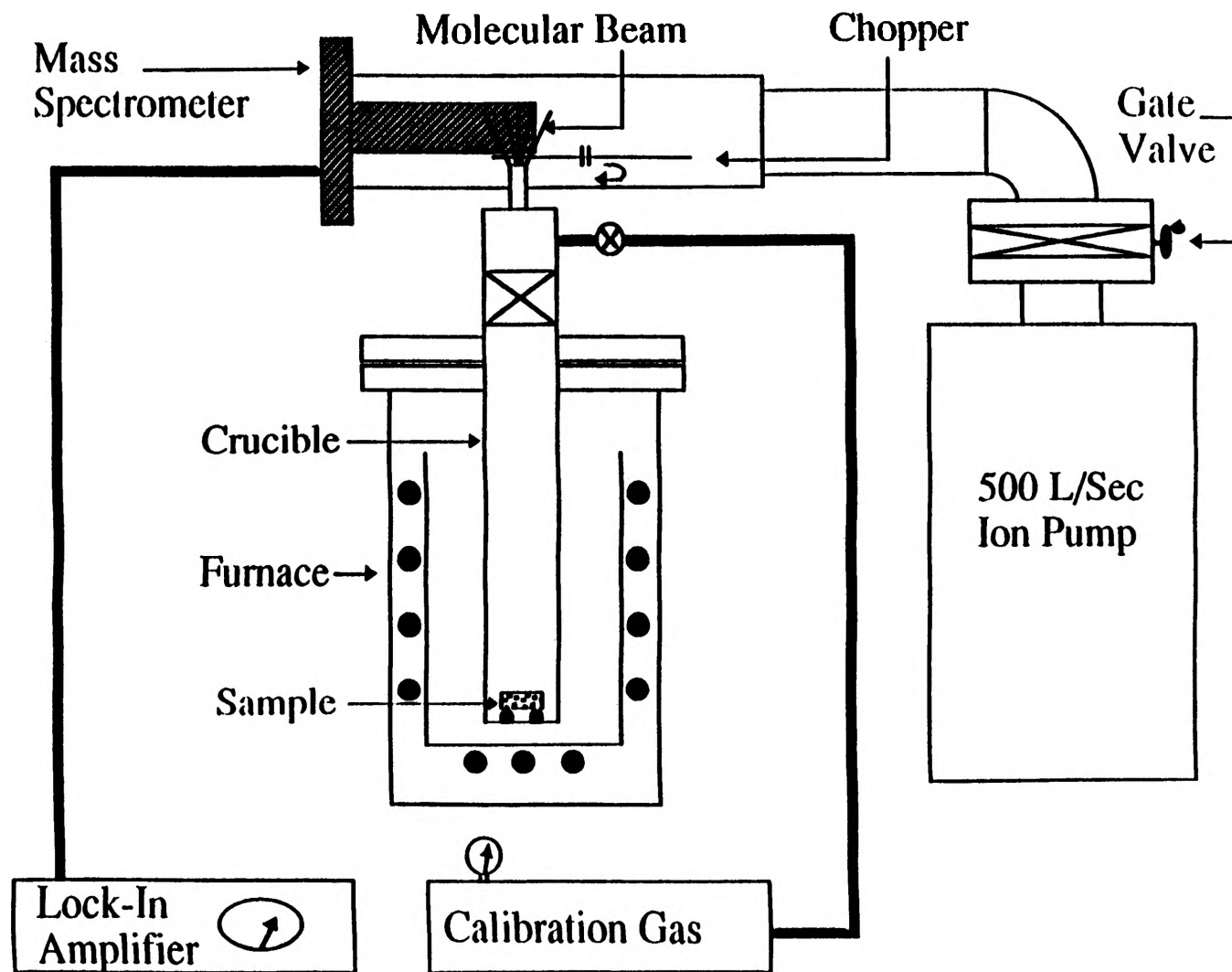


Fig. 1 Apparatus for Characterizing Gases

Another theory is the hydrogen induces embrittlement by migrating to the tips of existing microcracks. The hydrogen migrates to the crack tip through stress assisted diffusion. The high curvature tip of the microcrack has a high energy associated with it which due to the tendency of the tip of the crack to act as a stress concentrator. The highly mobile hydrogen lowers the free energy of the crack tip by migrating to it, which in turn lowers the cohesive force of the atoms surrounding the crack tip. This in turn lowers the strength of the material. This mechanism of embrittlement would also require slow strain rates for the hydrogen to diffuse to the cracks.

Results and Discussion

Galvanized steel seat belt holders and clips for automotive upholstery were analyzed for their hydrogen content. Three different types of samples were analyzed for each of the following: galvanized, galvanized then baked for four hours, and 'as received' which were the same as the other samples but had not been galvanized or baked. The three things listed above had been done by industry before the investigation began.

The 'as received' seat belt holder samples desorbed hydrogen only at temperatures in excess of 160 deg. C for 4 hours a total of 0.04 ppm (40 ng/g of sample of hydrogen was released. When the temperature was increased from 160 to 460 deg. C at 10 deg. C per minute a total of 0.175 ppm (175 ng/g of sample) was released. A galvanized sample (mechanically polished to remove Zn) was given the same treatment as the 'as received'. A total 0.488 ppm (488 ng/g of sample) of hydrogen was released with 80% coming out at temperatures above 160 deg. C.

When the results of the mechanically polished galvanized sample are compared to the results of a galvanized sample in which the Zn was removed with acid the hydrogen release is almost twice as much for the acid washed sample. It is concluded that the mechanical polishing removed not only the Zn plating but also some of the hydrogen rich layer on the steel surface.

A galvanized seatbelt holder sample (Zn removed with acid) was heated from room temperature to 200 deg. C at 4 deg. C per minute and maintained at 200 deg. C for 40 minutes. The total hydrogen release was 1.679 ppm (1679 ng/g of sample). In another experiment using the same sample the temperature was increased to 660 deg. C at 10 deg. C per minute and held for 40 minutes. The temperature was then increased at the same rate to 800 deg. C having a total annealing time of 8 hours with a total release of 13.11 ppm. The total release of from the sample in both experiments was 14.78 ppm of hydrogen.

Figure 2 shows hydrogen released from a galvanized seat belt holder with Zn left intact. When these results are compared with the results of a sample with the Zn removed with acid it is shown that Zn contains considerable hydrogen and also acts as a barrier to diffusion of hydrogen from the steel. In a 4 hour anneal a total of 5.08 ppm (5.08 micrograms per gram of sample) of hydrogen is released at 200°C in comparison to only 1.679 ppm for the sample with Zn removed by acid. Furthermore, the peak of the release curves occurs at ~3 hours from the start of the experiment as compared to only 50 min for the sample with the Zn removed with acid. Therefore, it appears that Zn plating delays hydrogen release and acts as a barrier for hydrogen diffusion.

Conclusions for galvanized clips are similar to those of seat belt holders. Figures 3 and 4 show hydrogen release rates up to 200°C from galvanized clips (Zn removed with acid) and galvanized clips with Zn plating intact, respectively. The total hydrogen release during 3 hours of annealing was 1.01 ppm for 'Zn removed' samples and 1.37 ppm for 'Zn not removed' samples. Just like the galvanized seat belt holders, the Zn plated clips contain a significant amount of hydrogen. Furthermore, the peak of the hydrogen desorption curve occurs at 140°C for

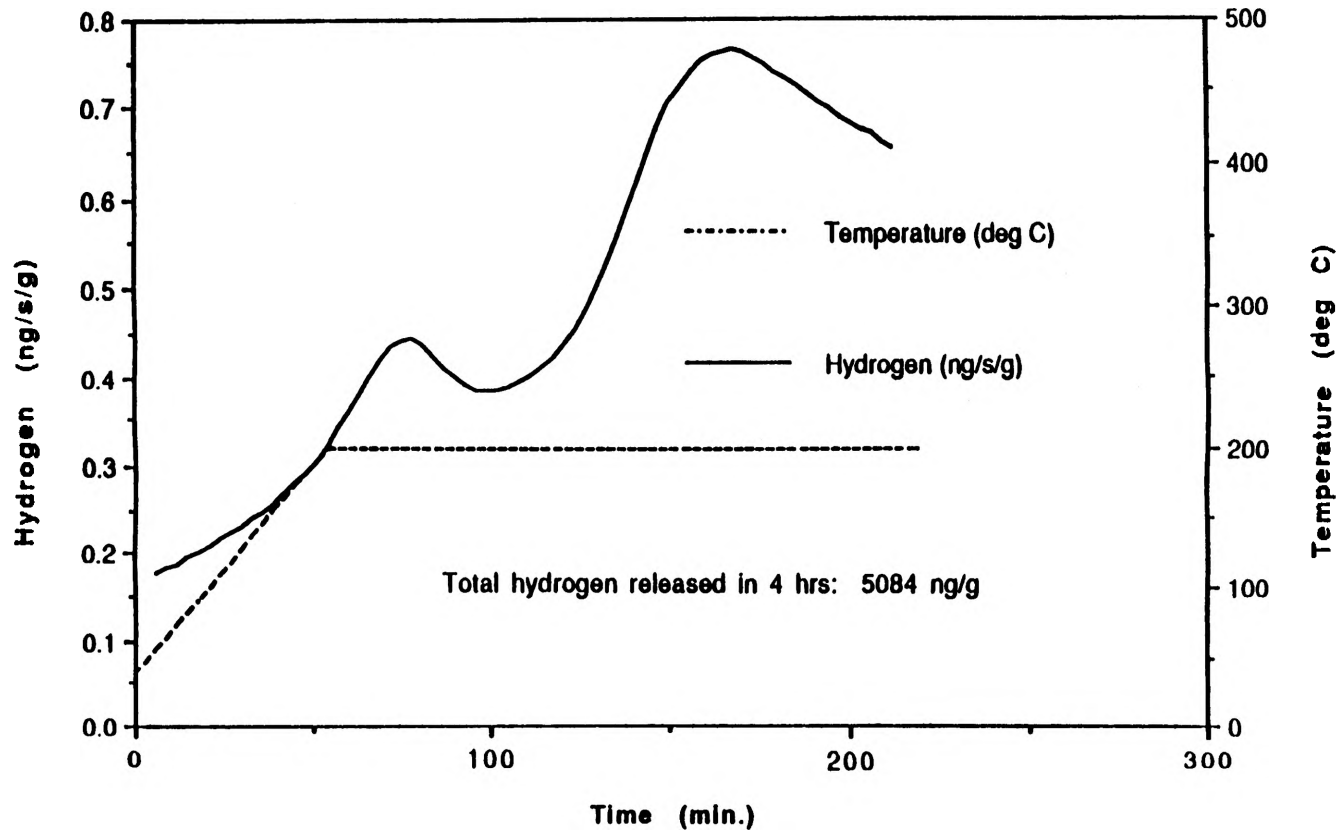


Figure 2. Galvanized seat belt holder. Zn not removed.

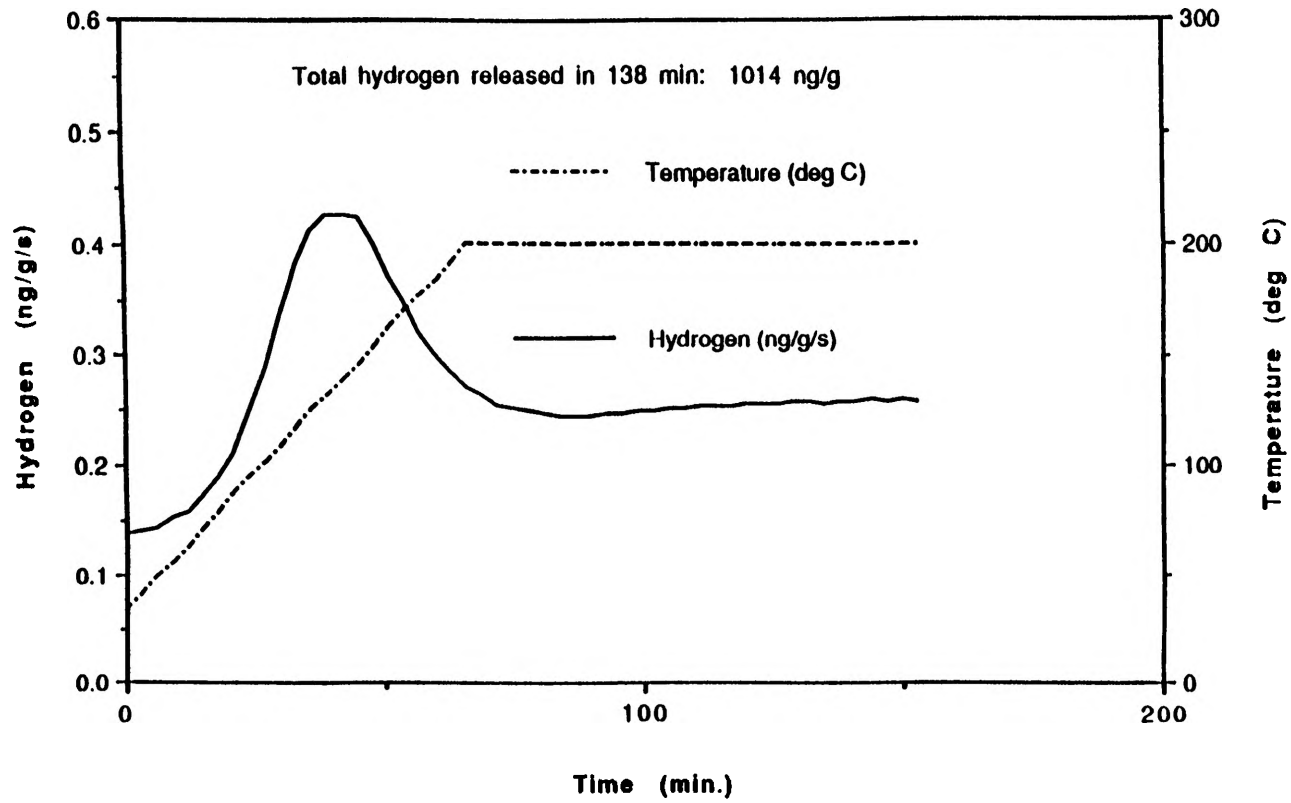


Figure 3. Galvanized clips. Zn removed with 1.5M HCl.

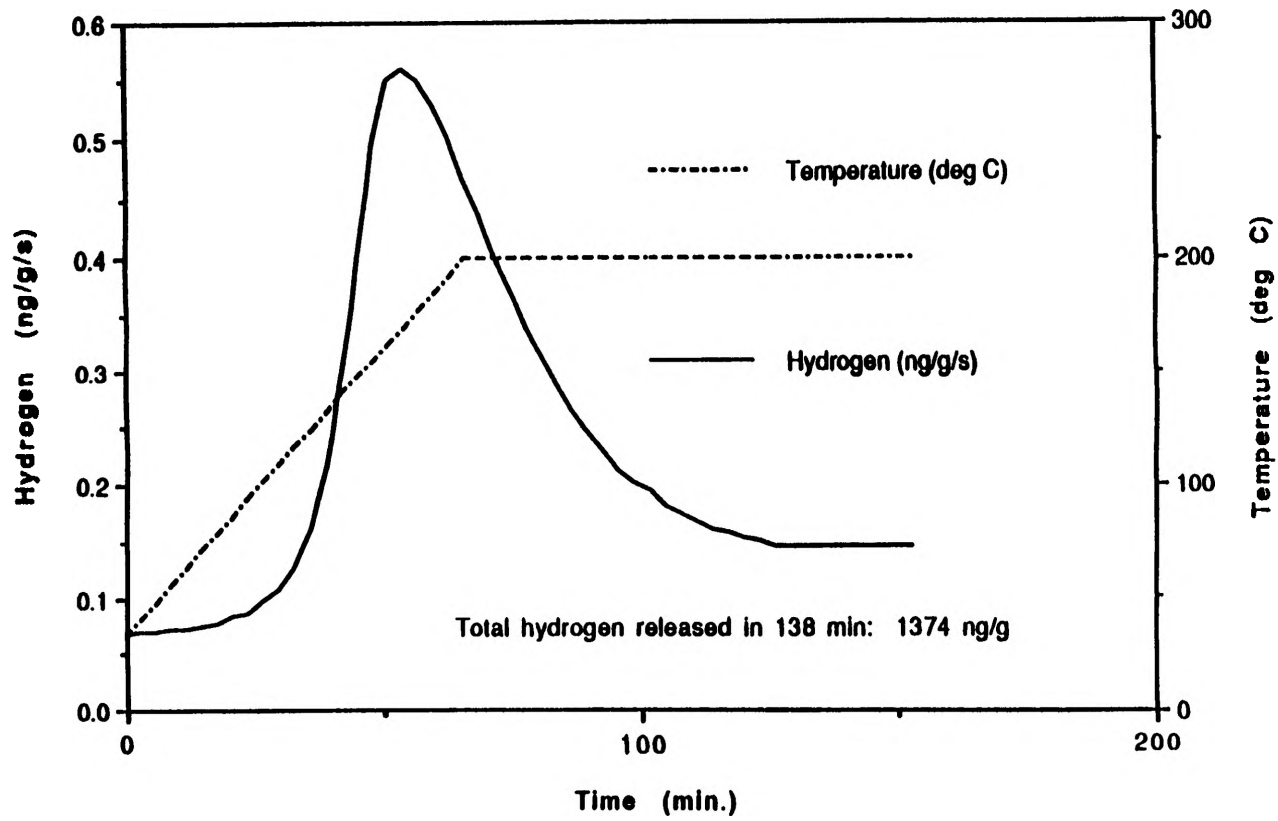


Figure 4. Galvanized clips, Zn not removed.

'Zn- removed' samples as opposed to 180°C for 'Zn not removed' samples. The shift in the peak to higher temperatures is an indication that the Zn plating acts as a barrier to hydrogen diffusion.

Figure 5 shows the hydrogen desorption curve up to 800°C from galvanized clips when the Zn is removed by acid (1.5 M HCl). A total of 3.13 ppm of hydrogen is released. This is considerably lower than 13.11 ppm for the seat belt holders (Zn removed with acid).

Conclusions

The following conclusions were drawn from the present work:

1. Modulated Beam Mass Spectrometry (MBMS) is capable of measuring hydrogen release rates of the order of 0.01 ng/sec. For one gram of sample, MBMS can conveniently measure concentrations of hydrogen on the order of a hundredth of 1 ppm.
2. The Zn plated layer contains a significant fraction (up to 20%) of the total hydrogen in the galvanized steels.
3. Zn plating acts as a barrier to hydrogen diffusion during annealing, requiring longer times or higher temperatures for hydrogen release.
4. Annealing at 200°C for 4 hours releases only a fraction of the total hydrogen uptake. The fraction is 30% for clips and only about 10% for seat belt holders.
5. Annealing at 200°C redistributes the high concentration of subsurface hydrogen into the bulk. This may be the reason why thicker (0.5 cm) seat belt holders release a lower fraction of hydrogen than the clips (radius ~0.1 cm).
6. The electroplated surface, with or without the Zn removed, acts as a barrier to hydrogen release. This promotes hydrogen redistribution in the bulk.

References

1. P. Gardner *et al.*, Hydrogen in metals and Alloys, Research Report to AESFS, University of Missouri-Rolla, 1990.
2. G. S. Holister *et al.*, J. Chem. Physics, Vol. 34, 1961.
3. A. Srivastava (aka Kumar) and D. Olander, 'Retention and Release of Water by Uranium Dioxide,' Trans. Am. Nuc. Soc., Vol. 23, 1978, p. 216.
4. A. S. Kumar, "Hydrogen in Galvanized Steels and Copper Reprocessed from Waste". Work in Progress, Supported by Bureau of Mines, U.S. Dept. Interior.
5. D. N. Williams, Hydrogen in Metals, University of Chicago Press, Chicago, 1948.
6. R. E. Reed-Hill, Physical Metallurgy Principles, PWS-Kent, Boston, 1973.
7. H. L. Ewalds, Fracture Mechanics, Edward Arnold, London, 1985.

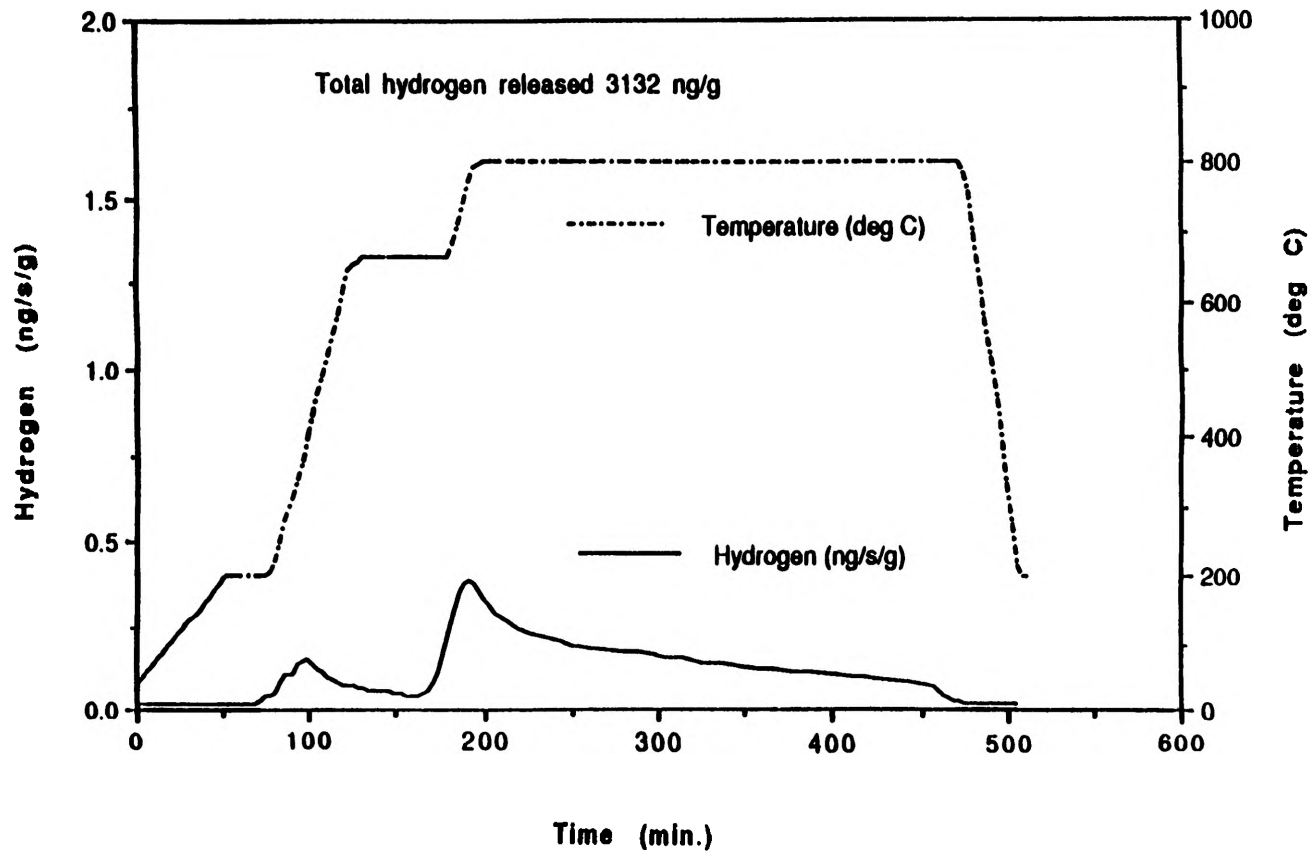


Figure 5. Galvanized clips. Zn removed with 1.5M HCl.

THE SYNTHESIS AND CHARACTERIZATION OF METAL BINDING POLYMERS CONTAINING 2, 2'-BIIMIDAZOLE

Renee Proctor

Abstract

Epoxides are known to form ring-opened polymer products that have demonstrated improved material strength, high heat stability, and chemical resistance as adhesives, coatings, and molding materials. It has been suggested that imidazoles can be used in the catalysis of this polymerization, and that the pyridyl nitrogen of the imidazole ring participates in epoxy ring-opening and is then incorporated in the polymeric structure. This study was conducted to test this theory of the role of pyridyl nitrogen in the reaction of 1,1'-dihydroxyethyl-2,2'-biimidazole (HEB) and metal-HEB complexes in reactions with the diglycidyl ether of bisphenol A (DGEBA). Of particular interest in this study is that HEB also exhibits two alcohol functionalities which are known to induce epoxy ring-opening and that HEB also forms an alkoxide ion adduct which promotes chain growth. I used DSC and IR to monitor the reactions of HEB and its metal complexes with DGEBA. These studies support the conjecture that the pyridyl nitrogen participates in epoxide ring-opening. They also suggest that the pyridyl nitrogen ring-opening is the first reaction, followed by the formation of the alkoxide adduct formation and the hydroxyethyl group etherification.

Introduction

Epoxides are known to form epoxide ring-opened polymer products in the presence of various reactive organic compounds such as acids (anhydrides), amines, alcohols and phenolics. These polymer products have found significant utility as adhesives, polymeric coating materials, and molding materials and have demonstrated improved material strength, high heat stability, and chemical resistance in these capacities.

Among known catalysts for the ring-opening and subsequent homopolymerization of epoxy compounds are imidazoles. Imidazoles are added to initiate esterification reactions in epoxy-anhydride systems, are used to catalyze specific epoxy-phenolic hydroxyl reactions, and are used as hardeners in a variety of commercial epoxy resin systems.

Previous investigations¹⁻³ on epoxy/imidazole systems have put forth some general conclusions about the formation of epoxy/imidazole adducts. As can be seen in Figure 1, these conclusions say that for a 1:1 epoxy/imidazole reaction in which the imidazole is a 1-unsubstituted imidazole, both a 1:1 hydroxide (OH) adduct and a 2:1 alkoxide (O-) adduct are formed. In these reactions, the imidazole becomes a part of the polymeric structure. In fact, in the formation of the 2:1 alkoxide (O-) adduct it has been suggested that the pyridyl nitrogen of the imidazole ring participates in epoxy ring-opening and is then incorporated in the polymeric structure.

In a similar fashion, the formation of a 1:1 alkoxide (O-) adduct is expected for 1-substituted imidazole/epoxide reactions. In this case the pyridyl nitrogen is again utilized in the adduct formation.

Suppose the 1-substitution on the imidazole is a hydroxyl ethyl group as suggested by Figure 2. Then one must not only consider the previously mentioned 1:1 alkoxide adduct formed by epoxy ring opening by the pyridyl nitrogen of imidazole, but one must also consider the possibility of the formation of a 1:1 imidazole/hydroxy ether adduct via hydroxyethyl ring-opening.

Imidazoles as Epoxy Catalysts

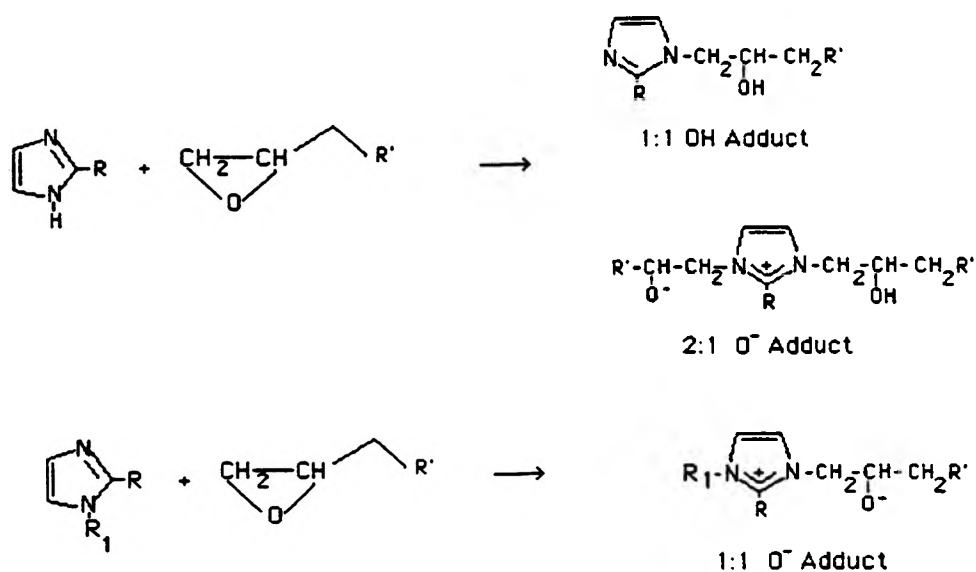


FIGURE 1

1-SUBSTITUTED IMIDAZOLE EPOXIDE CATALYST

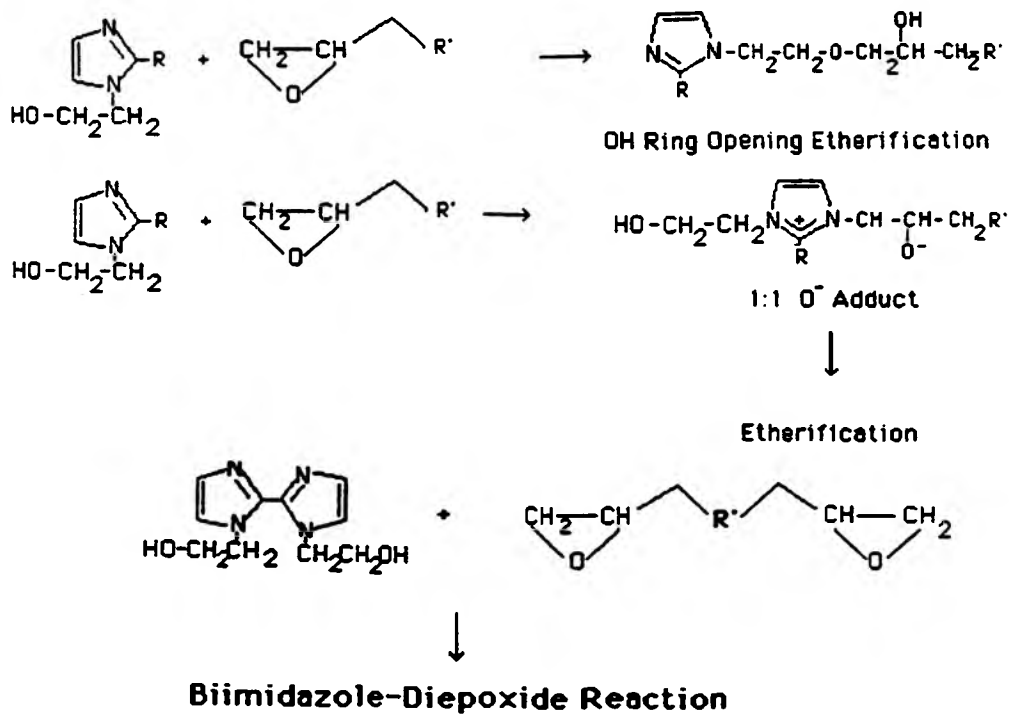


FIGURE 2

Subsequent to the formation of these adducts, which have been proposed to occur rapidly and initially, is the etherification reaction, which results in chain growth via OH-etherification and O-etherification reactions.

Another important consideration is that the alkoxide ion is highly reactive, and once placed in such a situation, will promote the O-etherification reaction.

The question posed by this phase of the investigation is: "is it possible to observe some discernment in the reaction of 1,1'-dihydroxyethyl-2,2'-biimidazole (HEB) with diepoxides?" For example, can the formation of the imidazole pyridyl nitrogen-epoxy adduct and the formation of the hydroxyethyl-epoxy adduct be observed? Can the proposed etherification reactions be observed? And what is the metal ion effect when it is used to block the pyridyl nitrogen sites?

I plan to discover the role of HEB and cobalt-HEB, or Co-HEB, complexes in reactions with the diglycidyl ether of bisphenol A, or DGEBA. If it is expected that there is an ordering of reactive groups for this and related reactions, then one might expect that the thermal monitoring of this reaction as a function of temperature may provide insight to what actually occurs.

In this particular case, the reaction order was expected to proceed as follows: the epoxide ring opening with the formation of the imidazole ring pyridyl nitrogen-epoxy alkoxide adduct; and the more rapid reaction of the alkoxide adduct with epoxide groups as well as the hydroxyethyl group ring-opening etherification.

It is proposed that if the pyridyl nitrogen site is occupied by a transition metal ion, then the principle reaction should be the hydroxyethyl group ring- opening etherification.

Experimental Section

The first problem confronted in this experiment was the task of purifying the 1,1'-dihydroxyethyl-2,2'-biimidazole. Testing a sample to determine its purity entailed a simple thin layer chromatographic analysis. First the sample of the crude HEB was dissolved in methanol and was dotted on a 1x6 inch thin layer chromatography silica plate. Once dry, it was placed in a covered graduated cylinder and allowed to develop for approximately 90 minutes to 2 5 hours in an 8:3:1 hexane: propanol:ethanol solvent mixture. The crude HEB was found to resolve into two basic components: mono-substituted HEB and the desired di-substituted HEB.

It was decided to employ flash chromatography in the purification process. After a lot of procedures were tried and sample purity was tested by the procedure outlined above, a sketchy method of purification was developed that gave consistently pure HEB. First, approximately 0.5 g of the crude HEB was dissolved in methanol. This often required a little heating, and usually, there was some insoluble solid present that was assumed to be impurities and was filtered out of the solution. Second, the flash chromatography column was rinsed with 8:3:1 hexane : propanol : ethanol solvent mix. Next, the dissolved HEB was introduced to the column and pumped down into the silica. Then the HEB mixture was chased through with the 8:3:1 solvent mix until pure white silica became discolored. At this point, the solvent was switched to methanol and the methanol was pumped through the column. A distinct yellow band was observed to form and move slowly down the silica column. This band contained the pure, golden HEB. The methanol wash was continued until the band reached the bottom of the column. Now, in a separate vial, the pure product was able to be collected by continuing the methanol strip until the yellow band was gone, and approximately 30 mL of the liquid was collected

beyond that point. Finally, the methanol was allowed to evaporate in a beaker so that only the pure HEB sample remained.

From the purified HEB and the Co-HEB samples, 1:1 molar HEB:DGEBA reaction samples were prepared in vials. These samples were weighed out on a Mettler PM460 Tare Scale. They were then mixed with a spatula, and stored under Argon gas in a 6° to 8° Celsius refrigerator. These precautions were taken to ensure a moisture and heat-free atmosphere so that no reactions occurred during storage.

Thermal analysis of the samples involved monitoring by Differential Scanning Calorimetry, or DSC. Five milligrams of the previously prepared reaction mixture were placed in aluminum sample pans and covered with a lid. These samples were placed in the DSC and scanned between 50° and 250° Celsius at a heat rate of 20 degrees per minute. They were then analyzed and sent to the printer. Four samples of each of the two reaction mixtures were run to ensure reproducibility.

Next, a thin film of the HEB reaction mixture and the Co-HEB reaction mixture was spread on NaCl salt plates. These plates were first heated in a 70°C oven for 2 minutes. They were then quenched cool in the 6° to 8° C oven, and, once cool, were scanned by a Fourier Transform Infrared Spectrometer, or FTIR. The plates were heated in the same oven for 5, 15, and 90 minutes respectively, cooled, and scanned each time. After these tests, the salt blocks were placed in a 185° C oven for 15 minutes. They were once again quench cooled in the refrigerator and scanned on the FTIR. Peak assignments and percent transmittances were printed out for each plot.

Results and Discussion

The monitoring by DSC of HEB with DGEBA and CoHEB, with DGEBA is illustrated in Figure 3. The endotherm for the HEB-DGEBA reaction is presumably due to the heat of reaction required for the pyridyl nitrogen to initiate ring-opening. The wide exotherm thereafter, at about 150°C, is thought to account for the alkoxide and hydroxyethyl reactions with epoxide. Compare this to the DSC scan obtained for the reaction of CoHEB with DGEBA, which clearly shows a single exotherm at approximately 200°C. Since, in the case of CoHEB, the pyridyl nitrogen has been blocked, this peak is due to the reaction of the hydroxyethyl group with the diepoxide.

In the next phase of the experiment, the sample was heated for four different time intervals in a 70° C oven and scanned by FTIR after each period. The intention was to catch the reaction in various stages towards completion. However, little to no change was actually observed. The samples were then heated in the 185° oven for 15 minutes to prove that the reaction reached completion as expected through observation of the epoxy peak.

The infrared examination of the mixture of HEB and DGEBA before the reaction is shown at the top of Figure 4. The epoxy peak can be seen here at approximately 916 cm^{-1} , and at the end of the 15 minute period, the scan for which is shown at the bottom of this figure, the reaction is completed and the epoxide is gone as expected. Note also the band assignments at 1670, the C=N, and the broad band appearing in the 3200 to 3400 cm^{-1} region, the N-H stretching region of the 1-substituted imidazole, as proof of the incorporation of HEB into the polymeric network. This band is especially exciting since the substance scanned initially is believed to be only DGEBA since the reaction mixture was rather heterogeneous. The growth of this peak from the initial to the final scans is further proof of the incorporation of the biimidazole in the polymer.

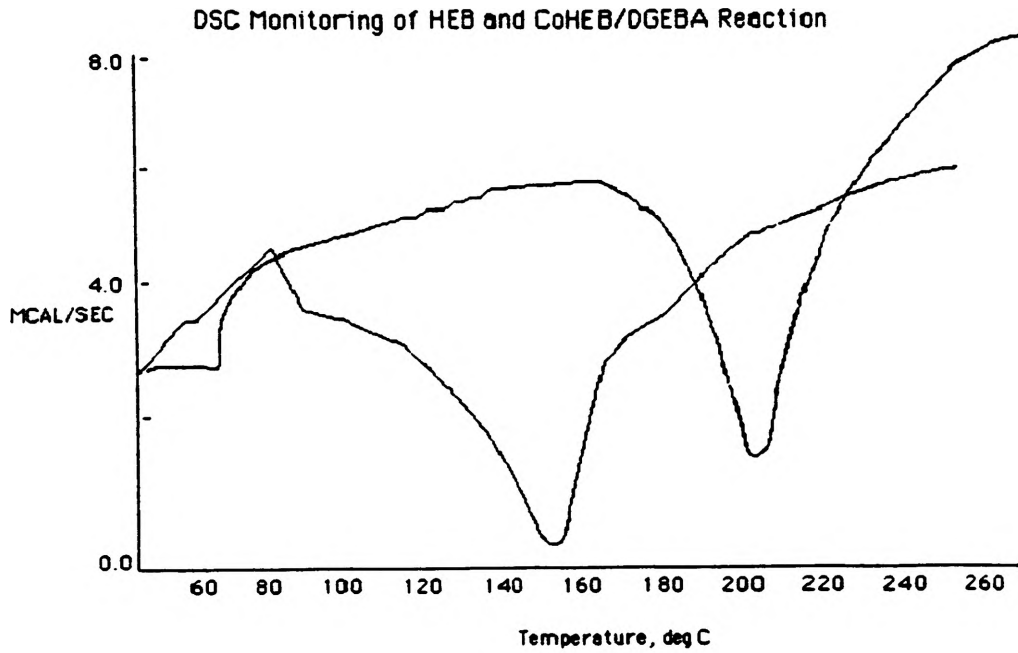


FIGURE 3

Infrared Spectra of HEB/DGEBA Before and After Polymerization

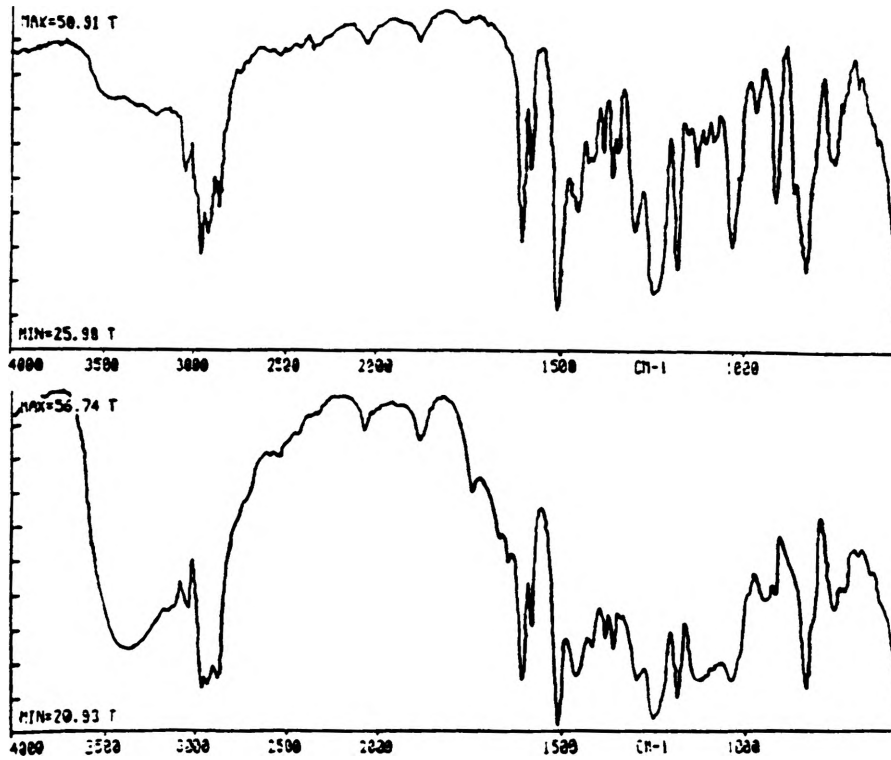


FIGURE 4

The FTIR scan in Figure 5 shows similar results for the reaction of CoHEB with DGEBA. Before heating for 15 minutes in the 185° C oven, an epoxy peak can be observed at 915 cm⁻¹, but after the heating the peak is gone and the reaction is complete. These FTIR results help to justify that the expected is occurring, and it is producing an epoxy ring-opened product.

Once again the C=N can be observed at 1670 and the broad 1-substituted imidazole band can be observed between 3200 and 3400 cm⁻¹ as the HEB is incorporated into the final polymeric structure.

Conclusions

So far, by blocking the pyridyl nitrogen sites of HEB with cobalt, support has been given to the conjecture that the pyridyl nitrogen participates in epoxide ring-opening. An order of reaction for the different functional groups has also been proposed. Further thermal analyses with a slower scanning rate on the Differential Scanning Calorimeter need to be run in order to differentiate among the steps even further. That is, with a slower heating rate, perhaps the wide exotherm containing the reaction of both the alkoxide adduct with epoxide groups as well as the hydroxyethyl group ring-opening etherifications can be separated into its two component reactions so that a definite order can be assigned to these reactions. Also, a method to stop the reaction at different stages by cold quenching needs to be developed so that further differentiation and characterization of the steps of this reaction may be made with FTIR. Characterization of the final polymer products of the HEB/DGEBA and the CoHEB/DGEBA reactions will be made by Nuclear Magnetic Resonance and Gel Permeation Chromatography analyses.

Future plans include the study of the effects of other metal ions, such as nickel and copper, on the reaction. Also, the study will be expanded to reactions with other diepoxides to witness if the reaction proceeds in a similar manner as described here.

References

1. Barton, J. M.; Shepard, P. M. *Makromol. Chem.* 1975, 176, 919.
2. Dearlove, T. J. *Appl. Polym. Sci.* 1970, 14, 1615.
3. Heise, M. S.; Martin, G. C. *Macromolecules* 1989, 22, 99. Syracuse University.

Infrared Spectra of CoHEB/DGEBA Before and After Polymerization

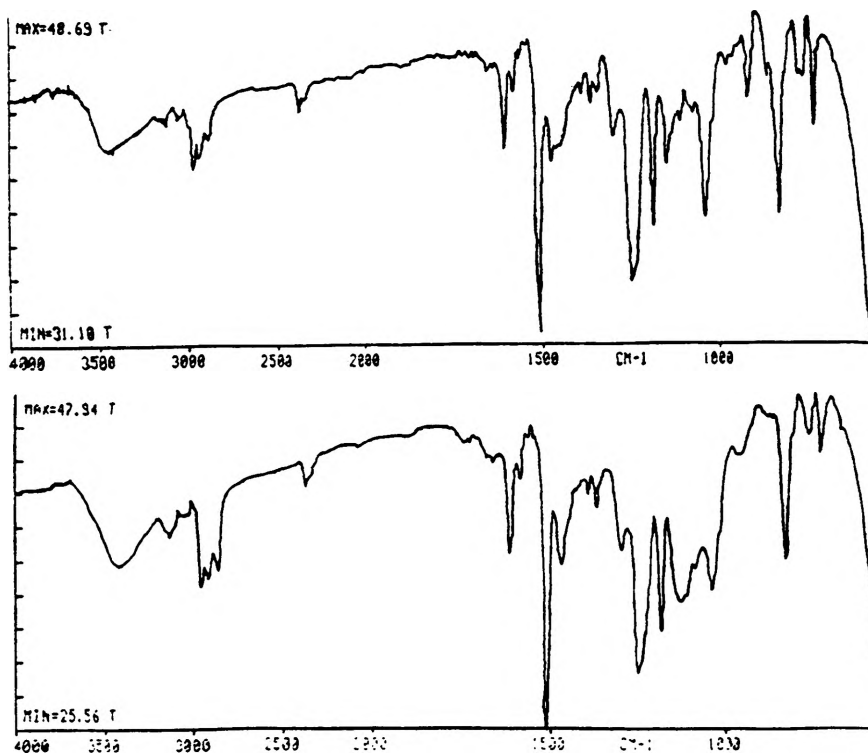


FIGURE 5

THE ELECTROCHEMICAL CHARACTERIZATION OF FERROCENE AS A GUEST MOLECULE IN THE PRESENCE OF β -CYCLODEXTRIN

Anne T. Roberson

Abstract

This experiment involves the development of electrochemical experimental methods for the determination of the oxidation/reduction potentials of a guest ferrocene complex ($C_{10}H_{10}Fe$) hosted by β -cyclodextrin. The project was conducted so that the specific interaction of two molecules forming a unique inclusion compound can be used as a model for rapid analysis of other small molecules. In principle, the study is based on the expected equilibrium interaction of the iron compound with β -cyclodextrin resulting in a complexed and an uncomplexed species equilibrium. The project's experimental objective is to determine if the redox potentials of both complexed and uncomplexed iron compounds are influenced sufficiently by β -cyclodextrin to allow simultaneous determination of the redox potentials in equilibrium mixtures. This analysis will allow the determination of equilibrium constants for interaction of guest molecules with β -cyclodextrin.

Introduction

Cyclodextrins are a series of cyclic compounds constructed from at least six units of linked glucose. (β -cyclodextrin, the one under consideration, is made up of seven linked glucose units.) Cyclodextrins are torus-shaped molecules with central cavities in which guest molecules of suitable size can be accommodated. The requirement for this inclusion formation appears only to be spatial, because all kinds of guest molecules, ranging from molar to ionic in character, are accepted. One of the most distinctive characteristics of cyclodextrins is that they are hydrophilic outside owing to the primary and secondary hydroxyl groups occupying both rims, and they are hydrophobic within the cavity because it is lined by hydrocarbon groups and ether-like oxygens.¹

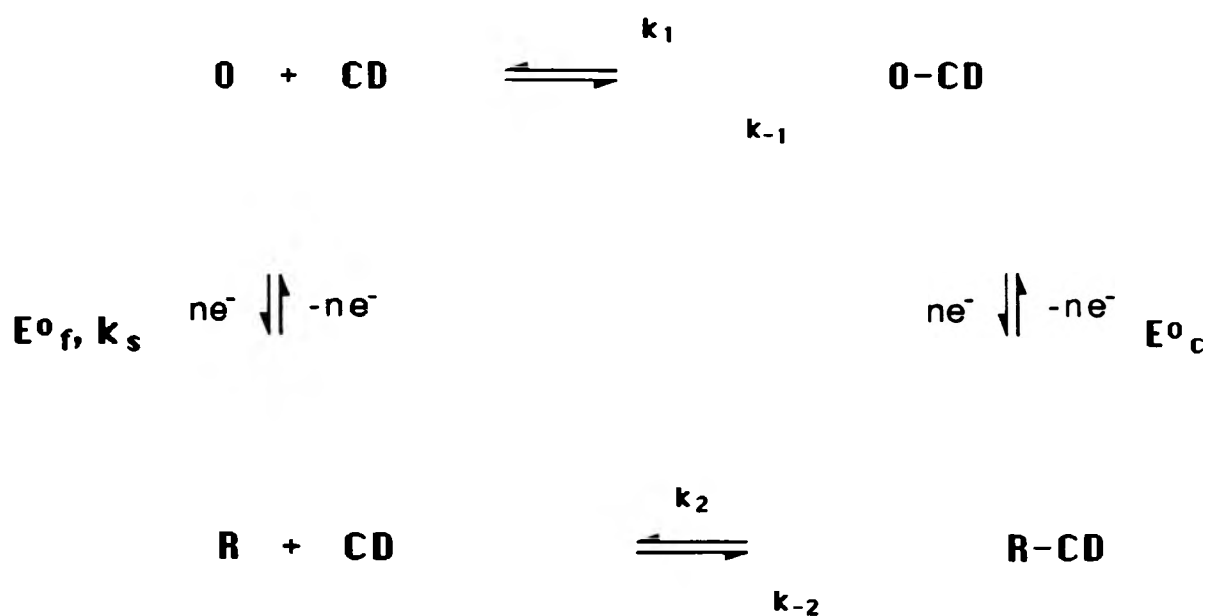
The inclusion reaction is promoted due to recognition of the guest molecules based on their size. It is also promoted upon hydrophobic interaction between the non-polar cyclodextrin interior and the guest molecule created on accommodation of the guest in the cyclodextrin cavity from the polar environment outside the cyclodextrin. Cyclodextrins become a host for guest molecules, and if the guests are electroactive in nature, this inclusion phenomena influences the electrochemistry of the guest molecules. This can be measured by cyclic voltammetry.

A cyclic voltammogram is analogous to conventional spectrum in that it conveys information as a function of an energy scan. Cyclic voltammetry is perhaps the most versatile electroanalytical technique for the study and identification of electroanalytical species.² It consists of cycling the potential of an electrode, which is immersed in an unstirred solution, and measuring the resulting current. Its effectiveness results from its capability for rapidly observing the oxidation/reduction (redox) potential over a wide potential range. The potential of the working electrode is controlled versus a reference electrode such as a saturated calomel electrode. The controlling potential which is applied across the two electrodes can be considered an excitation signal. A cyclic voltammogram is obtained by measuring the current at the working electrode during the potential scan.³ A salt is used in the solution as a supporting electrolyte.

Cyclic voltammetry is capable of rapidly generating a new oxidation state during the forward scan, and then reducing the sample or producing a new species after the reverse scan. With a reversible reaction, the cyclic voltammogram forms a sort of square mechanism⁴ (Fig. 1).

Figure 1

The Square Mechanism



E°_c, E°_f ; Formal Potential

k_s ; Standard Electron Transfer Rate

O, R; Oxidized and Reduced Species

To perform a set of viable cyclic voltammetry experiments, two things must first be done. An appropriate test procedure must be developed, and an effective electrode cleaning procedure must be found.

Experimental

Ultra-clean (electrochemical grade) dimethyl formamide was found to be an appropriate solvent, and tetrabutylammonium fluoroborate was used as the supporting electrolyte. Ferrocene is the inclusion compound discussed because it depicts theoretical trends. It formed a documented inclusion compound with β -cyclodextrin,⁵ which resembles this (Fig. 2).

The testing procedure was as follows:

1. The electrode cleaning procedure was implemented. (This consisted of a documented, three-step process⁶ entailing treatment with aqua regia, pulsing, and flaming.)
2. All glassware was cleaned.
3. The solutions to be tested were prepared.
4. The fixed amount (25 mL) of solution was measured out and placed in the testing cup.
5. The liquid was flushed with Argon gas, in order to deoxidize the solution.
6. The scan was run.

Results and Discussion

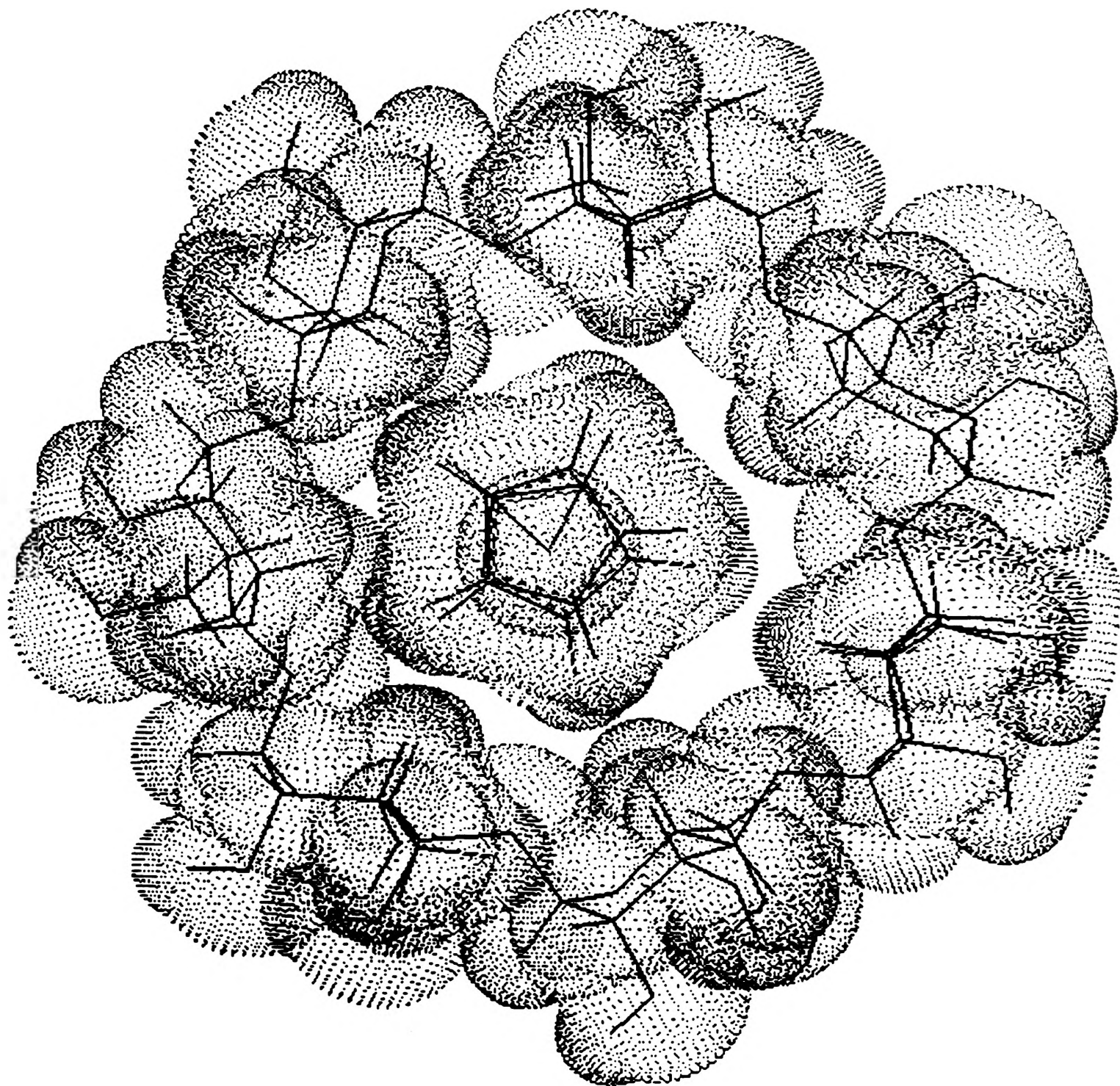
Inclusion phenomena do influence the electrochemistry of an electroactive guest molecule.⁷ Inclusion phenomena are usually characterized by the formation constant (equilibrium constant) and the formation rate constant (dissociation constant). When the guest molecule is electroactive, an electrochemical method is applicable for determining these constants and sometimes this method is superior to other methods, because information, not only on the substrate, but also on the electrogenerated species formed after the electron transfer reaction, can concurrently be obtained.

The shape of the voltammogram is sensitive to the heterogeneous electron transfer rate between the substrate and electrode, and also to the dissociation and formation rates. As demonstrated by the β -cyclodextrin/ferrocene data (Fig. 3), the addition of cyclodextrin to the electrolyte solution caused a decrease in the peak current.

Since cyclodextrin is a large macrocyclic compound, incorporation of a small guest molecule in the bulky cyclodextrin makes the apparent diffusivity of the guest lower. Diffusivity has the dimensions of a length times a velocity; obviously the greatly increased mass of the inclusion compound will slow any movement. Taking advantage of this phenomena, the formation constant of the inclusion complex can be easily determined by quantitative treatment of the variation of the peak current with a cyclodextrin concentration in solution.⁴ A much higher cyclodextrin concentration (an order of magnitude of about twenty times higher than that of the guest compound concentration) insures that all of the guest molecule goes into the inclusion state.

There is one more demonstrable change in the electrochemical nature of a transorganic metal upon the addition of cyclodextrin, and this is a shift in the apparent half-wave potential. This shift is dependent on the concentration of cyclodextrin. Detailed analysis of

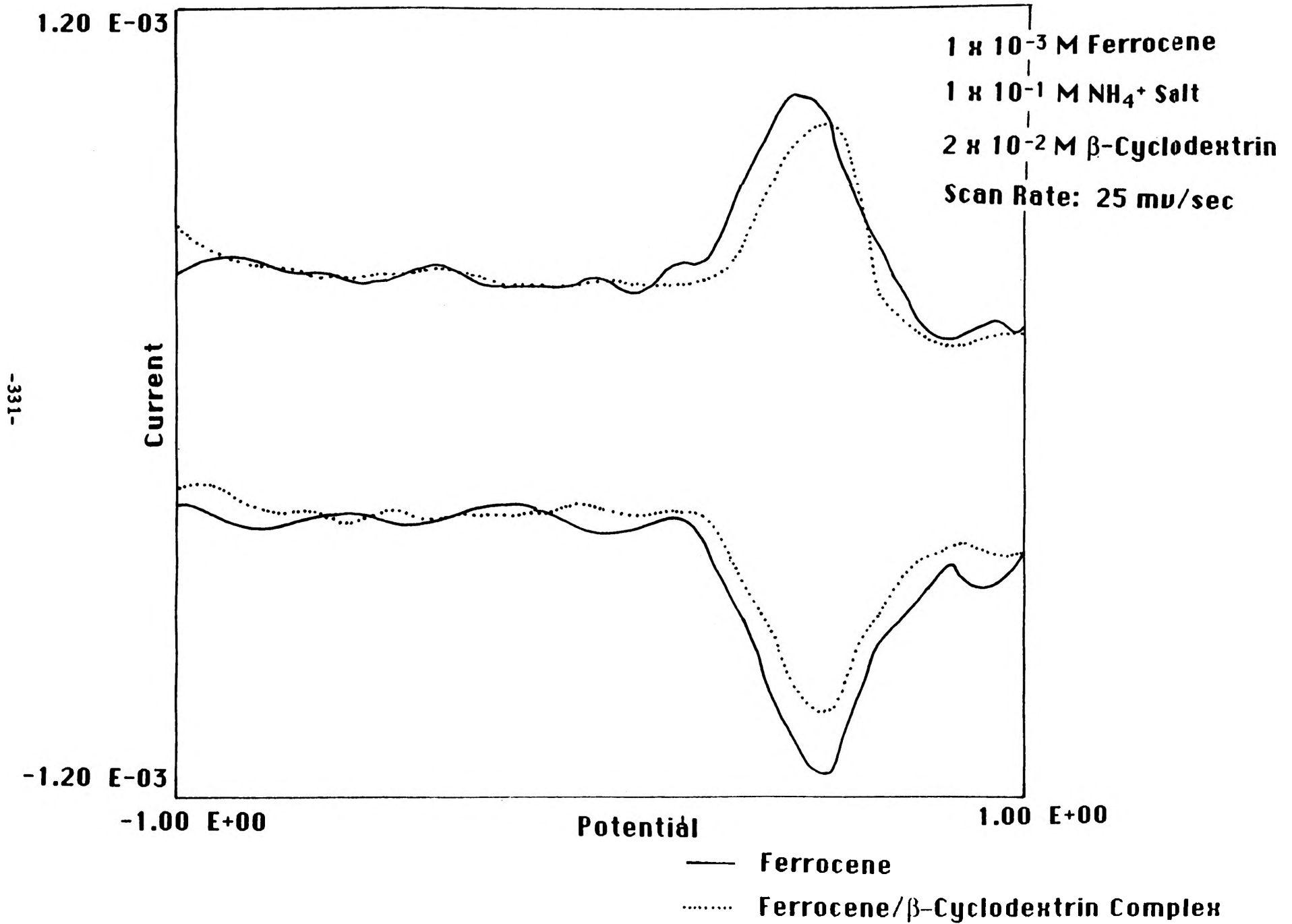
Figure 2



Ferrocene/ β -Cyclodextrin Inclusion Compound

Figure 3

Ferrocene/ β -Cyclodextrin Cyclic Voltammograms



this shift can also lead to the equilibrium constants of the cyclodextrin complexes.⁴ This was also readily observable in the β -cyclodextrin/ferrocene data (and can be seen in Figure 3).

Conclusion

The objectives of this study were to:

1. Discover the electrochemical conditions needed to monitor β -cyclodextrin and an inclusion compound.
2. Demonstrate the theoretical shift in electroanalysis of an active species upon bonding with β -cyclodextrin.

These were met successfully.

A third objective was to determine the equilibrium constant of the β -cyclodextrin/organometallic bonding. This is the point to which research has culminated. Future developments will include: the actual determination of the equilibrium constant for the ferrocene inclusion compound, the study of how species concentration affects the equilibrium constant, and expansion to consider other transorganometallic guest molecules.

References

1. Saenger, W., I. Intl. Symp. on Cyclodextrins. 1981, 1, 141.
2. Kissinger, P. T. and Heineman, W. R. J. Chem. Ed. 1983, 60, 702.
3. Evans, D. H., O'Connell, K. M., Petersen, R. A., and Kelly, M. J. J. Chem. Ed. 1983, 60, 290.
4. Matsue, T., Osa, T., and Evans, D. H. J. Inclusion Phen. 1984, 2, 547.
5. Armstrong, D. W. Anal. Chem. 1985, 57, 481.
6. Goldstein, E. L. and VanDeMark, M. R. Electrochem. Acta. 1982, 27, 1079.
7. Wojcik, J. F. Bioorg. Chem. 1984, 12, 130.

ENANTIOMERIC SEPARATION BY CLOUD POINT PRECIPITATION OF CYCLODEXTRINS

Deanna L. Schmid

Abstract

Certain cyclodextrins exhibit a diminishing solubility in water when heated. This phenomena of cloud point precipitation in conjunction with cyclodextrin's ability to form an inclusion complex with many compounds, can be used as a method of chemical separation. These cyclodextrins can be removed from the solution after precipitation by a hot filtration technique and the remaining solution analyzed by HPLC. Enantiomeric separations, concentration of compounds and removal of hazardous organic materials are all possible applications of cloud point extraction using cyclodextrins.

Introduction

Surface active agents have been used for years in many separation processes.¹ These processes are classified as either micellar or nonmicellar methods. A nonmicellar process is one in which no aggregation of the surfactant is required for the separation method to be effective. Examples of nonmicellar processes are foam flotation, precipitation and ion interaction chromatography.² A micellar process is one in which the surfactant must reach the critical micellar concentration and form micelles to be effective as a separation technique.³ Examples of micellar techniques are liquid-liquid extractions and membrane techniques.⁴ Cyclodextrins are surface active agents that form cloudpoint precipitates in a nonmicellar manner.⁵ Cloud point extractions have one other critical property that must be met. The temperature of the aqueous solution must reach the point where precipitation of the aggregated surfactant occurs. This temperature is called the cloud point temperature.

Cyclodextrins are cyclic oligosaccharides which have a toroidal shape. The interior of the cyclodextrin is hydrophobic, while the outside is lined with hydroxyl groups which are hydrophilic. These properties give cyclodextrin the capability of forming inclusion complexes with many organic molecules. Molecules that have been shown to form the best inclusion complexes with cyclodextrins have at least one aromatic ring.⁶ Cyclodextrins are also capable of chiral recognition and have become popular in that respect within the last decade.⁷

Experimental

The cyclodextrins were tested for cloud point precipitation at various temperatures and concentrations using the following method. Cyclodextrin was added to the specified amount of water in a test tube. That test tube was placed in a beaker filled with water. A magnetic stir bar was put into the beaker. The beaker was then placed on a hot plate/magnetic stirrer which was the source of temperature control and heat distribution. A thermometer was placed in the beaker to record the exact temperature.

The filtration was done using a Pyrex vacuum filtration apparatus, Nylon 66 0.45 micron filters and a standard oven set at 120 degrees Celsius. The filtration apparatus was heated for 20 minutes and quickly used for filtering. Before filtering the cyclodextrin was added to 10 ml of water and heated as previously described for 20 minutes at 65 degrees Celsius water bath.

The method to determine enhancement of the enantiomeric compounds was done using 0.005M permethyl-2-hydroxypropyl- β -CD and 0.005M compound. One filtration was done using only the compound in solution with water. This run was used as the standard to compare to the filtrate of the solution with the compound and cyclodextrin. Both filtrations were done as

described in the previous paragraph. HPLC with a B-cyclodextrin analytical column was used to analyze the standard and CD solutions after filtration. A mobile phase of methanol/1% TEAA (pH 4.1) was used in different ratios for all compounds. A flow rate of 1 ml/min was used. Ultraviolet detection at 254 nm was used for all compounds.

Results

Cyclodextrin	Critical Concentration	Cloud Point Temperature
Beta-Cyclodextrin	----	----
Hydroxyethyl-beta-CD	----	----
Hydroxypropyl-beta-CD	----	----
Methyl-beta-CD	----	----
Permethyl-2-hydroxypropyl-gamma-CD	0.0016	45
Permethyl-2-hydroxypropyl-alpha-CD	0.0017	49
Permethyl-2-hydroxypropyl-beta-CD	0.0016	45

Compound	Mobile Phase	Percent Enhancement
Mephobarbital	20/80	0
Mephénytoin	20/80	0
Dansyl-DL-leucine	35/65	0
Dansyl-DL-phenylalanine	35/65	0
Dansyl-DL-valine	35/65	0
Dansyl-DL-norleucine	35/65	0

Conclusions

All members of the permethyl-2-hydroxypropyl-cyclodextrin family were found to exhibit the cloud point precipitation phenomena. A hot filtration method was devised to filter off the precipitated cyclodextrin. Although no enantiomeric enhancement was evident in this limited study, further experimentation is underway to provide more complete results. There are also many other possible uses for the cyclodextrins that form a cloud point precipitate, many of which are currently being investigated.

Acknowledgments

Dr. Daniel W. Armstrong, Faculty Advisor for OURE Project, Professor of Chemistry, University of Missouri-Rolla.

References

1. D. W. Armstrong, *Separation and Purification Methods*, 14, 213(1985).
2. D. W. Armstrong, *Separation and Purification Methods*, 14, 213(1985).
3. B. Lindman, H. Wennerstrom, and H. F. Eicke, "Micelles", *Topics in Current Chemistry* No. 87, Springer Verlag, New York, 1980.
4. D. W. Armstrong, *Separation and Purification Methods*, 14, 213(1985).
5. D. W. Armstrong, *Separation and Purification Methods*, 14, 213(1985).
6. S. M. Han and D. W. Armstrong, *J. Chromatogr.*, 389(1987) 256.
7. S. M. Han and D. W. Armstrong, *J. Chromatogr.*, 389(1987) 256.

A Measurement of the Relative Efficiency of a Channeltron

Steve Scott

The original goal of this project was to determine the characteristics of a channeltron, a device used to detect electrons. While most channeltrons have entrance cones which are quite small, the channeltron we were to study had a significantly larger one. Due to its large size, the possibility existed that the channeltron would be more efficient at detecting electrons which hit near the center of the channeltron entrance than at detecting the electrons which hit near the edge. The main purpose of the experiment was to determine the relative detection efficiency of the channeltron as a function of the position where the electrons hit it.

Before describing the experiment itself, it is necessary to explain how a channeltron works and what the motivation for this experiment was. A channeltron is a device which amplifies a very weak electron signal to the extent that it can be detected by an ammeter. A schematic of a channeltron is shown in figure 1. When an electron strikes the semiconductor surface of the channeltron, secondary electrons are produced which are attracted toward the throat of the channeltron by an applied voltage. As the electrons enter the throat of the channeltron, they strike the sides, causing more secondary electrons to be produced. This "avalanche" process continues until the electrons reach the end of the channeltron, where they are collected and measured by an ammeter. This amplification is large enough to allow the detection of a single electron. In most channeltrons, the conical entrance surface has a diameter of about .5 cm which is small enough that the location where the electron first strikes is unimportant. However, the channeltron we are studying had an entrance cone with a diameter of 2.5 cm. This meant that an electron striking the channeltron near the edge of the entrance aperture would have a significantly lower chance of being detected than one which struck the device near its center.

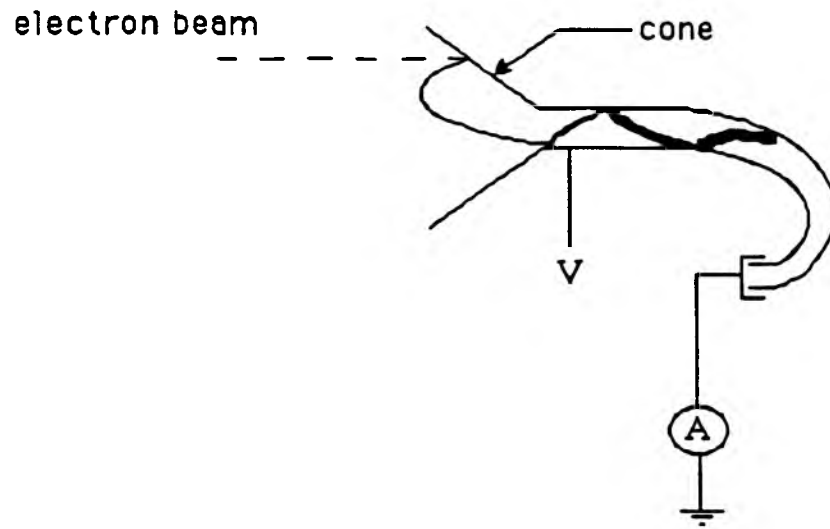


Fig.1 Schematic of channeltron.

In the experiments in which this channeltron was to be used, it was very important to know the relative detecting efficiency of the channeltron as a function of where the electron strikes. The efficiency was to be measured by scanning an electron beam across the mouth of the channeltron and measuring the current produced in the channeltron. Therefore, an electron beam whose characteristics were well-known and which could be finely controlled was needed.

I was required to use a vacuum system, since a channeltron is only operational under a vacuum. Fortunately, a facility was available which was small enough to allow the system to be quickly pumped down to vacuum and brought up to air, although it was necessary to thoroughly clean the system and replace some of the components of the system which had been removed. The vacuum system could be pumped down to a vacuum of approximately 10^{-6} torr in about 2 hours and could be brought up to air in about 5 minutes. This capability also greatly facilitated the testing of the electron gun, since the gun could not be tested at atmospheric pressure.

After familiarizing myself with the vacuum system, I began work on the electron gun, which was needed to supply the electron beam for the experiment. The electron gun was taken from an oscilloscope and slightly modified to withstand the stresses the gun would experience in going from atmospheric pressure to vacuum and back. The electron gun consisted of a simple tungsten filament, an Einsel lens, and two sets of deflectors. The electrons were emitted from the filament when a current passed through it. They were pulled through the Einsel lens, a set of three collimators used to focus the beam, and deflected by voltages applied to the deflectors. In order to obtain an electron beam from the gun, voltages were applied to the collimators and deflectors of the gun. After much trial and error, a combination of voltages was found which produced an acceptable electron beam of small cross sectional dimension. I then spent a great deal of time trying, unsuccessfully, to characterize the electron beam. Although an absolute value for the current produced by the beam was dependent on too many experimental conditions to make

it readily reproducible, a typical plot of the current coming from the gun versus the current flowing through the filament in the gun is shown in figure 2. This data was used to determine the optimum filament current.

The most difficult and most important characteristic of the beam was its profile. This information was necessary in order to minimize the width of the beam which was required in order to obtain the best measurements of the efficiency of the channeltron. An example of one of the better measurements is shown in Figure 3. From plots such as the one in figure 3, we could determine the width of the beam. Although some preliminary results looked respectable, in further experiments, the electron beam proved to be extremely sensitive to various experimental conditions such as pressure, the time that the gun had been running, the filament current, and possibly other unknown conditions. At this point, I voluntarily terminated my involvement in the project. Work on this project was continued by Jason Sutin.

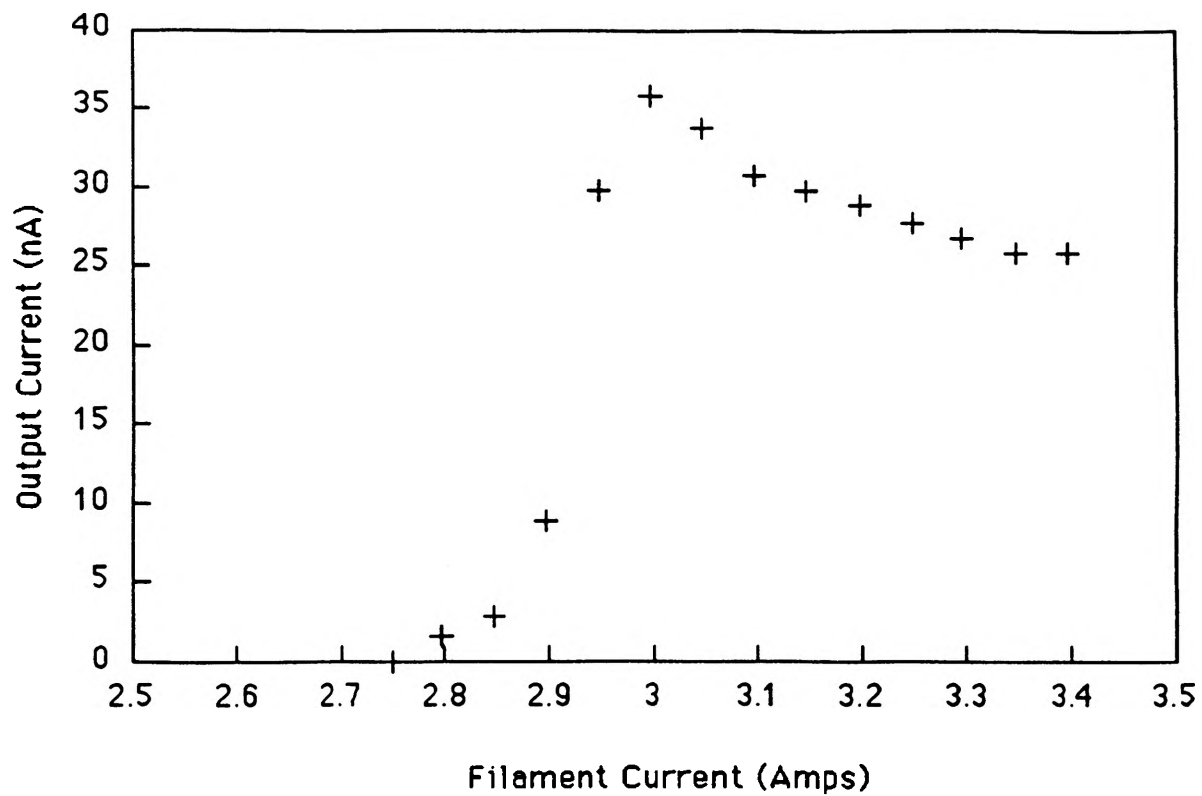


Figure 2. A plot of the output current from the electron gun versus the filament current.

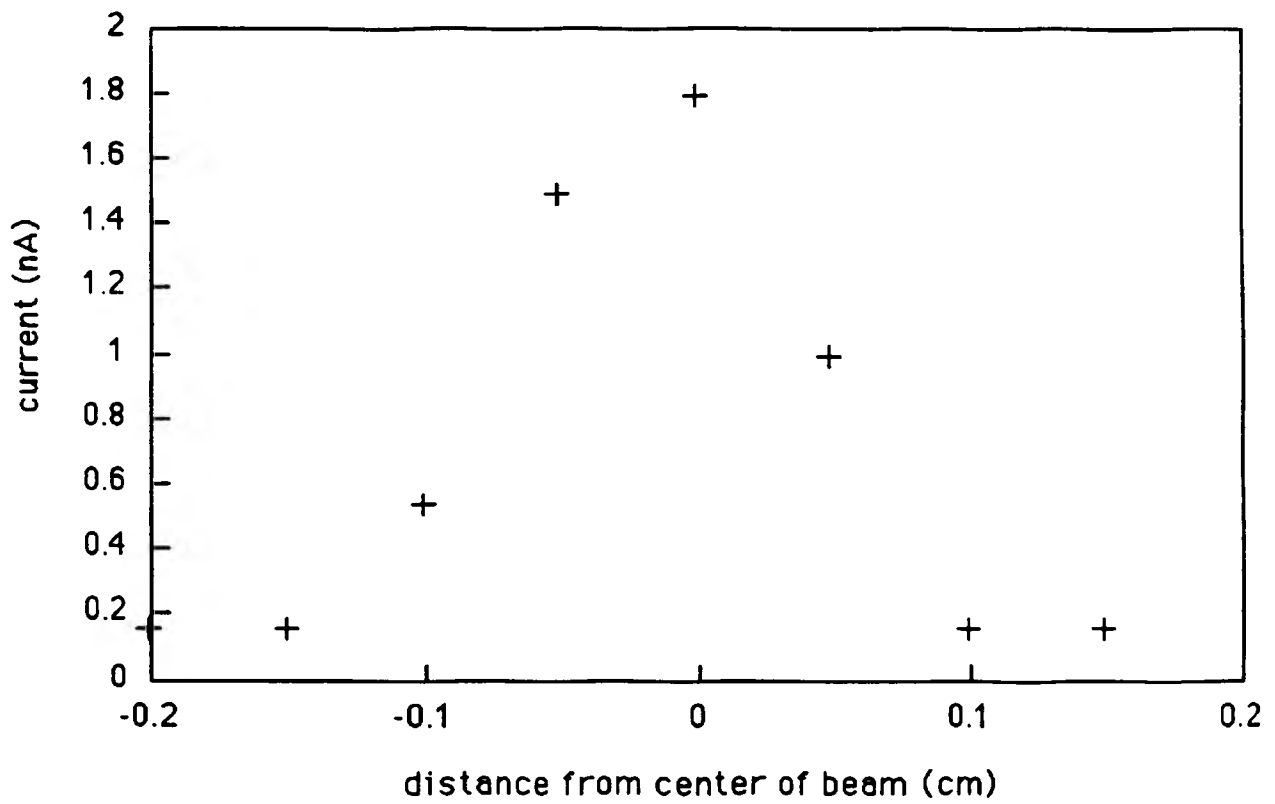


Figure 3. Profile of electron beam.

EVALUATION OF FILM COATED WINDOW GLASS SUBJECTED TO THE EFFECTS OF WINDSTORMS

Ronald B. Shankland Jr.

Introduction

The harm incurred by structures, equipment, and people due to window unit failure during a windstorm is drastically reduced if the glass remains in the frame until the storm has subsided.

There are basically two types of window glass used in curtain wall cladding systems: heat treated and annealed. Heat treated glass is tempered during its manufacture so that it retains residual surface stresses in the range of 3500 psi to 10,000 psi, or more. Annealed glass is cooled very slowly under controlled conditions in order to remove undesired internal stresses (Reznik, 1987). Also known as float glass, annealed glass is manufactured by floating molten glass on a bed of molten tin and then allowing it to cool very slowly (Minor, 1990a). Annealed glass is generally less expensive and easier to cut to size than heat treated glass. It is the basic type of glass used in architectural glazing (Minor, 1990a).

These two basic types of glass can be used as a single layer (monolithic) or combined (laminated or layered). Previous research (Behr *et al.*, 1985; Reznik *et al.*, 1987; Vallabhan *et al.*, 1987; and Pantelides *et al.*, 1991) has shown that laminated glass performs well in windstorm situations, especially if the glass is held in the frame with a silicone sealant.

In order to improve resistance against fallout after breakage, it has been proposed that a surface film (usually polyester) be applied to monolithic annealed glass. An economical way to make new window glass safer, it may also be a relatively inexpensive way to retrofit existing windows.

Background and Previous Research

Architectural glass has been receiving much scrutiny over the past two decades. Prior to this period, window glass was not given much attention during the design phase of a building project. The architect was primarily concerned with the aesthetics of glass treatment and selection of glass was a relatively simple procedure as noted by Minor (1990a). The architect would simply determine the thickness of the "plate" glass for a given opening size by referring to a single chart. This chart had been developed by glass manufacturers over 25 years ago. Many building codes still adhere to these principles, although they may have been slightly modified.

Past failures of glass in such high-rise buildings as the John Hancock building in Boston and the Sears Tower in Chicago have highlighted the need for a more in-depth analysis. In particular, these failures have drawn attention to a vital detail concerning the failure of glass cladding – what happens to the glass when the window breaks? In a ground floor office this can be inconvenient and somewhat dangerous, but when large glass shards plummet to street level from many tens of stories above, the danger is immediately apparent (Minor, 1990b). In addition, modern office buildings contain equipment and furnishings such as computers, copiers, and telephone systems, that are expensive and sensitive to adverse environmental conditions (Harris, 1978).

The energy crisis of the 1970's caused additional changes in the materials and techniques available for architectural glazing (Minor, 1990a). Tinted, coated, and insulating glass

appeared on the market as alternatives for standard "plate" glass. These new types of glass provide increased energy savings through their reflective and insulating properties. Also, laminated glass was made available to improve safety and is now seeing widespread popularity in the building industry.

It was determined through previous research (Beason, 1974; McDonald, 1976; Minor, 1976) that much of the glass breakage occurring during windstorms was attributable to two primary factors: uniform lateral pressure and missile impacts.

The term "uniform" may be misleading because it implies a steady-state loading condition. In truth, lateral loading of window glass can fluctuate both in magnitude and direction. The aerodynamics involved with a structure, or series of structures, in a windstorm can be extremely complicated. Understanding of this phenomena is being improved by the use of wind tunnel testing to determine wind pressures at various locations on the building (Minor, 1990b). Glass on the windward side of the building may experience strong pressures while the glass at the corners and on the leeward side may experience strong negative pressures, i.e., suction. As wind direction and velocity changes, so does the loading configuration on the glass. A single window may experience many cycles of positive and negative pressure in varying intensity due to gusts and turbulence. Minor (1976) noted that window breakage did not occur solely during extreme windstorms (i.e., tornadoes and hurricanes), but that many failures occurred when maximum recorded windspeed velocities were at or below the design velocity.

Missile impacts also effect glass breakage. Extreme wind conditions, such as those in effect during a tornado, may carry objects as large and heavy as automobiles, trees, lumber, and bricks. Wind velocities of a more moderate nature, however, can carry smaller objects which may also be hazardous to window glass. Minor (1976) discussed the propensity of roofing gravel being injected into the windstream through one of three mechanisms: explosive injection, ramp injection, and aerodynamic injection.

Explosive injection occurs when a roofing system fails due to a large pressure differential between the interior and exterior of a building and the gravel is injected into the windstream. Ramp injection occurs when roofing gravel, moving laterally due to horizontal wind pressures, strikes a protuberance. The gravel particle then incurs a vertical component to its velocity and is injected into, and carried by, the windstream. The Bernoulli Effect is primarily responsible for aerodynamic injection. Rapidly moving air above a layer of gravel has a lower pressure than the stagnant air below. If this pressure difference exceeds the weight of the gravel particle, it will be lifted into the windstream and carried away.

Once airborne, it becomes a question of whether or not the wind can sustain the gravel as missiles. Minor (1976) showed that it was indeed possible and that gravel could attain sufficient impact velocities to damage or break window glass.

Objectives

The purpose of this research was to determine the effectiveness of surface applied film on monolithic, annealed window glass for preventing excessive loss of glass particles after small missile damage and windstorm induced stresses. In addition, the missile damage characteristics of the "tin side" and the "air side" of the glass was explored. The "tin side" of the glass is the surface of annealed float glass that had been in contact with the molten tin during its manufacture. The other side of the glass pane is known as the "air side".

Research Plan

The research plan was designed to test twelve specimens of 58 by 96 by 3/8 inch annealed glass lights with a 0.004 inch (4 mil) thick polyester film applied to one surface. The film tested in this research was product number CL-400-X, manufactured by Madico, Inc. The advertised properties of the film include: 85% visible light and 0 to 4% ultraviolet light transmission, single-ply, 25,000 psi tensile strength, 100 pounds per inch width break strength, acrylic pressure sensitive adhesive, and 4 to 5 pounds per inch peel strength.

Two sets of parameters were evaluated. Three identical specimens were tested for each combination of the two parameters.

The first parameter to be evaluated was the film coverage. In all cases, the film was applied only to the surface that would be facing the interior of the building. This surface would not receive missile impacts. One set of six windows was fully covered with the film and the other set had the film trimmed back one-half inch all the way around the perimeter. If an existing window were to be replaced with a new window, it is possible that the new window could be completely covered with film. On the other hand, if an existing window were to receive an in-situ film application, it could only be applied up to the edge of the gasket holding the glass in the frame.

The second parameter to be evaluated was missile velocity. A 2.03 gm steel ball bearing was used as the missile. One half of the window specimens were impacted by missiles travelling at the lowest velocity capable of causing observable damage. This is known as the Minimum Damage Threshold Velocity (MDTV). Threshold damage is the lower limit of damage which can be seen at arm's length in good light. Generally it was a very small nick in the surface of the glass which would otherwise be barely noticeable. Minor (1990a) points out that as a rough general rule, any surface imperfection that is visible at arm's length reduces the strength of the glass at this point by half. Also, we took note of the differences, if any, in the velocities required to cause minimum damage between the "tin" side and the "air" side of the glass. The other six windows were impacted by missiles at a velocity of 80 miles per hour (117 fps). This velocity was chosen because it represents the average velocity of roofing gravel missiles being carried by a 100 year mean recurrence interval windspeed in most areas of the country.

All of the specimens in this test series were dry-glazed, that is, they were held in the frame by neoprene gaskets as commonly used in curtain wall glazing systems.

The numbering system employed to identify these specimens was based upon the above-listed conditions:

F = Surface Applied Film
D = Dry Glazed
DT = Minimum Damage Threshold Velocity
HV = High Velocity
T = Trimmed Film
F = Full Film Coverage

A numeric suffix identifies individual specimens. For example, F-D-DT-F-2 identifies the second specimen of the series which was dry glazed, impacted at MDTV, with full film coverage.

The following specimens were tested:

	<u>Full Coverage</u>	<u>Trimmed Coverage</u>
Minimum Damage	F-D-DT-F-1	F-D-DT-T-1
Threshold Velocity	F-D-DT-F-2	F-D-DT-T-2
	F-D-DT-F-3	F-D-DT-T-3
High Velocity	F-D-HV-F-1	F-D-HV-T-1
	F-D-HV-F-2	F-D-HV-T-2
	F-D-HV-F-3	F-D-HV-T-3

Test Equipment

The procedures followed and equipment used in this test closely parallel those used by Pantelides, Horst, and Minor (1991) for their work on "Evaluating Post-Breakage Behavior of Architectural Glazing in Windstorms". The glass testing facility at the University of Missouri-Rolla consists of a specimen holding table with pressure/vacuum chamber, two 500 gallon pressure/vacuum holding tanks, air cannon and alignment system, and control and data acquisition station.

The specimen holding table and chamber allowed the glass pane to be dry-glazed into a standard aluminum curtain wall frame and then be subjected to missile impacts and pressure/vacuum cycles. The chamber was instrumented with a liquid water manometer for measuring both the pressure and the vacuum applied to the specimen.

The pressure/vacuum holding tanks permitted relatively large volumes of air to be moved into or out of the pressure/vacuum chamber on the specimen table. This process was controlled for the most part by manually-operated valves; however, one window was partially cycled by a computer that monitored pressure transducers and controlled the valves. When manually operated, the valve operator would watch the manometer during pressure or vacuum application.

The air cannon was used to accelerate the 2.03 gm missiles to the required velocities. Cannon operation was managed from the control and data acquisition station. The operator was able to load and fire the cannon by remote control from this station and was also able to read and record the data relating to the muzzle velocity of the missile. Positioning the cannon was accomplished with the aid of guide tracks mounted on the floor and ceiling and a vertical standard mounted on wheels between the tracks. The cannon was affixed to the standard. Both the tracks and the standard were measured and marked to enable precise and repeatable alignment of the cannon.

Muzzle velocities were obtained through the use of a digital timer that measured the time required for the missile to travel 12 inches between two light beams in the cannon barrel. Velocities in feet per second were calculated by taking the reciprocal of this reading.

Other equipment included an ultraviolet lamp to detect traces of tin on the "tin side" of the glass, a dial gauge and mounting bar for measuring out-of-plane deflections of the pane, and an electronic balance for weighing the amount of glass ejected from the window.

Test Procedure

The film was applied to all glass specimens by technicians at Taylor Glass Company in Rolla, Missouri. They picked up the glass from the testing facility and took it to their

workshop where they applied the film in accordance with the manufacturer's specifications. An applicator solution, provided by Madico, was employed as a slip agent to neutralize the pressure sensitive adhesive during application. After the specified curing time, Taylor Glass Company returned the finished specimens to the glass testing facility.

The pressure/vacuum chamber was prepared for testing by affixing a plastic shroud to the inside of the chamber and sealing its perimeter with duct tape. The purpose for the shroud was to enable testing to continue even if the window partially failed and remained in the frame. The shroud would seal small holes and tears in the film, as well as breaches in the gasket system, and allow pressure to be maintained against the window. This step was necessary because of an inability to provide the volume of air commonly associated with actual windstorms. Use of a plastic shroud is permitted in accordance with ASTM 1233-88, paragraph 10.1.1, as long as the shroud does not impart any additional strength to the specimen. Similarly, a shroud was placed on the outside of the window when breaches occurred during the vacuum phase of the test.

Observations were made with the aid of ultraviolet lamp to determine if the "tin side" or the "air side" of the glass would be receiving the missile impacts. The window was then cleaned with a glass cleaning solution and mounted in the frame using standard dry-glazing techniques. Particular attention was paid to ensure that all specimens, especially the trimmed film specimens, were properly centered in the frame. The film side of the pane was on the inside of the chamber. Note that the inside of the chamber corresponds to the inside of a building, thus, a vacuum applied in the chamber would correspond to a pressure applied to the outside of the building. Pressure applied in the chamber would correspond to an outward acting pressure ("negative" pressure or suction) on the building.

The window was then subjected to missile impacts with the air cannon. Previous experience with observed field damage indicated that a window typically encounters approximately five impacts per square foot during a windstorm (Pantelides *et al.*, 1991). Consequently, a semi-random pattern of 190 impact locations was used. For the minimum damage threshold velocity, each location was impacted with a very low velocity missile and then the velocity was increased in very small increments until detectable damage occurred. For high velocity missile impacts, the velocity was adjusted as close to 80 mph as possible before actually impacting the window. Then the window was impacted with small adjustments being made to the cannon's air pressure to maintain the desired missile velocity. The glass dislodged by high velocity missile impacts was collected and weighed.

The next step was to subject the missile damaged windows to windstorm loadings. The pressure/vacuum cycles intended to simulate the loading conditions experienced during a windstorm were previously established by Pantelides *et al.* (1991). The vacuum sequence consists of 12 low vacuum cycles (33.8 psf) followed by one medium vacuum cycle (45 psf). This was repeated for a total of 5 times and then one high vacuum cycle was applied (56.3 psf). Each load was held for a duration of three seconds. The pressure sequence followed with the same pattern of low, medium, and high pressure cycles, but the magnitudes were 133% of the vacuum values (i.e., 45 psf, 60 psf, and 75 psf). These two sets of cycles were to be repeated eight times. The out-of-plane deflections were measured, if possible, for the last three loadings at the end of a sequence. Dislodged glass particles were collected and weighed at various times throughout the vacuum/pressure cycle sequence.

Failure of the window system occurred due to one of two events: either it became impossible to maintain loading due to excessive leaks or the window glass fell out of the frame. At this point the remaining loose glass was collected and weighed. The failed window was then disposed of after careful inspection for any abnormalities.

Results

Listed below is a brief group summary and then notes specific to each of the twelve windows tested in this research. Following the individual notes is a general summary of results.

<u>Specimen</u>	<u>Vacuum</u>	<u>Pressure</u>	<u>Failure Mode</u>
F-D-DT-T-1	60L, 5M, 1H	4L	Film Tear, Gasket
F-D-DT-T-2	60L, 5M, 1H	1L	Gasket
F-D-DT-T-3	60L, 5M, 1H	2L	Gasket
F-D-HV-T-1	24L, 2M,		Corner delam, Gasket
F-D-HV-T-2	50L, 4M,		Gasket
F-D-HV-T-3	36L, 3M,		Corner delam, Gasket
F-D-DT-F-1	60L, 5M, 1H	12L, 1M	Gasket
F-D-DT-F-2	60L, 5M, 1H	1L	Gasket
F-D-DT-F-3	60L, 5M, 1H	1L	Gasket
F-D-HV-F-1	48L, 4M,		Gasket
F-D-HV-F-2	20L, 1M,		Corner delam, Gasket
F-D-HV-F-3	36L, 3M,		Film tear, Gasket

F-D-DT-T-1: Average Minimum Damage Threshold Velocity (AMDTV) was 18.4 fps, "tin side" was impacted, Low Vacuum #60 (LV60) had a 0.450" inward deflection, Medium Vacuum #5 (MV5) had a 0.525" inward deflection, High Vacuum #1 (HV1) had a 0.600" inward deflection. After first low pressure loading there was extensive cracking from the center to the corners and some delamination along the larger cracks. Cracking seemed to have originated near the center of the pane. Edge damage which occurred during installation appeared to have no effect. A horizontal tear in the film near the middle of the pane one inch wide and nearly the width of the opening made it difficult to maintain full pressure. Gasket came out during the last pressure cycle causing the end of the test.

F-D-DT-T-2: AMDTV 19.4 fps, "tin" or "air" side not known, LV60 0.400", MV5 0.540", HV1 0.630". Full plate response cracking occurred on Low Pressure #1 (LP1). Gasket failed on Low Pressure #2 (LP2) and the window fell out of the frame onto the floor. About two feet of glass broke off into the frame.

F-D-DT-T-3: AMDTV 17.0 fps, "tin side", LV60 0.430", MV5 0.540", HV1 0.650". Gasket failure after LP2.

F-D-HV-T-1: Average missile velocity 116.3 fps. "Tin side". About 70% of missile damage was crushed cone and 30% was crushed cone with 1" local radial cracking. Crushed cone diameters averaged 2 inches with a 1/4" ring of film delamination around the cone. Low vacuum #1 (LV1), extensive full plate response cracking, glass is cracked into block about 65 sq in., some 1/8" wide delamination of film at the cracks, one inch permanent deflection (PD). LV12, 1-5/8" PD. MV1, 1-7/8" PD. MV2, about 72 sq in. of upper right corner film is delaminated. Unable to maintain vacuum. Applied a plastic shroud to seal the leak. LV25, failure. Top half of the window came out of the frame and was stopped only by the specimen table and chamber. Film was not torn; however, it was delaminated, especially in the corners.

F-D-HV-T-2: Average missile velocity 116.4 fps. "Tin side". About 50% of missile damage was crushed cone and 50% was crushed cone with 1" local radial cracking. Crushed cone diameters averaged 2 inches. LV1, cracked into blocks about 72 sq in., 1/2" PD, some 1/8" wide delamination along cracks. LV12, wedge gasket popped out from 12" to 20" along the top edge from left corner. LV24, gasket popping out from 18" to 30" from bottom on right side. MV4, 2-1/2" PD, gasket or small delamination is leaking, applied shroud to seal against further

leakage. LV50, failure. Glass came out of rabbet along left half of top and top 2/3 of left side. Window is still in the frame. Applied pressure to blow failed window out of frame. The window was angled 30 to 40 degrees about right edge before it fell out of the frame. The exposed film due to delamination was not as sticky as it was on other specimens.

F-D-HV-T-3: Average missile velocity 116.9 fps. "Tin side". About 50% of missile damage was crushed cone and 50% was crushed cone with local radial cracking. Crushed cone diameters averaged 2 inches with a 1/4" ring of film delamination around the cone. MV1, corners show serious evidence of delamination, film is about to pull away from upper right corner. MV2, 2-7/8" PD. MV3, upper left corner has pulled away, top wedge gasket coming out, 1-5/8" by 2-3/4" piece of glass falls from upper left corner. LV37, failure. Upper left corner half way down left side and half of the top wedge pulled out. Film did not tear: corner pulled away.

F-D-DT-F-1: AMDTV 14.0 fps, "air side", LV60 0.4", MV5 0.5", HV1 0.6". Explosive full plate response cracking originating near the center of the window during Medium Pressure #1 (MP1). The light cracked into several pieces. Failure occurred when the glass fell out of the frame due primarily to gasket failure. The exposed delaminated film was not very tacky. The film did not tear. Full pane film coverage and a full month of curing appeared to have made no difference.

F-D-DT-F-2: AMDTV 20.6 fps, "air side", LV60 0.456", MV5 0.544", HV1 0.640". All low vacuum loads were controlled by the computer, medium and high vacuums and the low pressure load were manually controlled. In general, the computer overshot the required loads by several psf. It does not appear that this made a difference in the failure mode. Failure occurred due to the gasket coming out of the frame. It peeled out along the top and then down the sides. Explosive full plate response cracking occurred just prior to gasket failure. The shroud pushed the window out of the frame, top first. Very little film delamination. Most of the delamination happened in the upper right and left corners, but this may have occurred due to falling on the floor.

F-D-DT-F-3: AMDTV 19.3 fps, "tin side", LV60 0.421", MV5 0.540", HV1 0.624". Top and left wedge gaskets peeled from upper left corner as window swung out as if hinged on the right. Glass then folded down upon itself. All four wedge gaskets and the right side preset gaskets were pulled out. Definitely gasket failure. There was explosive full plate response cracking just prior to failure. The shroud pushed the light out of the frame, top left corner first. Very little delamination. No tearing of the film. The film that was delaminated was somewhat sticky.

F-D-HV-F-1: Average missile velocity 116.2 fps. "Tin side". About 50% of the damage was a crushed cone and the other 50% was crushed cone with local radial cracking. Average diameter of the crushed cones was 2 inches. LV1, cracking started in middle of pane. LV4, 3/4" permanent deflection (PD). LV8, 7/8" PD. LV10, Bottom wedge gasket starting to pull out in middle of frame. LV12, deflected 0.870" during loading. MV1, 1- 7/8" PD. LV17, delamination begins in upper left and right corners. LV22, bottom wedge gasket almost all the way out. MV2, 2-1/8" PD. LV35, delamination starting in lower left corner, no tears in the film yet, very little leakage through areas of delamination, even in the corners. MV3, 2-1/2" PD. MV4, failure. Upper left corner pulled in, then the upper right corner, then the wedge gasket peeled out of both sides down to 2/3 of the window height. Then the upper wedge gasket failed and the glass pulled into the frame all the way across the top. Unable to maintain further pressure.

F-D-HV-F-2: Average missile velocity 116.2 fps. "Tin side". Average diameter of crushed cone was 2 inches. About 50% crushed cone and 50% crushed cone with local radial cracking. This specimen appears to have been poorly laminated. There are several spots where

insects, hair, dust, and dirt are trapped under the film. The worst places are in two areas: the first is in the upper right corner (8" high by 12" wide) and the other is about 12" wide and extends from 2 feet below the top to about 5 feet below the top. In these areas the film is about 50% delaminated due to improper quality control during the application process. These imperfections were observed prior to missile impacts. LV1 cracked into pieces that are about 64 sq in. LV2, 1/4" wide delamination along cracks. LV3, upper right corner starting to delaminate. LV12, deflected 1.610". MV1, deflected 2.490", permanent deflection is 2-1/2". LV19, upper right corner failed, sealed the breach with plastic to continue. LV20, failure started in upper right corner. 80% of top and right side is out of the frame. This was a gasket failure; however, it was definitely enhanced by the poor film application in the upper right corner.

F-D-HV-F-3: Average missile velocity 116.1 fps. "Air side". Almost all missile damage is two-inch diameter crushed cone with local radial cracking. LV1, full plate response cracking into pieces about 65 sq in., delamination along cracks, 1/4" wide. LV11, 1-1/2" PD. LV12, deflected 1.575". MV1, over 1.8" deflection, gauge ran out of travel. MV2, tear in film in upper right corner, 1-1/2" long. MV3, failure started in upper right corner, wedge gasket peeled out of right side and along top.

General Summary

The weight of glass particles dislodged during missile impacts and load cycling is, for the most part, insignificant when compared to the weight of the entire pane. The amount of glass dislodged when the window fails is significant. In addition to the hazard of an entire pane of windstorm damaged glass falling out of its frame, several large chunks of glass were dislodged as the window failed and either fell into the chamber or fell out onto the floor. It is difficult to estimate how much of this glass would have remained attached to the film if the failed pane had not contacted the floor.

Gasket pullout was, by far, the leading cause of window failure. It may prove worthwhile to investigate the possibility of alternate glazing systems for installing monolithic annealed glass with surface applied film, such as silicone sealant adhesive.

There appeared to be a propensity for gasket pullout to initiate in the upper corners of the frame. This is probably because the weight of the glass assists in resisting movement at the bottom of the pane. Tearing of the film was a deciding factor in only two of the twelve windows tested. In order of increasing influence on total window failure, the factors that are of most concern are 1) gasket failure, 2) delamination, and 3) tearing of the film. Gasket failure is inherent with this type of glazing system and resistance to tearing is a property of the film itself. Delamination tendencies could possibly be reduced if proper application of the film were adhered to more stringently.

Conclusions

Several valuable conclusions pertaining to the performance of film coated, annealed, monolithic, dry-glazed, curtain wall windows can be drawn from the results of this research:

- 1) Surface applied film of the type and configuration tested is not an effective means for retaining window glass in a curtain wall system that has been damaged by missile impacts and cyclic windstorm loading effects.
- 2) There is no significant difference between the performance of windows that have full film coverage and those that have trimmed film coverage.

- 3) Windows that have received minimum damage from airborne missiles may survive slightly longer than those that have received high velocity missile impacts; however, neither of these windows can be expected to survive a 100 year mean recurrence interval windstorm.
- 4) There is no statistically significant difference between the missile velocity required to cause minimum damage to the "air side" versus the "tin side" of monolithic annealed float glass.
- 5) The amount of glass lost from the window prior to total failure is trifling when compared to the weight of the pane and would not pose a significant hazard to life or property.

References

- ASTM, 1984: "Standard Test Method for Structural Performance of Glass in Windows, Curtain Walls, and Doors Under the Influence of Uniform Static Loads by Nondestructive Method", Standard E 998-84.
- ASTM, 1988: "Standard Test Method for Structural Performance of Exterior Windows, Curtain Walls, and Doors by Cyclic Static Air Pressure Differential", Standard E 1233-88.
- Beason, W. L., "Breakage Characteristics of Window Glass Subjected to Small Missile Impacts", Master's Thesis, Texas Tech University, Lubbock, Texas, 1974.
- Behr, R. A., Minor, J. E., Linden, M. P., Vallabhan, C. V. G., "Laminated Glass Units Under Uniform Lateral Pressure", Journal of Structural Engineering, ASCE, Vol. 111, No. 5, May, 1985, pp 1037-1050.
- Harris, P. L., Beason, W. L., Minor, J. E., "The Effects of Thickness and Temper on the Resistance of Glass to Small Missile Impacts", Institute for Disaster Research, Texas Tech University, Lubbock, Texas, May, 1978.
- McDonald, J. R., "Tornado Generated Missiles and Their Effects", Proceedings of the Symposium on Tornadoes, Texas Tech University, Lubbock, Texas, June, 1976.
- Minor, J. E., "Architectural Glass: Strength, Selection, Sizes", Progressive Architecture, April, 1990a, pp 47-49.
- Minor, J. E., "Selecting Glass for Tall Buildings", Architectural Record, June, 1990b, pp 105-107.
- Minor, J. E., "Window Glass Failure in Windstorms", Journal of the Structural Division, ASCE Proceedings, Vol. 102, No. ST1, January, 1976.
- Minor, J. E., Beason, W. L., Harris, P. L., "Designing for Windborne Missiles in Urban Areas", Journal of the Structural Division, ASCE Proceedings, Vol. 104, No. ST11, November, 1978, pp 1749-1759.
- Pantelides, C. P., Horst, A. D., Minor, J. E., "Post-Breakage Behavior of Architectural Glazing in Windstorms", Eighth International Conference on Wind Engineering, London, Canada, July 8-12, 1991.
- Reznik, P. L., Minor, J. E., "Failure Strengths of Laminated Glass", Journal of Structural Engineering, Vol. 116, No. 4, April, 1987, pp 1030-1039.
- Vallabhan, C. V. G., Minor, J. E., Nagalla, S. R., "Stresses in Layered Glass Units and Monolithic Glass Plates", Journal of Structural Engineering, vol. 113, No. 1, January, 1987, pp 36-43.

AN OVERVIEW AND EVALUATION: COMPUTER SOFTWARE TO AID STUDENTS IN PREWRITING, WRITING, AND REVISION

Mary Lou Shomaker

Executive Summary

The research on computer software to aid inexperienced writers was done from May, 1990 through August, 1990, and involved examining software that would help students improve their writing. The softwares also were evaluated according to their value for use in computer assisted writing classes. The project had three objectives: 1) to evaluate software designed to aid the writer in the pre-writing, writing, and revising stages; 2) to identify the components of this type of software; 3) to recommend software for the beginning academic writer.

The following recommendations are made to

UMR English Department:

1. Since there is evidence that writers' habits are changing, the "nature of text itself is changing," and "the character of writing instruction is changing," (Schwartz, *et al* 141-204) the UMR English Department should consider integrating computer assisted writing instruction in freshman English classes.
2. A pilot course should be developed and implemented as soon as possible.
3. Methods should be developed to evaluate writing classes that use computers to teach writing so their effectiveness can be judged in regard to quality of writing and retention of students.
4. A committee consisting primarily of English faculty, but not limited to the English faculty, should be established to make plans and set goals beyond the pilot program. This committee also should seek financial support within and outside the University to develop the computer writing program. The committee should also consider seeking funds for:
 - a. faculty training and development to integrate the use of computers in their writing classes (for example, funds to attend training workshops and release time or pay for faculty developing computer assisted writing classes).
 - b. a computer laboratory coordinator who will research and develop an effective writing laboratory on the UMR campus and who will help train faculty, staff, and students in its use once the laboratory is established.
5. The English Department should consider developing a mandatory introduction class to accompany computer assisted writing courses. The class could carry one hour of credit and would introduce students to the software used in writing classes and the English writing laboratory.
6. Research should be continued to to update information on the software already researched and to identify other software for writers, particularly a search for and purchase of a grammar handbook software package to be installed in the writing laboratory so students can easily look up points of grammar, punctuation, format, etc., while writing on the computer.

7. Research should be conducted by persons in the English Department along with academic computing staff and administrators to establish local area networks or other networks in the writing laboratory as deemed desirable and necessary.
8. A combination of software packages should be available for student use outside the classroom, such as Writer's Helper, WordBench, and Grammatik IV, to maximize the possibilities of teaching writing with computers.
9. The English Department should purchase the WordBench and Grammatik IV software packages for use in their computer laboratory.
10. The English Department should encourage the use of the software across the curriculum.

University of Missouri-Rolla

1. The University should work to achieve equity of access to computers for both faculty and students. For example, computer laboratories should be established on all dormitory floors and elsewhere as needed.
2. A committee should be established to research the possibility of expanding and upgrading the computer library to include indexing of all books, articles, and reviews dealing with computer software for education and business.
3. A committee should be formed to study the possibility of establishing a computer software library on campus where software can be reviewed or used on location similar to the concept of the reference book section of the current library.

An Overview and Evaluation: Computer Software to Aid Students in Prewriting, Writing, and Revision

The purpose of this research was to analyze and evaluate software designed for the writer and make recommendations concerning their use in or out of the classroom. I examined and evaluated five software packages, and briefly looked at three other packages for comparison purposes. The five packages analyzed were Norton Textra Writer, WordBench, Writer's Helper, PCSTYLE, and Grammatik IV. All five are menu driven and most are easy to learn. However, to use WordBench, Norton Textra Writer, Writer's Helper, and Grammatik IV effectively, a considerable amount of time should be spent becoming familiar with their various features.

I used each feature of the five software packages and judged each package according to how helpful it is to the writer, particularly the inexperienced student writer, in the prewriting, writing, and revision stages.

For the prewriting stage, I looked for components that would aid in the conception of ideas; problem solving and decision making about a topic. For the writing stage, I looked for aids in outlining; taking notes; sentence and paragraph development; and documentation. For the revising stage, I looked for components that provide help with grammar, punctuation, style, and inserting, rearranging, and deleting text.

Prewriting and Writing Tools

All of us have experienced the terror of a blank sheet of paper at one time or another and wondered how we would fill that space with meaningful dialogue. We hope that a classical

muse will appear like a genie in our brain and solve the problem. But a muse does not appear, at least not in the sense imagined.

Although "little is understood" about creativity and it is "almost impossible to teach," Valarie M. Arms, a humanities teacher at Drexel University, suggests that "creativity can be encouraged" by using computers (33-46). To date there is little conclusive research available regarding teaching writing with computers, but those who are using the computer in the college classroom feel optimistic that the computer can be used to teach writing to students in "new and better ways" (Wresch, "Questions, Answers, and Automated Writing" 1-12). Many agree that even though most "software packages for teaching writing are limited," these packages can help students learn to write better with instructor intervention (Barrett, Paradis "Teaching Writing ..." 154-171). Computer software will only point out problems and give assistance through a matching system decided on by programers (Stratton 119-134); therefore, instructor intervention is necessary to maximize the effectiveness of computer software in the classroom.

Three of the software packages I analyzed, Norton Textra Writer, WordBench, and Writer's Helper, have features that help students get past the blank page with freewriting and thought provoking activities. Norton Textra Writer and WordBench have prewriting activities and word processing capabilities that allow students to produce their texts (essays, research papers, reports, etc.) and use any prewriting activity without leaving the program. Writer's Helper does not have this capability. Writer's Helper is designed primarily to help students with prewriting, developing topics, and analyzing the finished writing project; it does not have complete word processing capabilities.

Prewriting

- I. Norton Textra Writer. Textra Writer has a handbook built into the program that provides on-screen suggestions for prewriting strategies. Accessed from the menu under Essays, the Textra Writer Handbook briefly describes brainstorming and tells the student writer how to order the ideas gained from a brainstorming exercise. Students also are encouraged to try free writing, invisible writing, and comparison tactics to get them started writing. For instance, the Handbook suggests that the display function of the computer be modified until the letters can no longer be seen on screen, then the students are to type uninterrupted for a chosen amount of time about anything that comes to mind. At the end of this session, the display lights are turned back up, and they read what they have written. These exercises are available in Textra Writer if the students or the instructors wish to use them, but they are not extensive nor a major part of the program.
- II. WordBench. Similar to Textra Writer, WordBench has prewriting activities that are a small part of the total program; however, the WordBench activities are more structured. The four prewriting activities under WordBench's Brainstorming menu are: A. Freewriting, B. Invisible writing, C. Nutshelling, and D. Goal Setting. These brainstorming tools allow students to focus on ideas rather than the mechanics involved in working on the computer.
 - A. **Freewriting** allows students to select a time limit and write without being able to make corrections to the text. The screen will keep scrolling during this activity and students can not go back to edit what has been typed. The inability to edit is supposed to free students from worrying about the text and allow them to concentrate on the ideas they wish to express. However, curbing the tendency to edit is difficult to do. In testing this exercise, I reacted immediately to correct the error once I realized I had made it. Yet Freewriting could be useful for students who become accustomed to using it or for those who are not as programmed as I am to correct errors immediately.

- B. **Invisible writing** lets students set down ideas without the distraction of seeing the words they type. The lack of visibility should help students concentrate on ideas and not the mechanics of typing. As with **Freewriting**, students cannot edit the typed line in this mode.
- C. **Nutshelling** provides a window limited to eight lines where students can type ideas or a thesis. This activity compels students to condense their ideas and focus on the main points.
- D. **The Goal Setting** feature has a window that asks students to name the subject of their writing, the point of view, the audience, and the purpose of the writing. Reminding students to consider these elements may help them produce better texts.

III. **Writer's Helper.** William Wresch, an English teacher from the University of Wisconsin Center, designed **Writer's Helper** to encourage students to prewrite. Mr. Wresch feels that most students do not use "prewriting activities outside of class, and even English teachers tend to go comatose when the subject comes up" (143-153). Doing a lot of prewriting, Mr. Wresch believes, prevents students from producing "correctly spelled drivel" (1984). The prewriting activities that **Writer's Helper** offers are found under **Find and Organize a Subject** on the menu. Students can choose **Find a Subject**, **Explore a Subject**, and **Organize Information** from the menu. Each menu choice has two or more activities to help students find a topic and explore its possibilities.

- A. **Find a Subject. Brainstorming, Lists, and The Questioner** are designed to help students choose a topic for their writing project.
 1. **Brainstorming.** This activity allows students to type three to ten lines of uninterrupted copy that they cannot edit. **Brainstorming** takes about two to ten minutes to do; and at the end of this activity students are asked to review what they have typed and consider what idea surprised them the most and what idea interested them the most. **Writer's Helper** further suggests that the ideas gained from brainstorming may be possible topics for a writing project.
 2. **Lists.** In this activity students may enter ten to fifty items to a list. The program makes no suggestions as to the form or content of the list; these decisions are left to the writers. For instance, a list might consist of sentences, items, or groups of words.
 3. **The Questioner.** The final activity in this series poses twenty questions for students to answer and is designed to prompt the students to think further about a topic and possibly narrow down the field. Examples of questions asked are: 1) "Who is the strangest person you know?," 2) "How much money does it take to live a good life?," and 3) "Why must we develop space travel? (**WH**)."
Both questions and answers may be printed out so that students can explore the possibilities for a topic at a later time.
- B. **Explore a Subject.** Once a topic has been chosen, students can begin to explore their topics' possibilities. **Explore a Subject** provides three ways to explore a topic: a. **Crazy Contrasts**, b. **Teacher's Questions**, c. **Three Ways of Seeing**.
 1. **Crazy Contrasts.** This activity helps students think about a familiar topic in a different way and may encourage students to "redefine, limit or select

another topic" (WH). For example, students may be asked to compare their own topics with a potted plant and type three ways it is like the plant and three ways it is not like it.

2. **Teacher's Questions.** This segment of the program gives instructors the opportunity to prepare their own questions for students to consider about a subject, writing project, or reading assignment. A total of twenty questions may be prepared for the students to answer.
 3. **Three Ways of Seeing.** In this activity students are asked to view their topics in "isolation, as a process of change, and as one item within a network of related items" (WH). Students then have one line to answer each question concerning their topics. The questions deal with how a topic can be described, how it has changed, its value in a larger network, and its relationship to that network.
- C. **Organize Information.** Two activities under this menu, **Debating an Issue** and **Comparing and Contrasting**, help students explore their topics in more depth.
1. **Debating an Issue.** This activity assists students to see more than one side of a topic by asking them to list several items in support of and opposition to their own opinions concerning their topics. Considering a topic from different points of view can help students prepare better support for their ideas.
 2. **Comparing and Contrasting.** Similar to **Debating an Issue**, this activity asks that students compare their topic with another topic that is similar and may be more familiar to their audience. Up to fifteen similarities and differences can be listed. Then students are asked to choose the three most important similarities or differences between the topics. Instructor intervention in this activity would be valuable since an instructor could ask students to compare characters, themes, relationships, and social issues in a reading assignment or for a writing project.

Writing

- I. **Norton Textra Writer.** Along with word processing capabilities, **Textra Writer** has a handbook and a **Split screen** function that are helpful to student writers.
 - A. **Split screen.** This function allows students to open windows to view different parts of their texts at the same time or create and retrieve documents. With this function students can add notes to their documents or view quotations for accuracy during the composing or editing process. Up to eight windows may be placed on the computer screen at one time.
 - B. **Handbook.** Basically a grammar handbook, **Textra Writer's Handbook** provides help on sentences, grammar, usage, punctuation, and documentation. The **Handbook** is available anywhere and anytime students may need it while writing. Should students have a question about punctuation, usage, or grammar, they can refer to this built-in handbook for answers without leaving the file.
 1. **Sentences.** Seventeen topic areas are available where students can find suggestions on revision, concreteness, and level of usage. For instance, under **Excessive coordination** and **Excessive subordination**, the **Handbook** gives examples of each and suggests how these sentences may be revised.

2. **Grammar.** The opening menu of **Grammar** includes subject areas such as pronoun agreement, case, and reference; subject/verb agreement; verb tenses; fragments; and adjectives and adverbs. General rules are available along with more specific information about correct grammar usage.
3. **Usage.** The usage glossary contains words that are commonly confused and misused, such as "accept/except." There are 125 entries listed in alphabetical order. Students will receive an explanation on screen of the correct usage of any word group selected.
4. **Punctuation.** Textra Writer's Handbook provides brief rules and/or examples for using ellipses, commas, the apostrophe, and quotation marks.
5. **Documentation.** The information on documentation is excellent. There are general rules about documentation and information about preparing citations in the MLA and APA styles. Each style has submenus that help students find examples for a citation within their text and the format to use in the bibliography.

II. **WordBench.** Like Textra Writer, WordBench is capable of doing most basic word processing functions; such as entering, moving, deleting, inserting, and copying text, as well as word searches and replacements. The WordBench program also provides bibliographical assistance to students. However, unlike Textra Writer, which has examples of the MLA and APA styles of documentation, WordBench's Reference Assistant is based only on the MLA Style Guide.

But the main feature of WordBench is the way it encourages and helps students organize their writing projects. The filing system is one of its best features. Under **Folder Manager** on the menu, students may create several files pertaining to their writing project that will be placed in the same "folder." It is like having a filing cabinet on disk. Each time notes, references, outlines, or texts are added to the folder, Wordbench stores them under the appropriate sub file. All the material needed for the writing project, including the main text, can be accessed within the folder which allows students to check data without having to exit the main document file and call up another file.

The tools available to aid students in organizing and writing include: A) **Notetaker**, B) **Outliner**, C) **Viewer**, and D) **Merge**.

- A. **Notetaker.** Students can compose and store notes in **Notetaker** and use them later in their writing projects. It is also possible to mark notes for editing, browse through all the notes entered, sort the notes according to subject title, and assign notes to levels of the outline. While working on the main text, notes can be called up in a window and viewed for reference.
- B. **Outliner.** The **Outliner** helps students develop and revise outlines up to four levels deep. The outline can be collapsed to check for logical development in the writing project. Collapsing the outline hides subheadings from view so only the most important points are seen and considered. Although creating an outline is easy since WordBench does not allow incorrect development, editing the outline is difficult and this is due to the same mechanisms that prevent incorrect development. In order to make major changes in the outline, entire lines and headings must be deleted before new headings may be inserted.

- C. **Viewer.** One of the most useful tools in the program is the **Viewer**. The **Viewer** is a window that can be placed at the bottom of the screen; information can be loaded into it so that students can reference both the main text and, for example, a note at the same time. While working on the main text students can load the viewer with anything contained in the folder or the **Library Folder**. The **Library Folder** contains lists of gender-related words and commonly misused words, and gives suggestions for the correct usage or suggests alternatives.
- D. **Merge.** **Merge** makes it possible to combine other documents – the outline, notes, or both the outline and notes -- with the main document. If notes are assigned to specific levels of the outline they can be merged to produce the first draft of a paper. This is very exciting since it allows students to collect data and ideas, tie these to the outline, then merge the two and print out what may be a very rough draft of the writing project. This allows students the chance to consider their divisions in the project and the strengths or weaknesses of presenting the material as outlined.

III. **Writer's Helper.** **Writer's Helper** has almost no word processing capabilities. The update, **Writer's Helper Stage II**, has a **Notepad** feature that allows students to enter about one large paragraph, but other than this the only word processing available involves the activities.

However, three activities offer help in organization and development of a writing project. **Trees**, **Develop a Single Paragraph**, and **Five-Paragraph Theme** lead students through a series of steps that should increase their understanding of organizing and developing their topics.

- A. **Trees.** In this activity students must type eight to fifteen items related to their topic, then they are to categorize these items according to their relationship to the writing topic. When this is accomplished, the program creates a "tree" or what one might consider a rough outline of the relationship between the items and the topic.
- B. **Develop a Single Paragraph.** **Writer's Helper** gives examples of two types of paragraphs--the descriptive and the argumentative--along with explanations and examples of each. For example, students are asked to make an assertion of their own and then write four sentences to support their assertion. After doing this, the program tells students to order their sentences. The activity ends by displaying the sentences in the requested order and reminds students that transitional words can link the sentences together into a readable paragraph.
- C. **Five-Paragraph Theme.** The **Five-Paragraph Theme** leads students through several steps that lead to the completion of a short theme that has an introduction, middle, and conclusion. The program does this by asking a group of questions about a topic. This activity makes students aware that writing about something requires purpose, audience, and information (**WP**).

Revising Tools

Roy Blount, Jr., author of nine books and a contributing editor to The Atlantic Monthly, said when he was 12, he "would wake up in a cold sweat. Because of the rumors." He relates that "'In high school,' it was whispered, 'you have to do everything in pen and ink. And you can't cross out.' Which meant I was dead. If I couldn't erase or cross out, I would have to turn in papers whose every other word was wrong. And if by some chance I mastered high school conditions well enough to get into college, what would be demanded of me there? Typing,

probably. Thousands of words a minute ... right off letter-perfect" (107). Blount's fears were exaggerated, but he did have to type on a typewriter and erase errors until there were holes in the paper. Computers eliminate these horrors of the past, including the fear that the instructor will ask for revisions or multiple drafts.

Students often resist turning in multiple drafts of their work; and instructors, particularly in the past, have been reluctant to require several drafts of a text due to the work involved in retyping (Gordon and Mansfield 9-13). Ellen W. Nold of Stanford University believes that writing instructors should "move from judging finished drafts" to promoting "the writing and revising of various drafts of the same paper – particularly with students who have not mastered" the many tasks involved in writing (13-23). Word processing programs make the production of several drafts less painful since students can easily delete, move, or insert text. Most word processing programs allow the user to insert, copy, delete, and move text, and both Textra Writer and WordBench have these capabilities.

However, revision involves more than just moving text or deleting it. Students also need to check punctuation, grammar, and style. WordBench has several features that analyze a text for word usage. Writer's Helper will check texts not only for word usage but also for paragraph and sentence length, and readability. There are also software packages available that only analyze style and are limited in scope, such as PCSTYLE, or are extensive in scope, such as Grammatik IV. Software packages that analyze grammar and style are not cure-alls and should be used with "appropriate guidance and caution" (Day 63-78). Students need to know how the software analyzes text and what the limitations of the software are. (See Charles R. Stratton's article "Anatomy of a Style Analyzer" for information about the mechanisms these software packages use to "read" a text.) Using these analyzers "will not guarantee the quality of a paper," but they will help "reinforce notions of good writing" (Day). In one study of a style analyzer, students reported that the program helped them remember a "variety of points about grammar and style" (Day).

Revision

- I. **WordBench**. In WordBench under **Library Folder**, there are several lists of words or expressions that can be checked against student texts. These lists include checks for cliches, gender, misused words, and wordy expressions. Lists also can be created by the instructors or students to check problem usage, and this flexibility is the best feature of the **Library Folder**. But the lists included in the package are disappointing as far as length and usability. For example, the **Misused Words** list contains only thirty words. Furthermore, WordBench will not flag a word as misused if it does not match the form of the word in the list. For instance, the word "elude" appears in the **Misused Words** list and if students use "eluded" incorrectly, the program will not flag it as incorrect.

Wordbench does not offer any suggestions for correction or alternatives when it checks for cliches and wordy expressions. There are explanations and suggestions for misused words and gender-related words, but they are not automatically shown on screen. Students would have to go through a series of commands to load the responses in the **Viewer** in order to obtain any advice.

- II. **Writer's Helper**. Writer's Helper is capable of analyzing a document up to about 3,000 words in length by outlining the document; computing the length of sentences and paragraphs; listing the document by sentences, computing its readability and giving a word frequency count; checking for homonyms, gender-related language, "to be" verbs, and usage errors. Of these, **List Document by Sentences** and **Compute Readability** are not especially helpful to inexperienced writers without instructor intervention. The checks for homonyms, usage errors, gender-related language, and "to be" verbs are based on

limited lists of words with suggestions and/or explanations for alternatives. There is some flexibility since instructors can modify any of the check lists and can create their own word lists.

- A. **List Document by Sentences.** This function is supposed to help students identify problems in individual sentences by isolating the sentence from the rest of the text (WP). However, without instructor direction, those who really need help in sentence structure will not find a listing of sentences very helpful since there are no concrete aids such as subject-verb agreement, etc.
 - B. **Compute Readability.** This analysis is based on the Fog Index readability formula and its value is minimal. However, it could make students aware that their audience may have different reading levels.
 - C. **Outline.** The **Outline** lists the first sentence of every paragraph which allows students to check transitions from one paragraph to another to see if their ideas are developing logically.
 - D. **Count of Words in Paragraphs.** All the paragraphs of a text are graphed with an asterisk and each asterisk represents five words. The graph visually points out any large discrepancies in paragraph length which may indicate underdevelopment of an idea or paragraphs that should be divided into two or more paragraphs. Sentences are graphed similarly with each asterisk representing one word.
 - E. **Word Frequency Count.** Computing the total number of times a word is used in a text, the **Word Frequency Count** function prints out each word used in the text in alphabetical order. The number of times the word was used and the total number of different words used also appears on the print-out. Knowing how many times a word is used in a text could be very helpful to students who have a tendency to overuse certain words. For example, if "however" appears an inordinate number of times, a student may want to go back and substitute another transitional word or the student may need to check for paragraph and sentence continuity.
 - F. **Teacher's Words.** With **Teacher's Words** instructors may create their own word check lists and messages concerning correct word usage. Instructors may want to use this to address common usage errors or spelling problems in particular classes or grade levels.
- III. **PCSTYLE.** PCSTYLE is a software package that is designed to analyze text only. It analyzes sentence length, total number of sentences, total number of words, and syllables per word. The program also gives a readability level for the document and a percentage count of the long words, personal words, and action verbs used. It does not check punctuation, grammar, or unique words, nor does it offer suggestions or alternatives for improving a text. PCSTYLE emphasizes three major areas: readability, personal tone, and action words. Although PCSTYLE is limited in scope, it does have merit. The emphasis on sentence length and word length, and average syllables per word could be used by freshman English students to help them reduce wordiness and overuse of long words.
- A. **Readability.** The program checks the average number of syllables per word, the average sentence length, and the percentage of long words in a text. The manual does not credit a reading index as the basis for the readability analysis. However, it does suggest you consult Rudolf Flesch's books (The Art of Readable Writing and How to Write Plain English) to learn more about readability. The best readability

scores go to texts with a low percentage of long words and with a small number of syllables per word.

- B. **Personal Tone.** PCSTYLE emphasizes using personal pronouns in writing whether the text is a report, book, speech, technical text, or a manuscript. If students use few personal pronouns in their texts, they will receive a low **Personal Tone** score.
- C. **Action Verbs.** There are forty action verbs in PCSTYLE'S dictionary and 260 words can be added to this list. Each time a word from the dictionary is found in a text the **Action** score of the text improves.

IV. **Grammatik IV.** A grammar analyst and style checker, Grammatik IV generates statistics, summarizes the data, flags errors in texts, and allows users to select how they wish to check a document. In addition, it permits users to create their own rule dictionaries and has a **Help System** that provides definitions of rule classes, defines the rules, and explains correct usage.

Grammatik IV checks grammar and usage, analyzes sentences and readability, checks spelling, and allows users to edit each problem before going on to the next one. As an aid to writing Grammatik IV can be useful as long as students keep in mind that it is not infallible. Like most text analyzers it "will miss some problems and will occasionally flag acceptable usages" (Paul, 1989). For example, it may not recognize nouns that also can be used as verbs. In addition, the program flags gender-related pronouns and suggests that writers change to non-gender alternatives whether it is appropriate or not.

The following is a brief description of the types of grammar and usage problems that Grammatik IV looks for in a text, the kinds of statistics it generates, and the different ways students can check their texts.

- A. **Grammar and Usage.** Under the **Preference** menu there are standard rules and user defined rules that students can turn on or off when checking a text. There are forty-two categories of rules listed under the **Standard Rules** option, including several punctuation, pronoun, adverb, preposition, and possessive rules. Students also can check for split infinitives, verb agreement, homonyms, incomplete sentences, passive voice, cliches, and long-winded or wordy expressions. Since there are several types of writing and the strictness of rules applied to the different types of writing varies, there are four rule dictionaries that can be used when checking a text. Instructors also can create four of their own rule dictionaries.
- B. **Statistics.** Among the statistics that Grammatik IV compiles are three readability levels: **Flesch Reading Ease**, **Flesch-Kincaid Grade Level**, and **Gunnig's Fog Index**. At the end of a checking session, the readability evaluations appear on screen along with information about passive voice usage, average sentence length, average word length, and average paragraph length. For graphed statistics, students can open the **Statistics** menu at the end of a checking session and choose **Comparison charts**. **Comparison charts** compares the text's readability with three other standard texts: the Gettysburg Address, a Hemingway short story, and a life insurance policy. Grammatik IV produces graphs that compare student text with each of the standard texts according to reading ease, grade level, average sentences per paragraph, average words per sentence, average letters per word, and the percentage of prepositions. If instructors do not want students to compare their texts to these built-in, standard texts, they can create their own comparison texts under a custom preferences file.

Word usage statistics are available at the end of a checking session also. The Word usage profile orders all the words in the text according to the number of times they were used. Students can choose to have the words listed in order so that the most frequent usage appears first or the least frequent usage appears first. Listings by alphabet and frequency are also available.

- C. **Ways to Check a Text.** There are five ways to check the document: **Begin full interactive check; Mark only; Mark only, add advice; Statistics only; and Read only.**
1. **Begin full interactive check.** This check reads the text, gives advice, and allows students to edit each problem that is flagged immediately. However, students also can skip the flagged "problem" if they see nothing wrong with their usage; replace a word or words with Grammatik IV's suggested alternative; mark the problem and check it later on a print out; or tell the program to ignore the problem when it comes across it in the text again.
 2. **Mark only.** This option puts a # sign in front of the problems it detects without giving students any advice and saves the mark in the file so errors can be checked later.
 3. **Mark only, add advice.** Unfortunately, **Mark only, add advice** is cumbersome. For each problem detected, Grammatik IV identifies the problem word, words, or punctuation; then specifies the rule class, and gives advice. The word or words flagged are printed out long with the rule class and advice, if any, and can be compared to the text at a later time. However, to check it later, requires that students print out their marked text and compare it with the printed advice or compare the printed advice with the marked text on screen. Finding the problem in the text and comparing the advice with it requires a constant back and forth referencing that is time consuming and often confusing.
 4. **Statistics only.** This option does exactly what it says – generates about a page of numbers and percentages concerning usage and style including readability scores and paragraph, sentence, and word statistics.
 5. **Read only.** The **Read only** option places the text on the screen and flags problems in the text. Students may choose to ignore the problem, note the problem, or go on to the next problem. Editing is not possible in **Read only**. However, if students have asked Grammatik IV to print the errors on the printer (this must be done under **Options** before starting a check), all flagged problems will be printed out along with a statistical summary.

Summary

All five software packages, PCSTYLE, Grammatik IV, Norton Textra Writer, WordBench, and Writer's Helper, have features that make them valuable to student writers and could be used in the college classroom or writing laboratory. The packages are menu driven and most are easy to learn and use. Each package has strengths and weaknesses and emphasizes different aspects of the writing process. For example, Writer's Helper is more process oriented, whereas WordBench is more product oriented. Norton Textra Writer combines word processing and a grammar handbook and seems to be more useful for individual use outside the classroom. Grammatik IV and PCSTYLE check a completed writing project for style and/or grammar.

No single package seems adequate for addressing all the aspects of writing. Therefore, using a combination of three or more packages would be more beneficial to students. WordBench can be used from the beginning of the writing process to the finished product. Although WordBench's brainstorming features are weak, it does provide flexibility and organization for writing projects and could be used across the curriculum. For help in the prewriting stages and style, Writer's Helper is a good choice. However, for revision Grammatik IV is the one to use.

Bibliography

- Arms, V. M. "The Right Answer to the Wrong Question." Computers and Composition, 6 No. 1 (Nov. 1988), 33-46.
- Barrett, E. "Textual Intervention, Collaboration, and the Online Environment." In The Society of Text. Ed. Edward Barrett. Cambridge, Mass.: The MIT Press, 1989.
- Barrett, E. and James, P. "Teaching Writing in an On-Line Classroom." Harvard Educational Review, 58 No. 2 (May 1988), 154-171.
- Barrett, E. and James, P. "The On-Line Environment and In-House Training." In Text, ConText, and HyperText: Writing with and for the Computer. Ed. E. Barrett. Cambridge, Mass.: The MIT Press, 1988.
- Blount, R., Jr. "Waking Up in a Cold Sweat." PC/COMPUTING, 2 No. 12 (Dec. 1989), 107.
- Bridwell, L. S., P. R. Nancarrow, and D. Ross. "The Writing Process and the Writing Machine: Current Research on Word Processors Relevant to the Teaching of Composition." In New Directions in Composition Research. Eds. R. Beach and L. S. Bridwell. New York: The Guildford Press, 1984.
- Burns, H. "Computers and Composition." In Teaching Composition. Ed. G. Tate. Fort Worth: Texas Christian Univ. Press, 1987.
- Burns, M. H. "Recollections of First-Generation Computer-Assisted Prewriting." In The Computer in Composition Instruction: A Writer's Tool. Ed. W. Wresch. Urbana, Ill.: Natl. Coun. Teachers, 1984.
- Button, J. and A. Fluegelman. PCSTYLE. Computer software. Buttonware, Bellevue, Wash., 1986.
- Collins, T., N. Engen-Wedin, and W. Margolis. "Persistence and Course Completion." Computers and Composition, 6 No. 1 (Nov. 1988), 27-32.
- Davidson, P. "Writing Across the Disciplines: A Memo to Colleagues." In Courses for Change in Writing. Upper Montclair, New Jersey: Boynton/Cook Publishers, Inc., 1984.
- Day, J. T. "Writer's WorkBench: A Useful Aid, But Not a Cure-All." Computers and Composition, 6 No. 1 (Nov. 1988), 63-78.
- Garvey, J. J. and D. H. Lindstrom. "Pros' Prose Meets Writer's WorkBench: Analysis of Typical Models for First-Year Writing Courses." Computers and Composition, 6 No. 2 (April 1989), 81-106.
- Gordon, N. and S. Mansfield. "Computers across the Curriculum: A Confluence of Ideas." Computers and Composition, 6 No. 1 (Nov. 1988), 9-13.
- Grammatik IV. Computer software. Reference Software International, Version 1.0, 1989.
- Nold, E. W. "Revision: Intentions and Conventions." In Revising. Ed. R. A. Sudol. Urbana, Ill.: ERIC Clearinghouse on Reading and Communication Skills and the Natl. Coun. Teachers of English, 1982.
- Paul, F. "Proofread." PC/COMPUTING, 2 No. 12 (Dec. 1989), 105.

- Peek, G. S., T. Eubanks, C. May, and P. Heil. "The Efficacy of Syntax Checkers on the Quality of Accounting Students' Writing." Computers and Composition, 6 No. 3, (August 1989), 47-62.
- Schenck, M. J. "Writing Right Off: Strategies for Invention." In Training the New Teacher of College Composition. Eds. C. W. Bridges, T. A. Lopez, and R. F. Lunsford. Urbana, Ill.: Natl. Coun. Teachers of English, 1986.
- Schwartz, H. J. "3 SEEN: A Tutorial and User Network for Hypothesis Testing." In The Computer in Composition Instruction: A Writer's Tool. Ed. W. Wresch. Urbana, Ill.: Natl. Coun. Teachers of English, 1984.
- Schwartz, H. J., *et al.* "Computers in Writing Instruction: Blueprint for Progress." In Computing Across the Curriculum: Academic Perspectives. Ed. W. H. Graves. McKinney, Texas: Acad. Comp. Pub., Inc., 1989.
- Stratton, C. R. "Anatomy of a Style Analyzer." Journal of Technical Writing and Communication, 19 No. 2 (1989), 119-134.
- Sudol, R. A. "Introduction." In Revising. Ed. R. A. Sudol. Urbana, Ill.: ERIC Clearinghouse on Reading and Communication Skills and the National Council of Teachers of English, 1982.
- The Bank Street College of Education and F. E. Smith. WordBench. Computer software. Addison-Wesley Pub. Co., 1988. IBM PC, XT, AT, PS/2 and 100% compatibles.
- Tuman, M. C. Norton Textra Writer. Computer software. AnnArbor Software and the W. W. Norton and Company, Inc., 1989.
- Wresch, W. "Introduction." In The Computer in Composition Instruction: A Writer's Tool. Ed. W. Wresch. Urbana, Ill.: Natl. Coun. Teachers of English, 1984.
- Wresch, W. "Questions, Answers, and Automated Writing." In The Computer in Composition Instruction: A Writer's Tool. Ed. W. Wresch. Urbana, Ill.: Natl. Coun. Teachers of English, 1984.
- Wresch, W. Writer's Helper. Computer software. CONDUIT, The Univ. Iowa, Iowa City, Ia., 1985.

MATHEMATICA CALCULUS ILLUSTRATIONS

Jeremy Squires

• Objectives

The purpose of this project was to create a collection of computer illustrations that would represent certain concepts of calculus. These illustrations were to be performed on a calculus based program called Mathematica. Another of the underlying objectives of this project was the potential of using these illustrations as classroom demonstrations. These demonstrations might convey an idea that is not easily understood on just verbal communication alone.

Since a large part of calculus is graphical by nature, the computer is a great tool in studying and understanding the ideas proposed by calculus. As former students of computer based calculus courses (Math 21 and Math 22), we found that the learning experience is greatly enhanced when a visual representation is involved. Overall it increased the understanding of the material.

Computer demonstrations are of great use in Math 22 when three dimensional functions and vectors are introduced. Concepts such as volumes of revolutions, BNT frames, triple integrals, cross product, etc. are easily depicted with the aid of a computer and Mathematica whereas portraying these ideas on the chalkboard might not be so easy. Animations are another useful feature that show space time relationships not easily illustrated on the chalkboard. With the aid of animation one can see how the BNT frame changes as it moves along a curve or how mixed partial derivatives are related to a three dimensional function.

One of the potential barriers involved in this type of project is the ease at which a student (or for that matter the professors) would have access to these demonstrations. For this reason, we believe, Macintosh along with Mathematica was chosen for this project. Using Macintosh as well as the program Mathematica have proven to be very easy for computer illiterate people.

Being the first of this type of project, the outcome was particularly unexpected. Due to our limited "hands on" exposure to Mathematica in previous calculus courses, computer and program limitations were not known and needed to be explored. However, the limited "hands on" exposure we *did* get provided a basis on deciding what demonstrations would be able to be attempted. Along with Professor Hall of the Math Department and our imagination we worked from a list of ten ideas of which the following were tried: volumes of revolution, BNT Frames, secant line becoming a tangent line, animation showing rectangle approximation of integrals, 3D coordinate axes to be used when displaying three dimensional surfaces.

• Procedure

Upon commencing this project, the first task was to determine Mathematica's limitations concerning colors, size of pictures, the maximum number of frames for animation, and any other constraint that might effect our results. Knowing this information would be a key factor in determining which ideas to explore and how to implement them.

We started by generating a sphere. With this sphere, we experimented with all the picture generation methods and options offered by Mathematica and attempted to answer some of our questions. The Macintosh's that we worked with had 8MB of memory of which the program, Mathematica, required 4MB to run. Therefore, we concluded that we had roughly 4MB of memory to work with.

Our first concern was color. When dealing with three dimensional surfaces, shading and color play an important role in visualizing and understanding what the surface is actually doing in space. The less color you have, the less descriptive the picture. Hence, we wanted to maximize the number of colors available for display. We set the number of colors initially at 256. This amount provided a nicely shaded image. It also allowed us to generate surfaces with different colors and still have good imagery. Macintosh's other color modes such as 128 and 64 also produce well images. However, as the number of objects (and other entities) with different colors increase, the number of colors must be distributed to accommodate the color needs. Thus, by using 64 colors, you may get a good image of a blue sphere, for example, but when you add a red one the imagery degrades. When you only had the blue sphere, you had all 64 colors to produce different shades of blue to properly shade the image. When you add the red one, you now only have 32 colors for each sphere. There is an advantage, and in some cases a necessity, in using a lower number of colors. The fewer colors you use, the less memory you use. Therefore, we would probably have to sacrifice imagery for an animation where large amounts of memory are needed. Due to the memory limitation we reduced the number of colors to 128 and even less for some animations.

Next we attempted animating the sphere to revolve 360 degrees about an axis to reveal the constraints we would be faced with. The results of these tests would determine the path of our project since most of our illustrations involved motion of some kind. Our first tests quickly demonstrated the vast amounts of memory required for animations. At this point we found the size of the pictures

greatly effected the amount of memory needed. By using smaller pictures, we might be able to produce more frames for a smoother animation. Size, however, was an important factor. If these illustrations were to be viewed by an entire class of students, the image would have to be large enough for every one to see when it was displayed.

During this process, we found other ways to increase the amount of available memory. Until now we were producing all of our images in postscript format. We discovered that by converting the images to screen bitmaps, the amount of needed memory significantly decreased. Unfortunately, dissimilar to the postscript format, the picture could not be resized and still maintain the quality of the original image. We, therefore, agreed on a size that would be suitable and made it a standard to the illustrations we would produce and used the screen bitmap format. Nevertheless, this format did prove to be advantageous. While using the postscript format, loading of the animation for viewing was a timely process. Utilizing the screen bitmap, the process was greatly accelerated.

Another memory conservation technique, which proved to be quite useful, was quitting the Kernel. In Mathematica, the Kernel is a part of the program which allows the user to carry out certain mathematical operations depending on what operations are loaded into the Kernel. By eliminating (from the Kernel) any operations irrelevant to the current illustration, those operations would not be loaded into memory, thus, increasing the total available memory.

For some of the animations it was necessary to unload the entire Kernel. Since no mathematical operations are needed to display an animation, the Kernel can be dislodged from memory. This option is called Quit Kernel in Mathematica. Once this is done, however, the program must be restarted if any mathematical operations are to be performed. This would be unfortunate in a classroom demonstration where the instructor wanted to display an animation and then illustrate the mathematics involved using Mathematica. Class time would be wasted while the program was restarting. Quitting the Kernel, however, did provide an extra 3MB to work with. Hence, most of the animations produced require the Kernel be quit so the animation can be viewed smoothly.

During the entire process, of all the variables associated with the project, time was the most constraining. Creating and executing the command statements necessary to produce an animation is lengthy process. Some illustrations took several days just to render the pictures necessary to compile the animation. Other delays were created when the virus checking programs installed on the harddrive

were "fighting" each other and in the process destroying essential files needed to carry out certain command statements; or when the harddrive decided to quit working all-together; and we lost count of how many times the computer "crashed" during a several day computation.

• Illustrations

• 3D Axes

One of the first items that came into good use was a three dimensional axes to be used when viewing surfaces. It originally was made so that we could tell what was going on during our preliminary tests. We had been observing difficulties in producing a smooth 360 degree rotation of surfaces; every time we reached a certain angle, the picture would go "haywire". There for we designed this axes which had the name of each axis positioned corresponding to the traditional x, y, and z variables (Figure 1). The letters were constructed in three dimensions so that when a surface was rotated, the letters would also rotate. Therefore, in some views, the axis name may appear backwards or even upside-down. That may seem to be confusing, however, it provides a distinct space relationship that enables the viewer to determine the specific display angle they are viewing the picture. The code that is used to generate the axes can be inserted

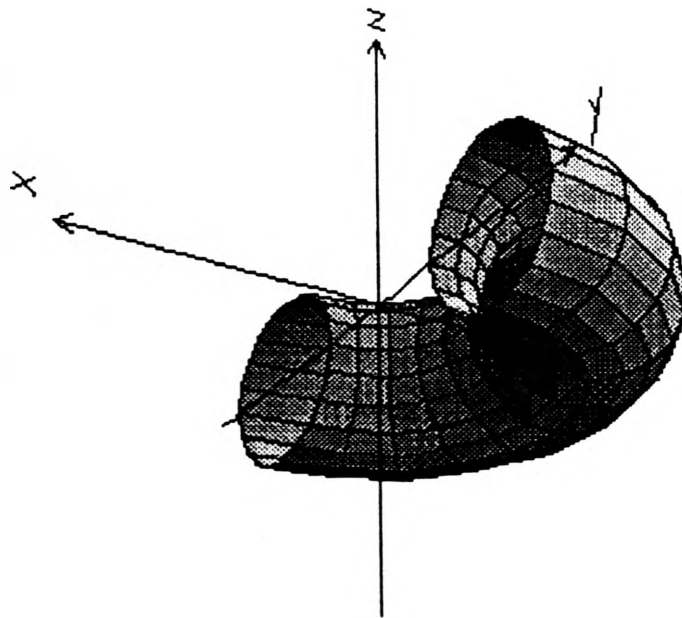


Figure 1 : Using the axis, it is easy to determine the viewing angle.

into any command sequence that displays three dimensional graphics. One who spends a little time with Mathematica will learn that it is very easy to change several aspects of the axes to suit their needs. For example, the color of the letters and axes can be changed as well as the thickness of the lines; in cases where one wanted the lines to stand out more. The code that follows was used for the axes in figure 1:

```
Graphics3D[
{Thickness[0.001],RGBColor[0,0,0],
Line[{{-1.7,0,0},{1.7,0,0}}],
Line[{{0,-1.7,0},{0,1.7,0}}],
Line[{{0,0,-1.7},{0,0,1.7}}],
Line[{{1.7,0,0},{1.6,0,0.05}}],
Line[{{1.7,0,0},{1.6,0,-0.05}}],
Line[{{0,1.7,0},{0,1.6,0.05}}],
Line[{{0,1.7,0},{0,1.6,-0.05}}],
Line[{{0,0,1.7},{0.05,0,1.6}}],
Line[{{0,0,1.7},{-0.05,0,1.6}}],
RGBColor[1,0,0],PointSize[0.01],
Point[{0,0,0}],
Thickness[0.003],RGBColor[0,0,1],
Line[{{1.8,0,0.1},{1.9,0,0.2}}],
Line[{{1.8,0,0.2},{1.9,0,0.1}}],
Line[{{0,1.8,0.2},{0,1.85,0.1}}],
Line[{{0,1.9,0.2},{0,1.8,-0.05}}],
Line[{{-0.05,0,1.8},{0.05,0,1.8}}],
Line[{{-0.05,0,1.9},{0.05,0,1.9}}],
Line[{{0.05,0,1.8},{-0.05,0,1.9}}]}]
<- Color and Thickness
specifications
<- Axes
<- Letters
```

• Volumes of Revolutions

Our next illustration was to show how certain space curves are revolved about an axis to generate a volume of revolution. For this example a sphere was used. The actual illustration involved an animation of the space curve being drawn out (a semi-circle) and then being revolved about the z-axis to generate a sphere. It is difficult to display the animation on paper, however, a frame of the animation is shown in figure 2. The following code is used to generate the animation:

```
Do[Show[
Graphics3D[
{Thickness[0.001],RGBColor[0,0,0],
Line[{{-1.7,0,0},{1.7,0,0}}],
Line[{{0,-1.7,0},{0,1.7,0}}],
Line[{{0,0,-1.7},{0,0,1.7}}],
Line[{{1.7,0,0},{1.6,0,0.05}}],
Line[{{1.7,0,0},{1.6,0,-0.05}}],
Line[{{0,1.7,0},{0,1.6,0.05}}],
Line[{{0,1.7,0},{0,1.6,-0.05}}],
Line[{{0,0,1.7},{0.05,0,1.6}}],
Line[{{0,0,1.7},{-0.05,0,1.6}}],
RGBColor[1,0,0],PointSize[0.01],
Point[{{0,0,0}},
Thickness[0.003],RGBColor[0,0,1],
Line[{{1.8,0,0.1},{1.9,0,0.2}}],
Line[{{1.8,0,0.2},{1.9,0,0.1}}],
Line[{{0,1.8,0.2},{0,1.85,0.1}}],
Line[{{0,1.9,0.2},{0,1.8,-0.05}}],
Line[{{-0.05,0,1.8},{0.05,0,1.8}}],
Line[{{-0.05,0,1.9},{0.05,0,1.9}}],
Line[{{0.05,0,1.8},{-0.05,0,1.9}}]}],
(*Sphere Definition*)
ParametricPlot3D[{{(Sin[u]) Cos[v],
(Sin[u]) Sin[v],
(Cos[u]) },
{u,0,Pi,Pi/10},{v,Pi/2,n,Pi/10},
Lighting->True,
DisplayFunction->Identity],
```

```
Graphics3D[RGBColor[0,1,0],
  (*SpaceCurve*)
  SpaceCurve[{0,(Sin[z]),(Cos[z])},
    {z,-Pi/2,Pi/2,Pi/50},
    DisplayFunction->Identity],

  PlotRange->{{-.9,.9},{-.9,.9},{-1,1.3}},
  DisplayFunction->$DisplayFunction,
  Boxed->False,
  (*RenderAll->False,*)
  ViewPoint->{4.5 Cos[50 Pi/180] Sin[60 Pi/180],
    4.5 Sin[50 Pi/180] Sin[60 Pi/180] ,
    4.5 Cos[60 Pi/180]},{n,Pi/2,5Pi/4,Pi/10}]
```

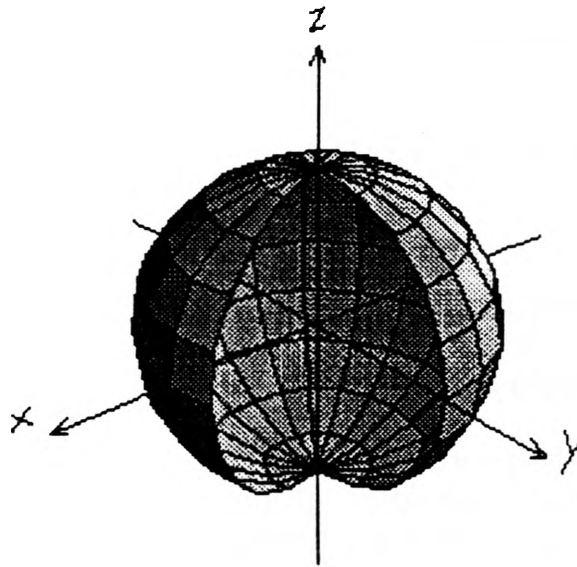


Figure 2. A frame of the animation showing how volumes of revolutions are generated

• BNT Frame

The BNT Frame illustration is another animation the shows how the unit binormal, normal and tangent vectors are related to a curve. A frame of the animation is shown in figure 3. The B, N, and T in figure 3 correspond to the binormal, normal , and tangent vectors respectively. The letters were designed in

three dimensional space and follow the vectors as they move along the curve. For this reason, the B in the frame shown in figure 3 appears backwards to the viewer. The code that follows generated the animation. It is quite lengthy due to the construction commands necessary to create the letters and make them move in the path of the curve:

```

a = Cos[n]
b = Sin[n]
c = 0.25 n

normv = Norm[D[{a,b,c},n]]
va = D[a,n]
vb = D[b,n]
vc = D[c,n]
tana = (va/normv) + a
tanb = (vb/normv) + b
tanc = (vc/normv) + c

normacc = Norm[D[D[{a,b,c},n],n]]
acca = D[va,n]
accb = D[vb,n]
accc = D[vc,n]
nora = (acca/normacc) + a
norb = (accb/normacc) + b
norc = (accc/normacc) + c

bina = (((tanb-b) (norc-c)) - ((tanc-c) (norb-b))) + a
binb = -(((tana-a) (norc-c)) - ((tanc-c) (nora-a))) + b
binc = (((tana-a) (norb-b)) - ((tanb-b) (nora-a))) + c

Do[Show[
Graphics3D[
{Thickness[0.001],RGBColor[0,0,0],
Line[{{-1.7,0,0},{1.7,0,0}}],
Line[{{0,-1.7,0},{0,1.7,0}}],
Line[{{0,0,-1.7},{0,0,1.7}}],
Line[{{1.7,0,0},{1.6,0,0.05}}],
Line[{{1.7,0,0},{1.6,0,-0.05}}],
Line[{{0,1.7,0},{0,1.6,0.05}}],
Line[{{0,1.7,0},{0,1.6,-0.05}}],

```

Undergraduate Research Report

```
Line[{{0,0,1.7},{0.05,0,1.6}},
Line[{{0,0,1.7},{-0.05,0,1.6}},
RGBColor[1,0,0],PointSize[0.01],
Point[{0,0,0}],
Thickness[0.003],RGBColor[0,0,1],
Line[{{1.8,0,0.1},{1.9,0,0.2}},
Line[{{1.8,0,0.2},{1.9,0,0.1}},
Line[{{0,1.8,0.2},{0,1.85,0.1}},
Line[{{0,1.9,0.2},{0,1.8,-0.05}},
Line[{{-0.05,0,1.8},{0.05,0,1.8}},
Line[{{-0.05,0,1.9},{0.05,0,1.9}},
Line[{{0.05,0,1.8},{-0.05,0,1.9}}}],
```

```
Graphics3D[RGBColor[0, 0, 1.000]],
SpaceCurve[{Cos[u],Sin[u],0.25 u},{u,0,2Pi,Pi/30},
DisplayFunction->Identity],
Graphics3D[
```

```
(*Unit Tangent Vector*)
{Thickness[0.003],RGBColor[.5, .5, .5],
Line[{{a,b,c},{tana,tanb,tanc}},
Line[{{tana,tanb,tanc},{1.4 Cos[n+ 40Pi/180],1.4 Sin[n+
40Pi/180],tanc}},
Line[{{tana,tanb,tanc},{1.3 Cos[n+ 43.5Pi/180],1.3 Sin[n+ 43.5Pi/180],
tanc}},
(*T*)
Thickness[0.004],
Line[{{1.36015 Cos[n +36.0274Pi/180],1.36015
Sin[n+36.0274Pi/180],
tanc},
{1.52643 Cos[n +31.6075Pi/180],1.52643 Sin[n+31.6075Pi/180],
tanc}},
Line[{{1.44222 Cos[n +33.6901Pi/180],1.44222
Sin[n+33.6901Pi/180],
tanc},
{1.34164 Cos[n +26.5651Pi/180],1.34164 Sin[n+26.5651Pi/180],
tanc}},
```

(*Unit Normal Vector*)

Thickness[0.003],RGBColor[.4, .4, .4],
Line[{{a,b,c},{nora,norb,norc}},
Line[{{nora,norb,norc},{0.141421 Cos[n+ 45Pi/180],
0.141421 Sin[n+ 45Pi/180],
norc}}],
Line[{{nora,norb,norc},{0.141421 Cos[n+ -45Pi/180],
0.141421 Sin[n+ -45Pi/180],
norc}}],

(*N*)

Thickness[0.004],
Line[{{0.28284 Cos[n + -45Pi/180],
0.28284 Sin[n + -45Pi/180],
norc},
{0.44721 Cos[n + -26.56505Pi/180],
0.44721 Sin[n + -26.56505Pi/180],
norc}}],
Line[{{0.40311 Cos[n + -60.25511Pi/180],
0.40311 Sin[n + -60.25511Pi/180],
norc},
{0.53151 Cos[n + -41.18592Pi/180],
0.53151 Sin[n + -41.18592Pi/180],
norc}}],
Line[{{0.44721 Cos[n + -26.56505Pi/180],
0.44721 Sin[n + -26.56505Pi/180],
norc},
{0.40311 Cos[n + -60.25511Pi/180],
0.40311 Sin[n + -60.25511Pi/180],
norc}}],

(*Unit Binormal Vector*)

Thickness[0.003],RGBColor[.3, .3, .3],
Line[{{a,b,c},{bina,binb,binc}},
Line[{{bina,binb,binc},{1.12145 Cos[n+ -11.2239Pi/180],
1.12145 Sin[n+ -11.2239Pi/180],
c+ 0.873129}}],
Line[{{bina,binb,binc},{0.926092 Cos[n+ -13.633Pi/180],
0.926092 Sin[n+ -13.633Pi/180],
c+ 0.873129}}],

(*B*)
Thickness[0.004],
Line[{{1.36387 Cos[n + -8.17884Pi/180],
1.36387 Sin[n + -8.17884Pi/180],c + 0.8 },
{1.26497 Cos[n + -8.82322Pi/180],
1.26497 Sin[n + -8.82322Pi/180],c + 0.8 }}],
Line[{{1.26497 Cos[n + -8.82322Pi/180],
1.26497 Sin[n + -8.82322Pi/180],c + 0.8 },
{1.21407 Cos[n + -8.73271Pi/180],
1.21407 Sin[n + -8.73271Pi/180],c + 0.76 }}],
Line[{{1.21407 Cos[n + -8.73271Pi/180],
1.21407 Sin[n + -8.73271Pi/180],c + 0.76 },
{1.21309 Cos[n + -8.42703Pi/180],
1.21309 Sin[n + -8.42703Pi/180],c + 0.733}}],
Line[{{1.21309 Cos[n + -8.42703Pi/180],
1.21309 Sin[n + -8.42703Pi/180],c + 0.733},
{1.26148 Cos[n + -7.73458Pi/180],
1.26148 Sin[n + -7.73458Pi/180],c + 0.7 }}],
Line[{{1.26148 Cos[n + -7.73458Pi/180],
1.26148 Sin[n + -7.73458Pi/180],c + 0.7 },
{1.21063 Cos[n + -7.59811Pi/180],
1.21063 Sin[n + -7.59811Pi/180],c + 0.66 }}],
Line[{{1.21063 Cos[n + -7.59811Pi/180],
1.21063 Sin[n + -7.59811Pi/180],c + 0.66 },
{1.20978 Cos[n + -7.29067Pi/180],
1.20978 Sin[n + -7.29067Pi/180],c + 0.633}}],
Line[{{1.20978 Cos[n + -7.29067Pi/180],
1.20978 Sin[n + -7.29067Pi/180],c + 0.633},
{1.25844 Cos[n + -6.64034Pi/180],
1.25844 Sin[n + -6.64034Pi/180],c + 0.6 }}],
Line[{{1.25844 Cos[n + -6.64034Pi/180],
1.25844 Sin[n + -6.64034Pi/180],c + 0.6 },
{1.35782 Cos[n + -6.15239Pi/180],
1.35782 Sin[n + -6.15239Pi/180],c + 0.6 }}],
Line[{{1.35782 Cos[n + -6.15239Pi/180],
1.35782 Sin[n + -6.15239Pi/180],c + 0.6 },
{1.36387 Cos[n + -8.17884Pi/180],
1.36387 Sin[n + -8.17884Pi/180],c + 0.8 }}],
Line[{{1.36063 Cos[n + -7.16784Pi/180],
1.36063 Sin[n + -7.16784Pi/180],c + 0.7 },

```
{1.26148 Cos[n + -7.73458Pi/180],  
  1.26148 Sin[n + -7.73458Pi/180],c + 0.7 ]}] ],  
Background->RGBColor[1,1,1],  
PlotRange->{{-1,1},{-1,1},{-.5,1.4}},  
DisplayFunction->$DisplayFunction,  
Boxed->False,  
(*RenderAll->False,*)  
ViewPoint->{4.5 Cos[45 Pi/180] Sin[50 Pi/180],  
  4.5 Sin[45 Pi/180] Sin[50 Pi/180],  
  4.5 Cos[50 Pi/180]},{n,170Pi/180,170Pi/180,5Pi/180}]
```

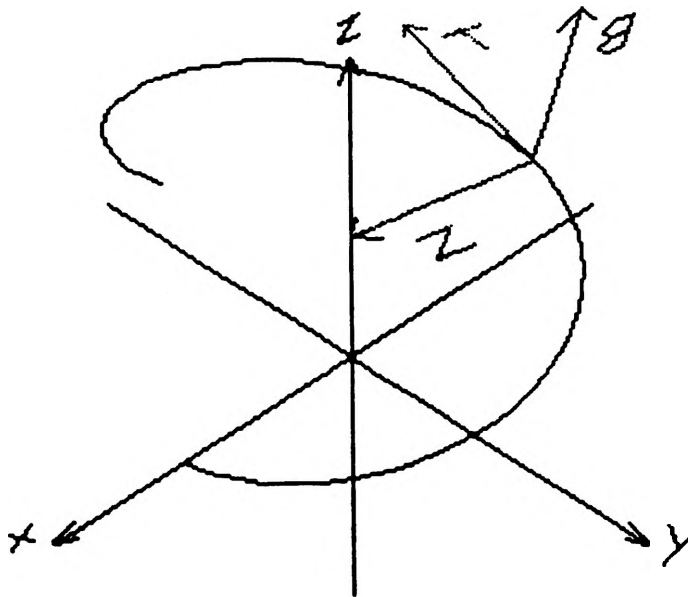


Figure 3. Frame from BNT Animation.

• Secant Line Becoming a Tangent Line

This illustration shows the process of a secant line of a curve becoming a tangent line to that curve. Figure 4 shows a frame of the animation. As the secant line moves, the slope is displayed in the animation. The following is the command used to generate this animation:

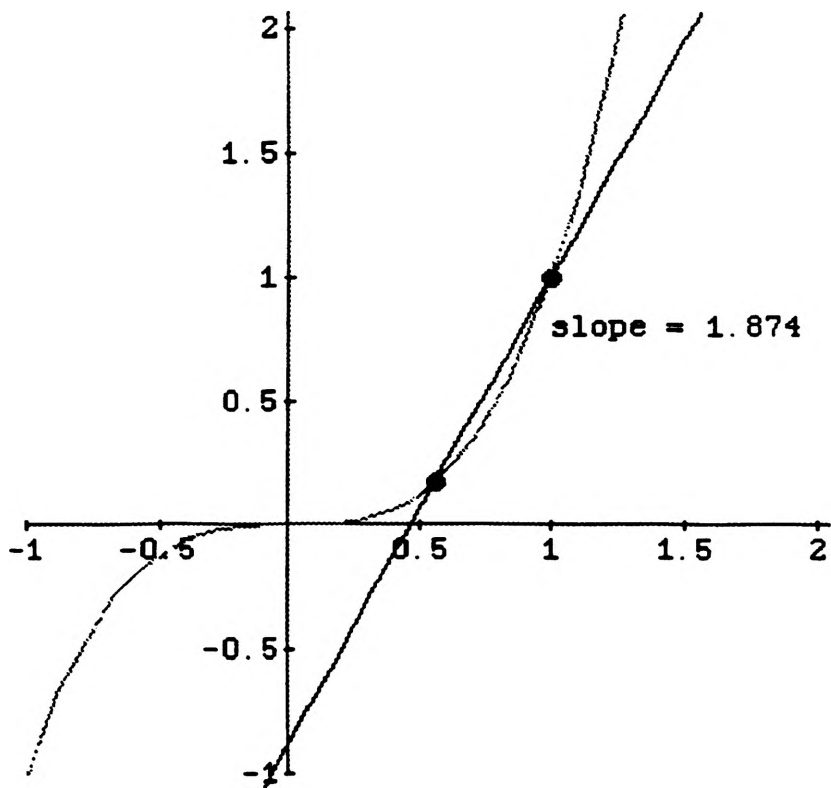


Figure 4. Frame of Secant Becoming Tangent Line

```
Clear[y,x,m,n,l,o,s]
s=((l-m)/(n-o))
y=(s x)+c
y=l
x=n
m=o^3
Solve[(y - (s x + c)) == 0,c,]
```

```
Clear[y,x]
n=1
l=1
y[x_]=((l-o^3)/(n-o))x-((o^3 n - l o)/(-n+o))
```

```

Do[If[o==1,s=3,j=7];
Show[
Graphics[{RGBColor[1.000, 0.000, 0.754],
Line[{{0,-1},{0,2.15}}],
Line[{{-1,0},{2.15,0}}],
RGBColor[1,0,0],Text[StringForm["slope = ``",N[s,4]},{1,.8},{-1,0}],
RGBColor[1,0,0],PointSize[.025],
Point[{o,o^3}],Point[{1,1}]}],

Plot[x^3, {x, -1, 2.15},PlotStyle->{RGBColor[0,1,0]}
,DisplayFunction->Identity],
If[o==1,Plot[3(x-1)+1, {x, -1, 2.15},
PlotStyle->{RGBColor[0.000, 0.146, 1.000]},
DisplayFunction->Identity],
Plot[y[x],{x,-1,2.15},PlotStyle->{RGBColor[0.000,0.146,1.000]},
DisplayFunction->Identity]],
AspectRatio->Automatic,
(*Background->RGBColor[0, 0, 0],*)

PlotRange->{{-1,2},{-1,2}},
DisplayFunction->$DisplayFunction},{o,0,1,.02]}

```

• Rectangle Approximation of Integration

This illustration was made to show how rectangles are used to approximate the area under a curve (See figure 5). As the width of the rectangles decrease and more rectangles are used to approximate the area, the approximation gets better. Eventually the rectangles become infinitesimal and the exact area is obtained; hence, the integral. The code that follows generated the animation:

```

rs=3.384 Sin[.2988Pi]
rc=3.384 Cos[.2988Pi]
Do[Do[b[n]=
Show[
Graphics3D[
{Thickness[0.001],RGBColor[1,0,0],
Line[{{-1.7,0,0},{1.7,0,0}}],
Line[{{0,0,-1.7},{0,0,1.7}}],
Line[{{1.7,0,0},{1.6,0,0.05}}],
Line[{{1.7,0,0},{1.6,0,-0.05}}],
Line[{{0,0,1.7},{0.05,0,1.6}}],

```

Undergraduate Research Report

```

Line[{{0,0,1.7},{-0.05,0,1.6}},
  Thickness[0.003],RGBColor[1,1,0],
  Line[{{1.8,0,0.1},{1.9,0,0.2}},
  Line[{{1.8,0,0.2},{1.9,0,0.1}},
  Line[{{0.1,0,1.85},{0.15,0,1.75}},
  Line[{{0.2,0,1.85},{0.1,0,1.6}}]],
  PlotRange->{{-1.1,1.3},{-1.,1.},{-1.1,1.3}},
Graphics3D[RGBColor[0.000, 1.000, 0.017],
  PlotRange->{{-1.1,1.3},{-1.,1.},{-1.1,1.3}},
  SpaceCurve[{x,0,x^2},{x,-1.3,1.3,.05},
    DisplayFunction->Identity],
Graphics3D[RGBColor[0.000, 0.008, 1.000]],
  SpaceCurve[{n+2 (1.200/m),0,y},
    {y,0,(If[n==1.2-(1.2/m),0,1])
    (n+(1.200/m))^2,.02},
    DisplayFunction->Identity],
Graphics3D[RGBColor[1.000, 0.994, 0.000]],
  SpaceCurve[{n+2 (1.200/m),0,y},
    {y,(n+(1.200/m))^2
    (If[n==1.2-(1.2/m)]|n==1.2-2(1.2/m),0,1)},
    (If[n==1.2-(1.2/m)]|n==1.2-2(1.2/m),0,1)
    (n+2(1.200/m))^2,.02},
    DisplayFunction->Identity],
Graphics3D[RGBColor[1.000, 0.994, 0.000]],
  SpaceCurve[{x,0,(n)^2},
    {x,n,n+1.200/m If[n==0,- (1.200/m),1],.02},
    DisplayFunction->Identity],
Graphics3D[RGBColor[1.000, 0.994, 0.000]],
  SpaceCurve[{x,0,0},
    {x,n,n+1.200/m If[n==0,- (1.200/m),1],.02},
    DisplayFunction->Identity],
Graphics3D[RGBColor[1.000, 0.994, 0.000]],
  SpaceCurve[{1.2,0,y},{y,0,(1.2-(1.200/m))^2,.02},
    DisplayFunction->Identity],
Graphics3D[RGBColor[0.000, 0.008, 1.000]],
  SpaceCurve[{1.200/m,0,y},{y,0,(1.200/m)^2,.02},
    DisplayFunction->Identity],
  Background->RGBColor[0,0,0],Boxed->False,
ViewPoint->{-0,-9,0.020},{n,0,1.200-(1.200/m),1.200/m}
;{c[m]=Show[b[0],b[.60(If[m==2,1,0])], b[.4(If[m==3,1,0])],b[.8(If[m==3,1,0])],
b[.3(If[m==4,1,0])],b[.6(If[m==4,1,0])],b[.9(If[m==4,1,0])],b[(1.2/5)1(If[m==5,1,0])],
b[(1.2/5)2(If[m==5,1,0])],b[(1.2/5)3(If[m==5,1,0])],b[(1.2/5)4(If[m==5,1,0])],b[(1.2/6)1(If[m==6,1,0])],
b[(1.2/6)2(If[m==6,1,0])],b[(1.2/6)3(If[m==6,1,0])],b[(1.2/6)4(If[m==6,1,0])],b[(1.2/6)5(If[m==6,1,0])],
b[(1.2/7)1(If[m==7,1,0])],b[(1.2/7)2(If[m==7,1,0])],b[(1.2/7)3(If[m==7,1,0])],b[(1.2/7)4(If[m==7,1,0])],
b[(1.2/7)5(If[m==7,1,0])],b[(1.2/7)6(If[m==7,1,0])],b[(1.2/8)1(If[m==8,1,0])],b[(1.2/8)2(If[m==8,1,0])],
b[(1.2/8)3(If[m==8,1,0])],b[(1.2/8)4(If[m==8,1,0])],b[(1.2/8)5(If[m==8,1,0])],b[(1.2/8)6(If[m==8,1,0])],
b[(1.2/8)7(If[m==8,1,0])],b[(1.2/9)1(If[m==9,1,0])],b[(1.2/9)2(If[m==9,1,0])],b[(1.2/9)3(If[m==9,1,0])],
b[(1.2/9)4(If[m==9,1,0])],b[(1.2/9)5(If[m==9,1,0])],b[(1.2/9)6(If[m==9,1,0])],b[(1.2/9)7(If[m==9,1,0])],
b[(1.2/9)8(If[m==9,1,0])],b[(1.2/10)1(If[m==10,1,0])],b[(1.2/10)2(If[m==10,1,0])],b[(1.2/10)3(If[m==10,1,0])],
b[(1.2/10)4(If[m==10,1,0])],b[(1.2/10)5(If[m==10,1,0])],b[(1.2/10)6(If[m==10,1,0])],b[(1.2/10)7(If[m==10,1,0])],
b[(1.2/10)8(If[m==10,1,0])],b[(1.2/10)9(If[m==10,1,0])],b[(1.2/11)1(If[m==11,1,0])],b[(1.2/11)2(If[m==11,1,0])],
b[(1.2/11)3(If[m==11,1,0])],b[(1.2/11)4(If[m==11,1,0])],b[(1.2/11)5(If[m==11,1,0])],b[(1.2/11)6(If[m==11,1,0])],
b[(1.2/11)7(If[m==11,1,0])],b[(1.2/11)8(If[m==11,1,0])],b[(1.2/11)9(If[m==11,1,0])],b[(1.2/11)10(If[m==11,1,0])],
b[(1.2/12)1(If[m==12,1,0])],b[(1.2/12)2(If[m==12,1,0])],b[(1.2/12)3(If[m==12,1,0])],b[(1.2/12)4(If[m==12,1,0])],
b[(1.2/12)5(If[m==12,1,0])],b[(1.2/12)6(If[m==12,1,0])],b[(1.2/12)7(If[m==12,1,0])],b[(1.2/12)8(If[m==12,1,0])],

```

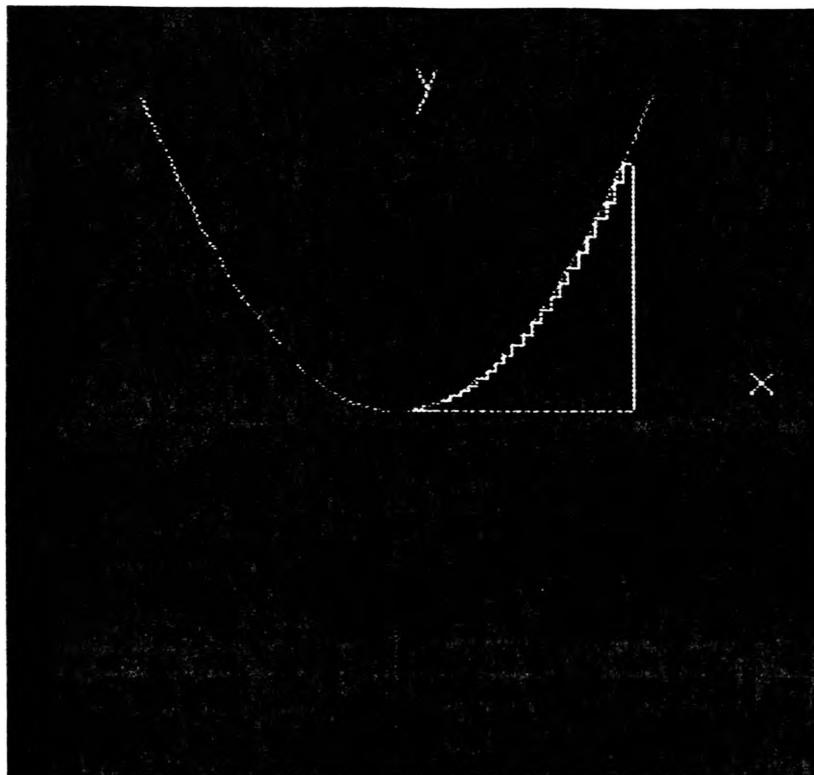



Figure 5. Frame from Rectangular Approximation of Integration.

• Newton's Method

This animation shows a graphical representation of using Newton's method to find where two curves intersect. Figure 6 shows a frame of this animation. The following code generated the animation:

```
f[x_] := (-2x + 3)-(6(x^3));  
Graphics[{a = Plot[-2x + 3, {x, -1, 2.15},  
  PlotStyle->{RGBColor[0,1,0]}  
  ,DisplayFunction->Identity],  
b = Plot[6(x^3), {x, -1, 2.15},  
  PlotStyle->{RGBColor[0.000, 0.146, 1.000]},  
  DisplayFunction->Identity]}];  
x = 1.6;  
Do[  
  x = x - (((-2x + 3)-(6(x^3)))/(-18(x^2)-2));  
  Show[
```

```
Graphics[{RGBColor[1.000, 0.000, 0.754],Line[{{0,-1},{0,3}},
Line[{{-1,0},{2.15,0}},
RGBColor[1,0,0],
Text[StringForm["x = `",N[x,4]],{1,1.5},{-1,0}],
RGBColor[1,0,0],PointSize[.025],
Point[{x,-2x + 3}],Point[{x,6(x^3)}]},
a,b,
AspectRatio->Automatic,
(*Background->RGBColor[0, 0, 0],*)
PlotRange->{{-1,2},{-0.5,3}},
DisplayFunction->$DisplayFunction],
{n,0,1,.1}]
```

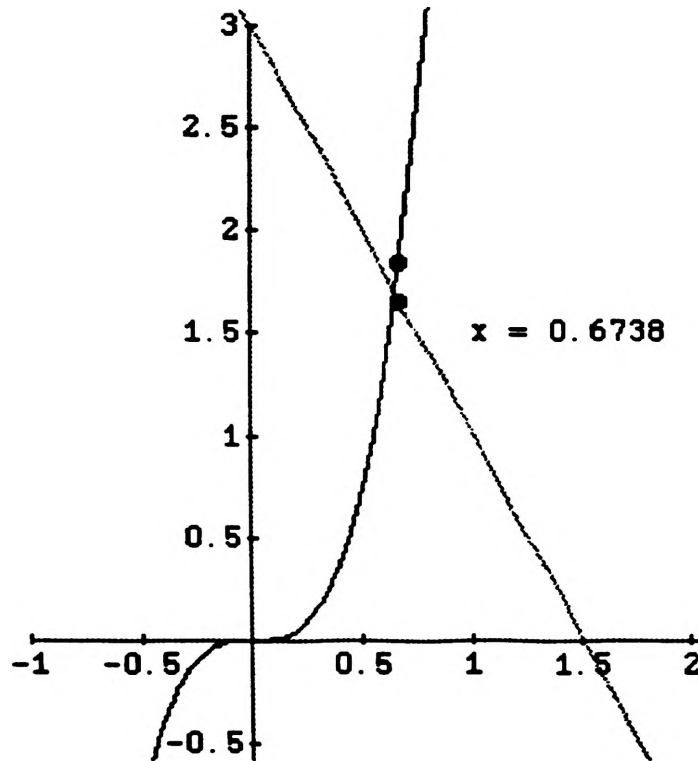


Figure 6. Frame from Newton's Method

• Conclusion

At the start of this project, we were very energetic as to what Mathematica might allow us to accomplish. That energy dwindled as we proceeded onward. Due to our limited knowledge and experience with Mathematica, we had to spend much time in learning how to use Mathematica and determine any limitations that would effect our progress. We feel that if we had more time, we could have exceeded our present output to produce more detailed and complex illustrations.

The entire process was very slow. Days passed as we waited for the computer to complete the commands we gave it. Thus, if the final output was wrong in some way, the process was started over. Perhaps our expectations were too high. Memory and hardware considerations drastically limited our imaginations. The computer's 8MB was not enough to accommodate our ideas; And if the computer *could* handle our ideas, its speed slowed our progress.

The project, however, was not a failure in our view. Mathematica performed very well. It produced some good results which sparked ideas for other demonstrations and illustrations. Time, however, was the key factor.

A COMPUTER GRAPHICS PROGRAM FOR DISPLAYING WATER MOLECULES ON A DN3500 APOLLO WORKSTATION*

Michael A. Stuller

Abstract

A computer graphics program is developed for displaying water molecule configurations on the screen of a DN3500 Apollo workstation. The motivation was to generate a fast display of output from molecular dynamics or Monte Carlo computer simulations. Input to the program consists of a listing of the Cartesian coordinates of the atomic constituents of the molecules. Options in the program include: 1) number of molecules; 2) plot size; 3) atomic radii; 4) superposition of substrate atomic positions; 5) viewing angle; and 6) color-coded and/or numbered atoms. The program is written in Fortran.

Introduction

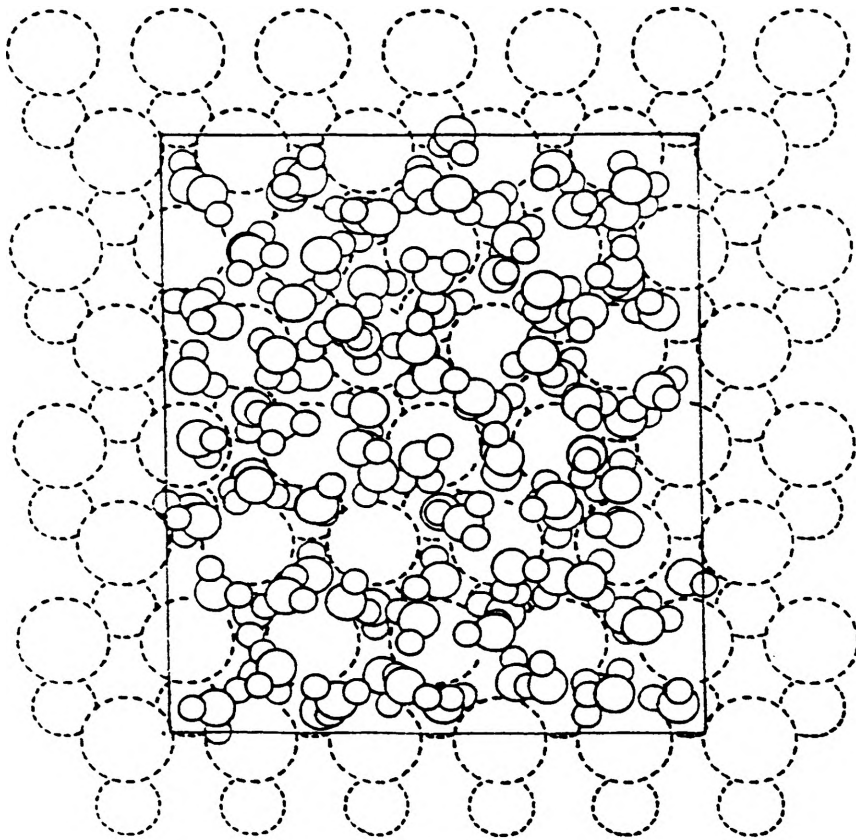
In computer simulations of molecular systems it is often necessary to display the atomic configurations. Plotting routines, such as those for the Hewlett-Packard (HP) plotters, are slow and take considerable time -- especially when the molecular system contains 100 or more atoms. In water systems one has three atoms per molecule and the number of atoms soon becomes large. The motivation for this work was to develop a plotting routine which would display #600 atomic configurations in a few seconds on the screen of an Apollo DN3500 workstation. In comparison, the HP plot takes about 30 minutes.

Description of the Plotting Routine

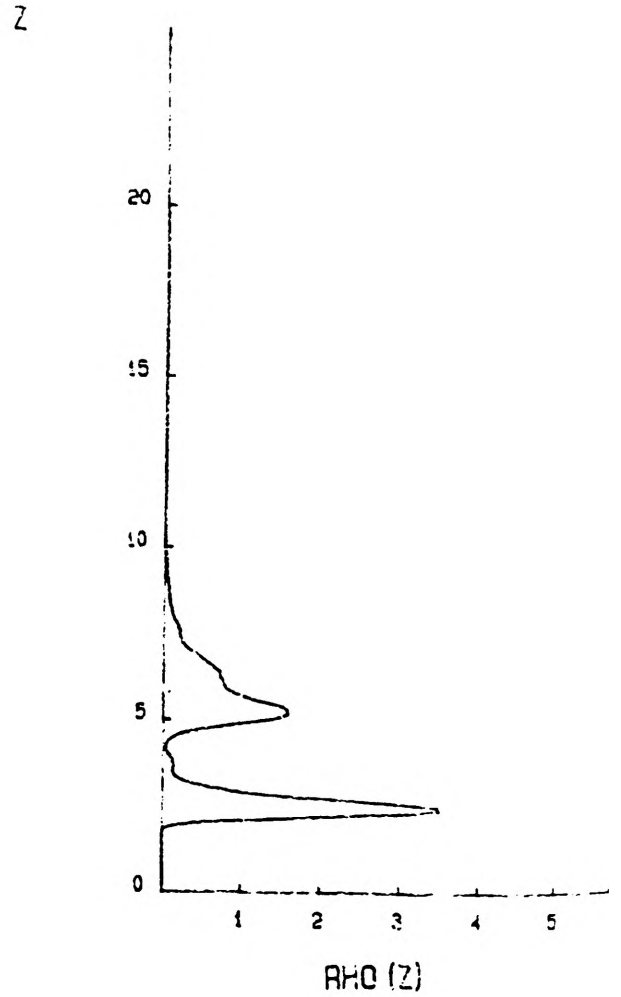
The basic plotting routine, called MASTERPLOT, is a Fortran code developed for the HP plotter. It reads the atomic coordinates and plots the atomic configurations in layers, so that the circles representing atoms in the bottom layers are hidden. The present work modified this code to send the output to the Apollo screen. In this version, the hidden line plotting was done by using filled circles for each atom, so that atoms in upper layers covered the circles lying below. The basic program also plots (if applicable) atoms of a substrate in contact with the molecular system.

One of the complications of this project was to make use of the multiple windows available on the Apollo with a mouse based operating system. Each plot appears in a window which can be re-sized with the mouse. The program rescales the output to fit in the new window by selecting a "REDRAW" option with the mouse. By opening new shells, one can display multiple plots and compare rotated or later time views of the atomic configurations. Many of new routines were developed from variations on code provided by the Apollo graphics manual.

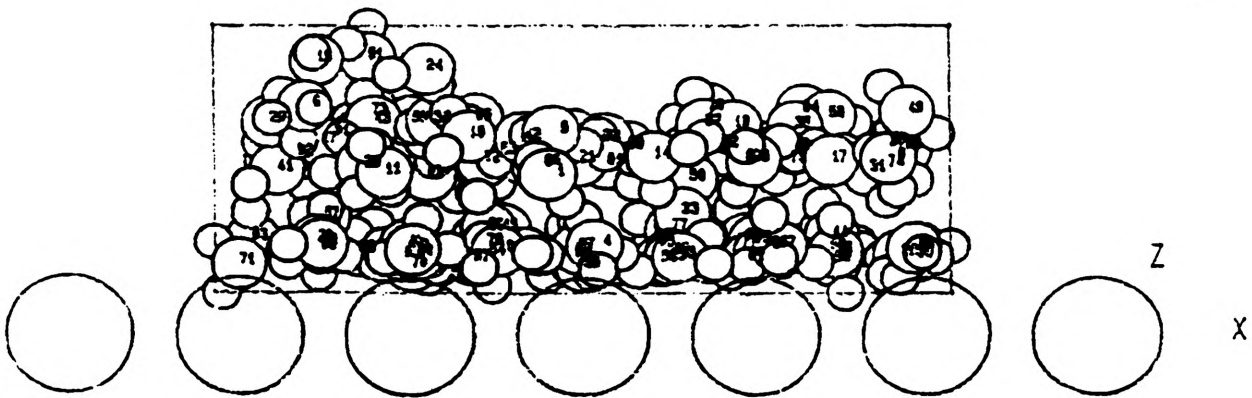
An example of the plot, applied to water molecules is shown in Figure 1. Three plots are shown: a) a view looking down (along the -z axis) on 96 water molecules adsorbed on a model AgI substrate; b) the same system looking along the y axis; and c) a plot of the molecular density perpendicular to the substrate. The information in part c) of Figure 1 must be read into the program in a separate file.



(a)



(c)



(b)

Figure 1

The Fortran Code

The code was written for the Apollo operating system SR 10.1. Modifications for later versions of the operating system should require minimal effort. However, if applied to the new HP-Apollo UNIX workstations some more extensive changes might be required.

Part of the Fortran code is given below, showing definition of input variables, dimensions of the arrays and open and close statements for files. A diskette containing the file can be obtained from B. Hale, Physics Department, University of Missouri-Rolla, Rolla, Missouri 65401.

Summary and Comments

This project, completed during the summer of 1990, was sponsored by the University of Missouri-Rolla undergraduate research program. It provided an opportunity to become familiar with the Apollo workstation, its operating system and some of the subtleties of screen graphics. In addition, the routine will be made publicly available. A diskette containing the file can be obtained from B. Hale, Physics Department, University of Missouri-Rolla, Rolla, Missouri 65401, or by sending a request message to hale@apollo.physics.umr.edu.

This computer graphics program displays water molecule configurations on the screen of a DN3500 Apollo workstation. The motivation was to generate a fast display of output from molecular dynamics or Monte Carlo computer simulations. Input to the program consists of a listing of the Cartesian coordinates of the atomic constituents of the molecules. Options in the program include: 1) number of molecules; 2) plot size; 3) atomic radii; 4) superposition of substrate atomic positions; 5) viewing angle; and 6) color-coded and/or numbered atoms. The program is written in Fortran.

rad

BORDER DETECTION OF SKIN TUMOR IMAGES

Mike Tiehies

Border detection of skin tumor images is part of a research project whose purpose is to identify key features in skin tumor images using machine vision techniques. The key features present in a skin tumor guide the dermatologist in making the proper diagnosis. A few examples of key features are crust, scale and ulcer.

The success of this research is largely dependent on accurate border detection. The border defines the boundary of the tumor. From this, features such as regular border and irregular border can be determined giving the dermatologist a measure for the smoothness of the tumor edge. Irregularity of the border often indicates the presence of a malignant tumor. The border also defines the area in the image to restrict the search for other key features present in the skin tumor. If the border errs to the outside of the tumor, features of the skin surrounding the tumor may be improperly identified as key features. If the border errs to the inside of the tumor, features present could be neglected completely. This creates the need for an algorithm which is capable of detecting an accurate border for the skin tumor in a digitized image.

Jeremiah Golston wrote the first version of a border detection program which used radial search methods on a luminance image. The luminance image was generated by replacing the original red, green, and blue (rgb) values with a weighted sum of the rgb values. The luminance border program, `lumborder`, searched radially outward from the defined center of the tumor looking for a dip in the luminance value with a sustained length. `Lum.border` would terminate the search on any radius when these conditions were satisfied. If the search reached the boundary of the image without satisfying the above condition the restrictions would be relaxed and the search on that radius performed until a point was found. Under these conditions `lumborder` may perform multiple searches on the same radius before returning a border point.

Stopping the search with the first point that satisfied the conditions may result in `lumborder` defining a border point at a false edge of the tumor. A border detection program which searches each radius one time and was capable of returning multiple border candidates would be capable of determining the true border of a tumor with multiple color changes and reduce processing time.

`Colborder.simple`, written by Michael Tiehies, employs radial search and color information for determining multiple border candidates on each radius of reduced resolution, color segmented images. As in the `lumborder` program a sustained length condition was required. Unlike `lumborder`, `colborder` looked for color changes in segmented images that satisfied the sustained length condition to determine the edge of the tumor. The point with the greatest sustained length was selected as the initial border point. The radial length of each possible border point on the adjacent radius was then compared to the radial length of the previously chosen border point. The point which reduced the difference in radial length to a minimum was selected as the true border point for that radius. The process was repeated for each successive radius until one point had been selected for each radius.

To have a measure of how accurate the selected border points were, a program called `Success`, written by Michael Tiehies, was used. `Success` compared the location of each selected border point with a data base, feature files, for that image. If the location of the selected border point was labeled as a partial tumor block in the feature files, the point was considered to be an accurate border point. `Success` also looked at the location of the selected border point if it wasn't located in a partial tumor block to determine if it was within half a feature block of

wt
I
ad
fol
:=
)hi
F
,I
p|c
F
L
.6;
= X
OM

a partial tumor block. If this condition occurred the point was labeled a near hit inside or near hit outside depending on its actual location. Success then returned a percentage rating for each image. Preliminary results implied that the colborder program had about a ten percent higher accuracy than lumborder.

The work this semester began by running a curve fitting program on the selected border points returned from colborder.simple for images 300 - 400. The closed curves were then compared with the closed curves obtained using the selected border points from lum.border for the same images. The results from the comparison illustrated that the luminance border program was superior despite preliminary results using the success program.

The selected border points from colborder were obtained from a 64 x 64 resolution image. Before the curve fitting program was applied to these points the resolution was increased to 512 x 512. The border points were then located at the left top corner of the 8 x 8 block in the 512 x 512 image. The resulting curve for the border points for the colborder program was extremely irregular and generally transposed slightly. This condition was not present for the border points used from lumborder since the image was 512 x 512 resolution. After further consideration a decision was made to increase the resolution of the image processed by colborder.simple to 128 x 128. This would help reduce the erroneous irregularity of the closed curve. Each pixel in the lower resolution would now represent a 4 x 4 block in a 512 x 512 image compared to the previous 8 x 8 block.

The 64 x 64 image which colborder.simple processed was generated through several processing stages and segmentation of the original 512 x 512 image. All the programs used to generate the segmented 64 x 64 images were written by Scott Umbaugh. Therefore changing the resolution to 128 x 128 would require modifications to the following programs written by Scott: avecol, mask.nskn, spher_xform, find_covmtrx, remap, seuccc, seuuccc, numcol and colfilter. Modifications were also required to colborder.simple and centerpoint.

Avecol will average a color, pixel-interleaved image over a specified block size and replace the block by the average RGB values. Mask.nskn reads the feature file for all nonskin blocks, it then sets the RGB values of the corresponding blocks in the image to zero. Spher_xform transforms the RGB color space, so the first plane is Angle A, the second plane is Angle B, and the third is length. After transforming, the data is converted to byte format. Find_covmtrx finds the covariance matrix for an RGB pixel interleaved image file. Remap transforms an image into principal components and then remaps to the range 1 to 254 for byte size. Seuccc and seuuccc performed a principle components transform which condensed most of the information into one color space, normally the red color plane. Find_numcol finds the number of colors to segment the image, based on a rule generated from First Class Fusion that uses RGB maximum, minimum, and variance to make the determination. Col_filter does spatial filtering by filling in holes and rounding off protruding pixels from objects. Center.point reads the feature file for partial and full tumor blocks. It calculates the center of the tumor and then adjust the coordinates to the resolution of the image being processed. Colborder.simple uses the center point as the starting point and searches out radially for color changes. The point is marked as a possible border candidate if the color change remains constant for the minimum sustained length condition. The radial search continues on the line until four points have been located or the edge of the image is reached. The final border point for each radial line is chosen so the smallest difference in radial length for two neighboring points results.

A test set of images was chosen to verify that the changes made to the programs would not alter their integrity. After the changes, certain images had the information in the red and blue planes reversed. Due to the unfamiliarity with the segmentation programs written by Scott Umbaugh they were checked several times for errors due to programming changes.

The results from the programs remained unchanged. The color border program seemed unaffected by the information being reversed in the red and blue planes. These results could be explained in that the colborder.simple looked for a color change in any of the three color planes. If the point found fulfilled the sustained length condition the point would be labeled a possible border point. For this reason no more time was spent on trying to explain the change of information from the red to blue plane.

When colborder.simple was changed to function on the higher resolution image the sustained length condition was written as a function of the resolution. The sustained length condition for the 64 x 64 images was two pixels; this became four pixels for the 128 x 128 images. Several images were viewed at the higher resolution before sending the data points to the curve fit program. These images reveal that little gain in accuracy of the data points to the actual border of the skin tumor occurred. The border points continued to err to the outside of the tumor.

The error to the outside of the tumor had one constant factor. There was usually a color change that occurred prior to the selected border points but that would be omitted because of the four pixel sustained length condition. The sustained length condition was then changed to two pixel for the 128 x 128 resolution. The change in sustained length moved the border points toward the center of the skin tumor, reducing the error to the outside. About twenty images were then run using the modified sustained length condition and displayed on the Conrac monitor. A significant improvement in the selected border points resulted.

Changing the sustained length condition to two pixels improved the capability of colborder to find the true border for small tumors considerably. Although these changes improved the accuracy of the border for small and medium sized tumors, at the same time the accuracy of the border points for large tumors decreased. Viewing the results of a few large tumors it became apparent; since colborder would terminate the search after finding the first four possible border points on each radius, that the true edge of the tumor often would not be reached. One solution to this problem was to increase the number of points on each radius. The program was modified to find four, five, six, and seven points on each radius for the same 279 images. Table I shows the results for the selected border points returned from colborder. Additionally the results were compared with the same 279 images with an 8 x 8 average block size or 64 x 64 resolution image. From Table I an image resolution of 128 x 128 and selecting four possible border points on each radius returned the highest success rate.

From these results colborder was set to find four possible border points on each radial line. Time did not permit generating the closed curves for images 300 - 400 for comparison with lumborder.

Using the color information in the image and finding multiple points on each radius should give colborder the capability of detecting the border of a tumor with greater accuracy than lumborder.

Point determination, a subroutine of colborder, selects one point on each radius. Selections are made to minimize the difference in radial length with neighboring selected border points. For the final selection process, this is a relatively primitive method. Selections which employ additional information from the image in conjunction with minimal difference in radial length would improve the accuracy of the border detection program, colborder. Future focus on border detection should be guided in this direction.

Table 1. Percent Accuracy for Valid Border Points

No. points per radius	Total Hits	Direct Hits	Near Hits Inside	Near HitsOutside	Image Resolution	Number of Tumors
4	54.84	35.61	15.00	4.22	64x64	279
4	66.90	44.02	13.18	9.69	128x128	279
5	66.43	43.84	12.76	9.83	128x128	279
6	65.32	43.11	12.36	9.85	128x128	279
7	64.44	42.71	12.10	9.63	128x128	279

SOME STABILITY AND CONTROL ASPECTS OF A VARIABLE PIVOT WING CONFIGURATION

Paul Vitt

Abstract

In supersonic flight, there is a large positive shift in the static margin, which causes extreme positive shifts in longitudinal stability, and is an undesirable characteristic. This paper investigates some of the stability and control aspects of an alternative configuration, that of a variable pivot wing aircraft -- an aircraft with two sets of wings, one set sweeps forward, the other set sweeps rearward. By prescribing a sweep schedule, it is desired to minimize the static margin shift with Mach number. The effects of the two lift elements -- that of mechanical shift of the center of pressure forward with sweep, and aerodynamic coupling with the reduction in aspect ratio which cause a decrease in lift-curve slope due to sweep -- on simple longitudinal stability and control parameters will be presented. Two cases are examined. The first case has four equal-area wings with a fuselage/strike; the second case has the area of the front wings twice the area of the rearward wings with a fuselage\strike.

Nomenclature

b	wing span
c	wing chord
$C_{L\alpha}$	lift-curve slope
$C_{L\alpha}(\Phi_f/\Phi_r)$	lift-curve slope for (wing sweep angles)
$C_{m\alpha}$	moment-curve slope
$C_{m\alpha}(\Phi_f/\Phi_r)$	moment-curve slope for (wing sweep angles)
M	Mach number
MAC	mean aerodynamic chord
S	wing area
ST	stagger (in chord lengths)
XMC	moment center location
/R	aspect ratio
Φ	wing sweep angle

Subscripts

f	forward wing pair
r	rear (or aft) wing pair

Introduction

The major trade-off of high speed flight is the conflicting requirements of high aspect ratio wings for high lift and maneuverability at low speeds with low aspect ratio wings for low gust loading and wave drag at supersonic speeds. Variable configurations were proposed to solve this problem, by varying the aspect ratio of the wings to fit the current flight regime. The two current designs are for aft-sweeping wings and oblique-sweeping wings. Both have their drawbacks: sweeping the wings aft causes a mechanical shift in center of pressure which augments the shift normally associated with supersonic flight; the oblique-swept wing causes obvious longitudinal-lateral-directional stability and control cross-coupling, which leads to undesirable handling qualities. A newer alternative is the scissor wing (ref [2]), which has four wings cross-joined (forward-to-aft) across a single center pivot. This paper does an initial investigation of some of the characteristics of a derivative of this concept, the variable pivot wing configuration. It also has four wings, but are set in pairs (two wings sweep forward

synchronously, and similarly two wings sweep rearward), and each wing has an individual pivot, which is close to the aircraft centerline. This gives the advantage of being able to have longitudinally unsymmetrical sweep scheduling: sweeping the forward wings faster than the aft wings, for example. The wings can be fully extended for low speed flight, in order to give good handling capabilities, and then can be swept to any combination of angles to minimize the shift in static margin, wave drag and gust loadings at high speeds. Cross-coupling of longitudinal and lateral-directional attributes is eliminated due to the centerline symmetry of the aircraft.

The preliminary investigation presented here deals with simple stability and control derivatives, specifically the lift-curve slope, the moment-curve slope, and the static margin. For this purpose, two variations of the variable pivot wing were examined: the first model has four equal-area wings, a strake or fuselage, and a horizontal tail; the second model has the total wing area split 2:1 between the forward reference wings and the aft reference wings, a fuselage or strake, and a horizontal tail.

The objective of this paper is to show that the static margin shift can be controlled for a large range of Mach numbers by prescribing a sweep schedule which takes advantage of the variable forward/aft sweep capabilities of the design. Also, the mechanisms which produce the resulting lift-curve slopes and moment-curve slopes will be examined, in order to determine how the control is achieved. High speed flight has many factors which are not considered here, and knowledge of the mechanics which control longitudinal stability will allow the designer to trade-off the stability and control with performance efficiently.

Method of Analysis

The linear vortex lattice method of reference [5] (NARUVLE) was used as a subroutine in a program to iteratively trim the aircraft, using the horizontal tail for a given flight condition, to determine the aerodynamic characteristics. Transonic results cannot be obtained with this method because it is linear. The method was limited to 200 panels, and in some cases gave some numerical oscillation. Reference [3] indicates that the trends obtained can be taken as accurate.

In order to study the effects of variable sweep on static margin, three models were developed and analyzed over a Mach number range of 0.4 to 3.4. All configuration used the same Λ/R and reference wing area (S), so that the results could be related (the Λ/R and S for the pivot wing configurations was taken from a basic sweep of $\Phi = 18$ degrees). The first is the baseline, which is a conventional, fixed wing aircraft based roughly on a F-18 layout, and is used to give the results a basis for comparison. This configuration is shown in Figure 1a. The second is the equal-area configuration, which has four paired equal-area wings. This is the basic variable pivot wing layout, and it is shown in Figures 1b, 1c, and 1d, for various sweep angles. In order to study the effects of wing area and aspect ratio on the static margin, a split-area configuration was developed. For the split-area configuration, there are four paired wings, but the forward pair have twice the area of the aft pair (or the total wing area is split 66%/33%). The equal-area and split-area models are shown in Figures 2a and 2b, respectively, in the basic sweep positions. The pivots for the wings are located 1.733 ft off of the centerline of the aircraft to allow for the necessary mechanisms for rotation of the wing, and also to allow the front section of the wings to fold into the fuselage without overlapping each other. The geometry of the different configurations is listed in Table 1. The total aircraft weight was taken to be 50,000 lbs, with the equal area wing weights 4000 lbs each, and the split-area wing weights 5333 lbs forward and 2667 lbs aft.

Table 1. Configuration Geometries

<u>Parameter</u>	<u>Baseline</u>	<u>Equal-Area</u>	<u>Split-Area</u>
S (ft ²)	426.0	427.9	424.5
b (ft ²)	39.33	41.35 ^c 39.33 ^d	41.35 ^c 39.33 ^d
c _{root} (ft)	16.00	6.84	9.00 ^a 4.44 ^b
c _{tip} (ft)	5.33	3.30	4.50 ^a 2.22 ^b
MAX (ft)	11.09	5.18 ²	6.81 ^{a,2} 3.45 ^{b,2}
Taper Ratio	0.33	0.48	0.5
/R ¹	3.63	4.00 ^c 3.62 ^d 2.00 ^e 1.00 ^f	4.03 ^c 3.64 ^d 2.01 ^e 1.01 ^f
/R ²	3.63	7.24	5.39 ^a 11.22 ^b
S _{H. Tail} (ft ²)	98.72	98.72	98.72
XMC (ft)	32.67	30.32	29.57

NOTES: 1 - total configuration
 2 - individual wings
 a - forward wing pair
 b - aft wing pair
 c - $\Phi = 0^\circ$
 d - $\Phi = 18^\circ$
 e - $\Phi = 45^\circ$
 f - $\Phi = 60^\circ$

Each of the variable-pivot models was evaluated for symmetrical ($\Phi_f = \Phi_r$) sweep cases of $\Phi = 0, 18, 30, 45,$ and 60 degrees, and the unsymmetrical sweep cases which were permutations of $\Phi = 30, 45,$ and 60 degrees. The unsymmetrical sweep cases will be denoted by ($\Phi_f = \Phi_r$).

Aerodynamic coupling between the wings has been linked to the stagger of the wings: the horizontal distance between the front and aft wings. The results of reference [6], which are used to interpret the results obtained here, are for two dimensional airfoils, so the stagger is measured from the leading edge of MAC_r , to the trailing edge of the MAC_f . The stagger for the equal-area models ranged from $1.64MAC$ for the no sweep case to $3.72MAC$ for the fully swept case. The split-area models had a similar range, based on an average $MAC_a = 5.13$ ft., of $1.62MAC_a$ to $3.71MAC_a$ for the unswept and fully swept cases, respectively. Reference [6] indicates that strong coupling (increasing the front wing lift and decreasing the rear wing lift significantly) occurs for stagger less than 3 and moderate coupling occurs for stagger between 3 and 10. This is the reason for XMC to be as far forward as it is relative to the wing locations.

All three models were designed with a 5% stable static margin (the pivot wing configurations were 5% stable with sweep $\Phi = 18^\circ$) at $M = 0.4$. The shift in XMC with unsymmetrical sweep is taken into account by using the wing weights listed above.

Results and Discussion

Equal-area Wing-Strake Model

The lift-curve results are shown in Figures 3a and 3b. The (0/0) case showed an increased lift-curve slope at subsonic and low supersonic speeds over the baseline case, and the curves all tended to follow the same trend of slowly decreasing as M increases. The lowest sweep (highest /R and closely coupled aerodynamically) wing pair dominates the $C_{L\alpha}$ response of the model. From Figure 3a, if the response of the low sweep configurations (0/0) and (30/30) is taken to be the trend, the (45/45) and (60/60) sweep settings require increased Mach number to converge to that trend. Figure 3b shows the effects of sweeping the alternate pair to an unsymmetric position. Sweeping the alternate to a lower sweep forces the response to the trend to converge at lower Mach number. The (30/60) and (45/30) follow the (30/30) trend very closely – although the (30/60) case is shifted slightly down due a reduction in total wing lifting area. The (45/60) case closely follows the (45/45) case. These results indicate that the lift-curve slope is very dependent on the magnitude of the largest /R and the stagger of the wings, both factors are linked together by sweep. The (60/60) case decreases very little with increasing Mach number.

The moment-curve results are shown in Figure 4. A large unstable moment-curve slope results at low supersonic speeds for two cases: a low front sweep/high rear sweep or for both wings highly swept. The first result is due to the much higher $C_{L\alpha}$ of the front wing forcing a positive couple. The second result is most likely due to a shift in the total center of pressure forward (after reference [4]), due to coupling ($ST = 3.72$) increasing the lift of the front wing (relative to the aft wing) and the mechanical forward sweep of the wing.

The combination of these results into the static margin is shown in Figure 5. The results are strongly influenced by any large changes in either $C_{L\alpha}$ or C_{ma} . The $\Phi = 45^\circ$ case exhibited a sharp increase in stability for $1.2 < M < 1.8$, and a similar pattern is followed by the (30/60) case. For this Mach number range, $C_{L\alpha}(45/45)$ is nearly constant, so the increase in stability is due to the shift of the center of the pressure of the wings aft from increasing Mach number, reducing the forward wing moment arm about XMC, reducing C_{ma} . The (30/60) case stability increase is due to a reduction in $C_{L\alpha}$ as well as the pressure shift. The least shift in static margin at higher Mach numbers occur for the (60/60) case, which is due to the almost constant lift-curve slope and the slowly changing moment-curve slope. The sweep schedule for the least shift in static margin is shown in Figure 6. The wings are initially swept to (45/30) by $M = 1.45$, and then to (60/60) by $M = 1.8$, keeping the static margin constant at 5% stable up to this point, and then increasing along the (60/60) curve. This result will be discussed later.

Split-Area Wing-Strake Model

The lift-curve slope results for the split-area wing-strake model are shown in Figure 7. The $\Phi = 0^\circ$ case showed a large improvement in $C_{L\alpha}$ over the wing-strake baseline case in both the subsonic and low supersonic regimes. The interesting result from this graph is the effect of forward wing sweep on the lift-curve slope, when the aft wing is fully swept. Comparing the (30/60), (45/60), and (60/60) cases shows that the sweep of the front wing controls $C_{L\alpha}$. As the front wings are swept forward the stagger is increased and the lifting ability of the rear wing is increased as the lifting ability and area of the front wing is decreased. So, because of the area distribution, the model's lifting ability is decreased. With both sets of wings fully swept, the lift-curve slope becomes virtually independent of Mach number.

The moment-curve slope results are shown in Figure 8. None of the curves shows a large negative gain (below the trend line) like the other models have. By sweeping the front wing

from (30/60) to (45/60) reduces the negative shift of the curve for low supersonic Mach numbers. As the forward wings are swept, the stagger is increased, which decreases the relative lifting ability of the front wing, while increasing the relative lifting ability of the rear wing. The aspect ratio of the front wing is also reduced, which further decreases C_{La} . Both of these effects induce a negative moment about XMC. The positive moment that is the result must then be because of the mechanical shift of the forward wing's aerodynamic center.

The static margin results are presented in Figure 9. The main result is that in order to control the static margin the aft wing needs to be fully swept at supersonic speeds, in order to minimize its λ/R and coupling effects and so reduce the impact it has on stability. Then the front wing can use its large lifting area to control the static margin. The sweep schedule for this case is shown in Figure 6. The relation between the front wing and the rear wing characteristics is shown here. The front wing is swept from 30 to 60 and then down to 45° as Mach number increases from 1.2 to 1.85, while the aft wing is swept to 60° before $M = 1.35$. The reason for the front wing gyrations is at low speeds and when the rear wing is at 45°, low stagger is required to maintain stability, hence the $\Phi_f = 30^\circ$. When the rear wing is initially swept to 60°, the forward wing must be fully swept in order to increase the stagger and reduce the effectiveness of the front wing to maintain stability. Then, as Mach number increases, the center of pressure shifts aft on the front wing and its sweep must be reduced to increase its effectiveness through an increased λ/R and aerodynamic coupling, and force the center of pressure to stay forward.

Comparison of the Scheduled Static Margins

The results of the applying the sweep schedules to the different wing-strake models are shown in Figure 10. The pivot wing models showed less static margin increase than the baseline model did. The pivot-wing configurations showed considerable improvement over the baseline models at the low end of the supersonic range (for $M < 2.0$), with the variable pivot wings able to maintain their 5% static margin to Mach = 1.8. The baseline model did not maintain the 5% margin above the subsonic range. The split-area model had the least center of pressure travel of all three models, with the increased front lifting surface being able to exert more control as

the center of pressure shifts aft. The equal-area wing-strake model did not have the same degree of control at higher supersonic Mach numbers.

Conclusions

A preliminary evaluation of the ability of a variable pivot wing aircraft to control the lift-curve and moment-curve slopes, and hence static margin, was presented. In comparison to a conventional highspeed aircraft layout, the variable pivot wing showed exceptional control over the static margin shift in the supersonic regime.

It was shown that the wing-strake models were able to maintain a 5% static margin up to Mach numbers of approximately 1.8, and the static margin rise after this point was minimal. The control of the static margin is a complicated function of the interaction between the aspect ratios of the wing pairs, the aerodynamic coupling between the wings, mechanical shifts in the aerodynamic centers of the wings, and reduction in wing area due to masking by the fuselage (or the symmetrical wing in the pair in the wing-only cases). The aerodynamic coupling and aspect ratio effects are linked through sweep: this study did not attempt to separate the effects, but incorporated them together into the results, as on an actual model they would be linked.

The effects of low- and high-speed control and other stability derivatives, and wave drag needs to be evaluated on the models, because these aspects were not considered in this paper. These factors will probably compromise the benefits of this design in some ways – for example, limiting the forward sweep to be within the nose shock. They should be investigated, since the design showed considerable improvement over the baseline conventional configuration in terms of control of stability at high speeds.

References

1. Housch, C. S. "Aerodynamic Characteristics of Scissor Wing Geometries". Master's Thesis, University of Missouri-Rolla, 1990.
2. Rokhsaz, K. "Scissor Wing, Patent Disclosure". Disclosure #87-UMR-023, 1986.
3. Rokhsaz, K., and Selberg, B. "Scissor Wing – An Alternative to Variable Sweep". 27th Aerospace Sciences Meeting, AIAA, 1989.
4. Selberg, B., Rokhsaz, K., and Housch, C. "Some Aerodynamic Characteristics of the Scissor Wing Configuration." SAE paper #892202, Aerospace Tech. Conf. and Exposition, 1989.
5. Tulinius, J. "Unified Subsonic, Transonic, and Supersonic NAR Vortex Lattice" North American Rockwell, TFD72-523, 1972.
6. Keith, M. W. and Selberg, B. P. "Aerodynamic Canard/Wing Parametric Analysis for General-Aviation Applications." J. Aircraft, Vol. 22, No. 5, May 1985, pp 401-485.

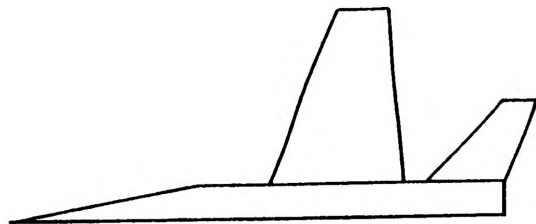


Figure 1a: Wing-strake baseline configuration

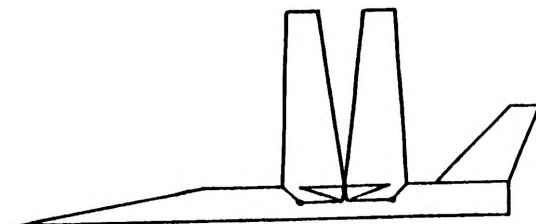


Figure 1b: Variable pivot configuration, $\phi = 0^\circ$

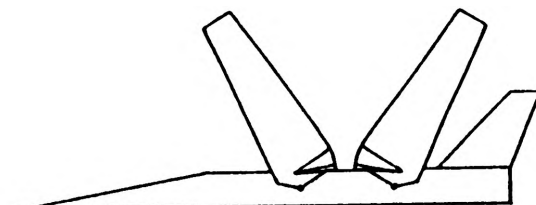


Figure 1c: Variable pivot configuration, $\phi = 30^\circ$

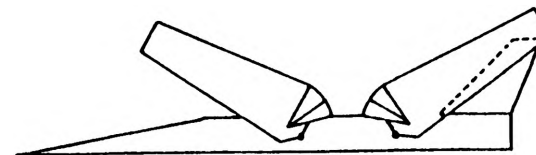


Figure 1d: Variable pivot configuration, $\phi = 60^\circ$

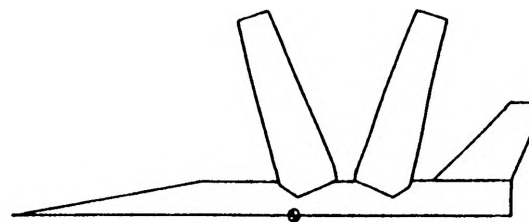


Figure 2a: Equal-area wing-strake model ($\phi = 18^\circ$)

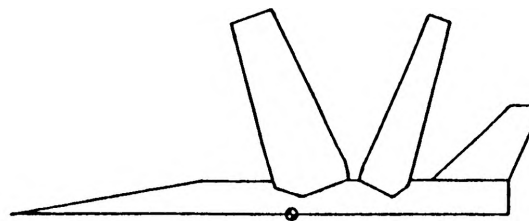


Figure 2b: Split-area wing-strake model ($\phi = 18^\circ$)

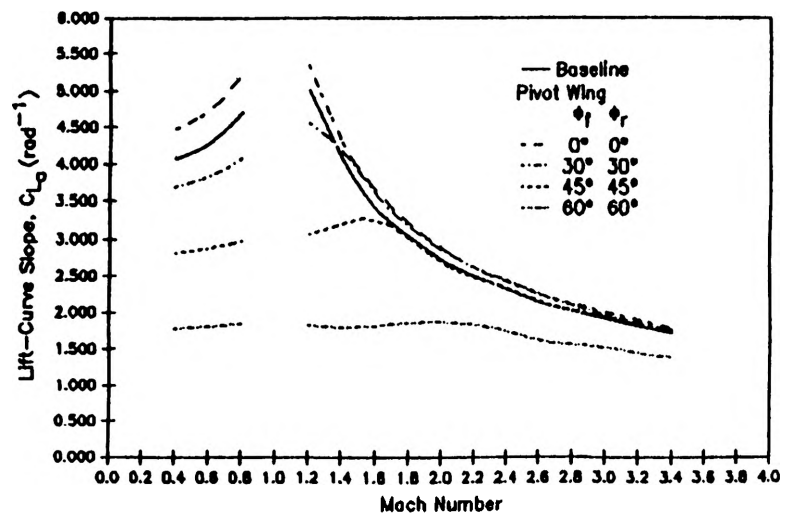


Figure 3a: Lift-curve slopes for the equal-area wing-strake model

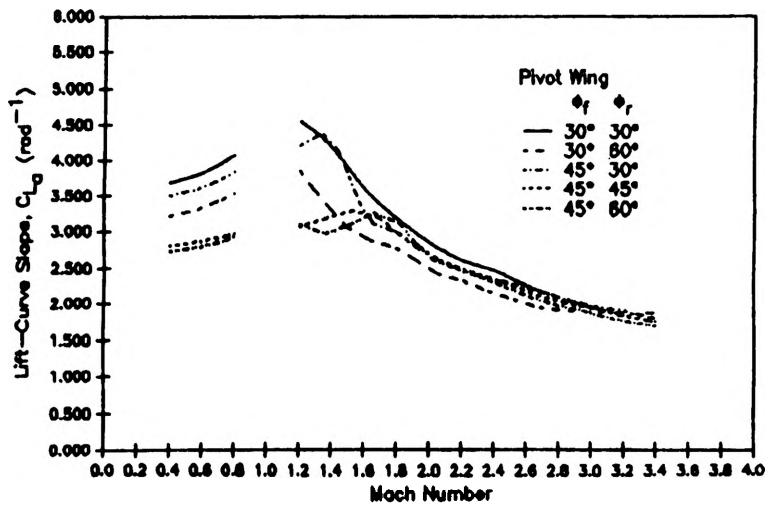


Figure 3b: Lift-curve slopes for the equal-area wing-strake model (continued)

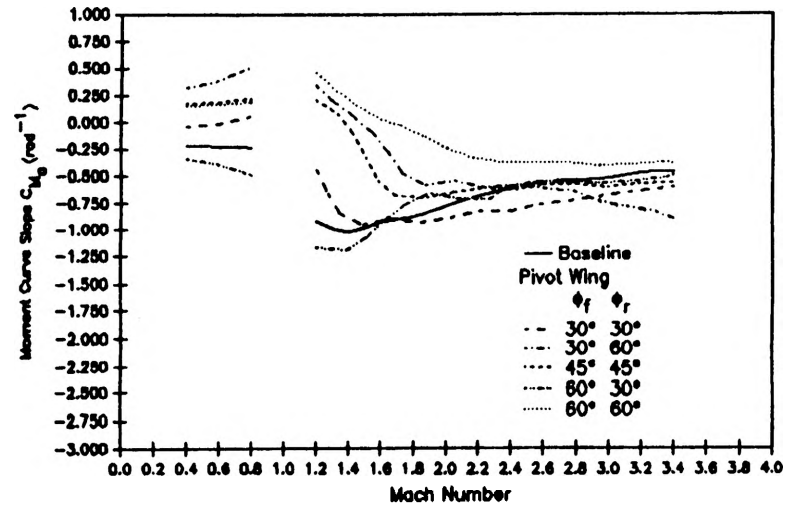


Figure 4: Moment-curve slopes for the equal-area wing-strake model

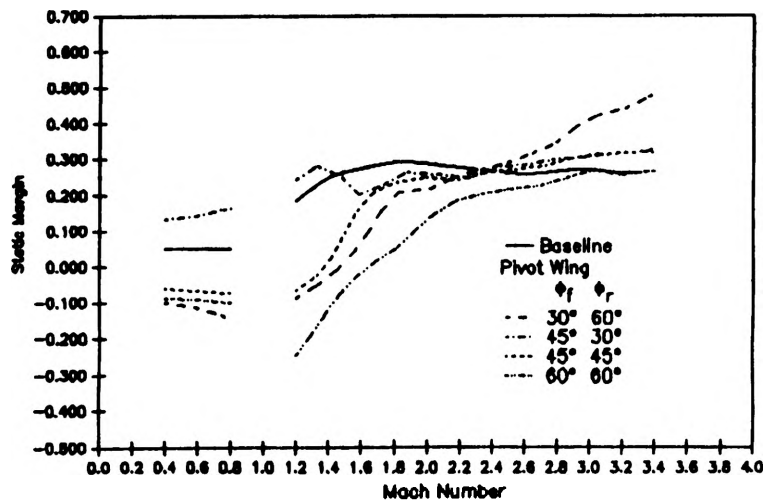


Figure 5: Static margin plots for the equal-area wing strake model

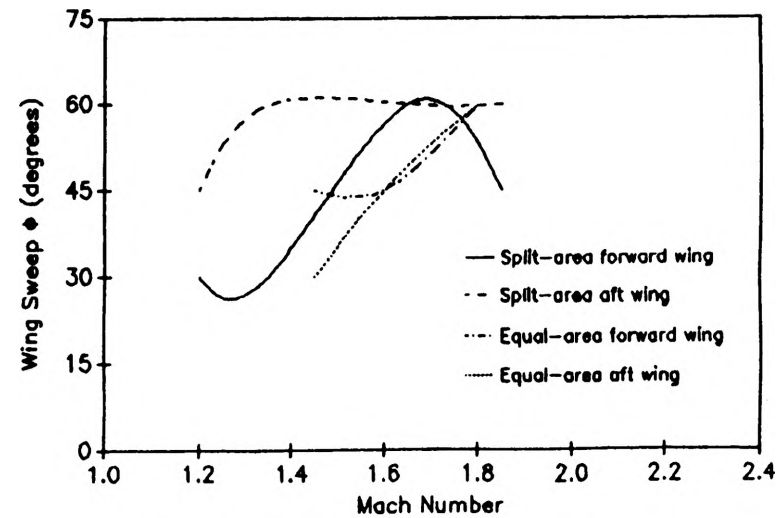


Figure 6: Sweep Schedule for the split-area and equal-area wing-strake models

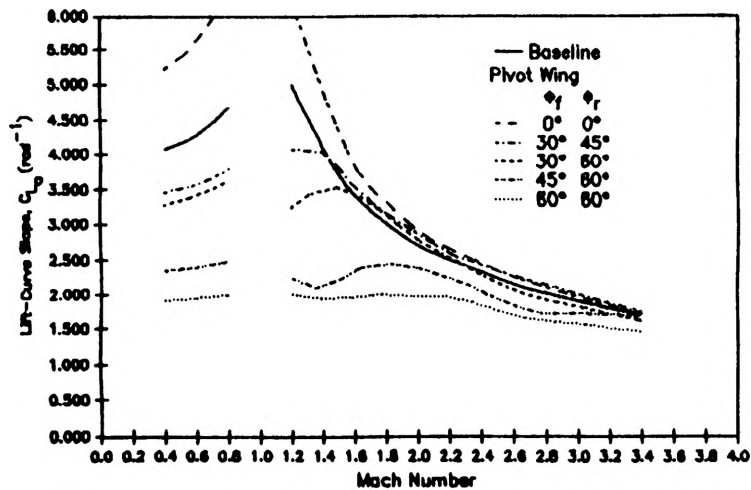


Figure 7: Lift-curve slopes for the split-area wing-strake model

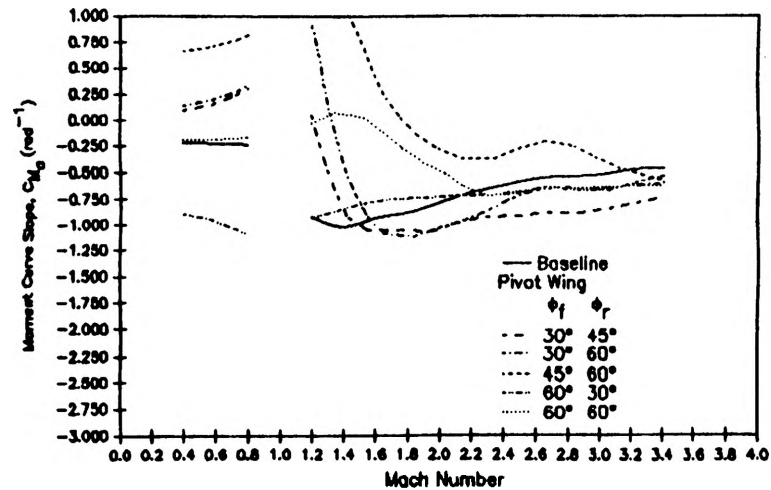


Figure 8: Moment-curve slopes for the split-area wing-strake model

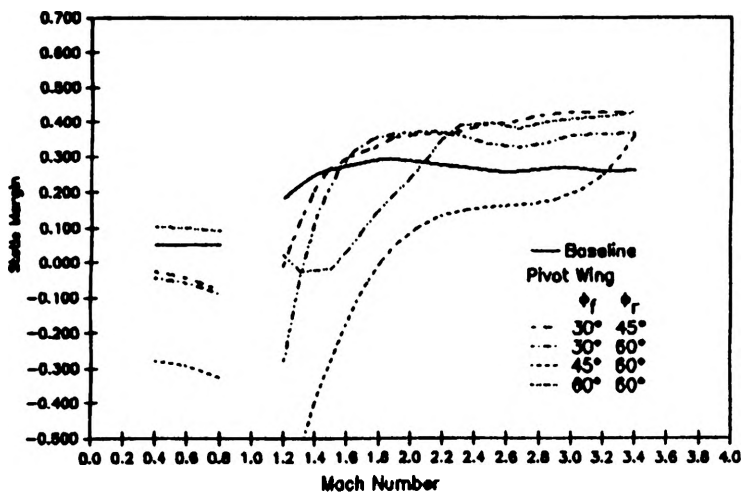


Figure 9: Static margin plots for the split-area wing-strake model

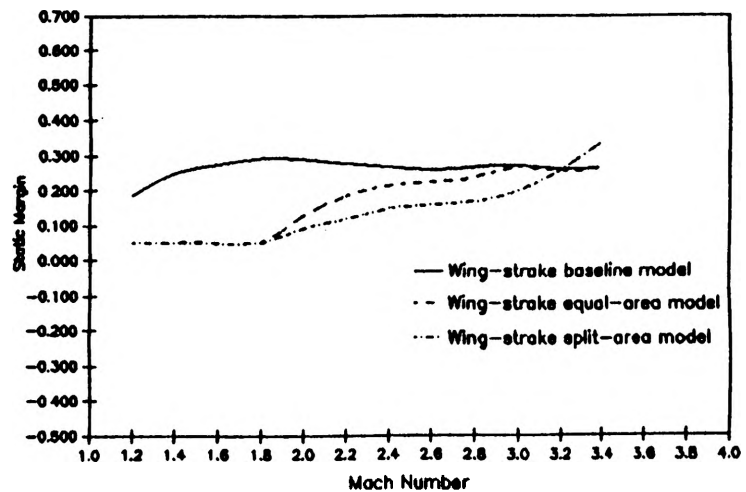


Figure 10: Static margin control comparison for the different models using the sweep schedules

BUNDLED CABLE PARAMETERS AND THEIR IMPACT ON EMI MEASUREMENT REPEATABILITY

Deanna L. Weil

ABSTRACT - This research project was 99% experimental, therefore, not many theoretical ideas will be presented. The main idea behind the project was centered around cable bundling. The effect of cable bundling using analytical measurements and data from a network analyzer was investigated.

INTRODUCTION - The FCC has stated Electro-Magnetic Interference (EMI) test procedures for cable bundling observation. The standard procedure states specifics about cable length and the location of the bundles. Cable bundles are to be "30 to 40 centimeters" in length and located near the center of the long cable. It also states they should be bundled in "serpentine fashion". Parameters such as a tightness, shape and the number of loops are not specified.

Because of this vagueness, the testing results were not repeatable. This paper delves in to find more specifics and to view the effects of various bundling.

DESCRIPTION OF SET-UP - A simplified model was constructed using a coaxial cable attached to an insulated wire. The wire acted as an antenna. It measured three meters in length. Analyzing the basic physical changes in the antenna, one can grasp the effects of the tightness and shape parameters. Although the data taken is not ideal given the experiment was not performed in a vacuum, approximations could be made. Ferrite cores were used to limit the noise; and the set-up, other than the antenna, was held constant for each measurement. These factors limited the error. The network held constant is shown in Figure 1.

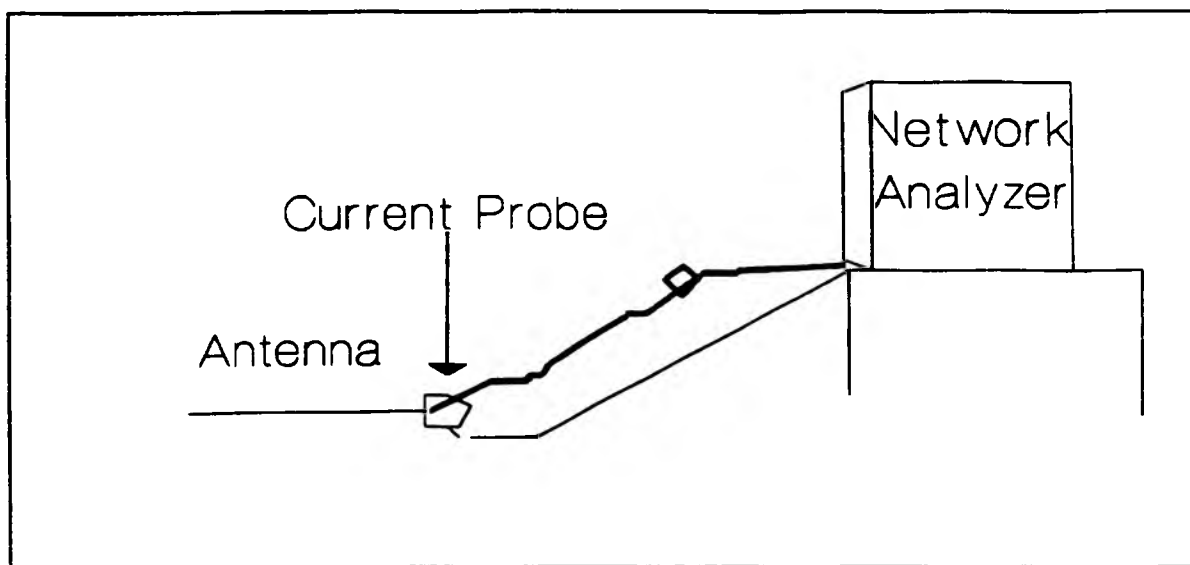


Figure 1: Simplified EMI Source Model

Originally the coaxial cable was the "bundling cable"; yet, after prolonged experimentation and observation, it became obvious this method would not work without a controlled environment. Therefore, the changing of the antenna and the formation of a transmission line were observed. This was another method by which bundling could be experimented with. Using this method, clear and precise results were found.

The resonant frequencies were sought out, using a small voltage driven by an unknown source attached to the cable and antenna, thereby creating a high current. This current was detected by a current probe located where the cable met the antenna. (See Figure 1.) The reading was displayed on the CRT as current verses frequency. Here, the peaks of the signal were the locations of the resonant frequencies. Resonant frequencies occur at frequencies where the length of the antenna (wire) is approximately one-quarter wavelength. The changes in the bundling of the antenna became very apparent using this displayed signal.

RESULTS - The following pages are the founded results of the experimentation completed by creating a transmission line and changing its length, width, and placement on the antenna. Finally, simple changes were observed in the bundles.

First, the straight antenna:

Null	Resonant Frequency Location (MHz)
1	37.001197
2	75.991098
3	120.286096
4	145.437353

Table 1

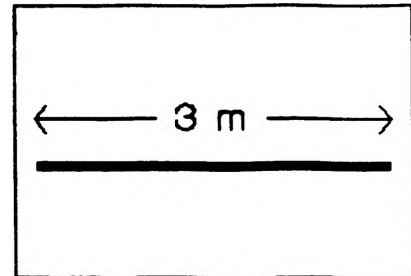


Figure 2

Refer to Graph 1. The respective signal is represented with a circled 1.

Second, the original transmission line:

Null	Resonant Frequency Location (MHz)
1	43.488164
2	68.312838
3	120.674397
4	144.775385

Table 2

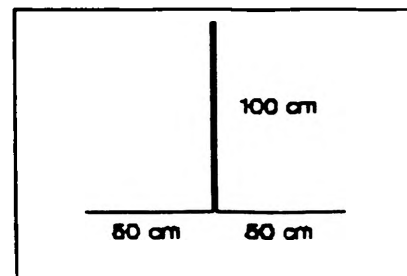


Figure 3

Refer to Graph 1. The respective signal is represented with a circled 2.

Third, a change in the transmission line's width:

Null	Resonant Frequency Location (MHz)
1	42.607466
2	72.468449
3	122.865976
4	143.286033

Table 3

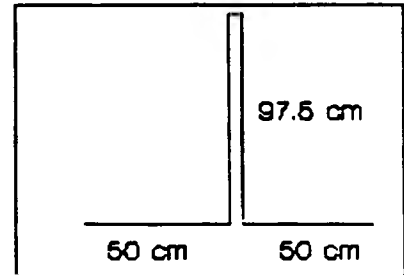


Figure 4

Refer to Graph 1. The respective signal is represented with a circled 3.

Fourth, a second change in the transmission line's width:

Null	Resonant Frequency Location (MHz)
1	39.906895
2	74.924578
3	119.848397
4	144.707873

Table 4

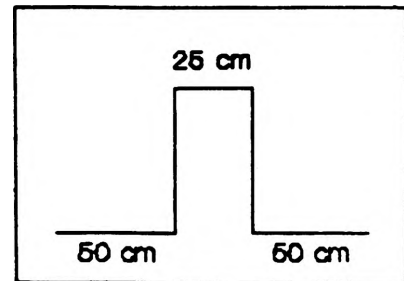


Figure 5

Refer to Graph 1. The respective signal is represented with a circled 4.

Fifth, a change in the length of the transmission line:

Null	Resonant Frequency Location (MHz)
1	43.910144
2	82.812232
3	125.272427
4	162.795557

Table 5

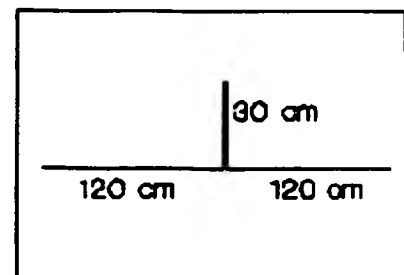


Figure 6

Refer to Graph 2. The respective signal is represented with a circled 1.

Sixth, a second change in the length of the transmission line:

Null	Resonant Frequency Location (MHz)
1	43.412667
2	76.625817
3	113.661067
4	179.274797

Table 6

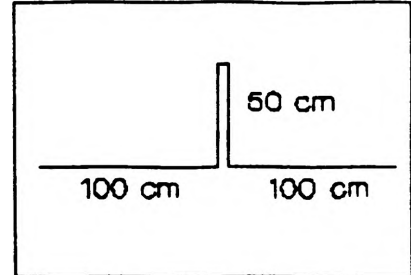


Figure 7

Refer to Graph 2. The respective signal is represented with a circled 2.

Seventh, a third change in the transmission line's length:

Null	Resonant Frequency Location (MHz)
1	43.413118
2	71.487329
3	112.224305
4	170.273529

Table 7

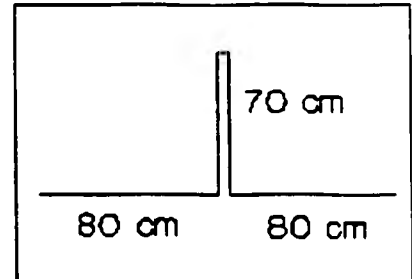


Figure 8

Refer to Graph 2. The respective signal is represented with a circled 3.

Eighth, a move in the transmission line's location:

Null	Resonant Frequency Location (MHz)
1	41.347888
2	74.955529
3	112.224305
4	146.235965

Table 8

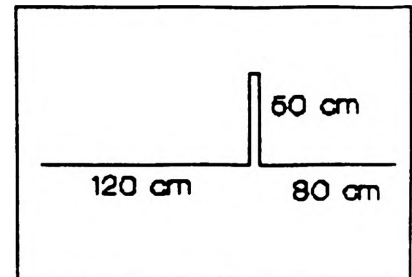


Figure 9

Refer to Graph 3. The respective signal is represented with a circled 1.

Nineth, a second move in the trasmission line's location:

Null	Resonant Frequency Location (MHz)
1	41.402628
2	85.131639
3	116.489545
4	145.932195

Table 9

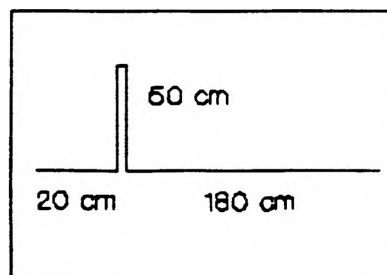


Figure 10

Refer to Graph 3. The respective signal is represented with a circled 2.

Lastly, a third move in the transmission line's location:

Null	Resonant Frequency Location (MHz)
1	41.860077
2	80.287814
3	109.111117
4	145.379895

Table 10

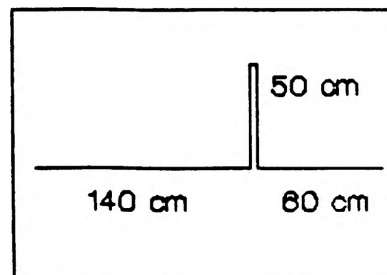


Figure 11

Refer to Graph 3. The respective signal is represented with a circled 3.

The final observation was changing the "bundles" of the transmission line. The circled 1 representation on Graph 4 is the original transmission line. The transmission line was bent. See table of resonant frequencies and figure below.

Null	Resonant Frequency Location (MHz)
1	44.267112
2	68.334523
3	120.978555
4	195.979618

Table 11

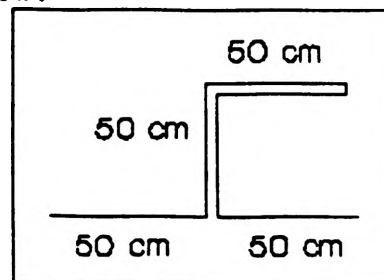


Figure 12

The second and final change in the transmission line bundle is represented on Graph 4. See the signal marked with the circled 3. The data is in the following table and the diagram is presented below.

Null	Resonant Frequency Location (MHz)
1	45.975133
2	67.753367
3	116.562962
4	198.867048

Table 12

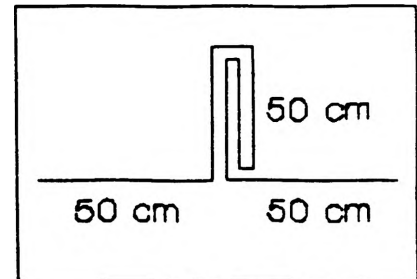
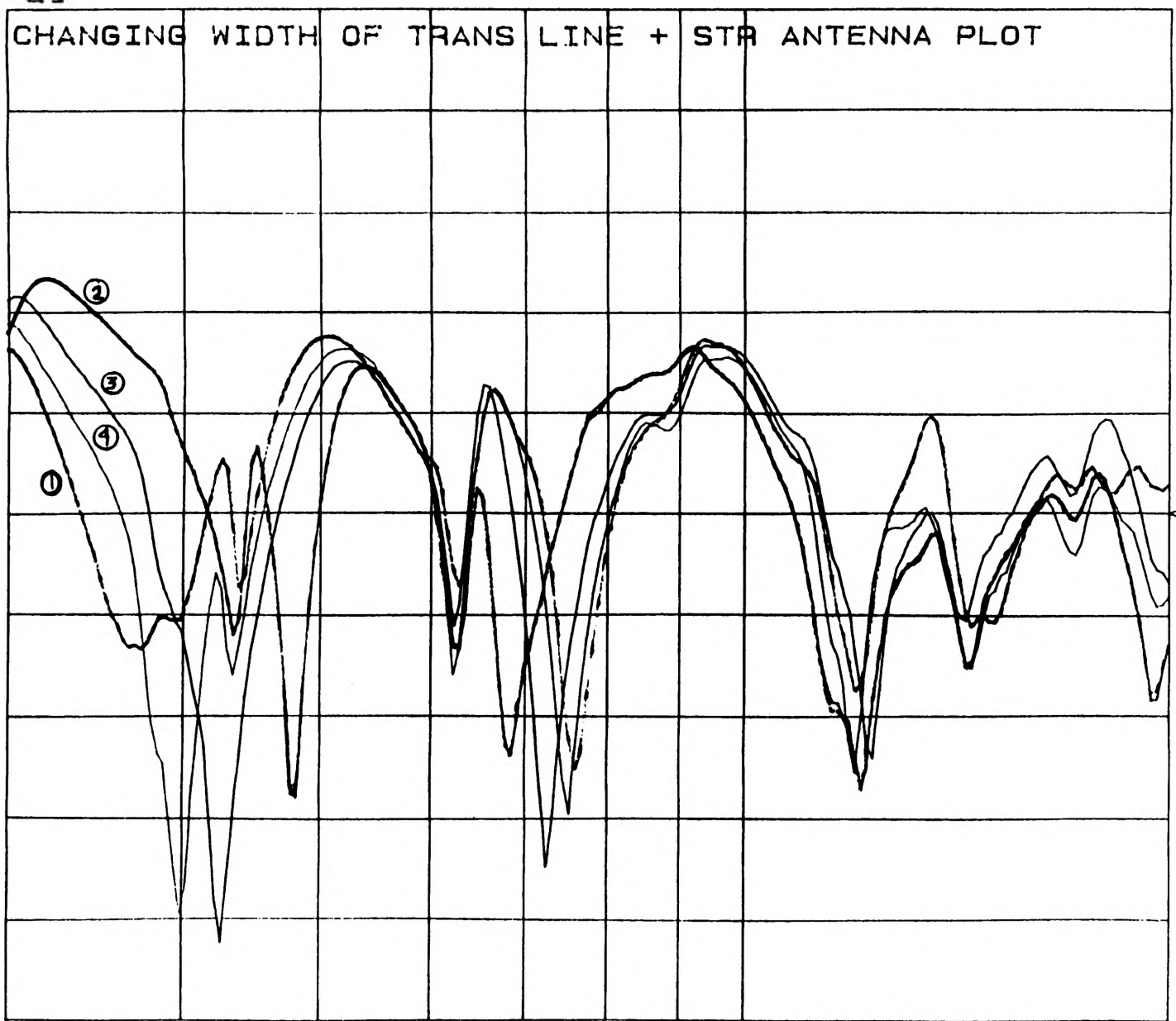


Figure 13

CONCLUSIONS - There is much consistency in the resonant frequency locations when the width of the transmission line was varied. In changing the length, again we had consistency at low frequencies but at high frequencies there were discrepancies. When the location varied, the resonant frequency locations stayed relative to the original transmission line. Bundling also gave results that did not vary much from the results of the original transmission line at low frequencies; yet, at higher frequencies the resonant frequency peaks changed dramatically. However, in the changes of the bundles observed in this paper, change is found among the resonant frequency locations from bundle to bundle; therefore justifying the need for more specific parameters when dealing with bundled cables.

Further research can be done in manipulating the computer program already established to give resonant frequencies of the transmission lines created in this project. This program was not used throughout this experiment. It must be developed further. This would provide more data for comparison and allow specific parameters to be developed and included in the FCC standards.

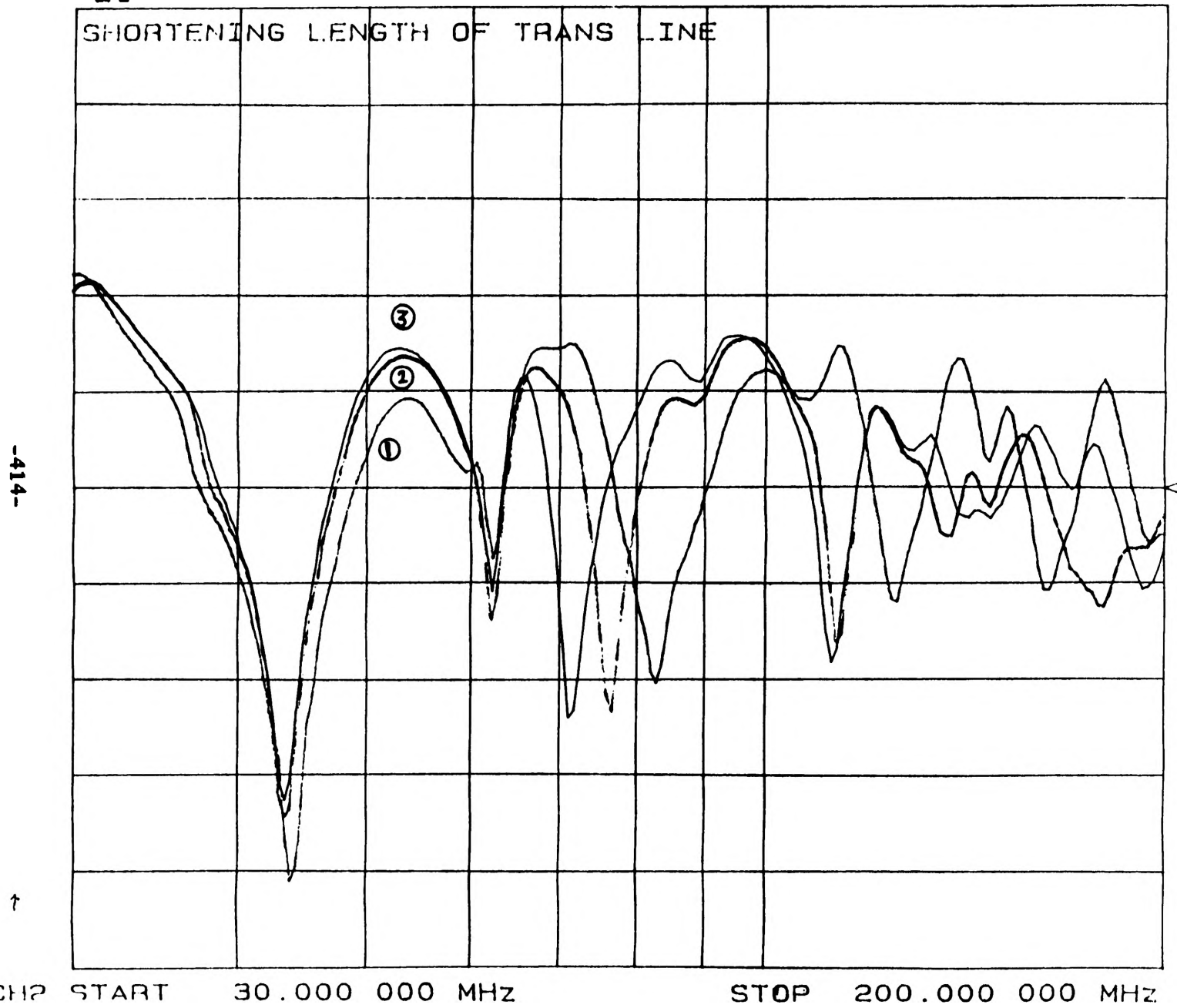
CH2 S₂₁ log MAG 5 dB/ REF -40 dB



CH2 START 30.000 000 MHz STOP 200.000 000 MHz

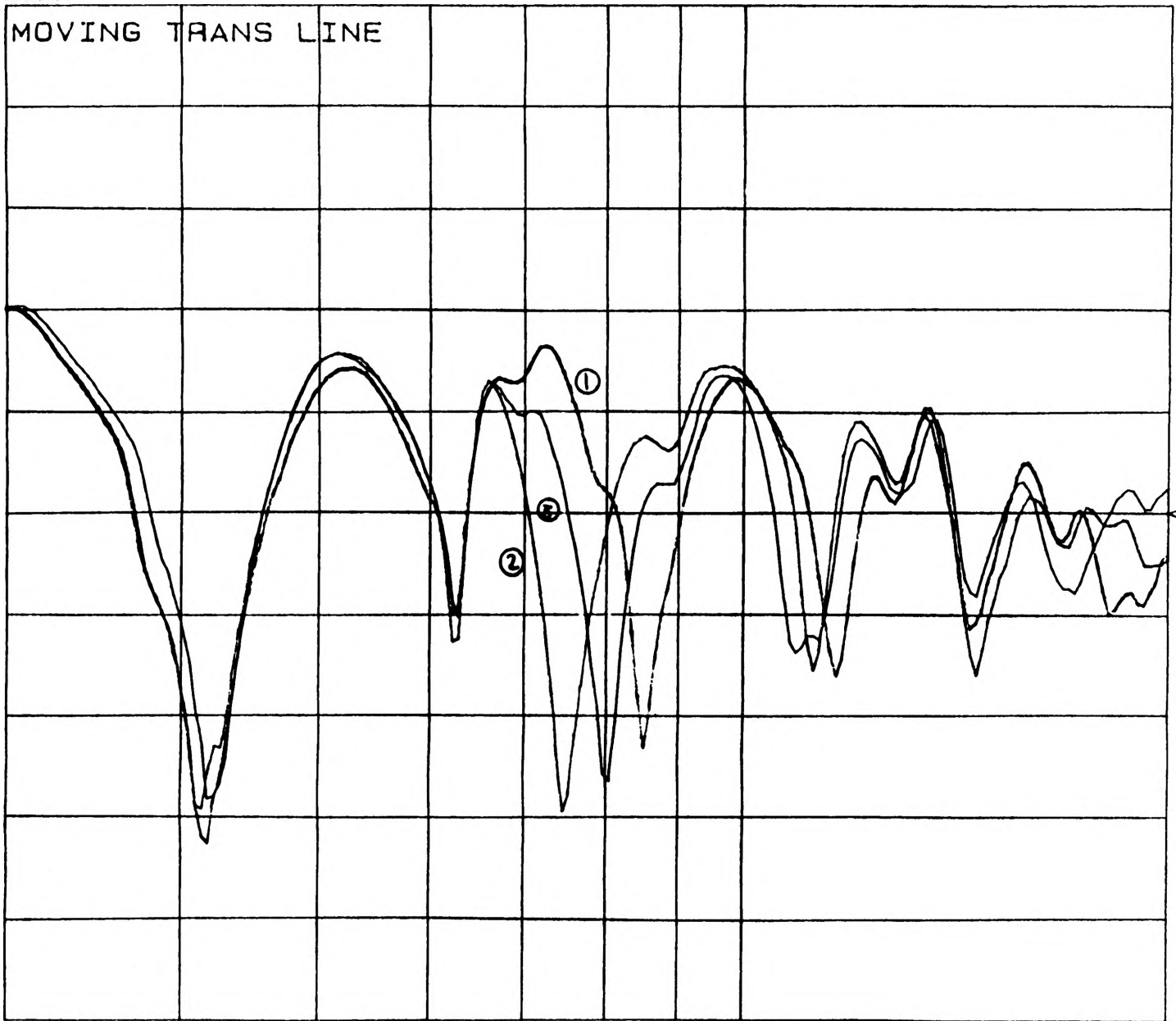
Graph 1

CH2 S₂₁ log MAG 5 dB/ REF -40 dB



Graph 2

CH2 S₂₁ log MAG 5 dB/ REF -40 dB

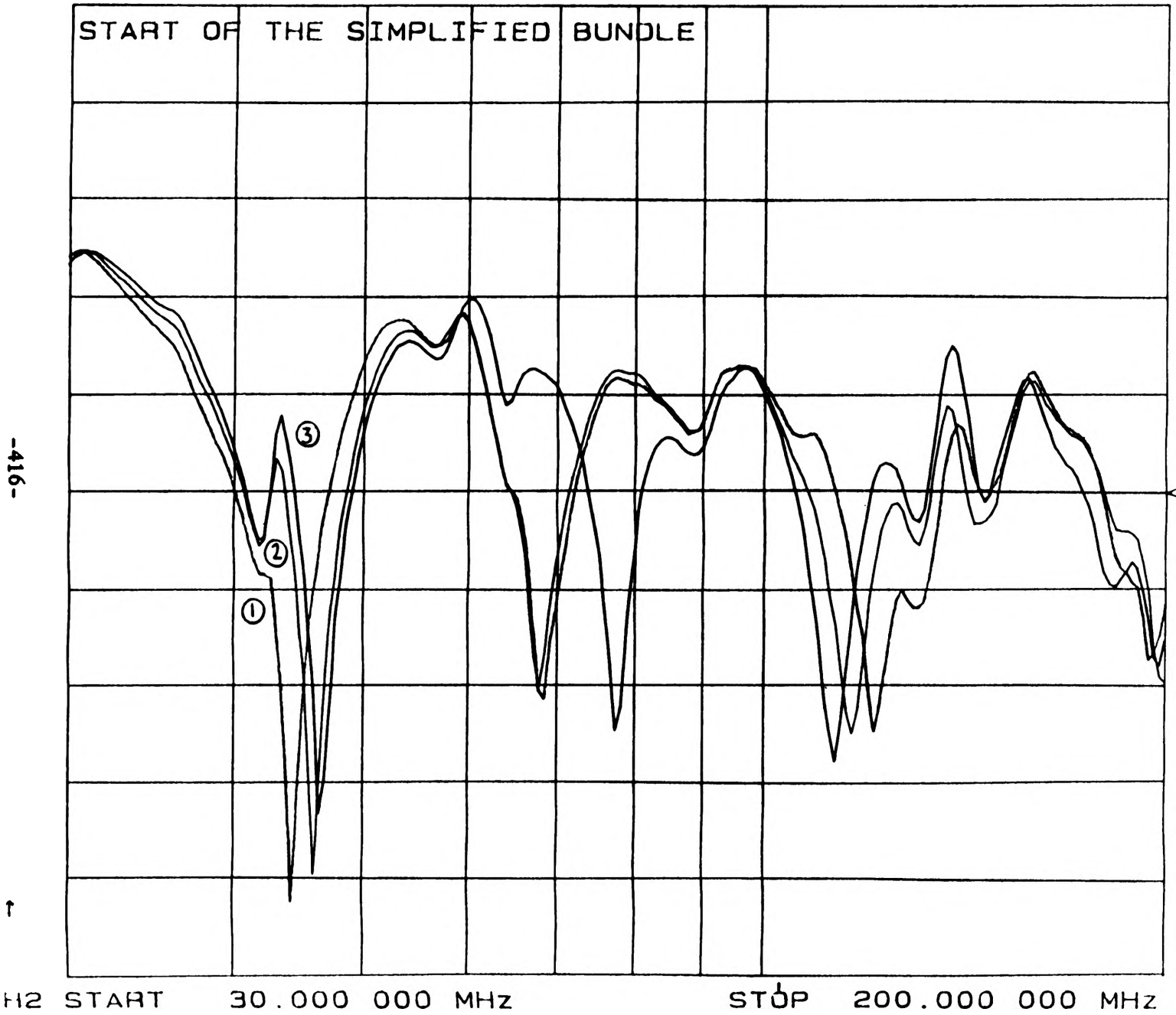


CH2 START 30.000 000 MHz

STOP 200.000 000 MHz

Graph 3

CH2 S₂₁ log MAG 5 dB/ REF -40 dB



Graph 4

A COMPUTER SIMULATION OF THE UMR REACTOR

H. Allen Wilkins

Introduction

The Opportunities for Undergraduate Research project entitled, "A Computer Simulation of the UMR Reactor" had two goals. To produce a reactor simulation to be used in creating an artificial intelligence based reactor simulation for the UMR Nuclear Reactor and to produce a means of teaching students the fundamentals of reactor operations.

The primary purpose was to create a program which would simulate all the situations one would encounter in actual reactor operation. With the simulator the artificial intelligence system could be thoroughly tested before use with actual reactor data.

This same simulator would be used as a teaching aid for students to observe events which would not be allowed to occur with the actual reactor. The ability to get actual hands-on experience with a real time simulation of the reactor would permit a student to obtain a better understanding of the initial reactor physics courses by allowing the student to actually see the subject matter put to use.

Previous Work

The starting point for the simulator was a program written by a former graduate student which represented the physical processes which occurred within the reactor. There were several features of this program which made it an excellent base from which to work.

First, the program was written in Pascal. The Turbo Pascal version of this language, as published by Borland International, has a very efficient compiler which aids the programmer in finding errors in the code. Modifications in this code would be fairly straightforward due to the self-documenting capabilities of properly written Pascal code. This language also allowed the actual screen display to appear more realistic due to the number of graphics routines available.

Second, the graduate student solved the reactor kinetics problem using Hamming's method for the solution of stiff equations. This method, when coupled with current reactor data, allows for up-to-date simulations of the reactor power response to a given transient condition.

Project Description

With the means of solving the reactor kinetics equations available, the main task was now to obtain the necessary input to enable the simulator to perform as the UMR reactor would in various situations. This would require the mating of physical equations to the reactor control systems.

In order to accomplish this, one must first understand how the reactor operates. The heart of the reactor is the core where fuel undergoes the fission process. The reactor is controlled from the control room. From there the reactor operator is able to see the current state of reactor operations with the various charts and gauges which are positioned on the control panel. Along the top of the panel is a series of multicolored lights which display the current status of all alarms. When the alarm is sounded, the light which corresponds to it will flash along with the alarm. The alarms are color coded to allow the severity of the problem to be ascertained at a glance. The alarm names on the red lights are major disturbances which

require immediate automatic response. The alarm names on the blue lights are disturbances which need attention because they may lead to worse events. The alarms which are on the yellow lights are warnings which require attention but are not of extreme significance. Beneath this alarm board there is a strip chart which gives the recent history of the reactor operation. With this the operator can detect a trend and make a correction for it. The control room also uses a series of switches to scale one of the strip charts to certain powers. These power scales are 2 watts, 20 watts, 200 watts, 2000 watts, 20 kilowatts and 200 kilowatts. The operator then judges the current power of the reactor based on a certain percentage of the given scale.

Located beneath the strip chart recorders are the reactor controls. It is with these manual controls that the operator is able to control the reactor power by raising and lowering control rods. As these rods are withdrawn, the number of fission reactions increases, which causes the power to increase. Above the controls, there is a clock style gauge for each individual rod which will display the current height of the rods. Also, there are lights used to display whether or not the rods have been removed past a certain length, or shim range.

A reactor cannot be operated safely without a number of safety features in place. These features are designed to automatically warn the operator of trouble and, in extreme cases, take steps to correct the event. There are three responses which these safety features can implement. They are, in order of least importance,

- A) **Rod Prohibits:** These relatively minor occurrences are listed on the alarm panel as the Period Less Than 30 Seconds alarm and as the Less Than 2 Counts Per Second alarm. These are both in the yellow section of the panel. The rod prohibits that are based on the current rod location are always in effect during startup so they are not considered alarming occurrences and do not set off the alarm. If they did the alarm would sound continuously during a normal startup.
- B) **Rod Rundowns:** This is a more severe problem. The blue section of the alarm panel is reserved for these problems. They are listed as the Period Less Than 15 Seconds alarm, the 120% Full Power alarm, and the 120% demand rundown.
- C) **Reactor Scrams (or rod drops):** This is an extremely severe occurrence. The alarms which have this safety response are the Period Less Than 5 Seconds alarm, the 150% Full Power alarm and the Manual Scram alarm. These alarms are located on the red areas of the alarm panel.

The alarm panel works in conjunction with these safety systems to allow the operator to understand what has happened and why.

This suggests that the simulator must include several procedures to make it perform all the safety checks and actions. The safety systems, or interlocks, which needed to be written included:

- *1 **Shim Range Regulating Rod Lock.** This prevents the regulating rod from being raised unless all three control rods are raised above the shim range (approximately 12.5 inches).
- *2 **Control Rod Lock Due to Extended Regulating Rod.** This prevents the control rods from being raised if the regulating rod is not fully inserted and at least one control rod is below shim range. This could occur if all three control rods were above shim range, allowing the regulating rod to move, and then one control rod were to be lowered below shim range.

- *3 **Manual Scram.** This is a button which will force all the control rods to drop at once.
 - *4 **150% Full Power Scram.** This will cause the rods to drop if the reactor reaches 150% of its full power which is 300 kilowatts.
 - *5 **Period Less Than 5 Seconds Scram.** This scram will automatically occur if the time it takes for the reactor power to increase by a factor of 'e', is less than 5 seconds.
- NOTE: All scrams prevent any further use of the reactor unless the scram reset button is depressed.
- *6 **120% Demand Rundown.** This causes the control rods to automatically perform a controlled descent into the reactor if the power exceeds 120% of what the current power scale is.
 - *7 **120% Full Power Rundown.** This causes the control rods to rundown into the reactor if the power ever exceeds 120% of full reactor power which amounts to 240 kilowatts.
 - *8 **Period Less than 15 Seconds Rundown.** This rundown will occur if the time it takes for the reactor power to change by a factor of e , is less than 15 seconds.
- NOTE: All rundowns require that the rundown reset button be pressed before the rods can be extended again.
- *9 **Less Than Two Counts Per Second Rod Interrupt.** This feature prevents the control rods from being withdrawn any farther unless the situation is corrected. The user is prevented from using the reactor without a neutron source thanks to this system.
 - *10 **Period Less Than 30 Seconds Rod Interrupt.** This prevents the control rods from being raised any further unless the period returns to a value greater than 30 seconds.

Another set of features which had to be installed were the Board Acknowledge and the Board Reset buttons. The Board Acknowledge button allows the alarm to be acknowledged, which silences the alarm yet leaves a light corresponding to that alarm lit above the control console. The Board Reset button clears all alarm lights and allows the alarms which were previously acknowledged to sound.

The first level safety interlocks, or rod prohibits, can be bypassed. This is done when the senior reactor operator wishes to operate the reactor under conditions which would set off a specific, low danger, safety alarm. When the safety system is bypassed, the alarm will still sound but the control rods will not be prohibited from moving further. This allows the regulating rod to be tested without the regular control rods withdrawn. It also allows for faster power changes and low source tests. Implementing the bypass procedure would be very similar to a reactor safety system failure procedure.

In order to determine how these safety features worked together, the senior reactor operators needed to be asked questions concerning the types of systems present in the reactor system. Questions concerning the order of alarm precedence were asked most frequently. This allowed the simulator to model the portions of the standard operating procedures which were based on hardware requirements.

A number of other questions dealt with how the reactor would respond if the various safety interlocks were to fail. To simulate this on the program a procedure to deactivate a given safety interlock needed to be written. This procedure would turn a particular safety system off when a particular sequence of keys was pressed.

The safety interlocks, alarms, and acknowledgements outlined above were all incorporated into the simulator with the exception of the Rod Prohibit Bypasses.

Recommendations for Future Work

The next step which needs to be implemented is a fission chamber. While the simulator works from an operational standpoint, in order for a true startup to be accomplished, the operator must have data which can only be made available from a log count meter and a linear power scale. This will require a series of measurements to be taken of the reactor fission chamber. These measurements must be taken over a short period of time since the exact counts from the fission chamber vary over the lifetime of the unit. Another area to look at would be the variance of the log power meter to take into account over or under compensation of the compensated ion chamber. A procedure to take the failure of magnetic current in the control rods could also be worked out. This would be similar to the current procedure for inducing a scram, only the reactivity would change by a smaller amount. From an operational standpoint, one could include a bridge radiation term in the readouts. This would make the inclusion of a nitrogen diffuser something worthwhile, instead of a set of lights and switches with no real purpose. The alarm board lights could also be made to fail in order to observe what the loss of one of one of the readout systems did to the ability of a student to diagnose what is happening inside.

In the future this program will be used in the evaluation of student performance under the stress of postulated accident scenarios. If some system fails while the reactor is being brought to a higher power, how will that student react? It will be necessary for these students to understand some sort of standard response to these situations. This is necessary since the real UMR reactor will never allow someone to do some of the things which can occur in the simulator.

Conclusions

In conclusion, this OURE project allowed me to gain insight into the workings of the UMR reactor safety system while also producing a program which is capable of being used in many projects. These projects can be as diverse as a room full of computers where an instructor gives students the basics of reactor operations, to a high powered computer which constantly presents solutions to current reactor problems after a set of simulation responses has been evaluated. This project will certainly aid the students as well as provide growth potential for future research efforts.

SUGGESTIONS FOR IMPROVEMENTS IN CURRENT COMPUTER IMAGE PROCESSING METHODS IN DETECTION AND QUANTIFICATION OF THE SEVERITY OF ATROPHIC RHINITIS IN PIGS

Jimmy Yu

Abstract.

This paper investigates several techniques to aid in the utilization of computer image processing methods to detect and quantify the severity of atrophic rhinitis in pigs. An algorithm for reducing the complexity of matrix multiplications from $O(n^3)$ to $O(n^{2.81})$ is explored. A one-pixel-wide edge detection method is also studied. These techniques are considered for improving the accuracy, repeatability, and speed of existing detection and quantification methods.

Introduction.

Atrophic rhinitis (AR) is a disease of swine involving the atrophy of bony structures (conchae) within the nose. AR rarely results in the death of a pig, but it can significantly decrease the pig's efficiency and rate of growth. Diagnosis of AR is usually confirmed after slaughter by making a transverse cross-section of the snout at the level of the second premolar teeth and by subjectively visually inspecting the nasal conchae.

The motivation for the use of computer image processing techniques to automatically detect and quantify Atrophic rhinitis stems from the conclusion [1] that a more objective measure of conchal atrophy in pigs will overcome problems associated with subjective evaluation even by trained observers. Subjective evaluations may produce accurate results, and are typically repeatable if performed by the same evaluator. However, subjective evaluations are labor intensive, expensive, and may be influenced by bias, fatigue, or training of the observer. Therefore, with an automated computer image processing system, a reliable, cost effective, and objective measure of AR might be possible.

Current methods used in the detection and quantification of AR in pigs do not yield satisfactory results. The correlations between the computer generated Morphometric Index (MI), a measure of AR, and the scores determined by pathologists are weak. Also, the speed of processing the images leaves much to be desired. Matrix multiplication, which is a fundamental operation in image processing, can create a huge burden on the computer system. To increase the speed of matrix multiplication of large matrices, an algorithm based on the divide and conquer methodology is studied. Strassen's algorithm allows the complexity of matrix multiplication to be reduced from $O(n^3)$ to $O(n^{2.81})$. While this does not seem much of an improvement, for large n (>100), the savings can be quite significant.

The problems encountered in previous works include the detection of edges of the images in order to threshold the image -- the grouping of certain ranges of gray levels into a single gray level to provide a sharper contrast. The problem lies with the line thinning process. A poor implementation would result in a totally different image than what was intended. The one-pixel-wide edge detection method by Shu [2] seems to offer a solution.

Strassen's algorithm.

The usual way to multiply two $n \times n$ matrices A and B , yielding the resultant matrix C , is as follows:

```
for i := 1 to n do
  for j := 1 to n do
    begin
      C[i,j] := 0;
      for k := 1 to n do
        C[i,j] := C[i,j] + A[i,k]*B[k,j];
      end;
```

where the three matrices A , B , and C are divided as:

$$\begin{bmatrix} A_{11} & A_{12} \\ A_{21} & A_{22} \end{bmatrix} \cdot \begin{bmatrix} B_{11} & B_{12} \\ B_{21} & B_{22} \end{bmatrix} = \begin{bmatrix} C_{11} & C_{12} \\ C_{21} & C_{22} \end{bmatrix}$$

A **B** **C**

This algorithm requires n^3 scalar multiplications (multiplications of single numbers) and n^3 scalar additions. Strassen's method [3] uses seven $(n/2) \times (n/2)$ matrix multiplications and eighteen $(n/2) \times (n/2)$ matrix additions and subtractions.

$$\begin{aligned} M_1 &= (A_{12} - A_{22})(B_{21} + B_{22}) \\ M_2 &= (A_{11} + A_{22})(B_{11} + B_{22}) \\ M_3 &= (A_{11} - A_{21})(B_{11} + B_{12}) \\ M_4 &= (A_{11} + A_{12})B_{22} \\ M_5 &= A_{11}(B_{12} - B_{22}) \\ M_6 &= A_{22}(B_{21} - B_{11}) \\ M_7 &= (A_{21} + A_{22})B_{11} \end{aligned}$$

$$\begin{aligned} C_{11} &= M_1 + M_2 - M_4 + M_6 \\ C_{12} &= M_4 + M_5 \\ C_{21} &= M_6 + M_7 \\ C_{22} &= M_2 - M_3 + M_5 - M_7 \end{aligned}$$

where M_i denotes the matrices and A_{rc} , B_{rc} , and C_{rc} are the values at the locations given by row, column (rc).

Performing this method recursively the seven $(n/2) \times (n/2)$ matrix multiplications gives the

recurrence equations used for solving the complexity of the algorithm:

$$\begin{array}{ll}
 T(1) = 1 & \text{single item array} \\
 T(n) = 7 T(n/2) & \text{sum of the 7 matrix multiplications each of } T(n/2) \text{ for } n \geq 2
 \end{array}$$

Solving the recurrence equation to derive the closed form expression of $T(n)$ using repeated substitution will provide a preferable expression. For the case $n = 2^k$ ($k = \log_2 7$):

$$\begin{array}{ll}
 T(2^k) = 7^1 T(2^{k-1}) & \text{substituting for } n \\
 = 7^2 T(2^{k-2}) & \text{unraveling the recurrence formula} \\
 = \dots & \\
 = 7^i T(2^{k-i}) & \text{generalizing for any } i \\
 = \dots & \\
 = 7^k T(1) & \text{terminating condition } (k = i) \\
 = 7^k * 1 & \\
 = 7^k & \log_2 n = k \log_2 2 = k \\
 = 7^{\log_2 n} &
 \end{array}$$

Therefore, by applying the identity $a^{\log_b c} = c^{\log_b a}$, the complexity is found to be $T(n) = n^{\log_2 7} = n^{2.81}$. The number of scalar additions performed is also $O(n^{2.81})$. This shows clearly that Strassen's algorithm is asymptotically more efficient than the standard algorithm. However, the additional overhead of managing the many small matrices imposed by Strassen's algorithm makes it feasible only for large n .

One-Pixel-Wide Edge Detection.

The goal of this method is the detection of spatially accurate one-pixel-wide edges within a gray-scale input image. This method first uses existing edge detectors such as the Sobel or Robert edge detectors as shown in Figure 1 to detect multi-pixel-wide edges. The Sobel and Robert edge detectors are commonly used edge detector operators in image processing. The detected edges are then thinned by a thinning edge operation.

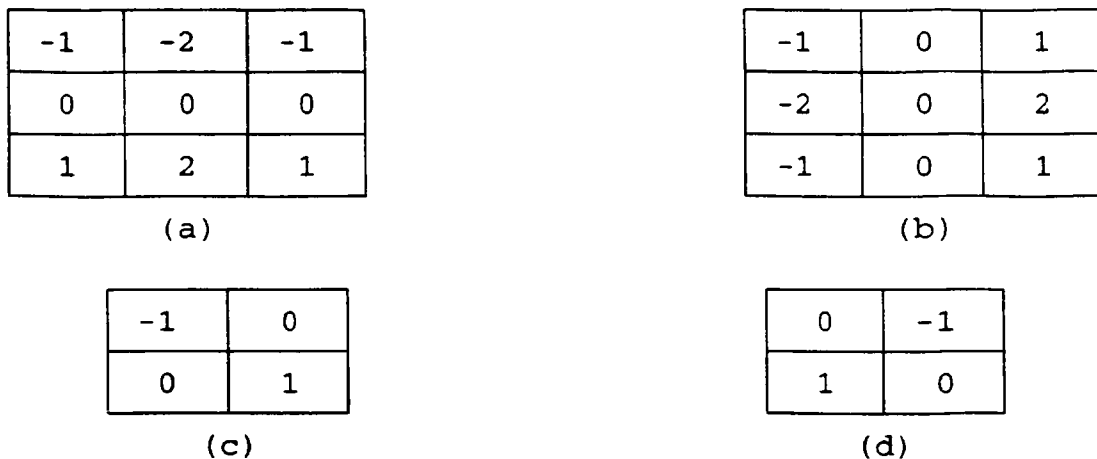


Figure 1. [2] Edge detection operators, (a), (b) Sobel edge detectors, (c), (d) Robert edge detectors.

The mathematical expressions for this operation are as follows [3]:

$$E_e(i,j) = \text{Input image for the thinning edge operation} \quad (1)$$

$$E_x(i,j) = \begin{cases} E_e(i-1,j) + E_e(i,j) + E_e(i+1,j); & \text{if } E_e(i,j) \geq E_e(i-1,j) \text{ and } E_e(i,j) \geq E_e(i+1,j) \\ 0; & \text{otherwise} \end{cases} \quad (2)$$

$$E_y(i,j) = \begin{cases} E_e(i,j-1) + E_e(i,j) + E_e(i,j+1); & \text{if } E_e(i,j) \geq E_e(i,j-1) \text{ and } E_e(i,j) \geq E_e(i,j+1) \\ 0; & \text{otherwise} \end{cases} \quad (3)$$

$$E_s(i,j) = \text{Output thinned edge image} \quad (4)$$

$$= \sqrt{E_x^2 + E_y^2}.$$

The values of $E_x(i,j)$, $E_y(i,j)$, and $E_s(i,j)$ lie in the range from 0 - 255 inclusive with any calculated value greater than 255 clipped into 255.

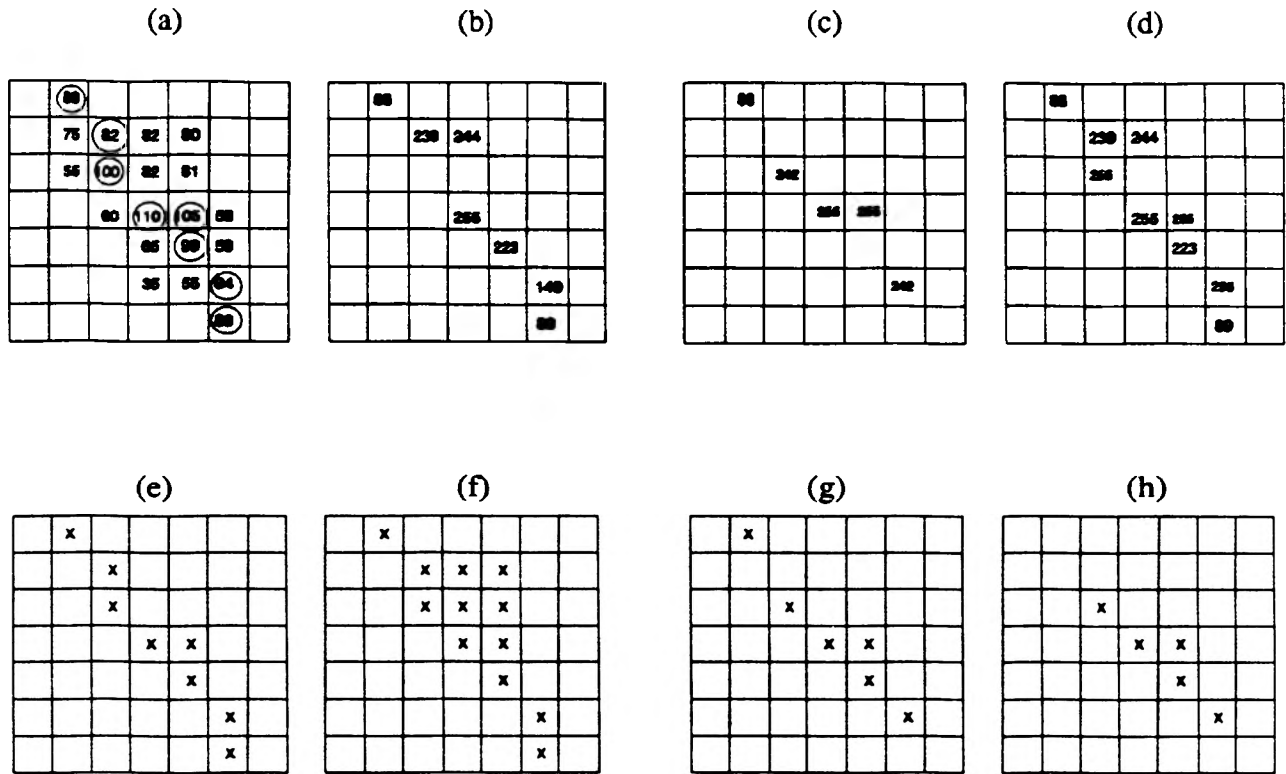


Figure 2. [2] Thinning edge processing example, (a) raw edge array $E_c(i,j)$, (b) after horizontal thinning edge operation, (c) after vertical thinning edge operation, (d) thinned edge array $E_n(i,j)$, (e) detected edge streaks by the heuristic search, (f) detected edge by thresholding Fig. 2(a) at 80, (g) detected edge by thresholding Fig. 2(a) at 85, (h) detected edge by thresholding Fig. 2(a) at 90.

Figure 2 [2] illustrates how the 2-dimensional edge thinning operation (expressed by equations (2)-(4)) processes the multi-pixel-wide edge array to reduce the edge widths. In Figure 2(a), the circled pixels in this raw edge intensity array indicate the desirable one-pixel-wide edge streak based on the human visual perception. Figure 2(b) shows the result of applying the vertical thinning edge operation (equation (2)) on the raw edge array in Figure 2(a). Figure 2(c) shows the results of the horizontal thinning edge operation (equation (3)) on Figure 2(a). Figure 2(d) shows the gray scale edges with reduced edge widths resulting from the thinning edge processing (equation (4)). After applying the heuristic search algorithm of Figure 3 which extracts optimal edge streaks whose width are exactly one-pixel wide, the detected one-pixel-wide edges of Figure 2(e) result. In Figures 2(f), (g), and (h), the detected edges by the direct thresholding of raw edges of Figure 2(a) at threshold value equal to 80, 85, and 90 respectively are shown. In these detected edges in Figures 2(e), (f), (g), and (h), the edge thinning operation followed by the heuristic search produces the best result.

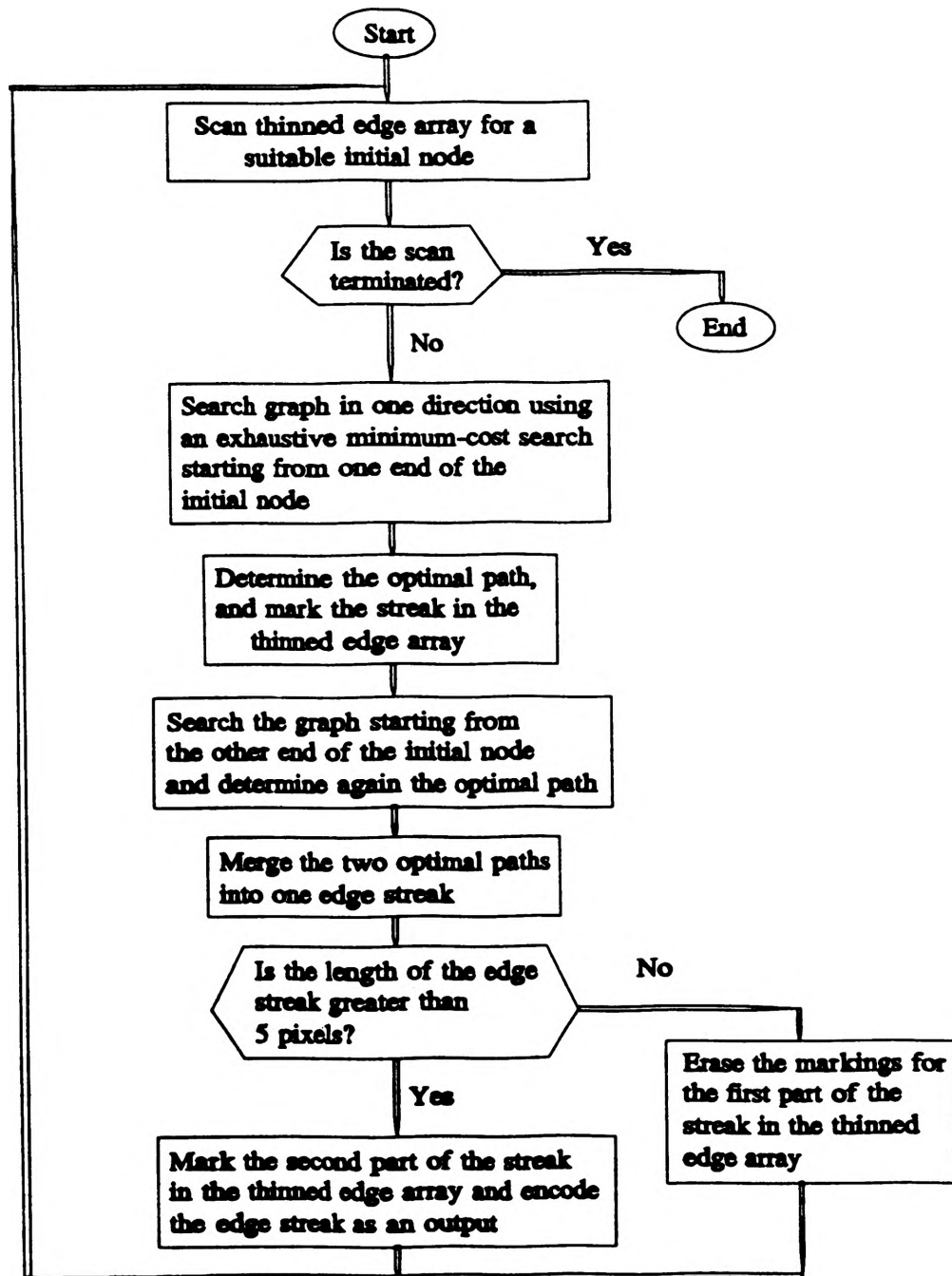


Figure 3. [2] Flow chart of the heuristic search algorithm.

Conclusions.

The utilization of computer image processing techniques in the study of atrophic rhinitis in pigs promises rewarding results. Improving upon previous techniques in the detection and quantification of images is the primary goal of this project. The major problems encountered with the old analysis system are speed, accuracy, and repeatability. The techniques described in this paper provide a new direction for further development in this area.

Strassen's algorithm provided for a faster multiplication of large matrices which is useful in the area of image processing since the images are commonly represented by matrices. It was shown that Strassen's algorithm allows the complexity of the matrix multiplication to be reduced from $O(n^3)$ to $O(n^{2.81})$. Shu's one-pixel-wide edge detection method clearly produces spatially accurate edges exactly one pixel wide. With these algorithms, the problems of speed, accuracy, and repeatability in the digital image processing system are addressed. However, due to time considerations, the implementation of these techniques was not performed.

References.

1. Cowart MT, Moss RH, et al., "Development of a digital image processing system for the diagnosis of porcine atrophic rhinitis." Proceedings of the 14th Annual Symposium on Computer Applications in Medical Care. Washington, D.C., November 4-7, 1990.
2. Shu, Joseph Shou-Pyng, "One-pixel-wide edge detection." Pattern Recognition, Vol 22, No. 6, 1989. pp. 665-673.
3. Kingston, Jeffrey H., Algorithms and Data Structures: design, correctness, analysis. Addison-Wesley, Singapore, 1990.
4. Done, J. T., "Atrophic rhinitis: Snout morphometry for quantitative assessment of conchal atrophy." The Veterinary Record, January 14, 1984.
5. Collins, M. T., "Turbinate perimeter ratio as an indicator of conchal atrophy for diagnosis of atrophic rhinitis in pigs." Am J Vet Res, Vol 50, No. 3, March 1989.
6. Hord, R. Michael, Digital Image Processing of Remotely Sensed Data. Academic Press, New York, 1982.